

THÈSE

Pour obtenir le grade de

DOCTEUR DE L'UNIVERSITÉ GRENOBLE ALPES

École doctorale : PHYS - Physique

Spécialité : Physique Subatomique et Astroparticules

Unité de recherche : Laboratoire de Physique Subatomique et Cosmologie

Mesure des corrélations photon-hadron dans les collisions Pb-Pb à 5.02 TeV avec l'expérience ALICE au LHC

Measurement of isolated photon-hadron correlations in Pb-Pb collisions at 5.02 TeV with the ALICE experiment at LHC

Présentée par :

CAROLINA ARATA

Direction de thèse :

Gustavo CONESA BALBASTRE

CHARGE DE RECHERCHE, CNRS - Délégation Alpes

Directeur de thèse

Julien FAIVRE

MAITRE DE CONFERENCES, Université Grenoble Alpes

Directeur de thèse

Rapporteurs :

Cvetan Valeriev CHESHKOV

DIRECTEUR DE RECHERCHE, CNRS Délégation Rhône Auvergne

Matthew NGUYEN

CHARGE DE RECHERCHE HDR, CNRS Délégation Ile de France Gif sur Yvette

Thèse soutenue publiquement le **8 octobre 2024**, devant le jury composé de :

Johann COLLOT,

PROFESSEUR DES UNIVERSITES, Université Grenoble Alpes

Président

Cvetan Valeriev CHESHKOV,

DIRECTEUR DE RECHERCHE, CNRS Délégation Rhône Auvergne

Rapporteur

Matthew NGUYEN,

CHARGE DE RECHERCHE HDR, CNRS Délégation Ile de France Gif sur Yvette

Rapporteur

Marie GERMAIN,

CHARGEDE DE RECHERCHE, CNRS Délégation Bretagne et Pays de Loire

Examinateuse

Pol Bernard GOSSIAUX,

PROFESSEUR, IMT Atlantique

Examinateur



Alla nonna Mari,

Acknowledgements

E alla fine è arrivato il momento di scrivere i famosi ringraziamenti.

Questi tre anni sono stati costellati da incontri inaspettati, esperienze e avventure che non avrei mai potuto immaginare all'inizio del mio dottorato. Il risultato di questa tesi è frutto di innumerevoli scambi, professionali e personali, per cui desidero ringraziare chiunque ne abbia fatto parte.

First of all, I want to sincerely thank my supervisors, Gustavo and Julien, for taking a chance on me three years ago by accepting my application and offering me a PhD position. At that time, none of us could predict where this journey would lead. Despite the challenges, unclear results, and moments of doubt, we persevered, and here we are. Thank you for the valuable discussions, the constant support, and for always believing in me.

Gustavo, thank you for always finding encouraging words, even when results were inconclusive, and for patiently answering my questions at any time of the year—holidays included! Julien, thank you for your pedagogical approach and for teaching me how to confidently defend my ideas.

Je veux remercier tout le groupe ALICE de Grenoble:

Merci, Christophe, de m'avoir écoutée et de toujours trouver un mot sympa pour égayer mes journées. Merci, Rachid, pour les shifts passés ensemble et pour les bons conseils. À vous deux, un immense merci pour votre honnêteté et pour m'avoir donné la force de continuer, même lorsque la lumière au bout du tunnel semblait lontaine.

Thank you, Ran—you were the first person I met in the office. I know I talked a lot, but you were always there to listen. I will never forget your hug that cold day of December, when we were both exhausted from our analyses!

Merci, Aimeric, tu as été un super collègue de bureau. On a beaucoup ri, on a beaucoup grimpé, et on s'est épaulés quand les codes ne marchaient pas, quand la vie semblait compliquée et quand les simulations tardaient à arriver.

Je tiens à remercier le service électronique : travailler avec vous a été un plaisir ! Un remerciement particulier à Olivier pour avoir ravivé mon intérêt pour le hardware. Merci pour ton soutien constant et pour toutes tes réponses, qu'elles concernent l'électronique ou la grammaire française!

I want to thank the FoCal group for giving me the opportunity to do my service work with you—I learned so much! A beam test can be stressful, many things can go wrong, but with a great team, every problem finds a solution. Many thanks to Tommaso, Emilie,

Norbert, Heidi, Laura, Tea and Ton.

Je tiens également à remercier le groupe MFT pour m'avoir confié des shifts on-call. Cela m'a offert une pause bienvenue dans l'écriture de ma thèse! Merci Charlotte, Yorito, et Sarah pour vos précieux conseils et votre écoute!

At this point, I want to acknowledge the many people who marked my path over these three years:

la *gang* du 3ème étage¹, Constantin et Eduardo², Thomas et Max³, Corentin et Tim⁴, Maurice⁵, Rebecca⁶, Sara⁷, Chiara⁸, Nicolò⁹, Paolo¹⁰, Chiara e Michele¹¹, Luigi¹².

Ci tengo molto a ringraziare il mio gruppo des “Italiens” de Grenoble: avete segnato il mio percorso di dottorato; potrei raccontare aneddoti su ciascuno di voi—momenti divertenti e non—ma la verità è che siete stati una vera famiglia, rendendo indimenticabili questi anni. Ringrazio chi c’è stato sempre e non mi ha mai lasciato, chi c’è stato per un po’ condividendo solo un tratto di strada con me, e chi si è rivelato una piacevole scoperta verso la fine del percorso.

Infine ringrazio la mia famiglia, che mi ha supportato e sopportato durante questi anni, con tutti i miei deliri e la mia voglia di fare sempre di più. Questa dovrebbe essere la mia ultima tesi, quindi potete finalmente stare tranquilli! Grazie per esserci sempre, anche nei momenti più complicati, quando sono complicata io, o quando stravolgo i vostri piani all’ultimo minuto.

Ringrazio la mia sorellina, che mi ha sempre ascoltato—lamentandosi un po’, è vero—ma dandomi sempre consigli preziosi. Quest’anno mi sono resa conto di quanto tu sia cresciuta! Ringrazio i miei nonni, acquisiti e non: grazie per tutti i pranzi quando tornavo da scuola o durante sessione e grazie per avermi insegnato a sognare in grande.

¹Merci pour les déjeuners ensemble et pour avoir rendu la vie au 3ème bien plus agréable!

²Merci pour toutes nos pauses café qui m’ont aidée à préparer Quark Matter!

³Merci pour toutes les séances d’escalade et le bivouac. Il nous reste la randonnée du Néron à faire!

⁴Merci pour nos sessions intensives de rédaction. Après trop de week-ends passés au labo, ce jour est enfin arrivé!

⁵Merci pour cet appel de deux heures à écouter tous mes doutes et questions et merci de m’avoir accompagné dans les joies et les difficultés de notre thèses.

⁶Grazie alla mia amica di sempre, che anche da lontano è sempre tanto vicina, che ha sempre le parole giuste e che a volte mi capisce meglio di me.

⁷Grazie alla mia fisica Fotonica preferita per i passaggi al lavoro, le cene al volo e la nostra vacanza!

⁸Grazie per la nostra coloc, i nostri discorsi sul divano e i pranzi della domenica!

⁹Ore 6:30 del mattino: “Non è che posso passare un attimo?”

¹⁰Grazie al mio coinquilino acquisito e snowboardista preferito!

¹¹Grazie perché nonostante la distanza e i tre anni trascorsi, quando ci vediamo è come se nulla fosse cambiato dai nostri pranzi a “fisica beach”!

¹²Grazie al mio compagno di masterclasses, anche nominatosi “co-relatore ad honorem”!

Abstract

Ultra-relativistic heavy-ion collisions, produced at the Large Hadron Collider (LHC) at CERN, allow to produce a state of strongly interacting matter, the quark-gluon plasma (QGP), in which quarks and gluons are deconfined.

Direct prompt photons are produced in Compton ($qg \rightarrow \gamma q$) and annihilation ($q\bar{q} \rightarrow \gamma q$) processes. Since they are colour-neutral, they do not interact strongly with the QGP and they can tag the parton emitted back-to-back to the photon at the origin of the process, which will interact strongly with the QGP losing energy. Such tagging gives a calibrated reference of its initial momentum and direction. The study of the direct prompt photon-hadron correlations gives access to the modification of the yield of the produced hadrons, originated from the parton fragmentation, and permits to understand how the lost energy of the parton, because of the presence of the QGP, is redistributed. The work presented in this manuscript is articulated around the study of the hadron from parton fragmentation modification via the measurement of the photon-hadron correlations in Pb–Pb collisions at center of mass energy of 5.02 TeV per nucleon measured with the ALICE experiment during the LHC Run 2 (years 2015 and 2018). At first, the selection of isolated photons is discussed: photons are detected with the ALICE calorimeter EMCAL and identified via calorimeter cluster shape analysis; then the purity of the candidates sample is enhanced using the isolation method. Later on, the challenges of the analysis due to the large amount of underlying event and to the presence of background photons from various sources, such as neutral meson decays and fragmentation, are illustrated.

My thesis demonstrates the feasibility of the measurement in three different centrality bins in Pb–Pb collisions and the main observation made, is the strong suppression of the hadron yield in central events compared to peripheral events and pp NLO simulations, in agreement with theoretical calculations.

The last part of the thesis is dedicated to the FoCal upgrade, a forward calorimeter to upgrade the ALICE detector during the Run 4 (2030-2032). My contribution to the electromagnetic calorimeter (Focal-E) is presented, illustrating the tests and the calibrations done and implemented. A few results obtained at the test beam campaigns at CERN are also presented.

In conclusion, this thesis illustrates the first measurement of isolated photon-hadron correlations in Pb–Pb collisions done by the ALICE Collaboration and produces an extensive benchmarking for the future data delivered by the LHC, which will help to reduce the dominant uncertainties.

Résumé

Les collisions d’ions lourds ultra-relativistes, produites au Large Hadron Collider (LHC) au CERN, permettent de produire un état de matière en forte interaction, le plasma quark-gluon (QGP), dans lequel les quarks et les gluons sont déconfinés.

Les photons prompts directs sont produits dans les processus de Compton ($qg \rightarrow \gamma q$) et d’annihilation ($q\bar{q} \rightarrow \gamma q$). Étant neutres de couleur, ils n’interagissent pas fortement avec le QGP et peuvent identifier le parton émis en sens opposé au photon à l’origine du processus, qui interagira fortement avec le QGP en perdant de l’énergie. Une telle identification fournit une référence calibrée de son impulsion et de sa direction initiales. L’étude des corrélations directes prompt photon-hadron permet d’accéder à la modification du taux de production des hadrons produits, issus de la fragmentation du parton, et permet de comprendre comment l’énergie perdue par le parton, en raison de la présence du QGP, est redistribuée.

Le travail présenté dans ce manuscrit est articulé autour de l’étude de la modification de la production des hadrons issus de la fragmentation du parton via la mesure des corrélations photon-hadron dans les collisions Pb–Pb à une énergie de centre de masse de 5.02 TeV per nucleon mesurée avec l’expérience ALICE lors du Run 2 du LHC (années 2015 et 2018). Tout d’abord, la sélection des photons isolés est discutée : les photons sont détectés avec le calorimètre EMCal d’ALICE et identifiés via une analyse de la forme des amas calorimétriques ; puis la pureté de l’échantillon des candidats est améliorée en utilisant la méthode d’isolation. Ensuite, les défis de l’analyse dus à la grande quantité d’événements sous-jacents et à la présence de photons de fond provenant de diverses sources, telles que les désintégrations de mésons neutres et la fragmentation, sont illustrés.

Ma thèse démontre la faisabilité de la mesure dans trois différentes classes de centralité dans les collisions Pb–Pb et l’observation principale faite est la forte suppression du production des hadrons dans les événements centraux par rapport aux événements périphériques et aux simulations pp NLO, en accord avec les calculs théoriques.

La dernière partie de la thèse est consacrée à la mise à niveau du FoCal, un calorimètre avant pour améliorer le détecteur ALICE lors du Run 4 (2030-2032). Ma contribution au calorimètre électromagnétique (Focal-E) est présentée, illustrant les tests et les calibrations effectués et mis en œuvre. Quelques résultats obtenus lors des campagnes de test de faisceau au CERN sont également présentés.

En conclusion, cette thèse illustre la première mesure des corrélations photon-hadron isolées dans les collisions Pb–Pb réalisée par la collaboration ALICE et produit une référence exhaustive pour les futures données fournies par le LHC, ce qui aidera à réduire les incertitudes dominantes.

Contents

1 From the Standard Model to the Quark–Gluon Plasma	10
1.1 Quantum Chromodynamics	12
1.2 Hadron-hadron collisions and the factorization theorem	15
1.2.1 Parton distribution functions	16
1.3 The Quark–Gluon Plasma	19
1.4 Heavy–ion collisions	20
1.4.1 Nuclear parton distribution functions	22
1.4.2 Key variables in heavy–ion collisions	23
1.5 Experimental Probes	28
1.5.1 Soft probes: strangeness enhancement	29
1.5.2 Soft probes: collective flow	31
1.5.3 Hard probes: quarkonium suppression and regeneration	34
1.5.4 Hard probes: high p_T particles and jets	36
1.6 Conclusions	42
2 Photons: a way to probe the QGP	44
2.1 Photon sources	44
2.1.1 Direct photons	47
2.1.2 Prompt photons	48
2.2 Isolated photons measurements	50
2.3 Conclusions	64
3 The ALICE experiment at the LHC	65
3.1 The Large Hadron Collider	65
3.2 The ALICE Detector	67
3.2.1 Inner Tracking System	68
3.2.2 Time Projection Chamber	70
3.2.3 V0 Detector	71
3.3 The ALICE data acquisition and offline framework	72
3.4 Track and vertex reconstruction	73
3.5 Centrality determination in Pb–Pb collisions	75
4 The electromagnetic calorimetry and its role in the ALICE experiment	78
4.1 Photon interaction with matter	78
4.2 The EMCal calorimeter	81
4.2.1 From the cell to the supermodule	82

4.2.2	Electronics acquisition and EMCal triggers	85
4.2.3	Calibrations: energy and time	88
4.3	The EMCal performance	89
5	How to identify and select photons using the ALICE EMCal	91
5.1	Signal detection in the calorimeter cells	91
5.1.1	Track-calorimeter cluster matching	92
5.1.2	Exotic clusters	96
5.1.3	Summary of basic cluster selections for photon measurements	97
5.2	Photon identification via cluster shape analysis	98
5.2.1	Cross-talk	103
5.3	The isolation method	104
5.4	Isolated photon purity P	111
5.4.1	The ABCD-ALICE method	111
6	Azimuthal correlation distributions of isolated photons with hadrons in Pb–Pb collisions	115
6.1	Data selection	116
6.2	Monte Carlo simulations	117
6.3	How an azimuthal correlation distribution can be defined?	120
6.3.1	Underlying event subtraction	122
6.3.2	Purity Correction	127
6.3.3	Correction of the track momentum resolution	130
6.3.4	$D(z_T)$ distributions	133
6.4	Systematics uncertainties	135
6.4.1	Mixed event and UE estimation	135
6.4.2	Purity	139
6.4.3	Variation of the Shower Shape	141
6.4.4	Track momentum resolution	143
6.4.5	Number of centrality bin used for filling the mixed event pool	144
6.4.6	Total uncertainties	145
6.5	Theoretical models	148
6.5.1	The nuclear-modification factor I_{AA}	150
6.5.2	I_{CP}	150
6.6	Results from other experiments	152
7	Future prospects for isolated photons measurements at forward rapidity with ALICE	154
7.1	FoCal calorimeter design	155
7.2	Prototype electronics and associated tools	159
7.3	HGCROC-V2 calibration procedure	160
7.3.1	Pedestals calibration	162
7.3.2	Timing measurement	164
7.3.3	Charge injection response	165
7.3.4	Calibration of the TOA and of the TOT	166
7.4	Beam test configuration and calibrations	168

7.4.1	ADC response	169
7.4.2	TOA and TOT response	172
8	Conclusions	176
A	Data run numbers	178
A.1	Data periods	178
B	Hit maps	180
C	Azimuthal correlation distributions	184
C.1	Azimuthal correlation distributions in 0-10% Pb–Pb collisions for isolated cluster narrow	184
C.2	Azimuthal correlation distributions in 10-30% Pb–Pb collisions for isolated cluster narrow	187
C.3	Azimuthal correlation distributions in 30-50% Pb–Pb collisions for isolated cluster narrow	189
C.4	Azimuthal correlation distributions in 50-90% Pb–Pb collisions for isolated cluster narrow	192
C.5	Azimuthal correlation distributions in 0-10% Pb–Pb collisions for isolated cluster wide	195
C.6	Azimuthal correlation distributions in 10-30% Pb–Pb collisions for isolated cluster wide	197
C.7	Azimuthal correlation distributions in 30-50% Pb–Pb collisions for isolated cluster wide	199
C.8	Azimuthal correlation distributions in 50-90% Pb–Pb collisions for isolated cluster wide	199
C.9	Azimuthal correlation distributions: purity correction	205
C.10	$D(z_T)$ distributions for all p_T^γ intervals	215
D	I_{CP} systematics	219
D.0.1	Mixed event and UE estimation	219
D.0.2	Purity	219
D.0.3	Variation of the Shower Shape	220
D.0.4	Number of centrality bin used for filling the mixed event pool	222
D.0.5	Total uncertainties	222
E	Synthèse en français	224
List of Figures		236
List of Tables		256
Acronyms		257
Bibliography		260

Chapter 1

From the Standard Model to the Quark–Gluon Plasma

1.1	Quantum Chromodynamics	12
1.2	Hadron-hadron collisions and the factorization theorem	15
1.2.1	Parton distribution functions	16
1.3	The Quark–Gluon Plasma	19
1.4	Heavy–ion collisions	20
1.4.1	Nuclear parton distribution functions	22
1.4.2	Key variables in heavy–ion collisions	23
1.5	Experimental Probes	28
1.5.1	Soft probes: strangeness enhancement	29
1.5.2	Soft probes: collective flow	31
1.5.3	Hard probes: quarkonium suppression and regeneration	34
1.5.4	Hard probes: high p_T particles and jets	36
1.6	Conclusions	42

The Standard Model of particle physics is a theory that allows us to study the interaction between the fundamental constituents of our universe: it describes the electromagnetic, weak, and strong interactions along with the particles that make up matter [1]. Gravity is negligible on the small scales of particle physics and is not part of this Standard Model.

The Standard Model classifies the elementary particles into three groups: **fermions**, **gauge bosons** and **scalar bosons**; this division is shown in Fig. 1.1. **Fermions** are particles of spins 1/2 from which matter is built and they can be divided into two sub-categories: **leptons** and **quarks**. They are each composed of six particles and the corresponding anti-particles. **Leptons** and **quarks** are classified based on how they interact and on the charge that they carry (electric, weak, and color charges for the electromagnetic, weak and strong interactions, respectively). They are divided into three generations, as indicated in the top of Fig. 1.1: the lightest and stable particles belong to the first generation, while second and

third generation particles decay rapidly through the weak interactions. The first generation of **leptons** is made of (e^\pm, ν_e) , followed by (μ^\pm, ν_μ) and then (τ^\pm, ν_τ) . The e^\pm, μ^\pm, τ^\pm carry positive or negative electromagnetic charge; while the neutrinos ν_e, ν_μ, ν_τ have null electromagnetic charge and interact very feebly with matter only through the weak interaction.

The three generations of **quarks** (q) are characterised by a **flavour**, that defines their nature. These generations are composed of: the lighter quarks **up** (u) and **down** (d) for the 1st generation, followed by the **charm** (c) and **strange** (s) in the 2nd generation, and then **top** (t) and **bottom** (b), also called *beauty*, for the 3rd one. Quarks are the only fermions carrying a **colour** charge, which can be red, blue or green, and they can exist in three different colour states, hence they are sensitive to the strong force, more details will be given in the next Sections. In addition, they mix into colourless composite particles, known as **hadrons**, divided into **baryons** (composed of three quarks: qqq) and **mesons** (composed of $q\bar{q}$).

Gauge vector bosons are particles of spin 1 and they are the mediators of interactions. It is possible to distinguish among:

- **photons** (γ): they are electrically neutral, hence there is no direct interaction taking place between photons. They are the carriers of electromagnetic interactions and can be exchanged between fundamental particles with electric charges.
- **W^\pm and Z** bosons: they are the carriers of the weak interactions. They can be exchanged among fermions and they allow the change of the fermions' **flavour**.
- **gluons** (g): they carry colour charge and they are the mediators of the strong interaction.

The **Higgs boson** is a **scalar boson**, discovered at the Large Hadron Collider ([LHC](#)) in 2012: it is a massive scalar field, with neither electric nor colour charge. The masses of all elementary particles are related to their coupling constants with the Higgs field: the higher, the heavier.

All these particles are reported in Fig. 1.1.

The interactions among all the particles are described by the Quantum Field Theory ([QFT](#)) [3], which provides the mathematical framework to understand and quantify the interactions found in the Standard Model. In essence, in [QFT](#) every particle is viewed as an excitation of a quantum field, which is defined over all space and time. How and if a force is mitigated is determined by the properties of the boson and the [QFT](#), that is associated with the given interaction. The masses of all elementary particles are related to their coupling constants with this field.

For the electromagnetic interaction, the corresponding theory is known as Quantum Electrodynamics ([QED](#)), while the strong interaction is described by Quantum Chromodynamics ([QCD](#)). Weak interactions are usually described within the electro-weak theory, which allows a unified description of the electromagnetic- and weak forces.

Since the focus of this Thesis is on the strong force in the next section we will concentrate on [QCD](#).

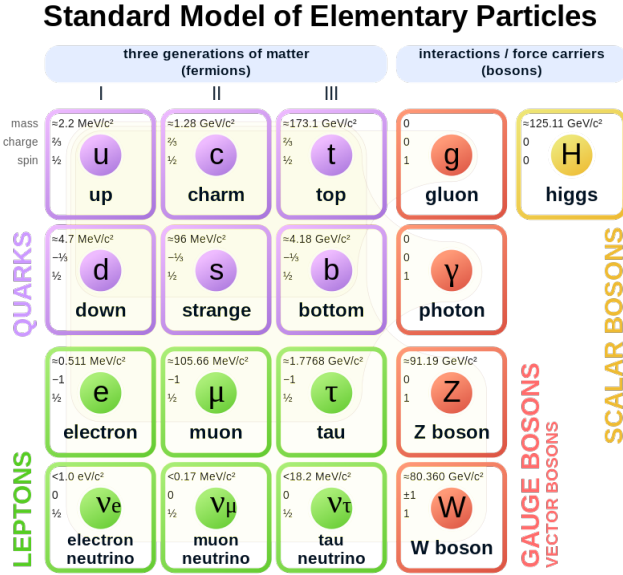


Figure 1.1: The elementary particles of the Standard Model [2].

1.1 Quantum Chromodynamics

The strong force is responsible for holding the protons and neutrons of a nucleus together and governs the internal structure and interactions of hadrons. Hadrons make up most of the visible matter in the universe and they are described as combinations of fundamental constituents: quarks and gluons [1]. The strong interaction, described with QCD, is a non-abelian (non-commuting) quantum field theory, invariant under SU(3) Lie's group. The colour charge, forming the fundamental representation of a SU(3) symmetry group, is made of three primary colours: red, green, and blue (R, G, B), and the respective anticolours: ($\bar{R}, \bar{G}, \bar{B}$). This quantum variable is deemed necessary after the formation of the quark model in order to respect Pauli's exclusion principle¹, which would have been violated while implementing the quark scheme for the Δ^{++} baryon: $\Delta^{++} = uuu$, with each u quark having the same spin of $1/2$. Thus, the colour charge allows to re-write Δ^{++} wavefunction as $u_R u_G u_B$, preventing the violation of Pauli's exclusion principle.

The interaction between colour charges is mediated by eight gluons [1], forming a SU(3) octet, as follows:

$$R\bar{G}, R\bar{B}, G\bar{R}, G\bar{B}, B\bar{R}, B\bar{G}, \frac{1}{\sqrt{2}}(R\bar{R} - G\bar{G}), \frac{1}{\sqrt{6}}(R\bar{R} + G\bar{G} - 2B\bar{B}). \quad (1.1)$$

Gluons, being coloured, can interact with each other and can couple to other objects carrying a non-zero colour charge, such as quarks. However, no free quarks or gluons have been observed so far: the colour is confined to the hadrons. The absence of “free” colour charged particle states is referred to as colour confinement [4].

¹The Pauli exclusion principle states that two or more identical particles with half-integer spins (i.e. fermions) cannot simultaneously occupy the same quantum state within a system that obeys the laws of quantum mechanics.

1.1. Quantum Chromodynamics

The QCD Lagrangian describes mathematically the strong interaction taking place between quarks and gluons and it can be written as:

$$\mathcal{L}_{QCD} = \sum_{q=1}^{N_f} \bar{\psi}_{q,a} (i\gamma^\mu \delta_{\mu b} - g\gamma^\mu t_{ab}^C A_\mu^C - m_q \partial_{ab}) \psi_{q,b} - \frac{1}{4} G_{\mu\nu}^C G^{C,\mu\nu}, \quad (1.2)$$

where $\psi_{q,a}$ is the quark fields with flavour q , with the colour-index $a \in \{R, G, B\}$ and with a mass m_q . The quantity g is a free parameter, defined as the QCD “coupling constant”, and it quantifies the interaction strength between the different QCD fields. The γ^μ are the Dirac matrices, the t_{ab}^C are 3×3 matrices which are the generators of the SU(3) group, and the A_μ^C represent gluon fields (with C running from 1 to 8, for each possible colour configuration). The indices μ and ν are spacetime indices that run over the four dimensions of spacetime. They are used to indicate the components of four vectors and tensors in the theory. The quantity $G_{\mu\nu}^C$ is the gluon field strength tensor and is constructed as:

$$G_{\mu\nu}^A(x) = \partial_\mu A_\nu^A(x) - \partial_\nu A_\mu^A(x) - g f_{abc} A_\mu^B(x) A_\nu^C(x), \quad (1.3)$$

where f_{abc} is the constant structure and it is different than zero because the elements of the group do not commute. The gluon field strength tensor ensures invariance with respect to SU(3) colour symmetry for QCD.

The Feynman diagrams, describing the interaction between quarks and gluons and corresponding to each term in the Lagrangian which involves the coupling parameter g , are reported in Fig. 1.2. The $g(\bar{\psi}\gamma^\mu A_\mu\psi)$ term from Eq. (1.2) describes the interaction between a quark, an anti-quark and a gluon field (Fig. 1.2–left). The $g(f A_\mu A_\nu A^\mu A^\nu)$ terms describe the interaction between three gluon fields (Fig. 1.2–middle). Finally, the $g^2(f^2 \partial_\mu A_\nu A^\mu A^\nu)$ term describes the interaction between four gluons (Fig. 1.2–right). From these last two terms, we see that gluons interact with other gluons due to the non-abelian nature of QCD. The

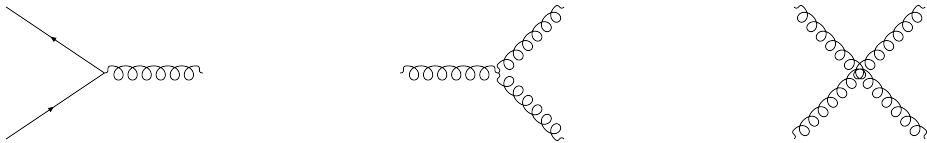


Figure 1.2: QCD vertices [5].

presence of the gluon-gluon self-interaction makes QCD very different from QED and leads to important implications, in particular regarding the coupling constant g , that is usually indicated via $\alpha_s = g^2(Q^2)/4\pi$. The strength of the interaction depends on the probed scale, that is the transferred momentum Q^2 : at short distances (or large momentum exchange), the strength of the interaction will be different than at large distances (or small momentum exchange). This scale dependence is very pronounced in QCD and can be studied by looking at the dependence of α_s on Q^2 [6], which permits to understand the characteristics of the strong interaction.

The evolution of α_s with the squared transferred momentum Q^2 can be described at leading order (LO) by:

$$\alpha_s(Q^2) = \frac{g^2}{4\pi} = \frac{4\pi N_C}{(11N_C - 2N_f)\ln(Q^2/\Lambda_{QCD}^2)} \quad (1.4)$$

where N_C is the number of colour degrees of freedom ($N_C = 3$), N_f is the number of flavours taken into account in the theory ($N_f = 6$) and Λ_{QCD}^2 is the characteristic energy scale of

QCD ($\Lambda_{QCD}^2 \sim 200$ MeV). The $\alpha_s(Q^2)$ decreases with increasing transferred momentum as

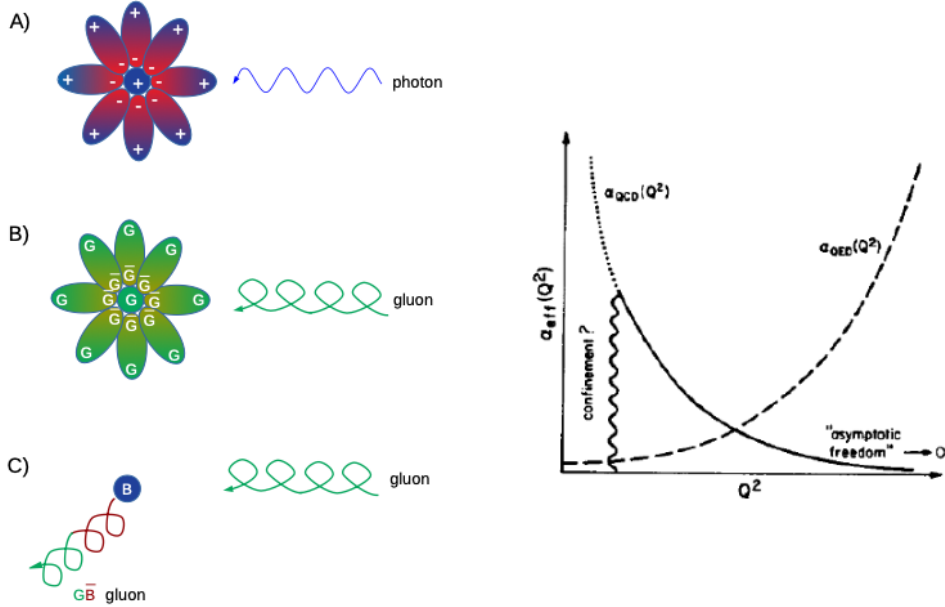


Figure 1.3: Left: (a) Illustration of how vacuum polarization in QED shields a bare charge. (b) is the same as (a) but for a QCD charge. (c) shows how in QCD a charge can radiate away its colour via gluon radiation, adapted from [7]. Right: Coupling constants behaviour of the QED and QCD as a function of Q^2 [7].

shown in Fig. 1.3-right, a direct consequence of the fact is that the $(11N_C - 2N_f)$ at the denominator of Eq. (1.4) is positive. The drastic change of α_s as a function of Q^2 is commonly referred to as “running of α_s ” and its decrease for large Q^2 is known as **asymptotic freedom** [8, 9]. This dependence is related to the renormalisation process, typical of every perturbative quantum field theory, used to remove divergences.

The coupling parameter of QED (α_{QED}) evolves oppositely and this can be seen in Fig. 1.3-right: at high Q^2 , $\alpha_{QED}(Q^2)$ becomes infinite; while for low Q^2 , it is small $\alpha_{QED}(m_e^2) \sim 1/137$, where $m_e^2 = 511$ keV is the electron mass.

It is possible to explain the different behaviour between QCD and QED using the left panel of Fig. 1.3. A virtual photon is characterised by the virtuality Q^2 , if it is too small the virtual photon cannot interact with the point charge because it is shielded by the vacuum polarization, but if Q^2 is sufficiently high, the photon can overcome the shielding. In QCD the situation is exactly the opposite because the gluons can interact with themselves. Quark-anti-quark vacuum polarization shields the colour charge as in QED. However, since the source can radiate colour, as shown in Fig. 1.3 (c), the colour is no longer located at a definite place in space. It is spread out due to gluon emission and absorption. If the Q^2 of the gluon probe increases, the spatial distances become smaller and smaller and it becomes less likely to find the “bare” colour (green in Fig. 1.3 (b)). This effect is known as “anti-screening” and is due to the non-abelian nature of QCD [7]. Considering the Eq. (1.3), as long as $11N_C > 2N_f$, the anti-screening prevails in comparison to the screening property.

Figure 1.4 reports a summary of experimental findings of the scale dependence of α_s as a function of Q [9, 10]. The different experimental techniques to determine the α_s are

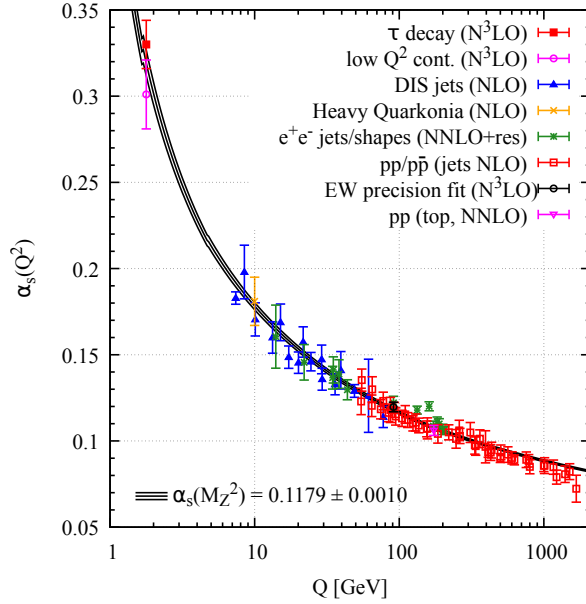


Figure 1.4: Summary of measurements of $\alpha_s(Q^2)$ as a function of the respective energy scale Q . The acronyms in the brackets specify the order used in perturbative QCD calculations that went into the extraction of α_s [10].

indicated in the legend: they differ in the precision and the Q^2 scale probed, allowing them to cover a wide momentum range. The running coupling constant α_s is not a measurable observable, but it can be extracted from physical quantities using calculations made by the perturbative QCD (pQCD).

1.2 Hadron-hadron collisions and the factorization theorem

Hadron-hadron colliders, such as the LHC (more details will be presented in Sect. 1.4 and in Chapter 3), enable the exploration of particle physics at energy scales far beyond the reach of circular e^+e^- colliders. In addition, because hadron-hadron collisions involve quarks and gluons carrying color charge, they provide an excellent platform for testing pQCD. However, theoretically modeling these collisions and making accurate predictions for particle production is challenging. As already said, hadrons are composite particles with a complex and time-dependent structure, where valence quarks are surrounded by dynamic clouds of partons that continuously evolve due to the creation of virtual $q\bar{q}$ pairs and the emission or absorption of gluons [11]. The complex structure within a proton is sketched, as an example, in Fig. 1.5.

Perturbative QCD can only be applied to the scattering of quasi-free partons with sufficiently large momentum transfers, Q . However, these conditions are not met for the initial and final states of collisions, where partons are confined within hadrons. As a result, calculating cross-sections for QCD processes in hadron-hadron collisions is complex, since not all aspects of the interaction can be described by pQCD alone. To address this, the *factorization theorem* is introduced, which allows the cross-section to be expressed as a convolution of perturbatively calculable hard parton-parton scatterings and process-independent descriptions of the non-perturbative regimes in the initial and final states. Because hard scatterings occur on a much shorter timescale than the processes in the initial and final states, the different

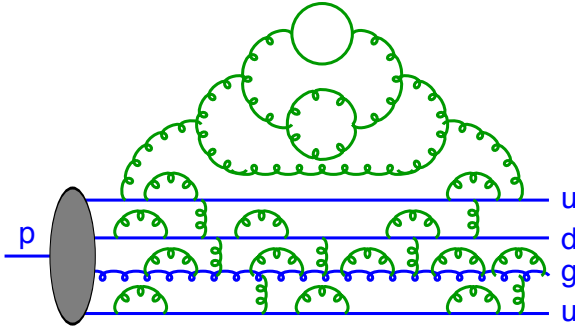


Figure 1.5: [11].

regimes can be treated independently. The factorization theorem remains valid up to corrections of order $O(\Lambda_{\text{QCD}}^2/Q^2)$. The nature of such a factorization and the objects involved are exemplified in the cross-section $\sigma^{A+B \rightarrow h+X}$ of a process of two colliding nucleons A and B which produce a hadron h :

$$d\sigma^{A+B \rightarrow h+X} = f_a(x_1, Q^2) f_b(x_2, Q^2) \bigotimes d\sigma^{ab \rightarrow c+X}(x_1, x_2) \bigotimes D_{c \rightarrow h}(z, Q^2), \quad (1.5)$$

where:

- $f_a(x_1, Q^2)$ and $f_b(x_2, Q^2)$ are the Parton Distribution Functions (PDFs), that indicate the probability of finding a parton of flavour a or b inside the hadron A or B with a momentum fraction $x_a = p_a/p_p$ ($x_b = p_b/p_p$). The PDFs describe the initial state of the interaction. They cannot be calculated perturbatively and need to be constrained by fits to data.
- $d\sigma^{ab \rightarrow c+X}(x_1, x_2)$ is the production cross section of the parton c , estimated using the pQCD at a given order in α_s
- $D_{c \rightarrow h}(z, Q^2)$ is the fragmentation function (FF), that represents the probability that the parton c fragments into a final state hadron h with a momentum fraction $z = p_h/p_c$. Like the PDF, the fragmentation function cannot be calculated a priori, and requires input from experimental data. The fragmentation function is associated with the hadronization process in the final-state.

1.2.1 Parton distribution functions

Parton distribution functions describe the probability density of finding a specific parton a within a nucleon or nucleus. Specifically, a PDF represents the density of partons at a given momentum fraction x , integrated over all transverse momenta up to an arbitrary factorization scale, which is often chosen to match the momentum transfer Q of the scattering process [12]. PDFs are extracted from global fits to experimental data, while their evolution with respect to Q is governed by pQCD through evolution equations such as DGLAP [13] and BFKL [14]. Once a PDF is constrained in a particular region of x and Q , these evolution equations allow for its extrapolation to other regions of phase space. Precise knowledge of parton distribution functions is essential, as uncertainties in the PDFs propagate into the theoretical predictions for physical observables, impacting a wide range of measurements conducted at the LHC. Beyond their role in measurements, PDFs also encapsulate our understanding of

the substructure of protons and neutrons. The ongoing effort to constrain PDFs across a broad phase space in x and Q is directly tied to probing the proton in various regimes, allowing us to test our understanding of QCD evolution across scales spanning several orders of magnitude.

A PDF is typically modelled using a parametrization for each parton species that adheres to fundamental theoretical constraints, such as energy conservation and the positivity of hadronic observables. These parametrizations involve several adjustable parameters that must be fine-tuned to best align with the available experimental data. The region of x and Q^2 in which the PDF is constrained by data, as well as the sensitivity to various parton species (e.g., valence quarks, sea quarks, and gluons), depends on the specific physical process under investigation. Most experimental data are derived from Deep Inelastic Scattering (DIS) measurements, where quark densities are directly probed by scattering leptons off nucleons via the exchange of a virtual photon, W , or Z boson. Figure 1.6 shows the NNPDF4.0 NNLO proton PDF as a function of x for different parton species, evaluated at $Q = 3.2$ GeV and $Q = 100$ GeV [15].

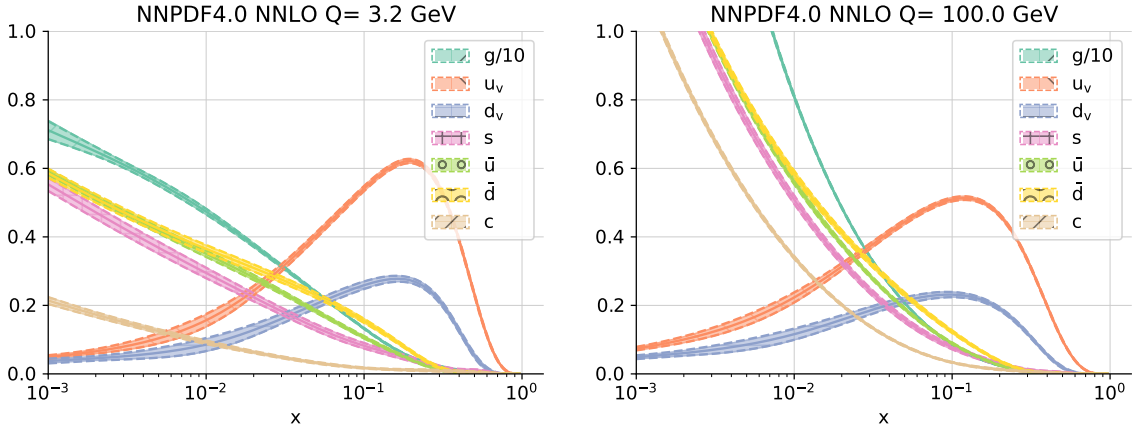


Figure 1.6: NNPDF4.0 NNLO proton PDF as a function of momentum fraction x , evaluated at two different scales $Q = 3.2$ GeV (left) and $Q = 100$ GeV (right). Each colour represents the PDF of a different parton species, as indicated in the legend [15].

The complex substructure of the proton is highlighted: the up and down valence quarks u_v and d_v are dominant at large x , where one finds $u_v \simeq 2 \cdot d_v$, consistent with proton valence quark combination uud . In addition to the valence quarks, there is a sea of gluons and virtual quark-antiquark pairs, predominantly with low momentum fractions (which increase as x decreases). This occurs because, in QCD, gluons with large momenta are suppressed by the $1/Q^2$ gluon propagator. Consequently, sea quark contributions that originate from the process $g \rightarrow q\bar{q}$ are similarly suppressed. Overall, one finds that roughly only 50 % of the proton's momentum is carried by quarks and anti-quarks, whereas the rest is carried by gluons. If we compare the PDFs obtained for different Q values, interesting insights into the scale dependence of the proton's substructure can be extracted. Since quarks and gluons are believed to be point-like particles, one does not expect a dependence of the PDF on the scale Q^2 . This independence of the PDF on Q^2 is known as Bjorken scaling. However, as reported in Fig. 1.6 there is a small dependence on the scale can be observed. For a larger Q , there is an increase at low x : the scale is more sensitive to gluon radiation $q \rightarrow qg$ on smaller length scales. This dependence on Q implies that the Bjorken-scaling is broken and

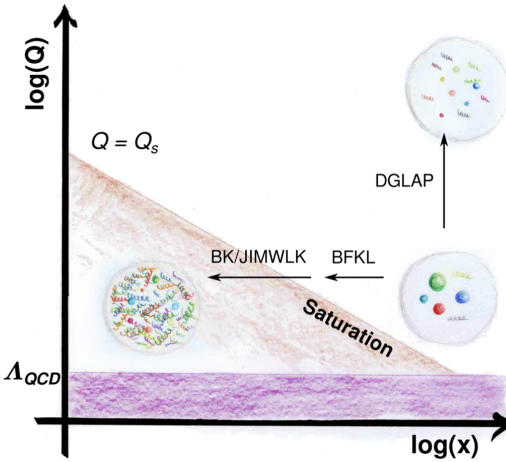


Figure 1.7: Map of QCD as a function of (Q, x) .

that the PDF, rather than being static, evolves with the scale.

The evolution of a PDF in (x, Q^2) phase-space can be described with QCD evolution equations, which incorporate parton splitting probabilities via dedicated functions, and allow interpolating from one region to the next. Figure 1.7 reports the evolution of QCD as a function of (Q, x) , where sketches of a proton portray the parton density in each regime.

Different regions of (x, Q^2) phase-space are described by different equations: at large x and Q^2 the parton densities are low enough and the evolution can be described using DGLAP [13]; at small x and moderate Q^2 the BFKL calculations take over [14].

In the limit $x \rightarrow 0$ there is a drastic increase of the gluon density, which cannot be taken into account by DGLAP and BFKL linear equations. This enhancement continues until when, at small enough x , the density of gluons is so high that gluons recombine in a process of gluon fusion ($gg \rightarrow g$). This requires non-linear equations to describe the evolution in this low- x regime, such as JIMWLK [16] or BK [17]. The non-linear effect of gluon fusion counteracts gluon splitting eventually leading to an equilibrium at which the gluon densities are saturated. The parametric form of gluon saturation scale Q_s is approximately [18]:

$$Q_s \approx \frac{\alpha_s}{\pi R_h^2} x G(x, Q^2), \quad (1.6)$$

where α_s is the running coupling constant, R_h the radius of the hadron and $G(x, Q^2)$ is the gluon density. For perturbative calculations to work well in the saturated regime, the saturation scale should be an order of magnitude larger than the QCD scale Λ_{QCD} 0.2 GeV/c. A prominent model to describe the properties of saturated gluons is the Colour-Glass Condensate (CGC) [19], which is an effective field theory describing the weakly coupled state of gluons packed with a high density inside a hadron by approximating the low- x gluons with classical fields. The CGC is of special importance in the initial stages of nuclear collisions, where it produces a so-called glasma-field configuration from gluons liberated from the partons inside the colliding nuclei.

1.3 The Quark–Gluon Plasma

The evolution of α_s implies the existence of distinct phases of the nuclear matter, related to two properties of the QCD: the asymptotic freedom and the colour confinement. At low Q^2 , the confinement prevails, corresponding to our macroscopic world. At high Q^2 , the running coupling constant decreases until a deconfinement phase is reached: in this condition, quarks and gluons are not anymore “stuck” into hadrons and are almost free to move. This soup-like state [20] can be formed under extreme temperatures and/or densities and it is called the Quark–Gluon Plasma (QGP). The different states of the strongly interacting matter can be shown in a phase diagram as the one reported in Fig. 1.8. The phase diagram is presented in terms of temperature T on the y -axis and baryon chemical potential μ_B on the x -axis. The baryon chemical potential μ_B is defined as the energy needed to increase by one unity the total baryon number.

The ordinary nuclear matter is located at approximately $T \approx 0$ MeV and $\mu_B \approx 1$ GeV. If the baryon chemical potential starts to increase, a transition to the QGP state is expected to happen [21]. This high- μ_B QGP has been hypothesised to be present in the core of compact stars [22]. If the baryon chemical potential continues to increase, there should be the formation of Cooper pairs and therefore of a colour-superconductive state [23]. In the limit of $\mu_B = 0$ MeV, increasing the temperature, there will be a transition around $T \approx 145 - 165$ MeV ($\approx 1.7 \times 10^{12}$ K), corresponding to an energy density of about $\varepsilon \approx 0.18 - 0.5$ GeV/fm 3 . This hot QGP state is believed to have been formed in the first phases (10^{-6} s) of the primordial Universe, subsequently the Big Bang.

Theoretical calculations of the features of the phase diagram and the properties of the different phases of QCD matter cannot be performed using perturbative expansions, due to the large values of α_s at small Q^2 . Therefore, two different approaches are employed:

- **Effective models:** these models describe the behaviour of the nuclear matter under specific conditions focusing on some aspects of the QGP. The MIT Bag Model [24] is an effective model, which describes phenomenologically the confinement of quarks and gluons into hadrons. It assumes that quarks are massless fermions, free to move in a finite region of space, called the bag; the confinement derives from the equilibrium between an external bag pressure direct inward and the internal pressure due to the kinetic motion of quarks.
- **Lattice QCD:** it is a theoretical technique, based on a discretization of space-time by a finite step-size lattice that allows to perform numerical QCD calculations. The estimations obtained applying Lattice QCD are related to the assumption on quark masses. Precise calculations are available only in the case of null chemical potential ($\mu_B \sim 0$). Therefore, it is not possible to investigate the entire phase diagram. The computational resources limit the minimum step size of the lattice and therefore the Lattice QCD calculations.

The region at low μ_B is based on Lattice QCD calculations, which predict a crossover between the hadron gas to the QGP [26]. The presence of this crossover is due to the chiral symmetry, which is restored in case of vanishing quark masses. On the other hand, the zone

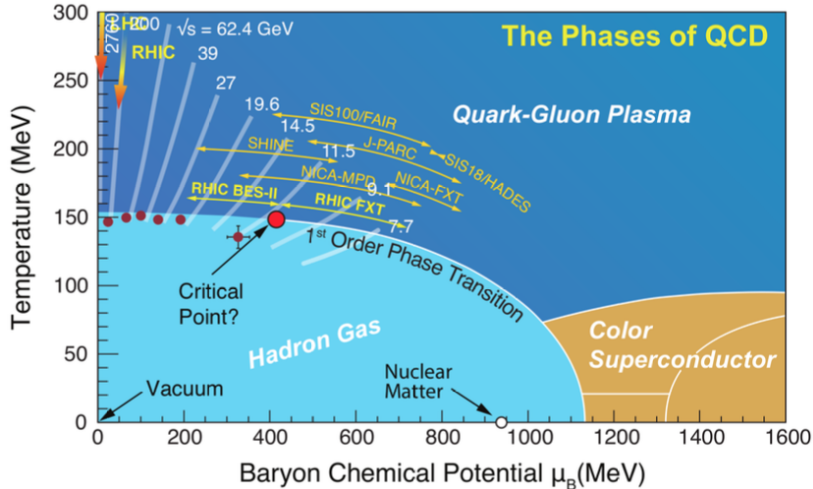


Figure 1.8: The QCD phase diagram as a function of the temperature and the baryon-chemical potential [25].

at high μ_B is described by phenomenological models, such as the MIT one, which foresees a first-order transition and a critical point [27].

1.4 Heavy-ion collisions

Lattice QCD calculations have thus shown the existence of a state of strongly interacting matter at temperatures larger than the pseudo-critical temperature $T_C \approx 155$ MeV [28], which corresponds to a critical energy density ε_C of the order of 1 GeV fm^{-3} [29]. The QGP can be reproduced in the laboratory using ultrarelativistic collisions of large nuclei, called “heavy-ions”, which allow us to reach the required extreme conditions of temperature and energy density.

This kind of collisions can currently be performed at *Conseil Européen pour la Recherche Nucléaire (CERN)* with the *Large Hadron Collider* [30] and with the *Super Proton Synchrotron* (SPS) and at *Brookhaven National Laboratory (BNL)* via the *Relativistic heavy-ion Collider (RHIC)*. The first experimental studies of AA collisions were initiated in 1970 at the Synchrophasotron (JINR Dubna) [31, 32] and in 1975 at the Bevelac (LBL Berkeley) [33]. Then in the second half of the 1980s they will be followed by heavy-ion experiments at the SPS at CERN [34] and the *Alternating Gradient Synchrotron* (AGS) at BNL [35]: they were fixed-target experiments operating at a center-of-mass energy per nucleon-pair ($\sqrt{s_{NN}}$) between 7.7 - 17.3 GeV and probing a μ_B different from zero (between 200 and 500 MeV). At these energies, the nucleons are in a regime defined as *stopping*: they are stopped in the collision region and the net-baryon density is high. The heavy-ion physics moved to colliders, first with the RHIC at BNL and then with the LHC at CERN. The accelerators permitted to reach different center-of-mass energies $\sqrt{s_{NN}}$ per nucleon pair, allowing to probe of different regions of the QCD phase diagram as a function of the temperature T and the baryon chemical potential μ_B . The top center-of-mass energies of the two previously cited accelerators are 200 GeV and 5.36 TeV per nucleon with Au and Pb ions, respectively. These energies permit to explore the QCD phase diagram in the region of μ_B close to zero, defined as the *Bjorken regime* or the *transparency regime* [36].

Consequently, heavy-ion collision experiments allow to probe of the constituents of the hadrons in extreme conditions and explore the properties of the nuclear matter, testing the QCD predictions/calculations. Three categories of collision systems can be used to study the QGP:

- proton-proton (pp) collisions: small system collisions used to study QCD properties in the vacuum. The proton-proton collision measurements are used as references to compare with other collision systems;
- proton-nucleus (pA) collisions: collision systems composed of a proton and a nucleus used to investigate the so-called Cold Nuclear Matter (CNM) effects. Because of nuclear interactions in nuclei, parton distribution functions differ between the proton and nuclei. Moreover, the particles generated in the collision can interact with the nuclei, inducing modifications in their observed production rates and momentum distributions. In addition, coherent energy loss effects between the initial and final state may arise [37].
- nucleus-nucleus (AA) collisions: due to the large number of nucleons involved in the collision a large number of collisions and particles are produced. The system can thermalize and create a new medium, potentially the QGP. With this collision system, it is possible to characterize the QGP properties.

The space-time evolution of heavy-ion collisions can be summarized with the following successive phases, which are schematically presented in Fig. 1.9:

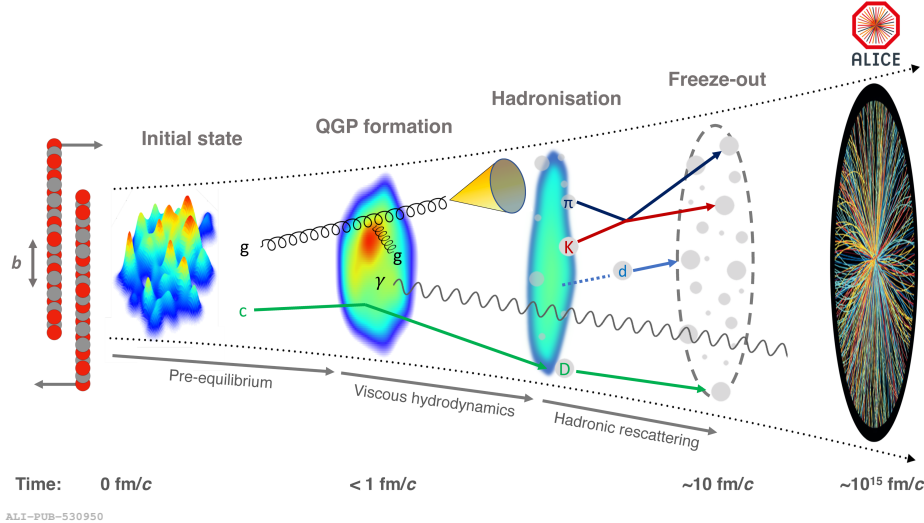


Figure 1.9: The space-time evolution of heavy-ion collisions at LHC [38].

1. **Collision:** at the time $t = 0 \text{ fm}/c$ the collision of the two nuclei takes place. The nuclei are highly Lorentz contracted, and an extremely dense region of partons is generated with a large energy deposit in the overlap region of the collision. The superposition of the nuclei occurs in a very short time $\tau_{\text{coll}} = 2R_N/\gamma$, where τ_{coll} is the crossing time of the nuclei, R_N is the nucleus radius and γ is the Lorentz factor. In Pb–Pb collisions at $\sqrt{s_{\text{NN}}} = 5.02 \text{ TeV}$ at the LHC, τ_{coll} is about $6 \times 10^{-3} \text{ fm}/c$, which is smaller than the strong-interaction timescale $\tau_{\text{QCD}} \simeq 1 \text{ fm}/c$.

2. **Pre-equilibrium** or **initial state**: during this phase, secondary particles are produced due to the inelastic nucleon-nucleon collisions, after a formation time $\tau_f > \tau_{\text{coll}}$. The formation time τ_f can be estimated via the Heisenberg's principle $\tau_f \approx \hbar/\langle m_T \rangle$ where \hbar is the Planck's constant, $m_T = \sqrt{m^2 + p_T^2}$ is the transverse mass and p_T is the momentum in the traverse plane.

The system in this phase is still not in equilibrium. Some hard processes occur between partons, thus particles with either a large mass or large transverse momenta are produced.

3. **QGP**: particles produced in the primary collisions continue to mutually interact, giving rise to a region of high matter and energy density at the thermal equilibrium from which the **QGP** can be produced in less than 0.1-0.3 fm/ c . In these early stages, most of the interactions between partons involve small momentum exchange, that is soft interactions. Due to pressure gradients, the system expands and the temperature cools down. The rapid expansion of the **QGP** is usually modelled using relativistic hydrodynamics [39]. The **QGP** lifetime for the energy densities reached at the **LHC** is of the order of 10 fm/ c [40].

4. **Hadronization**: it happens when the critical energy density is reached ($\varepsilon_C \sim 1 \text{ GeV/fm}^3$). The system gradually evolves into an interacting hadron resonance gas and it continues to expand and cool down.
5. **Freeze-out**: the hadronic gas continues to expand and cool down until when the particle average energies are too low to allow inelastic scatterings. At this moment, the abundance of the different hadronic species is fixed. This condition is defined as *chemical freeze-out*. At the **LHC**, the chemical freeze-out occurs at $T_{\text{ch}} \simeq 153 \text{ MeV}$. At a certain point also elastic scatterings cease, the *thermal freeze-out* is reached, and the particles' momentum spectra are frozen. The experimental measurement can take a screenshot of this moment, in fact after the thermal freeze-out, the light hadrons freely travel to the detectors.

1.4.1 Nuclear parton distribution functions

If the nuclei were a simple collection of almost free nucleons, the only modification expected for the **PDFs** of nucleons bound in nuclei relative to free nucleons would be due to the Fermi motion of the protons and neutrons inside the nucleus. This would lead to a modification of the distribution of the fraction of the nucleon momentum, the Bjorken x , carried by the partons. However, deep-inelastic scattering experiments have underlined that other effects should be taken into account and that they depend on the x momentum distribution of partons.

Figure 1.10 shows that it is possible to distinguish four different regions of x :

- $x < 0.1$: in this region, a significant suppression is observed, which increases with the mass number of the nucleus. This interval is called *shadowing* region [41].
- $0.1 < x < 0.3$: this interval identifies the *anti-shadowing* region, where the ratio is slightly above the unity.

- $0.3 < x < 0.8$: in this range, the ratio is lower than unity, reaching a minimum around $x \approx 0.7$. This suppression is called *EMC effect* [42].
- $0.8 < x < 1$: in this region, the ratio is above unity because of the *Fermi motion*.

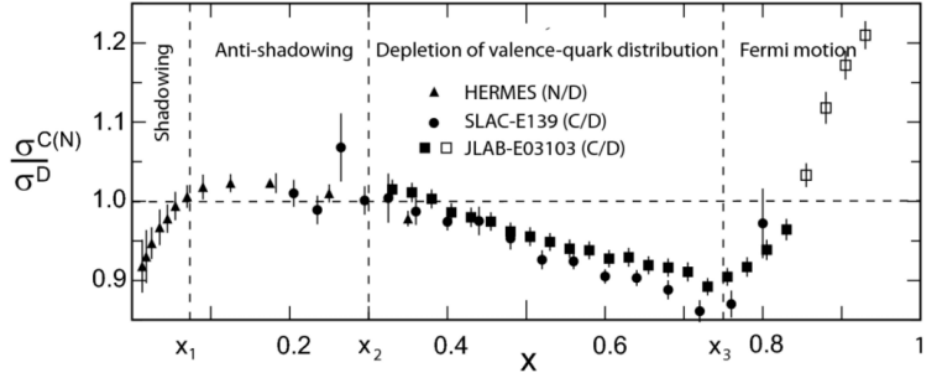


Figure 1.10: Measurements of the nuclear modification of the PDFs performed by several experiments in a wide range of Bjorken x .

The parton distribution functions of nucleons within nuclei (**nPDFs**) are different to the **PDFs**. The nuclear modification of the **nPDFs** is usually defined as:

$$R(x; Q^2) = \frac{f_a(x; Q^2)}{A \cdot f_P(x; Q^2)} \quad (1.7)$$

where $f_P(x; Q^2)$ is the **PDF** in the free nucleon, while $f_a(x; Q^2)$ is the one in a nucleon bound inside a nucleus with A nucleons.

Figure 1.11 reports the modification of **nPDFs** in Pb at a scale $Q = 10$ GeV with respect to the free-proton baseline for six different parton species [43]. The lines represent the central values for different **nPDFs** indicated in the legend, and the bands show the associated uncertainties at a 68 % confidence level. The different **nPDFs** almost display the features of the previously outlined nuclear effects, but the magnitude is different depending on the parametrisation. Although a lot of progress has been made in recent years to better constrain **nPDFs**, the amount of data available for various nuclei is much smaller compared to their free-proton counterparts, therefore the **PDFs** are still better described than the **nPDFs**.

1.4.2 Key variables in heavy-ion collisions

In this Section, the variables necessary to describe the collisions of the heavy ions and how they collide will be presented.

Kinematics

The geometry of the collision is described considering the reference frame of the laboratory, which is shown in Fig. 1.12. The incident beam direction axis is known as the longitudinal axis (the z -axis by convention). The plane perpendicular to the longitudinal axis, the (x, y) plane, forms the transverse plane in which is defined the transverse momentum of particles with:

$$p_T = \sqrt{p_x^2 + p_y^2} \quad (1.8)$$

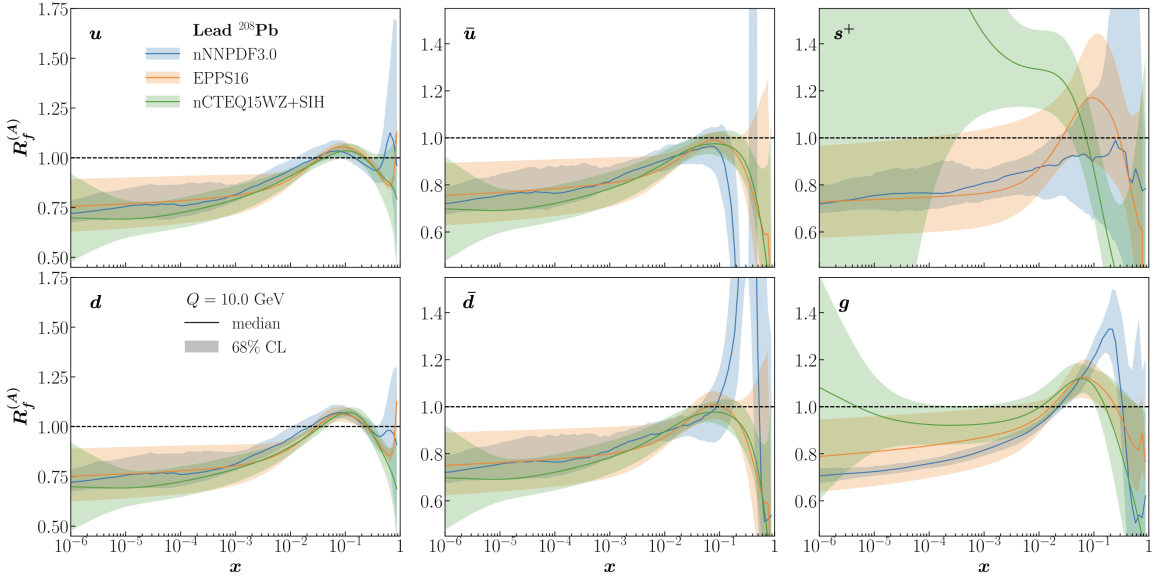


Figure 1.11: Nuclear modification of nPDFs at $Q^2 = 10 \text{ GeV}^2$ for different parton species with respect to the free proton baseline. The calculations for nNNPDF3.0 [43], EPPS16 [44] and nCTEQWZ+SIH [45] are shown, where the bands illustrate the uncertainties at a 68% confidence level [43].

The p_T is invariant under Lorentz boost along z and this permits to determine the transverse energy of the particle:

$$E_T = \sqrt{p_T^2 c^2 + (mc^2)^2} \quad (1.9)$$

where m is the mass of the particle and c is the speed of light. The azimuthal angle φ and the polar angle θ define the propagation direction of the particle. The total energy of the collision in the center-of-mass is extracted using the Mandelstam variable \sqrt{s} , which is invariant for Lorentz transformation. This energy can be evaluated from the four-momenta vector $p = (E, p_x, p_y, p_z)$ of the colliding particles: $s = (p_1 + p_2)^2$.

Another important variable for the particle is the rapidity y , which is related to the particle's propagation along the beam axis:

$$y = \frac{1}{2} \ln \left(\frac{E + p_z}{E - p_z} \right) \quad (1.10)$$

This formula contains the particle's energy E and the longitudinal momentum $p_z = p \cos(\theta)$. Under a Lorentz boost along z -axis (β_z), the rapidity y is shifted by the same amount: $y = y' + \Delta y$, with $\Delta y = \frac{1}{2} \ln \left(\frac{1+\beta_z}{1-\beta_z} \right)$. Thanks to this property, experimental rapidity distributions can be easily compared when they are measured in fixed target and collisional modes.

Another fundamental variable is the pseudorapidity η defined as:

$$\eta = -\frac{1}{2} \ln \left(\frac{|p| + p_z}{|p| - p_z} \right) = -\ln \left(\tan \frac{\theta}{2} \right) \quad (1.11)$$

where θ is the particle emission angle relative to the beam direction, i.e. the polar angle. At relativistic energy scale and around mid-rapidity, that is the rapidity of a particle close to the axis of a beam of particles, $\eta \simeq y$. The pseudo-rapidity η is used when the measured particle mass is unknown.

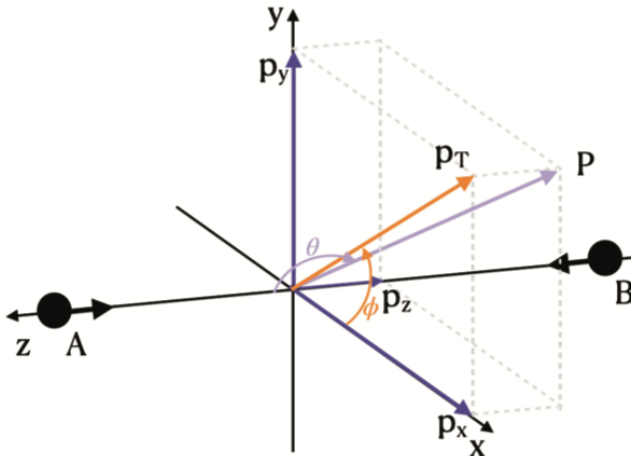


Figure 1.12: Coordinate system describing a collision between A and B nuclei.

The Glauber model and the impact parameter

The Glauber Model [46] allows to describe quantitatively the geometrical configuration of nucleus-nucleus collisions, which are described in terms of an incoherent superposition of elementary nucleon-nucleon collisions. One important variable is the impact parameter \vec{b} , the distance between the centres of the two colliding nuclei. The model allows the calculation of other variables, such as the number of participant nucleons $N_{\text{part}}(\vec{b})$, those which have interacted at least once during the collision; the total number of binary nucleon-nucleon collisions $N_{\text{coll}}(\vec{b})$ and the interaction probability.

In the Glauber Model formulation, the nucleons are supposed to be point-like and independent inside nuclei. In addition, the nucleons inside the nuclei do not deflect during the collision, their trajectory is along a straight line; the nucleon-nucleon inelastic cross-section does not vary during the collision. All these assumptions go under the name of *optical limit*: the collision between two nuclei (or a target A and a projectile B) can be analytically described using the nuclear density function ρ (typically parametrised with a Wood-Saxon function) and the inelastic nucleon-nucleon cross section $\sigma_{\text{inel}}^{\text{NN}}$.

Figure 1.13 shows the coordinate system used to describe the collision between the nucleus A and the nucleus B. The origin of the coordinate system is placed in the centre of A, and the position in the transverse plane of the nucleons inside A is expressed by the vector \vec{s} . For what concerns the nucleus B, the nucleon position is given by $\vec{b} - \vec{s}$. The probability to find a nucleon in A per unit of transverse area is given by the *nuclear thickness function*:

$$\hat{T}_A(\vec{s}) = \int_{-\infty}^{+\infty} \rho_A(\vec{s}, z_i^A) dz \quad (1.12)$$

A similar expression can be extracted also for the nucleus B. Then it is possible to define the probability of having an overlap between two nucleons of the nuclei:

$$p(\vec{b}) = \sigma_{\text{inel}}^{\text{NN}} \cdot \int d^2 s \cdot \hat{T}_A(\vec{s}) \cdot \hat{T}_B(\vec{b} - \vec{s}) = \sigma_{\text{inel}}^{\text{NN}} \cdot T_{AB}(\vec{b}) \quad (1.13)$$

where $T_{AB}(\vec{b})$ is the *nuclear overlap function*. The probability of having n nucleon-nucleon interactions is given by the binomial distribution:

$$P(n, \vec{b}) = \binom{AB}{n} \left[T_{AB}(\vec{b}) \sigma_{\text{inel}}^{\text{NN}} \right]^n \left[1 - T_{AB}(\vec{b}) \sigma_{\text{inel}}^{\text{NN}} \right]^{AB-n} \quad (1.14)$$

From the mean value of the binomial probability distribution, we can get the average number of nucleon-nucleon collisions:

$$\langle N_{\text{coll}}(\vec{b}) \rangle = AB \cdot \sigma_{\text{inel}}^{\text{NN}} \cdot T_{AB}(\vec{b}) \quad (1.15)$$

The number of participants is given by the following equation:

$$\begin{aligned} \langle N_{\text{part}}(\vec{b}) \rangle &= A \cdot \int d^2 s \cdot T_A(\vec{b}) \cdot \left[1 - \left(1 - \sigma_{\text{inel}}^{\text{NN}} \cdot T_B(\vec{b} - \vec{s}) \right)^B \right] \\ &\quad + B \cdot \int d^2 s \cdot T_B(\vec{b} - \vec{s}) \cdot \left[1 - \left(1 - \sigma_{\text{inel}}^{\text{NN}} \cdot T_A(\vec{s}) \right)^A \right] \end{aligned}$$

We can obtain the inelastic nucleus-nucleus interaction cross section and it is related to the probability to have at least one binary nucleon-nucleon collision:

$$\frac{d\sigma_{\text{inel}}^{\text{AB}}}{d\vec{b}} = 1 - P_{0,\text{AB}}(\vec{b}) = 1 - \left[1 - \sigma_{\text{inel}}^{\text{NN}} \cdot T_{AB}(\vec{b}) \right]^{AB} \quad (1.16)$$

In the case of hard processes, for which the cross section is small, the Eq. (1.16), in which σ_{inel} is substituted by σ_{hard} , can be expanded in Taylor series:

$$\frac{d\sigma_{\text{AB}}^{\text{hard}}}{d\vec{b}} \simeq 1 - \left[1 - AB \cdot \sigma_{\text{hard}}^{\text{NN}} \cdot T_{AB}(\vec{b}) \right] = AB \cdot \sigma_{\text{hard}}^{\text{NN}} \cdot T_{AB}(\vec{b}) \propto \sigma_{\text{hard}}^{\text{NN}} \cdot \langle N_{\text{coll}}(\vec{b}) \rangle \quad (1.17)$$

As a consequence, the Glauber Model predicts that the yield of particles produced via hard processes in nucleus-nucleus collisions is proportional to the one in proton-proton collisions, with proportionality constant $\langle N_{\text{coll}} \rangle$. This property is typically addressed as *binary-scaling* or $\langle N_{\text{coll}} \rangle$ -scaling and will be useful in the following.

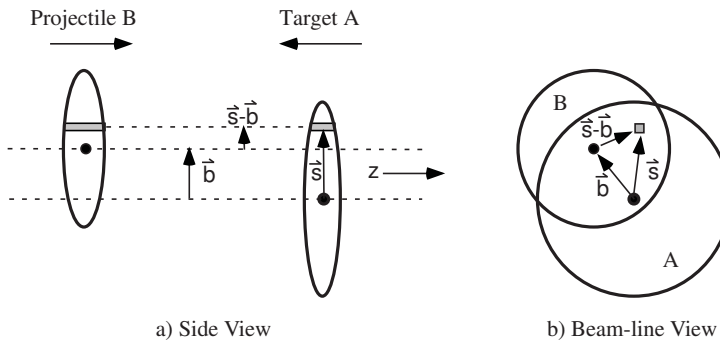


Figure 1.13: Schematic representation of the Optical Glauber Model geometry, with transverse (a) and longitudinal (b) views [46].

It is possible to generally classify nucleus-nucleus collisions in terms of centrality, which varies with continuity and depends on the overlapping of the nuclei. Two main classes of collisions are defined: **central** and **peripheral**, according to the impact parameter. The former class is characterised by a small value of the impact parameter and the superposition of the nuclei is almost complete: the N_{part} is close to the overall number of nucleons in the

projectile and target nuclei, the N_{coll} is high, and the number of produced particles is large. On the contrary, very peripheral collisions are characterised by $|\vec{b}| \sim 2R_N$, where R_N is the nuclear radius and the overlap region is limited. In this case, N_{part} and N_{coll} are low and consequently a small number of final particles are produced in the collision. The Glauber Model can successfully compute some quantities related to the geometry of the collision. However, its usage of continuous density functions for quantities that are discrete and that can fluctuate event by event represents a limitation. In order to take into account the event-by-event fluctuations it is possible to use Glauber Monte Carlo (MC) simulations, in which the nucleon positions are randomly sampled from the nuclear density function, and a random impact parameter is generated according to the differential cross section $d\sigma/db \propto 2\pi b$. The collision between two nuclei is considered as a superposition of independent binary nucleon-nucleon collisions. A collision between two nuclei distant d in the transverse plane can occur if the following condition is satisfied

$$d < \sqrt{\frac{\sigma_{\text{NN}}^{\text{inel}}}{\pi}} \quad (1.18)$$

Thanks to this approach, the N_{part} and N_{coll} values are obtained for each generated event. Another variable that can be obtained is the number of “spectators”, that is the number of nucleons which do not interact and is defined as: $N_{\text{spect}} = 2A - N_{\text{part}}$. Figure 1.14 illustrates an example of collision simulated with the Glauber Monte Carlo model showing participant and spectator nucleons.

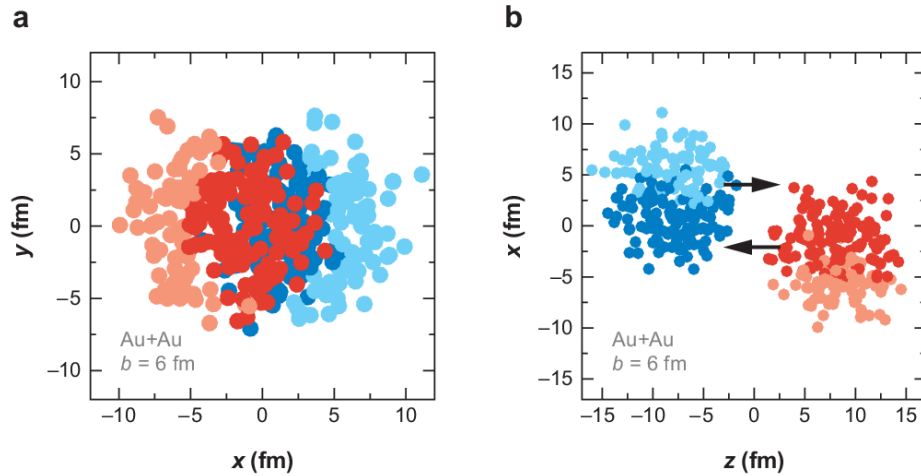


Figure 1.14: A Glauber Monte Carlo simulation of an Au–Au collision event at $\sqrt{s_{\text{NN}}} = 200$ GeV with impact parameter $b = 6$ fm. (a) shows the transverse plane visualisation, while (b) the visualisation along the beam axis. Darker circles represent participating nucleons [46].

We have learned that the impact parameter is not directly measurable; therefore the centrality is used to characterise the amount of nuclear overlap in the collisions. In theory, any observable that scales monotonically with impact parameter could be used for classification according to centrality. However, the centrality can be measured experimentally for example by exploiting these observables:

- the number of charged particles produced in the collision, that is the average charged-particle multiplicity N_{ch} ;

- the energy in the forward region, measured for example using the number of spectator nucleons not involved in the collision.

In A Large Ion Collider Experiment ([ALICE](#)), during Run 1 and 2 data taking periods, centrality classes were defined by measuring the signal amplitudes in the scintillator arrays, placed at forward rapidity, i.e. close to the beam axis, of the [V0](#) detector [47] (more details will be given in Sect. 3.2.3 and Sect. 3.5). The signal amplitudes are proportional to the multiplicity of particles produced in the event, which is correlated to the centrality of the collision. For example, the 0-5% centrality class corresponds to the 5% of events with the highest [V0](#) amplitude; the same principle applies to other classes. Centrality classes are therefore expressed via a percentage of the total hadronic interaction cross section measured by the forward scintillators.

1.5 Experimental Probes

The short lifetime of the [QGP](#) ($\simeq 10 \text{ fm}/c \simeq 10^{-23} \text{ s}$) makes it impossible to be studied directly. However, it is still possible to shed light on this phase by studying the particles produced in the final stages of the collision. There are different observables which are sensitive to the [QGP](#) properties, which are commonly grouped into two main categories of probes:

- **Soft probes** include low p_T hadrons (below $p_T \lesssim 1 \text{ GeV}/c$ at [RHIC](#) and below $p_T \lesssim 4 \text{ GeV}/c$ at [LHC](#)) composed by light quarks (i.e. u, d, s), that originate from the [QGP](#) hadronization and partons produced at low Q^2 . The measurement of soft hadrons permits to access to macroscopic and collective properties of the [QGP](#), such as the equation of state, thermodynamic and dynamical characteristics.

Into the soft probes we can include also real and virtual photons, and lepton-antilepton pairs, emitted by the hot plasma as black body radiation in the early phases of the collision. Photons and di-leptons do not carry colour charge and thus are not affected by the strongly interacting medium. Their measurement allows to access to thermodynamic properties of the [QGP](#). The majority of the total number of particles produced in the collision are soft processes [48].

- **Hard probes** for $Q \gg \Lambda_{\text{QCD}}$. They are partons or electro-weak particles (γ , Z, W^\pm) produced in the early stages of the collision and they include particles characterised by a high-transverse momentum, above $\sim 5 \text{ GeV}/c$.

They include jets and the production of particles containing heavy flavour quarks (c, b) in open charm/beauty and quarkonia ($q\bar{q}$). This kind of probe is particularly sensitive to the [QGP](#) phase, because the hard scatterings occur on short time scales and the partons produced in such scatterings interact with the medium. On the contrary, electro-weak particles do not interact strongly with the medium, and provide direct information on the initial conditions of the collision. This Thesis is dedicated to the high p_T photons produced in hard processes, particularly their correlations with hadrons from parton fragmentation particle jets. The Chapter 2 will be specifically dedicated to hard photon measurements.

All these probes provide access to various types of information about the nature of the [QGP](#). In the following, a selection of the main observables will be presented.

A fundamental quantity used for many observables is the Lorentz-invariant differential yield of final state particles, given by:

$$E \frac{d^3N}{dp^3} = \frac{1}{2\pi p_T} \frac{d^2N}{dp_T dy} \quad (1.19)$$

which is the number density of the particle three-momentum scaled by the particle energy E . It depends on the measured particle species in question, the transverse momentum, p_T , and rapidity, y .

Hard probes, as mentioned, are produced in the earliest times of the collision. One of the ways they can be explored is by extracting their nuclear modification factor R_{AA} . This observable is sensitive to the evolution of hard processes in heavy-ion collisions relative to the vacuum. It is defined as the ratio between the invariant yield of particles in AA with respect to the one in pp scaled by the $\langle N_{coll} \rangle$, i.e. the average number of nucleon-nucleon collisions, according to the Glauber model (see Sect. 1.4.2). It is expressed by the following equation:

$$R_{AA} = \frac{1}{\langle N_{coll} \rangle} \times \frac{d\sigma_{AA}/dp_T}{d\sigma_{pp}/dp_T} \quad (1.20)$$

Basically, the following possible conclusions could be extracted from R_{AA} measurement among others:

- $R_{AA} = 1$, no medium modification;
- $R_{AA} > 1$, QGP thermal emission or multi-parton interactions;
- $R_{AA} < 1$, yield suppression due to parton energy loss in the medium.

Any departure from unity reveals how the studied processes are modified in heavy-ion collisions.

1.5.1 Soft probes: strangeness enhancement

The strangeness enhancement [49] is an enhancement in nucleus-nucleus collisions of the relative yield of strange and multi-strange hadrons with respect to hadrons which contain only up and down quarks. In small colliding systems, the production of strange particles is disfavoured with respect to the production of particles containing u and d quarks, because of the higher mass of s quarks [50]. Instead in heavy-ion collisions, the enhancement of strange hadron production is possible due to the high gluon density of the QGP. This is thanks to the dominance of gluonic production channels, such as the processes $gg \rightarrow s\bar{s}$, $u\bar{u} \rightarrow s\bar{s}$ and $d\bar{d} \rightarrow s\bar{s}$.

The strangeness enhancement was initially observed in heavy-ion collisions at SPS [51] energies and later on at LHC [52] ones. The NA57 Collaboration measured the strange baryons (hyperons) enhancement at the SPS [51], evaluating the yield per participant in Pb-Pb collisions relative to the yield per participant in p-Be. The result is reported as a function of the average number of participants, defined $\langle N_{wound} \rangle$ in Fig 1.15. The magnitude of the enhancement increases with the strangeness content of the particles, reaching the highest increase with the Ω baryon, which contains only strange quarks. This enhancement of

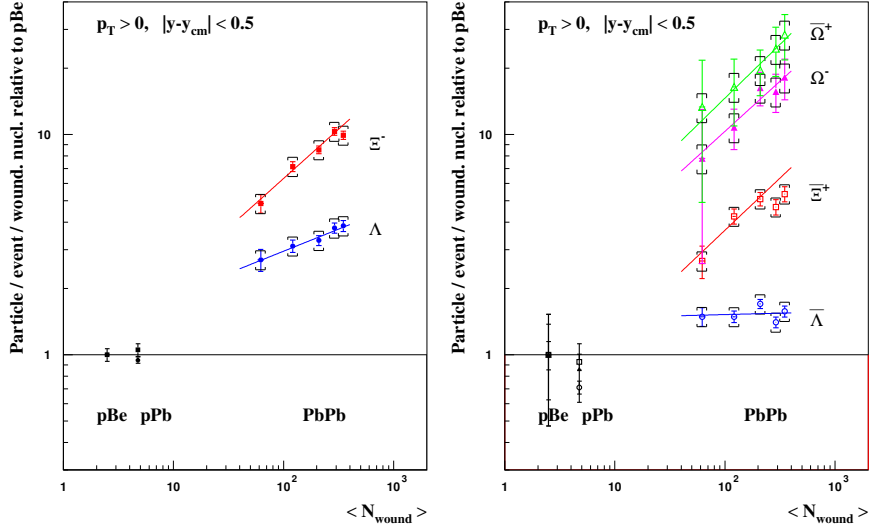


Figure 1.15: Hyperon enhancements as a function of $\langle N_{\text{wound}} \rangle$ in Pb–Pb, p–Pb and p–Be collisions at $\sqrt{s_{\text{NN}}} = 158$ GeV measured by NA57 Collaboration [51].

strange hadron production in heavy-ion collisions relative to p–Be collisions, was historically considered as one of the signatures of QGP formation.

The ALICE Experiment has performed a similar measurement at the LHC energies, computing the relative production of strange hadrons with respect to pions as a function of the charged-multiplicity at mid-rapidity [53]. The results are reported in Fig. 1.16 for different collision systems and center-of-mass energies per nucleon pair.

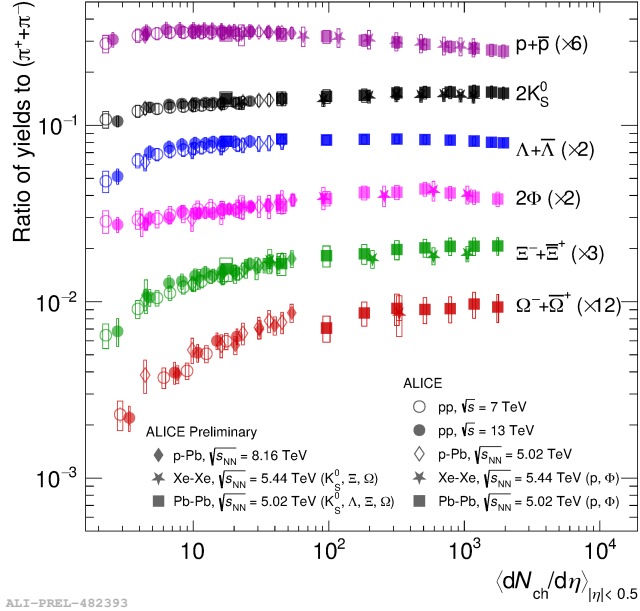


Figure 1.16: Ratios of the p_T -integrated yield of hadrons with strange-quark content and charged pions as a function of the charged-particle multiplicity at midrapidity, measured by the ALICE Collaboration in various collision systems and at different center-of-mass energies [53].

The measured strange-hadron production is larger in Pb–Pb collisions with respect to low-multiplicity pp collisions. Nevertheless, in pp and p–Pb events, the strangeness produc-

tion increases smoothly with increasing charged-particle multiplicity and in high-multiplicity it reaches values similar to those observed in Pb–Pb collisions. This continuous evolution of particle production (event multiplicity) from pp to Pb–Pb collisions, is quite surprising because small systems like pp and pA were considered as reference cases, where the formation of the QGP was not possible. The production yields are compatible in collisions characterized by similar final state multiplicities, implying no significant dependence on the center-of-mass energy or the collision system. This suggests that the origin of strangeness production in hadronic collisions is driven by the properties of the final state. The observed enhancement is more pronounced for hadrons with a higher strange-quark content, as can be seen in Λ/π , Ξ/π and Ω/π ratios and as it was already observed by NA57.

A future experiment NA60+ [54], foreseen at the SPS intends to investigate the dependence of the strangeness enhancement on the collision centrality and on collision systems as a function of the multiplicity. In particular, the charged-particle multiplicity appears to be a useful tool which allows for direct comparison among different collision systems, reflecting the final hadronic state produced in the collision and also being strongly related to the initial energy at play. As a consequence, the future NA60+ measurements will permit to update the results obtained by NA57 at the SPS energies and will offer a comparison with the ALICE ones.

1.5.2 Soft probes: collective flow

Essential insights into the understanding of strongly-coupled matter are related to the dynamical properties of the Quark–Gluon Plasma. These properties are identified through measurements sensitive to the collective motion of the particles superimposed on their thermal motion. The collective motion is related to radial and anisotropic flows, which have a significant role during heavy-ion collisions.

Radial flow occurs because the pressure at the centre of the QGP is greater than at its outer regions, causing a uniform outward velocity field. The rate of hydrodynamic expansion is affected by the bulk viscosity, which is the medium’s resistance to volume growth. This radial flow, coming from the collective motion in the transverse plane, can be measured experimentally through the momentum distribution of identified particles. The radial flow leads to flatter transverse momentum distributions with increasing mass, particularly at low values of p_T . In this region, the p_T distribution has contributions from the random thermal motion and the collective expansion. While the former depends on the decoupling temperature, the latter is dependent on the hadron mass because all hadrons acquire an additional transverse momentum given by their mass multiplied by the common radial flow velocity. Figure 1.17 shows the p_T spectra as a function of p_T for various particles in Pb–Pb collisions measured by ALICE [38]. The spectral shapes vary with centrality, showing maxima radial flow at higher transverse momenta in central collisions compared to peripheral ones. Moreover, at low- p_T the distributions result harder and this effect is mass-dependent, more pronounced for heavier particles.

Another important collective motion observed in non-central collisions is the *anisotropic flow*. When two nuclei collide with a non-zero impact parameter (non-central collisions), the

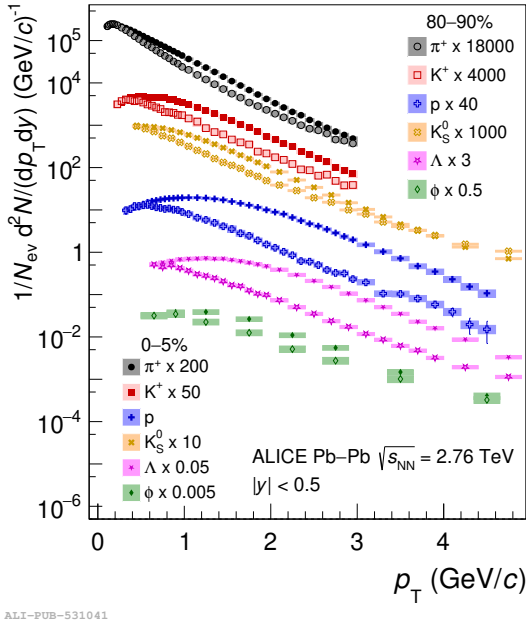


Figure 1.17: Transverse momentum spectra of charged pions, kaons, protons, Λ baryons, and ϕ mesons for central (0–5%) (full marker) and peripheral (80–90%) (empty marker) Pb–Pb collisions at $\sqrt{s_{\text{NN}}} = 2.76 \text{ TeV}$ measured by ALICE [38].

interaction volume is asymmetrical and is characterised by an almond shape, as shown in Fig. 1.18. This initial spatial anisotropy is converted into anisotropies in particle emission and momentum distribution. These anisotropies are generated before the medium reaches the critical temperature and the hadronisation phase, hence the anisotropic flow is sensitive to the early and hot strongly interacting phase of the evolution of Quark–Gluon Plasma. This anisotropic flow can be measured from the azimuthal angle distributions of the particles in the final state, as shown in Fig. 1.18. The final azimuthal distribution of emitted particles

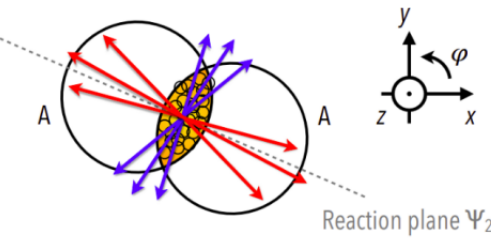


Figure 1.18: Sketch of a collision to highlight the almond shape.

can be written in terms of the azimuthal Fourier coefficients of the transverse momentum spectrum:

$$\frac{dN}{d(\varphi - \Psi_{RP}) dp_T} = \frac{dN}{2\pi dp_T} \left\{ 1 + 2 \sum_{n=0}^{\infty} v_n(p_T) \cos[n(\varphi - \Psi_{RP})] \right\} \quad (1.21)$$

where φ is the azimuthal angle of the particle momentum, Ψ_{RP} is the angle of reaction plane,

n is the order of the harmonic, v_n are the Fourier coefficients defined as

$$v_n = \langle \cos[n(\varphi - \Psi_{RP})] \rangle \quad (1.22)$$

Measuring these v_n coefficients is extremely important because they are linked to the initial geometric conditions and inhomogeneities, providing insight into the properties of the medium. The v_n generally depend on p_T and y . In a non-central collision, the typical almond shape of the overlapping region generates a pressure gradient along the reaction plane (Ψ_2 in Fig. 1.18). In this case, the dominant term of Eq. (1.22) is the second-harmonic coefficient v_2 , called *elliptic flow*. It is sensitive to the equation of state (EoS) in the medium in the early stages of the collision, when in fact the anisotropic pressure gradients are the highest. The elliptic flow of different species is reported in Fig. 1.19 measured by the ALICE Collaboration for several centrality classes in Pb–Pb collisions at $\sqrt{s_{NN}} = 5.02$ TeV [55].

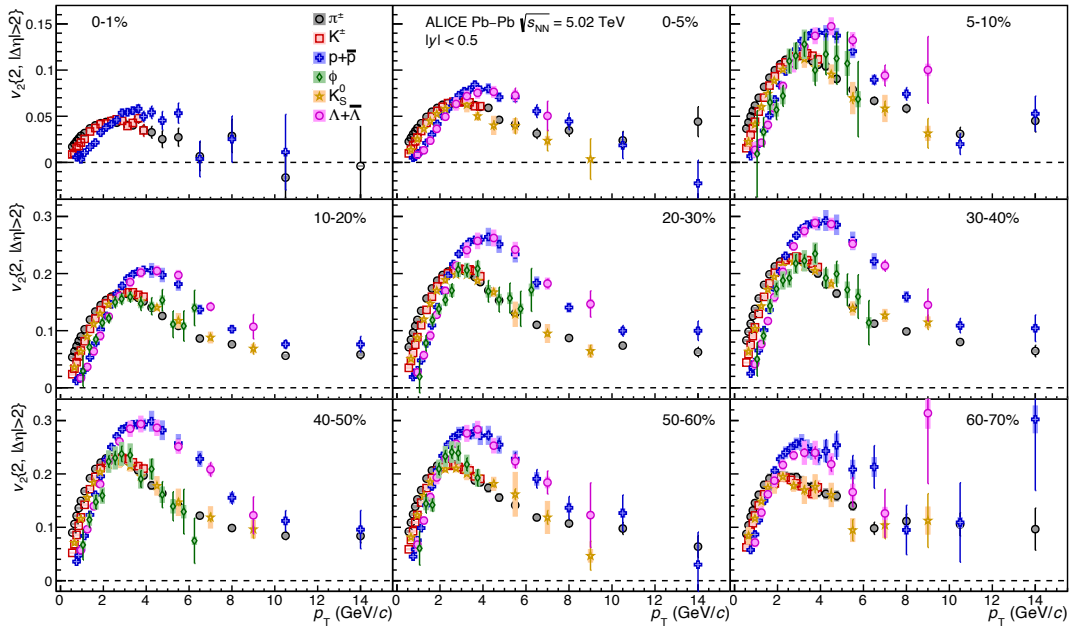


Figure 1.19: Elliptic flow coefficient v_2 of charged pions, charged and neutral kaons, protons, ϕ mesons, and hyperons as a function of p_T , measured by the ALICE Collaboration for several centrality classes in Pb–Pb collisions at $\sqrt{s_{NN}} = 5.02$ TeV [55].

The elliptic flow increases from the most central collisions to the semi-central ones because of the higher spatial anisotropy, since the almond shape is more pronounced in semi-central collisions. On the other hand, it decreases in more peripheral collisions because the smaller the density of the medium, the smaller the generated pressure gradients. It is possible to appreciate a mass-ordering of the v_2 coefficients in the low- p_T region ($p_T \lesssim 3$ GeV/ c): lighter particles have a larger v_2 than the heavier ones. This is caused by the radial flow, which overlaps with the elliptic flow and imposes an equal velocity boost to all particles, thus pushing more massive hadrons to higher p_T .

For the p_T region between 3 and 8 GeV/ c , there is a separation between the v_2 coefficients of baryons and mesons, with baryon elliptic flow coefficients larger than meson ones. In particular, the ϕ meson, whose mass is similar to the proton one, has a v_2 value compatible with that of the other mesons in this p_T interval. It is possible to conclude that there

is a dependence on the number of constituent quarks rather than the hadron mass. This behaviour aligns with the hypothesis of quark hadronisation via coalescence [56], where the elliptic flow of each constituent quark contributes to the v_2 of the final-state hadron. For $p_T > 10 \text{ GeV}/c$, the elliptic flows of different particle species are compatible within uncertainties and depend only weakly on the transverse momentum.

The comparison of the measured v_n harmonics with viscous hydrodynamic models gives information on medium properties, such as the equation of state or shear viscosity η/s . It has been found that a value of η/s of about 0.12 and 0.2 allows for a good parametrisation of the measurements in Au–Au collisions at the top of RHIC energy and Pb–Pb collisions at $\sqrt{s_{\text{NN}}} = 2.76 \text{ TeV}$, respectively [57].

1.5.3 Hard probes: quarkonium suppression and regeneration

The high mass of charm and beauty quarks implies that they are produced in the early stages of the collision. Since these processes take place with a characteristic timescale smaller than the typical QGP formation time, charm and beauty quarks live through the medium expansion, interacting with the free partons in the plasma. The measurement of open heavy-flavour hadrons, namely hadrons containing at least one heavy valence quark (c or b), and quarkonia, bound states of heavy quark-antiquark pairs, provides access to the entire QGP space-time evolution and is sensitive to the initial state.

In particular, quarkonia consist in bound states $c\bar{c}$ *chamonia* (such as the J/ψ , $\Psi(2S)$, ...) and $b\bar{b}$ *bottomonium* ($\Upsilon(nS)$). The presence of the QGP leads to a colour-screening effect which can dissociate the quarkonia in the medium, causing the so-called **quarkonia suppression**; in 1986 Matsui and Satz proposed this phenomenon as a signature of the QGP [58]. The colour screening can be explained using the definition of the non-relativistic interaction potential between a quark and anti-quark in vacuum as a function of r :

$$V(r) = -\frac{\alpha}{r} + \sigma r \quad (1.23)$$

where σ is the confinement string tension and α is computed by the lattice QCD. The first term is the Columbian-like contribution that describes $q\bar{q}$ interactions; while the second one is related to the confinement, which prevails at high distances. When the system reaches high-energy densities and/or temperatures, that is in the presence of the QGP phase, the number of coloured partons increases, giving origin to a screening effect, known as the Debye screening, which reduces the interaction potential of the $q\bar{q}$ and leads to the melting of quarkonium states and therefore to the so-called suppression of their production. Due to the existence of a wide range of quarkonium states with binding energies varying from a few tens of MeV ($\psi(2S)$) to over 1 GeV ($\Upsilon(1S)$), it is possible to observe a process known as sequential suppression. This process involves the gradual disappearance of different quarkonium resonances as the temperature of the system increases. Because of this property, quarkonia can be considered effective thermometers, and by comparing their nuclear modification factors with theoretical predictions, it may be possible to estimate the temperature of the QGP.

Measurements of quarkonia suppression can be quantified with the nuclear modification factor R_{AA} .

Figure 1.20 reports the R_{AA} for different bottomonium states as a function of the number of participants measured by the CMS Collaboration [59]. This result is particularly important

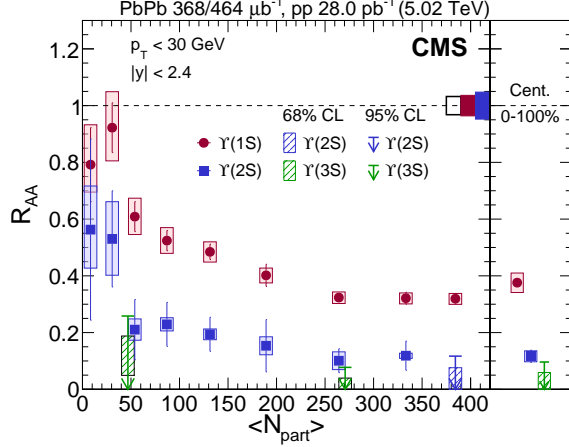


Figure 1.20: Nuclear modification factors for the $\Upsilon(1S)$, $\Upsilon(2S)$ and $\Upsilon(3S)$ mesons as a function of $\langle N_{\text{part}} \rangle$ measured by CMS [59].

because the sequential melting is clearly visible. The ground state ($\Upsilon(1S)$) exhibits a R_{AA} lower than unity for more central collisions, while the excited states ($\Upsilon(2S)$ and $\Upsilon(3S)$) are even more suppressed, given their smaller binding energy.

Figure 1.21-left shows the J/ψ R_{AA} as a function of the charged multiplicity measured by the NA50, the Solenoidal Tracker at RHIC (STAR) and the ALICE experiments at different center-of-mass energies per nucleon-pair.

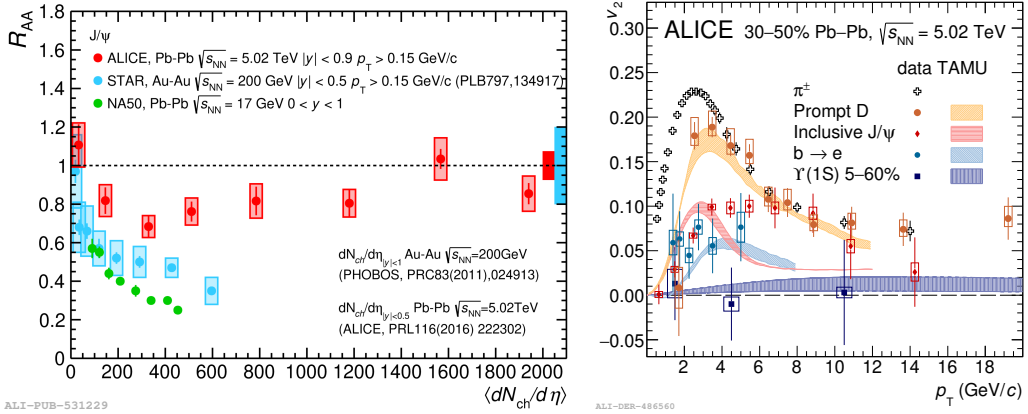


Figure 1.21: Left: R_{AA} of the J/ψ hadron measured in heavy-ion collisions at different center-of-mass energies as a function of the charged multiplicity by ALICE (red full circle), by NA50 (green full circle) and by STAR (light blue full circle) experiments [38]. Right: v_2 coefficient of charged pions, prompt D mesons, electrons from beauty-hadron decays, J/ψ mesons, and Υ mesons as a function of p_T for Pb-Pb collisions at $\sqrt{s_{NN}} = 5.02$ TeV in the 30-50% centrality class [38].

The nuclear modification factors measured by the three experiments are below unity. Specifically, the R_{AA} estimated by NA50 at $\sqrt{s_{NN}} = 17$ GeV shows a suppression that increases with multiplicity. In contrast, the ALICE results in Pb-Pb collisions at $\sqrt{s_{NN}} = 5.02$ TeV indicate that at LHC energies, the J/ψ suppression is less pronounced and its dependence on multiplicity is reduced. This is due to the higher production of c quarks at greater

energies. Consequently, the recombination of a quark from a dissociated $q\bar{q}$ pair with an antiquark from another dissociated $q\bar{q}$ pair is more likely to occur. This effect, known as **quarkonia regeneration**, indicates that part of the charmonia production arises from the statistical recombination of charm and anti-charm quarks originating from unrelated hard scatterings. The regeneration effect is expected to be stronger for charmonia than for bottomonia states, as it depends on the number of heavy-quark pairs produced in the collisions, which is smaller for bottom quarks compared to charm quarks.

Since heavy quarks are produced in the initial hard scattering, they are not expected to be in equilibrium at the formation time of the **QGP** and their dynamical properties can be different from that of light partons. Heavy quarks participate marginally to **QGP** collective motions and the bulk flow is transferred to the charm and beauty quarks via the multiple interactions with the medium constituents. For this reason, it is interesting to study the heavy quark elliptic flow (see Sect. 1.5.2) of different open heavy-flavour hadrons (prompt D mesons) and quarkonia. They are reported together with the elliptic flow of pions in Fig.1.21-right. D mesons, which are the lightest hadrons containing a charm-quark, are characterised by a v_2 with a p_T trend similar to pions elliptic flow. This suggests that D mesons are strongly affected by the surrounding medium, participating in the collective motion of the **QGP**. For what concerns the J/ψ mesons, which do not contain light-flavour quarks, they exhibit a significant positive elliptic flow with a similar p_T dependence. This relatively large flow is in agreement with the scenario of J/ψ formation via recombination during the late stages of the collision and when the charm-quark flow is fully developed. The beauty quark seems to be less affected by flow effects and the v_2 of open beauty hadrons is significantly smaller than open charm hadron one. In contrast to the other particles, Υ mesons do not show any significant elliptic flow. Below $p_T < 4$ GeV, an apparent mass hierarchy can be appreciated: the lighter the particle, the greater the elliptic flow, as expected in a hydrodynamical description of **QGP** evolution.

1.5.4 Hard probes: high p_T particles and jets

High- p_T partons are produced in hard-scattering processes in the early stages of the collision. Nevertheless, partons from the hard process cannot be observed directly since they hadronise into a collimated spray of particles. This object is defined as a **jet** and can be measured experimentally. To reconstruct it, an algorithm is used to combine the particles that belong to the jet, mapping the final state particle momenta to jet momenta. Various algorithms are available and therefore there is a no unique definition of a jet. From a theoretical perspective, the jets which are reconstructed experimentally should correspond to objects which can be calculated perturbatively. One way to ensure calculability is to require that the jet reconstruction algorithms satisfy the conditions of Infrared and Collinear (**IRC**) safety [60]. **IRC**-safe jet reconstruction algorithms satisfy two conditions:

- Infrared (IR) safety: it means that the result of the jet algorithm doesn't change if a very low-energy (infrared) particle is added or removed. Such a particle is usually too weak to significantly alter the jet's structure, so the algorithm should ignore it.
- Collinear (C) safety: the reconstructed jets in an event will not change if a track is split into two collinear tracks which together carry the same four-momentum of the

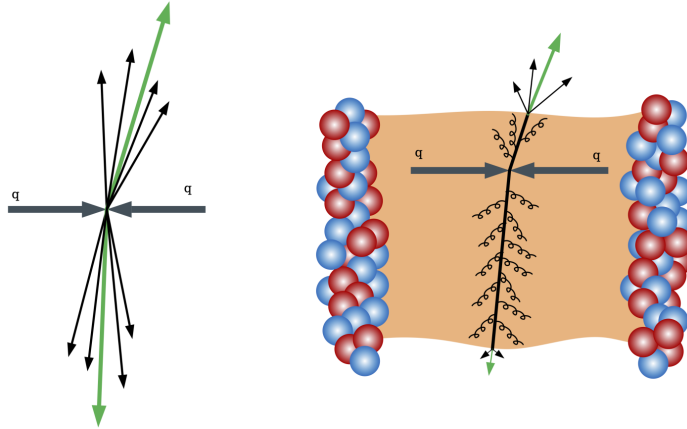


Figure 1.22: Sketch of jet production in pp collisions (left) and in AA collisions (right).

original track.

These requirements remove divergences in jet calculations and ensure theoretical calculations can be done.

One class of algorithms is represented by sequential clustering algorithms. It is based on the distance between particles inside the cone and assumes that particles have small differences in transverse momenta. This algorithm determines the smallest distance and verifies if it is between two particles or if it is between a particle and the jet axis: in the first case particles are combined, in the latter the algorithm stops. An example of a sequential clustering algorithm is the so-called “anti- k_T ”, which is widely used to reconstruct jets [61]. A typical parameter used in the jet properties is the jet radius R , which defines up to which point separate particles are associated to a single jet.

Jets are largely produced at high energy colliders and Fig. 1.22 shows a sketch of jet production in pp and AA. In pp collisions, these sprays of hadrons arise from the fragmentation of energetic quarks and gluons generated in high- Q^2 interactions, as sketched in Fig. 1.22–left. Since their production cross sections in the vacuum can be calculated analytically in pQCD, they permit to test various theoretical calculations. On the contrary, when the parton shower evolves in the QGP, the parton colour-charged constituents interact with the medium and lose energy via inelastic (gluon radiation) and elastic (scattering) processes, as sketched in Fig. 1.22–right. This modification of the parton shower was first proposed by Bjorken in 1983 [62] and it is commonly defined as *jet quenching*.

This has been explored for instance in the BDMPS-Z framework [63, 64], which shows that interference between scattering and emission processes generates a characteristic dependence of the energy loss on the square of the in-medium path length. Since at high- p_T , radiative processes are the dominant energy loss mechanism, the loss of energy can be approximated by:

$$\Delta E_{\text{loss rad}} \propto \alpha_S C_F \hat{q} L^2 \quad (1.24)$$

where α_S is the running coupling parameter (see Eq.(1.4)), L is the length of the medium crossed, and \hat{q} is the medium transport coefficient, that corresponds to the momentum

transferred to the medium per squared unit path-length. Finally, C_F is the Casimir factor, that takes into account the different interaction of quarks and gluons with the medium: gluons lose more energy than quarks ($C_F = 3$ for gluons and $C_F = 4/3$ for quarks). The energy loss of quarks and gluons is expected to follow this ordering:

$$\Delta E_{\text{loss rad}}(g) > \Delta E_{\text{loss rad}}(u, d, s) > \Delta E_{\text{loss rad}}(c) > \Delta E_{\text{loss rad}}(b) \quad (1.25)$$

At LHC energies, partons scatter with high probability into other two partons, producing two back-to-back jets in the final state (dijet). The presence of the jet quenching implies these effects on the final state in Pb–Pb collisions with respect to pp ones:

- suppression of the high- p_T hadrons, observed comparing the measurement of yield of particles in AA to pp ones;
- in jet back-to-back processes, attenuation or total suppression of one of the jets, usually measured with angular correlations;
- modification of the energy distribution of the particle produced from the hadronization: enhancement of low- p_T particles and suppression of the high- p_T ones, estimated measuring the fragmentation functions or jet structures.

One of the ways to explore the effects of jet quenching is by extracting the nuclear modification factor R_{AA} , which was defined in Eq. (1.20). Figure 1.23–left reports the nuclear modification factor as a function of the transverse momentum for charged particles measured by ALICE at $\sqrt{s_{NN}} = 5.02$ TeV for central and peripheral Pb–Pb collisions and p–Pb collisions [38].

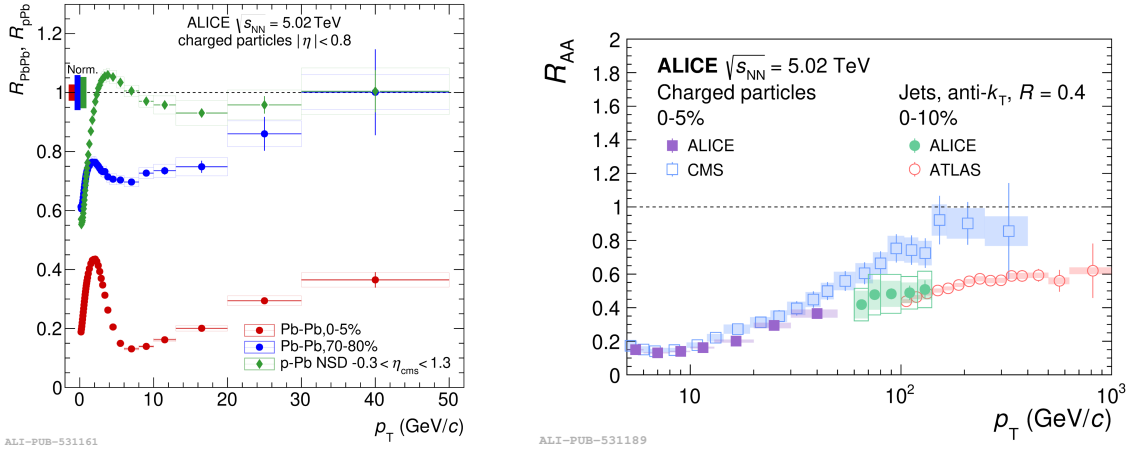


Figure 1.23: Left: R_{AA} for charged particles in central (0-5%) (full red circle) and peripheral (70-80%) (full blue circle) Pb–Pb collisions and R_{pA} for p–Pb collisions (full green diamond) at $\sqrt{s_{NN}} = 5.02$ TeV by ALICE [65]. Right: nuclear modification factor for charged particles by ALICE (full violet square) and CMS (empty light blue square) and inclusive jets by ALICE (full green circle) and ATLAS (empty red circle) in central Pb–Pb collisions at $\sqrt{s_{NN}} = 5.02$ TeV [38].

The R_{pA} is close to unity for $p_T > 2$ GeV/ c , hence the particle production approximately follows the $\langle N_{\text{coll}} \rangle$ scaling. In central Pb–Pb collisions, the nuclear modification factor shows a peak around 2–3 GeV/ c , partly due to collective radial flow and enhancement in the baryon-to-meson yield ratio; then at high- p_T the R_{AA} is suppressed. In peripheral collisions, the

R_{AA} is below unity at $p_T \simeq 6 \text{ GeV}/c$ and increases to unity as the p_T increases. For p_T below $3 \text{ GeV}/c$, the R_{AA} and the R_{pA} are both below one. This is because binary scaling fails in this p_T range, where soft processes dominate and the yield of produced particles is expected to scale with $\langle N_{\text{part}} \rangle$.

Another way to investigate the parton energy loss is with the measurement of the jet fragments' angular distributions. Estimating the angular distributions consists of measuring the azimuthal correlations $\Delta\varphi = \varphi^{\text{trig}} - \varphi^{\text{assoc}}$ between two objects: a high- p_T trigger particle or jet and the associated objects, hadrons or jets, emitted in the opposite direction relative to the trigger. The $\Delta\varphi$ distributions are usually characterised by a two peaks correlation distribution: the peak around $\Delta\varphi \simeq 0$ is defined as **near side** peak and it is typical of jet production, while the peak around $\Delta\varphi \simeq \pi$ is called **away side** peak and it is due to back-to-back jet events. Figure 1.24-left reports the di-hadron azimuthal correlations as a function of $\Delta\varphi$ measured by the STAR Collaboration [66, 67] at RHIC.

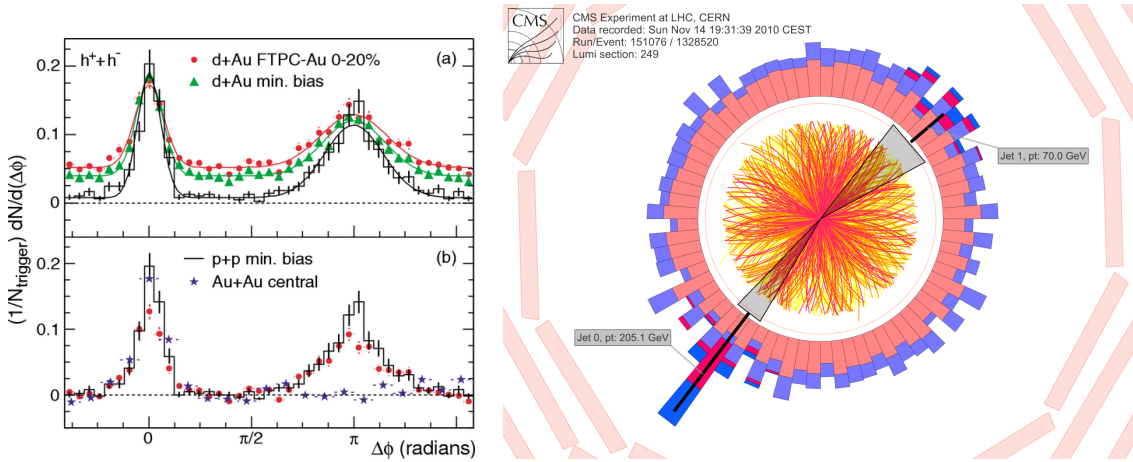


Figure 1.24: Left: azimuthal correlation distributions in pp (black line), in central $d\text{-Au}$ (full red circle), in minimum bias $d\text{-Au}$ (full green triangle) and central $Au\text{-}Au$ (full blue star) collisions measured by the STAR Collaboration. The trigger hadron p_T is $4 < p_T < 6 \text{ GeV}/c$, while the selected charged particles p_T are between $2 < p_T^{\text{assoc}} < p_T^{\text{trig}} \text{ GeV}/c$ [66, 67]. Right: CMS event display at LHC for a single $Pb\text{-}Pb$ collision, showing a dijet event [68].

The $\Delta\varphi$ distributions measured in pp and $d\text{-Au}$ collisions measured at RHIC show the typical two-peak distribution, as reported in Fig. 1.24-top left. Figure 1.24-bottom left reports the angular distributions in pp , central $d\text{-Au}$ and $Au\text{-}Au$ collisions. The near side peaks are similar in all three systems, while the away-side peak in central $Au\text{-}Au$ shows a dramatic suppression relative to pp and $d\text{-Au}$ [67]. This suppression is because of the presence of the medium and the apparent disappearance of the peak is due to the selection done on the p_T of associated particles, which in this case is quite high. When the correlated hadrons are selected with a relaxed cut, the away side jet can be recovered, but the number of correlated particles, that is the peak integral, is lower and the distribution is wider than the one found in pp and $d\text{-Au}$ collisions. It is possible to appreciate this phenomenon by looking at the Compact Muon Solenoid (CMS) experiment event display at LHC [68] shown in Fig. 1.24-right for a single $Pb\text{-}Pb$ collision: the trigger jet is the one indicated as “*Jet 0*” with a p_T of about $200 \text{ GeV}/c$, while the associated jet, defined as “*Jet 1*” is emitted in the opposite direction with a p_T of about $70 \text{ GeV}/c$. The associated jet does not disappear, but

it is lower in energy and broader in shape than the trigger jet.

The two jets, emitted back-to-back as in Fig. 1.24-right, are expected to experience asymmetric energy loss due to traversing unequal path lengths in the QGP. This asymmetry is driven by the geometry of the overlapping nuclei and the relative orientation of the jet trajectories through the evolving medium. A way to access this asymmetric energy loss is by measuring the momentum balance x_J , defined as:

$$x_J = \frac{p_{T,2}}{p_{T,1}}, \quad (1.26)$$

where $p_{T,1}$ is the transverse momentum of the highest- p_T (leading) jet and $p_{T,2}$ is the transverse momentum of the second-highest- p_T (subleading) jet. The dijet momentum balance is sensitive to the difference in energy loss between the leading and sub-leading jets. Figure 1.25-left reports the di-jet yield-normalized x_J distributions for a $p_{T,1}$ (p_T^{leading}) between 128 and 141 GeV/c in pp collisions and in central and peripheral Pb–Pb ones measured by the A Toroidal LHC ApparatuS (ATLAS) experiment [69].

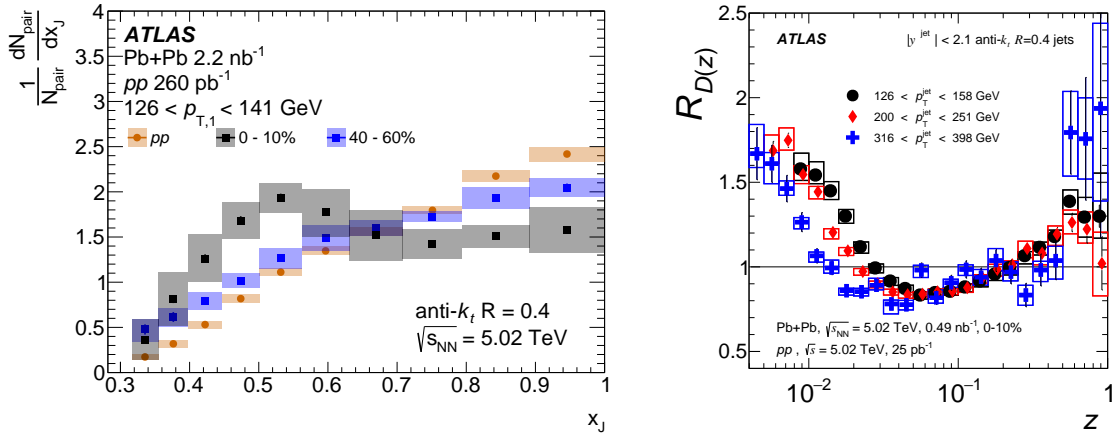


Figure 1.25: Left: measurement of di-jet yield-normalized x_J distributions measured by the ATLAS Collaboration in 0–10% (full black square) and 40–60% (full blue square) Pb–Pb and in pp (full orange circle) collisions at $\sqrt{s_{\text{NN}}} = 5.02 \text{ TeV}$ [69]. Right: ratio $R_{D(z)}$ between fragmentation functions in central Pb–Pb and pp collisions at $\sqrt{s_{\text{NN}}} = 5.02 \text{ TeV}$ measured by ATLAS. Ratios are shown for three different $p_{T,\text{jet}}^{\text{jet}}$ ranges: 126–158 GeV (full black circle), 200–251 GeV (full red diamond) and 316–398 GeV (full blue cross) [70].

The x_J distribution in pp collisions reports a peak at $x_J \simeq 1$, corresponding to nearly symmetric dijet events. On the other hand, in central Pb–Pb collisions, the distribution has a peak around $x_J \simeq 0.5$, indicating that the p_T of the jets is more unbalanced than in pp collisions where the QGP is not present. This maximum suggests that asymmetric dijets, that is dijets highly imbalanced in p_T are more probable in central Pb–Pb collisions than in pp. This is also an indication that one of the partons (jet) is more quenched due to the larger QGP medium path traversed. This peak feature becomes less pronounced with decreasing centrality and as well as with increasing $p_{T,1}$. These measurements can help constrain models that describe the path-length dependence of jet energy loss and its fluctuations. Energy loss fluctuations are the main contributor to dijet imbalance, as they reflect the random interactions of partons with the medium, variations in the distances they travel, and the effects of jet quenching. Together, these factors lead to differences in the final energy of the two jets. During a collision, the energy distribution within the jets can

fluctuate due to processes like parton energy loss or hadronization. In a dense medium such as the QGP created in heavy-ion collisions, one jet can lose more energy than the other as it passes through, causing the imbalance. However, it is not possible to precisely determine the distance partons traverse because the location of the hard process within the QGP is unknown.

Until now we have discussed the presence of energy loss using jets as compact objects. However, since the parton at the origin of the jet radiates energy in the presence of the QGP, we would like to probe the medium modifications of the internal components of the jet and to understand how the energy is redistributed in the final state. The jet radiation pattern can be explored via measurements of the fragmentation functions. One typically checks this by comparing the jet fragmentation functions $D(z_T)$ in pp and in Pb–Pb collisions. The fragmentation functions are estimated by counting the number of constituents within a jet according to their relative contribution to the overall jet energy. The fragmentation function is defined as:

$$D(z_T) = \frac{1}{N^{\text{trig}}} \frac{dN^{\text{charg}}}{dz_T} \quad (1.27)$$

$$z_T = p_T^{\text{charg}} / p_T^{\text{jet}} \quad (1.28)$$

where N^{trig} is the number of jet triggers, N^{charg} is the number of charged particles in the jet and z_T (z) is the momentum fraction of the jet carried by the charged particles.

Figure 1.25–right shows the ratio of jet fragmentation functions $D(z_T)$ in central Pb–Pb collisions relative to pp collisions as a function of z_T for three p_T^{jet} intervals measured by ATLAS [70]. At low- z_T a strong enhancement is observed; while in the intermediate region $0.03 < z_T < 0.1$, the ratios are below unity. Partons would normally contribute in this intermediate region, but since partons interact with the medium, the energy lost is transferred mainly to soft particles, resulting in the observed low- z_T enhancement. At high- z_T ($z_T > 0.5$) there seems to be an enhancement of high- z_T particles in Pb–Pb collisions, consistent for all the three p_T^{jet} ranges. This excess can be related to a selection bias: the measured jets with high- z_T hadrons are jets with a harder fragmentation, such as narrow jets, that have been quenched less than wider jets. Otherwise, since quark jets generally exhibit harder fragmentation than gluon jets, this can also be interpreted as evidence for stronger energy loss in gluon-initiated jets compared to quark-initiated jets (see Eq. (1.25)), resulting in an enhanced quark fraction at a given p_T^{jet} [71].

To better understand the medium modification of the parton fragmentation process, it is also possible to explore the jet transverse characteristics. This can be achieved by measuring, for example, the angular distribution of hadrons with respect to the jet axis within the jet cone that corresponds to the jet radial momentum profile. The latter observable can be defined as:

$$P(\Delta r) = \frac{1}{\delta r} \frac{1}{N_{\text{jets}}} \sum_{\text{jets}} \sum_{\text{tracks} \in (\Delta r_a, \Delta r_b)} p_{\text{T}}^{\text{track}} \quad (1.29)$$

$$\Delta r = \sqrt{(\varphi_{\text{jet}} - \varphi_{\text{track}})^2 + (\eta_{\text{jet}} - \eta_{\text{track}})^2}$$

where Δr is angular distance from the jet axis; Δr_a and Δr_b define the annular edges of Δr and $\delta r = \Delta r_b - \Delta r_a$. Figure 1.26 reports the ratio of the jet radial momentum profile in

Pb–Pb collisions relative to pp ones as a function of the angular distance Δr for leading and subleading jet, measured by CMS [72].

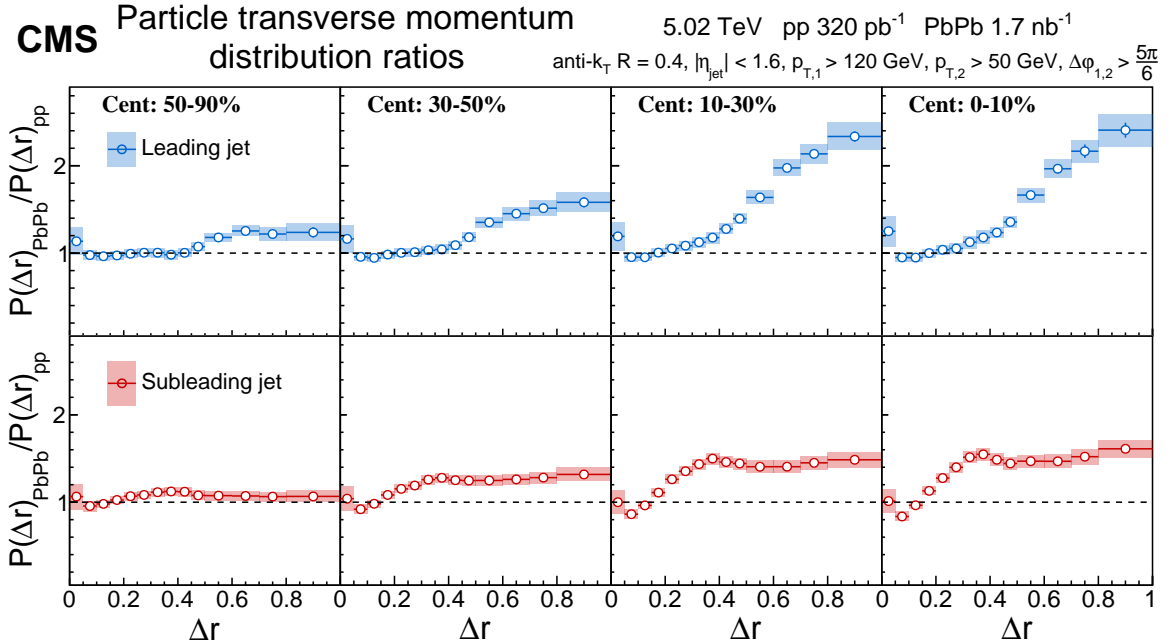


Figure 1.26: Ratio of the jet radial momentum distributions as a function of the angular distance Δr from the jet axis in Pb–Pb for various centrality intervals relative to that measured in pp collisions for leading jets (empty blue circle) with $p_T > 120 \text{ GeV}/c$, $R = 0.4$ and subleading jets (empty red circle) $0.7 < p_T^{\text{track}} < 300 \text{ GeV}/c$ [72].

Regarding the leading jets, shown in Fig. 1.26–top, there is a clear enhancement of the Pb–Pb jet radial momentum over the pp distribution. This enhancement is visible for $\Delta r > 0.4$, that corresponds to charged particles emitted farther away from the jet axis, and it is most pronounced in the most central collisions. On the other hand, the subleading jets, shown in Fig. 1.26–bottom, have a lower enhancement. This is because they have significantly lower p_T compared to leading jets and their jet shapes are wider. Overall, a redistribution of energy is observed from small angles with respect to the jet axis to larger angles when comparing Pb–Pb and pp events. This behaviour suggests significant out-of-cone radiation associated with the jet. Thus, jets defined with a larger cone radius R should recover more of this large-angle radiation than jets defined with a smaller cone and therefore should be expected to incorporate more sources of potential energy loss. The magnitude of the out-of-cone radiation will depend on the parton-medium interactions and also differences in the energy-loss mechanisms between quark and gluon jets [73].

1.6 Conclusions

Through the selection of (di)jet measurements presented in the last Section, we have understood that jets have complex structures characterized by both macroscopic quantities (such as their energy and direction) and microscopic properties. Probing the medium with a jet is not equivalent to using a single parton with a fixed (hard) perturbative scale: the measurement of the jet energy in Pb–Pb collisions is not exactly the parton energy at the origin of

the process. This is because, also when the leading jet is selected, it traverses the medium and loses energy. In addition, the measured jet area is restricted to limit the large quantity of combinatorial background and part of the particles belonging to the jet can be missed. Thus, these measurements cannot always be interpreted easily.

An alternative is to find a way to tag the parton at the origin of the hard process. This can be done by selecting high- p_T photons produced in $2 \rightarrow 2$ processes from Compton and annihilation processes. Since the photon does not lose energy in the QGP via the strong interaction, it provides a calibrated reference of parton initial momentum and direction. Thanks to the unmodified photon energy, the γ -tagged jet events are an ideal configuration to study medium modification. Moreover, jets opposite in azimuth from a high momentum photon can also provide an enhancement of quark-jets over gluon-jets (jets initiated by a quark or a gluon, respectively).

The topic of this Thesis is dedicated to the study of partons recoiling from high energy photons, to extract the angular correlations between these photons and hadrons. For this reason, the next Chapter will be devoted to photons in heavy-ion collisions and to the various measurements that can be done with them.

Chapter 2

Photons: a way to probe the QGP

2.1 Photon sources	44
2.1.1 Direct photons	47
2.1.2 Prompt photons	48
2.2 Isolated photons measurements	50
2.3 Conclusions	64

In the previous Chapter, we explored various probes of the quark-gluon plasma, with a particular focus on those that reveal modifications due to jet quenching in heavy-ion collisions. As mentioned, photons are of significant interest in this context because they do not interact via the strong force. However, to study photons originating, specifically from high-energy partonic processes before QGP formation, it is essential to understand the various production mechanisms involved. In this Chapter, we will discuss the different photon sources in heavy-ion collisions and their properties. Additionally, we will explore the observables that can be studied with photons and the insights that can be obtained on the nature of the QGP.

2.1 Photon sources

In high-energy heavy-ion collisions, photons are produced during all the phases of the collision. The main difference between quarks and gluons is that photons are colour-neutral, therefore they do not interact with the QGP; however, they can still be used to “probe” the medium in very different ways. Considering which is the photon production origin, four main classes can be distinguished [74]:

- photons produced in the initial hard scattering from two incident partons of the incoming nuclei. At LO, their production primarily occurs through Compton scattering ($qg \rightarrow \gamma q$) and annihilation ($q\bar{q} \rightarrow \gamma g$) processes, with a much smaller contribution from the $q\bar{q} \rightarrow \gamma\gamma$ process. At NLO corrections are coming from subprocesses such as $qg \rightarrow \gamma gg$ and $q\bar{q} \rightarrow \gamma gg$ [75]. Since at LO, their production is mainly from $2 \rightarrow 2$ processes, in this Thesis, those photons are denoted as $\gamma_{2 \rightarrow 2}$;

2.1. Photon sources

- fragmentation photons, γ_{fragm} : they derive from the collinear fragmentation of a final-state parton into a photon [75]. They are accompanied by hadronic activity;
- thermal photons, γ_{therm} , emitted by the quark-gluon plasma or by the hadron gas;
- decay photons, γ_{decay} , produced by the hadronic decays, mainly from neutral mesons decays ($\pi^0 \rightarrow \gamma\gamma$ or $\eta \rightarrow \gamma\gamma$).

In this Thesis, the following notation will be used: the term **inclusive** (γ_{inc}) will indicate all the types of photons produced in a collision; the term **prompt** (γ_{prompt}) will define the group that includes fragmentation photons γ_{fragm} and photons $\gamma_{2 \rightarrow 2}$. Then, the term **direct** (γ_{dir}) will be referred to as the sum of prompt and thermal photons. The sum of all these contributions is reported in Eq. (2.1):

$$\gamma_{\text{inc}} \simeq \underbrace{\gamma_{2 \rightarrow 2} + \gamma_{\text{fragm}}}_{\gamma_{\text{prompt}}} + \gamma_{\text{therm}} + \gamma_{\text{dec}}. \quad (2.1)$$

The different types of photons produced in a heavy-ion collision are sketched in Fig. 2.1.

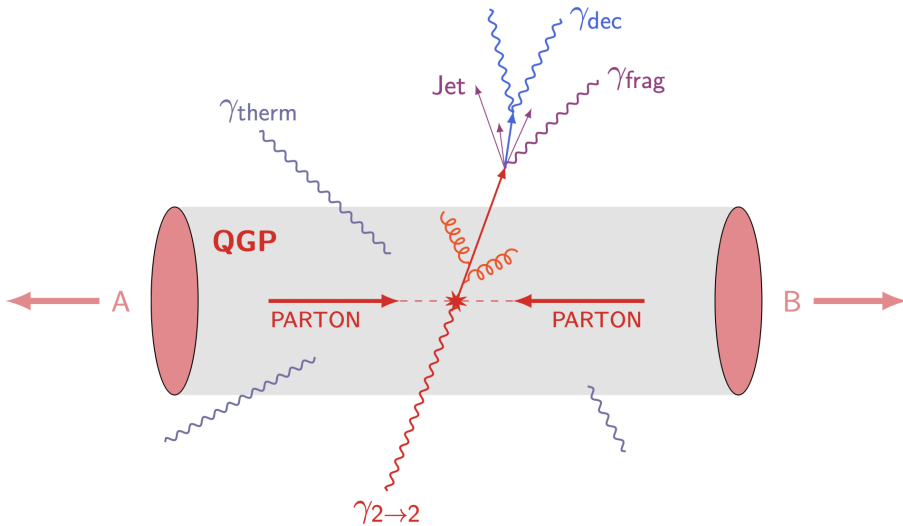


Figure 2.1: Sketch of photon production during a heavy-ion collision between nuclei A and B. They include: $\gamma_{2 \rightarrow 2}$, γ_{decay} , γ_{fragm} and γ_{therm} .

The $\gamma_{2 \rightarrow 2}$ and γ_{fragm} are produced in the early stages of the collision and it is not possible to clearly separate them by applying a “hard cut” neither experimentally nor from the theory side. Nevertheless, it is feasible to apply a measurable criterium to select $\gamma_{2 \rightarrow 2}$: the isolation method, which consists of requiring the sum of the transverse energies (or transverse momenta) of produced particles in a cone around the photon candidate direction to be smaller than a given threshold value [76]. Since fragmentation photons are accompanied by other jet fragments, the isolation selection permits the suppression of their contribution. For the same reason, the isolation criterium suppresses the γ_{decay} . Thermal photons can be emitted in the presence of the QGP medium or the hot hadron gas. Their production and the QGP properties they probe (temperature and size) depend on the time of γ_{therm} emission: from early production from the expanding QGP (high T , small size) to late production from the

hadron gas (low T , larger size).

Although photons are colour-neutral, some of the previously listed photons can be “influenced” by the presence of the medium. This is the case for example of γ_{decay} , that are affected by the **QGP** because they derive from hadronic decays. In the same way, the γ_{fragm} are sensitive to the **QGP** phase because they come from the fragmentation of a parton. The photons from $2 \rightarrow 2$ processes are not affected by the **QGP** and they can have a “memory” of the recoiling parton’s properties before its propagation in the medium.

These different properties of photons can be inspected by measuring the nuclear modification factor. Figure 2.2–left shows the R_{AA} of direct γ (in this case corresponding to $\gamma_{2 \rightarrow 2}^1$), of π^0 and η mesons, and of hadrons as a function of p_{T} in central Au–Au collisions at $\sqrt{s_{\text{NN}}} = 200$ GeV measured by **RHIC**’s experiments.

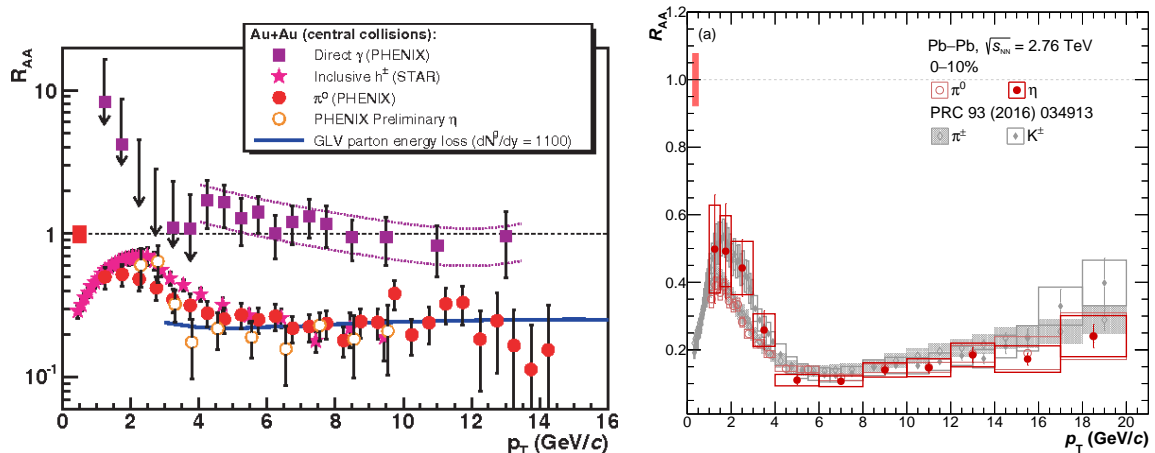


Figure 2.2: Left: nuclear modification factor of direct γ (full violet square), inclusive hadrons (full pink star), π^0 mesons (full red circle) and η mesons (empty yellow circle) as a function of p_{T} for central Au–Au collisions at RHIC [77, 78]. Right: nuclear modification factor for the π^0 (empty red circle), η mesons (full red circle), kaons (full grey circle) and charged pions (empty grey circle) in 0–10% Pb–Pb collisions at $\sqrt{s_{\text{NN}}} = 2.76$ TeV measured by **ALICE** [79].

The direct photons R_{AA} is compatible with unity, confirming that the yield of $\gamma_{2 \rightarrow 2}$ is not affected by the presence of the **QGP**. Instead, the nuclear modification factors of π^0 and η mesons are strongly below unity above $p_{\text{T}} > 4 \text{ GeV}/c$. Below $p_{\text{T}} < 4 \text{ GeV}/c$, the R_{AA} of the mesons is less suppressed and the presence of the bump is related to the binary scaling failing because of the soft probes production (see Sect. 1.4.2). Since the π^0 and η mesons are affected by the **QGP**, their daughter photons γ_{decay} inherit as well as a suppression. The hadron R_{AA} follows a similar suppressed trend. Figure 2.2–right reports the nuclear modification factor of charged and neutral pions, η mesons and charged kaons as a function of p_{T} measured by the **ALICE** experiment in central Pb–Pb collisions at $\sqrt{s_{\text{NN}}} = 2.76$ TeV. The π^0 and η mesons R_{AA} are suppressed above $p_{\text{T}} > 4 \text{ GeV}/c$, while there is a maximum around $p_{\text{T}} \sim 2 \text{ GeV}/c$, again because of the binary scaling failing. The R_{AA} obtained at **RHIC** and **LHC** follow a similar trend at low p_{T} but the π^0 and the η mesons measured by **ALICE** show a larger suppression compared to the one measured at **RHIC**. The **ALICE** results confirm a dependence of the suppression on the center-of-mass energy and indicate

¹RHIC’s experiments use a different notation with respect to the one used in this Thesis

a larger suppression for increasing collision energy. Moreover, the results obtained at LHC report a rise trend for $p_T \gtrsim 10 \text{ GeV}/c$, not measured at RHIC.

Before focusing on the $\gamma_{2\rightarrow 2}$, which are one of the main interests of this Thesis, an overview on the direct photon measurements will be presented.

2.1.1 Direct photons

The direct photons include γ_{prompt} and γ_{therm} . The $\gamma_{2\rightarrow 2}$ production is dominant above $p_T \gtrsim 5 \text{ GeV}/c$ [80] with a spectrum that follows a power law. On the other hand, the thermal photons are mostly generated below $p_T \lesssim 4 \text{ GeV}/c$ with an exponential spectrum. Since they are originated by interactions between the constituents of the thermalized QGP or hadron gas, they contain information about the plasma such as its temperature and collective flow [81]. The measurement of direct photons is interesting because it permits to distinguish between the different photon classes, displaying the contribution of thermal photons and prompt photons. One can quantify the fraction of direct photon signal produced via the measurement of the double ratio R_γ , defined as:

$$R_\gamma = \frac{\gamma_{\text{incl}}}{\gamma_{\text{decay}}} = \left(\frac{\gamma_{\text{incl}}}{\pi_{\text{param}}^0} \right) / \left(\frac{\gamma_{\text{decay}}}{\pi_{\text{param}}^0} \right), \quad (2.2)$$

where γ_{incl} is the measured inclusive photon production, π_{param}^0 is a parameterization of the measured π^0 spectrum, and γ_{decay} is the calculated decay photon spectrum. Using the double ratio, the direct photon yield can be calculated from the inclusive photon yield as [80]:

$$\gamma_{\text{direct}} = \gamma_{\text{incl}} - \gamma_{\text{decay}} = \left(1 - \frac{1}{R_\gamma} \right) \cdot \gamma_{\text{incl}} \quad (2.3)$$

If the R_γ is above 1 in the p_T range between 1 and 5 GeV/c it implies the presence of another type of photons apart from the prompt ones. Figure 2.3–left shows the R_γ as a function of p_T for two centralities in Pb–Pb collisions.

It is possible to appreciate a clear excess for a p_T between 1 and 3 GeV/c and it cannot be attributed to the prompt photons, which dominate above 5 GeV/c . To confirm the origin of this excess, the results are compared with models. At high- p_T , the R_γ is consistent with prompt photon production described by pQCD and JETPHOX theory calculations. Hence, the significant excess at lower p_T indicates that there is an excess of thermal photons coming from the QGP. The non-prompt direct-photon spectrum at $\sqrt{s_{\text{NN}}} = 2.76 \text{ TeV}$ is obtained by subtracting the scaled pQCD prompt photon contribution from the direct photon spectrum in central and semi-central collisions. The residual thermal photons spectrum is shown, as a function of p_T , in Fig. 2.3–right. From the thermal photon spectrum, it is feasible to extract an effective temperature T_{eff} using an exponential fit ($f = Ae^{-p_T/T_{\text{eff}}}$), where T_{eff} is a convolution of the evolution temperature over all the collision phases [80]. The spectra can be fitted in two different p_T regions characterised by different slopes, thus by different temperatures. The effective temperatures T_{eff} in the intermediate p_T range (in 0-10%, $T_{\text{eff}} \simeq 400 \text{ MeV}$) are systematically larger compared to those obtained at low p_T (in 0-10%, $T_{\text{eff}} \simeq 350 \text{ MeV}$), although consistent within uncertainties. This may indicate an earlier photon emission, and thus a sensitivity to pre-equilibrium photon production [80]. The measured values suggest initial temperatures well above the critical temperature

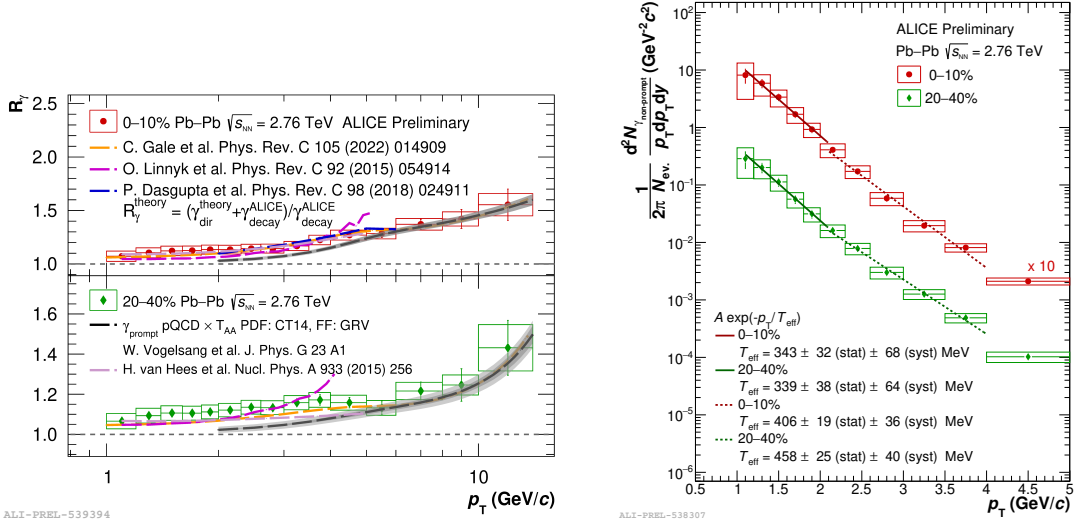


Figure 2.3: Left: R_γ as a function of p_T for 0–10% central (top, red full circle) and 20–40% semi-central (bottom, green full diamond) Pb–Pb collisions at $\sqrt{s_{NN}} = 2.76$ TeV compared with different model calculations by ALICE. Right: thermal photon spectra as a function of p_T for 0–10% central (red full circle) and 20–40% semi-central (green full diamond) in Pb–Pb collisions at $\sqrt{s_{NN}} = 2.76$ TeV by the ALICE Collaboration [80]

$T_C \sim 150 - 160$ MeV (approx. 1.8×10^{12} K) at which the transition between ordinary hadronic matter and the QGP occurs. The ALICE measurement also indicates that the LHC has produced the hottest piece of matter ever formed in a laboratory.

2.1.2 Prompt photons

As already said, the $\gamma_{2\rightarrow 2}$ and γ_{fragm} , which are part of the prompt photons are in principle indistinguishable experimentally, but by applying the isolation method, previously referenced and to be discussed in detail later (Sect. 5.3), it becomes possible to suppress the γ_{fragm} contribution.

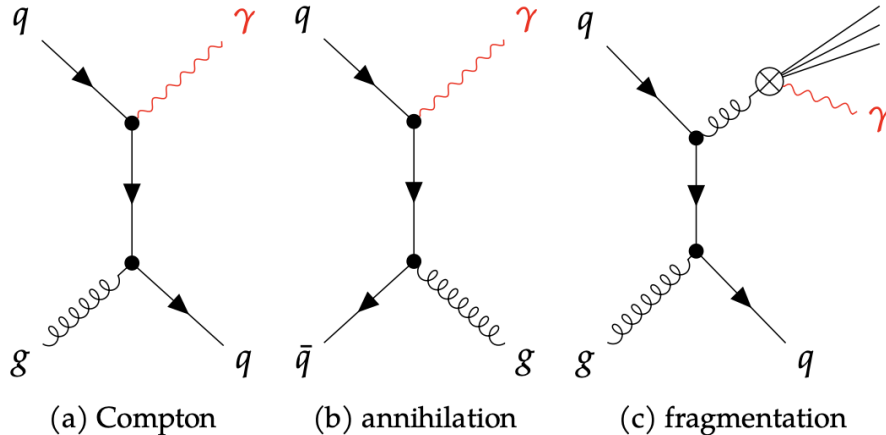


Figure 2.4: Feynman diagrams for prompt photon production.

Figure 2.4–left and middle reports the Feynman diagrams for Compton (a) and annihilation (b) processes, which consist in the emission of a photon and a parton back-to-back. Then the parton fragments and hadronises, giving origin to a jet of particles. This is the

2.1. Photon sources

γ -jet (GJ) process. Since these productions involve electromagnetic interaction, they are less probable than purely QCD processes. Examples of QCD processes are $qg \rightarrow qg$ or $q\bar{q} \rightarrow gg$ and they lead to two jets produced back-to-back, which are called jet-jet (JJ) process. Furthermore, prompt photons can also be produced by fragmentation, as shown in Fig. 2.4-right (c). Since the production is due to the parton fragmentation, it can happen in any collision phase. Once emitted, these photons are surrounded by the hadrons from the jet fragmentation.

Photons produced in Compton and annihilation processes can also be referred to as direct prompt photons, due to their point-like connection, at leading order (LO), to the incoming partons. However, calculations performed beyond LO also include contributions of the fragmentation type, which result from a cascade of successive collinear splittings of an outgoing parton, that end up with a quark-photon splitting. The fragmentation of an outgoing quark or gluon to a photon can be absorbed in a non-perturbative parton-to-photon fragmentation function $D_{q/g}^\gamma(z, \mu_f)$, that is defined within a certain factorization scheme at given factorization scale μ_f [82]. The following equation reports the cross-section of prompt photons $\sigma(p_\gamma)$:

$$\sigma(p_\gamma) = \sum_{a=q,\bar{q},8} \int_0^1 \underbrace{\frac{dz}{z} \hat{\sigma}^a \left(\frac{p_\gamma}{z}; \mu_R, \mu, \mu_f \right)}_{\text{fragmentation}} \cdot D_a^\gamma(z; \mu_f) + \underbrace{\hat{\sigma}^\gamma(p_\gamma; \mu_R, \mu, \mu_f)}_{\text{direct}}, \quad (2.4)$$

where $\hat{\sigma}^a$ is the partonic cross-section for the production of a parton a , $\hat{\sigma}^\gamma$ is the partonic cross-section for a γ and $D_a^\gamma(z, \mu_f)$ is the parton-to-photon fragmentation function. The calculation depends on three different arbitrary scales: the renormalization scale μ_R , which enters the partonic cross-section via the determination of α_s , the factorization scale μ coming from the PDFs as well as the fragmentation scale μ_f of the fragmentation function. Figure 2.5-left shows the magnitude of the three processes that contribute to the total prompt photon production cross-section as a function of the photons transverse energy E_T^γ at mid-rapidity. The results derive from a simulation in pp collisions at $\sqrt{s} = 14$ TeV at LHC.

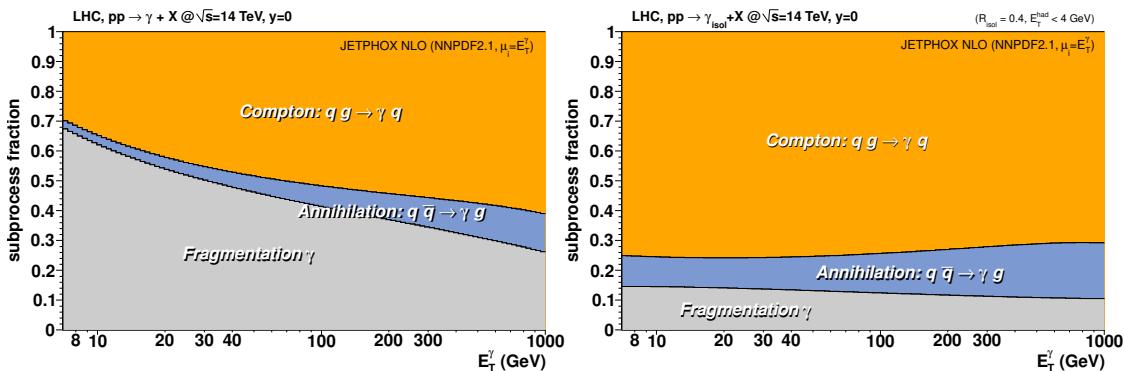


Figure 2.5: Fraction of different processes, Compton (orange), annihilation (blue) and fragmentation (grey), that contributes to the prompt photon production in pp collisions at $\sqrt{s} = 14$ TeV at LHC from simulation without (left) and with (right) the isolation method [83].

Below $E_T^\gamma < 20$ GeV, the dominant contribution is given by the fragmentation photons. At higher energies, the contribution from Compton processes takes over and becomes

predominant. The fraction of the annihilation processes is much lower than Compton and fragmentation ones. Apart from the presence of the γ_{fragm} , one of the major difficulties for the measurement of $\gamma_{2 \rightarrow 2}$ is the enormous production in a collision of photons from hadron decays (mainly π^0 and η). To suppress the contribution of γ_{fragm} and γ_{decay} , the isolation criterion is applied, defining a condition on the hadronic activity (energy) in the vicinity of the photon. The isolation method works because of the different production of the $\gamma_{2 \rightarrow 2}$ with respect to the γ_{decay} and γ_{fragm} : the latter are often produced in jets of particles originating from hadronization of the same parent parton, and therefore they will be surrounded by hadronic and electromagnetic activity. A sketch of how the isolation method works is presented in Fig. 2.6. The isolation consists in considering photons where the sum of the

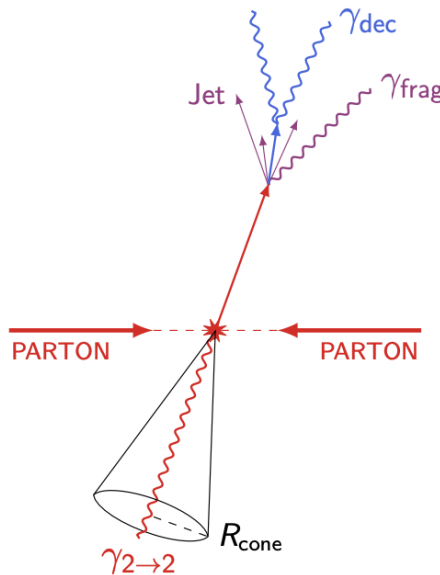


Figure 2.6: Sketch of a collision in which $\gamma_{2 \rightarrow 2}$, γ_{decay} and γ_{fragm} are produced. The isolation method is applied to select the $\gamma_{2 \rightarrow 2}$.

transverse energy p_T of particles within a cone radius R around the photon is below an energy threshold, more details will be illustrated in Sect. 5.3. In Fig. 2.5–right, it is possible to appreciate the power of the isolation method to select the $\gamma_{2 \rightarrow 2}$ in a sample of γ_{prompt} . It reduces the contribution from γ_{fragm} to less than 15% also at very low E_T^γ values and the fraction of γ_{fragm} remains almost constant in the entire energy range. Furthermore, the isolation permits to enhance the selection of $\gamma_{2 \rightarrow 2}$: with a contribution of about 70% by Compton process and 15% by annihilation. From now on the photons selected with the isolation method will be indicated with the notation γ^{iso} .

In the following, various measurements that involve the isolated photons will be illustrated: initially, the γ^{iso} cross section will be discussed, and then the last part of the chapter will be dedicated to the state-of-the-art of γ^{iso} tagged measurements.

2.2 Isolated photons measurements

Isolated photons cross sections

The measurement of isolated photons in pp, pA, and AA collisions is an important tool for studying nuclear matter, as γ^{iso} production occurs early in the evolution of the collision via hard scattering of incoming partons.

The measurement of the isolated-photon rate can be used to test perturbative Quantum Chromodynamics (pQCD) theory calculations, and, in particular, the need to include higher orders than LO and next-to-leading order (NLO). Moreover, isolated photons can also be used to constrain the PDFs and nPDFs in the proton and the nucleus, especially through measurements at p_T^γ below 20 GeV/c, where cold nuclear matter shadowing effects are more significant. The dominant contribution to prompt photon production at the LHC is the quark-gluon Compton diagram [75], which is directly sensitive to the gluon density in the colliding hadrons, that has the largest uncertainty among the PDFs. Therefore, isolated-photon measurements allow us to probe the low- x gluon content of one of the incoming protons.

Additionally, since isolated photons are produced before the QGP formation and do not interact strongly, pQCD can be applied and theoretical models can be easily tested also in AA collisions. The γ^{iso} cross section measurements in AA collisions can also serve as a calibrated reference with which other processes can be compared.

The measurement of the isolated prompt photons p_T spectrum has been explored in pp(\bar{p}) collisions at different fixed-target and collider experiments, producing results at various collisional energies from $\sqrt{s} = 20$ GeV [84] up to 13 TeV [85, 86, 87, 88]. For comparing cross sections measured at different \sqrt{s} , it is better to use the variable $x_T^\gamma = 2p_T^\gamma/\sqrt{s}$, which is also closely related to the Bjorken x [85]. Figure 2.7–left shows the various cross section measurements done at Tevatron, RHIC, SPS and LHC as a function of x_T^γ .

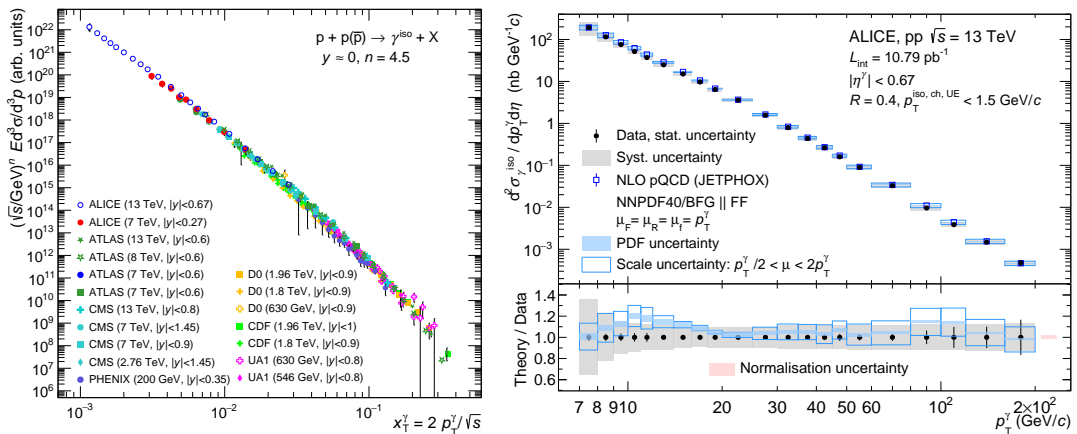


Figure 2.7: Left: Overview of various isolated-photon spectra in pp and $p\bar{p}$ collisions as a function of $x_T = 2p_T^\gamma/\sqrt{s}$ [85]. Right top: isolated-photon differential cross section (full black square) measured in pp collisions at $\sqrt{s} = 13$ TeV. The blue boxes correspond to pQCD calculations with JETPHOX. Right bottom: ratio between JETPHOX calculations and data displayed in the blue boxes, vertical boxes size shows the theory scale and PDF uncertainties. Experimental uncertainties are shown here on the black points centred at unity [85].

All the x_T^γ spectra follow a power-law dependence that corresponds to $\propto 1/\sqrt{s}^n$. The different spectra at different energies are scaled with \sqrt{s}^n and for a $n = 4.5$ they overlap [85].

on a common curve. This scaling behaviour indicates a universal production mechanism of prompt photons, where the extracted exponent is very close to the expected scaling behaviour of a $2 \rightarrow 2$ scattering [89]. This measurement helps to constrain further the gluon PDF at midrapidity in the region $x \approx 1 - 3 \times 10^{-3}$ and reduce its uncertainty values [85]. It is worth noticing: the extremely low x_T^γ (i.e. a p_T^γ around 7 GeV/c) reached by ALICE and the very high x_T^γ reached by CMS [86] and ATLAS [90] experiments (i.e. a p_T^γ around 1–2 TeV/c).

Figure 2.7-right top shows the isolated-photon cross section in pp collisions at $\sqrt{s} = 13$ TeV measured by ALICE [85] as a function of p_T^γ (same points as in Fig. 2.7-left as a function of x_T^γ). The cross section is compared to NLO pQCD calculations using JETPHOX 1.3.1 [85] and data and theory are in agreement.

The γ^{iso} cross section has also been evaluated in pA collisions: this type of measurement allows for the investigation of possible nuclear modifications of the parton densities, which can be investigated using the nuclear modification factor R_{pA} . The R_{pA} of isolated-photon production at $\sqrt{s_{\text{NN}}} = 8.16$ TeV measured by ALICE as a function of p_T is shown in Fig. 2.8-top. The pp reference was measured at $\sqrt{s} = 8$ TeV and extrapolated to 8.16 TeV.

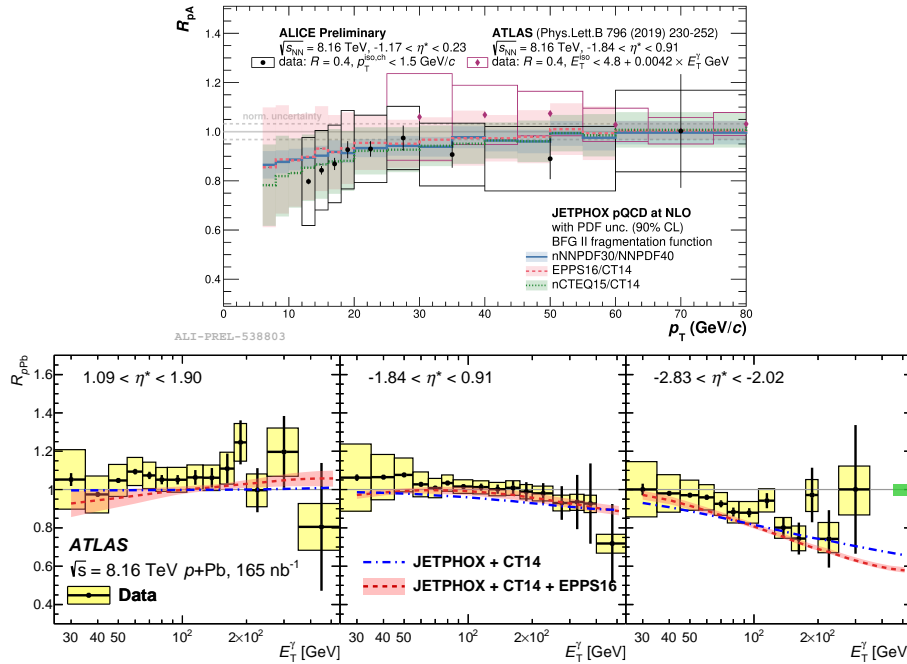


Figure 2.8: Top: R_{pA} of isolated-photon production in p-Pb collisions at $\sqrt{s_{\text{NN}}} = 8.16$ TeV by ALICE (full black circle) and by ATLAS (full pink circle) compared with different JETPHOX calculations using nNNPDF30 (blue line), using CT14 proton PDF + EPPS16 Pb nPDF (red dashed line) and using CT14 proton PDF + nCTEQ15 Pb nPDF (dotted green line) [91]. Bottom: nuclear modification factor R_{pA} at $\sqrt{s_{\text{NN}}} = 8.16$ TeV in p-Pb collisions measured purely by ATLAS (full black circle) at different rapidities confronted with JETPHOX calculations using CT14 proton PDF (blue dotdashed line) and using CT14 proton PDF + EPPS16 Pb nPDF (red dashed line) [92].

The result is in agreement with unity within the uncertainties and for $p_T > 25$ GeV/c and it is in line with the findings obtained by ATLAS at mid-rapidity [92]. The low- p_T reached by ALICE reveals a hint of an increasing suppression for $p_T \lesssim 20$ GeV/c of up to 20%, which is however not (yet) significant within the experimental uncertainties. The measured R_{pA}

is compared to various JETPHOX calculations at **NLO** using different nuclear PDFs and the BFG II fragmentation function. The different nPDFs used include cold nuclear matter effects such as gluon shadowing. The theory predictions well describe the data for all the different nPDFs used, within the uncertainties, displaying a similar suppression pattern below $p_T \lesssim 20$ GeV/ c . This suppression is often attributed to low- x shadowing of gluons inside the lead nucleus [91].

For completeness, the results by **ATLAS** [92] in the same collision system, but in different rapidity regions, are shown in Fig. 2.8–bottom. The data are compared with theory: JETPHOX **NLO** calculations using the CT14 proton PDF for the proton beam and the corresponding EPPS16 nPDF for the Pb beam. At forward rapidities, shown in Fig. 2.8–bottom left, the R_{pA} is consistent with unity over the full covered momentum range; the slight reduction at low E_T and enhancement above 100 GeV, could be related to shadowing and anti-shadowing effects. However, this effect is not foreseen by the calculation using only the CT14 proton PDF, therefore it is related to the chosen model. At mid-rapidity and backward-rapidity, shown in Fig. 2.8–bottom middle and right, respectively, there is an increasing suppression of isolated prompt photons at high E_T relative to pp. Since this suppression is compatible with both JETPHOX predictions, it implies that it derives from the proton-neutron asymmetry inside the Pb nucleus and not from a nuclear modification of the parton densities inside the nucleus.

Globally, **ATLAS** results agree with theoretical calculations in all three rapidity regions.

The **ALICE** experiment has measured the isolated-photon differential production cross section as a function of p_T^γ for various centralities in Pb–Pb collisions and in pp at $\sqrt{s_{NN}} = 5.02$ TeV [93]. The results have been obtained testing two different radii of the isolation cone R ($R = 0.2$ and $R = 0.4$) used in the isolation criterium, as sketched in Fig. 2.6. Here, only the results with $R = 0.2$ are presented in Fig. 2.9–left.

The measurements are compared to next-to-leading order pQCD calculations using JETPHOX 1.3.1 [82, 94]. The fragmentation function used is BFG II [95]. The parton distribution function used in the calculations for pp collisions is NNPDF4.0 [15], and the nuclear parton distribution function used in the calculations for Pb–Pb collisions is nNNPDF3.0 [43], which has been calculated for 0–100% centrality. For Pb–Pb collisions the theory has been scaled by $\langle N_{\text{coll}} \rangle$. The ratio data over theory, reported in Fig. 2.9–right, shows that the isolated-photon cross sections in data and theoretical predictions are in agreement for the full transverse momentum range measured in pp and each of the Pb–Pb centrality classes. A similar agreement is obtained for $R=0.4$.

The measurement of the cross-section using different isolation radii (R) can be exploited to calculate the ratio $d\sigma(R = 0.4)/d\sigma(R = 0.2)$. This ratio has the potential to constrain the non-perturbative part of the fragmentation functions because it is sensitive to the fraction of fragmentation photons passing the isolation [90, 96]. Figure 2.10 shows the ratio in pp collisions between 11 and 80 GeV/ c and in Pb–Pb collisions between 10–14 and 40–140 GeV/ c (depending on the centrality class).

All data systems are in agreement: no modification of the ratio is observed in central Pb–Pb collisions compared to peripheral Pb–Pb and pp collisions. The ratio ranges between 0.8 and 1 in the data, while in **NLO** pQCD calculation it is around 0.9, with a small increase for increasing p_T^γ . The data are in agreement with the JETPHOX **NLO** ratios of

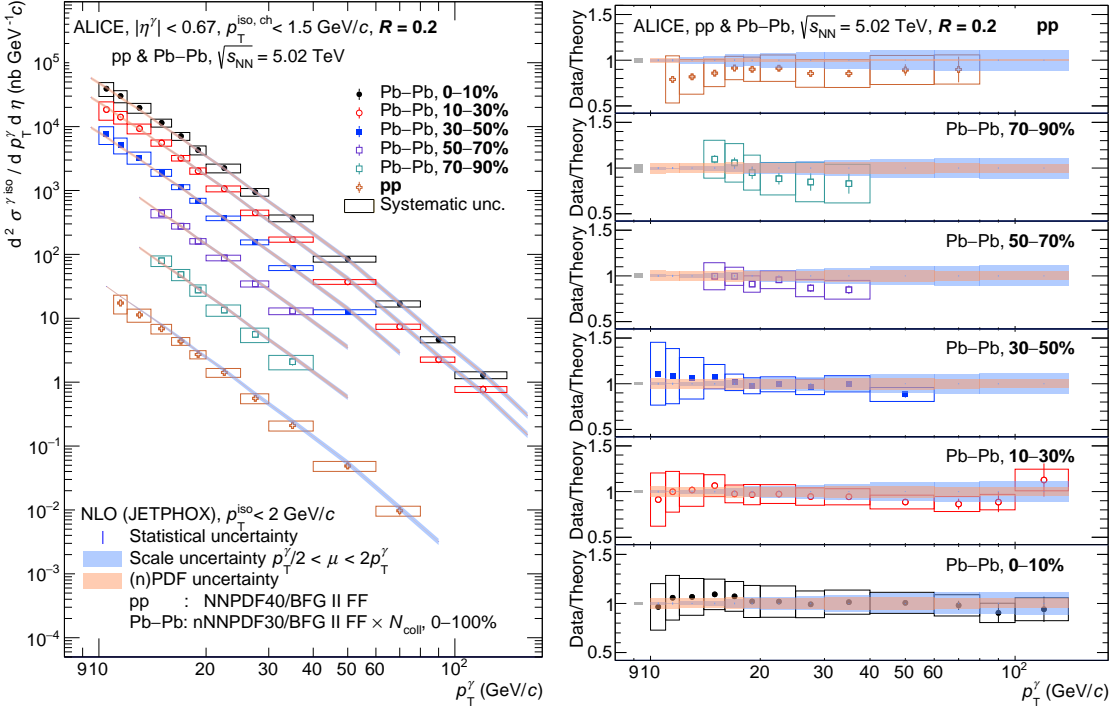


Figure 2.9: Left: isolated-photon differential cross section measured in pp and Pb–Pb collisions at $\sqrt{s_{NN}} = 5.02$ TeV for five Pb–Pb centrality classes for $R = 0.2$. Right: ratio of data over JETPHOX NLO pQCD calculations. The bands centred at unity correspond to the JETPHOX pQCD calculations, their width represents the scale (blue) uncertainty and PDF (orange) uncertainty, and blue vertical bars indicate the statistical uncertainty of the calculation [93].

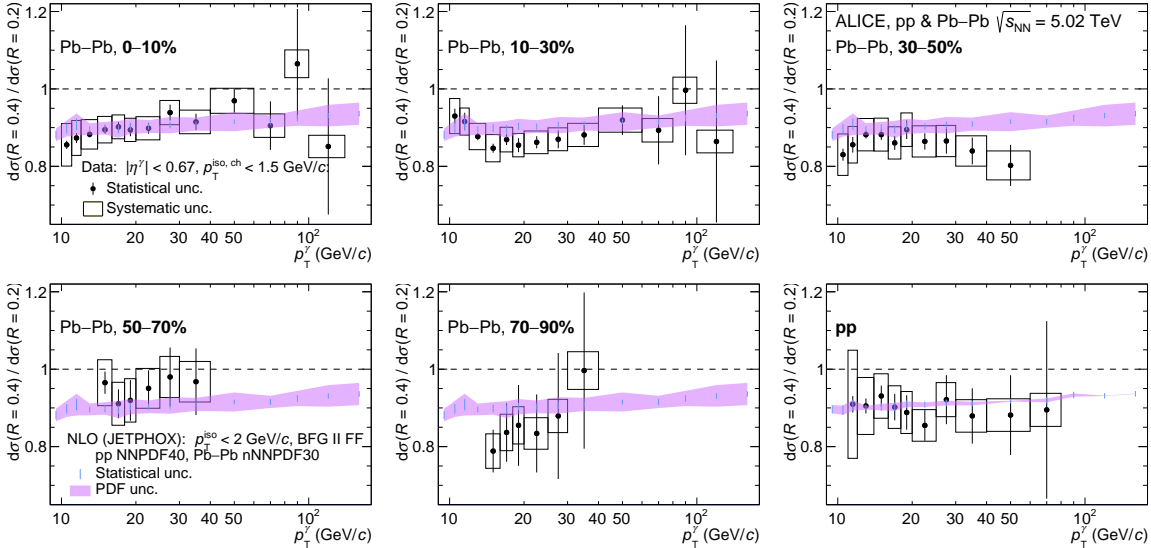


Figure 2.10: Ratio of isolated-photon spectra measured with $R = 0.4$ over $R = 0.2$, for Pb–Pb and pp collisions at $\sqrt{s_{NN}} = 5.02$ TeV. Each panel corresponds to a Pb–Pb collisions centrality class or to pp collisions. The pink band corresponds to pQCD calculations with JETPHOX [93].

2.2. Isolated photons measurements

different radii R yields in both collision systems. The dependence on the isolation-cone size is well described by pQCD NLO calculations incorporating an isolation criterion [93]. Also, all data systems are in agreement: while a ratio closer to unity could be naively expected in central collisions if the fragmentation photon production was suppressed in the medium, no modification of the ratio is observed comparing central Pb–Pb collisions to peripheral Pb–Pb and pp collisions. The ATLAS Collaboration also conducted this measurement in pp collisions at $\sqrt{s} = 13$ TeV with p_T^γ above 250 GeV/ c , observing agreement between the data and theoretical predictions [90].

From the ALICE cross section results, it is possible to estimate the nuclear modification factor, defined in Eq. (1.20), of γ^{iso} in Pb–Pb collisions at $\sqrt{s_{\text{NN}}} = 5.02$ TeV. Figure 2.11 shows the isolated-photon R_{AA} for the five Pb–Pb centrality classes measured for the cone radii $R = 0.2$ and 0.4 .

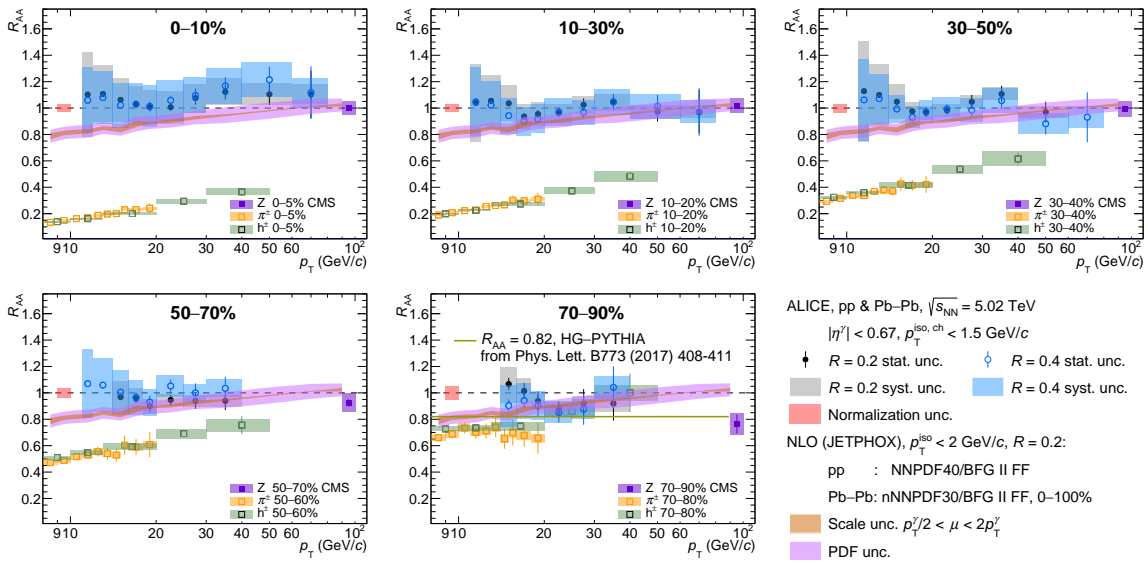


Figure 2.11: Nuclear modification factor for isolated photons at $\sqrt{s_{\text{NN}}} = 5.02$ TeV for isolation cone radii $R = 0.2$ (full black circle) and $R = 0.4$ (empty blue circle). Distribution compared to the R_{AA} for charged particles [65] (empty green square) and charged pions [97] (empty orange square) from ALICE, and to the ratio of the Z bosons (full violet square) production in each centrality class to the 0–90% class measured by CMS [98]. The bands correspond to pQCD calculations with JETPHOX for Pb–Pb collisions (nPDF) for 0–100% centrality over pp collisions (PDF). The width of each band corresponds to the scale (orange) and PDF (pink) uncertainties [93].

In sharp contrast with the charged-particles [65] and charged-pions [97] R_{AA} , the isolated-photon R_{AA} is found compatible with unity, except for a deviation for the most peripheral class. The strong suppression observed for hadrons in central Pb–Pb collisions with respect to pp collisions is not observed for isolated photons. The isolated-photon R_{AA} in peripheral collisions is below unity. Such a behaviour can be explained by biases in the centrality selection and collision geometry that the Glauber model cannot account for, more detail can be found in Ref. [99] and will be discussed in Sect. 3.5. In the 70–90% centrality class, the expected R_{AA} bias calculated with the HG-PYTHIA model [99] is indeed 0.82, significantly below unity and in agreement with the measurement within the uncertainties. The Z boson production was measured by CMS [98] in Pb–Pb collisions at $\sqrt{s_{\text{NN}}} = 5.02$ TeV, and like the isolated photons, it is not affected by the QGP. As shown in Fig. 2.11, the R_{AA} of Z bosons

agrees with unity for centrality classes from 0 to 70%, while a deviation is visible in the most peripheral centrality class 70–90%. The ALICE data have been compared with NLO (JETPHOX) calculations. Like the data, the NLO R_{AA} is close to unity for $p_{\text{T}}^{\gamma} > 50$ GeV/ c . In contrast, theory predicts a suppression of the R_{AA} at lower p_{T}^{γ} for all the centralities. This can be attributed to differences in the proton and nucleus PDFs of about 0.8 at low p_{T}^{γ} . This suppression is not seen in the data, which shows tension with the theory at low p_{T}^{γ} .

Isolated photons tagged measurements

It has been demonstrated that isolated photons are not modified by the medium, making them particularly valuable in studies of heavy-ion collisions. Since their energies remain unchanged when crossing the QGP, isolated photons can tag the parton, giving a calibrated reference of its initial momentum and direction. For this reason, they are used as triggers in correlation measurements and they allow us to compare processes with the same initial momentum in pp and AA collisions, probing jet quenching effects.

Despite these advantages, the limitation due to the photon-tagged jet events with respect to inclusive jet production is related to the lower statistics, which made these measurements particularly challenging.

In the following, part of the jet quenching measurements, already presented in Sect. 1.5.4, will be revisited and the results obtained using photon-tagged jet events will be illustrated.

We have learned in Sect. 1.5.4 that high-energy partons originated in the pre-equilibrium phase in heavy-ion collisions lose energy while travelling through the thermalized and coloured QGP medium. The loss of energy happens through collisional and mostly radiational (gluon emission) processes. Theory predicts an ordering in quark energy loss described in Eq. (1.25) (see Sect. 1.5.4) and the quark $\Delta E_{\text{loss rad}}(q)$ is expected to be lower than gluons $\Delta E_{\text{loss rad}}(g)$. Experimentally, this ordering can be tested by comparing quark jets with gluon jets. Since γ^{iso} -tagged jets are mainly initiated by a hard-scattered quark at LHC, this enables potential discrimination between the energy loss of a primary quark with the medium and that of a mixture of quarks and gluons that constitute an inclusive jet sample. Figures 2.12–left illustrates the R_{AA} as a function of the jet $p_{\text{T}}^{\text{jet}}$ for γ^{iso} -tagged jets measured by ATLAS [100].

The R_{AA} of γ^{iso} -jets is below unity and the suppression is larger for more central collisions, as expected from the presence of the QGP. Figure 2.12–right compares the photon-tagged jet R_{AA} to inclusive jet results. The nuclear modification factor of photon-tagged jets is significantly higher than the corresponding values for inclusive jets for $p_{\text{T}}^{\text{jet}} < 200$ GeV. Above $p_{\text{T}}^{\text{jet}} > 200$ GeV, the statistical and systematic uncertainties in the photon-tagged jet results are larger and the R_{AA} values become compatible. The results confirm larger jet quenching for gluon jets compared with quark jets in central Pb–Pb collisions.

Momentum balance measurements are based on the fact that high- p_{T} objects must be produced in momentum conserving processes and that these derive mainly from 2→2 scatterings. For the dijets measurements, the back-to-back jets momentum and direction can be changed by interacting with the QGP, as already shown in Sect. 1.5.4. On the contrary, the γ^{iso} -tagged jets offer a controlled configuration of the initial hard scattering and give access

2.2. Isolated photons measurements

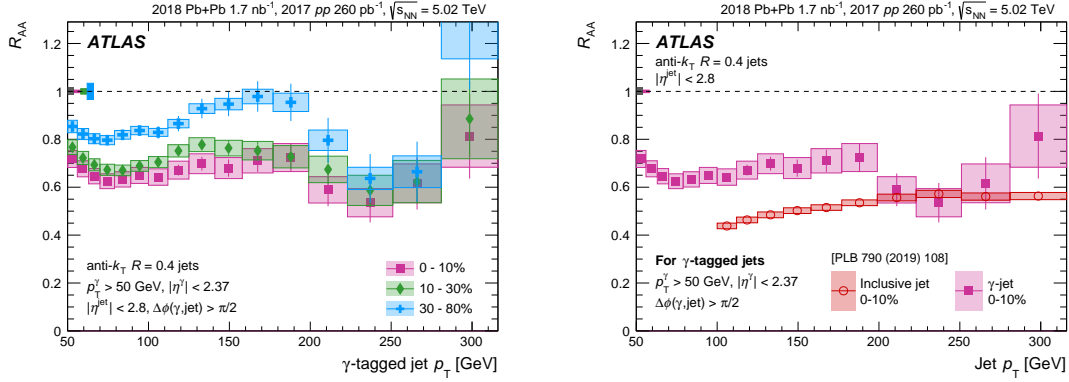


Figure 2.12: Left: nuclear modification factor of γ^{iso} -tagged jet as a function of p_T^{jet} for 0-10% (full pink square), 10-30% (full green diamond) and 30-80% (full blue cross) Pb-Pb collisions at $\sqrt{s_{\text{NN}}} = 5.02$ TeV measured by ATLAS. Right: nuclear modification factor of γ^{iso} -tagged jets (full pink square) and inclusive jets (empty light pink circle) as a function of p_T^{jet} for 0-10% Pb-Pb collisions at $\sqrt{s_{\text{NN}}} = 5.02$ TeV measured by ATLAS [100].

to the “absolute” parton energy loss. For γ^{iso} -jet events the variable $x_{\text{j}\gamma}$ is defined as:

$$x_{\text{j}\gamma} = \frac{p_{\text{T}}^{\text{jet}}}{p_{\text{T}}^{\gamma}} \quad (2.5)$$

Figure 2.13 shows the momentum balance $x_{\text{j}\gamma}$ distributions in pp and various centrality classes in Pb-Pb collisions at $\sqrt{s_{\text{NN}}} = 5.02$ TeV measured by the CMS Collaboration [101].

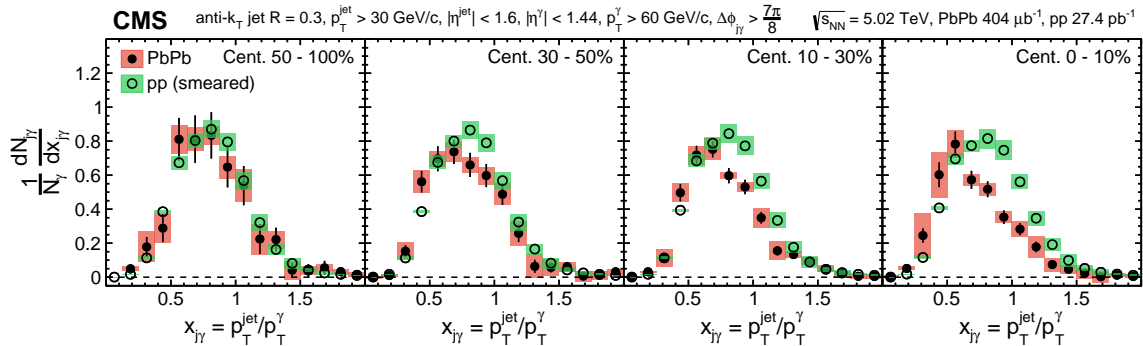


Figure 2.13: The p_T balance observable as a function of $x_{\text{j}\gamma}$ for various centralities in Pb-Pb (full markers) and pp (open markers) collisions. Vertical lines display the statistical uncertainties while the coloured boxes (red for PbPb, green for pp) show the systematic uncertainties [101].

Going from peripheral to central collisions, the fraction of balanced photon-jet pairs (those with $x_{\text{j}\gamma} \approx 1$) decreases. The Pb-Pb distributions shift towards lower $x_{\text{j}\gamma}$ and the fraction of pairs in which the photon has more p_T than the jet increases. This is consistent with the expectation that a significant amount of parton energy is transported out of the jet cone due to the longer average path length that the parton must travel through in more central Pb-Pb collisions [101].

To be more sensitive to the hadronization process, the fragmentation functions can be estimated. The FFs reflect the momentum distribution inside the parton shower in the longitudinal direction, as already illustrated in Sect. 1.5.4.

In inclusive jet measurements, the medium-induced modifications are studied by comparing populations of jets in Pb–Pb and pp within the same measured jet p_T window. Due to the jet energy loss that occurs in Pb–Pb collisions, the comparison is not done for the same initial parton energies and the momentum of the jet is estimated after jet interactions with the QGP. Therefore, this can lead to a selection bias by which broad jets, that are more strongly quenched, are filtered out from the selected reconstructed jet p_T interval, while the population of narrow jets, that are less suppressed, is included and highlighted in the final state [71]. On the other hand, the use of γ^{iso} -tagged jet samples avoid this bias by triggering on the photon p_T^γ and help to understand if the observed modifications are induced by the presence of the quark–gluon plasma or by selection biases. The comparison between the inclusive jets fragmentation functions and γ^{iso} -jets ones in Pb–Pb over pp collisions is reported in Fig. 2.14. The results measured by the CMS Collaboration [102, 103] are reported as a function of ξ_T , a variable parent of z_T . These variables are defined as:

$$z_T = \frac{p_T^{\text{trk}}}{p_T^\gamma} \quad \text{or} \quad \xi_T = \ln\left(\frac{1}{z_T}\right), \quad (2.6)$$

where p_T^γ is the transverse momentum of the photon, that tags the parton at the origin of the hard process and p_T^{trk} is the transverse momentum of the tracks. The low- ξ_T region corresponds to high- p_T particles, while the high- ξ_T , corresponds to the low- p_T hadrons.

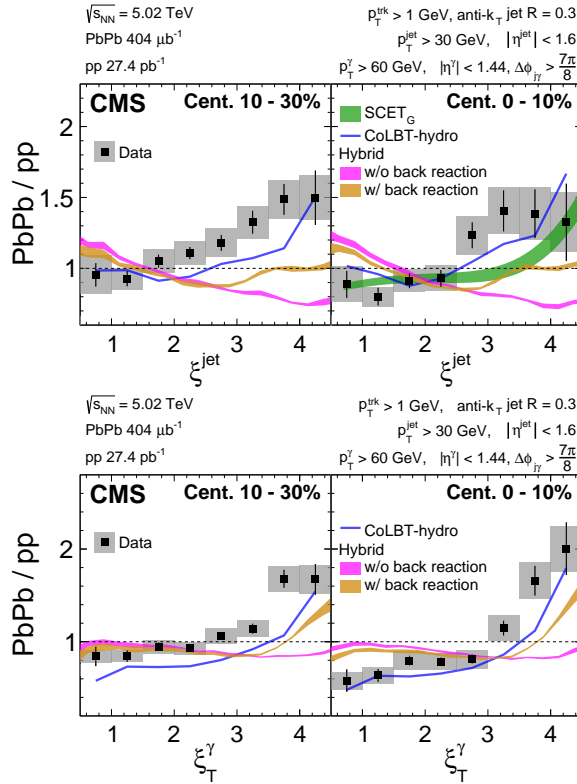


Figure 2.14: Comparison of photon-tagged fragmentation functions in centrality bins 10–30% (left) and 0–10% (right) as a function of the observables ξ_T^{jet} (top) and ξ_T^γ (bottom). The distributions are compared with CoLBT-hydro model (blue line) and HYBRID model with back reaction (yellow line) and without back reaction (pink line) [102, 103].

Jets in central Pb–Pb events show an excess of low- p_T particles and a depletion of high- p_T particles inside the jet. The enhancement is larger in the most central collisions and is better

2.2. Isolated photons measurements

highlighted in γ^{iso} -tagged jet samples. The conventional fragmentation function using ξ_T^{jet} displays a minor enhancement of soft particles alongside a corresponding reduction of hard particles (at large and small ξ_T^{jet} , respectively) and this is also confirmed by comparing with the ATLAS results shown in Fig. 1.25-right. The p_T^{jet} selection is applied to the jets in the final state, hence after the quenching has changed the jet population as compared to the pp reference data. In contrast, those using ξ_T^γ avoid this bias by selecting the p_T^γ of the photon and demonstrate that once the influence of jet energy loss is eliminated, the enhancement and the suppression become notably more pronounced, exhibiting a clear centrality dependence. The results are compared with several theoretical models, such as the Coupled Linear Boltzmann Transport and hydrodynamics (CoLBT-hydro) [104] and HYBRID [105] models, with varying degrees of agreement. Concerning the HYBRID model, it can describe the data qualitatively well only when incorporating the medium response (labelled HYBRID with back reaction). Both the HYBRID with back reaction and CoLBT models capture the general features seen in the data. The CoLBT model will be used in comparison to the results shown in this Thesis.

It is worth noting that the γ^{iso} -tagged jet fragmentation functions are a bit different from inclusive (dijet) ones: the tagging with the photon limits the statistics and identifies jets at lower p_T^{jet} ; in addition the selected jets can have a much higher fraction of quark jets than the inclusive jet sample.

A similar study can be done with the measurement of charged hadrons from the shower of a parton (quark or gluon) produced in association with a Z boson. Z bosons are selected by measuring their invariant mass from $Z \rightarrow \mu^+\mu^-$ and (sometimes) $Z \rightarrow e^+e^-$, hence they can be more easily identified than γ^{iso} ; on the other hand, their production rate is lower than isolated photons. Figure 2.15 shows the Z-jet fragmentation functions as a function of $\xi_T^{\text{trk},Z}$ measured in pp and in Pb–Pb collisions at $\sqrt{s_{\text{NN}}} = 5.02$ TeV by CMS [106].

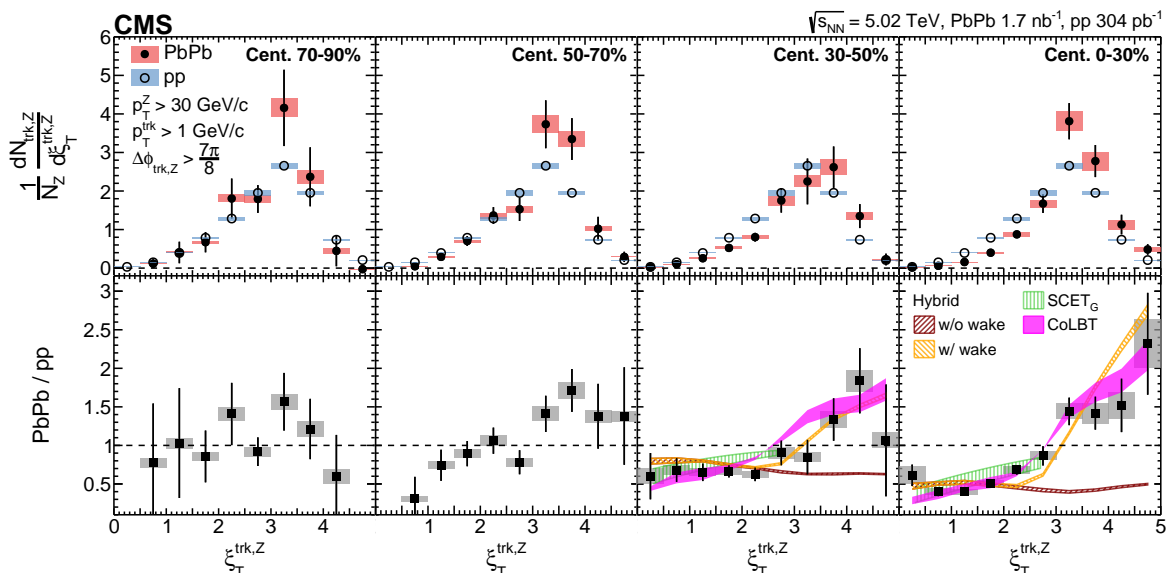


Figure 2.15: Top: distributions of $\xi_T^{\text{trk},Z}$ in pp collisions compared to Pb–Pb collisions in various centrality bins. Bottom: ratios of the Pb–Pb to pp distributions. The vertical bars and coloured boxes represent the statistical and systematic uncertainties, respectively. The distributions are compared with CoLBT-hydro model (pink line) and HYBRID model with wake (yellow line) and without wake (brown line) [106].

As before, there is no modification in peripheral Pb–Pb collisions with respect to pp results; while in central collisions there is an enhancement of low- p_T particles for $\xi_T^{\text{trk},Z} > 3$ and suppression of high- p_T particles for $\xi_T^{\text{trk},Z} < 3$. The same conclusions as before can be drawn: the enhancement is consistent with a scenario where additional low-energy particles are produced from the parton traversing the medium. This measurement will be compared with the final results obtained in this Thesis.

The jet radial distributions can be investigated using the density of the radial momentum distribution $\rho(r)$ from γ^{iso} -tagged jets, defined as

$$\rho(r) = \frac{1}{\delta r} \frac{\sum_{\text{jets}} \sum_{r_a < r < r_b} \left(p_T^{\text{trk}} / p_T^{\text{jet}} \right)}{\sum_{\text{jets}} \sum_{0 < r < 0.3} \left(p_T^{\text{trk}} / p_T^{\text{jet}} \right)}, \quad (2.7)$$

where $\delta r = r_b - r_a$ is the width of the annulus of inner and outer radii r_a and r_b with respect to the jet axis and $r = \sqrt{(\varphi_{\text{jet}} - \varphi_{\text{track}})^2 + (\eta_{\text{jet}} - \eta_{\text{track}})^2}$ is the distance between the track and the jet axis. Figure 2.16 reports the density of the radial momentum distribution in pp and in different centrality classes in Pb–Pb collisions and the corresponding ratio measured by the CMS Collaboration [107].

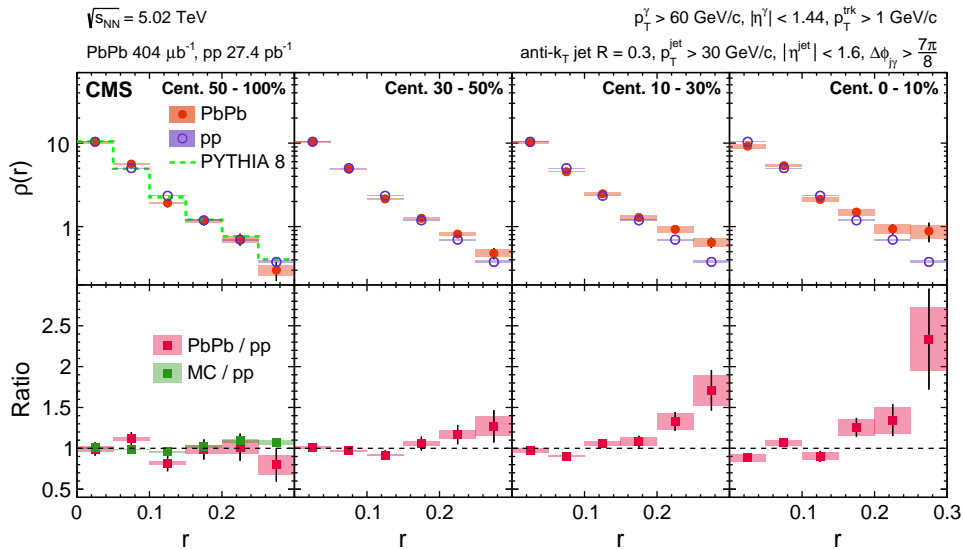


Figure 2.16: Top: Differential jet shape, for jets associated with an isolated-photon from peripheral to central Pb–Pb (full circles), and pp (open circles) collisions at $\sqrt{s_{\text{NN}}} = 5.02$ TeV. Bottom: Ratios between the Pb–Pb and pp distributions by CMS [107].

In peripheral collisions, there are no differences with respect to pp. In central collisions, a modification of the jet shape is evident: the $\rho(r)$ increases for the distances between the track and the jet axis of $r \gtrsim 0.15 - 0.20$. A larger fraction of the jet momentum is observed at larger distances from the jet axis compared to pp and this effect is stronger in central collisions. This represents an observation of the jet broadening due to the presence of the QGP [107].

Another observable that can be used to study jet angularities is the jet girth g , which is a measure of the width of the jet. It is defined as the sum of the product of the momentum

2.2. Isolated photons measurements

fraction of the jet constituents and their distance relative to the anti- k_T jet axis, namely:

$$g = \frac{1}{p_T^{\text{jet}}} \sum_i p_T^i \Delta R_{i,\text{jet}}, \quad (2.8)$$

where $\Delta R_{i,\text{jet}} = \sqrt{(\Delta y_{i,\text{jet}})^2 + (\Delta \varphi_{i,\text{jet}})^2}$ is the distance in $y - \varphi$ of the i -th jet constituent with respect to the anti- k_T jet axis.

The γ^{iso} -tagged jets events can be exploited to disentangle the potential modification of the jet angular substructure due to the energy loss from the selection bias effects. They can increase the number of quenched jets at a certain p_T value in the measured samples and the jet girth distribution of these events can be used to study how narrow or broad a jet is. The jet girth distributions have been measured in pp and in central Pb–Pb collisions at $\sqrt{s_{\text{NN}}} = 5.02$ TeV by the CMS Collaboration [108]. These distributions are estimated selecting jets in two different intervals of momentum balance: $x_{j\gamma} = p_T^{\text{jet}}/p_T^\gamma > 0.4$ and $x_{j\gamma} = p_T^{\text{jet}}/p_T^\gamma > 0.8$. The results are reported in Fig. 2.17–left and right, respectively.

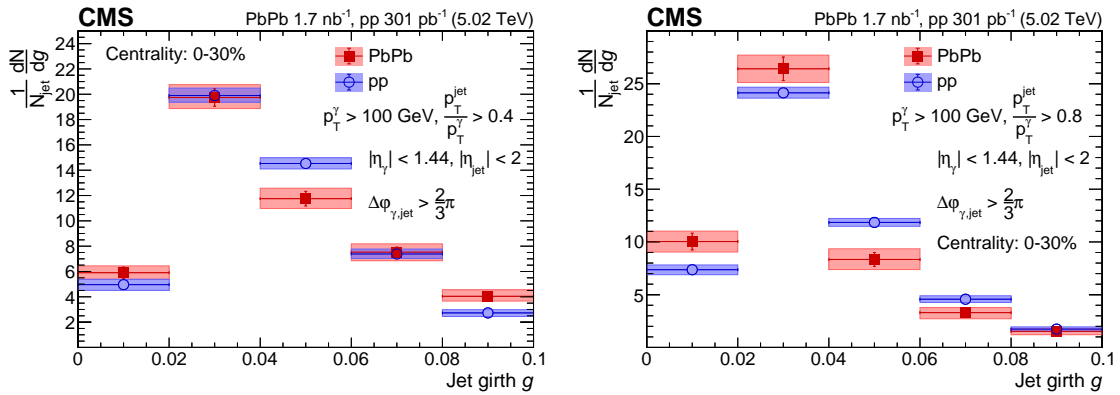


Figure 2.17: Distributions of jet girth g of γ^{iso} -tagged jets in Pb–Pb (full red square) and pp (empty blue circle) collisions for $x_{j\gamma} = p_T^{\text{jet}}/p_T^\gamma > 0.4$ (left) and for $x_{j\gamma} > 0.8$ (right) measured by CMS [108].

The momentum balance selection intervals permit to investigate jet reconstructed in a large p_T window. Jets with $p_T^{\text{jet}}/p_T^\gamma > 0.4$ correspond to an inclusive jet selection where both quenched and less quenched jets are included. As reported in Fig. 2.17–left, no narrowing of the angular structure of jets is produced in Pb–Pb collisions relative to pp. On the other hand, when jets with $p_T^{\text{jet}}/p_T^\gamma > 0.8$ are considered, the jets are closely balanced with the photon (p_T^{jet} and p_T^γ are close) and the distribution is enhanced at low- g , namely jets are narrower in Pb–Pb than in pp collisions. These observations suggest that selection bias effects play an important role in the interpretation of the modification of the angular scales of jets in terms of medium-induced effects [108].

Until now, the Section has focused γ^{iso} -jet events, however, the energy redistribution in the final state due to the jet quenching can be also studied with γ^{iso} -hadron correlations. This measurement was historically done for the first time at RHIC [109], before measuring photon-jet events. It is simpler because it does not require the reconstruction of the associated jet, which can be quite complicated, especially at low p_T ; instead, it is sufficient to select hadrons emitted in the opposite azimuthal direction. Nevertheless, γ^{iso} -hadron correlations do not permit to explore other effects due to the jet quenching, such as its impact on jet

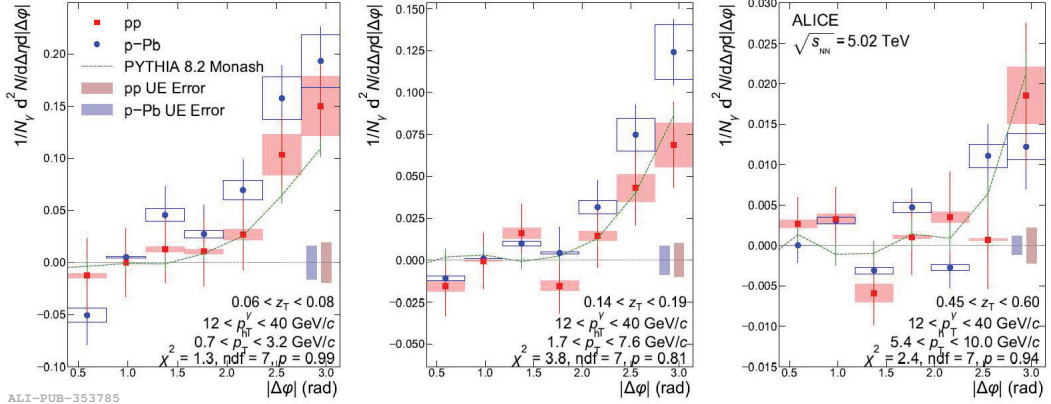


Figure 2.18: Top: γ^{iso} -hadron azimuthal correlation distributions for pp (full red square), p-Pb (full blue circle) data and PYTHIA 8.2 Monash Tune simulation (dashed green line) at $\sqrt{s} = 5.02$ TeV measured by the ALICE Collaboration. The different panels correspond to different z_{T} bins [110].

substructures and angularities.

The **ALICE** experiment has measured the γ^{iso} -hadron correlations in various z_{T} intervals in pp and p-Pb collisions at $\sqrt{s_{\text{NN}}} = 5.02$ TeV [110]. The z_{T} variable, indicated in Eq. (1.28), represents the momentum fraction of the parton p_{T} inherited by the hadron. Figure 2.18 shows the azimuthal correlation distributions in various z_{T} ranges as a function of $\Delta\varphi = (\varphi^{\gamma} - \varphi^{\text{h}})$, where φ^{h} is the hadron azimuth direction.

The correlation functions in pp and in p-Pb report a similar trend: both show a signal consistent with zero at small $\Delta\varphi$ and an away side peak at large $\Delta\varphi \sim \pi$, due to the hard-scattered parton opposite to the trigger photon. The $\Delta\varphi$ distributions are compared with PYTHIA 8.2 Monash Tune and an agreement within uncertainties between pp, p-Pb and theory simulation is obtained.

The measured γ^{iso} constrains the parton kinematics, hence, the distribution of away side associated hadrons with momentum fraction z_{T} represents a “proxy” to the fragmentation function $D(z_{\text{T}})$ of the parton (see Eq.(1.27)). The $D(z_{\text{T}})$ functions are obtained integrating the region of the $\Delta\varphi$ distributions with $\Delta\varphi > \frac{7}{8}\pi$ for every z_{T} bin and they are estimated in a larger p_{T}^{γ} range: $12 < p_{\text{T}}^{\gamma} < 40$ GeV/ c . The $D(z_{\text{T}})$ distributions are reported in Fig. 2.19.

No difference is observed in the $D(z_{\text{T}})$ distributions between pp and p-Pb data. The ratio of the two z_{T} functions in the different collision systems, reported in Fig. 2.19-bottom, is consistent with unity. This result is in agreement with the expectation of no medium modifications in p-Pb collisions with respect to pp.

The same measurement can be done in AA collisions to quantify hot nuclear matter effects. The **STAR** experiment has measured the $D(z_{\text{T}})$ for γ -hadron correlations in pp and Au-Au collisions at $\sqrt{s_{\text{NN}}} = 200$ GeV at **RHIC** [111]. Figure 2.20-left reports the $D(z_{\text{T}})$ distribution as a function of z_{T} .

We can appreciate that there is a suppression of the high- p_{T} particles at high- z_{T} with respect to pp collisions, in agreement with what has been obtained for example by **CMS**, as shown in Fig. 2.15. In this case, though, the enhancement of the low- p_{T} particles, expected for a z_{T} below 0.1, is not visible. The reason could be that the selection on the associated

2.2. Isolated photons measurements

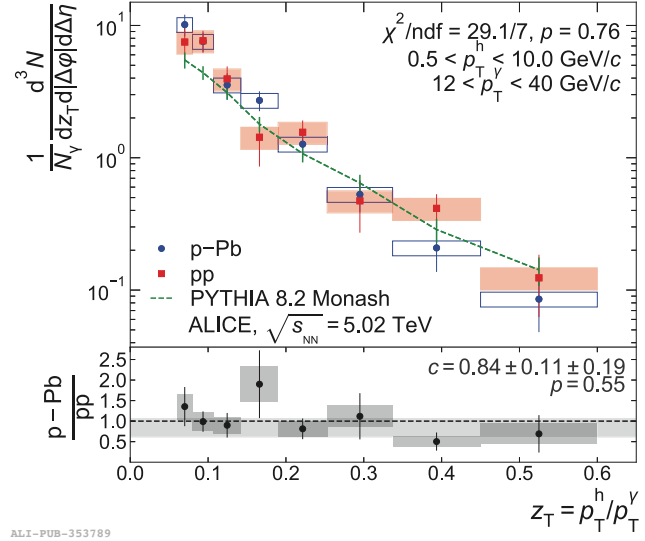


Figure 2.19: γ^{iso} -hadron fragmentation function for pp (full red square), p–Pb data (full blue circle) and PYTHIA 8.2 simulation (dashed green line). The ratio between p–Pb and pp distributions (black marker) is shown in the bottom panel. The boxes represent the systematic uncertainties while the vertical bars indicate the statistical uncertainties [110].

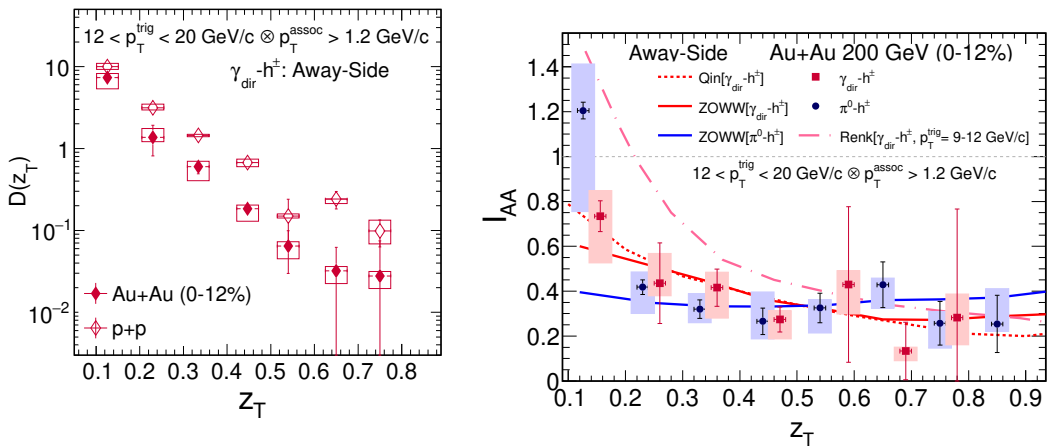


Figure 2.20: Left: $D(z_T)$ distributions for γ^{iso} -hadron correlations as a function of z_T for central Au–Au (full red dot) and for pp (empty red dot) collisions measured by the STAR Collaboration. Right: I_{AA} for γ^{iso} -hadron (red squares) and for π^0 -hadron (blue circles) correlations as a function of z_T . The vertical lines represent statistical error and the vertical boxes represent systematic errors. The curves represent theoretical model predictions [111].

hadrons ($p_T^{\text{assoc}} > 1.2 \text{ GeV}/c$) does not allow probing of low- p_T hadrons enhancement [111]. To quantify the medium modification of γ -hadron correlations, the I_{AA} , defined as:

$$I_{\text{AA}} = \frac{D(z_T)_{\text{AA}}}{D(z_T)_{\text{pp}}} \quad (2.9)$$

that is the ratio between the $D(z_T)$ in Au–Au and in pp collisions. Figure 2.20–right shows the I_{AA} obtained for γ^{iso} -hadron correlations and of π^0 -hadron ones as a function of z_T . There is a clear suppression for $z_T > 0.2$. While for $0.1 < z_T < 0.2$, there is an indication of less suppression, but this observation is not significant for the dependence of I_{AA} because the uncertainties in the lowest z_T bin are large. The data are consistent with model calculations, in which the suppression is caused by parton energy loss in a thermalized medium [111].

2.3 Conclusions

The goal of this Thesis is to measure the γ^{iso} -hadron correlations in Pb–Pb collisions at $\sqrt{s_{\text{NN}}} = 5.02 \text{ TeV}$ with the ALICE experiment, repeating the same measurement already done by the STAR Collaboration, but at a higher center-of-mass energy per nucleon $\sqrt{s_{\text{NN}}}$ than at RHIC. The aim is to explore the medium-induced modifications and the energy redistribution because of the QGP with the isolated photon-hadron correlations, trying to reach a lower p_T^γ than those previously measured by ATLAS and CMS. The ALICE experiment has already measured the γ^{iso} -hadron correlations in pp and p–Pb collisions, therefore the measurement in Pb–Pb represents the last missing piece of the puzzle.

Chapter 3

The ALICE experiment at the LHC

3.1	The Large Hadron Collider	65
3.2	The ALICE Detector	67
3.2.1	Inner Tracking System	68
3.2.2	Time Projection Chamber	70
3.2.3	V0 Detector	71
3.3	The ALICE data acquisition and offline framework	72
3.4	Track and vertex reconstruction	73
3.5	Centrality determination in Pb–Pb collisions	75

ALICE [112] is one of the four main experiments at the Large Hadron Collider [113], the accelerator built to collide protons and ions at unprecedented energies (TeV scale). ALICE has been designed and optimised for the high-multiplicity environment of ultrarelativistic heavy-ion collisions, to study the deconfined state of matter produced in the collision, the QGP (see Sect. 1.3). This Chapter will give a description of the ALICE detector systems employed to collect the data analysed in this work.

3.1 The Large Hadron Collider

The LHC is a circular accelerator and collider of hadrons (protons or heavy ions) with a circumference of 26.7 km. It is made of two rings of superconductive magnets, located between 50 and 175 m underground (it is 1.3° inclined with respect to the horizontal plane) on the CERN site near Geneva. There are 1600 superconducting magnets made from a niobium-titanium alloy used to maintain the charged particles in a circular orbit. These magnets operate at a temperature of 1.9 K, cooled by superfluid helium, and generate a magnetic field of approximately 8 T.

The LHC was constructed to collide protons with a maximum centre-of-mass energy of 14 TeV at a peak luminosity¹ of $\mathcal{L} = 10^{34} \text{ cm}^{-2}\text{s}^{-1}$ as well as Pb ions at a centre-of-mass

¹The instantaneous luminosity is dependent on the particle beam parameters and it is defined as the ratio

energy per nucleon of 5.5 TeV at a peak luminosity of $\mathcal{L} = 10^{27} \text{ cm}^{-2}\text{s}^{-1}$. A complex injection chain, in which the particles are pre-accelerated, is needed to reach such high energies. Hydrogen atoms are stripped of their electrons to create a proton beam using an electric field. The resulting protons are then injected from a linear accelerator (**LINAC**) [114] into the Proton Synchrotron Booster (**PSB**) [115], where their energy is increased. Next, the beams are transferred to the Proton Synchrotron [116] for further acceleration, followed by the Super Proton Synchrotron, before finally being injected into the **LHC**. Lead nuclei follow a similar path, but they are accelerated via the **LINAC 3** and Low-Energy Ion Ring (**LEIR**) before being passed into the Proton Synchrotron (**PS**). Their injection energy at the **LHC** is 177 GeV per nucleon. After injection, they are further accelerated around the **LHC** ring before colliding at the interaction points (**IP**) of each detector. The various collisions systems and the corresponding energies that were accelerated at **LHC** during Run 1 (2009–2013) and Run 2 (2015–2018) are summarised in Table 3.1.

Collision system	$\sqrt{s}, \sqrt{s_{\text{NN}}} \text{ (TeV)}$	
	Run 1	Run 2
pp	0.9, 2.76, 7, 8	5.02, 13
p–Pb	5.02	5.02, 8.16
Pb–Pb	2.76	5.02
Xe–Xe	-	5.44

Table 3.1: Collision systems and energies at the LHC Run 1 and 2 [117].

Along the **LHC** ring there are four experiments surrounding each beam interaction point:

- **ATLAS** (A Toroidal LHC ApparatuS) [118];
- **CMS** (Compact Muon Solenoid) [119];
- **LHCb** (Large Hadron Collider beauty) [120];
- **ALICE** (A Large Ion Collider Experiment).

The **CMS** and **ATLAS** experiments were designed to investigate the creation and properties of the Higgs boson and to explore phenomena beyond the Standard Model. The primary aim of the **LHCb** experiment is to examine CP violation in the heavy-quark sector. Meanwhile, **ALICE** focuses on studying the properties of quark–gluon plasma in heavy-ion collisions.

The CERN accelerator complex is shown in Fig. 3.1.

of the number of inelastic events detected in a certain time to the pp inelastic cross-section:

$$\mathcal{L} = \frac{1}{\sigma_{\text{MB}}} \frac{dN_{\text{ev}}}{dt} \quad (3.1)$$

The integrated luminosity is the integral of the luminosity with respect to time:

$$\mathcal{L}_{\text{int}} = \frac{N_{\text{ev}}}{\sigma_{\text{MB}}} \quad (3.2)$$

3.2. The ALICE Detector

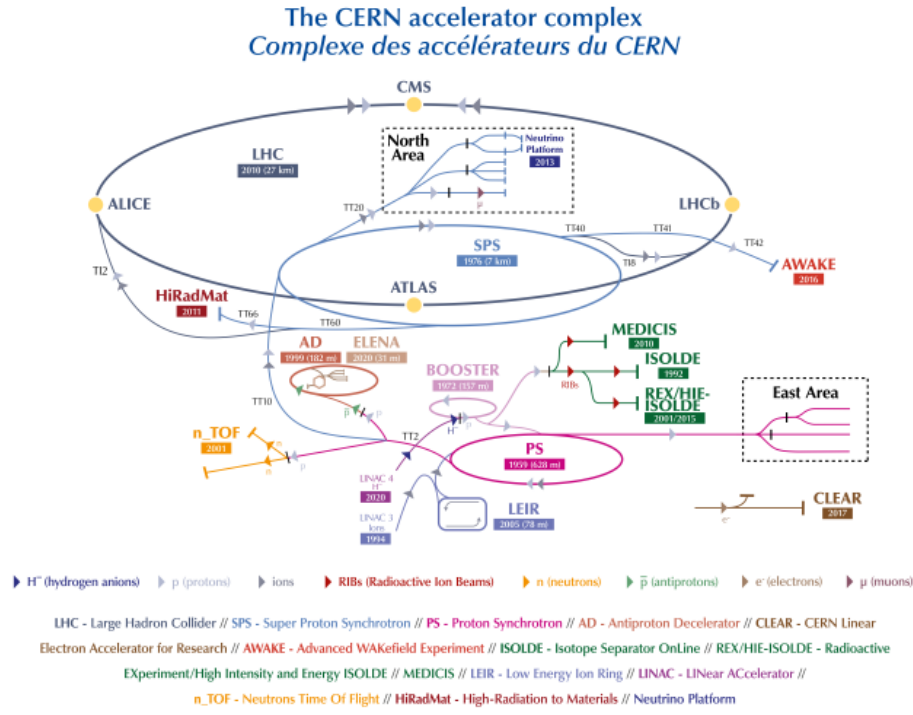


Figure 3.1: Scheme of the CERN accelerator complex. The locations of the four main LHC experiments (ALICE, ATLAS, CMS and LHCb) around the LHC ring are also shown.

3.2 The ALICE Detector

ALICE is a general-purpose detector designed to study hadronic matter under extreme temperature and energy density conditions, similar to those moments after the Big Bang. Its primary goal is to test QCD predictions about the phase transition from common hadronic matter to quark-gluon plasma, where quarks and gluons are not confined within hadrons. ALICE also investigates proton-proton (pp) collisions as a reference and proton-nucleus (pA) collisions to distinguish effects related to the presence of nuclei in the system, which could mimic final-state medium-related effects (Cold Nuclear Matter effects).

To conduct measurements in heavy-ion collisions, ALICE must operate in a high-track density environment, with charged particle multiplicity at mid-rapidity in central Pb-Pb events reaching up to $dN/d\eta = 2500$. To manage the high particle rate, high-granularity detectors are used to reduce detector occupancy. Additionally, excellent tracking down to very low transverse momentum p_T and particle identification (PID) across a wide momentum range are essential. To meet these requirements, ALICE employs a low material budget to minimize multiple scattering at low p_T and a larger tracking distance to enhance resolution at high p_T , along with various PID techniques.

The ALICE detector is located at the interaction point IP2 at LHC and the setup used during Run 2 is shown in Fig. 3.2. The apparatus, that was in operation during LHC Run 1 and Run 2, is defined as ALICE 1. ALICE sub-detectors are categorized into three main groups: the barrel detectors, which cover central pseudorapidities; the forward detectors, positioned at forward rapidities; and the muon arm, dedicated to muon identification. The

ALICE reference coordinate system is a right-handed orthogonal Cartesian system with its origin (x, y, z) = 0 at the **IP**. In this system, the z -axis is parallel to the beam direction, with the two sides of the detector along the z -axis labelled A (anti-clockwise, for positive z) and C (clockwise, for negative z).

- central barrel detectors: they include, starting from the interaction point and going outward:
 - the Inner Tracking System (**ITS**);
 - the Time Projection Chamber (**TPC**);
 - the Transition Radiation Detector (**TRD**);
 - the Time of Flight (**TOF**)

This group of subsystems have full azimuthal ($0 \leq \varphi < 2\pi$) coverage with rapidity acceptance $|\eta| < 0.9$ and is enclosed in the L3 solenoid magnet, which provides a 0.5 T nominal magnetic field. These subsystems are mostly dedicated to vertex reconstruction, tracking, particle identification and momentum measurement.

In the mid-rapidity region, there are also some specialised detectors with limited acceptance:

- High-Momentum Particle Identification Detector (**HMPID**);
- PHOton Spectrometer (**PHOS**);
- ElectroMagnetic CALorimeter (**EMCal**) and Di-jet Calorimeter (**DCal**).
- The forward detectors are placed in the high pseudorapidity region with different acceptances. These detectors include the muon spectrometer and specialised systems for event triggering and measuring global event characteristics. They include:
 - Muon Spectrometer ($-4.0 \leq \eta \leq -2.5$). It consists of a dipole magnet, tracking and trigger chambers; it is optimised to reconstruct heavy quark hadrons through their $\mu^+ \mu^-$ decay channel and single muons.
 - Forward Multiplicity Detector (**FMD**) ($-3.4 < \eta < 5.1$);
 - Photon Multiplicity Detector (**PMD**) ($2.3 < \eta < 3.7$);
 - Zero Degree Calorimeters (**ZDC**) ($|\eta| > 8.8$ for ZN, $6.5 < |\eta| < 7.4$ for ZP, $4.8 < |\eta| < 5.7$ for ZEM);
 - **V0** Detectors ($2.8 < \eta < 5.1$ for **V0-A** and $-3.7 < \eta < -1.7$ for **V0-C**);
 - **T0** Detectors ($4.6 < \eta < 4.9$ for **T0-A** and $-3.3 < \eta < -2.9$ for **T0-C**).

This Section presents details regarding some of these detectors, focusing on the ones that are more relevant to this Thesis. Since the **EMCal** is essential for this work, the next Chapter (4) will be dedicated to it.

3.2.1 Inner Tracking System

The Inner Tracking System [121] is the **ALICE** detector closest to the interaction point. The detector is attached to the beam pipe, covering the region from 3.9 cm to 43 cm in radius. The **ITS**, which is schematised in Fig. 3.3, is composed of six cylindrical layers of silicon

3.2. The ALICE Detector

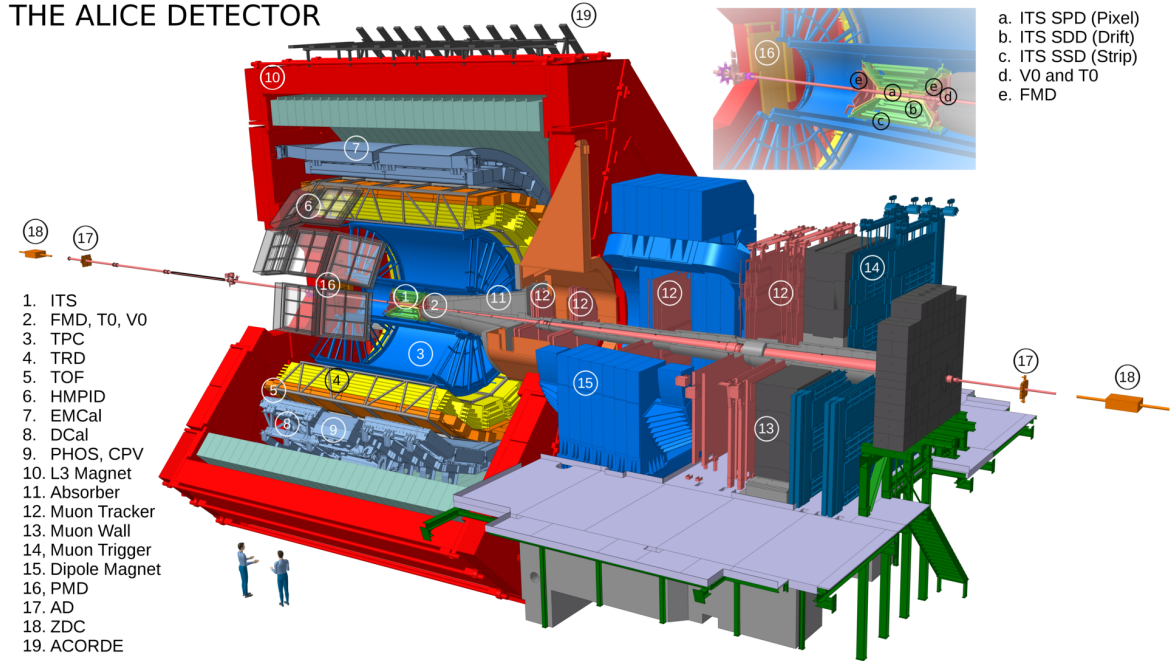


Figure 3.2: The [ALICE](#) experimental apparatus with individual sub-detectors labelled during Run 2.

detectors placed coaxially around the beam vacuum tube. The layers are instrumented with sensors based on different technologies. The two innermost layers are silicon pixel detectors (**SPD**), the third and fourth ones are silicon drift detectors (**SDD**), and the last two layers are double-sided silicon strip detectors (**SSD**). The details about the position, spatial extension, material budget, and spatial resolution of each layer are reported in Table 3.2.

The two layers of the Silicon Pixel Detector are based on hybrid silicon pixels. The **SPD**'s main purpose is to equip [ALICE](#) with sufficient secondary vertexing capability for detecting charm and beauty particles in a high-multiplicity environment. Specifically, the first layer of the **SPD** is utilized to measure the charged-particle multiplicity at midrapidity. Each readout chip in the **SPD** layers provides a binary output, delivering only hit information on the track without measuring energy loss.

The two Silicon Drift Detector layers are the two intermediate layers of the **ITS**, which, together with the two outermost layers Silicon Strip Detector, have analogue readout and can be used for **PID** via dE/dx measurement for low momentum particles.

Finally, the two **SSD** layers, besides providing energy loss measurements, play a crucial role in tracking the particles produced in the collisions connecting the tracks from the external detectors (i.e. Time Projection Chambers) to the **ITS** inner layers.

The **ITS** is characterised by a low total material budget, which reduces the particle multiple scattering with the detector structures. A particle crossing the **ITS** at $\eta = 0$ traverses an amount of material corresponding to about 7.2% of a radiation length X_0 , including the support structures and the thermal shields. The **ITS** has these main tasks:

- to localise the collision position, that is the primary vertex with a resolution better than 100 μm in pp collisions and 3–4 μm in central Pb–Pb collisions;
- to improve the spatial, angular, and momentum resolution for tracks reconstructed by

the TPC;

- to identify and track particles with momentum below $100 \text{ MeV}/c$, which do not reach the TPC.

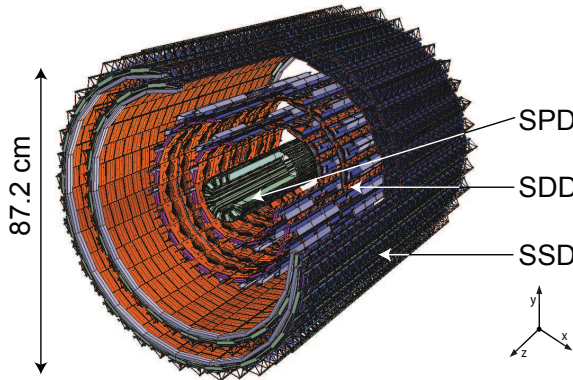


Figure 3.3: Schema of the Inner Tracking System [122].

Layer	Detector	r (cm)	$\pm z$ (cm)	Material budget (% X_0)	Spatial resolution $r\varphi \times z$ (μm^2)
1	SPD	3.9	14.1	1.14	12×100
2	SPD	7.9	14.1	1.14	12×100
3	SDD	15.0	22.2	1.13	35×25
4	SDD	23.9	29.7	1.26	35×25
5	SSD	38.0	43.1	0.83	20×830
6	SSD	43.0	48.9	0.86	20×830

Table 3.2: Properties of the six layers of the ITS detector [121].

3.2.2 Time Projection Chamber

The main detector of the central barrel is the Time Projection Chamber [123]. Its tasks are: to provide the charged particle momentum measurement ($0.1 \text{ GeV}/c < p_T < 100 \text{ GeV}/c$), to contribute to the primary vertex determination and to perform particle identification via the measurement of the ionisation energy loss dE/dx .

The TPC is an 88 m^3 gas-filled cylinder with dimensions of an 85 cm inner radius, a 250 cm outer radius, and a length of 5 m along the beam direction. It spans the pseudo-rapidity range of $|\eta| < 0.9$ and offers full azimuthal acceptance. A central electrode divides the detector into two drift regions. The detector was filled with an Ar/CO₂ (88/12) or Ne/CO₂/N₂ (90/10/5) gas mixture during 2016 and 2018, or 2017, respectively. The Ar and CO₂ mixture was used to enhance PID resolution in the relativistic rise region. As charged particles pass through the TPC, they ionize the gas, generating free electrons and ions. The drift field separates these charges, causing the electrons to move towards the end-plates. The parameters of the particle trajectory within the known magnetic field are used to measure the particle's momentum. The applied external electric field accelerates the electrons and

ions generated during ionization, causing them to drift towards the readout chambers and the Central Electrode (CE), respectively. The readout chambers are comprised of multi-wire proportional chambers (MWPC) with cathode pad readout. In the high electric fields near the anode wires, an electron avalanche is produced, which amplifies the primary ionization signal. The electrical signal induced by the positive space charge on a segmented pad plane is shaped, amplified, digitized, processed, and read from each readout pad by the data acquisition system. A schematic view of the TPC detector is shown in Fig. 3.4.

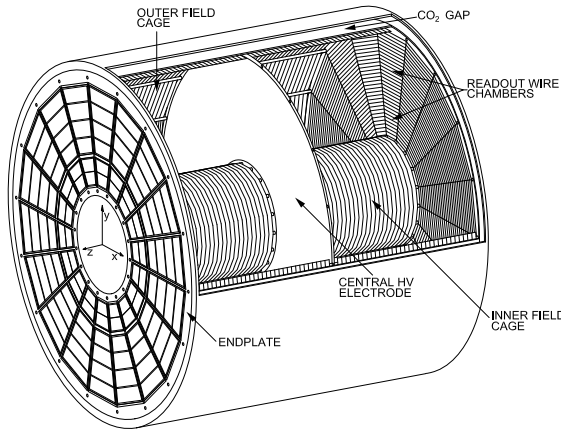


Figure 3.4: Schema of the Time Projection Chamber [122]

The maximum drift time of the electrons is $\sim 88 \mu\text{s}$, setting in this way a limit on the sustainable event rate of the TPC. At high interaction rates, pile up becomes relevant. This effect can be rejected considering that tracks from pileup point to a different primary vertex.

With this configuration, shown in Fig. 3.4, the detector provide a very high tracking efficiency, larger than 90%, for track of p_T between 100 MeV/ c and 100 GeV/ c and guarantee a good two-track separation with a resolution in relative momentum of few (below 5) MeV/ c . Measuring the tracks deflection in the magnetic field, the TPC is able to determine the momentum of charged particles with a resolution better than 1% at low p_T and better than 20% for $p_T \sim 100 \text{ GeV}/c$.

3.2.3 V0 Detector

The VZERO (V0) detectors [47] are composed of two arrays of scintillator counters, known as V0-A and V0-C. V0-A is positioned on the positive z -direction approximately 3.4 m from the ALICE vertex, opposite the muon spectrometer, and covers the pseudorapidity range $2.8 < \eta < 5.1$. V0-C is located on the opposite side of the vertex in the negative z -direction, about 90 cm away, with pseudorapidity coverage of $-3.7 < \eta < -1.7$. Each V0 array is segmented into four rings in the radial direction, with each ring further divided into eight sections in the azimuthal direction, as illustrated in Fig. 3.5.

This detector system serves multiple functions, including providing minimum bias (MB) and high multiplicity (HM) triggers for the central barrel detectors in pp, p-Pb, and AA collisions. During the initial data-taking periods in 2009, the ALICE MB trigger was activated by a hit in the Silicon Pixel Detector or either of the V0 arrays (V0-A or V0-C). Due

to increasing **LHC** luminosity and beam background in more recent data-taking periods, the trigger conditions were tightened to require coincidence between both **V0** arrays and the **LHC** bunch crossing signals. A significant source of background comes from interactions between the beams and the residual gas within the beam pipe, as well as between the beam halo and various accelerator components, such as the collimators. However, by using the time of flight of particles detected by each **V0** array, it is possible to efficiently distinguish between particles from collisions and those from beam-gas backgrounds. Additionally, the **V0** detector measures charged particle multiplicity based on the signal amplitude in the scintillators, which is used to define percentile classes and it is discussed with more details in Sect. 3.5.

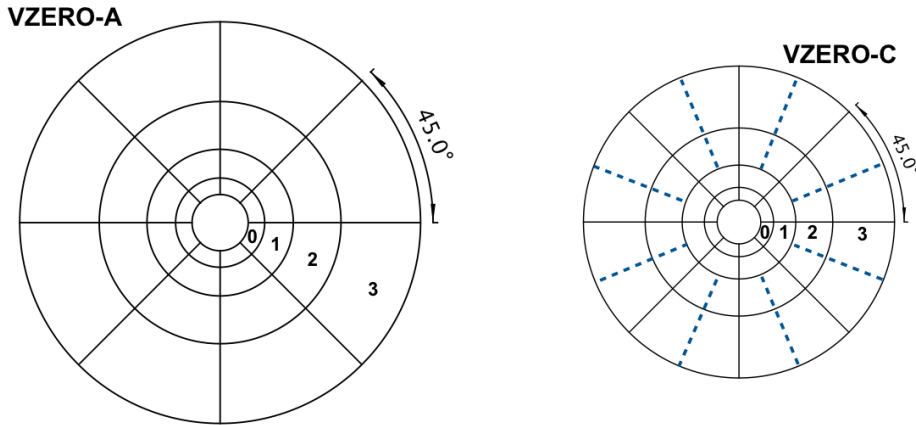


Figure 3.5: Sketches of **V0**-A and **V0**-C arrays showing their segmentation. Scintillator thicknesses are 2.5 and 2 cm respectively. The scintillator segments on both sides of the dashed lines are connected to the same PMT [47].

3.3 The ALICE data acquisition and offline framework

ALICE data-taking activities during Run 1 and 2 were managed by several central online systems. The Detector Control System (DCS) operated the detector hardware from a central interface. The Data Acquisition (**DAQ**) system controlled the configuration of the detectors during data collection. The Trigger (TRG) systems facilitated the selection of interesting physics events.

The **ALICE** trigger system consisted of a low-level hardware trigger, the Central Trigger Processor (**CTP**), and a High-Level software Trigger (**HLT**). The **CTP** made trigger decisions by integrating information from different detectors, which had varying readout times. Consequently, the system was divided into three levels: L0, L1, and L2. The Level 0 trigger decision (**L0**) was made approximately 0.9 μ s after each collision. Events that passed this initial selection were then evaluated by Level 1 (**L1**) approximately 6.5 μ s later, allowing time for computation and signal propagation from more distant detectors. If both **L0** and **L1** criteria were met, a Level 2 (**L2**) decision was made after about 100 μ s, which was necessary for the complete drift of ionization charges in the **TPC**.

Events that successfully passed all hardware trigger levels were accepted and processed by

the Data Acquisition system. The **DAQ** was connected to the **HLT**, which performed a rapid reconstruction of each event and further skimming to reduce data volume while preserving essential physics information. Finally, the processed events were permanently stored at the **CERN** computing center.

The extensive data collected by the **ALICE** experiment necessitates a robust infrastructure for processing and analysis. This is managed through the Worldwide **LHC** Computing Grid project [124, 125], which distributes data processing across various global computing centers. It operates as a hierarchical system with three tiers:

1. Tier-0: the largest computing center, located at CERN, serves as the primary data storage and processing hub;
2. Tier-1: large computing centers, handling significant data storage and contributing to raw data management;
3. Tier-2: smaller centers, involved in data processing tasks such as calibration, reconstruction, simulation, and analysis.

This grid infrastructure supports not only data storage but also comprehensive processing and analysis tasks, ensuring efficient management and utilization of the vast amount of data generated. The **ALICE** collaboration has developed a service named **AliEn** (**ALICE** Environment) [126], which facilitates easy access to data on the Grid. Data collected during Run 1 and Run 2 is analyzed using the **ALICE** software environment known as **AliRoot** [127], which is based on **ROOT**, a data analysis framework primarily written in C++. **AliRoot** interfaces with various Monte Carlo generators, such as **PYTHIA**, to simulate particle production in collisions. Detailed simulations of particle interactions with materials are carried out using **GEANT3** [128], **GEANT4** [129], and **Fluka** [130] transport codes. More details regarding **PYTHIA** and **GEANT3** will be presented in Sect. 6.2.

The final analysis is organized in a data repository called **AliPhysics**. The reconstruction process produces Event Summary Data (ESD), which contains comprehensive information about each event at the track and collision levels. From the ESDs, a summary of the most relevant data is extracted and formatted into Analysis Object Data (AOD) to facilitate more efficient analysis.

3.4 Track and vertex reconstruction

In **ALICE**, the track-reconstruction procedure is performed offline. A charged particle passing through the detectors leaves a number of discrete hits at corresponding positions in space.

The reconstruction process begins with a local cluster-finding algorithm executed by each detector within its sensitive volumes. This algorithm combines the signals generated by particles crossing the detectors' sensitive areas into individual clusters, each characterized by positions, signal amplitudes, times, and associated errors. Next, a preliminary determination of the primary vertex is made using SPD tracklets, which are defined as lines connecting two clusters found in the two SPD layers of the ITS. The primary vertex is identified as the point in space where the maximum number of tracklets converge. Track finding and fitting are

performed using ITS and TPC clusters through the Kalman filter technique [131] in three stages, following an inward-outward-inward scheme.

The track-finding algorithm in **ALICE** starts with the reconstruction in the **TPC**. It builds track seeds from the clusters in the two outermost pad rows of the **TPC** and the primary vertex estimated using the **SPD** tracklets. These seeds are then propagated inward, with the Kalman Filter algorithm selecting the cluster closest to the track at each step based on a proximity cut. This process continues until the inner radius of the **TPC** is reached. The tracks reconstructed in the **TPC** are then matched to hits in the outermost **SSD** layer, becoming seeds for track finding in the **ITS**. Similar to the previous step, the seeds are propagated inward, attaching the closest clusters within a proximity cut to the seed. Consequently, each **TPC** track generates a corresponding tree of track hypotheses in the **ITS**. Track candidates are selected based on their χ^2 values. To increase efficiency for tracks with low transverse momentum ($p_T < 200$ MeV/ c) and to reconstruct tracks of particles that traverse dead zones of the **TPC** or decay before entering the **TPC**, the hits in the **ITS** that are not attached to tracks propagated from the **TPC** are used for an **ITS** stand-alone reconstruction.

In the second iteration, the tracks obtained with clusters in both the **ITS** and **TPC** detectors are extended outward to match the reconstructed points in the outer detectors (i.e., TRD, TOF, **EMCal**, **DCal**, PHOS, and HMPID). Finally, the tracks are re-fitted inward using all the previously found clusters and propagated to their Distance of Closest Approach (**DCA**) to the **SPD** vertex.

After the full tracking procedure, if at least two tracks are reconstructed, the position of the primary vertex is recomputed using global tracks (tracks with both **ITS** and **TPC** reconstruction). To remove contributions from secondary tracks originating from interactions with detector material or particle decays, a cut on the distance of closest approach between the tracks and the primary vertex is applied.

During some data taking periods, part of the **SPD** was not operational, causing a non uniform reconstruction efficiency in azimuth. For this reason, the tracks, used in this analysis that requires a uniform detector response, were reconstructed using a hybrid approach. This method distinguishes between two track classes accepted [132]: (i) tracks containing at least three hits in the **ITS**, including at least one hit in the **SPD**; their momentum is determined without using the primary vertex position in the fit, and (ii) tracks containing less than three hits in the **ITS** or no hit in the **SPD**, with the primary vertex included in the momentum determination. Class (i) contributes to 90% and class (ii) to 10% of all accepted tracks, independently of p_T .

To ensure high track quality, several selection criteria are applied. All selected tracks must lie within a pseudorapidity range of $|\eta| < 0.9$, as determined by the geometrical coverage of the **ITS** and **TPC**. Additionally, each reconstructed track must contain at least 70 out of a possible 159 clusters in the **TPC**, ensuring enough clusters for a reliable fit with satisfactory p_T resolution while suppressing “fake” tracks that do not originate from particles produced in the collision. To further guarantee good track fit quality, the χ^2 value of the track fit calculated between the track helix and the associated **TPC** clusters must not exceed

5 per TPC cluster. To prevent multiple tracks from being reconstructed for the same charged particle, candidates sharing more than 40% of their TPC clusters with another track in the same event are rejected. A lower transverse momentum threshold of $p_T > 100$ MeV/ c is applied to eliminate tracks that bend too much in the magnetic field to be reconstructed with sufficient momentum resolution. Finally, all tracks are required to originate from the primary collision vertex, with a loose selection based on their DCA to the vertex. Specifically, charged-particle tracks are selected if their DCA to the primary vertex is less than 2.4 cm in the plane transverse to the beam and less than 3.0 cm in the beam direction.

All these criteria, that are summarized in Table 3.3, are applied to the tracks selected and used in this Thesis.

name	selection
Min. clusters in TPC tracking fit quality acceptance transverse momentum DCA to primary vertex	$N_{\text{clust}}^{\text{TPC}} > 70$ $\chi^2/\text{clust.} < 5$ $ \eta < 0.9$ and full azimuthal angle $p_T > 100$ MeV/ c $d_{xy} < 2.4$ cm $d_z < 3.2$ cm

Table 3.3: Overview of the track selection criteria.

3.5 Centrality determination in Pb–Pb collisions

Heavy ions are extended objects, hence their collisions are typically classified by the collision centrality, which is the volume of the overlapping region and directly related to the collision impact parameter b , as discussed in Sect. 1.4.2. Centrality is usually expressed as a percentage c of the total hadronic interaction cross section σ_{AA} :

$$c(b) = \frac{\int_0^b \frac{d\sigma}{db'} db'}{\int_0^{+\infty} \frac{d\sigma}{db'} db'} = \frac{1}{\sigma_{\text{AA}}} \int_0^b \frac{d\sigma}{db'} db'. \quad (3.3)$$

The impact parameter of a collision cannot be accessed directly, experimentally, thus to obtain the collision centrality, the relation between the number of particles produced in the collision and the number of spectator nucleons is exploited. In the ALICE experiment, two primary observables related to the collision geometry are measured: the energy deposited by spectator nucleons in the ZDC detector and the signal amplitude produced by charged particles in the V0 detector, which is proportional to the particle multiplicity N_{ch} [133]. The latter result will be discussed more in detail, because it is employed to determine the centrality classes used in this Thesis.

Assuming the particle multiplicity N_{ch} increases monotonically with the overlap volume, the centrality can be computed as:

$$c \simeq \frac{1}{\sigma_{\text{AA}}} \int_{N_{\text{ch}}}^{+\infty} \frac{d\sigma}{dN'_{\text{ch}}} dN'_{\text{ch}} = \frac{1}{n_{\text{ev}}^{\text{tot}}} \int_{N_{\text{ch}}}^{+\infty} \frac{dn_{\text{ev}}}{dN'_{\text{ch}}} dN'_{\text{ch}}. \quad (3.4)$$

The total hadronic cross section σ_{AA} and the differential cross section $d\sigma$ in the Eq. (3.4), can be substituted with the total number of events (n_{ev}^{tot}) corrected for the trigger efficiency and with the number of observed events dn_{ev} within a given multiplicity interval dN'_{ch} , respectively. For a given value of the V_0 amplitude, the percentile of the hadronic cross section can be determined by integrating the distribution of the measured V_0 amplitudes normalized at an *anchor point*. The anchor point is defined as the V_0 amplitude corresponding to 90% of the hadronic cross section and sets the absolute scale for centrality.

The *anchor point* is determined by fitting the distribution of V_0 amplitudes measured in Pb–Pb collisions with a parametrisation based on a Glauber Monte Carlo simulation. For each simulated event, the number of participant nucleons N_{part} and the number of binary collisions among nucleons N_{coll} are obtained from Glauber model calculations (see Sect. 1.4.2). The multiplicity distribution is modeled assuming $fN_{\text{part}} + (1-f)N_{\text{coll}}$ particle sources, where the f parameter represents the contribution of soft processes to the particle production. Each source produces particles following a negative binomial distribution (**NBD**) with fit parameters μ and k .

The **NBD** distribution is defined as:

$$P_{\mu,k}(n) = \frac{\Gamma(n+k)}{\Gamma(n+1)\Gamma(k)} \times \frac{(\mu/k)^n}{(\mu/k+1)^{n+k}} \quad (3.5)$$

where μ is the mean multiplicity per ancestor and k is a parameter controlling the width of the distribution. The fit provides the integrated number of events N_{ev} needed for the absolute centrality scale and relates the number of participants and binary NN collisions to the centrality.

Figure 3.6 reports the distribution of the V_0 amplitude measured in Pb–Pb collisions at $\sqrt{s_{\text{NN}}} = 2.76$ TeV together with the fitted **NBD**-Glauber parametrisation. The bands report the limits of the centrality classes which are defined in terms of percentiles of the integral of the distribution up to the anchor point.

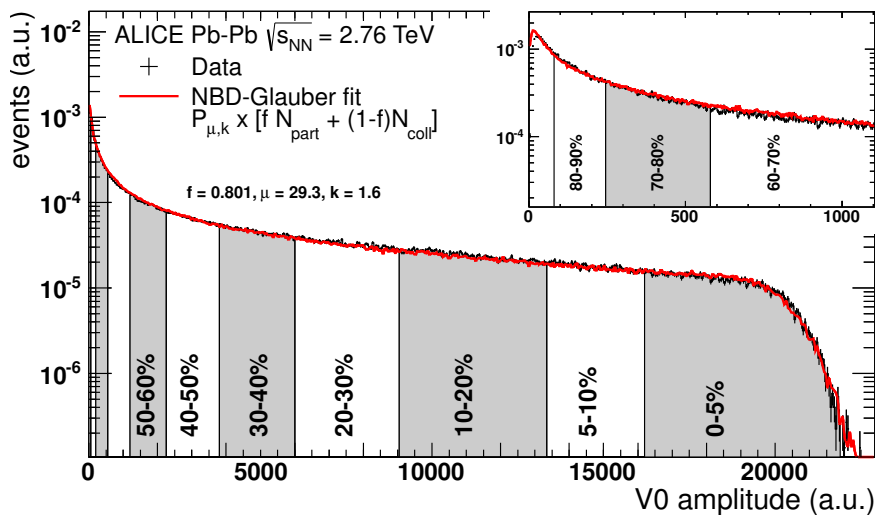


Figure 3.6: Distribution of the V_0 amplitudes measured in Pb–Pb collisions at $\sqrt{s_{\text{NN}}} = 2.76$ TeV. The red line reports the **NBD**-Glauber fit, while the bands show the different centrality classes [122].

Centrality estimation biases

The centrality classification, based on the measured V0 amplitude and on the MC Glauber model, can bias the mean number of charged particles of individual NN collisions, that is the multiplicity, and, in case of correlations between soft and hard particle production, it can influence the yield of hard processes in AA collisions. There are two main origins for these selection biases. Firstly, the spatial distribution of nucleons bound in nuclei in the plane transverse to the beam direction differs from those of protons in a beam leading to a bias on the NN impact parameter. Secondly, centrality selection is based on measurements related to bulk, soft particle production [99].

These biases have to be taken into account when interpreting measurements that use these parameters, such as the nuclear modification factor R_{AA} . Figure 3.7 reports the simulated R_{AA} taking into account the effect of the geometry bias only (cross markers) and the outcome obtained with the geometry and event selection biases (circle markers) as a function of the centrality.

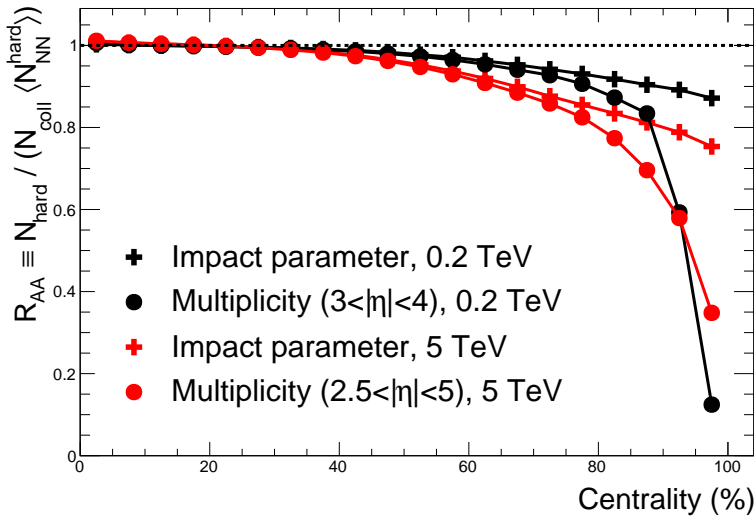


Figure 3.7: R_{AA} versus centrality for Au–Au and Pb–Pb collisions at $\sqrt{s_{NN}} = 0.2$ TeV (black markers) and $\sqrt{s_{NN}} = 5.02$ TeV (red markers), respectively, calculated with HG-PYTHIA model [99].

The biases introduced a suppression in the R_{AA} that becomes stronger as the collision events are more and more peripheral. This apparent suppression is present in all high energy collisions and it is expected to be larger at lower collision energies. In conclusion, it is important to consider these biases in the estimation of the medium effect with the R_{AA} ; in fact they can generate artificial suppressions, not related to nuclear modification effects. In contrast, centrality measurements based on zero-degree energy should not introduce any selection bias, but the geometric bias could still play a role.

Chapter 4

The electromagnetic calorimetry and its role in the ALICE experiment

4.1	Photon interaction with matter	78
4.2	The EMCal calorimeter	81
4.2.1	From the cell to the supermodule	82
4.2.2	Electronics acquisition and EMCal triggers	85
4.2.3	Calibrations: energy and time	88
4.3	The EMCal performance	89

It is possible to distinguish between two types of calorimeters: hadronic and electromagnetic; their difference depends on which particles are intended to be detected and the calorimeter’s structural characteristics [134]. The hadronic calorimeter (HCAL) is designed to measure particles that interact via the strong nuclear force (see Chapter 1). On the other hand, the electromagnetic calorimeter (ECAL) is specifically designed to measure the energy of particles that interact primarily via electromagnetic interaction.

In the next sections, the focus will be on electromagnetic calorimeters, which are the main detectors used to measure the photon used as triggers in the γ^{iso} -hadron correlations. Initially, I will discuss the interaction of photons with matter, then I will concentrate on the [ALICE EMCal](#) calorimeter by presenting its structure and properties. More details can be found in the [EMCal](#) performance paper [135].

4.1 Photon interaction with matter

Photons can interact with matter through various electromagnetic processes, which are well described by [QED](#) (see Chapter 1). Among them there are three main interactions:

- **photoelectric effect**: a photon is absorbed by an atom of the medium and due to this excitation, an electron of the corresponding energy is emitted;
- **Compton effect**: a photon interacts with one of the e^- of the matter and results in the electron emission. The photon is not absorbed, but deflected with lower energy;
- **pair production** ($\gamma \rightarrow e^-e^+$): the entire energy of the incident photon is converted into matter/antimatter, with the production of an electron and a positron.

Figure 4.1 reports the photon-matter interaction cross section for two different elements, carbon (C) and lead (Pb), which are characterised by different atomic numbers Z . As

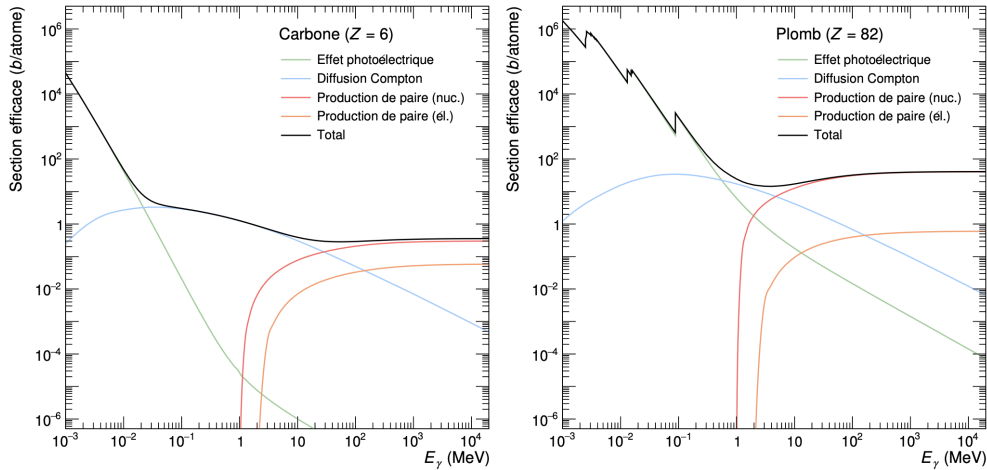


Figure 4.1: Photon-matter interaction cross section and its three main contributions as a function of incident photon energy in carbon (left) and lead (right) [136]. Pair production actually has two components, linked to the nuclear (nuc.) and electronic (el.) electric fields of the atom near which the process takes place [137].

Fig. 4.1 shows, below 10^{-2} - 10^{-1} MeV the photoelectric effect is the dominant one, while the Compton dominates around 1 MeV; increasing much more the energy, at several MeV, the pair production takes over and becomes the principal effect. Comparing this trend to the relevant energies for the ALICE experiment, from a few GeV up to 200 GeV, it is possible to conclude that the pair production contributes the most.

Once pairs are generated, e^- and e^+ can also interact with the material and to illustrate this behaviour we can look at Fig. 4.2, which reports the probability of an electron interaction per process in the lead matter depending on its energy.

At LHC energies, the most probable process is the Bremsstrahlung radiation: the electron/positron interacts with matter nuclei, emitting a photon. This phenomenon is sketched in Fig. 4.3: the process propagates with subsequent emissions of photons and pair production until the energy of the photon/pair production is not sufficient anymore for the next step. The combination of Bremsstrahlung and pair production generates a large number of photons, positrons and electrons in a small volume and this is referred to as **electromagnetic (EM) shower**. The development of the shower can be seen in Fig. 4.3: it is characterized by longitudinal (L) and radial (l) expansions: these properties define constraints on calorimeter construction.

The longitudinal expansion is related to the **radiation length** X_0 , which characterizes the stopping power of the calorimeter [139]. X_0 is defined as the length needed for the initial

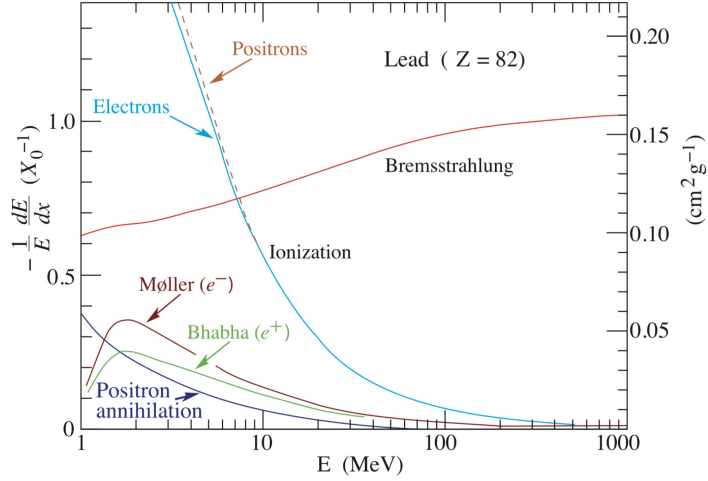


Figure 4.2: Contributions related to the loss of energy per unit radiation length (quantity defined in the text) suffered by an electron or positron in the lead (Pb) as a function of its energy [138].

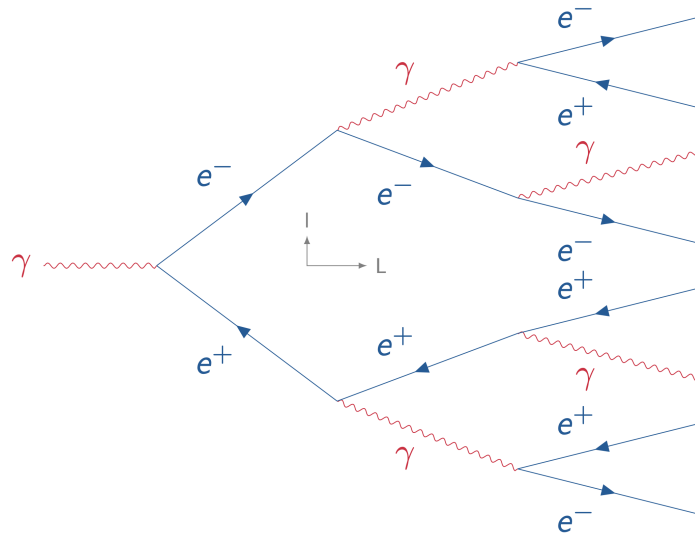


Figure 4.3: Sketch of the development of an electromagnetic shower induced by an incident photon. The axes "L" and "l" represent the longitudinal and radial components of this development respectively. Figure taken from [137]

electron with an energy E_0 to reach an energy E_0/e . Indeed, the energy loss in the material via photon emission is described by an exponential function:

$$E = E_0 e^{x/X_0} \text{ with } X_0(\text{cm}) \simeq \frac{716.4A}{Z(Z+1)\ln(287)} \cdot \frac{1}{\rho} \quad (4.1)$$

where x is the distance and A is the mass number of the material. Thus, the energy loss depends on the considered material and its density (ρ): the larger the atomic number (Z) and the density, the lower the radiation length X_0 . Since the **EMCal** is designed to study electrons until hundreds of GeV, X_0 needs to be low enough to let electrons lose all their energy inside a calorimeter of reasonable size.

Figure 4.1 shows that the interaction cross-section is larger for heavier elements: Pb can therefore be used to keep the detector compact; it is not a case that the **ALICE** calorimeters (**EMCal** and **PHOS**) use Pb material as converter.

Another important property of the shower is the **radial expansion**, that is the width of the shower in the plane perpendicular to the direction of the incident particle. The radial expansion is related to the **Molière radius**, which is the radius of a cylinder containing on average 90% of the shower's energy deposition. The Molière radius [139] R_M is approximately expressed as:

$$R_M \simeq \frac{21.2 \text{ MeV}}{E_C} X_0 \quad (4.2)$$

where E_C is the critical energy of the considered medium for which the energy loss via ionisation becomes equivalent to the energy loss via pair creation.

If the radial expansion of the electromagnetic shower of particles is too large, the showers of two incident particles will be merged and the discrimination of them is more difficult. The Molière radius sets limits to the granularity of the calorimeter so that most of the particle shower is contained in the smallest sensible unit of the detector.

4.2 The EMCal calorimeter

The **ALICE** central barrel includes two electromagnetic calorimeter systems: the PHOton Spectrometer (**PHOS**) and the ElectroMagnetic Calorimeter (**EMCal**).

The **PHOS** is composed of 12544 lead-tungsten PbWO_4 crystals with a size of $22 \times 22 \times 180 \text{ mm}^3$ each, covering a pseudo-rapidity range $|\eta| < 0.12$ and azimuthal angles $260^\circ < \varphi < 320^\circ$ during Run 1 and $250^\circ < \varphi < 320^\circ$ during Run 2. The **PHOS** is a homogeneous calorimeter where the **EM** shower is created and measured in the lead-tungstate crystals of the **PHOS**. This technology generally allows to achieve a better energy resolution than sampling calorimeters [9], however comes with a larger cost, which is reflected in the smaller acceptance of the **PHOS** with respect to the **EMCal**. It was designed to measure spectra of thermal and direct photons, and neutral mesons via their decay into photon pairs.

The **EMCal** [140] is composed of towers of $6 \times 6 \times 20 \text{ cm}^3$ each one constituted of 76 alternating layers of lead and scintillator (not uniform in contrast to **PHOS**); it was designed for the measurements of electrons from heavy-flavor hadron decays, the electromagnetic component of jets, spectra of direct photons and neutral mesons and correlations of those photons with hadrons or jets. It has been completed by the **DCal**, at the opposite side of the beam

pipe, during the LHC long shut-down (LSD) before the Run 2 (2013-2014). The DCal, built with the same technology as EMCal, is located around PHOS, as shown in Fig. 4.4-right, it was added to ease the study di-jet events and photon/ π^0 -jet events. Both calorimeters are trigger detectors and they select collisions when there is a high energy deposition, typically a few GeV, in a small area of 2×2 cells, called photon trigger (more details in Sect. 4.2.2). They also provide a dedicated trigger for jets, typically in the range of several tens of GeV, over a larger area like 32×32 cells [135].

In the following, I will call the sum of EMCal + DCal, the “EMCal calorimeter”: they have different names, but they are identical, except for the acceptance. I will describe the EMCal calorimeter properties and performances and illustrate its central role for the thesis analysis.

4.2.1 From the cell to the supermodule

The two parts of the EMCAL calorimeter, shown in Fig. 4.4 and mentioned in the previous section, have:

- EMCAL: 12288 towers covering $80^\circ < \varphi < 187^\circ$ and $|\eta| < 0.7$
- DCal: 5376 towers covering $260^\circ < \varphi < 320^\circ$ and $0.22 < |\eta| < 0.7$ and $320^\circ < \varphi < 327^\circ$ and $|\eta| < 0.7$. The $|\eta| < 0.22$ is covered by PHOS and its services.

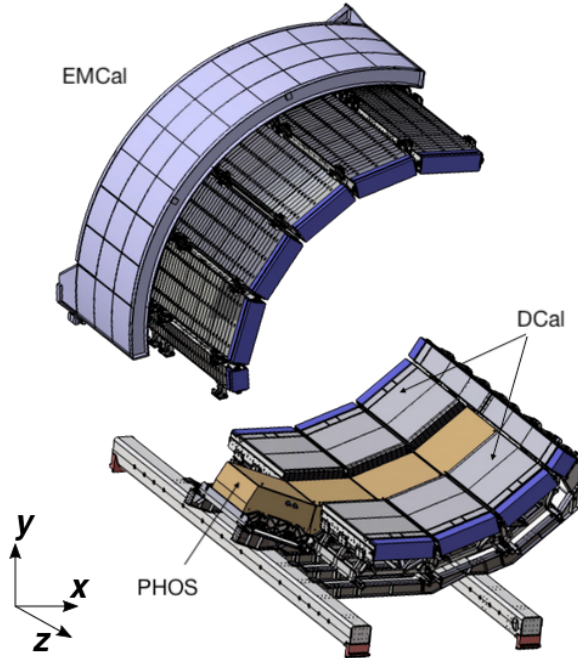


Figure 4.4: Schematic view of the EMCAL calorimeter illustrating the module position on two approximately opposite locations in azimuth φ . The PHOS calorimeter is inside the DCal and is indicated in brown [135].

The **towers** or **cells** are the elementary units of the calorimeter with a dimension of $\simeq 0.0143 \times 0.0143 \text{ rad}^2$, or $6 \times 6 \text{ cm}^2$, all pointing approximately towards the interaction point of the experiment. The EMCAL calorimeter is located 4.28 m in radial distance from the beam pipe.

4.2. The EMCal calorimeter

Each tower/cell is made of 76 layers of lead (Pb), 1.44 mm thick, interleaved with 77 plastic scintillator layers. The electromagnetic shower mostly develops in the Pb scintillator layers, to detect ionization due to e^+ and e^- .

The collection of the light, generated by the **EM** shower, is assured by 36 optic fibres, which cross the tower along its longitudinal section. The fibres are collected outside of the tower, as it is shown in Fig. 4.5 (indicated by number 14) and they are connected using a waveguide to the Avalanche Photo Diodes (**APDs**) (15), that convert the light into an analogic signal and transfer it to the Front End Electronics (**FEE**).

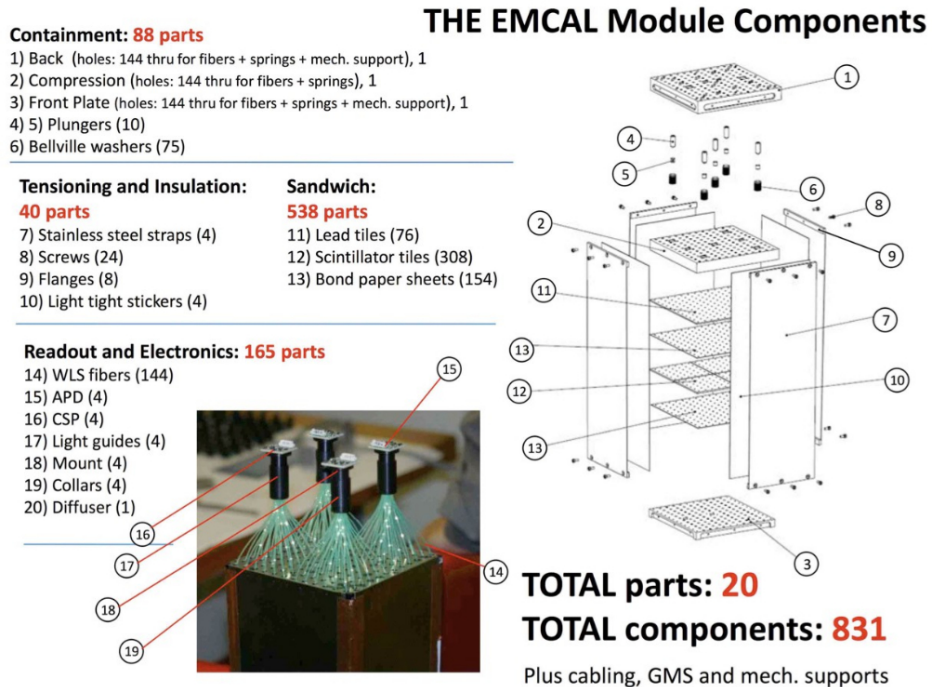


Figure 4.5: Photo and drawing of the **EMCal** module components [132].

The **EMCal** has different segmentation levels, as shown in Fig. 4.6: the towers are grouped in sets of four (2×2) to form a **module**, which are assembled linearly in sets of 12 in the φ direction into strips called **strip-modules**. The grouping of these strip-modules forms the highest level of segmentation of the calorimeters, called a **supermodule SM**. Each full-size **SM** is assembled from $12 \times 24 = 288$ modules arranged in 24 strip modules of 12×1 modules each. There are three types of supermodules: two types of complete supermodules consist of 24 strip-modules for **EMCal** and 16 strip-modules for **DCal** (to make space for the **PHOS** modules), and the third type of supermodule for **EMCal** and **DCal** consists of an assembly of 24 thirds of strip-modules, therefore containing only 4 modules each instead of 12.

The towers are characterised by an effective X_0 of 1.23 cm and an effective Molière radius of 3.20 cm. Since these values are only twice larger than the lead ones, the calorimeter towers are particularly compact; the **EMCal** towers' height is 24.6 cm, which corresponds to 20.1 X_0 and it is sufficient to fully contain the electromagnetic showers formed by photons and electrons with energies up to 200 GeV, enabling the fulfilment of the physics program of the experiment.

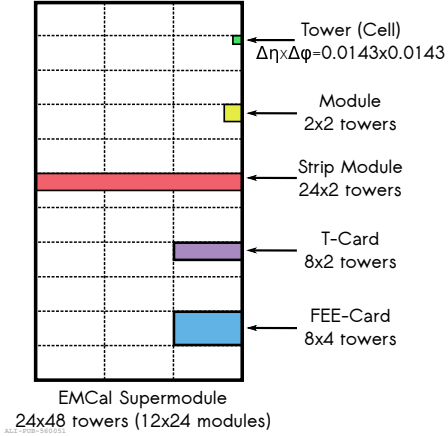


Figure 4.6: Illustration of one EMCAL supermodule with the different segmentation levels: tower (green), module (yellow), strip module (pink), T-Card (violet) and FEE-Card (light blue) [132].

Quantities	Values
Tower/cell dimension	$z \times \varphi \times r = 6 \times 6 \times 24.6 \text{ cm}^3$
Tower/cell acceptance	$\Delta\eta \Delta\varphi \simeq 0.0143 \times 0.0143 \text{ rad}^2$
Sampling report	1.44 mm Pb/1.77 mm scintillator
Numb. of layers of Pb (plastic)	76(77)
Radiation length X_0	12.3 mm
Molière radius R_M	3.2 cm
Number of towers	EMCal: 12288 DCal: 5376
Number of supermodules	EMCal: $10 + 2 \times 1/3$ DCal: $6 + 2 \times 1/3$
Total acceptance	EMCal: $80^\circ < \varphi < 187^\circ; -0.7 < \eta < 0.7$ DCal: $260^\circ < \varphi < 320^\circ, 320^\circ < \varphi < 327^\circ;$ $-0.7 < \eta < -0.12 \cup 0.12 < \eta < 0.7$

Table 4.1: Summary of the EMCAL and DCAL properties.

Table 4.1 summarizes the properties of the EMCAL and DCAL reported before.

4.2. The EMCal calorimeter

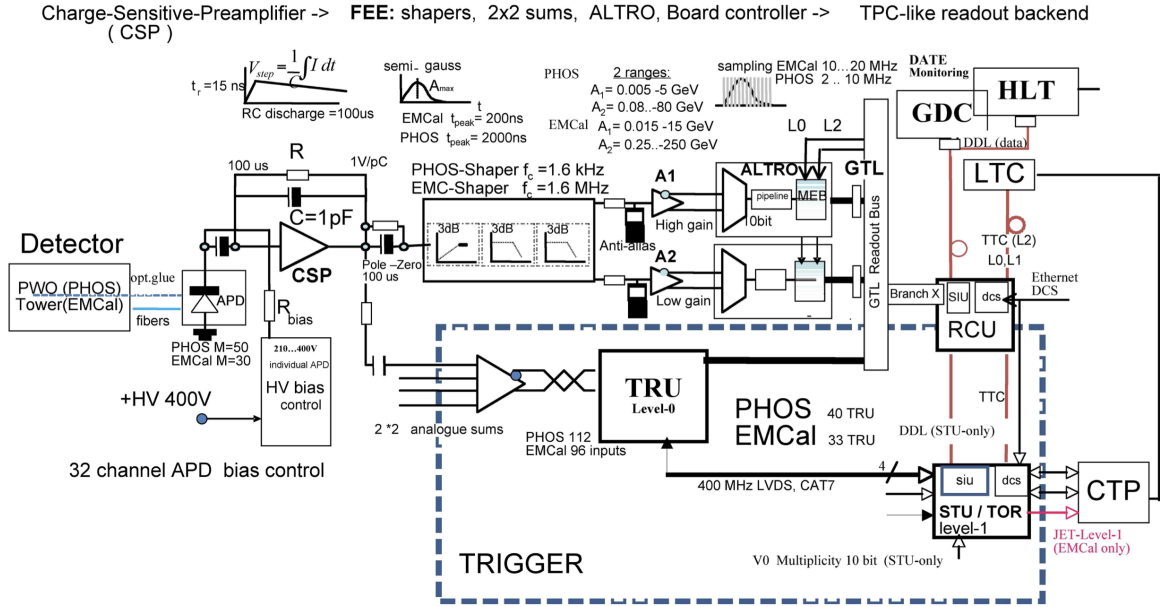


Figure 4.7: Scheme of the EMCal front end electronics [140].

4.2.2 Electronics acquisition and EMCal triggers

The Avalanche Photo Diodes convert the light into an electrical signal via the photoelectric effect. After the conversion of the light to an electric input, the signal is sent to the Charge Sensitive Pre-amplifier (CSP), which converts it to a pulse. This electronic chain is reported in Fig. 4.7.

The APDs amplify the signal with low gain (15 MeV - 15 GeV) and high gain (250 MeV - 250 GeV), and generate two digitized time-dependent electronic pulse shapes that are stored in raw data format and that are proportional to the number of photo-electrons collected by the APD. If the signal amplitude corresponds to energies below $E \simeq 16$ GeV, the high gain is applied, otherwise the low gain signal is used. At this point, the obtained pulse shape is fitted using a Γ -function ($\Gamma_n(t)$):

$$\Gamma_n(t) = p + Ax^n(t) \exp\{n[1 - x(t)]\} \quad (4.3)$$

with

$$x(t) = \frac{t - t_{\max} + \tau}{\tau} \quad \text{and} \quad \tau = n\tau_0 \quad (4.4)$$

where t_{\max} is the time in which the maximum of the input signal is expected and τ_0 is the characteristic time of the ADC. From the fit, the signal amplitude (linked to the energy of the incident particle) and arrival time can be extracted. This procedure is called **raw data fitting** and an example of it is reported in Fig. 4.8.

The obtained pulse is transferred to a FEE card and the signal goes through a shaper to be in the correct form to be transmitted to the Analog to Digital Converters (ADCs), allowing its digitalisation. This procedure allows us to measure the energy and position of EM probes.

In addition, the EMCal provides hardware-based event triggers used to enhance photon and jet signal measurements [140]. It allows to select high- p_T photons, electrons and jets, that otherwise would not be easily obtained using the minimum bias. That is why

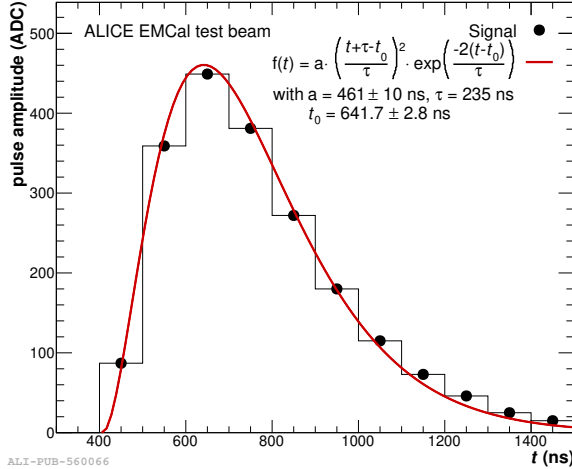


Figure 4.8: Digital signal (full black circle) of a tower obtained at the output of a FEE card as a function of time, fitted by the function $\Gamma_n(t)$ (full red line) defined in Eq. (4.3) [132].

the **EMCal** incorporates into its electronic design the ability to trigger data based on the information gathered in its towers, as shown in Fig. 4.7. The digitised signals are sent to the trigger chain. The first step consists of summing the digitised signals in groups of 2×2 towers to reconstruct the signal corresponding to a complete module. Each **FEE** card thus produces eight summed signals called **FastORs**. The **FastORs** signals are sent to a Trigger Region Unit card (**TRU**) to enable a fast Level-0 trigger. The **L0** algorithm integrates the signals over time using a sliding window of 2×2 **FastORs** (i.e. 4×4 towers), referred to as a trigger patch, and produces a summed signal. This signal has to satisfy the following criteria: an amplitude larger than a predefined threshold and the presence of a peak in the temporal distribution of this signal. Since it is a sliding algorithm, it means that the window scans all 96 towers in the one-third supermodule managed by the **TRU** card in which it is implemented. Consequently, the Level 0 trigger provided by **EMCal** is relatively localized and cannot combine information from multiple **TRU** cards and even less so from multiple supermodules, making it suitable for measuring photons but not jets. When the two selection criteria are met by a summed signal within a given window, the corresponding **TRU** card transmits this information to the central **ALICE** trigger system via the Summary Trigger Unit (**STU**). If the feedback from the Central Trigger Processor is positive (considering, for example, information from other detectors in the experiment), the data collected with the **L0** trigger level can be transmitted to the **DAQ** for storage and reconstruction.

Beyond the Level 0 algorithm, a stricter selection of signals produced by the **EMCal** towers is possible within the **STU** through the Level 1 trigger system [141]. This system is based on the **FastOR** signals prepared by the **TRU** cards for the entire calorimeter and includes two algorithms: **L1- γ** , dedicated to photon measurement, and **L1-jet**, oriented towards jet measurement. Both algorithms operate similarly to **L0** by using sliding windows that scan the surface of the calorimeter. However, unlike **L0**, these windows are not physically restricted to one-third of a supermodule but can cover the entire detector surface. The algorithms are defined with the following criteria:

- **L1- γ** is implemented similarly to **L0**, with the amplitude required to exceed a pre-defined threshold, but it does not involve searching for a peak in the summed signal

distribution.

- L1-jet also uses an amplitude threshold but integrates 16×16 FastOR signals, covering 32×32 towers, to better capture the spatial extent of a particle jet.

It is important to note that the thresholds chosen for the L1 algorithms are not fixed but can depend on the multiplicity of charged particles measured by the V0 detector, which is proportional to the centrality of collisions in heavy-ion systems (p–Pb and Pb–Pb). This precaution is motivated by the fact that a central event tends to emit more particles and induce larger energy deposits in the calorimeter towers, affecting the amplitude of the signals processed by the trigger algorithms. In any case, the EMCal Summary Trigger Unit transmits the results of the L1 algorithm to the CTP, which then decides whether or not to trigger an event/a collision. If triggered, the data collected by the calorimeter with the L1 trigger are transmitted to the ALICE DAQ for storage and reconstruction [137].

The trigger performance can be studied using the ratios of the event-normalized energy spectra of EMCal clusters measured in triggered events to the spectra measured in MB events. The EMCal L1- γ trigger efficiency is the probability that the trigger selects events in which a high-energy cluster is reconstructed in the EMCal acceptance above a given trigger energy threshold. This result is reported in Fig. 4.9–left as a function of p_T for the Pb–Pb and pp samples at $\sqrt{s_{NN}} = 5.02$ TeV taken in years 2015 and 2018 (Pb–Pb) and 2017 (pp). The trigger efficiency is of the order of 90% with a small p_T dependence. It does not reach

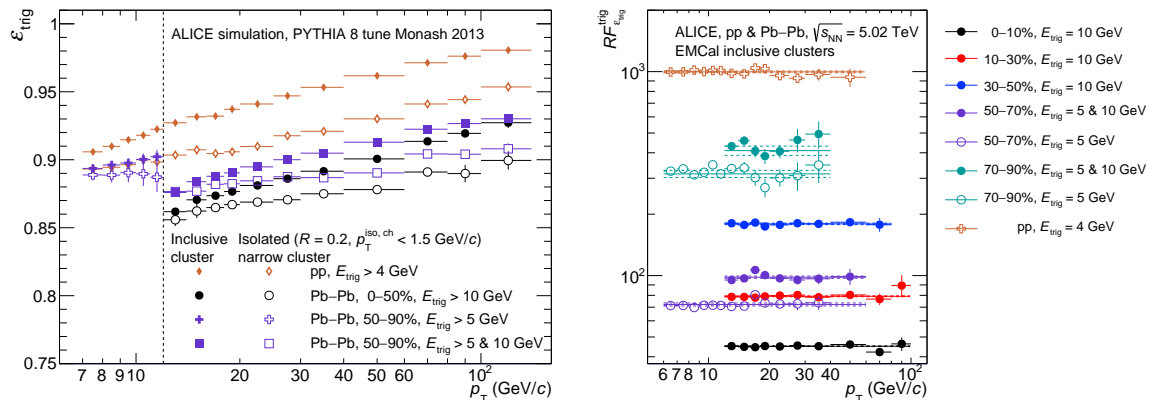


Figure 4.9: Left: L1- γ trigger efficiency for inclusive clusters (see Table 5.1) and isolated narrow clusters (see Sect. 5.3), obtained with PYTHIA simulation combining γ -jet (empty markers) and jet-jet (full markers) processes for pp and embedded in data for Pb–Pb collisions, considering the corresponding trigger thresholds in each system. Right: L1- γ trigger rejection factor calculated by applying the trigger efficiency for each of the pp and Pb–Pb centrality classes considered at $\sqrt{s_{NN}} = 5.02$ TeV. Solid lines over points result of a constant fit and dashed lines indicate the fit uncertainty [93].

100% above the trigger threshold because of the reduced geometric coverage of the trigger compared to the EMCal acceptance, because of FastOR channels or full TRU cards that are masked at trigger level whereas the corresponding towers are not always masked in the Front-End readout [132].

Another variable that can be taken into account for the trigger performances is the EMCal trigger rejection factor $RF_{\epsilon_{\text{trig}}}$, which quantifies the enhancement fraction of calorimeter triggers with respect to MB triggers. Figure 4.9–right reports the trigger rejection factor

$RF_{\varepsilon_{\text{trig}}}^{\text{trig}}$ for pp and for various centrality classes in Pb–Pb collisions at $\sqrt{s_{\text{NN}}} = 5.02$ TeV. For cluster energies beyond the trigger threshold (given in the legend of Fig. 4.9–right), an almost constant plateau region can be observed, corresponding to the maximum efficiency of the trigger.

Thanks to the triggering capabilities of the [EMCal](#), Run 1 and Run 2 analyses can reach p_T beyond 100 GeV, impossible to obtain with the limited minimum bias samples.

4.2.3 Calibrations: energy and time

The goal of the energy calibration is to obtain for each cell a coefficient such that all cells generate the same value to an identical stimulation.

A pre-calibration has been done before the detector installation in [ALICE](#), using cosmic rays as Minimum Ionizing Particles ([MIPs](#)), which deposit on average an energy of ~ 260 MeV. A relative calibration of $\sim 2\%$ was obtained after fixing the [MIP](#) position of each cell to a common value with the appropriate voltage gains.

The main calibration method involves photons from π^0 decays, whose measured mass depends on the measured energy of the photons. It was executed using the pp collisions data measured by [ALICE](#). Neutral pions decay into two photons, therefore the mass of the mesons can be extracted from the energy and the opening angle of the two photons measured in the calorimeter cells, using the formula:

$$M_{\gamma\gamma} = \sqrt{2E_{\gamma_1}E_{\gamma_2}(1 - \cos\theta_{12})} \quad (4.5)$$

where θ_{12} is the opening angle and E_{γ_i} is the photon's energy. A photon deposits its energy in a high energy cell surrounded by smaller energy cells, a cluster. Summing the cell energy of the cluster one obtains the photon energy. Combining all the clusters in the collisions it is possible to calculate Eq. (4.5) and to obtain an invariant mass distribution such as the one shown in Fig. 4.10–left (for a fully calibrated detector). Since most of the energy of a photon falls in a single cell, one can extract the energy calibration factor per cell by comparing the invariant mass obtained for π^0 for which one photon of the two decay photons cluster is centered in the cell and the Particle Data Group [138] mass value for π^0 ($M_{\gamma\gamma} \simeq 135$ MeV/c²). Starting from the invariant mass distribution, the π^0 mass can be obtained by fitting the measured distribution with a gaussian (signal) plus a polynomial of order two (combinatorial background). An energy de-calibration would reflect a deviation in the invariant mass distribution peak and width. Since the position of the invariant mass peak depends mainly on the calibration of the main cell of the reference cluster, but also the calibration of the secondary cells of the cluster, and the calibration of the clusters paired to construct the invariant mass, the π^0 calibration was an iterative procedure: three iterations were needed to finalize the calibration to achieve about 1 - 2% accuracy [142]. The calibration factor c_i of cell i is calculated via:

$$c_i = \left(\frac{m_{\pi^0}^{\text{PDG}}}{m_{\pi^0}^{\text{rec}}} \right)^n \quad (4.6)$$

where n is a coefficient chosen between 1 and 2: the convergence is faster with values around $n = 1.5$ [135]. Fig. 4.10–right shows an example of the variation of the energy calibration coefficient per cell from first to last iteration in 2012 [142]. The results obtained in the last calibration are more precise than the first one.

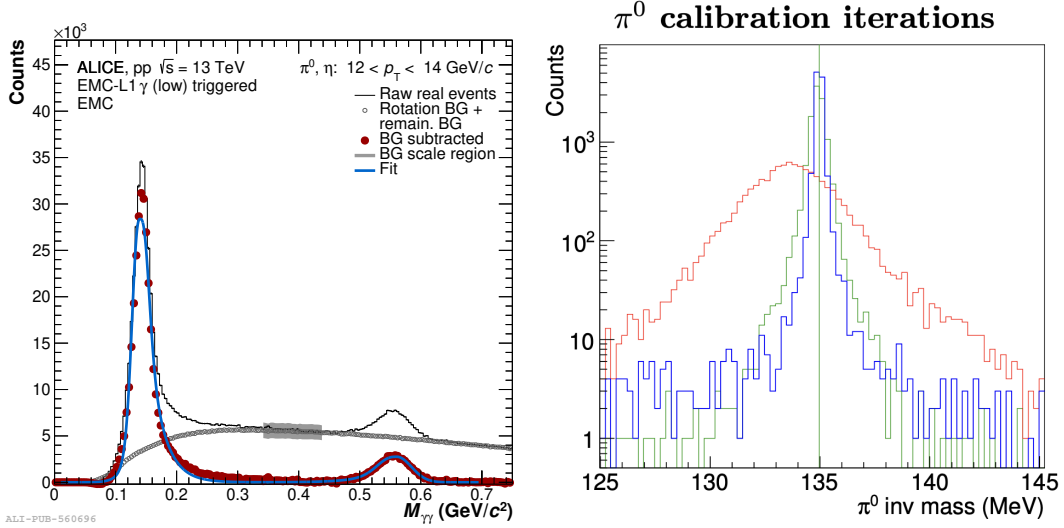


Figure 4.10: Left: Invariant mass distribution for neutral pion and η meson candidates at intermediate transverse momenta $12 < p_T < 14$ GeV/c reconstructed with both photons in the EMCal in pp collisions at 13 TeV using the L1- γ trigger sample. Distribution obtained with a fully calibrated EMCal [135]. Right: Variation of the π^0 energy calibration coefficient in all channels of 2012 data from the last iteration (blue) compared to the first iteration (red), and compared to the last iteration of 2011 data (green).

The average timing resolution of a cell with an energy above 2 GeV is below 3 ns, which is smaller than the **LHC** bunch spacing of 25 ns [135]. The **EMCal** signals are sampled at 10 MHz, i.e. approximately every 100 ns, differing from the **LHC** clock speed. This discrepancy leads to four possible shifts in the registered cell times relative to the triggered bunch crossing time. Additionally, signal propagation through the **EMCal** cables introduces a constant offset of around 600 ns, resulting in a total shift of the triggered bunch registered by a cell to be between 600 ns and 700 ns. A calibration procedure, conducted for each run, determines the time offset for each cell, and the stored timing information is adjusted accordingly. The mean of the calibrated cell times deviates by no more than about 0.8 ns from the triggered bunch crossing time.

4.3 The EMCal performance

Precise knowledge of a calorimeter's energy response to incoming particles is essential. Consequently, the relationship between the reconstructed energy and the true energy of an incoming particle is often studied in controlled environments that provide beams of particles with known energies. This consists in determining the energy nonlinearity of the detector response. The energy response is shown in Fig.4.11-left where the ratio of reconstructed energy over true beam energy ($E_{\text{rec}}/E_{\text{beam}}$) as a function of E_{rec} measured in the test-beam data is reported. The ranges indicated at the top of the figure show which energy ranges could be accessed by the test setup at the PS and SPS, respectively. The energy response is almost linear for reconstructed energy below 10 GeV, after it becomes non-linear. This non-linearity is common to various calorimeters and for the **EMCal** is due to the signal shapers in the **FEE** cards or effects due to the shower hit position not being in the centre of a cell, as well as energy losses due to material interactions in front of the **EMCal**. The non-linearity due to the shapers has been studied in the laboratory and it was possible to parametrize it,

applying a correction to cell energies.

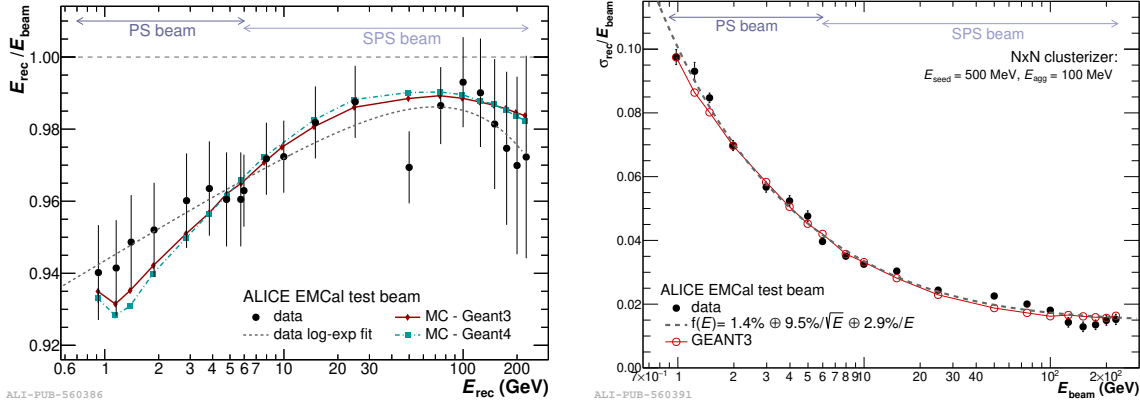


Figure 4.11: Left: Energy nonlinearity correction as a function of reconstructed energy for electrons obtained from test beam data (black points), and from MC simulations with GEANT3 (red points) and GEANT4 (cyan points) transport codes. Right: energy resolution of the EMCAL as a function of the incident particle energy [135].

The remaining nonlinearity is parameterized with:

$$f(E_{\text{rec}}) = \frac{p_0 + p_1 \ln(E_{\text{rec}})}{1 + p_2 \exp(E_{\text{rec}}/p_3)} \quad (4.7)$$

where E is the incident energy and the parameters are: $p_0 = 4.3 \pm 0.6$, $p_1 = 0.06 \pm 0.02$, $p_2 = 3.5 \pm 0.6$, $p_3 = 4172 \pm 2276$.

It is also possible to define the energy dependence of an electromagnetic calorimeter energy resolution, which is parameterized as:

$$\frac{\sigma}{E} = a \oplus \frac{b}{\sqrt{E}} \oplus \frac{c}{E} \quad (4.8)$$

where: E is the energy of the electromagnetic shower; a , b and c are characteristic parameters of the calorimeter. The parameter b arises from stochastic fluctuations due to intrinsic detector effects such as energy deposition, energy sampling and light-collection efficiency. The constant term, a , originates from systematic effects, such as shower leakage, detector nonuniformity or channel-by-channel calibration errors. The third term, c , is due to electronic noise summed over the towers of the cluster used to reconstruct the electromagnetic shower. The energy resolution is shown in Fig. 4.11–right. The following numerical values have been found from a fit to data for the energy resolution parameters: $a = 1.4 \pm 0.1\%$, $b = 9.5 \pm 0.2\% (\text{GeV}^{1/2})$, $c = 2.9 \pm 0.9\% (\text{GeV})$ [135]. Thus, the energy resolution of the EMCAL in a range of energy from 0.5 to 100 GeV goes from 10% to 2%.

Chapter 5

How to identify and select photons using the ALICE EMCal

5.1	Signal detection in the calorimeter cells	91
5.1.1	Track-calorimeter cluster matching	92
5.1.2	Exotic clusters	96
5.1.3	Summary of basic cluster selections for photon measurements	97
5.2	Photon identification via cluster shape analysis	98
5.2.1	Cross-talk	103
5.3	The isolation method	104
5.4	Isolated photon purity P	111
5.4.1	The ABCD-ALICE method	111

In the previous Chapter, the various technicalities of the EMCal have been illustrated; now the idea is to present how photons are reconstructed and selected in the ALICE calorimeter, to have all the ingredients to enter the heart of the Thesis topic.

5.1 Signal detection in the calorimeter cells

A particle interacting with the calorimeter material produces a shower spreading its energy over several neighbouring cells; the width of the shower is almost twice the effective $R \sim 6.40$ cm, which is larger than the cell/tower surface.

Hence, the question is how we could reconstruct the energy and the arrival position of the incident particles from the energy deposited in the activated cells. A cluster can be defined as a set of calorimeter cells activated by an energy deposit in neighbouring cells. Each cluster is ideally generated by one particle, but in reality, clusters can also originate from the superposition of the showers produced by two or more particles.

Different clusterization algorithms are available to select the cells to be aggregated into a cluster and are schematically shown in Fig. 5.1. All clusterizers build clusters starting

from the highest energetic cell in a region of the calorimeter, referred to as **seed cell** with an energy E_{seed} . All the cells in the cluster must have minimum energy to be aggregated: $E > E_{\text{agg}}$, where E_{agg} is the aggregation energy. The energy E_{agg} is defined to be more than three times above the nominal electronic noise. The clusterization parameters values used are $E_{\text{seed}} = 500$ MeV and $E_{\text{agg}} = 100$ MeV and the choice of a specific clusterizer depends on the analysis one wants to perform and on the collision system. In the following list, the different clusterizers are illustrated:

- **V1** clusterizer: it is the simplest clusterizer and it is used for analyses that heavily rely on separating the signal and background through Particle Identification (PID) selections: for example, it is usually used for isolated photon analyses in pp and p–Pb collisions. The algorithm associates to that **seed cell** all cells in the vicinity that share a common side with one of the cells already in the cluster;
- **V2** clusterizer: it is similar to **V1**, but before aggregating a cell to the cluster, it checks if the energy of the cell is smaller than the energy of the cell already belonging to the cluster and with which it shares a side. If the energy is larger, the cell is not added and the clusterization does not propagate further towards that direction. This algorithm is more robust against shower overlaps and performs better in Pb–Pb collisions because clusters, that are more closely related to the incident particles in terms of energy and position, are produced. Hence, **V2** is the default clusterizer in Pb–Pb collisions, which are characterised by a large particle multiplicity, a large contribution of the underlying event and inputs from several particles can easily be merged into the same cluster in central heavy-ion collisions.
- **N × N** clusterizer: it is based on **V1** but restricts the cluster size to a $N \times N$ cell window in the η and φ directions around the seed cell.

Figure 5.1 shows how a cluster is reconstructed by the different types of clusterizers presented above.

Once clusters are reconstructed, several properties can be attributed to them and used in the analyses:

- energy: sum of the energy of all cells associated with the cluster;
- time: measured time of the highest energy cell of the cluster;
- global position in (η, φ) , weighted by the cells energy as in [143];
- cluster shape: distribution of energy within a cluster (see Sect. 5.2).

My Thesis involves photons produced in Pb–Pb collisions and the clusterizer used is the **V2**. More details will be presented in Sect. 5.2.

5.1.1 Track-calorimeter cluster matching

The **EMCal** is designed to measure the energy of particles that interact electromagnetically with the material, i.e. photons and electrons. However, hadrons can also deposit energy in the **EMCal**, most commonly charged hadrons via ionization, but also via nuclear interactions, generating hadronic showers. Therefore, selecting photons imposes to distinguish between

5.1. Signal detection in the calorimeter cells

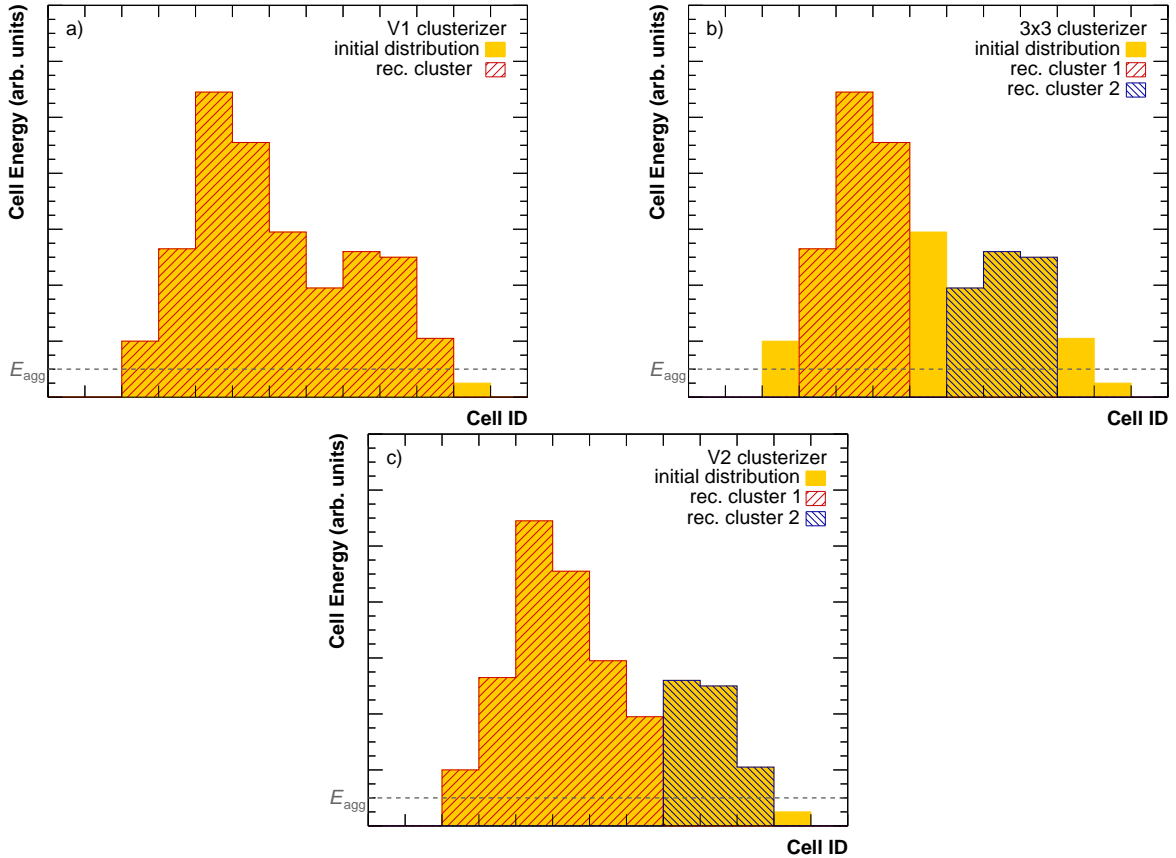


Figure 5.1: Schematic comparison of different clusterization algorithms: a) V1, b) 3×3 , c) V2. Yellow boxes represent the energy in each cell. E_{agg} is the aggregation energy. Different clusters are indicated by blue and red hatched areas [135].

showers originating from charged and neutral particles. To do that, the tracking detectors' information is considered. Charged particles are reconstructed in a hybrid approach using the **ITS** and the **TPC** measurements, as presented in Sect. 3.4. To determine whether a charged particle points to a reconstructed **EMCal** cluster, tracks are extrapolated to the **EMCal**, taking into account the energy loss of the particle when it traverses the detector materials.

Figure 5.2 displays the distributions of the residuals of clusters to the closest track in $\Delta\eta^{\text{residual}} = |\varphi^{\text{track}} - \varphi^{\text{cluster}}|$ (left) and $\Delta\varphi^{\text{residual}} = |\eta^{\text{track}} - \eta^{\text{cluster}}|$ (right) as a function of track p_T in pp collisions at $\sqrt{s} = 13$ TeV.

The $\Delta\varphi^{\text{residual}}$ distributions are significantly wider than $\Delta\eta^{\text{residual}}$ ones, this is due to the orientation of the magnetic field: tracks incidence in the calorimeter is less perpendicular in φ than in η direction due to their curvature along z , which causes a larger spread for low energy tracks and has an important effect for $p_T < 2$ GeV/ c . The fact that the distributions are different in $\Delta\eta^{\text{residual}}$ and $\Delta\varphi^{\text{residual}}$ implies different limit values to be used for the matching. As the width of the distribution depends on the transverse momentum of the particle, a p_T -dependent window in the $\Delta\eta^{\text{residual}}\text{-}\Delta\varphi^{\text{residual}}$ plane is used to select cluster-track pairs [135].

For clusters originating from neutral particles, the separation of the position of any tracks extrapolated to the **EMCal** surface from the cluster position must fulfil the following selections,

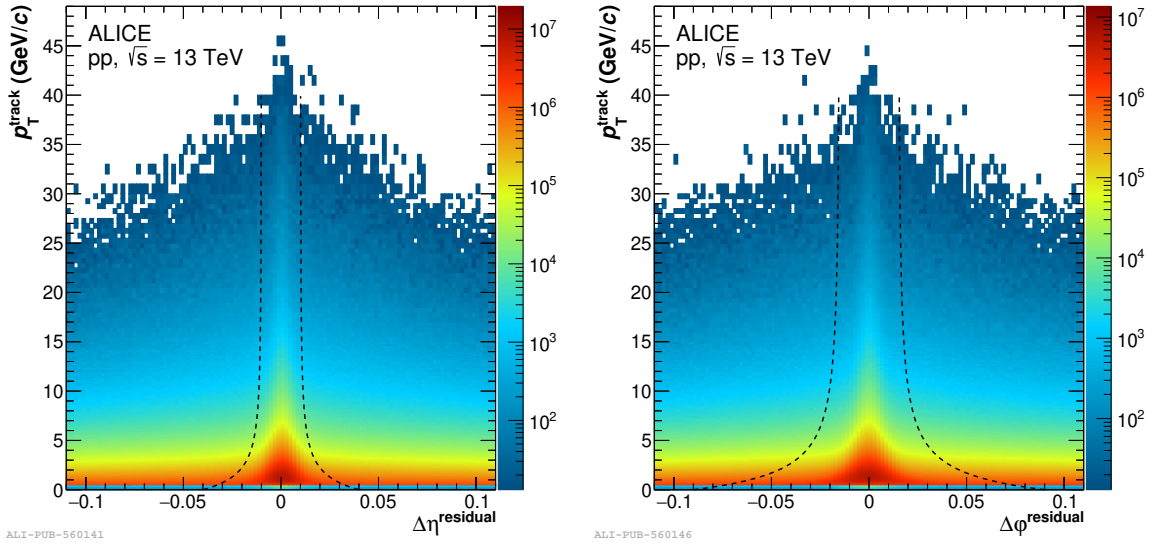


Figure 5.2: Distance between a cluster and the closest projected track in $\Delta\eta^{\text{residual}}$ (left) and $\Delta\varphi^{\text{residual}}$ (right) angle versus the track momentum p_T^{track} in pp collisions at $\sqrt{s} = 13$ TeV. The black lines indicate the selection reported in Eq. (5.1) and (5.2) [135].

indicated with black lines in Fig. 5.2:

$$\Delta\eta^{\text{residual}} > 0.010 + (p_T^{\text{track}} + 4.07)^{-2.5} \text{rad}; \quad (5.1)$$

$$\Delta\varphi^{\text{residual}} > 0.015 + (p_T^{\text{track}} + 3.65)^{-2} \text{rad}; \quad (5.2)$$

where p_T^{track} is the track transverse momentum expressed in GeV/c . This residual selection is applied only if the ratio of cluster energy over track momentum is smaller than 1.7 ($E_{\text{clust}}/p_T^{\text{track}} < 1.7$), to avoid fake matches. This same method is used in other ALICE measurements using the EMCAL in pp, p–Pb and Pb–Pb collisions.

Since this Thesis focuses on Pb–Pb collisions data, we report the residuals obtained in Pb–Pb collisions at $\sqrt{s_{\text{NN}}} = 5.02$ TeV. Figure 5.3 shows the residual parameters distributions as a function of the track transverse momentum in 0–10% and 50–90% Pb–Pb collisions.

There is almost no centrality dependence, the $\Delta\eta^{\text{residual}}$ and $\Delta\varphi^{\text{residual}}$ are well-centred at 0 and rather narrow. Thus, the same selection cuts reported in Eq. (5.1) and (5.2) are applied for all centralities in Pb–Pb collisions.

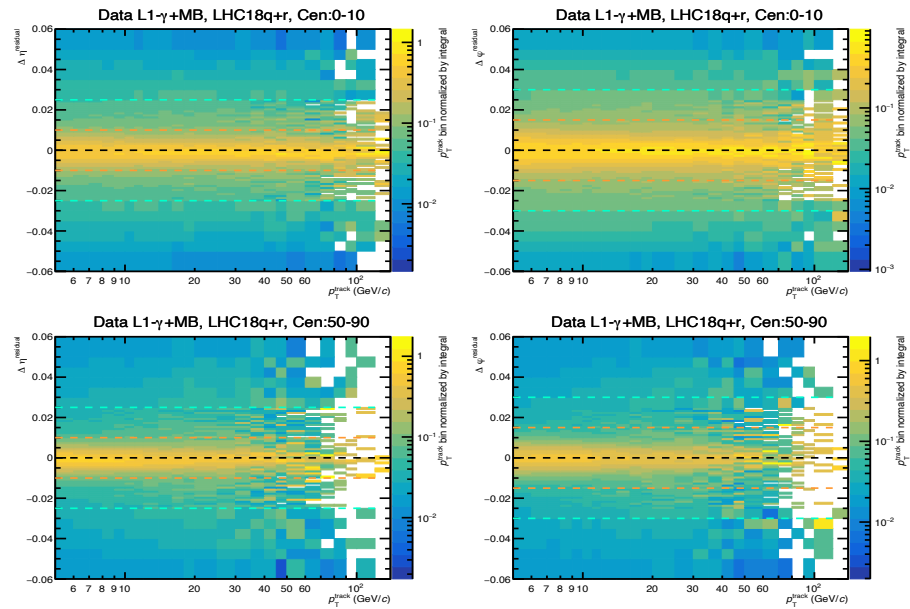


Figure 5.3: Positive charge track-cluster matching residuals of $\Delta\eta^{\text{residual}}$ (left) and $\Delta\varphi^{\text{residual}}$ (right) as a function of p_T^{track} for central (0-10%, top rows) and peripheral Pb-Pb collisions (50-90%, bottom rows). The orange dashed lines indicate the limit at high p_T cut given by Eq. (5.1) and (5.2) and the teal dashed line is the loose cut used for systematic studies in the spectrum analysis [93].

5.1.2 Exotic clusters

We have learned that in electromagnetic calorimeters, in addition to the electromagnetic response, hadrons can deposit a fraction of their energy. Most of these hadrons only interact by EM diffusion and deposit only energy of a MIP passing through the calorimeter, they can be removed using the previous technique. However, also slow neutrons/anti-neutrons can produce a signal in the calorimeter and their typical energy deposition is different, because they hit a nucleus in the APD of a cell.

These hits produce an abnormal signal [135, 144], which is most frequently observed as a single high-energy cell with no or few surrounding low-energy cells. Such characteristic clusters are called *exotic clusters* and are observed in both calorimeters, **EMCal** and **PHOS**, but also in other **LHC** experiments calorimeters. Exotic clusters can be easily identified as they typically have a low number of cells in the cluster despite large energy: it is sufficient to require that the clusters have at least 2 cells ($n_{\text{cell}} > 1$) to remove most of them.

A topological cut on a variable denoted F_+ , called the *exoticity*, can be used to remove such clusters, similar to the method developed by the **CMS** Collaboration [144]. The exoticity describes the degree of homogeneity of the energy partition within the cluster, allowing to reject clusters with a dominant contribution from a single cell. The exoticity is defined as $F_+ = 1 - E_+/E_{\text{Max}}$, where E_+ is the sum of the energy if the four surrounding cells that share a common edge with the cell with the highest energy E_{Max} in the cluster.

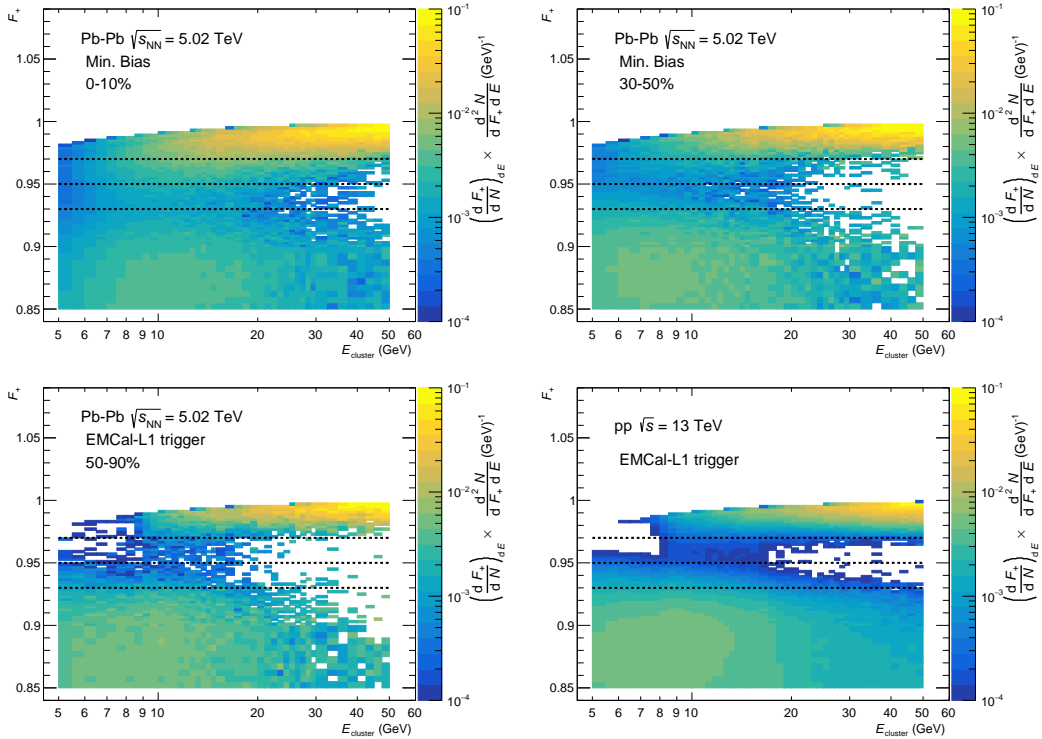


Figure 5.4: The exotoxicity F_+ versus E_{cluster} for 0-10% and 30-50% in minimum bias Pb–Pb collisions at $\sqrt{s_{\text{NN}}} = 5.02$ TeV (top rows) and for 50-90% Pb–Pb collisions at $\sqrt{s_{\text{NN}}} = 5.02$ TeV and pp collisions at $\sqrt{s} = 13$ TeV (bottom rows) with $n_{\text{cells}} > 1$. Lines at $F_+ = 0.97, 0.95$ and 0.93 are added to guide the eye on the exotics upper band limits [93].

Figure 5.4 shows the exotoxicity F_+ as a function of the cluster energy in pp and Pb–Pb

5.1. Signal detection in the calorimeter cells

collisions at different centralities, with $n_{\text{cells}} > 1$. We can see that in pp collisions the upper band populated by exotic clusters is above $F_+ > 0.97$, but increasing the Pb–Pb centrality, the band gets wider. Therefore to reject these signals, one requires that $F_+ < 95\%$ as a common cut, even if in central collisions a tighter cut might be needed at lower cluster energies.

5.1.3 Summary of basic cluster selections for photon measurements

Various cluster quality selection criteria are applied. A cluster must contain at least two cells ($n_{\text{cells}} > 1$) to ensure a minimum cluster size and to remove single-cell electronic noise fluctuations. To limit energy leakage at the calorimeter supermodule borders, a distance of at least one cell between the highest-energy cell in the cluster and the SM border is required, except at the $\eta = 0$ border, where supermodules are in contact and clusters can be shared between two supermodules. These requirements, in addition to the exclusion of the two “1/3 SM” located at the highest φ because of unsatisfactory energy calibration, lead to the calorimeter acceptances for this measurement. The acceptance are of $|\eta| < 0.67$ for $81.2^\circ < \varphi < 185.8^\circ$ and $0.25 < |\eta| < 0.67$ for $261.2^\circ < \varphi < 318.8^\circ$. During Pb–Pb collisions data-taking periods, the LHC delivered events in bunches separated by 75 to 150 ns in the year 2018 and by 100 to 225 ns in the year 2015, respectively. The EMCal time resolution is between 1 and 2 ns for clusters with energy below 80 GeV and reaches close to 3 ns above 100 GeV. Consequently, it was possible to require the time of the highest-energy cell in the clusters relative to the main bunch crossing to satisfy $|\Delta t| < 20$ ns, ensuring the selection of clusters from the main bunch crossing.

Table 5.1 summarizes the various clusterization parameters and basic cluster cuts used in

Parameter	Cut value std
Cluster seed threshold	$E_{\text{seed}} > 500$ MeV
Cluster aggregation threshold	$E_{\text{agg}} > 100$ MeV
Number of cells	$n_{\text{cells}} > 1$
N cells from highest E cell to SM border	$n_{\text{border}} > 1$
Cluster time - bunch crossing time	$ \Delta t < 20$ ns
Abnormal signal removal	$F_+ < 0.95$
Acceptance	
EMCal	$81.2^\circ < \varphi < 185.8^\circ$ $ \eta < 0.67$
DCal	$261.2^\circ < \varphi < 318.8^\circ$ $0.25 < \eta < 0.67$
Charged particle veto:	
when	$E_{\text{clust}}/p^{\text{track}} < 1.7$
track–cluster η residual	$ \Delta\eta^{\text{residual}} > 0.010 + (p_T^{\text{track}} + 4.07)^{-2.5}$ rad
track–cluster φ residual	$ \Delta\varphi^{\text{residual}} > 0.015 + (p_T^{\text{track}} + 3.65)^{-2}$ rad

Table 5.1: Cluster basic selection cuts for this Thesis.

this Thesis. In the following, clusters that pass the previous selection criteria will be called “inclusive clusters”.

5.2 Photon identification via cluster shape analysis

The shape of the energy distribution within a cluster, sketched in Fig. 5.5, can be described as an ellipse. The ellipse axes size are used as **PID** parameters. The shower surface is defined by the intersection of the cylinder containing the shower with the front plane of the calorimeter. This surface can be represented by a covariance matrix with four terms representing the average cluster position in η and φ direction in the calorimeter plane, weighted logarithmically by the cell energy [143].

The diagonalization of this covariance matrix gives the eigenvalues, which correspond to the shower surface ellipse axis parameters: σ_{long} (long axis) and σ_{short} (short axis) defined as:

$$\sigma_{\text{long}}^2 = 0.5(\delta_{\varphi\varphi} + \delta_{\eta\eta}) + \sqrt{0.25(\delta_{\varphi\varphi} - \delta_{\eta\eta})^2 + \delta_{\eta\varphi}^2}, \quad (5.3)$$

$$\sigma_{\text{short}}^2 = 0.5(\delta_{\varphi\varphi} + \delta_{\eta\eta}) - \sqrt{0.25(\delta_{\varphi\varphi} - \delta_{\eta\eta})^2 + \delta_{\eta\varphi}^2}, \quad (5.4)$$

where α_i and β_i are the cell indices in the η and φ directions. The $\delta_{\varphi\varphi}$, $\delta_{\eta\eta}$ and $\delta_{\eta\varphi}$ are coefficients weighted by the cell energy:

$$\delta_{\alpha\beta} = \sum_i \frac{w_i \alpha_i \beta_i}{w_{\text{tot}}} - \sum_i \frac{w_i \alpha_i}{w_{\text{tot}}} \sum_i \frac{w_i \beta_i}{w_{\text{tot}}}, \quad (5.5)$$

with

$$w_i = \text{Max}(0, w_0 + \ln(\frac{E_i}{E_{\text{cluster}}})) , \quad w_{\text{tot}} = \sum_i w_i, \quad (5.6)$$

where i indicates a cell that belongs to the cluster, η_i and φ_i are the indexes of the cell inside a **SM** (see Sect. 4.2.1) in longitudinal and azimuthal direction, respectively, with $0 \leq \eta_i < 48$ and $0 \leq \varphi_i < 24$, and $w_0 = 4.5$ [143]. This latter value is chosen according to the amount of proportional energy a cell in the cluster has. The selected value leads to limit down which cells contribute to the shower shape parameters. In this case, $w_0 = 4.5$ corresponds to a limit of 1.1% of the cluster energy, below which the cells are not used in the computation.

Figure 5.5 shows schematically the cell cluster energy E repartition and what corresponds to the ellipse axes.

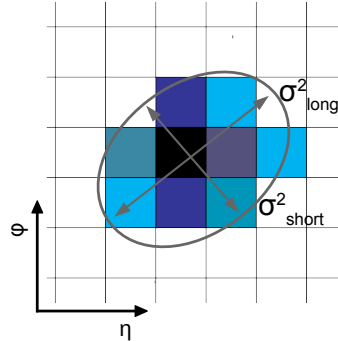


Figure 5.5: Schematic view of cluster energy repartition in cells and the ellipse axes. Darker colours indicate higher energy cells [135].

The cluster shape can be used to discriminate between clusters from single electromagnetic showers (photons, electrons) and from multiple showers (merged clusters). In particular, we need to distinguish between single photons and decay photons from neutral meson decays, when both of them contribute to the same cluster. To do that the long axis is used because it is the most discriminating axis; σ_{long}^2 is called “shower shape” parameter. Figure 5.6 shows a schematic example of clusters from two photons from meson decays at different meson energies, one can see that merged clusters are more elliptical (large σ_{long}^2) than not merged clusters that are more circular (small σ_{long}^2).

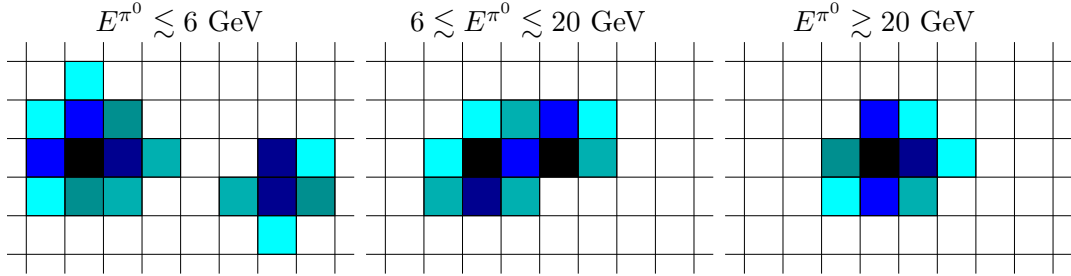


Figure 5.6: Schematic view of cluster energy repartition in cells in low particle multiplicity environment, for two decay photons from a neutral meson (π^0 or η for example) at low (left), medium (middle) and high meson energy (right). The opening angle of the decays gets smaller due to the Lorentz boost and thus the two showers tend to merge at high energy. Darker colours indicate higher energy cells [135].

As reported in Sect. 5.1, in pp and p–Pb collisions, the **V1** clusterizer is usually used: since it allows to reconstruct merged clusters with large σ_{long}^2 from high-energy meson decays, compared to single photons. The **V1** clusterizer permits to discriminate between single photons and meson decays, especially at intermediate energies $6 < E^{\pi^0} < 20$ GeV, such as the clusters shown in Fig. 5.6–middle.

In central Pb–Pb collisions, a cluster is likely formed from multiple particle contributions, essentially from the underlying event; therefore, the shower shape discrimination with **V1** is less performant and the energy resolution for identified particles from such clusters gets worse. For a low-energy high-multiplicity particle environment, the clusterizer **V2** is better for reducing the UE contribution to the cluster since it tries to split the merged showers, improving energy resolution. Nevertheless, it is less optimal for shower shape discrimination of single and merged decay clusters at intermediate energies. In order to improve this clusterization in Pb–Pb, a change in the definition of σ_{long}^2 is introduced:

- the clusterizer **V2** is used to obtain the cluster energy and position;
- the shower shape is calculated taking only the cluster cells which lay in a 5×5 window centred around the highest energy cell of the **V2** cluster.

Figure 5.7 shows schematically, for intermediate energy merged cluster from π^0 decays, the cells selected by the different clusterization approaches and as well as those used for the σ_{long}^2 calculation.

This approach rejects cells that are out of the 5×5 window and cells sharing only one corner, and thus reduce the UE contribution while keeping part of the cells belonging to the cluster of the 2nd decay γ . The shower shape, determined in this way and used in Pb–Pb

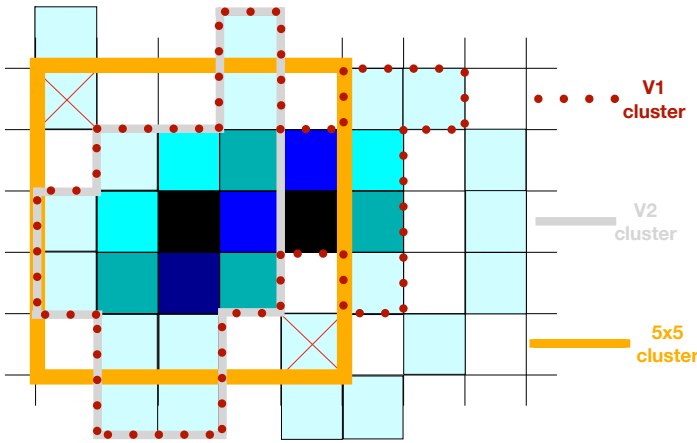


Figure 5.7: Schematic view of the cell energy repartition of two high-energy decay photons from a neutral meson, each centred in the black-filled cells, on top of a high-multiplicity low-energy particle underlying event environment, the lightest blue cells. The grey lines are the contour of cells selected restricting the growth of the cluster (V2) used to calculate the cluster energy and position. The orange square is the 5×5 region around the highest-energy cell used for the shower shape calculation, excluding cells that only have a common corner, red cross. The red dotted lines are the contour of a cluster without growth restriction (V1), as used in previous pp and p–Pb isolated photon analyses [93].

collisions, is denoted as $\sigma_{\text{long}, 5 \times 5}^2$. Now we have all the ingredients to distinguish between single photons and showers from meson decays.

Figure 5.8 shows the inclusive cluster $\sigma_{\text{long}, 5 \times 5}^2$ distributions versus the cluster p_T in pp collisions and in various centralities in Pb–Pb collisions at $\sqrt{s_{\text{NN}}} = 5.02$ TeV.

Most of the single photons are reconstructed as clusters with $\sigma_{\text{long}, 5 \times 5}^2 \simeq 0.25$. At higher $\sigma_{\text{long}, 5 \times 5}^2$ we can see a clear p_T -dependent band mostly populated by merged π^0 -decay photons for a p_T between 8 and 20 GeV/ c ; while a less clear band appears above 40 GeV/ c due to the merged η meson decays. Because of the kinematic boost and the resulting opening angle, the $\sigma_{\text{long}, 5 \times 5}^2$ value for merged photons decreases with increasing energy, causing a progressive overlapping with the single photon band for p_T above 20 to 40 GeV/ c . In pp collisions, photons can be distinguished from the merged meson decays by selecting clusters with $\sigma_{\text{long}}^2 < 0.3$. In Pb–Pb collisions instead, there are two different conditions depending on the p_T range: for $p_T \geq 18$ GeV/ c , we can select photons if $\sigma_{\text{long}, 5 \times 5}^2 < 0.3$. At lower p_T a p_T -dependent $\sigma_{\text{long}, 5 \times 5}^2$ selection is applied: $\sigma_{\text{long max}}^2 = 0.6 - 0.016 \cdot p_T$. This p_T -dependent cut allows to select narrow clusters with significant UE contribution, which are frequent at low p_T , without increasing the number of accepted merged decay photon clusters. A lower limit at $\sigma_{\text{long}, 5 \times 5}^2 = 0.1$ is used in all collisions system to clean the cluster narrow sample from a few anomalous high energy depositions that still pass the F_+ selection.

In this Thesis, “photon candidates” will refer to clusters with a narrow shape $0.1 < \sigma_{\text{long}, 5 \times 5}^2 < 0.3$, narrow cluster ($\text{cluster}_{\text{narrow}}$); while clusters with an elongated wide shape $0.4 < \sigma_{\text{long}, 5 \times 5}^2 < 1.0$ will be indicated as a wide cluster ($\text{cluster}_{\text{wide}}$).

Figures 5.9 display the inclusive cluster $\sigma_{\text{long}, 5 \times 5}^2$ distributions for two selected cluster p_T ranges: $12 < p_T < 14$ GeV/ c and $40 < p_T < 60$ GeV/ c for central Pb–Pb collisions and pp

5.2. Photon identification via cluster shape analysis

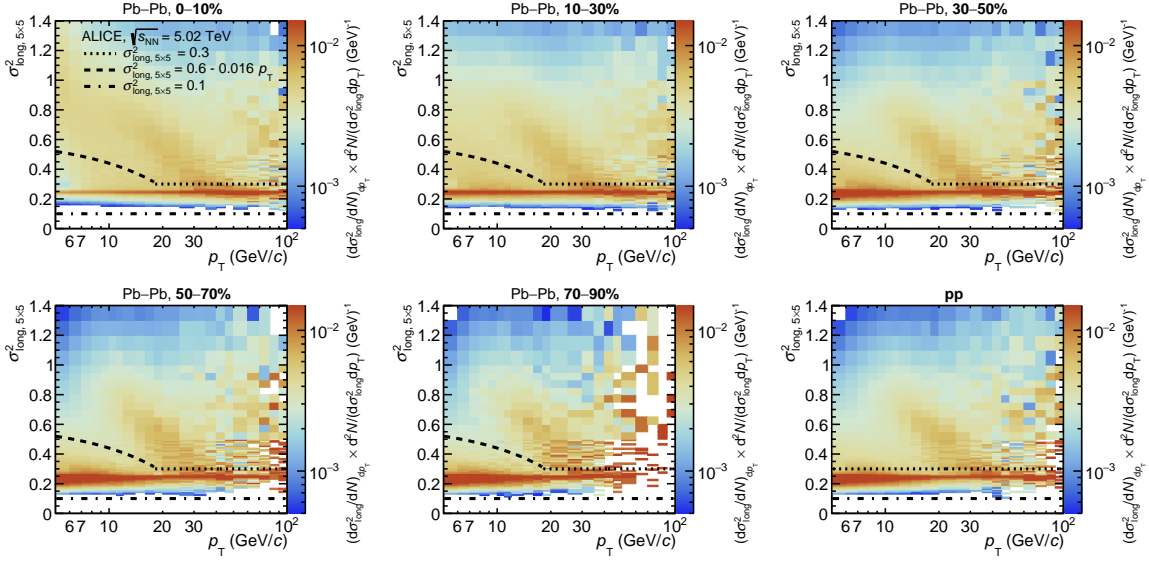


Figure 5.8: Inclusive cluster $\sigma_{\text{long}, 5\times 5}^2$ distribution as a function of p_T in data for five different centralities in Pb–Pb collisions and for pp collisions. The dotted line corresponds to the tight value of the upper selection limit ($\sigma_{\text{long}, 5\times 5}^2 = 0.3$) for single photon candidate clusters (narrow clusters), the dashed line corresponds to a looser photon upper selection used in Pb–Pb collisions below 18 GeV/ c . The dot-dashed line defines a lower selection limit ($\sigma_{\text{long}, 5\times 5}^2 = 0.1$) used in Pb–Pb and pp collisions.

collisions.

At low p_T , the dominant contributions to the narrow shower shape region are from single π^0 -decay photons (MC γ_{decay}), while the merged photon clusters from π^0 decay-photons (MC γ_{decay}) contribute more at high p_T . Prompt-photon clusters show a peaked distribution at 0.25, which has in central Pb–Pb collisions a significant tail at high $\sigma_{\text{long}, 5\times 5}^2$ due to the UE contribution. Decay-photon clusters without contribution from a second decay photon in the cluster show a similar distribution to prompt photons, but the tail is more significant due to nearby particles originating from the same jet and overlapping with the cluster. Merged clusters from π^0 (MC π^0) and η (MC η) meson decays have two maxima in the $\sigma_{\text{long}, 5\times 5}^2$ distribution for $12 < p_T < 14$ GeV/ c and $40 < p_T < 60$ GeV/ c : one, in the range $\sigma_{\text{long}, 5\times 5}^2 = 0.6 - 0.9$, is due to the merging of rather symmetric energy photon decays; the second, at 0.25, is due to clusters for which most of the energy comes from one of the decay photons, while the contribution of the second one does not affect the shower shape parameter. For $p_T > 20$ GeV/ c , the merged clusters from π^0 meson decays have only one maximum at $\sigma_{\text{long}, 5\times 5}^2 = 0.25$ but with a significant tail at high $\sigma_{\text{long}, 5\times 5}^2$.

Figure 5.9 permits also the comparison of the $\sigma_{\text{long}, 5\times 5}^2$ distributions in data and simulation: a reasonable description is achieved in simulation after including modelling at the cell energy level of the electronics cross-talk. The cross-talk parametrization used is different to previous measurements to match better the data since the cross-section measurement in central collisions is too sensitive to the shape of this distribution; a few more details on the cross-talk are presented in the next Sect. 5.2.1.

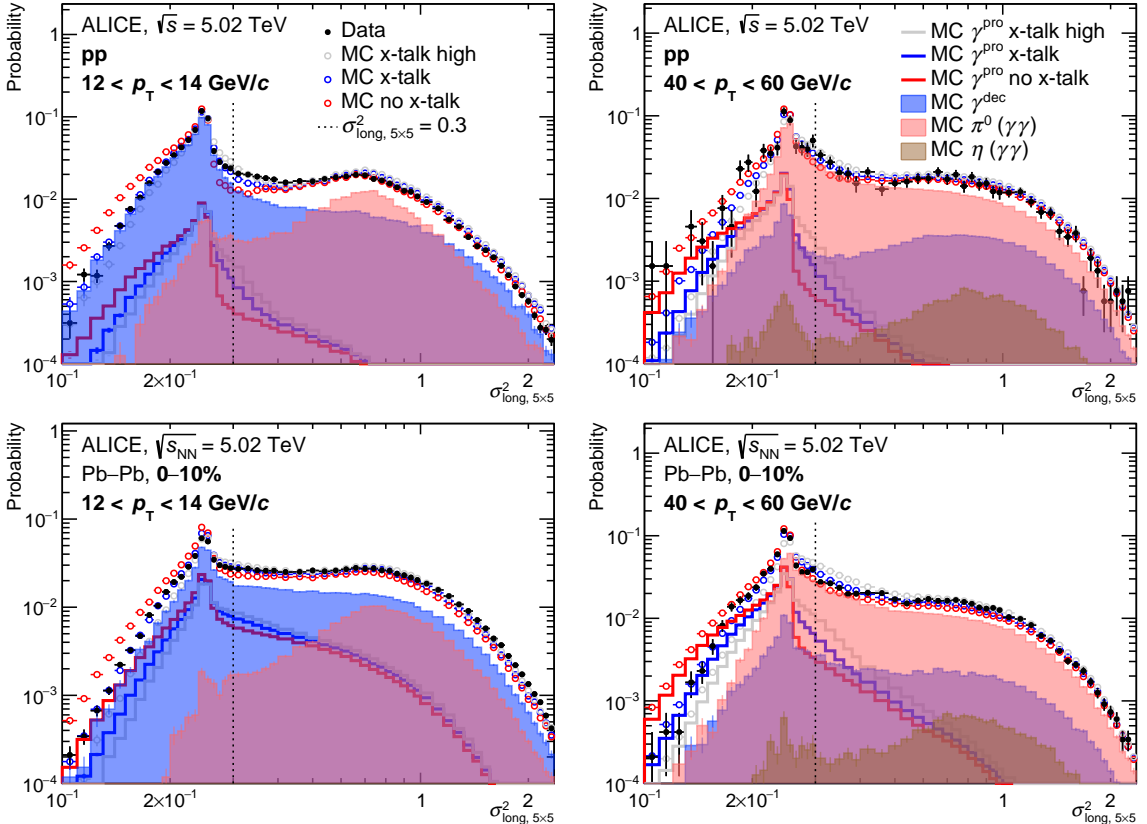


Figure 5.9: Inclusive-cluster $\sigma_{\text{long}, 5\times5}^2$ distribution in data (black bullets) and PYTHIA simulations. The simulation is decomposed in its different particle origins: prompt photons (blue line), not merged decay photons (MC γ_{decay} , blue area), merged decays from π^0 (MC π^0 , red area) or η (brown area). Three different treatments of cross-talk (x-talk) were considered in the simulation: “no x-talk” (open red circles); “x-talk high” (open grey circles), stronger cross talk obtained for the previous isolated-photon measurements [76, 85, 135]; and “x-talk” (open blue circles), obtained for this measurement. The four panels display these distributions for two selected cluster p_T ranges, $12 < p_T < 14 \text{ GeV}/c$ on the left and $40 < p_T < 60 \text{ GeV}/c$ on the right, and two collision systems: pp (top) and Pb–Pb 0–10% central (bottom) at $\sqrt{s_{\text{NN}}} = 5.02 \text{ TeV}$ [93].

5.2.1 Cross-talk

The cross-talk is an effect that was revealed during tests in the laboratory; it implies that a signal in one channel can induce a signal in a different channel belonging to the same T-card. The T-card, shown in Fig. 4.6, is an adaptor which connects the preamplifiers of 8×2 cells ($\eta \times \varphi$) via a ribbon cable to the FEE cards. The laboratory studies demonstrated that the cross-talk between channels is of random nature and causes modifications in the energy and time distribution of adjacent cells. The cross-talk between cells modifies the shower shape distributions, widening the single-photon-cluster peak distribution to $\sigma_{\text{long}, 5\times5}^2$ values larger than 0.25. This effect needs to be included in simulations to avoid a disagreement of the cluster shape in data and MC.

The cross-talk was modelled in the simulation by adding, for a given cell, a small fraction of its energy E_{cell} into the surrounding cells with energy $E_{i,j}$ (column i , row j with respect to the reference cell) in the same T-Card. The induced energy is then $E_{i,j}^{\text{ind}} = F_{\text{ind}} E_{\text{cell}}$, with $F^{\text{ind}} = \mu_1 + \mu_2 E_{\text{cell}}$, where μ_1 and μ_2 depend on the supermodule. If F^{ind} is above or below a given value $F_{\text{min}}^{\text{ind}}$ or $F_{\text{max}}^{\text{ind}}$, respectively, those values are used instead. Each resulting $E_{i,j}^{\text{ind}}$ is smeared by a Gaussian random distribution with width σ_{ind} . Additionally, the amount of induced energy is limited for lower energies in order not to provoke additional cluster non linearity, by requiring: $E_{i,j} + E_{i,j}^{\text{ind}} > 100$ MeV, the same limit as the clusterization minimum cell energy. Finally, the total induced energy after smearing in the nearby T-Card cells is subtracted from the main signal $E_{\text{cell}}^{\text{final}} = E_{\text{cell}} - \sum E_{i,j}^{\text{ind}}$, so that the energy scale is conserved.

The modelling of the cross-talk is the same between pp and Pb–Pb collisions, with model parameters fine-tuned through detailed comparisons of cluster shapes in data and MC, primarily using pp collision data at $\sqrt{s} = 13$ TeV, as detailed in [135]. However, this parametrization has been found to induce an excessively strong shape modification in central Pb–Pb collisions. Decreasing the F_{ind} limit by a factor of two with respect to [135] has been found to result in a better agreement between data and simulation for central as well as peripheral Pb–Pb collisions, improving the agreement in pp collisions. The multiplicity enhances the effect of the cross-talk. Figure 5.9 shows various inclusive-cluster $\sigma_{\text{long}, 5\times5}^2$ distributions, where the effect of the three cross-talk treatments in the simulation are compared: no cross-talk emulation, previous parameterization (pp x-talk high) used for the previously published pp measurements, and the new parameterization. The final cross-talk emulation parameters for Pb–Pb collisions used in the simulation are summarized in Table 5.2.

	group 1	group 2	group 3	group 4
SM number	3, 7	1, 10	0, 2, 4, 5, 6, 11	8, 9
	-	-	12, 13, 16	14, 15, 17, 18, 19
$F_{\text{min}}^{\text{ind}}$	0.3%	0.25%	0.235%	0.175%
$F_{\text{max}}^{\text{ind}}$	1.8%	1.6%	1.6%	1.6%
μ_1	1.2%	1.2%	1.15%	0.8%
$\mu_2 (\text{GeV}^{-1})$	-0.11%	-0.11%	-0.11%	-0.11%
σ_{ind}	0.5%	0.5%	0.5%	0.5%

Table 5.2: Parameters used in the cross talk emulation in the simulation, for the different groups of supermodules.

5.3 The isolation method

The role of this Section is to present how to select and identify photons from $2 \rightarrow 2$ processes, discussed in Chapter 2. We know that these direct prompt photons are produced with no hadronic activity in their vicinity except for the underlying event of the collision. There are other sources of single γ such as fragmentation photons and decays of mesons; in particular, the latter represents the main source. The γ_{decay} and the γ_{fragm} are part of a particle jet and therefore they have a high probability of being accompanied by other fragments [75]. This is sketched in Fig. 5.10-middle and right, that report the γ_{fragm} and γ_{decay} emissions, respectively.

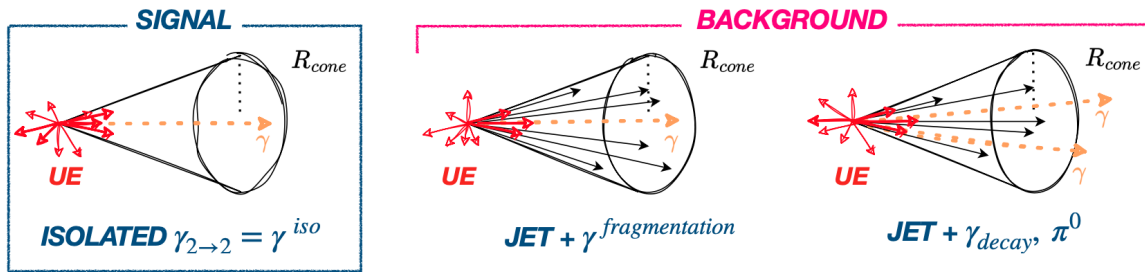


Figure 5.10: Production of different types of photons with the isolation cone sketched. Left: isolated photon produced alone. Middle and right: fragmentation photons and decay photons produced in combination with a jet.

The fact that the $\gamma_{2 \rightarrow 2}$ are produced **alone** can be used to increase the purity of the photons from $2 \rightarrow 2$ processes and suppress the contribution from fragmentation and hadron decay photons. This procedure is based on the selection via the so-called isolation momentum $p_{\text{T}}^{\text{iso}}$, which is the transverse momentum of all particles measured inside a cone around the photon candidate. Denoting η_γ and φ_γ the coordinates of the photon, the radius of the cone is defined as:

$$R = \sqrt{(\eta - \eta^\gamma)^2 + (\varphi - \varphi^\gamma)^2}. \quad (5.7)$$

The hadronic activity in the isolation cone can be measured by using the transverse momenta of the charged particle tracks ($p_{\text{T}}^{\text{track}}$) and the neutral particle clusters ($p_{\text{T}}^{\text{cluster}}$) after having excluded the candidate photon:

$$p_{\text{T}}^{\text{iso}} = \sum p_{\text{T}}^{\text{track}} + p_{\text{T}}^{\text{cluster}}. \quad (5.8)$$

In this analysis, neutral clusters are not included in the isolation momentum estimation and the previous formula becomes:

$$p_{\text{T}}^{\text{iso, ch}} = \sum p_{\text{T}}^{\text{tracks}} \quad (5.9)$$

Figure 5.10 shows the production of different types of photons and the isolation cone. The presence of the UE tracks needs to be taken into account and not included in the isolation momentum estimation:

$$p_{\text{T}}^{\text{iso, ch}} = \sum p_{\text{T}}^{\text{track}} - \rho_{\text{UE}}^{\text{track}} \pi R^2 \quad (5.10)$$

where $\rho_{\text{UE}}^{\text{track}}$ is the UE density and can be estimated event-by-event and subtracted from the transverse momentum content of the isolation cone.

5.3. The isolation method

In the following, we list the various methods used to estimate ρ_{UE}^{track} in different analyses by the **ALICE** Collaboration:

- **perpendicular cones** located at 90° in φ with respect to the candidate isolated cluster [145, 146], then:

$$\rho_{UE}^{\text{track}} = (\sum p_{\text{track}} \text{ in } \perp \text{ cone}) / (2\pi R^2); \quad (5.11)$$

- **perpendicular bands** located at 90° in φ with respect to the candidate isolated cluster, consists in a rectangular area with short side $\Delta\varphi = R$ and long side $\Delta\eta = 1.8$ (full **TPC** coverage), then:

$$\rho_{UE}^{\text{track}} = (\sum p_{\text{track}} \text{ in } \perp \text{ band}) / (2R\Delta\eta); \quad (5.12)$$

- **φ -band** centred in η of the candidate cluster, a rectangular area with short side $\Delta\eta = R$ and long side $\Delta\varphi = \pi$, half **TPC** coverage, avoid opposite side jet, then:

$$\rho_{UE}^{\text{track}} = (\sum p_{\text{track}} \text{ in } \varphi \text{ band}) / (R\Delta\varphi). \quad (5.13)$$

- **jet finder UE subtraction** techniques [110, 147]. For each event a k_T -jet finding algorithm is used, there: $\rho_{UE}^{\text{track}} = \text{median}\{p_{T,i}/A_i\}$ where $p_{T,i}$ and A_i are the transverse momentum and area of the k_T -jet denoted with the index i . To reduce the influence of jet signal on the estimation of the **UE** event, the two leading k_T -jets are excluded from the estimation. Furthermore, the use of the median ensures further stability against outliers entering the estimation.
- **η -band** centred around the φ of the candidate cluster, rectangular area with short side $\Delta\varphi = R$ and long side $\Delta\eta = 1.8$, full **TPC** coverage, default in this analysis, then:

$$\rho_{UE}^{\text{track}} = (\sum p_{\text{track}} \text{ in } \eta \text{ band}) / (R\Delta\eta), \quad (5.14)$$

Figure 5.11 shows schematically the location of the bands and cones compared to the reference cone centred at the cluster candidate to the isolation.

For the η and φ bands, an additional parameter is considered: a gap $\Delta R_{UE \text{ gap}}$ is introduced, so that the corona region $R^{\max} < R < R^{\max} + \Delta R_{UE \text{ gap}}$ is not considered in the **UE** calculation enlarging also the band in the shorter side by $\Delta R_{UE \text{ gap}}$, as shown in Figure 5.11. This was introduced in case the candidate cluster is the result of a jet fragmentation (neutral mesons decays), as jet hadronic remnants can still be found outside the selected isolation cone R and thus contribute to the area used for the **UE** estimation, biasing it to a higher value. In this Thesis, and also in other analyses [93, 85], the **η -band** method is used as default and a $\Delta R_{UE \text{ gap}} = 0.1$ is applied.

When the cluster candidate for isolation has a pseudorapidity $0.5 < |\eta| < 0.67$, a small fraction of the isolation cone of radius $R = 0.4$ is out of the tracking acceptance $|\eta^{\text{track}}| < 0.9$. To maximize the photon acceptance, such candidate clusters are still used in the analysis, but the measured isolation momentum is scaled up to account for the cone area that is out of the tracking acceptance [85, 110].

Figures 5.12 shows the $p_T^{\text{iso}, \text{ ch}}$ distribution for the different studied **UE** estimators for narrow clusters, $0.1 < \sigma_{\text{long}, 5 \times 5}^2 < 0.3$ in γ -jet PYTHIA 8 embedded into the Pb–Pb data.

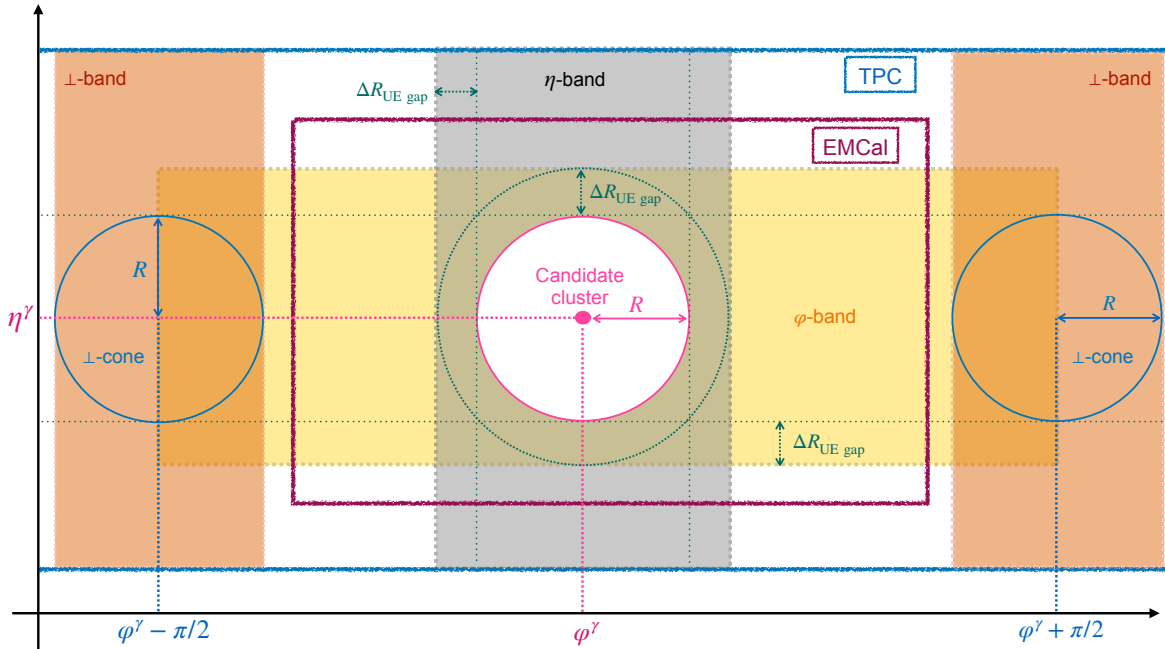


Figure 5.11: Illustration of the isolation cone and isolation UE estimation regions.

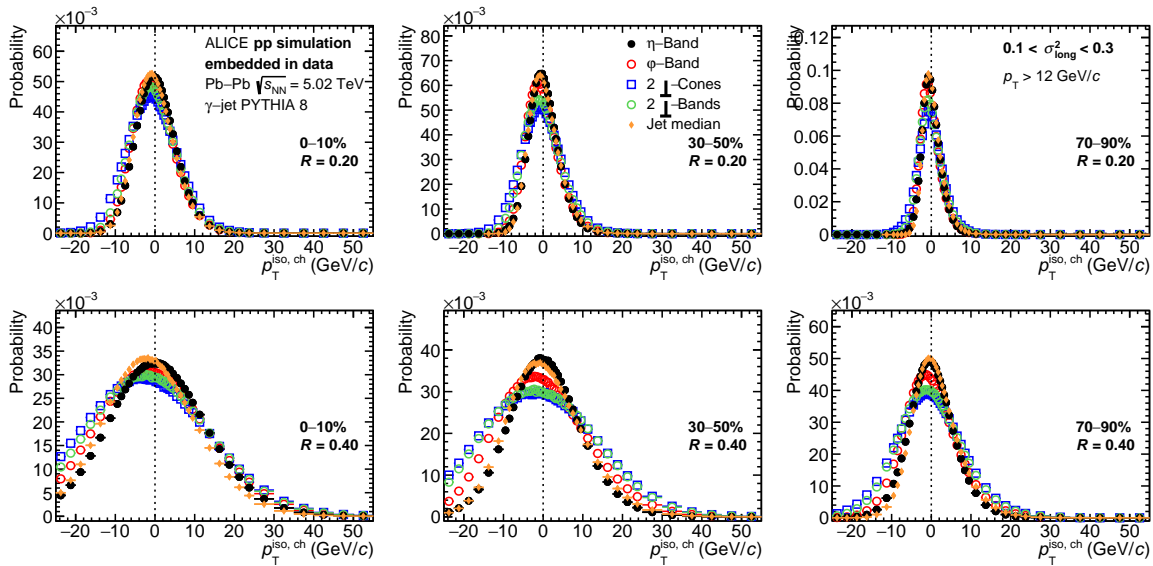


Figure 5.12: In γ -jet PYTHIA 8 simulation embedded into MB data, $p_T^{\text{iso, ch}}$ distribution for different UE estimation areas, $p_T > 12 \text{ GeV}/c$ and narrow clusters with $0.1 < \sigma_{\text{long}, 5 \times 5}^2 < 0.3$ in Pb-Pb central (left), semi-central (middle) and peripheral (right) collisions for $R = 0.2$ (top) and $R = 0.4$ (bottom) [148].

The distributions obtained show that the various methods have similar performances, but perpendicular cones and bands distributions are wider, and the mean of the distribution of φ -band, jet-median and the perpendicular methods tends to be lower than 0 for narrow clusters in the embedded signal simulation, unlike the η -band. All these methods are also more sensitive to the flow in the area inspected and could cause the observed differences, for this reason, they were not used as default.

Figure 5.13–left reports the UE track density $\rho_{\text{UE}}^{\text{track}}$ distribution in Pb–Pb data obtained with the η -band as a function of the centrality for a radius cone $R = 0.2$. The distribution has a large width due to the UE fluctuations event by event. As expected, the UE track density $\rho_{\text{UE}}^{\text{track}}$ depends strongly on the centrality.

Figure 5.13–right shows the UE track density $\rho_{\text{UE}}^{\text{track}}$ distributions for a radius cone $R = 0.4$ for different centrality classes in Pb–Pb collisions and in pp ones.

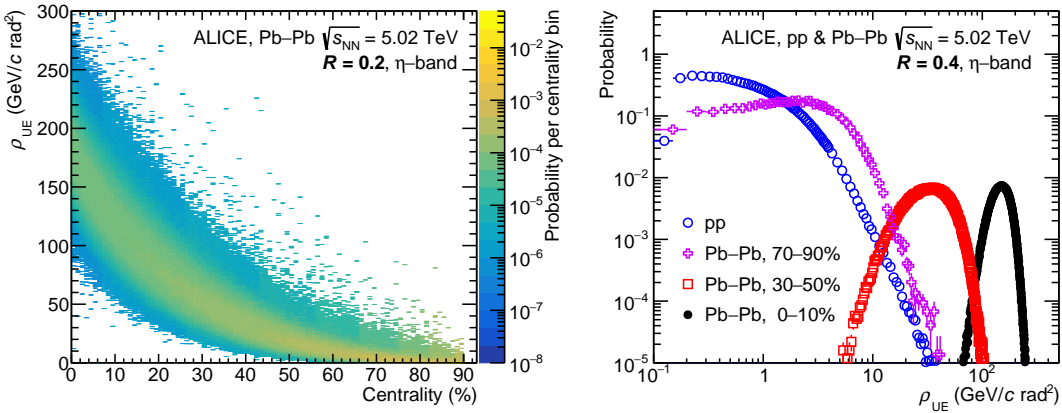


Figure 5.13: The $\rho_{\text{UE}}^{\text{track}}$ distributions in data calculated in the η -band. Left: for Pb–Pb collisions and the cone radius $R = 0.2$ as a function of centrality. Right: for pp and Pb–Pb collisions for different centrality classes for the cone radius $R = 0.4$ [93].

The UE density is beyond $100 \text{ GeV}/(c \text{ rad}^2)$ in central (0–10%) Pb–Pb collisions, still reaches several tens of $\text{GeV}/(c \text{ rad}^2)$ in semi-central (30–50%) collisions, but its value is only a few $\text{GeV}/(c \text{ rad}^2)$ for the most peripheral Pb–Pb collisions, and less than $1 \text{ GeV}/(c \text{ rad}^2)$ in pp collisions.

Figure 5.14 shows the $p_{\text{T}}^{\text{iso}, \text{ch}}$ distribution for both R values and all collision systems considered, for clusters with shower shape $0.1 < \sigma_{\text{long}, 5\times5}^2 < 0.3$, in data as well as in PYTHIA 8 simulations of prompt photons (γ -jet process), either native pp collisions or embedded into real Pb–Pb collisions data in two extreme centrality classes (other centrality classes reported in Ref. [148]).

Even though the UE energy to be subtracted is large, the distributions are centred around $0 \text{ GeV}/c$, even for the most central class. In the prompt-photon simulation, the distribution is symmetric since there is no jet contribution. On the contrary, the data contain a jet contribution when the cluster does not originate from a prompt photon, and that induces a widening of the distribution tail at positive values of $p_{\text{T}}^{\text{iso}, \text{ch}}$. The width of the distribution is larger for $R = 0.4$ than for $R = 0.2$, due to the larger UE fluctuations in the isolation cone. For the same reason, the width decreases when moving to more peripheral collisions.

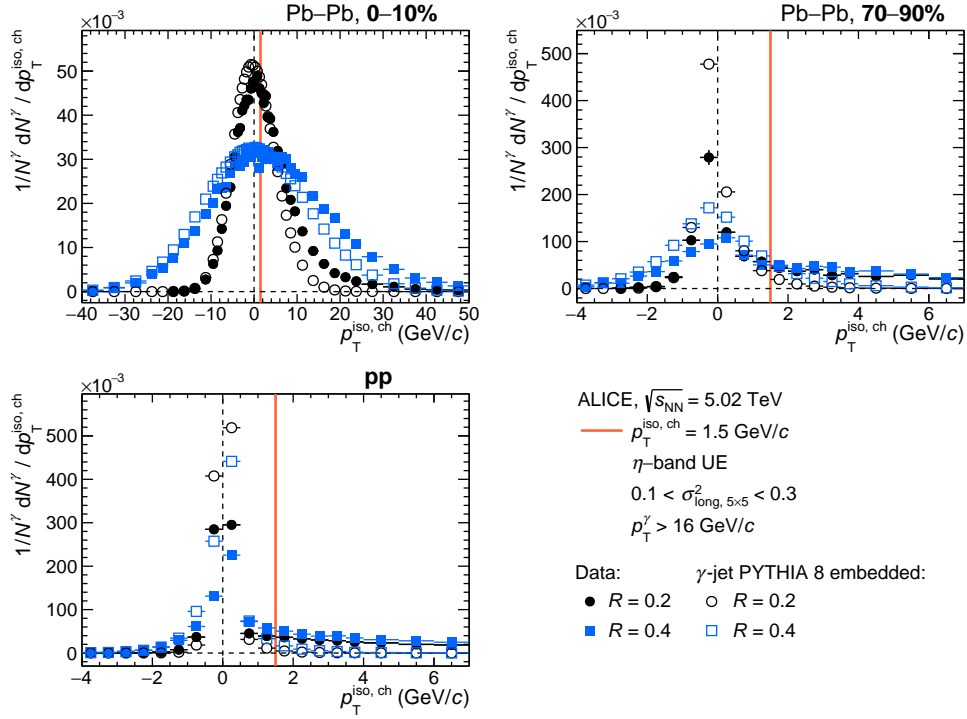


Figure 5.14: The $p_T^{\text{iso}, \text{ch}}$ distribution for narrow clusters with $0.1 < \sigma_{\text{long}, 5 \times 5}^2 < 0.3$ for $p_T > 16 \text{ GeV}/c$, in very central (0-10%) and peripheral (70-90%) Pb-Pb collisions (top left and right, respectively) and in pp ones (lower right frame) with $R = 0.2$ (black bullets) and $R = 0.4$ (blue squares), in data (full markers) and simulation (open markers) PYTHIA 8 γ -jet processes, embedded into data in case of Pb-Pb collisions [93].

In order to understand which value of the isolation cut should be applied to separate $\gamma_2 \rightarrow 2$ from the rest, it is possible to study the efficiency of the $p_T^{\text{iso}, \text{ch}}$ cut selection on known signal or background clusters, i.e. clusters from MC simulations.

Figure 5.15 shows the $p_T^{\text{iso}, \text{ch}}$ selection cumulative probability for wide clusters in data, that are mainly populated by background, for signal narrow clusters in γ -jet simulation and for wide clusters in jet-jet simulations for three different p_T bins.

The signal is largely accepted compared to the background if the $p_T^{\text{iso}, \text{ch}}$ cut is smaller than a few GeV/c . This selection is better in peripheral Pb-Pb and pp collisions than in central ones. Comparing both cone radii, the larger cone size gives a similar or a bit worse selection power in central collisions, but better in peripheral Pb-Pb and pp collisions at low $p_T^{\text{iso}, \text{ch}}$. The ratios of the distributions, γ -jet simulation signal over the data or jet-jet simulation background (not shown), are rather constant until a certain $p_T^{\text{iso}, \text{ch}}$ value depending on the centrality: for central collisions to approximately 8 GeV/c and for peripheral Pb-Pb and pp collisions up to 2 to 3 GeV/c , above these values the ratio decreases.

With these considerations, one can conclude that using a cut at $p_T^{\text{iso}, \text{ch}} = 1.5 \text{ GeV}/c$ like in previous pp and p-Pb analyses [110], is possible also in Pb-Pb collisions for all centralities. The choice of a lower $p_T^{\text{iso}, \text{ch}}$ value would not offer much more gain in background rejection power and would cause problems when compared to theoretical predictions. In central collisions (0-10%), it seems feasible to increase the $p_T^{\text{iso}, \text{ch}}$ up to 5 GeV/c to gain a bit of signal. This is supported by the fact that the purity, presented in the next Section, does not change with a sharper $p_T^{\text{iso}, \text{ch}}$ cut. However, for simplicity, we use the same selection value at $p_T^{\text{iso}, \text{ch}} < 1.5 \text{ GeV}/c$ for each of the centrality classes measured.

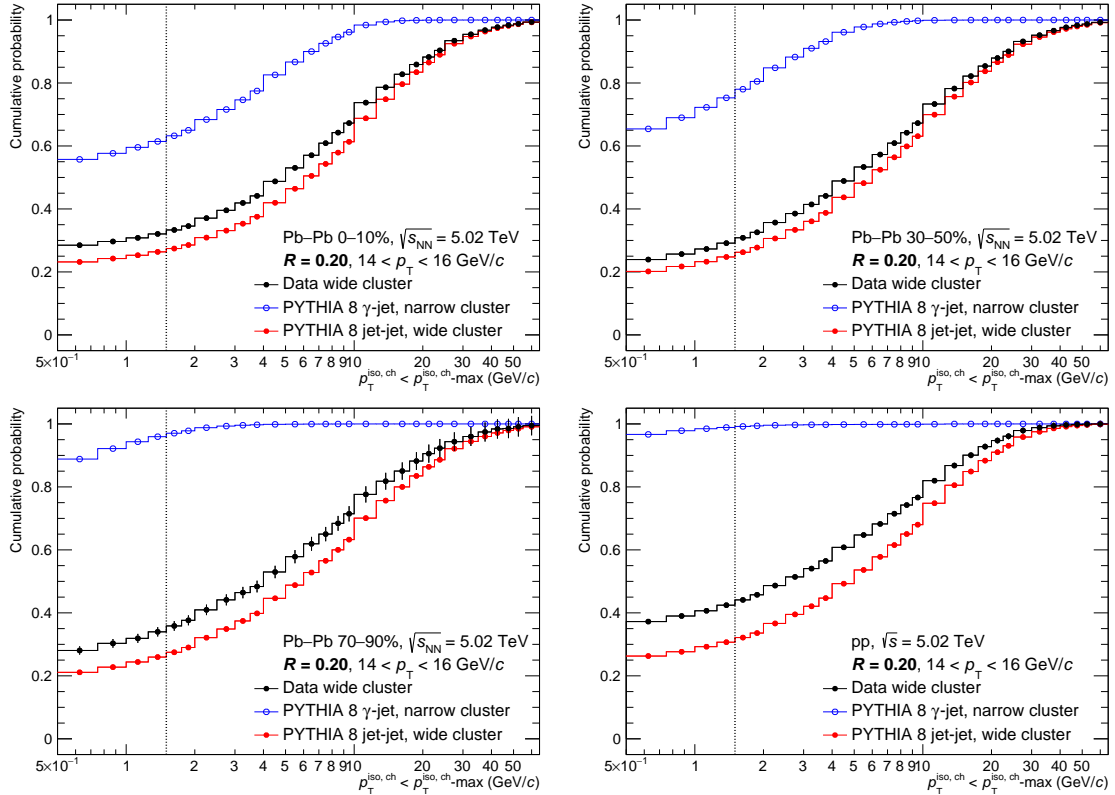


Figure 5.15: $p_T^{\text{iso}, \text{ch}}$ cumulative probability distribution (clusters with $p_T^{\text{iso}, \text{ch}} < p_T^{\text{iso}, \text{ch}}\text{-cut}$ overall) for clusters with $14 < p_T < 16 \text{ GeV}/c$ for signal narrow clusters in a γ -jet simulation (empty blue circle) and background wide clusters in data (full black circle) and background wide clusters in jet-jet simulation (full red circle) with $R = 0.2$. From top to bottom, 0–10% Pb–Pb collisions, 30–50% Pb–Pb collisions, 70–90% Pb–Pb collisions and pp collisions. The η -band is used to subtract the UE from $p_T^{\text{iso}, \text{ch}}$. Dashed line at selected isolation value of $1.5 \text{ GeV}/c$ [148].

5.4 Isolated photon purity P

Despite the cluster shape selections and the isolation cut, the isolated photon candidate sample is still affected by a significant amount of background, mainly from meson decays. This is corrected by estimating the sample purity. In the following, the ABCD-ALICE method for estimating the purity (P) is presented, since it is the one used in this Thesis and it has been applied in different ALICE measurements [76, 93, 85, 146, 147]. The purity values have been taken from the isolated photon spectra analysis [93] as the same photon selection are used.

Another way to estimate the purity is the template fit method. This method and its results have been used in other spectra analysis in pp and p–Pb collisions at $\sqrt{s_{\text{NN}}} = 5.02$ TeV, at 8.16 TeV and at $\sqrt{s_{\text{NN}}} = 8$ TeV, and in the γ^{iso} -jet correlations analysis in Pb–Pb collision at $\sqrt{s_{\text{NN}}} = 5.02$ TeV [145, 147, 149] done by the ALICE Collaboration. It was found that the template method needs better statistics to get stable results, in particular at low p_{T} , hence it was not selected to be used in this analysis.

5.4.1 The ABCD-ALICE method

The ABCD method is based on the fact that the cluster shape $\sigma_{\text{long}, 5\times5}^2$ and the isolation energy $p_{\text{T}}^{\text{iso}}$ contain information about whether or not a photon candidate is likely to be a $\gamma_{2\rightarrow2}$. To estimate the purity of the measured isolated photon sample, the phase-space populated by the clusters isolation $p_{\text{T}}^{\text{iso}}$ and cluster shape $\sigma_{\text{long}, 5\times5}^2$ is divided into four regions, as reported in Fig. 5.16. The yield of isolated photon candidates is labelled with the letter **A** in Fig. 5.16. The three other classes, contain predominantly background clusters and they are labelled as **B**, **C** and **D**.

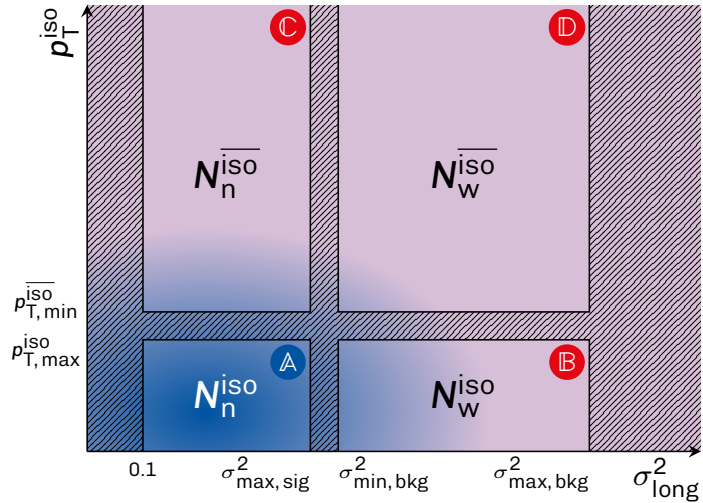


Figure 5.16: Illustration of the parametric-space of the photon $p_{\text{T}}^{\text{iso}}$ (or $p_{\text{T}}^{\text{iso}, \text{ch}}$, etc) and σ_{long}^2 ($\sigma_{\text{long}, 5\times5}^2$), used to estimate the background yield in the signal region (**A**) from the observed yields in the three control regions (**B**, **C**, **D**). The red regions indicate areas dominated by background and the blue regions by the photon signal. The color gradient indicates mixture of signal and background [135].

It is possible to distinguish classes based on the shower shape $\sigma_{\text{long}, 5\times5}^2$, i.e. **wide** ($\sigma_{\text{long}, 5\times5}^2 > 0.4$, most often elongated, i.e. non-circular) and **narrow** ($0.1 < \sigma_{\text{long}, 5\times5}^2 <$

0.3), and classes defined by the isolation momentum, i.e. **isolated** ($p_T^{\text{iso}, \text{ch}} < 1.5 \text{ GeV}/c$) and **anti-isolated** ($4 < p_T^{\text{iso}, \text{ch}} < 25 \text{ GeV}/c$), where the upper bound value is chosen to ensure that the background sample is still close enough to the isolation region.

The different classes are denoted by sub- and superscripts: for example, isolated narrow clusters are written as X_n^{iso} and non-isolated, wide clusters as $\overline{X_w^{\text{iso}}}$.

The yield of isolated photon candidates in this nomenclature is N_n^{iso} . It consists of signal (S) and background (B) contributions: $N_n^{\text{iso}} = S_n^{\text{iso}} + B_n^{\text{iso}}$. The contamination of the candidate sample is then $C = B_n^{\text{iso}}/N_n^{\text{iso}}$, or respectively, the purity is then $P \equiv 1 - C$. Assuming that the proportion of background in the narrow cluster areas (\mathbb{A} and \mathbb{C}) is the same as in the wide cluster areas, that means $\frac{A}{C} = \frac{B}{D}$ and assuming that the proportion of signal in the control regions (\mathbb{B} , \mathbb{C} and \mathbb{D}) is negligible compared to the proportion of background, the purity can be derived in a data-driven approach (dd) as

$$P_{\text{dd}} = 1 - C_{\text{dd}} = 1 - \frac{\overline{N_n^{\text{iso}}}/N_n^{\text{iso}}}{\overline{N_w^{\text{iso}}}/N_w^{\text{iso}}} \approx 1 - \frac{\overline{B_n^{\text{iso}}}/N_n^{\text{iso}}}{\overline{B_w^{\text{iso}}}/B_w^{\text{iso}}}, \quad (5.15)$$

unfortunately, both assumptions do not hold fully.

The correlation between the classes is due to the detector granularity and kinematical reasons that the MC should reproduce. An additional MC term is used in the purity:

$$P = 1 - C_{\text{dd}} \times \alpha_{\text{MC}} = 1 - \left(\frac{\overline{N_n^{\text{iso}}}/N_n^{\text{iso}}}{\overline{N_w^{\text{iso}}}/N_w^{\text{iso}}} \right)_{\text{data}} \times \left(\frac{\overline{B_n^{\text{iso}}}/N_n^{\text{iso}}}{\overline{N_w^{\text{iso}}}/N_w^{\text{iso}}} \right)_{\text{MC}}, \quad (5.16)$$

where the MC term contains all the corrections coming from the simulation.

For completeness, the parametric space of the cluster isolation momentum and the shower shape parameter in data for $R = 0.2$ is reported in Fig. 5.17. It has been used to estimate the background yield in the signal class long (A) from the observed yields in the three control classes (B, C, D).

The purity obtained with this method and for two radii cones ($R = 0.2$ and $R = 0.4$) is shown in Fig. 5.18 as a function of p_T^γ in pp collisions and in different centrality classes in Pb–Pb collisions at $\sqrt{s_{\text{NN}}} = 5.02 \text{ TeV}$. The p_T^γ dependence of the purity is caused by an interplay of physics and detector effects. On the one hand, the p_T^γ spectra of prompt photons are harder than that of neutral pions, mainly because the latter undergo fragmentation. Because of this, the $\gamma_{\text{dir}} / \pi^0$ yields ratio rises with p_T^γ , and as a consequence, the photon purity in the cluster sample should also increase. Also, the probability of finding a photon as isolated varies with p_T^γ : at higher p_T^γ , isolation of jet fragments is more probable for a fixed isolation momentum cut; on the contrary, due to the decreasing mesons decay opening angle at high p_T^γ and the corresponding higher probability to obtain a narrow shower from the merged photons, the contamination from π^0 mesons increases with p_T^γ . The combined effect of these mechanisms leads to the rise of the purity at low p_T^γ , consistent with more meson merging and good shower shape discrimination, and saturation for $p_T^\gamma > 18 \text{ GeV}/c$, which corresponds to poor shower shape discrimination, and then rises again above $\approx 40 \text{ GeV}/c$, where there is almost no shower shape discrimination, but higher photon yield.

The purity correction can have rather strong statistical fluctuations. To reduce them, the purity distribution is fitted by two sigmoid functions to reproduce the trend of the

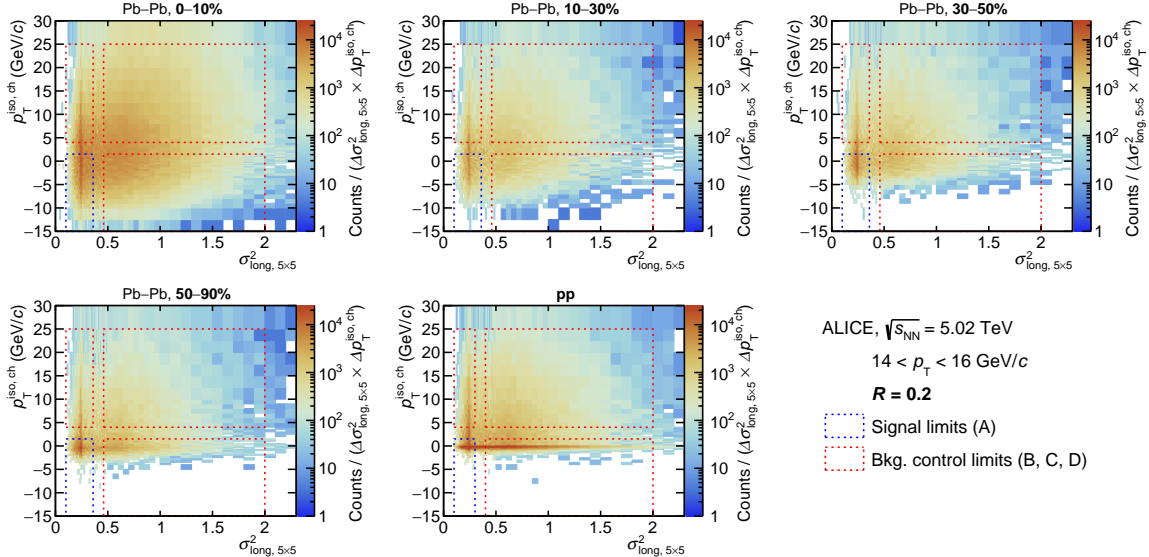


Figure 5.17: Illustration of the parametric-space of the photon $p_{\text{T}}^{\text{iso}}$ and $\sigma_{\text{long}, 5\times 5}^2$ for and $14 < p_{\text{T}} < 16 \text{ GeV}/c$ in five centrality classes in Pb–Pb collisions and in pp collisions, used to estimate the background yield in the signal region (A) from the observed yields in the three control regions (B, C and D). The dashed boxes indicate the limits of each class [148].

distribution with p_{T}^{γ} :

$$f_{\text{fit-sig}}(p_{\text{T}}^{\gamma}) = \frac{a}{1 + \exp(-b \cdot (p_{\text{T}}^{\gamma} - c))}. \quad (5.17)$$

The first fit is from $p_{\text{T}}^{\gamma} = 7$ to $60 \text{ GeV}/c$ and the second from $p_{\text{T}}^{\gamma} = 20$ to $140 \text{ GeV}/c$, as reported in Fig. 5.18. The second sigmoid fit starting at $20 \text{ GeV}/c$ seems reliable in central collisions 0-30% and semi-central 30-50%, but in the other systems the lack of statistics does not help to see a reliable trend. To validate the use of the fit on the purity and in particular at high- p_{T}^{γ} , it is possible to compare the previous results with other measurements that apply the fits. The purity obtained in pp at $\sqrt{s} = 13 \text{ TeV}$ by the ALICE Collaboration is shown in Fig. 5.19.

The purity distribution in pp collisions at $\sqrt{s} = 13 \text{ TeV}$ is fitted by two sigmoid functions to reproduce the trend of the distribution with p_{T}^{γ} , also at very high- p_{T}^{γ} . The use of the fit instead of the points, as demonstrated in Fig. 5.18 and 5.19, permit to get a clear reduction in the fluctuations.

The measured purity in Pb–Pb collisions at $\sqrt{s_{\text{NN}}} = 5.02 \text{ TeV}$ with $R = 0.2$ is slightly higher than that obtained with $R = 0.4$, particularly in central collisions, while in peripheral collisions, the distributions are nearly identical. In addition, the use of a small cone permits reduce the effects of the fluctuations in the underlying event. For these reasons, the purity obtained with $R = 0.2$ has been chosen for the γ^{iso} -hadron correlation analysis, that will be presented in the next Chapter.

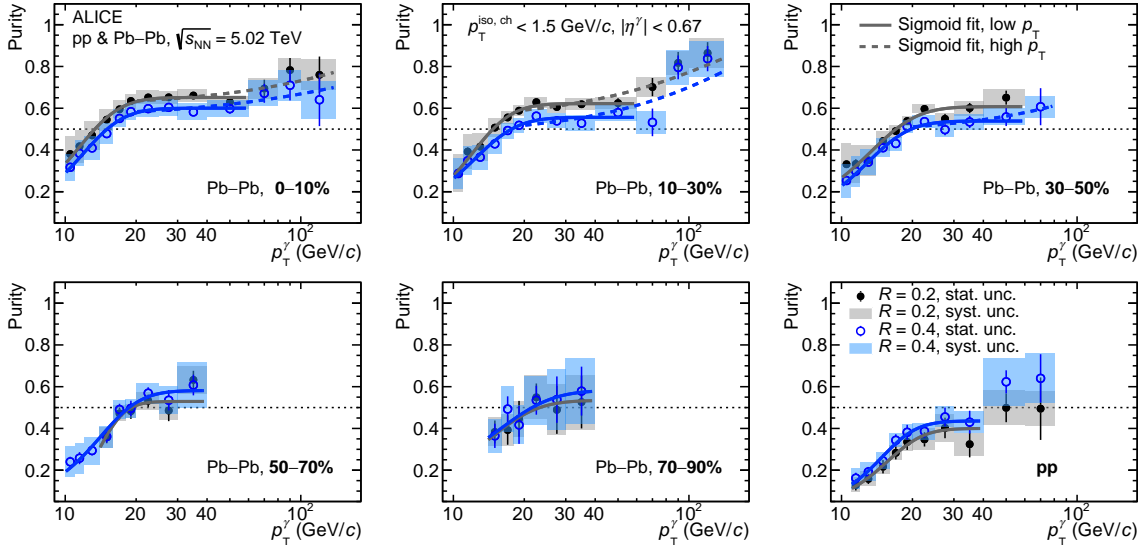


Figure 5.18: Purity of the isolated-photon sample as a function of p_T^γ in pp and different centrality classes in Pb–Pb collisions at $\sqrt{s_{NN}} = 5.02$ TeV for $R = 0.2$ (full black circle) and for $R = 0.4$ (empty blue circle). The lines are the result of the two sigmoid functions fit (see Eq. (5.17)) to the points, plain line for low p_T^γ and dashed for high p_T^γ [93].

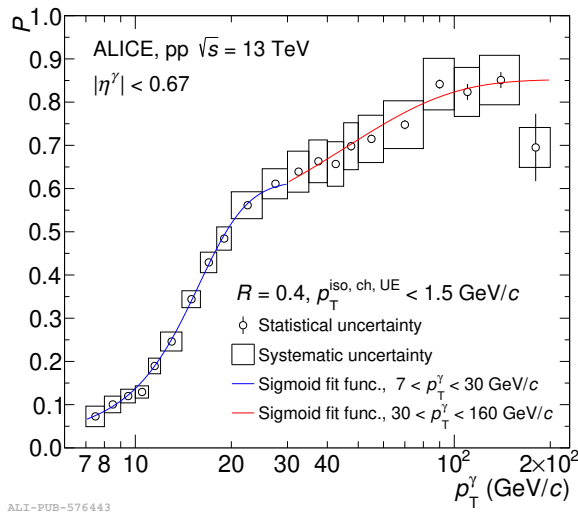


Figure 5.19: Purity of the isolated-photon sample as a function of p_T^γ in pp collisions at $\sqrt{s} = 13$ TeV. The red and blue lines are the results of a fit to the measured purity using a two-sigmoid-function described by Eq. (5.17) for two different transverse momentum intervals [85].

Chapter 6

Azimuthal correlation distributions of isolated photons with hadrons in Pb–Pb collisions

6.1	Data selection	116
6.2	Monte Carlo simulations	117
6.3	How an azimuthal correlation distribution can be defined?	120
6.3.1	Underlying event subtraction	122
6.3.2	Purity Correction	127
6.3.3	Correction of the track momentum resolution	130
6.3.4	$D(z_T)$ distributions	133
6.4	Systematics uncertainties	135
6.4.1	Mixed event and UE estimation	135
6.4.2	Purity	139
6.4.3	Variation of the Shower Shape	141
6.4.4	Track momentum resolution	143
6.4.5	Number of centrality bin used for filling the mixed event pool	144
6.4.6	Total uncertainties	145
6.5	Theoretical models	148
6.5.1	The nuclear-modification factor I_{AA}	150
6.5.2	I_{CP}	150
6.6	Results from other experiments	152

The photon-hadron correlation measurement can be used to characterize the energy and topology of hadron distributions resulting from parton fragmentation and to understand how parton propagation is modified by the presence of the medium, as it was illustrated in Chapters 1 and 2.

The main purpose of this Thesis is to measure the azimuthal correlation distributions of isolated photons and hadrons via $\Delta\varphi = \varphi^\gamma - \varphi^{\text{hadron}}$ in different $z_T = p_T^{\text{hadron}}/p_T^\gamma$ intervals for different centrality classes in Pb–Pb collisions at $\sqrt{s_{\text{NN}}} = 5.02$ TeV.

6.1 Data selection

The data used in this analysis derive from the Pb–Pb data-taking periods of 2015 and 2018 measured at $\sqrt{s_{\text{NN}}} = 5.02$ TeV with the [ALICE](#) experiment. The measurements have been performed in four centrality classes (0–10%, 10–30%, 30–50% and 50–90%), chosen considering the minimum bias interaction and the [EMCal L1- \$\gamma\$](#) triggers, presented in Sect. 4.2.2. The number of [MB](#) or [EMCal L1- \$\gamma\$](#) triggered events is shown for different event selections in Fig. 6.1.

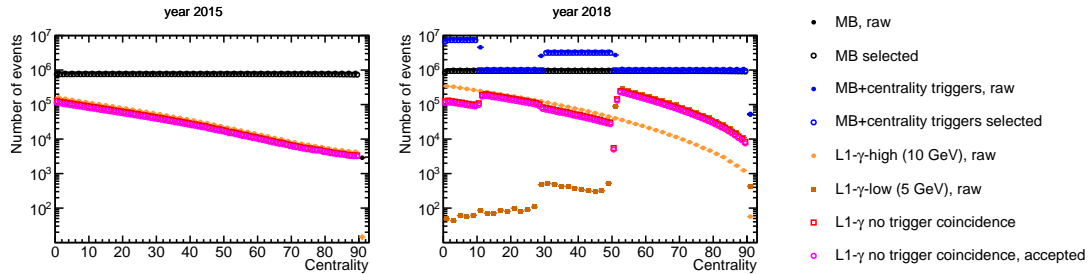


Figure 6.1: Centrality distributions for minimum bias events (black marker) or minimum bias plus centrality triggers (blue marker) or EMCAL L1- γ (yellow, orange, pink and red markers). Distributions are shown for events without selection (full markers) and after all the selections (open markers). The L1- γ triggers have an additional offline selection ("accepted" in the legend) based on masked trigger regions offline and energy thresholds.

Minimum bias data with centrality triggers in 2018 have the same constant dependence with centrality with and without the selection, apart from central (0–10%) and semi-central (30–50%) collisions, where dedicated triggers enhanced these centrality classes. [EMCal L1- \$\gamma\$](#) triggered data are shown in Fig. 6.1 with three different selections: raw, selected without [MB](#) triggers coincidence and selected without [MB](#) triggers coincidence, but applying trigger rejection based on the energy threshold and bad maps (more details relative to bad maps can be found in Appendix B). The [L1- \$\gamma\$](#) trigger centrality distributions look quite similar in 2015 and 2018, except for peripheral events: the 2018 peripheral distributions tend to be higher. Table 6.1 reports the number of selected events per each of the triggers considered and the centrality class.

Trigger	Trig. threshold	Pb–Pb	Pb–Pb	Pb–Pb	Pb–Pb
		0–10%	10–30%	30–50%	50–90%
MB	-	$80.38 \cdot 10^6$	$35.30 \cdot 10^6$	$78.65 \cdot 10^6$	$70.47 \cdot 10^6$
L1- γ -high	10	$1.975 \cdot 10^6$	$3.733 \cdot 10^6$	$1.449 \cdot 10^6$	$0.30228 \cdot 10^6$
L1- γ -low	5	-	-	-	$3.4493 \cdot 10^6$

Table 6.1: Number of selected events in Pb–Pb collisions, per centrality class.

An offline event selection is applied to remove beam background events, using the information from two zero-degree calorimeters positioned at 112.5 m on either side of the nominal interaction point: beam background events are removed by using the [V0](#) timing information and the correlation between the sum and the difference of times measured in each of the [ZDCs](#) [132]. Furthermore, all events with more than one reconstructed primary vertex were rejected in the analyses to exclude pileup events within the same bunch cross-

ing and out-of-bunch pileup was removed with cuts on the **V0** timing [132]. Finally, only events with a primary vertex along the beam direction within ± 10 cm from the centre of the apparatus were considered in this analysis, to grant a uniform pseudorapidity acceptance. Appendix A.1 collects the different run numbers for data.

The central classes (0-10% and 10-30%) will be combined for the final result in a larger single interval (0-30%) to increase the statistics.

6.2 Monte Carlo simulations

Monte Carlo (**MC**) event generators are used to obtain the isolated photon purity P , presented in Sect. 5.4, and in this analysis to get corrections such as the detector tracking efficiency, that will be discussed later in Sect. 6.3.3. The simulation must be able to describe the physics processes and also the propagation of particles through the **ALICE** detector.

For our aims, we use the PYTHIA 8 event generator [150], which is a general-purpose generator, largely used in high-energy particle physics to describe the properties of a high-energy collision and which provides event-by-event collision data using a combination of perturbative calculations and phenomenological models. The hard process of two partons from incoming hadrons is described by calculating the matrix elements of $2 \rightarrow 2$ scatterings using **LO** perturbation theory, where additional fixed-order radiative correction can be incorporated via additional matrix elements. Additional radiation and corrections (such as gluon emissions) are modeled through parton showers, specifically Initial-State Radiation (ISR) and Final-State Radiation (FSR), which describe the emission of additional particles by the incoming- and outgoing partons of the scattering, respectively. Multiple parton-parton scatterings in a single collision, which are known as Multi Parton Interactions (MPIs), are also modelled in a dedicated framework. The non-perturbative process of hadronisation is incorporated in Pythia through various models, where the default is based on the Lund string fragmentation model [151] that iteratively models the probability that the “strings” spanned by self-interacting gluons between $q - \bar{q}$ pairs break into hadronic states.

In this Thesis, pure PYTHIA 8 simulations are used to generate pp collisions at $\sqrt{s_{\text{NN}}} = 5.02$ TeV. Two types of simulations are used and they differ for the choice of scattering processes used in PYTHIA: the γ -jet simulations (**GJ MC**), which allow producing photons from $2 \rightarrow 2$ **LO** processes that contain one (Compton and annihilation processes) or two photons (negligible amount) in the final state; the jet-jet simulations (**JJ MC**), which permit to produce an inclusive sample of hard **QCD** scatterings, including $2 \rightarrow 2$ (3) processes involving light quarks and gluons as well as heavy flavour production. The event is accepted for the γ -jet event generation when the prompt photon enters the **EMCal** acceptance. For the jet-jet event generation, the event is accepted when at least one jet produces a high- p_T photon, requested to be originated from a hadron decay, in the **EMCal** acceptance (see Sect. 4.2.2). This is done to enhance the number of such photons, which are the main background in this analysis. To increase the probability of producing high- Q scatterings, which is reduced more and more at high p_T , the simulations are done in different bins of momentum transfer of the scattering process (p_T^{hard}).

In this Thesis, for **GJ MC**, six p_T^{hard} intervals are used and they correspond to:

- **GJ:** [5–11], [11–21], [21–36], [36–57], [57–84], [> 84] GeV/c .

For what concerns the **JJ** simulations, there is a distinction between **JJ-low**, corresponding to a decay photon p_T threshold of $3.5 \text{ GeV}/c$ and **JJ-high**, corresponding to a decay photon p_T threshold of $7 \text{ GeV}/c$. The corresponding p_T^{hard} are:

- **JJ-low:** [5–7], [7–9], [9–12], [12–16], [16–21], [> 21] GeV/c ;
- **JJ-high:** [8–10], [10–14], [14–19], [19–26], [26–35], [35–48], [48–66], [> 66] GeV/c ;

The **JJ** simulations have been only used to calculate the **MC** correction for the purity calculation, presented in Sect. 5.4.

When generating PYTHIA events in different p_T^{hard} intervals, a scale factor per range needs to be applied before merging them. This scaling factor is related to the event generated cross-section and the fraction of generated and selected events (i.e. the fraction of total events generated by PYTHIA and the events selected that match our requirements on photon acceptance or p_T). The effects of using p_T^{hard} intervals applying a scaling factor are reported in Fig. 6.2 for **GJ** simulations distributions and in Fig. 6.3 for **JJ-low** and **JJ-high** ones.

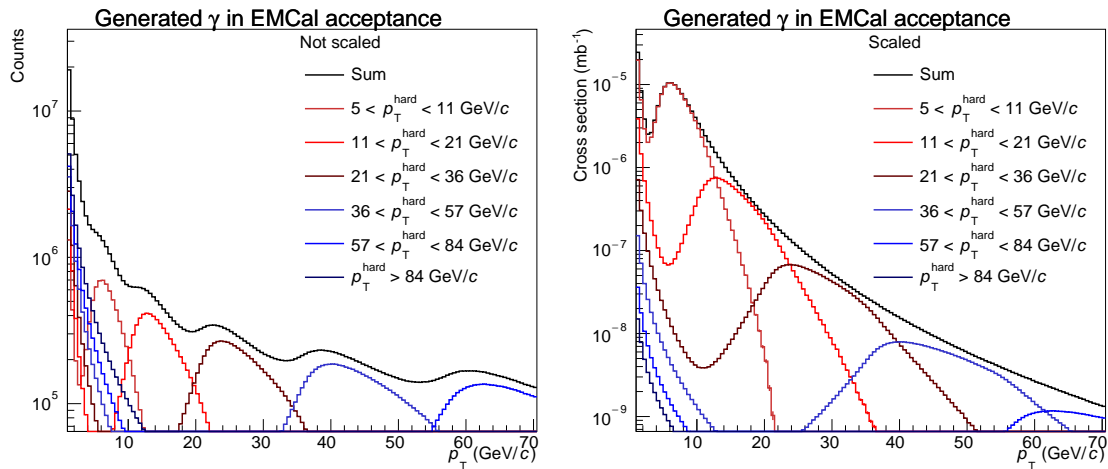


Figure 6.2: Left: Not scaled GJ MC distributions as a function of p_T . Right: Scaled GJ MC distributions as a function of p_T . The distributions are presented for various p_T^{hard} intervals.

The p_T of the photon is very close to the one of the parton, therefore there are different **GJ** distributions for every p_T^{hard} , as shown in Fig. 6.2–left. The scaling is necessary to obtain the usual logarithmic distribution, reported in Fig. 6.2–right.

Referring to the **JJ-low** and **JJ-high** distributions, reported in Fig. 6.3–left top and bottom, they are already logarithmic because the π^0 derive from parton fragmentation, but the π^0 cross-sections in different p_T^{hard} intervals have the same weight, which is not reasonable. The scaling effect is needed to set the correct weight for every p_T^{hard} , as illustrated in Fig. 6.3–right top and bottom.

In order to reproduce Pb–Pb collisions data, the pp PYTHIA simulations, aimed at describing the hard process, are embedded into real Pb–Pb minimum bias events, so that

6.2. Monte Carlo simulations

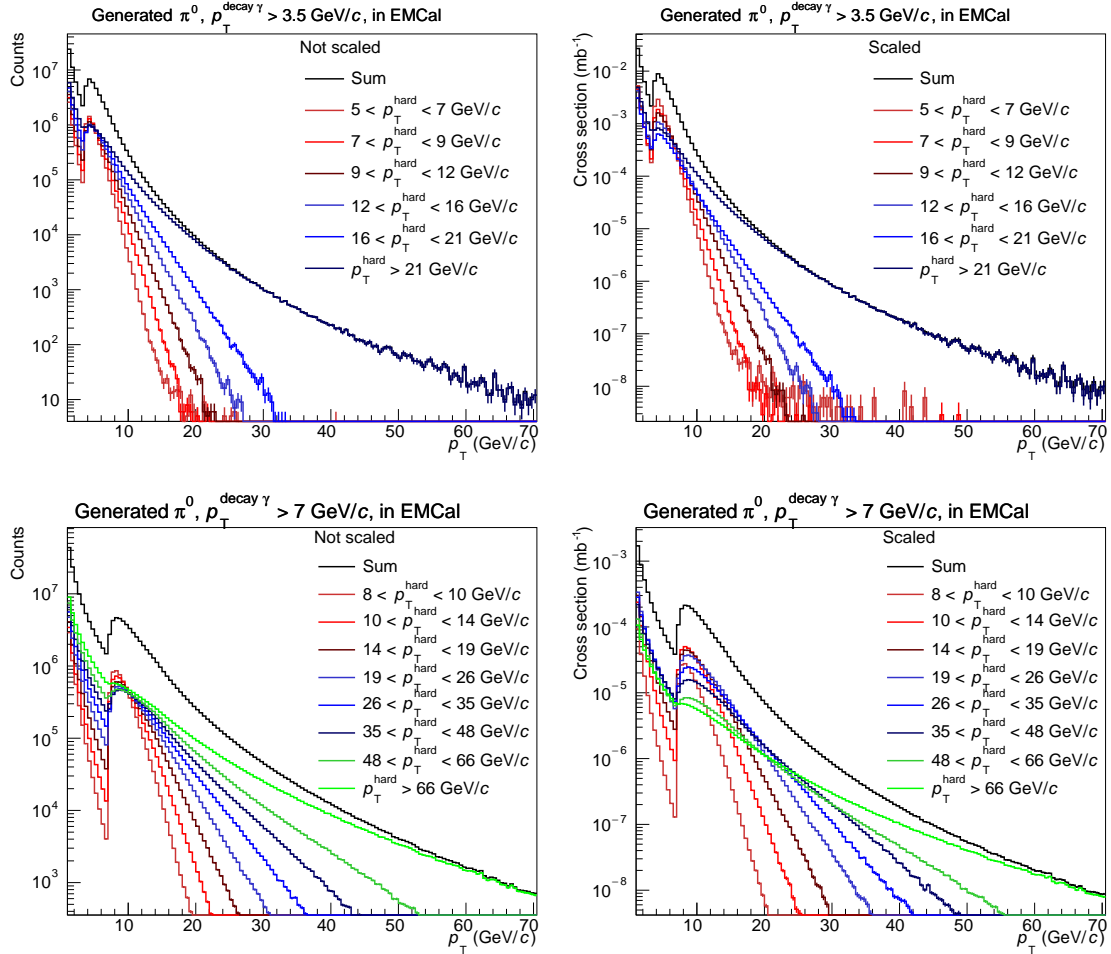


Figure 6.3: Left: Not scaled JJ-low (top) and JJ-high (bottom) MC distributions as a function of p_T . Right: Scaled JJ-low (top) and JJ-high (bottom) distributions as a function of p_T . The distributions are presented for various $p_{T_{\text{hard}}}^{\text{hard}}$ intervals.

the effect of the UE low-energy particles is properly taken into account. For the calorimeter, the embedding is made by summing the minimum bias data and the simulated energy at the cell level. For the charged particles measured with the tracking systems, the embedding is done at the track level, adding to the list of available tracks from the simulation those coming from the data. The hadron suppression, observed in heavy-ion collisions, can be reproduced in the jet-jet simulation by weighting down the contribution of the particles of hadronic origin by the merge of the nuclear modification factor of charged particles, obtained by combining the ALICE [65] and CMS results [152] to cover as much as possible the low and high p_T of the particle spectrum. This is not done for the γ -jet simulations since prompt photons are not expected to be suppressed in Pb–Pb.

The used R_{AA} weights are shown in Fig 6.4.

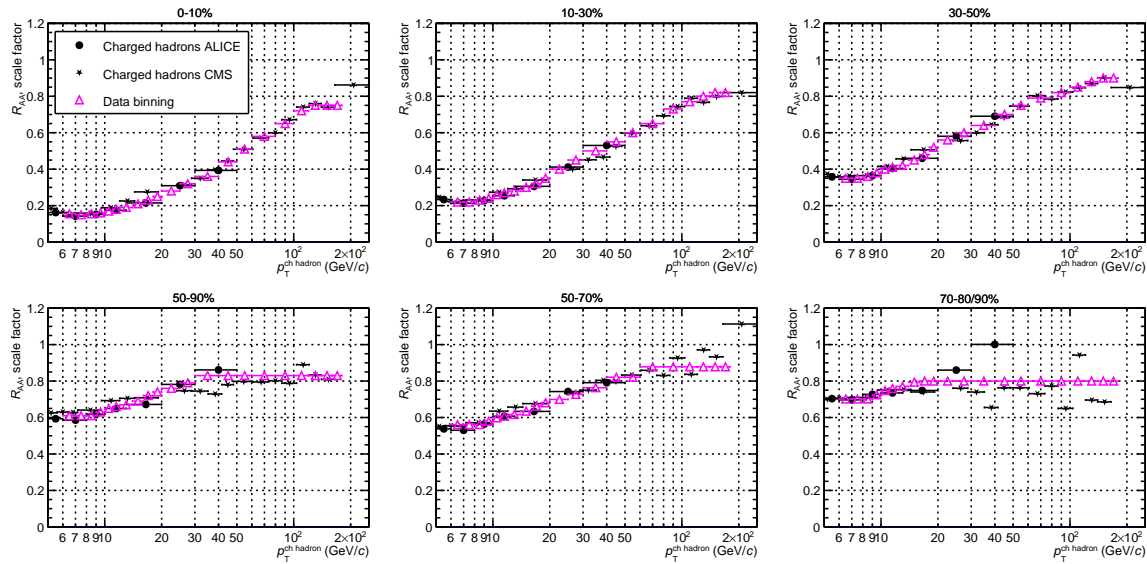


Figure 6.4: The R_{AA} distributions for charge hadrons by ALICE (full black circle), by CMS (full black star) and R_{AA} weights (empty pink triangle) as a function of $p_T^{\text{ch, hadron}}$ from central to peripheral Pb–Pb collisions (clock-wise) by ALICE [65] and CMS [152] at $\sqrt{s_{\text{NN}}} = 5.02$ TeV.

The propagation of the particles produced by an event generator through the active and passive material of ALICE is done by the GEANT3 [128] program. The framework allows the implementation of so-called volumes with various material properties. The interactions of the produced particles with the material are simulated in steps along their trajectory using MC methods, where effects such as various energy loss mechanisms and pair creation are taken into account according to the corresponding theoretical models.

6.3 How an azimuthal correlation distribution can be defined?

The azimuthal correlation distributions, as already introduced in Chapters 1 and 2, can be constructed using a trigger object, in our case a narrow isolated cluster with a trigger momentum p_T^{trig} , and associated particles, that are selected to be tracks with a momentum between $0.5 < p_T^{\text{had}} < 100$ GeV/c emitted in the opposite direction of the trigger. In this analysis, various p_T^{trig} are investigated: the lower p_T^{trig} limits of the considered intervals are:

6.3. How an azimuthal correlation distribution can be defined?

18, 20, 25, 30, 35, 40 GeV/ c . In addition, different z_T (see Eq. (1.28)) ranges are considered and the lower limits of the z_T intervals in which the correlation distributions are estimated are: 0.10, 0.15, 0.20, 0.40, 0.60, 0.80, 1.00.

The azimuthal correlation distribution can be written as:

$$\frac{d^2N(\Delta\eta\Delta\varphi)}{d\Delta\eta|d\varphi|} = \frac{1}{N^{\text{trig}}} \frac{dN^{\text{hadr}}}{d\Delta\eta\Delta\varphi} \quad (6.1)$$

where $\Delta\eta = \eta^\gamma - \eta^{\text{hadron}}$, $\Delta\varphi = \varphi^\gamma - \varphi^{\text{hadron}}$, N^{trig} is the number of trigger particles, in our case isolated narrow or wide clusters, and N^{hadr} is the number of associated hadrons.

The side with the trigger is defined as the **near side**, centred in $\Delta\varphi = 0$ rad, while the side containing the correlated objects, is the **away side**, centred in $\Delta\varphi = \pi$ rad. There is no selection in $\Delta\eta$ and all the **TPC** pseudorapidity coverage of $|\eta^{\text{track}}| < 0.9$ is considered for a selected trigger cluster pseudorapidity coverage of $|\eta^{\text{cluster}}| < 0.67$. As the trigger object is isolated, no correlation peak is expected to be in the **near side**, but only a back-to-back peak around $\Delta\varphi = \pi$ rad should be found.

The analysis strategy consists of three main steps, which are shown in Fig. 6.5, and they will be discussed in detail in the next Sections.

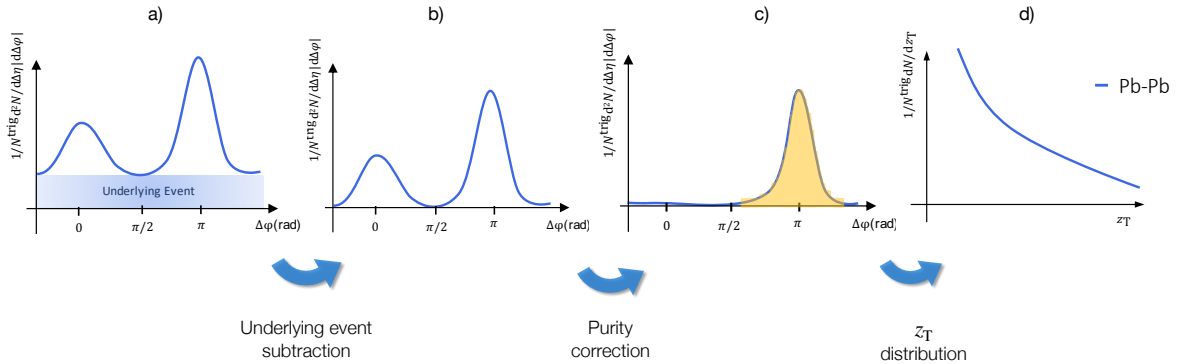


Figure 6.5: Sketch of the three main steps of the analysis.

First of all, the raw azimuthal correlation distributions need to be corrected for the combinatorial background, due to the large **UE** of the collision from low p_T tracks. The **UE** generates a sort of pedestal, as sketched in Fig. 6.5–left (a) and it must be subtracted. Secondly, the angular correlation distributions of isolated photons with hadrons should ideally exhibit only an **away-side** peak due to the photon isolation. However, the presence of residual background in our sample of isolated photon candidates, such as π^0 decays, introduces correlations that result in a small leftover **near-side** peak. This leftover can be removed by applying the purity correction using the correlation of a background triggered sample (isolated wide clusters), as shown in Fig. 6.5–middle (b-c). Afterwards, the correlation distributions are integrated over $2/3\pi$, namely the **away side** peak for each z_T interval, and the $D(z_T)$ distributions (see Eq. (1.27)) can be obtained. This step corresponds to Fig. 6.5–right (c-d).

In the next Sections, every step of this methodology will be discussed in detail. The azimuthal correlation distributions will be displayed with the $\Delta\varphi$ range along the x -axis

between 0 and π rad, differently to what is sketched in Fig. 6.5. The mirroring around $\Delta\varphi = \pi$ has been done to reduce the statistical uncertainties.

6.3.1 Underlying event subtraction

In high-energy pp, p–Pb and Pb–Pb collisions, there are other lower energy processes produced together with the hard process, that generate a particle combinatorial background to the azimuthal correlation distribution. This phenomenon is represented schematically in Fig. 6.5–left (a) and is known as the collision underlying event. This uncorrelated background is composed of all the soft particles not associated with the hard scattering of the collision. It is almost uniform in $\Delta\varphi$ because there is uniformity between the reaction plane angle and the angle of the hard process, but not necessarily flat. It can be affected by the presence of the flow v_n and detector inefficiencies. Two possible methods allow us to estimate the amount of UE to be subtracted before the number of particles correlated with the trigger particle can be estimated.

The ZYAM (Zero Yield At Minimum) [153] method relies on the assumption that the amount of UE is flat in $\Delta\varphi$. The UE is extracted by fitting or by making an integral of a $\Delta\varphi$ region where the hard process is not expected to contribute, for example $[1, \pi/2]$ rad and this value is subtracted bin by bin. This method is typically used in pp and p–Pb [110]. However, the flatness assumption may not be true.

The other method is the mixed event technique, which can describe the potential variation of UE as a function of $\Delta\varphi$. The mixed event (**mixed event ME**) is an artificial dataset created combining our trigger particle (such as a candidate single photon) from a given collision, and tracks from a different **MB** triggered collisions, but with the same global properties as the event to which the trigger particle belongs (**same event SE**). A pool of events from **MB** triggers is filled, depending on different values of the vertex position along z axis (z_{vtx}), centrality and event plane angle φ_{EP} (see Fig. 1.18). To fill the mixed event pool: nine intervals of 10% of centrality are considered between 0 and 90%; the φ_{EP} can vary between 0 and π with a step of $\pi/4$; the z_{vtx} vertex is between +10 cm and -10 cm in intervals of 2 cm. In addition, there is a maximum number of mixed events used to fill the pool, which is based on the number of events in data per centrality range: 50 events for 0-10%; 100 for 10-30%; 500 for 30-50% and 1000 for 50-90%. In central collisions, the number of triggers is larger than in peripheral collisions, hence less events are necessary to fill the pool in central collisions than in peripheral ones. By construction, in the mixed event, there is no correlation between the chosen trigger and the other particles, therefore the distributions obtained can reproduce the UE component.

In this Thesis, the mixed event technique is used; the reason for this choice is that it is based on real data and it can reproduce the status of the detector at the corresponding data-taking moment, additionally, it is not only flat.

The azimuthal correlation distribution is obtained by normalizing it to the number of triggers (N^{trig}). Four per-trigger types of correlations can be measured, defined from the purity parametric-space plot, shown in Fig. 5.16. We consider in this analysis two triggers: isolated narrow clusters $N_{\text{narrow}}^{\text{iso}}$ (signal plus background sample) and isolated wide clusters $N_{\text{wide}}^{\text{iso}}$ (background sample). The number of triggers is measured from the p_T^{trig} distributions

6.3. How an azimuthal correlation distribution can be defined?

for every cluster class for the same event, that is the real events, and the mixed event pools. Figure 6.6 reports the number of candidate isolated narrow and wide triggers as a function of p_T^{trig} . For a given p_T^{trig} interval the number of triggers isolated narrow clusters or wide can be extracted.

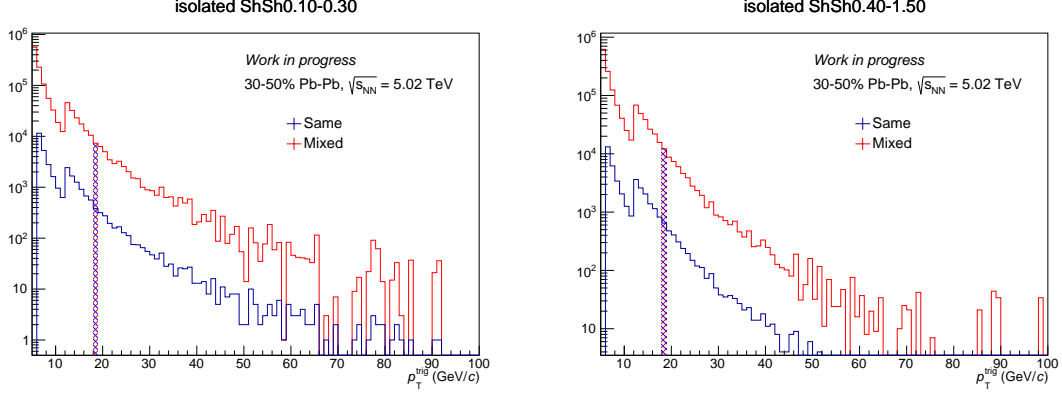


Figure 6.6: p_T^{trig} distribution for the same event (blue) and mixed event (red) in 30-50% Pb–Pb collisions. Left: distributions for isolated narrow clusters. Right: distributions for isolated wide clusters. As an example one p_T^{trig} bin has been coloured, corresponding to a certain number of triggers at that transverse momentum.

The p_T^{trig} distributions for the same event and the mixed event for both cluster classes show an exponential trend, decreasing as the p_T^{trig} augments. The evolution is the same by construction because the same trigger is reused a certain number of times for the mixed event. The sharp enhancement at 12 GeV/ c is due to the hard transition imposed at the analysis level from clusters purely from **MB** events and clusters from **MB** and **EMCal L1- γ** events. The normalisation per number of triggers is shown in Eq. (6.1) and is given by the integral of the trigger momentum distribution in a specific p_T^{trig} interval.

Once the same event and the mixed event $\Delta\varphi$ distributions are normalised to the corresponding number of triggers, $N_{\text{SE}}^{\text{trig}}$ and $N_{\text{ME}}^{\text{trig}}$, it is possible to subtract the **UE** according to this equation:

$$\frac{1}{N^{\text{trig}}} \frac{d^2 N(\Delta\eta\Delta\varphi)}{d\Delta\eta d\Delta\varphi} = \frac{1}{N_{\text{SE}}^{\text{trig}}} \frac{d^2 N_{\text{SE}}(\Delta\eta\Delta\varphi)}{d\Delta\eta d\Delta\varphi} - \frac{1}{N_{\text{ME}}^{\text{trig}}} \frac{d^2 N_{\text{ME}}(\Delta\eta\Delta\varphi)}{d\Delta\eta d\Delta\varphi}. \quad (6.2)$$

Figures 6.7 and 6.8 report the azimuthal correlation distributions for isolated narrow and wide clusters, respectively, for a p_T^{trig} between 20 and 25 GeV/ c in 30-50% Pb–Pb collisions for the same and the mixed events and after the subtraction of Eq. (6.2).

The mixed event azimuthal correlation distribution is quite flat and does not present a correlation peak. It is close to the same event distribution in the region $1 < \Delta\varphi < \pi/2$ rad. The same event $\Delta\varphi$ distributions for isolated narrow and wide clusters show a correlation peak, that seems visible for all of the z_T intervals around $\Delta\varphi \sim \pi$ and which is less visible at lower z_T due to the large **UE**. In addition, a residual peak seems to appear around $\Delta\varphi \simeq 0$ rad, this is a consequence of the fact that our sample of isolated candidate photons is still affected by a residual background that originates these correlations.

If the mixed event describes the underlying event, once it is subtracted, the uncorrelated background of the same event distribution in the region $1 < \Delta\varphi < \pi/2$ rad has to be com-

AZIMUTHAL CORRELATION DISTRIBUTIONS OF ISOLATED PHOTONS WITH HADRONS IN Pb-Pb COLLISIONS

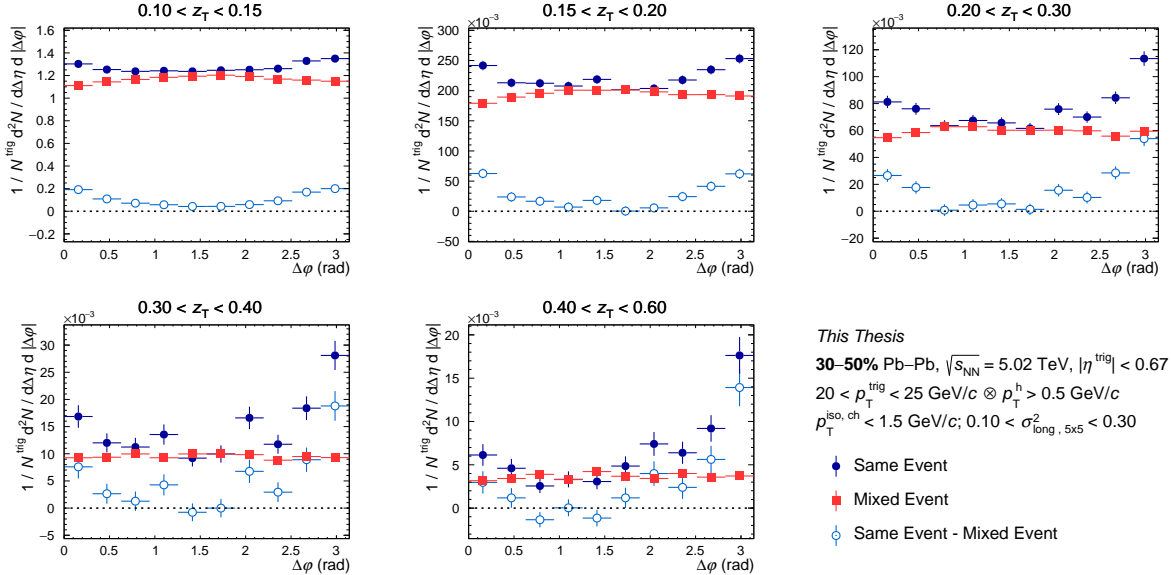


Figure 6.7: Azimuthal correlation distributions in **30–50%** for isolated **narrow** clusters for the same event (full blue circle), for the mixed event (full red square) and the result of the subtraction (empty light blue circle) as a function of $\Delta\varphi$ for different z_T bins with $20 < p_T^{\text{trig}} < 25$ GeV/c.

patible with zero and the pedestal should not be present anymore. The **UE** is expected to be independent of the type of clusters because the mixed event is built from the same set of **MB** events. This can be observed by comparing the **UE** distributions in Fig. 6.7 and 6.8, the mixed event for narrow and wide distribution is of the same order of magnitude.

Figures 6.9 and 6.10 show the azimuthal correlation distribution for isolated narrow clusters in central and in peripheral Pb–Pb collisions.

In central collisions, it is difficult to appreciate the correlation peak in particular at very low z_T : the **UE** covers almost all the signal. On the other hand, in peripheral collisions, the away side peak is visible and arises on top of the **UE** in all the z_T intervals. This is due to the lower quantity of uncorrelated background in 50–90% collisions than in 0–10% ones. The trend among centralities can be better appreciated in Fig. 6.11, which reports the azimuthal distributions for two z_T intervals in central, semi-central and peripheral collisions. For all centralities, it is possible to appreciate a marginal near side peak in all the z_T bins. It is important to note that, for isolated narrow clusters, no near side correlation is expected.

The other distributions obtained for different p_T^{trig} bins and for wide clusters are collected in Appendix C for all centralities.

6.3. How an azimuthal correlation distribution can be defined?

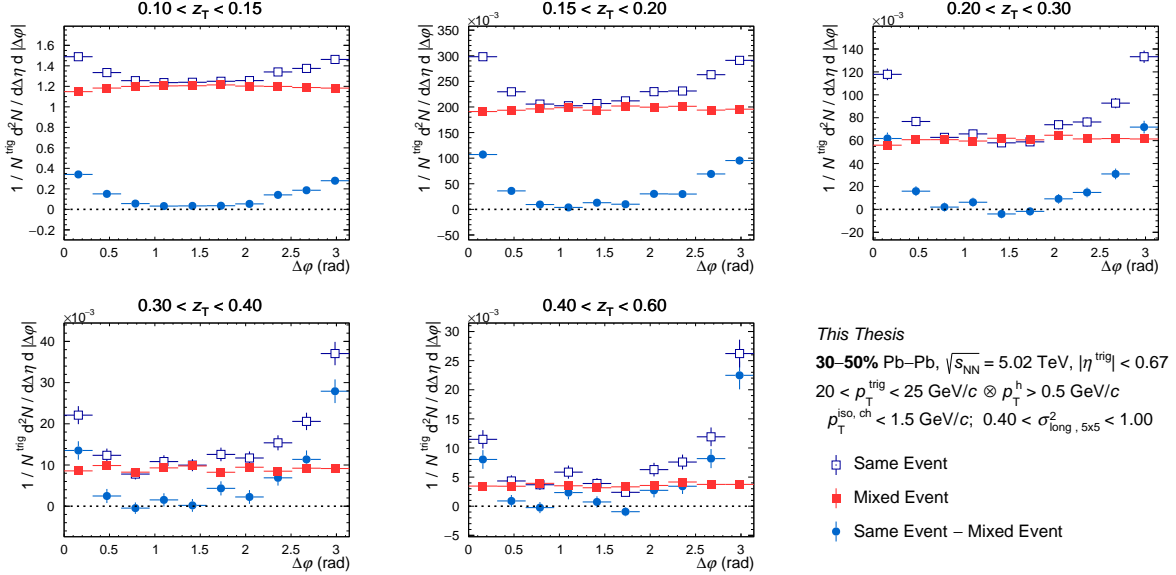


Figure 6.8: Azimuthal correlation distributions in **30–50%** for isolated **wide** cluster for the same event (empty blue square), for the mixed event (full red square) and the result of the subtraction (full light blue circle) as a function of $\Delta\varphi$ for different z_T bins with $20 < p_T^{\text{trig}} < 25$ GeV/c.

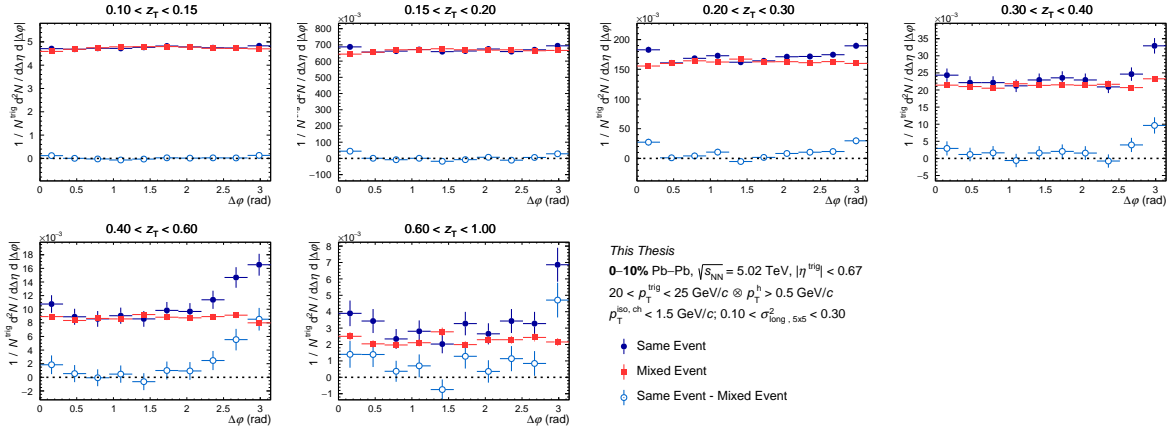


Figure 6.9: Azimuthal correlation distributions in **0–10%** for isolated **narrow** clusters for the same event (full blue circle), for the mixed event (full red square) and the result of the subtraction (empty light blue circle) as a function of $\Delta\varphi$ for different z_T bins with $20 < p_T^{\text{trig}} < 25$ GeV/c.

AZIMUTHAL CORRELATION DISTRIBUTIONS OF ISOLATED PHOTONS WITH HADRONS IN Pb–Pb COLLISIONS

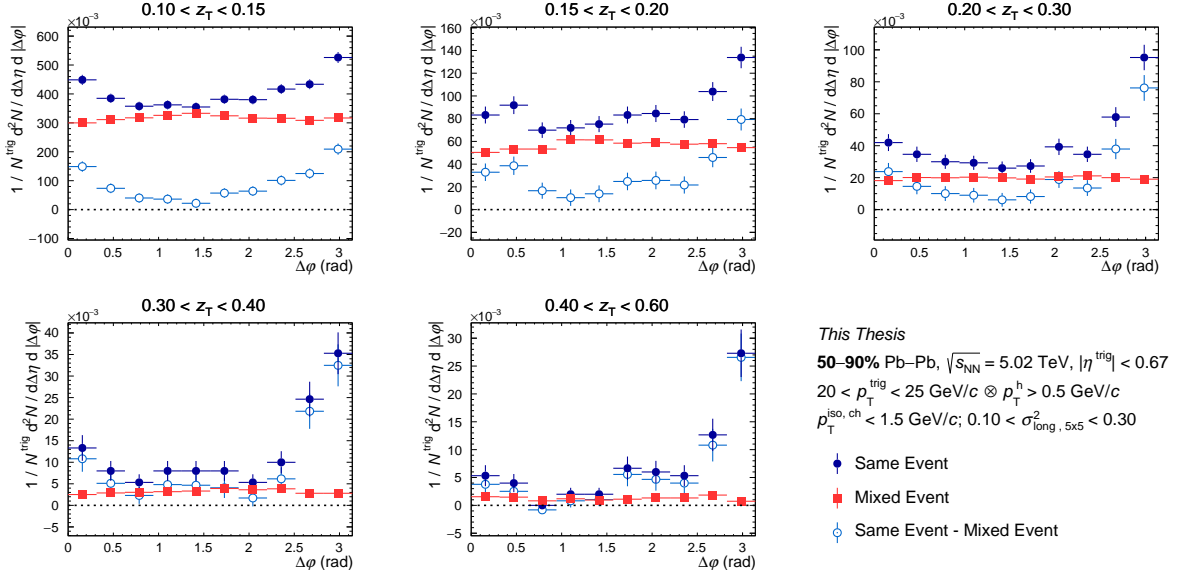


Figure 6.10: Azimuthal correlation distributions in **50–90%** for isolated **narrow** clusters for the same event (full blue circle), for mixed event (full red square) and the result of the subtraction (empty light blue circle) as a function of $\Delta\varphi$ for different z_T bins with $20 < p_T^{trig} < 25$ GeV/c.

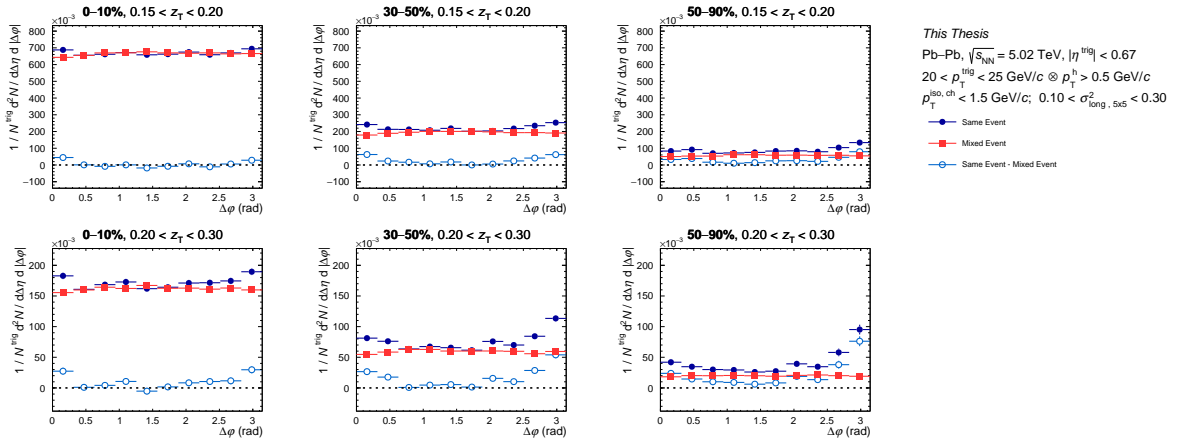


Figure 6.11: Azimuthal correlation distributions for isolated **narrow** clusters for the same event (full blue circle), for mixed event (full red square) and the result of the subtraction (empty light blue circle) as a function of $\Delta\varphi$ for two z_T intervals with $20 < p_T^{trig} < 25$ GeV/c. Comparing three centralities: **0–10%** (left), **30–50%** (middle) and **50–90%** (right) Pb–Pb collisions.

6.3.2 Purity Correction

After the subtraction of the UE, one must remove the background contamination in the isolated photon candidates sample, visible in the residual correlation in the near side peak of the isolated narrow cluster $\Delta\varphi$ distribution (see, for example, Fig. 6.7). Since γ_{decay} from π^0 represent by far the largest fraction of this contamination, as can be appreciated in Fig. 5.9 in Chapter 5, and assuming that such γ_{decay} clusters with narrow or wide shape have the same azimuthal correlation distribution, one can subtract the remaining background from the isolated narrow clusters–hadron correlation according to this equation:

$$\frac{1}{N^{\text{trig}}} \frac{dN(\Delta\varphi)}{d\Delta\varphi} \Big|_{\gamma^{\text{iso}}} = \frac{1}{P} \frac{1}{N^{\text{trig}}} \frac{dN(\Delta\varphi)}{d\Delta\varphi} \Big|_{\text{narrow}}^{\text{isolated}} - \frac{(1-P)}{P} \cdot \frac{1}{N^{\text{trig}}} \frac{dN(\Delta\varphi)}{d\Delta\varphi} \Big|_{\text{wide}}^{\text{isolated}} \quad (6.3)$$

where P is the purity, obtained in Sect 5.4 (the purity fit function of Fig. 5.18 for $R = 0.2$ and the point uncertainties are used here).

The assumption of using the isolated wide cluster as background relies on pure relativistic kinematic: the higher the energy, the more boosted the π^0 , as a consequence the decay photons are nearly always emitted merged and so they look like a narrow cluster, and those single decays that are not merged are paired with a very low energy photon and thus, a single photon carries almost all the meson energy. At such high p_T^{trig} , background clusters, narrow and wide, are mostly those containing two photons from the meson decay; the few single photon clusters, that remain appearing as narrow, have their photon decay partner with very low energy. Multiplying the isolated wide cluster azimuthal distributions by $1 - P$ permits to estimate of the background of the isolated narrow cluster sample. The results of this procedure are shown in Fig. 6.12 for semi-central Pb–Pb collisions.

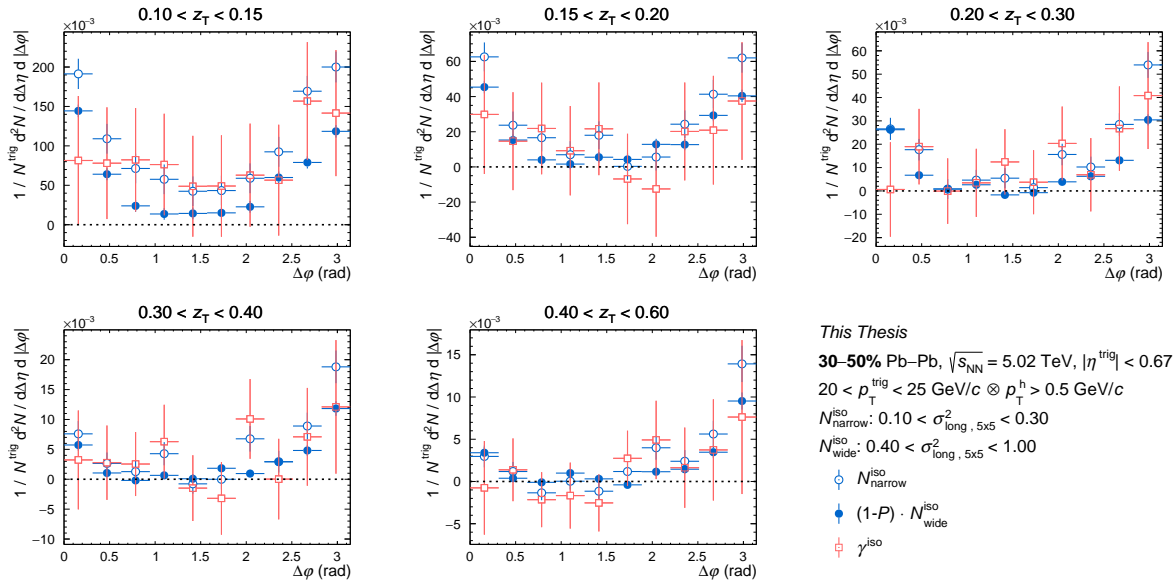


Figure 6.12: Azimuthal correlation distributions in **30-50%** for isolated narrow clusters (full light blue circle), for isolated wide clusters (empty light blue circle) and γ^{iso} (empty orange square) as a function of $\Delta\varphi$ for different z_T bins with $20 < p_T^{\text{trig}} < 25 \text{ GeV}/c$.

The γ^{iso} -hadron correlation distributions for 30-50% Pb–Pb collisions show a correlation peak for all the z_T ranges and the near side peak seems to have disappeared.

Figures 6.13 and 6.14 reports γ^{iso} -hadron correlation distribution for 0-10% and 50-90% Pb–Pb collisions.

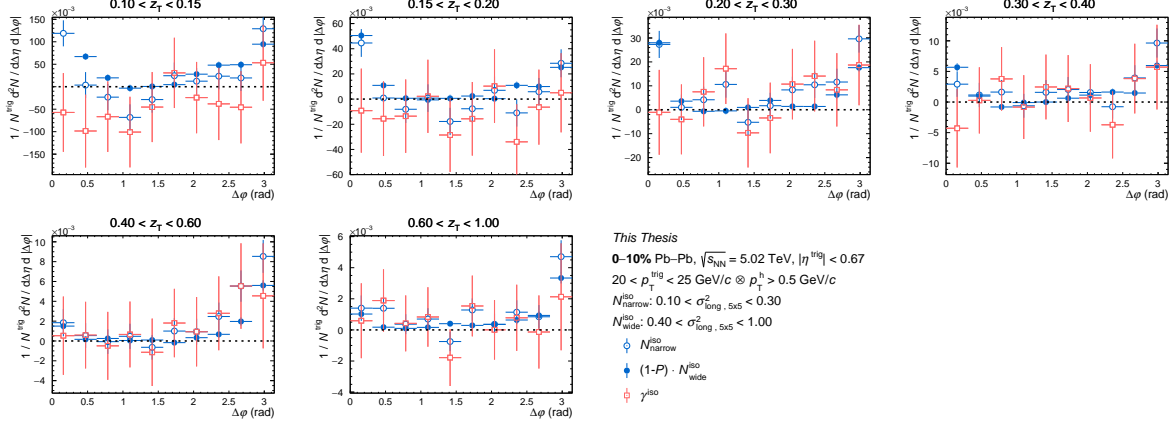


Figure 6.13: Azimuthal correlation distributions in **0-10%** for isolated narrow clusters (full light blue circle), for isolated wide clusters (empty light blue circle) and γ^{iso} (empty orange square) as a function of $\Delta\varphi$ for different z_T bins with $20 < p_T^{\text{trig}} < 25 \text{ GeV}/c$.

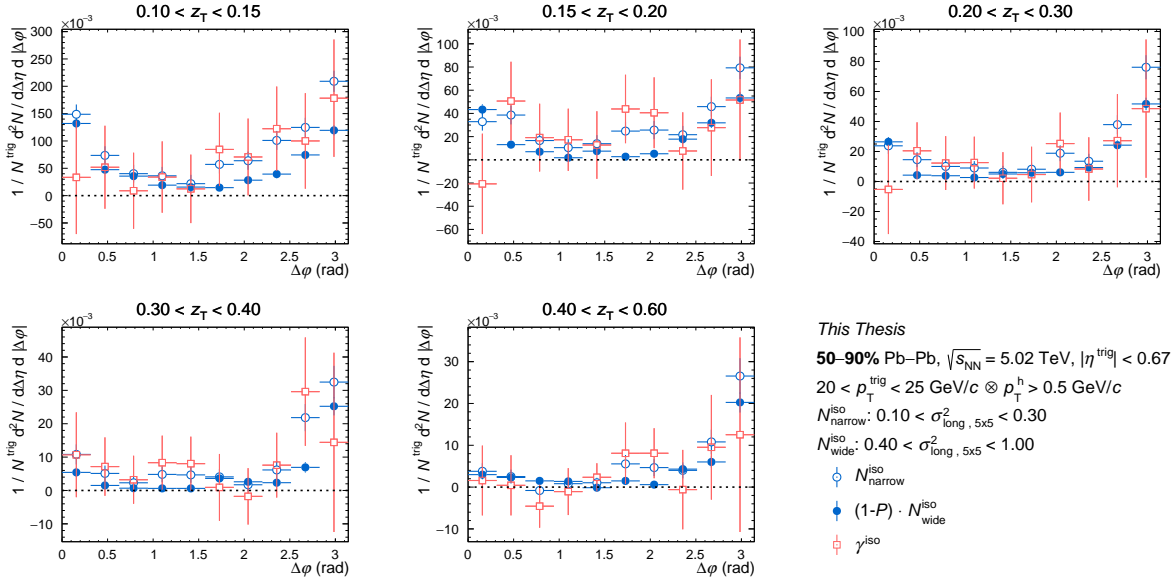


Figure 6.14: Azimuthal correlation distributions in **50-90%** for isolated narrow clusters (full light blue circle), for isolated wide clusters (empty light blue circle) and γ^{iso} (empty orange square) as a function of $\Delta\varphi$ for different z_T bins with $20 < p_T^{\text{trig}} < 25 \text{ GeV}/c$.

In central collisions, the correlation peak is almost always negative, but with large statistical uncertainties, for low z_T intervals, confirming that the statistics of the γ^{iso} photons is not sufficient to make them emerge from the UE and although the purity of the sample is larger than the other centralities, this is not enough to measure a γ^{iso} -hadron correlations. In peripheral collisions, the situation is different: the away side peak appears for low z_T bins, although the signal is pretty small.

6.3. How an azimuthal correlation distribution can be defined?

To conclude, the γ^{iso} -hadron azimuthal distributions obtained after the purity correction for all the centralities fluctuate strongly: this is due to the larger statistical error bars of the isolated narrow cluster with respect to the isolated wide cluster. In addition, the subtraction between two very close distributions increases the error bars. The results obtained for other p_T^{trig} intervals are reported in Appendix C.

The measured γ^{iso} constrains the parton kinematics, hence, the distribution of away side associated hadrons with momentum fraction z_T is the $D(z_T)$, which represents a proxy to the parton fragmentation function. We recall the formula for the $D(z_T)$:

$$D(z_T) = \frac{1}{N^{\text{trig}}} \frac{dN^{\text{hadr}}}{dz_T}. \quad (6.4)$$

To extract the $D(z_T)$ distributions, the away side peak ($3/5\pi < \Delta\varphi < \pi$ rad) of the γ^{iso} -hadron azimuthal correlations is integrated for every z_T range.

The $D(z_T)$ distributions for all centralities with a p_T^{trig} between 20 and 25 GeV/c are shown in Fig. 6.15.

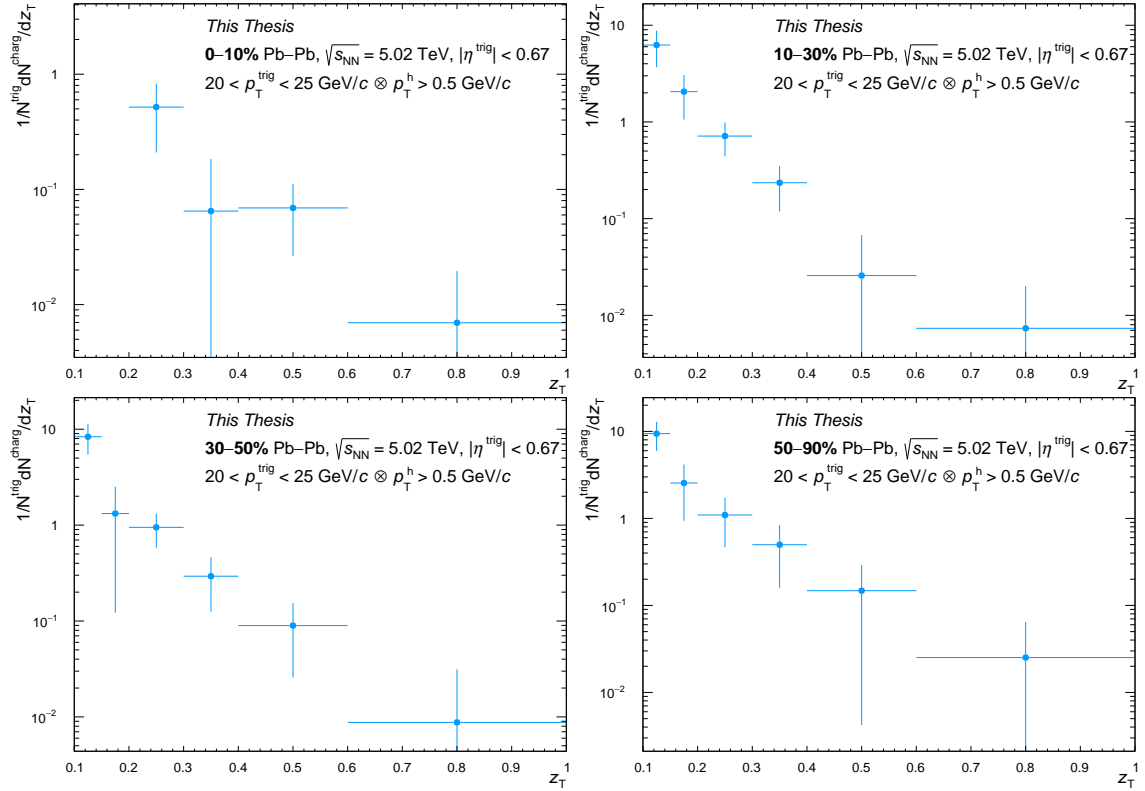


Figure 6.15: $D(z_T)$ distributions as a function of z_T for a p_T^{trig} between $20 < p_T^{\text{trig}} < 25$ GeV/c. From top to bottom, 0-10% Pb-Pb collisions, 10-30% Pb-Pb collisions, 30-50% Pb-Pb collisions and 50-90% Pb-Pb collisions.

The distributions decrease and are characterised by large statistical error bars. These results are dominated by the statistical limitation: the number of isolated photons is very low compared to other processes and, in particular, in central collisions, the signal is almost compatible with zero.

6.3.3 Correction of the track momentum resolution

The γ^{iso} -hadron correlation distributions should also be corrected from experimental effects such as the track energy resolution and the reconstruction efficiency. To do that, we use **GJ MC** simulations (see Sect. 6.2) distinguishing between γ -jet at the generator level and the reconstructed level. The **GJ MC** at the generated level corresponds to a production in vacuum. The simulated **GJ** events are affected by the presence of a small quantity of **UE**, which is removed using the **ZYAM** method (see Sect. 6.3.1).

Figure 6.16 shows the azimuthal correlation distributions for **GJ MC** generated with and without the **UE** once the **ZYAM** method has been applied. The away side peak can be identified and it is caused by the jet recoil from the γ^{iso} ; no near side peak is observed, as expected. The **UE** decreases from low to high z_T .

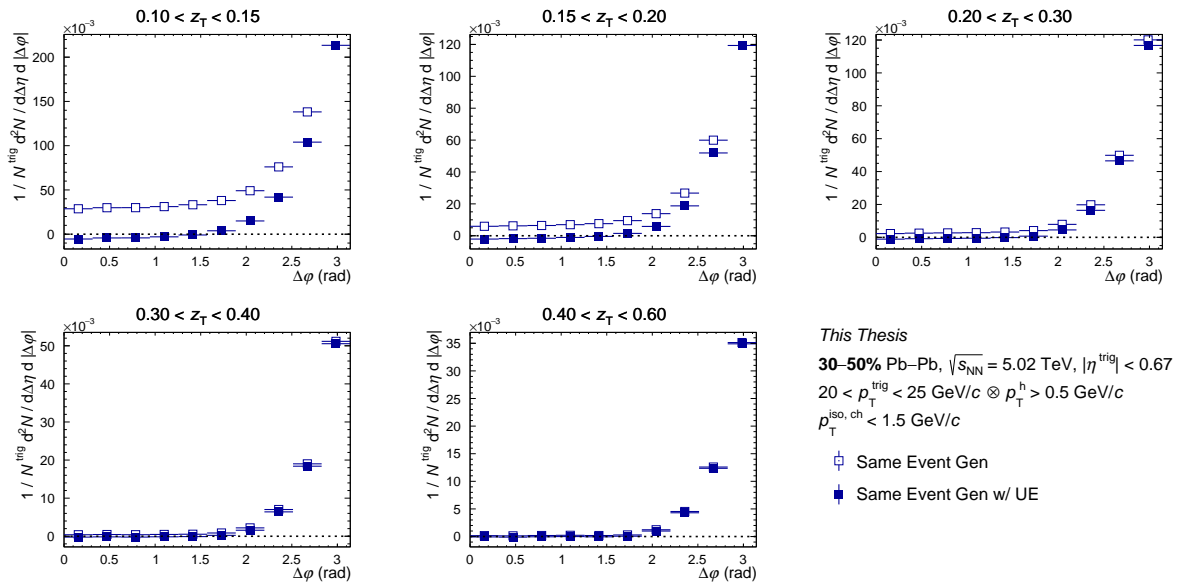


Figure 6.16: Azimuthal correlation distribution for PYTHIA 8 pp generator level before (empty blue square) and after the subtraction of the **UE** (full blue square) as a function of $\Delta\varphi$ for different z_T bins with $20 < p_T^{\text{trig}} < 25 \text{ GeV}/c$.

The **MC** reconstructed is affected by a quantity of **UE**, due to the embedding with **MB** data; as in the data, this combinatorial background is subtracted using the mixed event technique (see Sect. 6.3.1). Figure 6.17 illustrates the azimuthal correlation distributions at the reconstructed level for **GJ** simulation embedded in 30–50% Pb–Pb collisions. Again, a clear away side peak can be recognised. It survives after the **UE** subtraction. In the embedded simulation, the effect of the **UE** is significantly larger than at the pp collisions generated level, especially at low z_T . By construction, the azimuthal distributions from **GJ MC** simulations in pp collisions and embedded in Pb–Pb **MB** events do not display a near side peak.

By integrating the away side peak of the azimuthal distributions generated and reconstructed from the **MC** simulations for each z_T bin, we can extract the $D(z_T)$ distributions. They are displayed as a function of z_T in Fig. 6.18 for all centrality classes. The $D(z_T)$ dis-

6.3. How an azimuthal correlation distribution can be defined?

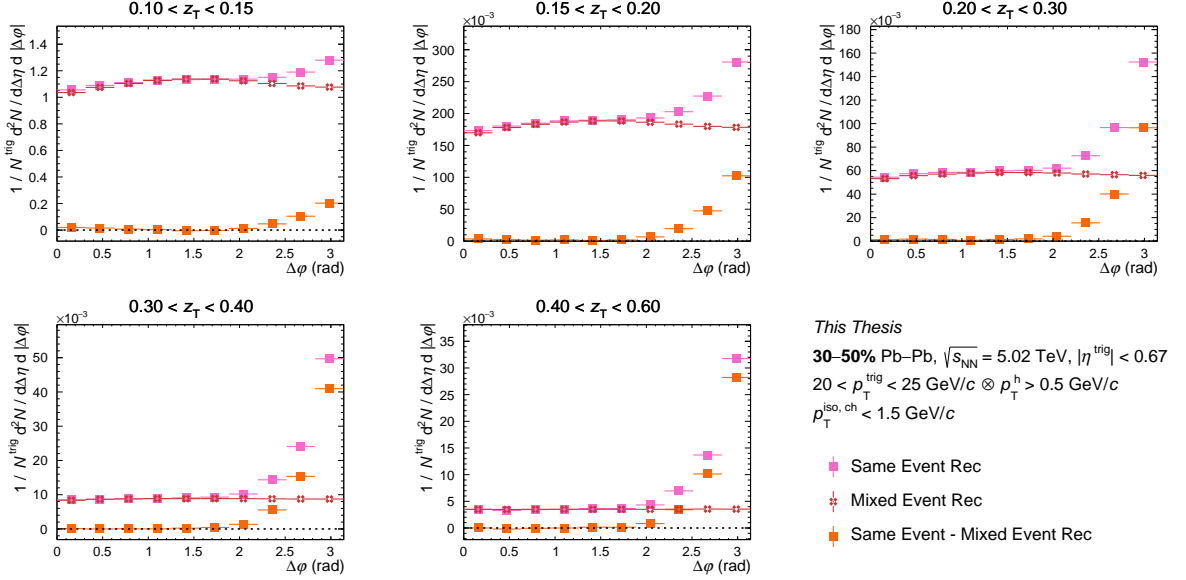


Figure 6.17: Azimuthal correlation distribution 30-50% Pb–Pb collisions for pp PYTHIA 8 γ -jet events embedded into MB data of the Same Event (full pink square), of the Mixed Event (red cross) and of the Same Event without UE (full orange square) as a function of $\Delta\varphi$ for different z_T bins with $20 < p_T^{\text{trig}} < 25$ GeV/c .

tribution for the GJ MC at the generator level is the same in every panel. The reconstructed $D(z_T)$ distributions have the same trend as the generated ones, but they are different for the various centralities, due to the embedding in MB Pb–Pb events. In central collisions (0-10% and 10-30%), the $D(z_T)$ distributions are more separated from the corresponding generated distributions. In semi-central and peripheral collisions, the $D(z_T)$ distributions are closer to the pp generated ones.

To take into account the detector effects, such as detector inefficiencies and the error on the reconstruction of p_T^γ and p_T^{hadr} , the α_{corr} is calculated. It is defined as the ratio of the $D(z_T)$ MC distributions at the generated level over the reconstructed one:

$$\alpha_{\text{corr}} = \frac{f(z_T^{\text{Gen}})}{f(z_T^{\text{Rec}})}. \quad (6.5)$$

Figures 6.18-bottom panels show the correction factor for all centralities for a p_T^{trig} between 20 and 25 GeV/c .

The α_{corr} is almost constant for all the centralities starting from $z_T \sim 0.15$. α_{corr} in the first z_T bin in 0-10% is unexpectedly high, because of the atypical value of $D(z_T)$ distribution at the reconstructed level in the first z_T bin. The correction factor accounts for both geometrical acceptance, detector inefficiencies, and dead channels.

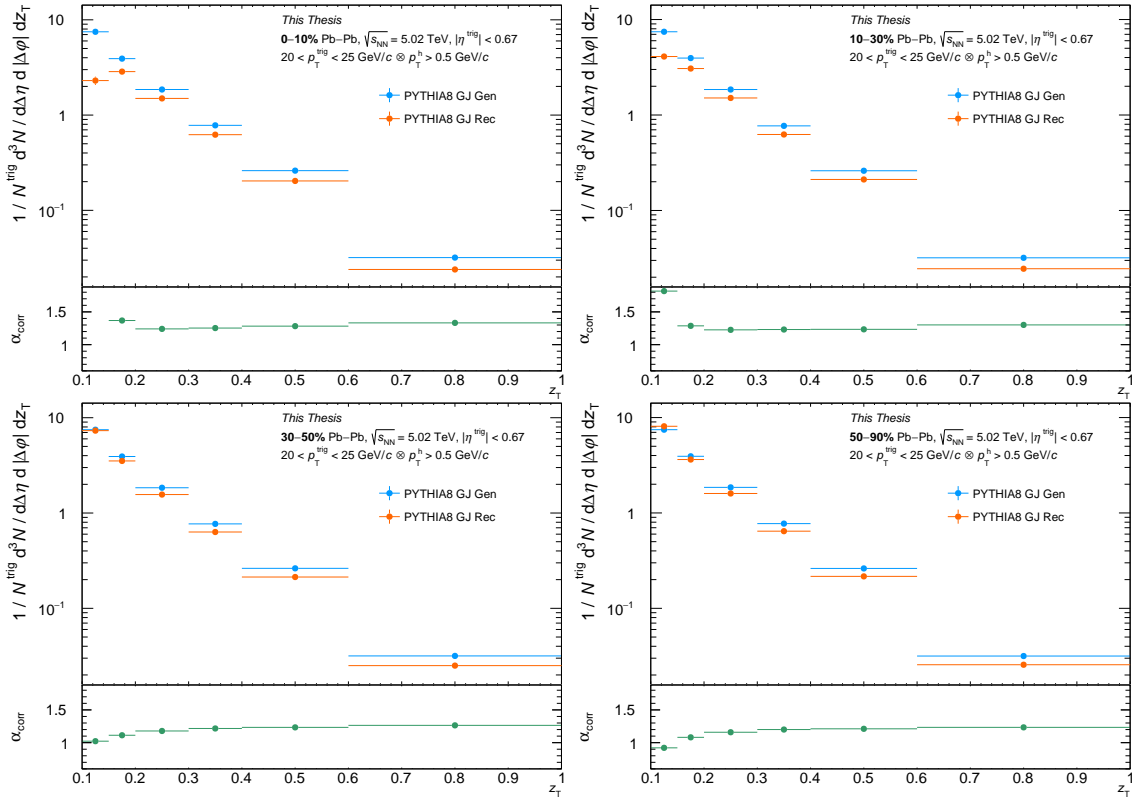


Figure 6.18: Top panels: the $D(z_T)$ distributions as a function of z_T for GJ MC simulation at generated (full light blue square) and reconstructed (full orange square) levels with $20 < p_T^{\gamma} < 25 \text{ GeV}/c$. Bottom panels: the α_{corr} factor (full green square) as a function of z_T . From top to bottom, 0-10% Pb–Pb collisions, 10-30% Pb–Pb collisions, 30-50% Pb–Pb collisions and 50-90% Pb–Pb collisions.

6.3.4 $D(z_T)$ distributions

The z_T distributions obtained in the Sect. 6.3.2 and reported in Fig. 6.15 are multiplied for the corresponding values of $\alpha_{\text{corr}}(z_T)$. Figure 6.19 illustrates the $D(z_T)$ distributions for all the centralities for a p_T^γ between $20 < p_T^{\text{trig}} < 25 \text{ GeV}/c$.

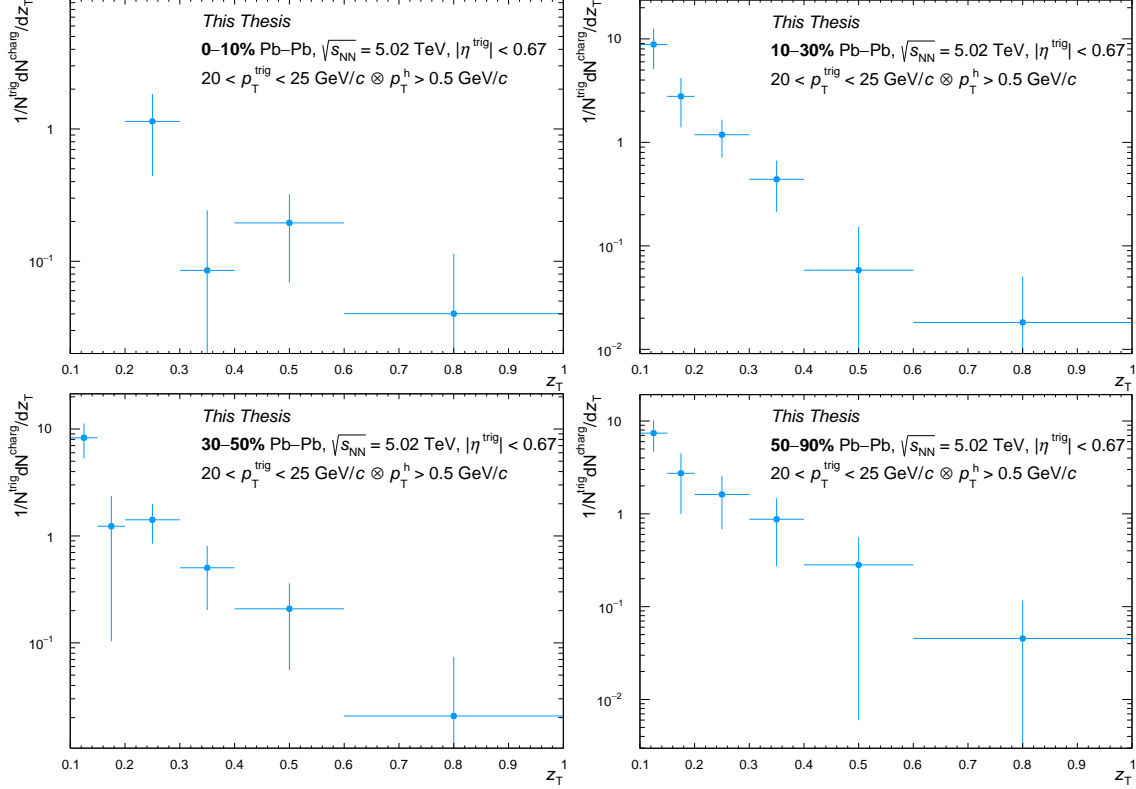


Figure 6.19: The $D(z_T)$ distributions as a function of z_T from γ^{iso} -hadron correlations for a p_T^γ between $20 < p_T^\gamma < 25 \text{ GeV}/c$. From top to bottom, 0-10% Pb-Pb collisions, 10-30% Pb-Pb collisions, 30-50% Pb-Pb collisions and 50-90% Pb-Pb collisions.

These results are dominated by statistical fluctuations, which represent the major difficulty of the analysis. To try to mitigate their impact, we have decided to combine the different p_T^γ ranges into a single, larger p_T^γ interval. The different p_T^γ bins have been merged using the formula:

$$D(z_T) = \frac{1}{\sum_i P_i N^{\text{trig},i}} \sum_i P_i N^{\text{trig},i} D(z_T)_i, \quad (6.6)$$

where $N^{\text{trig},i}$ is the number of isolated narrow cluster triggers in an i -th p_T^γ bin and P_i is the corresponding purity.

The weight of purity is necessary to obtain $N^{\gamma^{\text{iso}},i}$, which corresponds to $N^{\gamma^{\text{iso}},i} = P_i N^{\text{trig},i}$. The results obtained in the range p_T^γ between 18 and 40 GeV/c are shown in Fig. 6.20.

The results found in central collisions (0-10%) are not significant as they are; thus it was decided to combine the results in 0-10% with the ones in 10-30% in a larger bin: 0-30%. A weighted average on the number of triggers has been calculated from this formula:

$$\frac{N_{(0-10\%)}^{\text{trig}} f(\Delta\varphi_{(0-10\%)}) + N_{(10-30\%)}^{\text{trig}} f(\Delta\varphi_{(10-30\%)})}{N_{(0-10\%)}^{\text{trig}} + N_{(10-30\%)}^{\text{trig}}}, \quad (6.7)$$

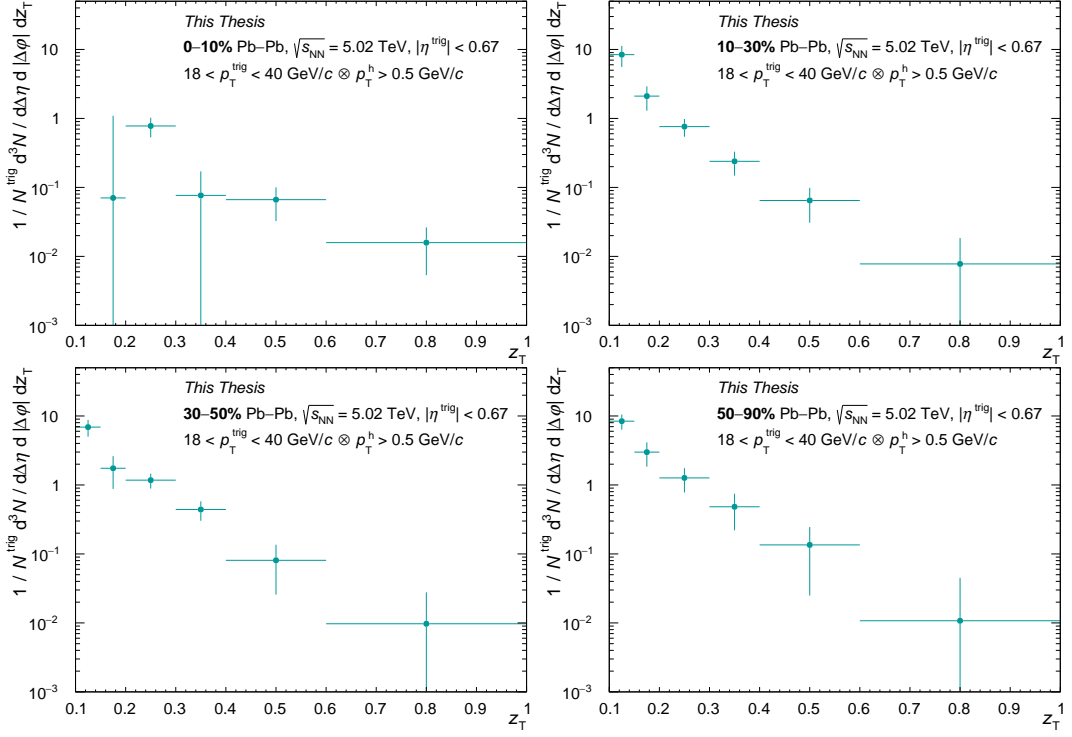


Figure 6.20: The $D(z_T)$ distributions as a function of z_T from γ^{iso} -hadron correlations for a p_T^γ between $18 < p_T^\gamma < 40$ GeV/c. From top to bottom, 0-10% Pb-Pb collisions, 10-30% Pb-Pb collisions, 30-50% Pb-Pb collisions and 50-90% Pb-Pb collisions.

where $f(\Delta\varphi_{(x-x\%)})$ corresponds to the azimuthal correlation distribution in a centrality interval. The combination has been done on the azimuthal distributions after the purity correction and on the MC $\Delta\varphi$ distributions. Figure 6.21 shows the z_T distribution for 0-30% Pb-Pb collisions, after the combination of different p_T^γ bins, as indicated in Eq.(6.6).

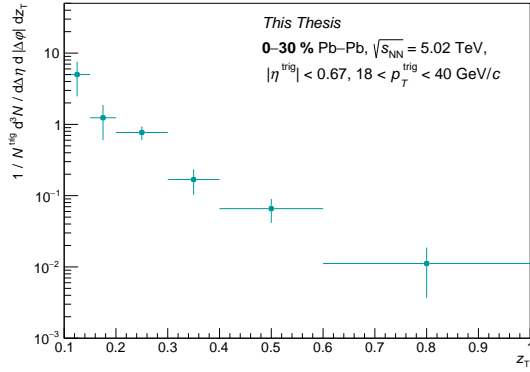


Figure 6.21: z_T distribution in 0-30% for the γ^{iso} -hadron correlation after merging the various $\Delta\varphi$ distributions in 0-10% and 10-30% Pb-Pb collisions for a p_T^γ in $18 < p_T^\gamma < 40$ GeV/c.

6.4 Systematics uncertainties

Before discussing the obtained results and comparing them with theoretical models, it is essential to identify the systematic effects present in the analysis. Therefore, the following variables have been evaluated to determine if they can introduce any systematic uncertainty:

- the mixed event and its estimation of UE;
- the purity;
- the $\sigma_{\text{long}, 5\times 5}^2$ background range variations;
- the tracks reconstruction efficiency;
- the number of centrality intervals used for filling the mixed event pool.

For most sources, the systematic effects have been estimated with a variation of the selection criteria.

In the next Sections, the various systematic uncertainties will be discussed together with the reasons to take them into account. The systematics are calculated considering relative variations (in %):

$$\Delta_i^{\text{rel}}(x) = \left| \frac{x_{\text{reference}} - x_i}{x_{\text{reference}}} \right| \quad \text{or} \quad \Delta_i^{\text{rel}}(x) = \frac{1}{2} \left| \frac{x_i^{\max} - x_i^{\min}}{x_{\text{reference}}} \right| \quad (6.8)$$

The relative uncertainty for every item listed above is evaluated and then used to calculate the total systematic uncertainty, given by the quadratic sum of the various uncertainties. When the selection criteria are changed up and down with respect to the reference (i.e. middle value), half of the relative variations are used.

6.4.1 Mixed event and UE estimation

To determine if the mixed event technique effectively removes the total UE affecting the correlations measurement or if there is a systematic effect, the compatibility with zero of the uncorrelated background region ($1 < \Delta\varphi < \pi/2$) has been tested. The azimuthal correlation distributions of the isolated narrow and wide clusters, after the subtraction of the UE, have been compared. A constant fit has been applied in the $\Delta\varphi$ range $1 < \Delta\varphi < \pi/2$ to assess the presence of any residual background. Figure 6.22 shows the azimuthal correlations distributions for isolated narrow and wide clusters for different z_T intervals with the corresponding fit to the uncorrelated background region for a p_T^{trig} between 20 and 25 GeV/ c in 30-50% Pb–Pb collisions.

The distributions of isolated wide clusters, largely from π^0 decays, seem to fluctuate less than those of isolated narrow clusters. This is because isolated wide clusters have larger statistics than isolated narrow correlations. On the other hand, some $\Delta\varphi$ bins of isolated narrow cluster distributions are characterized by very small statistical uncertainties. These small uncertainties are not reliable because, in those bins, the same event value is zero, and the uncertainty is driven by the small statistical uncertainty of the mixed event.

The results of the fits are not always compatible with zero. For example, the fit applied to isolated narrow clusters in the first z_T interval (0.10 to 0.15) yields a constant value of 0.05 with an error of 0.013. Within the 3σ uncertainty range, the uncorrelated background region

AZIMUTHAL CORRELATION DISTRIBUTIONS OF ISOLATED PHOTONS WITH HADRONS IN Pb–Pb COLLISIONS

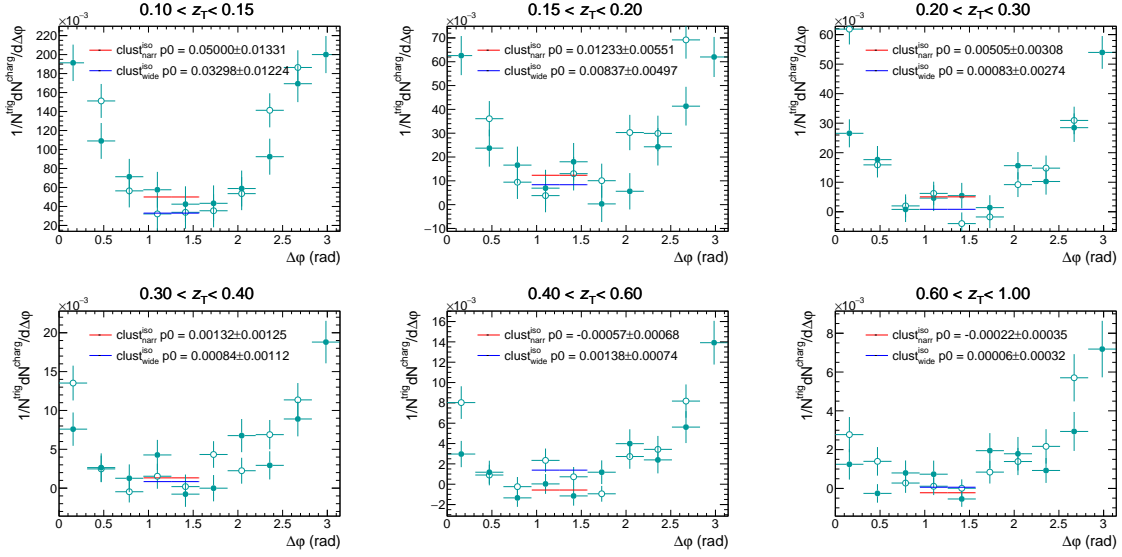


Figure 6.22: Azimuthal correlation distributions as a function of $\Delta\varphi$ for isolated narrow (full green circle) and for isolated wide (empty green circle) clusters after UE subtraction and corresponding constant fits (narrow: red; wide: blue) for different z_T intervals with $20 < p_T^{\text{trig}} < 25 \text{ GeV}/c$ in **30-50%** Pb–Pb collisions.

remains incompatible with zero, being at 0.011. For these reasons, the deviation from zero must be estimated for every z_T interval and accounted for as a systematic uncertainty of the mixed event. This systematic uncertainty is referred to as ε_{ME} .

The systematic uncertainty is given by the value of the constant fit C_{fit} in $1 < \Delta\varphi < \pi/2$ normalised by the integral of the away side peak:

$$\varepsilon_{\text{ME}} = \frac{B}{I} \quad (6.9)$$

where $I = \int N(\Delta\varphi)d\Delta\varphi$ is the integral of the away side, $B = \int C_{\text{fit}}d\Delta\varphi$ is the integral over $\Delta\varphi$ of the fit value. To estimate the uncertainty a few assumptions have been introduced:

- the fit value is the maximum residual UE not subtracted with the mixed event technique;
- the residual UE cannot be lower than zero.

With these considerations, B has to be divided by two and the uncertainty becomes:

$$\varepsilon_{\text{ME}} = \frac{B/2}{I - B/2} = \frac{B}{2I - B}. \quad (6.10)$$

Figures 6.23 show the uncertainty due to the mixed event as a function of z_T for p_T^{trig} between 18 and 40 GeV/ c for isolated narrow and wide clusters for all the centrality classes.

The systematic uncertainty is larger at low z_T and decreases at high z_T for both types of clusters and across almost all centralities. In 0-10% and 10-30% Pb–Pb collisions, where the UE is the largest, the systematic uncertainty is more significant. The trend for isolated wide clusters appears cleaner, and the uncertainty distribution fluctuates less. The limited

6.4. Systematics uncertainties

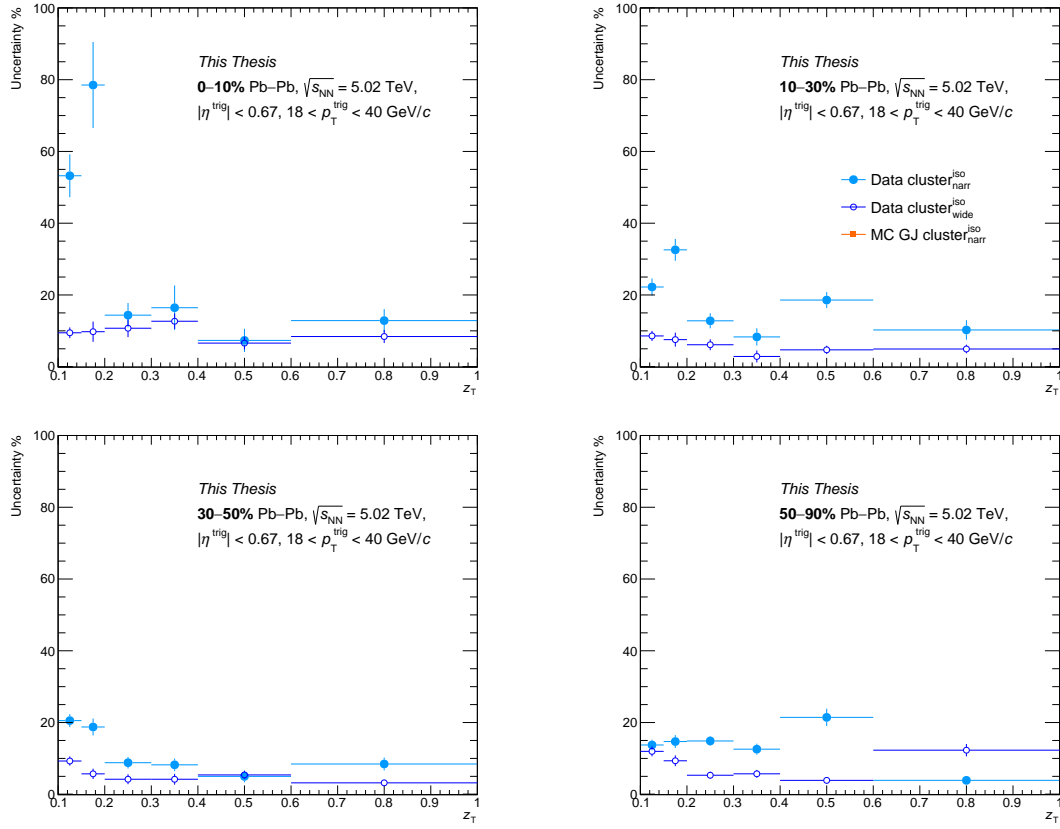


Figure 6.23: Systematic uncertainty of the mixed event for isolated narrow (full light blue circle) and wide (empty blue circle) clusters as a function of z_T . From top to bottom, 0-10% Pb-Pb collisions, 10-30% Pb-Pb collisions, 30-50% Pb-Pb collisions and 50-90% Pb-Pb collisions.

statistics of isolated narrow clusters result in more pronounced statistical fluctuations. In the first two z_T bins for 0-10%, the uncertainties are extremely large, and a similar effect is observed in 10-30%. These deviations in 0-10% are primarily driven by statistical limitations, especially when compared to isolated wide clusters. After combining 0-10% and 10-30%, this effect is a bit reduced, as reported in Fig. 6.24-left.

In order to smooth the trend in central collisions, a constant fit has been applied in the first two z_T intervals, to take into account the deviation towards large uncertainty values; while an exponential fit has been used above $z_T > 0.2$. Figure 6.24-right shows the uncertainty after the fit procedure. The systematic uncertainty of isolated narrow clusters in 30-50% and 50-90% Pb-Pb collisions are reported in Fig. 6.23-bottom. The corresponding points for isolated narrow clusters have been used as uncertainties.

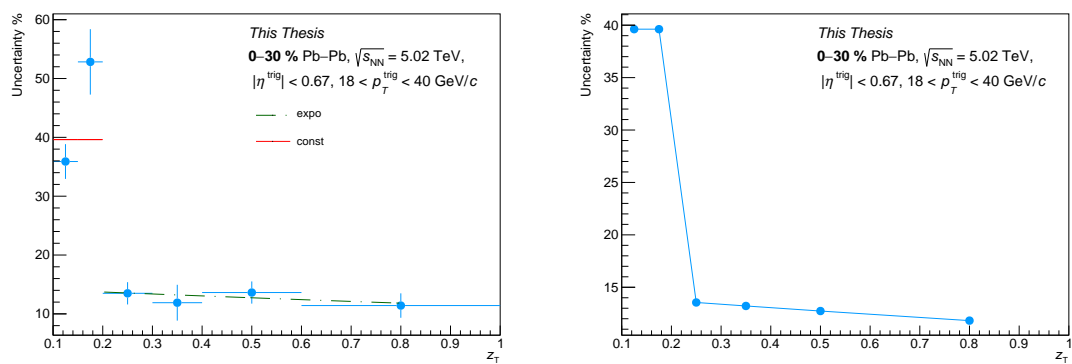


Figure 6.24: Systematic uncertainty of the mixed event for isolated narrow clusters (full light blue circle) as a function of z_T in 0–30% Pb–Pb collisions before smoothing the trend with fits (left) and after (right).

6.4.2 Purity

The purity used for the correlation measurement has been estimated with the ABCD method (see Sect. 6.3.2) in the isolated photon spectrum analysis at $\sqrt{s_{\text{NN}}} = 5.02 \text{ TeV}$ [93]. To take into account a possible variation of the purity on the z_T distribution, the error bars of the P are used. The uncertainty on the purity estimation depends on various sources: at low p_T^γ , it is driven by the systematic of the isolation probability, which estimates the uncertainty due to the correlations between the $p_T^{\text{iso}, \text{ch}}$ and $\sigma_{\text{long}, 5\times5}^2$ signal and background regions; at intermediate p_T^γ in central collisions by the signal over background scale, and at high p_T^γ , it is due to the statistics. The total uncertainty on the purity, in the range of interest for this analysis ($18 < p_T^\gamma < 40 \text{ GeV}/c$), is almost constant around $\sim 5\%$ ($\sim 10\%$) in central (peripheral) collisions. The uncertainty on the purity as a function of p_T^γ is reported in Fig. 6.25 for various centralities.

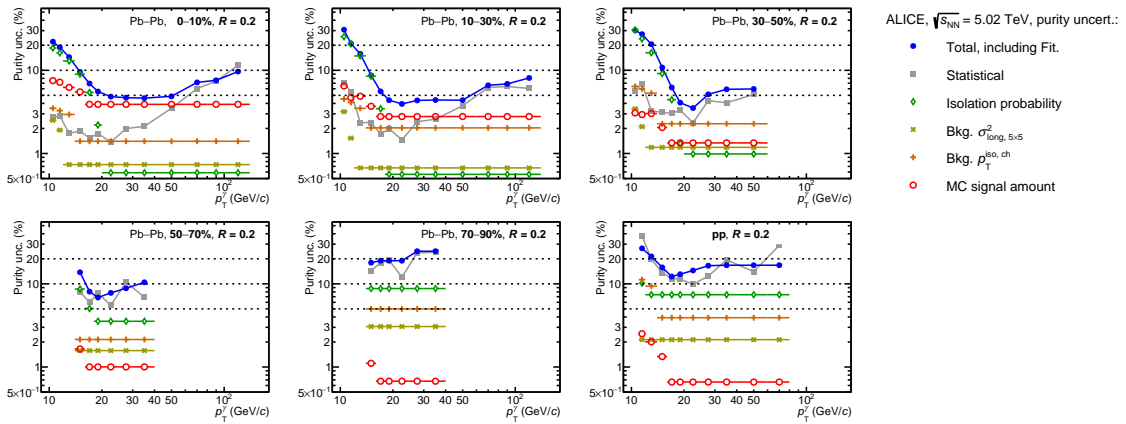


Figure 6.25: Isolated photon purity uncertainty components for $R = 0.2$ in pp and Pb–Pb collisions. Purity calculated with the ABCD method [93].

The total uncertainties are used to calculate the maximum and minimum values of purity available in the analysis. By adding and subtracting the corresponding uncertainty, the analysis is repeated using the extreme values of purity. This permits the estimation of the maximum variation that a deviation in purity can have on the $D(z_T)$ distributions. Figures 6.26 show the $D(z_T)$ distributions obtained with different purity values.

The z_T distributions obtained for the various centralities are shifted up for the highest purity and down for the lowest one: the systematic uncertainty is evaluated using Eq. (6.8)–left.

Figure 6.27–left reports the systematic uncertainties for all the centralities: in general there is an increase in the uncertainty at high z_T : this is because the statistic becomes significantly lower for z_T between 0.6 and 1.0 with large error bars on the $D(z_T)$ and this affects the estimation of the systematic error. The systematic error due to the purity, shown in Fig. 6.27–left, has been fitted with an exponential to smooth the trend. The result is reported Fig. 6.27–right. The systematic uncertainty is larger in central collisions at low z_T .

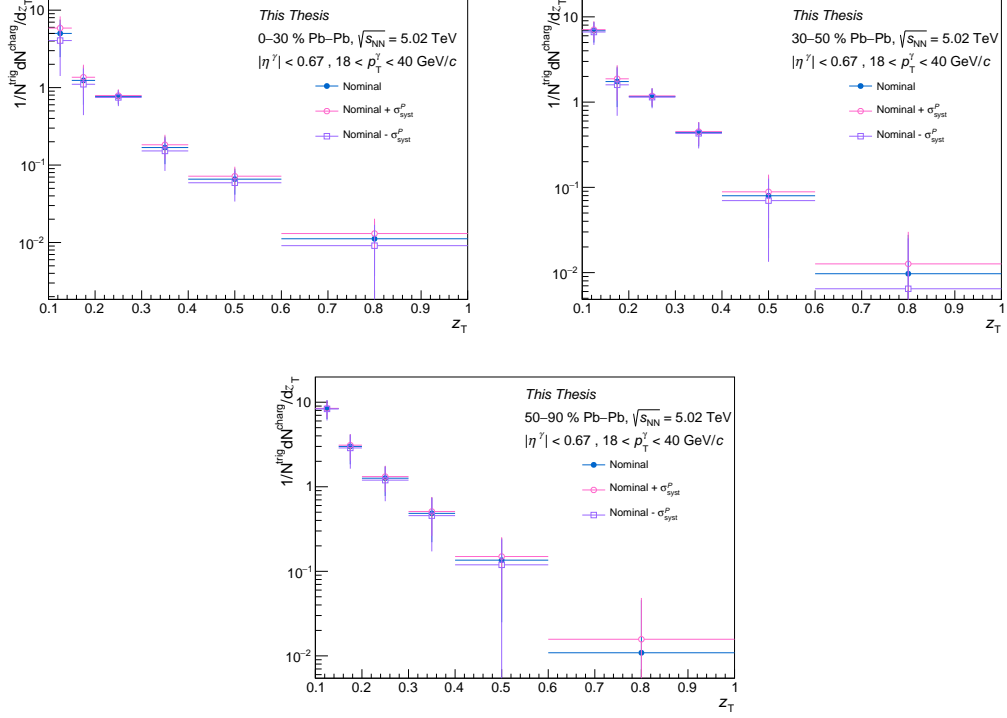


Figure 6.26: The $D(z_T)$ distributions for different purity values: nominal (full blue circle), nominal + σ_{syst}^P (empty pink circle) and nominal - σ_{syst}^P (empty violet square) in 0-30% (top left), in 30-50% (top right) and in 50-90% (bottom) Pb-Pb collisions.

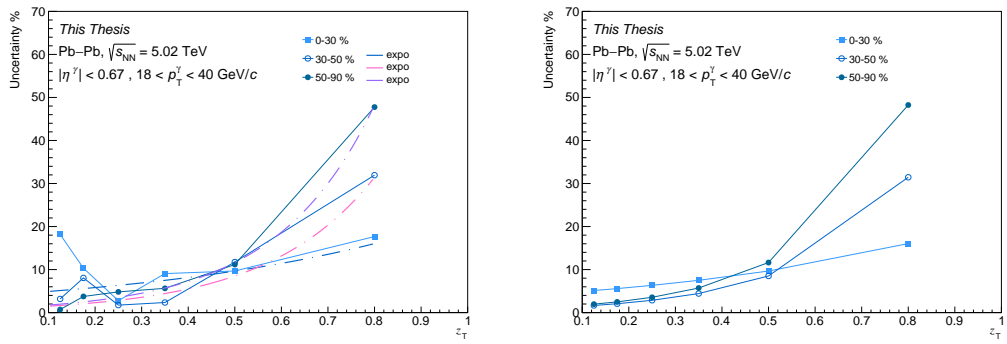


Figure 6.27: Left: Systematic uncertainties of the purity in 0-30% (full light blue square), 30-50% (empty blue circle) and 50-90% (full blue circle) Pb-Pb collisions. smoothing of the systematic uncertainties using an exponential fit in 0-30% (blue dot-dashed line), 30-50% (pink dot-dashed line) and 50-90% (violet dot-dashed line) Pb-Pb collisions. Right: Systematic uncertainties of the purity obtained from the fit.

6.4.3 Variation of the Shower Shape

The $\sigma_{\text{long}, 5\times5}^2$ background limits can be varied to determine if there is a systematic effect. Various combinations have been tested; some are standard and have been used in other **ALICE** correlation analyses [110, 149], while others are new. The different $\sigma_{\text{long}, 5\times5}^2$ selections that were taken into account are reported in the following list:

- $0.35 < \sigma_{\text{long}, 5\times5}^2 < 1.00$;
- $0.40 < \sigma_{\text{long}, 5\times5}^2 < 1.00$ (default);
- $0.40 < \sigma_{\text{long}, 5\times5}^2 < 1.50$ [110];
- $0.40 < \sigma_{\text{long}, 5\times5}^2 < 2.00$ [149];

The cluster shower shape distributions were introduced in Sect. 5.2 and reported in Fig. 5.8 as a function of the cluster p_{T} for various Pb–Pb centrality classes and pp collisions. The inclusive $\sigma_{\text{long}, 5\times5}^2$ distributions show that the π^0 band is mainly in the range $0.40 < \sigma_{\text{long}, 5\times5}^2 < 1.00$.

Previous **ALICE** analyses [110, 149] modified only the upper limit to study the systematic uncertainty, hence, we decided to verify the effect of changing the lower limit too. The first selection has been chosen because it modifies the lower $\sigma_{\text{long}, 5\times5}^2$ limit exploring a region where the population of pions should not change a lot and close to the single photon population, as shown in Fig. 5.8.

The majority of pions are found below $\sigma_{\text{long}, 5\times5}^2 < 1.00$, making our reference cut, indicated as default, effective in selecting most of them. The selections $0.40 < \sigma_{\text{long}, 5\times5}^2 < 1.50$ and $0.40 < \sigma_{\text{long}, 5\times5}^2 < 2.00$, which were already used in other **ALICE** analyses [110, 149], were applied to study the effect of different upper limits.

The analysis has been repeated using all the different background $\sigma_{\text{long}, 5\times5}^2$ selections and the $D(z_{\text{T}})$ distributions obtained are reported as a function of z_{T} in Fig. 6.28 for all centrality classes.

The z_{T} distributions obtained using a higher upper limit are in general driven down relatively to the default background selection; while the z_{T} distributions obtained with $0.35 < \sigma_{\text{long}, 5\times5}^2 < 1.00$ results are similar at low z_{T} and higher at high z_{T} .

The uncertainties are estimated using Eq. (6.8)–left; then the average of the uncertainty obtained with the three shower shape selections is calculated. The uncertainty points fluctuate at high z_{T} values in all centralities and in particular for semi-central and peripheral collisions. To smoothen the trend, the uncertainty given by the mean of the three systematic uncertainties has been fitted with an exponential in the range $0.15 < z_{\text{T}} < 0.60$. The results are reported in Fig. 6.29 and it has been used to describe the systematic uncertainty of the $\sigma_{\text{long}, 5\times5}^2$ background range.

AZIMUTHAL CORRELATION DISTRIBUTIONS OF ISOLATED PHOTONS WITH HADRONS IN PB-PB COLLISIONS

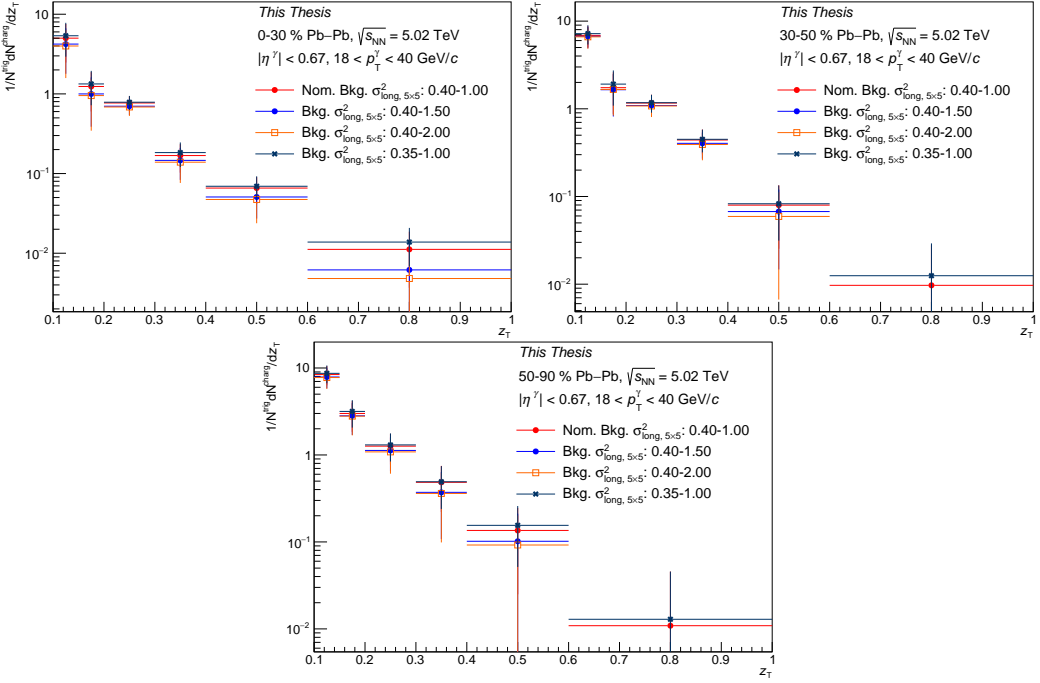


Figure 6.28: The $D(z_T)$ distributions obtained using different $\sigma_{\text{long}, 5\times 5}^2$ background ranges: $0.40 < \sigma_{\text{long}, 5\times 5}^2 < 1.00$ (full red circle) $0.40 < \sigma_{\text{long}, 5\times 5}^2 < 1.50$ (full blue circle); $0.40 < \sigma_{\text{long}, 5\times 5}^2 < 2.00$ (empty orange square) and $0.35 < \sigma_{\text{long}, 5\times 5}^2 < 1.00$ (full black cross) in 0-30% (top left), in 30-50% (top right) and in 50-90% (bottom) Pb-Pb collisions.

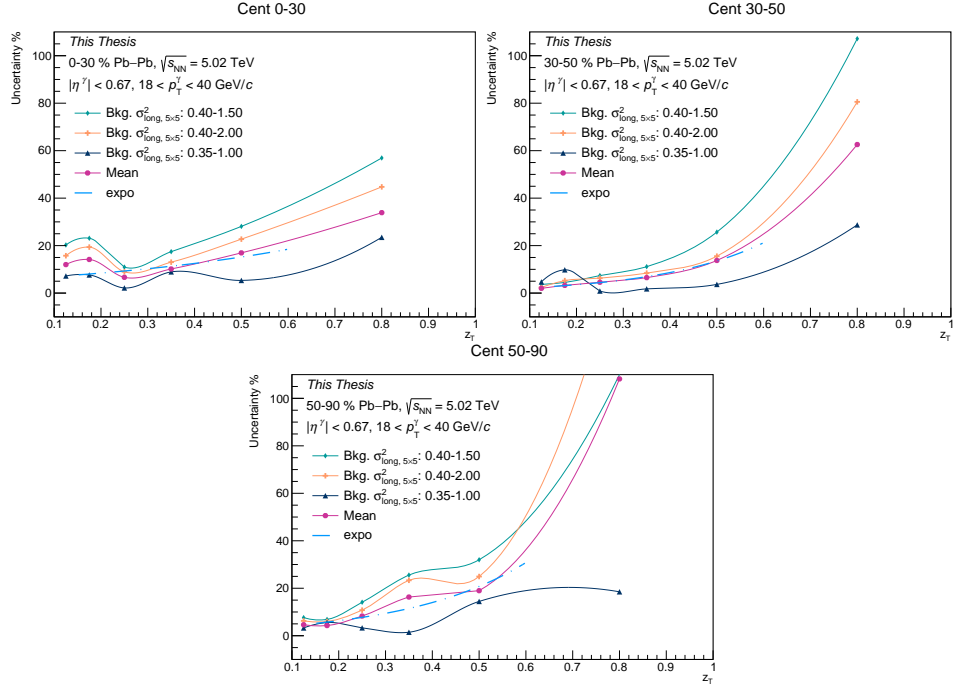


Figure 6.29: Systematic uncertainties due to $\sigma_{\text{long}, 5\times 5}^2$ background ranges: $0.40 < \sigma_{\text{long}, 5\times 5}^2 < 1.50$ (full green diamond); $0.40 < \sigma_{\text{long}, 5\times 5}^2 < 2.00$ (full orange cross) and $0.35 < \sigma_{\text{long}, 5\times 5}^2 < 1.00$ (full black triangle) in 0-30% (top left), in 30-50% (top right) and in 50-90% (bottom) Pb-Pb collisions. The average of the systematic uncertainties in the three ranges is pink, while the exponential fit is shown with a dashed light blue line.

6.4.4 Track momentum resolution

There is a p_T -dependent tracking uncertainty due to the uncertainty on TPC-ITS matching efficiency, defined as the fraction of tracks with clusters in both ITS and TPC over the total number of tracks with clusters in TPC. To the p_T -dependent tracking uncertainty contribute also the TPC track quality selections. This uncertainty, defined by the ALICE Data Particle Group (DPG), is of the order of 3% for the tracks considered in the analysis. To estimate its effect on the correlation distributions, a random p_T -dependent track rejection of the order of the uncertainty is applied in the MC at the level of the track selection. This permits us to verify the effect of losing a fraction of tracks on our measurement. The effect of this artificial selection is estimated by comparing the detector efficiency (see Sect. 6.3.3) with and without this selection. This method has also been used in Ref. [154]. The uncertainty is given by:

$$\frac{\alpha_{\text{corr}} - \alpha_{\text{corr}}^{\text{TrackEff}}}{\alpha_{\text{corr}}} \quad (6.11)$$

where α_{corr} is obtained from the ratio of GJ MC generated simulation over reconstructed one (see Eq. (6.5)) and $\alpha_{\text{corr}}^{\text{TrackEff}}$ is the one obtained after the tracking uncertainty selection. Figure 6.30 reports the systematic uncertainties obtained from Eq. (6.11) as a function of z_T for all the centralities.

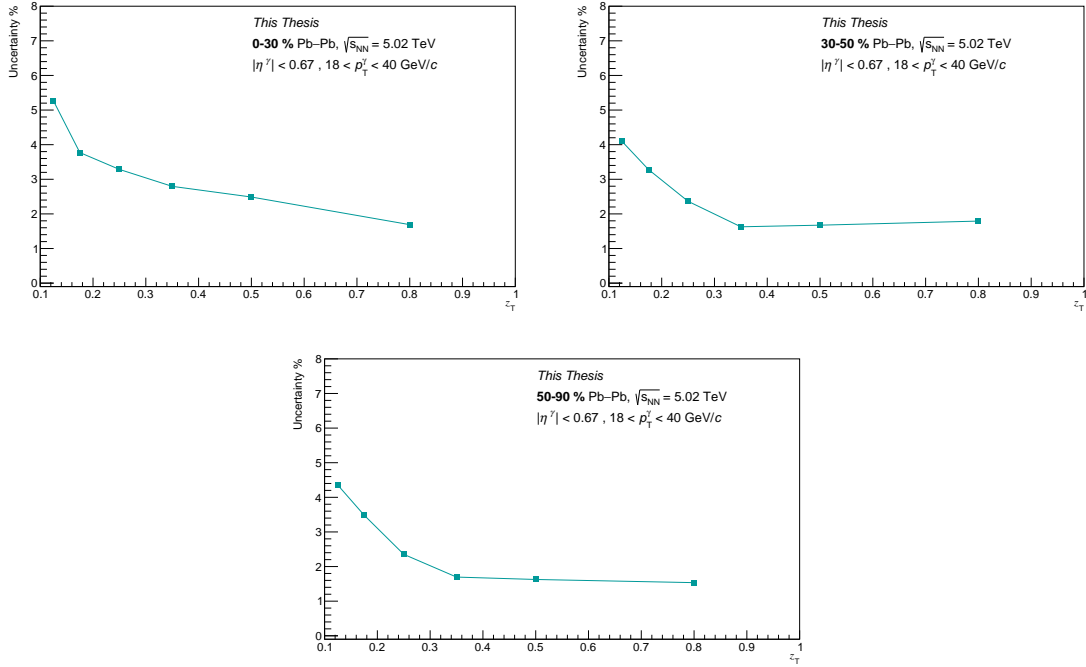


Figure 6.30: Systematic uncertainty due to the tracking efficiency in 0-30% (top left), 30-50% (top right) and 50-90% (bottom) Pb-Pb collisions.

The variations obtained are of the order of a few per cent: this is compatible with the 3% of track rejection that was introduced to consider the uncertainty of the matching efficiency. The points were considered as uncertainty.

6.4.5 Number of centrality bin used for filling the mixed event pool

The procedure involves determining whether varying the number of centrality ranges used to fill the event mixing pool has any effect, which means using finer centrality intervals. The comparison is between the nominal case, with $N_{\text{cent}} = 9$, corresponding to centrality intervals of 10%, and $N_{\text{cent}} = 45$, corresponding to centrality intervals of 2%. Figure 6.31 shows the z_T distributions obtained using different numbers of centrality bins for filling the mixed event. The distributions overlap in all cases, with only a few deviations visible in the 0-30% intervals. To understand if there is a systematic effect, the ratio between the

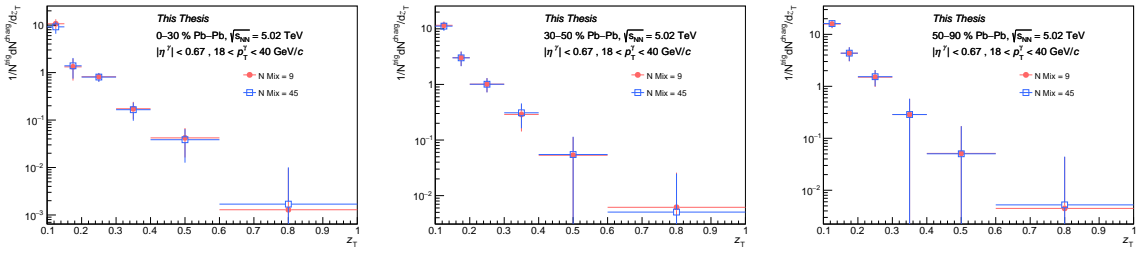


Figure 6.31: The differential z_T distributions obtained using 9 centrality bins (full pink circle) and 45 centrality bins (empty blue square) for filling the mixed event pool in 0-30% (left), 30-50% (middle) and 50-90% (right).

“nominal” z_T distributions and the ones obtained using $N_{\text{cent}} = 45$ is calculated. This result is shown in Fig. 6.32. The ratio is in general compatible with unity for all centralities, there

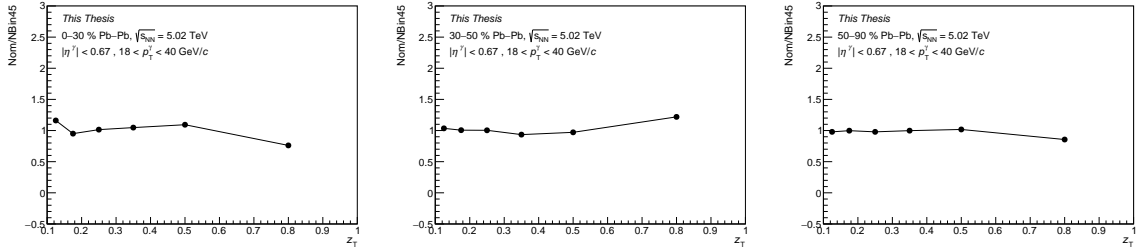


Figure 6.32: Ratio of the z_T distribution obtained with $N_{\text{centMix}} = 9$ and z_T distribution obtained with $N_{\text{centMix}} = 45$ in 0-30% (left), 30-50% (middle) and 50-90% (right).

is only a small deviation at low z_T in 0-30%. The systematic uncertainty is calculated using Eq. (6.8)-left and the results are shown in Fig. 6.33. The systematic uncertainty increases for all centralities at high z_T . In 0-30% the uncertainty is larger in the first z_T bin and this is related to the deviation from unity seen in Fig. 6.32-left. To smooth the trend of the systematic distributions an exponential fit has been applied over all the z_T range in 30-50% and 50-90% Pb–Pb collisions. In central collisions, a constant fit has been used for z_T between 0.1 and 0.2 and then an exponential has been applied. The systematic uncertainty has been evaluated from the fits.

6.4. Systematics uncertainties

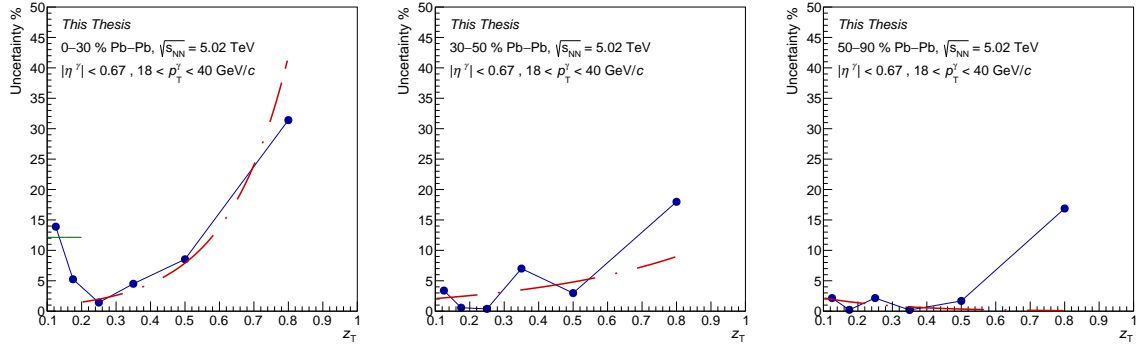


Figure 6.33: Systematic uncertainty for different numbers of centrality bins used for filling the mixed event pool in 0-30% (left), 30-50% (middle) and 50-90% (right).

6.4.6 Total uncertainties

In this Section, the different systematic uncertainties are compiled and added in quadrature.

$$\sigma_{\text{syst}}^{\text{tot}} = \sqrt{\sum_i \sigma_{\text{syst},i}^2}. \quad (6.12)$$

The result of this operation is reported in Fig. 6.34.

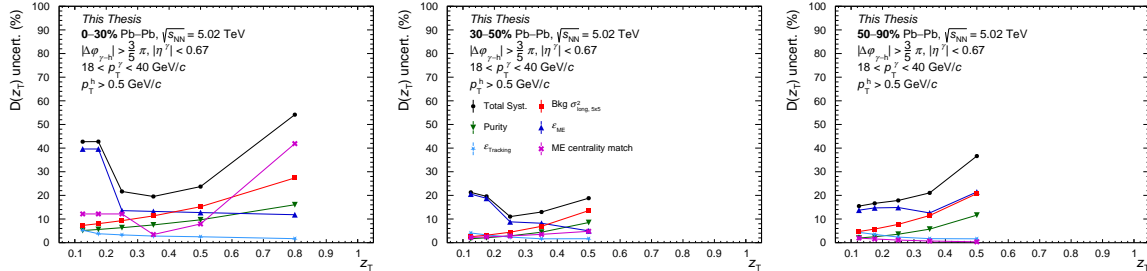


Figure 6.34: Various systematic uncertainty sources for the three centrality classes measured.

Considering the large statistical fluctuations that affects the last z_T interval in 30-50% and 50-90%, which makes deviate the distributions at large uncertainties value, it has been decided to exclude that z_T interval in semi-central and peripheral collisions. The dominant systematic uncertainty at low z_T is related to the mixed event (ϵ_{ME}), while at high z_T the biggest uncertainty seems to be related to the $\sigma_{\text{long}, 5 \times 5}^2$ of the background. The systematic uncertainties are worse in central collisions than in semi-central and peripheral collisions, in particular at low z_T . In central collisions, the large quantity of underlying event covers almost all the signal; it is not surprising that the uncertainty due to the mixed event have a large impact in that centrality interval.

Figure 6.35 shows the statistical and the total systematic uncertainties as a function of z_T for the three centrality classes. It is clear that the statistical uncertainty dominates most of the distributions. An important source of the statistical uncertainty is the subtraction of a too close background distribution. Correlation measurements are statistically ‘‘hungry’’, because they require selecting the trigger object and matching it with the associated hadrons emitted

AZIMUTHAL CORRELATION DISTRIBUTIONS OF ISOLATED PHOTONS WITH HADRONS IN PB-PB COLLISIONS

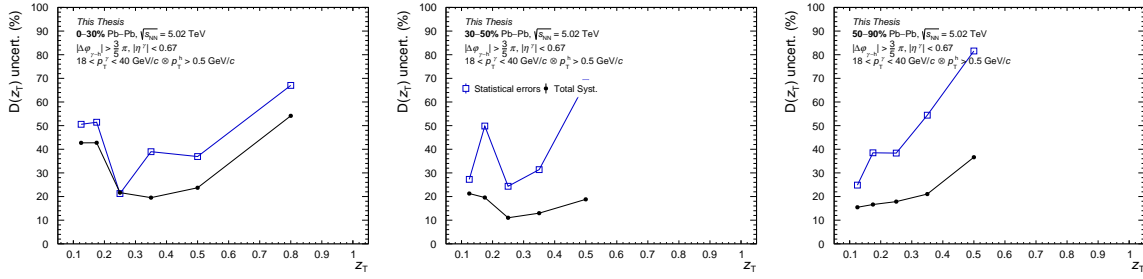


Figure 6.35: Comparison between statistical and systematic uncertainties for the three centrality classes measured.

in the opposite direction. Furthermore, the γ^{iso} -hadron correlations are much more complicated than di-hadron correlations because the γ^{iso} cross-section is lower than the hadron one, and the limited [EMCal](#) calorimeter acceptance does not help. The final $D(z_T)$ distributions including the systematics uncertainties are reported in Fig. 6.36.

6.4. Systematics uncertainties

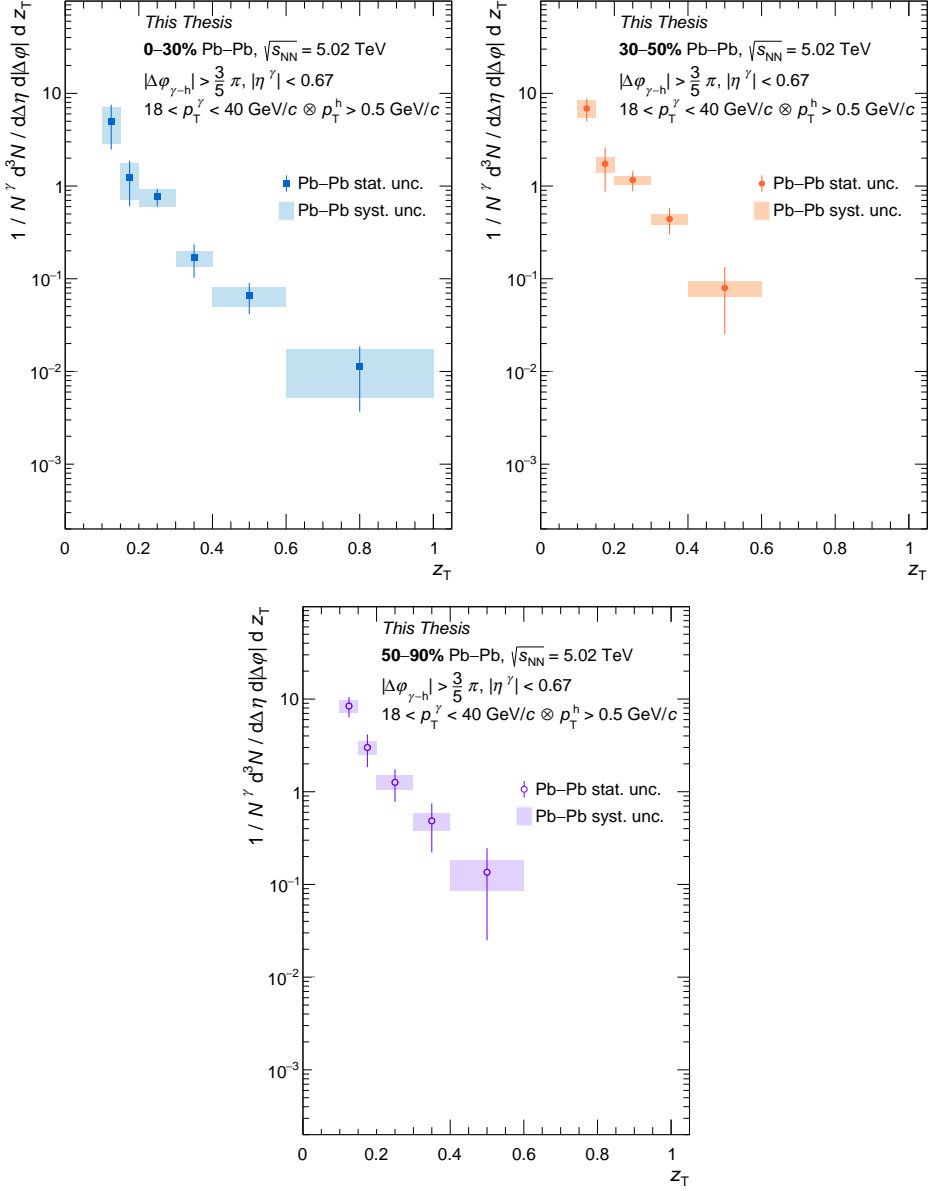


Figure 6.36: The $D(z_T)$ distributions as a function of z_T for a p_T^γ between $18 < p_T^\gamma < 40$ GeV/c in 0-30% (top left), 30-50% (top right) and 50-90% (bottom). The statistical uncertainties are indicated by bar, while the systematics uncertainties are shown with coloured boxes.

6.5 Theoretical models

In this analysis, two different theoretical models have been used to compare the obtained results. The models used are the pQCD NLO model [155, 156], used to describe the pp baseline and the QGP, in case of addition of quenching; and the CoLBT one [157], which also includes the quenching due to the presence of the medium. These two models are different at the generator level and they implement the loss of energy in a different way, hence in the following, the different characteristics are illustrated.

pQCD NLO model

These pQCD NLO calculations can include jet energy loss (ΔE), which is controlled by the \hat{q} and calculated by Higher-Twist formalism (see Sect. 1.5.4). The model obtains the parton-parton hard scattering cross-sections by perturbation calculation and convolves it with the PDF and FF. The \hat{q} value is extracted from single hadron, di-hadron, and γ -hadron suppression at different $\sqrt{s_{\text{NN}}}$ energies (0.2, 2.76, and 5.02 TeV). The various details of this model are reported in Table 6.2:. The pQCD NLO calculations include fragmentation

system	Pb–Pb collisions
colliding energy	$\sqrt{s_{\text{NN}}} = 5.02 \text{ TeV}$
centrality	0-30 %, 30-50 %, 50-90 %
rapidity	$ y^\gamma < 0.67, y^h < 0.9$
away side range	$ \Delta\varphi > 3\pi/5$
$p_T^{\text{trig}}(\gamma)$	[18 – 40] GeV/c
$p_T^{\text{assoc}}(h^\pm)$	[> 0.5] GeV/c
z_T	[0.15 – 0.2], [0.2 – 0.3], [0.3 – 0.4], [0.4 – 0.6], [0.6 – 0.8], [0.8 – 1.0]
PDFs	CT18A PDF [158]
FFs	Kniehl-Kramer-Potter FFs [159]
energy loss	High-twist approach [160] with $\hat{q}/T^3(T)$ extracted from single hadron, dihadron and γ -hadron data by the IF-Bayesian analysis [161, 162]

Table 6.2: Configurations for the NLO pQCD calculations.

photons, which are removed by applying the isolation method. The PDFs used are given by the CT18A [158] and the FFs are defined applying the KKP parametrization [159]. The uncertainty of the calculations is estimated by varying the factorization scale μ of the FFs.

CoLBT-hydro

Coupled Linear Boltzmann Transport and hydrodynamics (CoLBT-hydro) is developed for event-by-event simulations of jet transport and jet-induced medium excitation in high-energy heavy-ion collisions. This is made possible by a GPU parallelized (3+1)D hydrodynamics that has a source term from the energy-momentum deposition by propagating jet shower partons and provides a real-time update of the bulk medium evolution for subsequent jet transport [157].

In the **CoLBT** model the interactions are again driven by \hat{q} , but its value that describes the energy loss is extracted mainly from a single jet and γ -jet suppression at $\sqrt{s_{NN}} = 5.02$ TeV.

Comparison with models

Figure 6.37 compares final results in the three measured centrality classes with pQCD NLO calculations [155, 156] and the central Pb–Pb collisions results are also compared with the **CoLBT**-hydro model [157].

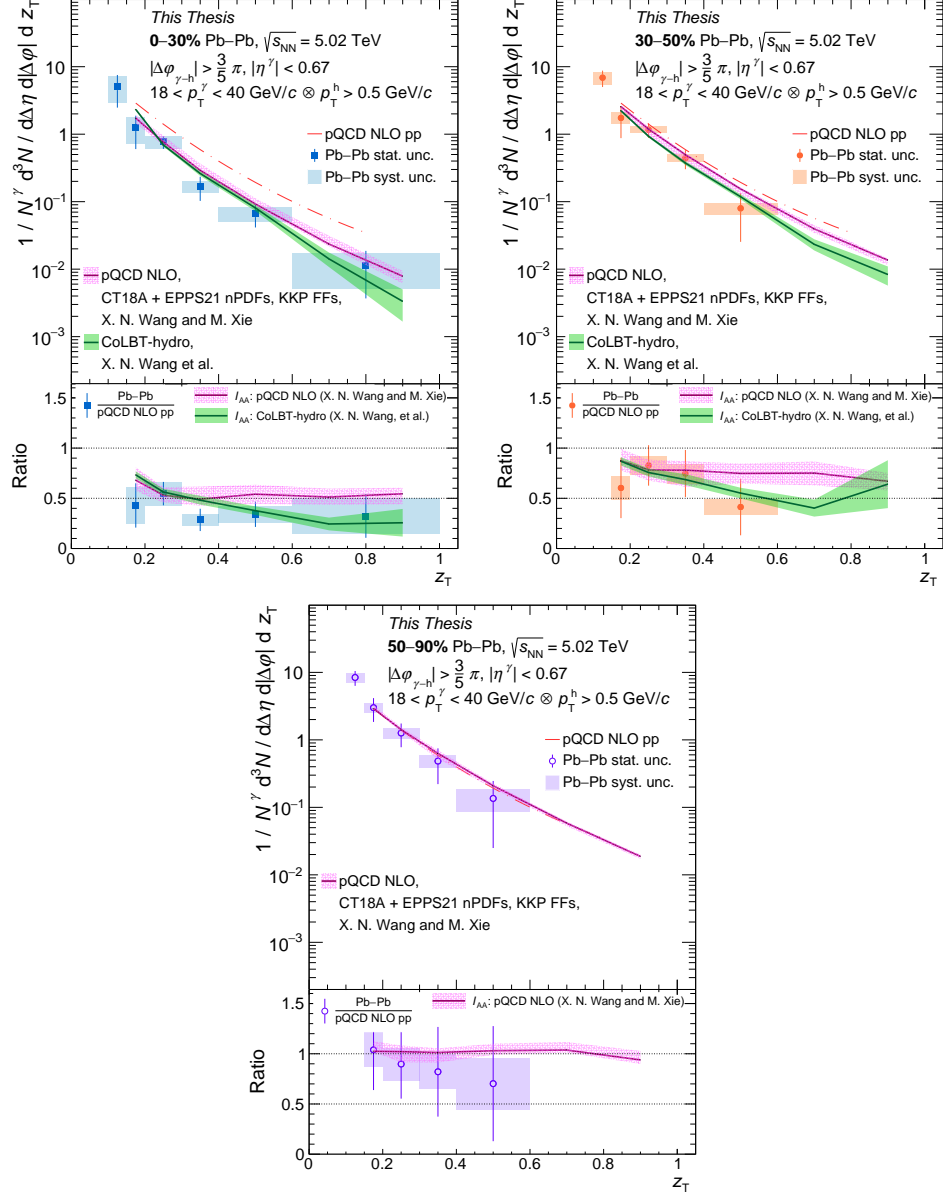


Figure 6.37: Top panels: The $D(z_\text{T})$ distributions as a function of z_T for a p_T^γ between $18 < p_\text{T}^\gamma < 40 \text{ GeV}/c$ in 0-30% (full blue square), 30-50% (full orange circle) and 50-90% (empty violet circle). The statistical uncertainties are indicated by bars, while the systematics uncertainties are shown with coloured boxes. Theoretical calulations are included pQCD NLO (pink) and CoLBT-hydro (green) models. Bottom panels: Ratio of $D(z_\text{T})$ in Pb–Pb collisions to pQCD calculations (bottom panels) as a function of z_T .

Good agreement is observed between data and theory, but the discrimination between the two models is not possible yet due to the current uncertainties. Figures 6.37 report also

the $D(z_T)$ distributions obtained from pp pQCD NLO simulations (top panels) as a function of z_T . The $D(z_T)$ distributions are suppressed compared to pp pQCD NLO calculations and this is a reflection of the high p_T hadron suppression in the presence of the QGP. This suppression becomes less important in peripheral collisions.

6.5.1 The nuclear-modification factor I_{AA}

The I_{AA} is the ratio between the z_T distribution in AA collisions with respect to the one in pp collisions, as it was already introduced in Sect. 2. It is defined as:

$$I_{AA} = \frac{D(z_T)_{AA}}{D(z_T)_{pp}}. \quad (6.13)$$

The $D(z_T)$ from γ^{iso} -hadron correlations has been measured by ALICE [110] in pp collisions at $\sqrt{s} = 5.02$ TeV, but with a different p_T^γ range ($12 < p_T^\gamma < 40$ GeV/ c). Unfortunately, the statistic of the pp sample does not allow us to repeat the measurement in our p_T^γ trigger range. On the other hand, in Pb–Pb collisions, it is not possible to measure the azimuthal correlations with a p_T^γ down to 12 GeV/ c because of the large amount of UE, which prevents the analysis at lower p_T^γ . For these reasons, we have decided to use pQCD NLO calculations as our pp reference. In this way, it is possible to calculate the $I_{\text{pQCD NLO}}$, defined as:

$$I_{\text{pQCD}} = \frac{D(z_T)_{AA}}{D(z_T)_{\text{pQCD NLO pp}}} \quad (6.14)$$

and that is a proxy for the I_{AA} .

The ratio of our data to this pp pQCD NLO calculation is shown in the bottom panel of each plot in Fig. 6.37. A clear difference can be seen in the data with respect to the pp pQCD NLO calculation. The ratios obtained are compared with the I_{AA} estimated from previous theoretical models and the results are consistent. To better visualize the trend with centrality, the $I_{\text{pQCD NLO}}$ of various centralities have been plotted in Fig. 6.38.

The ratios are below unity, as expected due to the QGP modification and more suppression is visible in central collisions with respect to peripheral. In peripheral collisions and in semi-central collisions, there are hints of a rising trend at low z_T intervals.

6.5.2 I_{CP}

Another interesting variable is the I_{CP} defined as the ratio between the $D(z_T)$ distributions in central or semi-central collisions relative to peripheral ones:

$$I_{CP} = \frac{D(z_T)_{0-30\%,30-50\%}}{D(z_T)_{50-90\%}}. \quad (6.15)$$

The I_{CP} is estimated using the $D(z_T)$ distributions presented before and the discussions regarding its systematics are reported in Appendix D. Figure 6.39 shows the I_{CP} as a function of z_T for central and semi-central centralities.

The results are dominated by statistical uncertainties, but it is possible to appreciate the larger suppression in central collisions than in semi-central. This result confirms the centrality dependence of the energy loss.

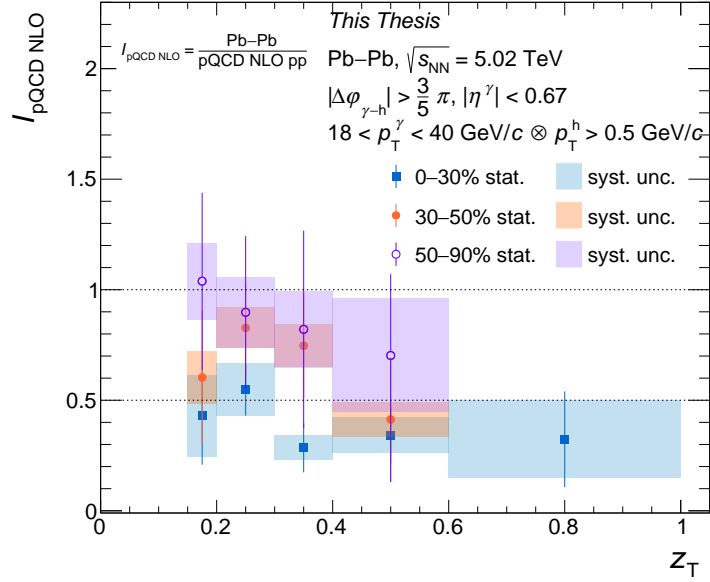


Figure 6.38: The $I_{\text{pQCD NLO}}$ distributions as a function of z_T in 0-30% (full blue square), 30-50% (full orange circle) and 50-90% (empty violet circle) Pb-Pb collisions.

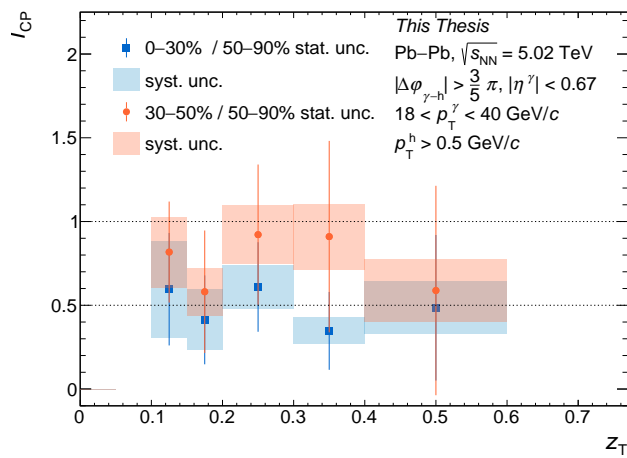


Figure 6.39: I_{CP} as a function of z_T for central (full blue square) and for semi-central (full orange circle) Pb-Pb collisions.

6.6 Results from other experiments

Our results have been compared with other measurements done at LHC by CMS [102, 106] and at RHIC by STAR [111] and PHENIX [163].

Relative to the measurements at LHC, the γ^{iso} -hadron correlations measured with the ALICE detector are compared with the γ -jet and Z -hadron correlations by CMS [102, 106] in Pb–Pb collisions at $\sqrt{s_{\text{NN}}} = 5.02$ TeV. The selections used by the two experiments are different: the CMS experiment can select higher energetic trigger objects ($p_T^\gamma > 60$ GeV/ c [102] or $p_T^Z > 30$ GeV/ c [106]) than ALICE ($18 < p_T^\gamma < 40$ GeV/ c). Additionally, the z_T range investigated by the two experiments is different. Figure 6.40 shows the I_{AA} obtained by CMS and the $I_{\text{pQCD NLO}}$ estimated by ALICE in this analysis.

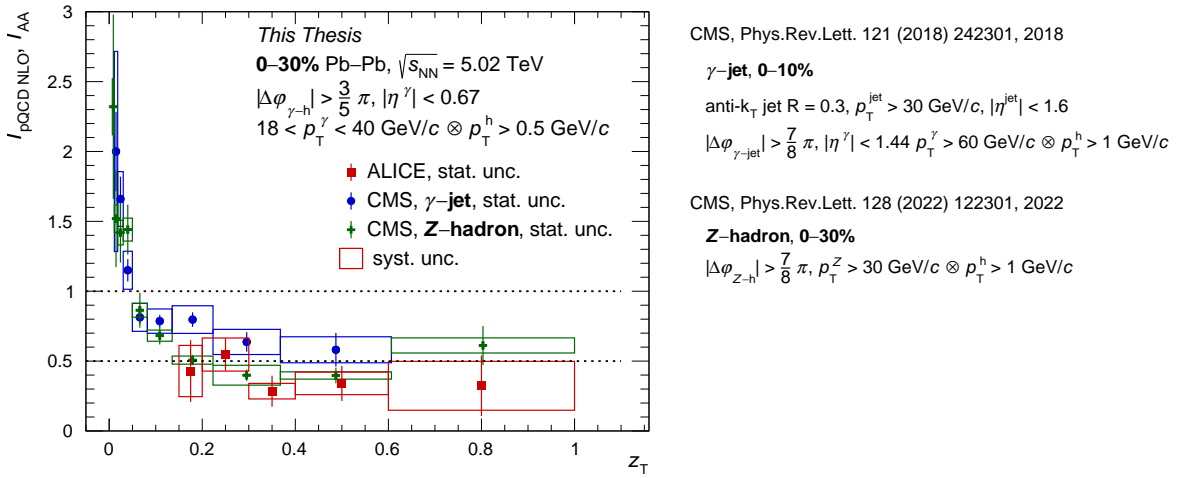


Figure 6.40: Top: The I_{AA} distributions as a function of z_T in central collisions for γ -jet (full blue circle) and Z -hadron (full green cross) correlation from the CMS Collaboration [102, 106] and the $I_{\text{pQCD NLO}}$ from the γ^{iso} -hadron (full red square) correlation by ALICE.

In the common z_T values, the three distributions are compatible and observe a suppression at high z_T . At low z_T (below $z_T < 0.15$) the CMS γ^{iso} -jet and Z -hadron correlations measurements are able to probe the enhancement of the low p_T hadrons.

Regarding RHIC’s experiments, the measurement is similar because STAR and PHENIX also measured γ -hadron correlations, but with different center-of-mass energy per nucleon $\sqrt{s_{\text{NN}}}$ (200 GeV) and collisional systems (Au–Au). The selections differ from those used in this analysis, though RHIC’s experiments tend to investigate a similar p_T region as ALICE. The PHENIX Collaboration selects γ^{iso} with $5 < p_T^\gamma < 9$ GeV/ c and correlates them with hadrons $0.5 < p_T^{\text{hadr}} < 7$ GeV/ c . The STAR experiment triggers on γ^{iso} with $12 < p_T^\gamma < 20$ GeV/ c and select with hadrons $p_T^{\text{hadr}} > 1.2$ GeV/ c . Both experiments have enough statistics to investigate low p_T^γ . Figure 6.41 reports the I_{AA} measured by the RHIC’s experiments and our $I_{\text{pQCD NLO}}$. The ALICE and the STAR results are compatible and overlap in the common z_T range. For what concerns the PHENIX results, the very low p_T^γ reached allows for the measurement of the enhancement of soft hadrons due to high- p_T hadron fragmentation through the medium.

Although this is not an apple-to-apple comparison, in the common z_T ranges the trends

6.6. Results from other experiments

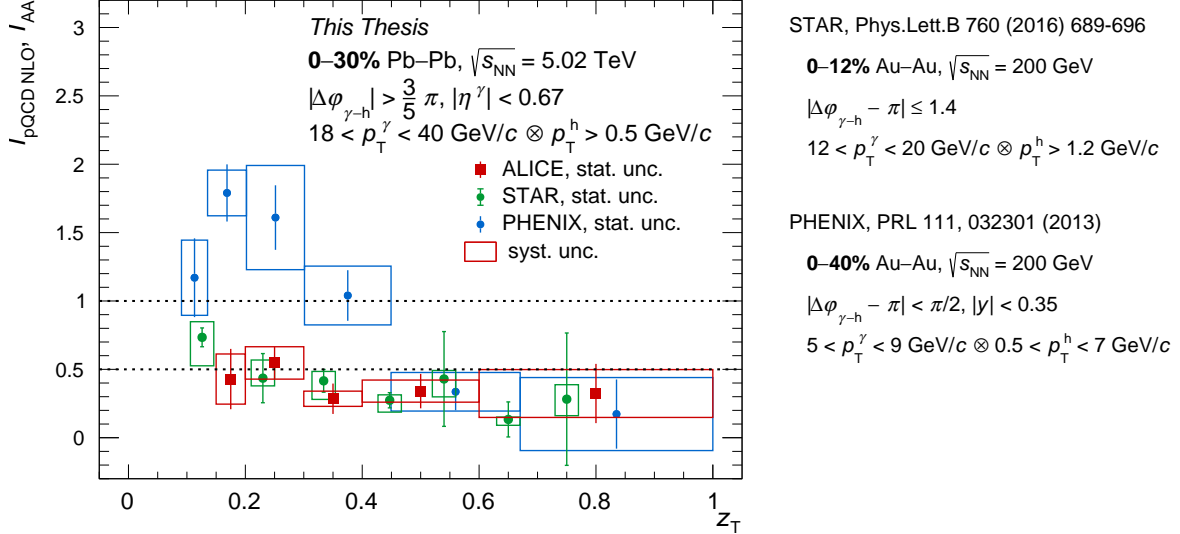


Figure 6.41: The I_{AA} distributions as a function of z_T in central collisions from γ -hadron correlation from the STAR Collaboration (full light green circle), the PHENIX experiment (full light blue circle) and the $I_{p\text{QCD NLO}}$ by the ALICE experiment (full red square).

and magnitude of the ratios (I_{AA} and I_{CP}) measured at **LHC** and at **RHIC** are quite similar. Deviations from **ALICE**'s results occur at low z_T for all experiments, where our results do not capture the enhancement. Similar deviations are observed in **STAR**'s results.

Chapter 7

Future prospects for isolated photons measurements at forward rapidity with ALICE

Gluon saturation arises from its non-Abelian nature (gluons carry colour charge and self-interact), which is a fundamental property of Quantum Chromo Dynamics. The gluon density in hadronic matter grows rapidly at low x . However, this growth is limited by the gluon self-interaction that may lead to a new state of gluon-saturated matter. Global fits to deep inelastic scattering (DIS) measurements with nuclear targets indicate that the gluon density at low momentum fraction $x \sim 10^{-2}$ is smaller in heavy nuclei than in free protons and neutrons [164]. The magnitude of gluon suppression in nuclei with respect to nucleons, called shadowing, can be evaluated with the measurement of direct photons at forward rapidity, which provides constraints of the gluon density and its x -dependence. Instrumentation of the forward region at LHC will enable measurements probing parton densities at small momentum fraction x of the proton or nucleus, down to $x \sim 10^{-6}$ with low momentum transfer $Q \sim 4 \text{ GeV}/c$.

In this perspective, after Long Shutdown 3 (LS3, 2025-2028) at LHC, the ALICE experiment intend to extend its forward physics program, installing the Forward Calorimeter (FoCal). It will cover pseudorapidities of $3.4 < \eta < 5.8$ and will enable measurements of isolated photon yields as well as correlations of isolated photons and hadrons.

At LHC the isolated photons originate predominantly in quark–gluon Compton scatterings: their high-precision measurement will be the primary objective of the FoCal with also the measurement of jets and coincident γ -jet and jet-jet measurements, in pp, p–Pb and Pb–Pb collisions [165], providing unique capabilities to investigate (n)PDFs in the unexplored regime of low Bjorken- x .

The Forward Calorimeter will have to be able to reconstruct and identify decay photons, with the capability to reconstruct photon pairs with a spatial separation of a few mm at the surface of the detector, providing precise discrimination between direct photons and decay photons. Hence, this upgrade will allow us to extend the isolated photon measurements that I discussed in the previous chapters of the Thesis to a different pseudorapidity region. Exploring jet quenching at forward rapidity in Pb–Pb collisions will allow us to map the

7.1. FoCal calorimeter design

QGP density as a function of rapidity and to study the difference between energy loss for quark and gluon jets since the fraction of quark-initiated jets is larger than at midrapidity [165].

7.1 FoCal calorimeter design

The **FoCal** conceptual design consists of a granular and compact silicon–tungsten electromagnetic calorimeter (**FoCal-E**) to measure and identify direct photons, followed by a spaghetti hadron calorimeter (**FoCal-H**) to reconstruct the hadronic fraction of the jets.

FoCal will be located on the A-side of ALICE (positive direction along the z -axis or beam line in the ALICE coordinate system), exterior to the ALICE solenoid. The front face of **FoCal** will be at 7 m from the nominal interaction point, providing sufficient space longitudinally for **FoCal-E** and **FoCal-H** (about 1.5 m). The **FoCal** transverse dimensions are about $1 \times 1 \text{ m}^2$ [166]. The geometry of **FoCal** at its intended location in front of the compensator magnet is shown in Fig. 7.1.

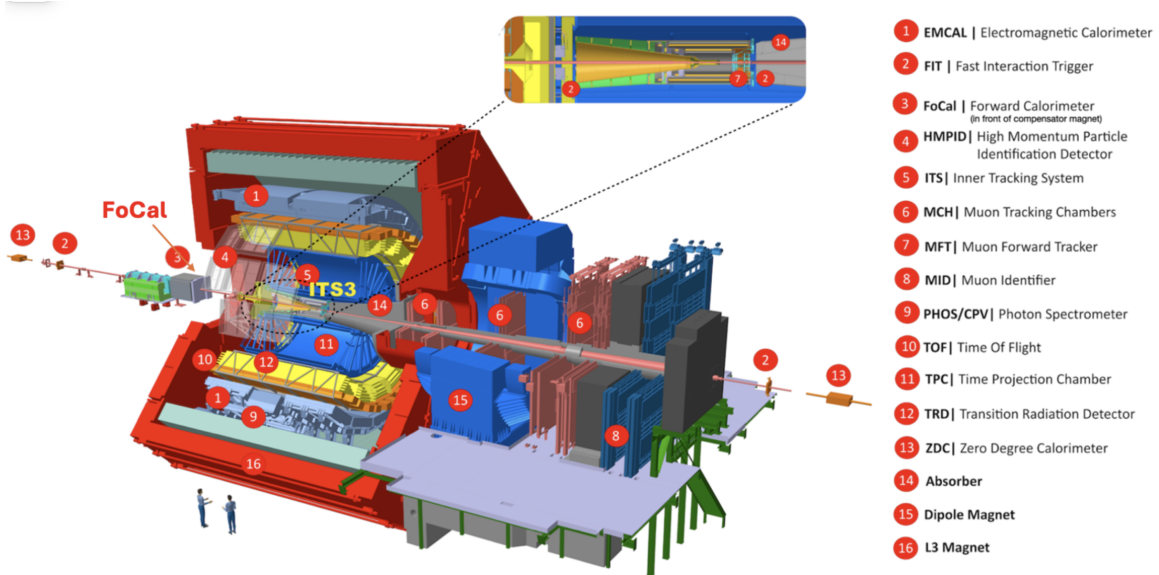


Figure 7.1: ALICE detector configuration for Run 4. **FoCal** is located in front of the compensator magnet and outside the magnet doors on the A-side, opposite the muon arm. Figure taken from [166].

Since the interest of this Thesis, is mainly related to photons, in the following, major attention will be dedicated to the electromagnetic calorimeter. The **FoCal-E** is composed of 22 modules and each one is made of 20 passive tungsten (W) absorber layers alternating with active Si detector layers. The Si silicon sensors layers are of two types: there are 18 layers of low-granularity ($\sim 1 \text{ cm}^2$) silicon pad detectors (**PADs**) and 2 layers of high-granularity ($\sim 30 \times 30 \mu\text{m}^2$) Monolithic Active Pixel Sensors (**MAPS**) [167].

The eighteen **PAD** layers of a module contain five pad sensors each, while the two **MAPS** layers consist of 15×6 ALPIDE [167] pixel sensor chips, therefore the **FoCal-E** is a sampling calorimeter, $x - y$ segmented in 110 towers. The longitudinal structure of the **FoCal-E** calorimeter is shown in Fig. 7.2.

The pad layers provide a measurement of the shower energy and its profile, while the pixel layers enable two-photon separation with high spatial precision to discriminate between

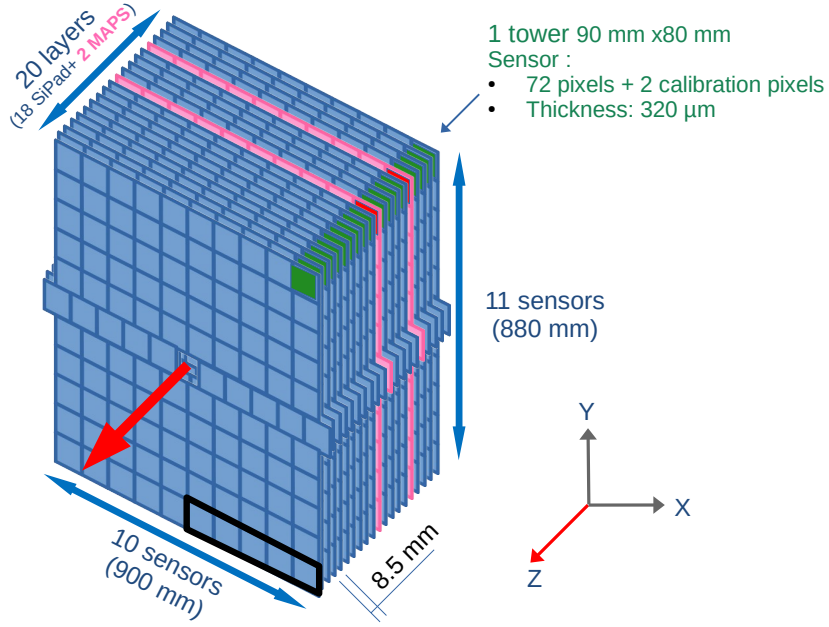


Figure 7.2: The longitudinal structure of the FoCal-E has a total of 20 layers: 18 layers of tungsten and silicon pads (blue) interleaved with two layers of tungsten and silicon pixels MAPS (pink) [168]. z is the beam direction.

isolated photons and merged showers of decay photon pairs from neutral mesons.

My technical service work within the [ALICE](#) Collaboration has been dedicated to test [PAD](#) layers existing calibrations and implementing new ones; hence, in the following, the focus will be on this topic. The [PAD](#) sensor is a p-type silicon PIN photodiode: a reverse-biased p-n junction characterised by a wide depletion region, which allows to produce a current signal when charged particles pass through the volume. Each sensor has a thickness of 320 μ m and it is segmented into 8 \times 9 channels plus two cells of smaller size that allow a more precise calibration, for a total of 74 channels.

The choice of using silicon pad sensors is motivated by their good energy resolution and signal-to-noise (S/N) ratio, as well as their wide dynamic range for the proposed [FoCal](#) physics program [169]. A sketch of a pad layer module is shown in Fig. 7.3.

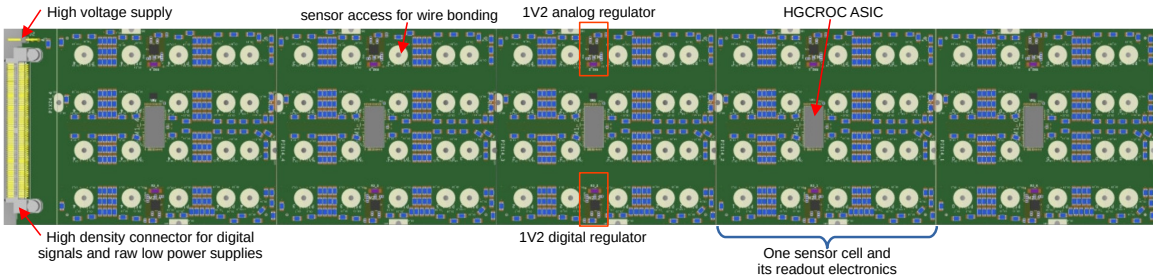


Figure 7.3: The pad-layer board is made out of 5 individual pad sensors each with 72 channels of $1 \times 1 \text{ cm}^2$, which will be readout by one HGCROC chip.

For reading out the analog signals of the [PADs](#), the High Granularity Calorimeter Readout Chip ([HGCROC](#)) Application Specific Integrated Circuit ([ASIC](#)) developed by the [\$\Omega\$ MEGA](#) (Organisation de MicroÉlectronique Générale Avancée) group for the [CMS](#) High

7.1. FoCal calorimeter design

Granularity Calorimeter [170, 171] has been chosen.

This ASIC is made of 72 channels of the full analogue chain achieving charge and timing information; 4 common mode channels for subtracting the coherent noise and 2 calibration channels for the Minimum Ionizing Particle.

An architectural overview of the ASIC is shown in Figure 7.4.

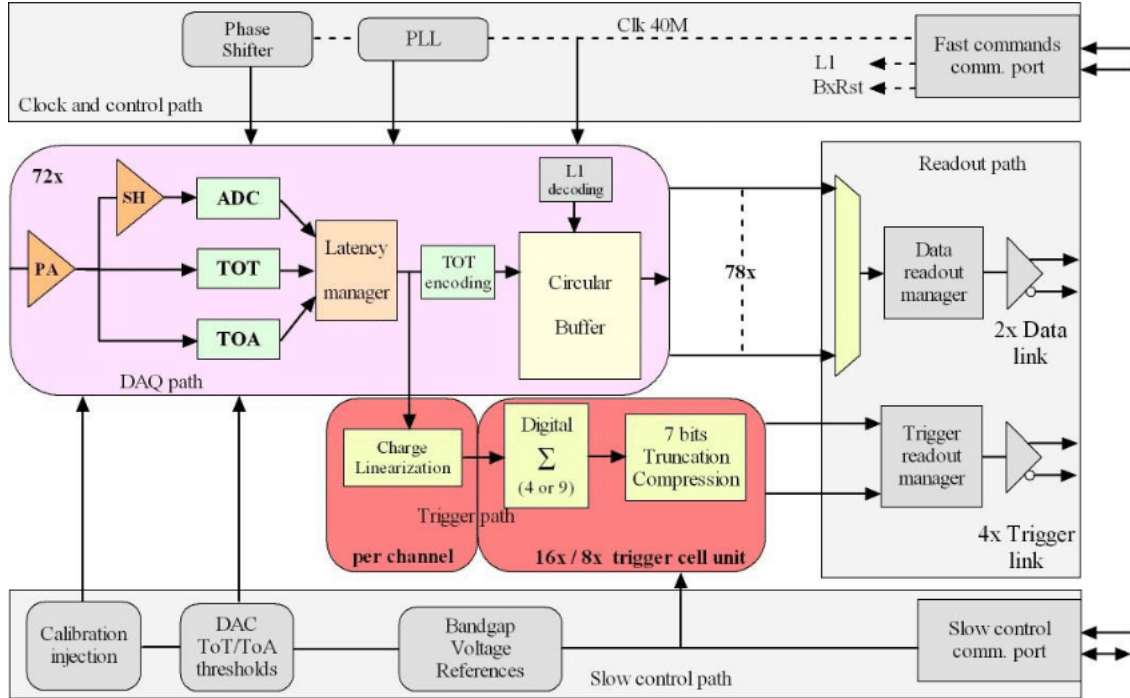


Figure 7.4: Architectural overview of the HGCROC-V2 [172].

Each channel has a low-noise preamplifier (**PA** on the sketch) that converts the input charge from the silicon diode to a voltage signal. This output signal can be sent to a shaper filter (**SH**), that feeds an Analog-to-Digital Converter (**ADC**), and to two discriminators: named Time of Arrival (**TOA**) and Time over Threshold (**TOT**).

The shaper action is divided into three stages:

- a Sallen-Key (S-K) shaper with gain 2, that shapes the integrated pulse;
- a RC^2 shaper, gain 3;
- a buffer to provide a good output impedance to drive the **ADC**.

One of the most important design considerations is the dynamic range of the readout system: in the forward direction it is necessary to cover shower energies of up to 2 TeV, that correspond to charge signals of few pC, and also to be able to measure signals as low as a few fC. In this perspective, the **HGCROC** allows to satisfy this objective thanks to its dual-range readout architecture with 10-bit **ADC** for small signals up to 100 **MIP** equivalent (~ 200 fC) and a 12-bit **TOT** measurement for large signals.

The **TOA** and the **TOT** are discriminators and they generate a trigger signal when the input signal exceeds a threshold value. In general, the **TOA** is used for precise timing measurements, but in **FoCal** its start time is necessary for activating the **TOT**. The **TOA**

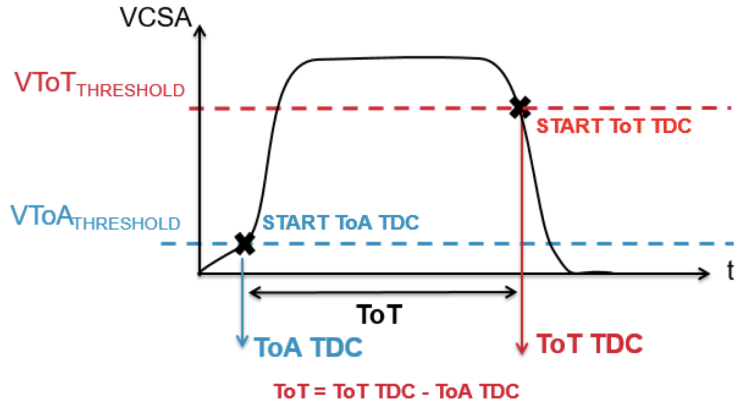


Figure 7.5: Sketch for describing the relationship between the **TOA** and the **TOT**. An analog signal as a function of the time is shown.

provides the timestamp corresponding to the instant when an event is triggered, that is when the impulse exceeds the **TOA** threshold with its rising edge. The Time Over Threshold measured the time difference between the start of **TOA** signal's rising edge and the start of the **TOT** signal's falling edge. Figure 7.5 shows the relationship between the **TOA** and the **TOT**.

The **TOT** measurement is based on a time width signal processing method: it deduces the charge from the time during which the pulse stays beyond a certain threshold, obtaining the energy by measuring the pulse width of the digital output. When the energy deposit is larger, the 10-bit **ADC** cannot be used because it saturates, therefore, the discriminator **TOT** is exploited.

More details will be given in the following Sections, because an important part of my work was dedicated to the implementation of **TOA** and **TOT** calibrations.

The three measurements (**ADC**, **TOA**, and **TOT**) are sampled at the so-called **LHC** frequency of 40 MHz (LHC clock) and stored continuously in a circular buffer. The 5-pad-layer boards will be read out on each side of the detector by FPGA-based aggregator boards. It is foreseen that four 5-pad-layer boards will be connected to one aggregator through a dedicated “final” interface board as shown in Fig. 7.6.

The aggregator board will be in charge of (i) controlling and reading out the 20 **HGCROC** through Ethernet connection, (ii) establishing the bidirectional communication channel through the GigaBit Transceiver (GBT) protocol [173] with the Common Readout Unit (CRU) [174] and (iii) distributing the low and high voltage power supplies.

The measurement to be transmitted to the aggregator is extracted from the circular buffer thanks to a timing offset programmed by slow control: the circular buffer induces a delay, expressed in counts of machine clock cycles, that has to be accounted for accessing and reading the triggered values. This delay is set in the initial configuration of the **HGCROC** and it can be modified [168].

7.2. Prototype electronics and associated tools

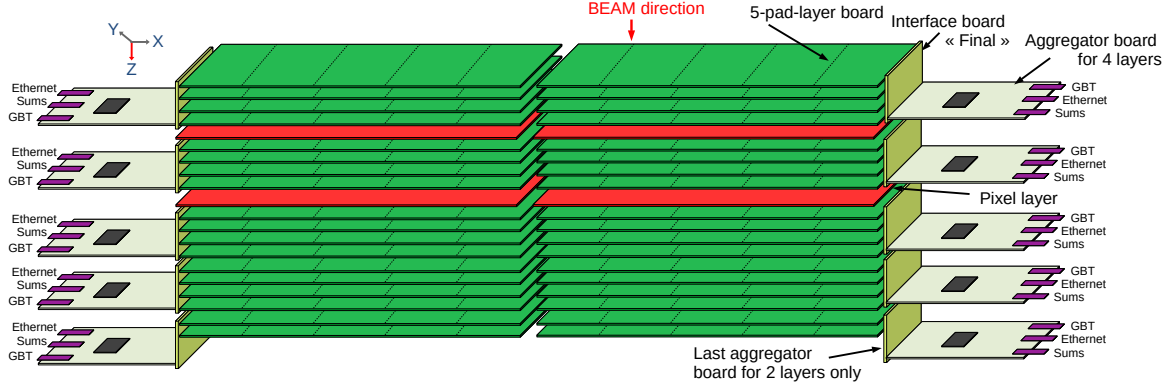


Figure 7.6: Overview of layer stacking in the beam direction. The silicon pad sensor layers and their associated front-end electronics are shown in green, and the MAPS layers (without their readout) are shown in red. The readout partition is shown for a full module: four 5-pad-layer boards per aggregator for the first four groups and two 5-pad-layer boards for the last silicon pad layers. The mechanical adaptation between the 5-pad-layer boards and the aggregator is achieved with a dedicated “final” interface board.

7.2 Prototype electronics and associated tools

For addressing the technical issues and to test the detector performances a fully instrumented tower prototype of the [FoCal-E](#), shown in Fig. 7.7 has been assembled: it consists of a sandwich of 20 tungsten layers and silicon sensors, out of these, 18 are [PADs](#), covering a surface of $9 \times 8 \text{ cm}^2$. In total 18 single pad [HGCROC](#) boards, a dedicated “prototype” interface board, and a prototype aggregator board were designed and manufactured.

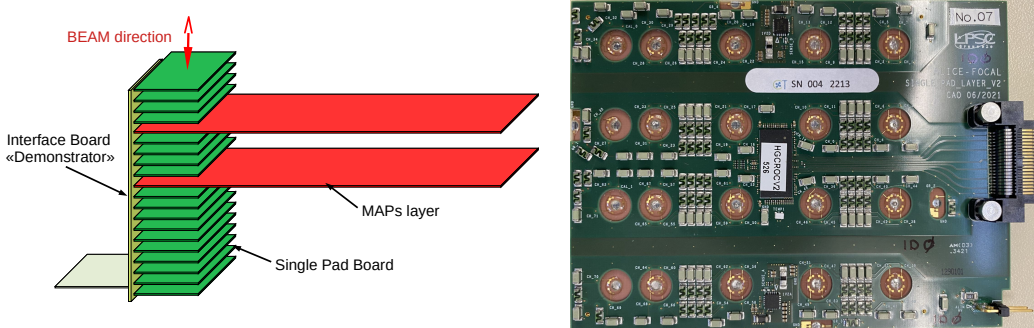


Figure 7.7: Left: Focal prototype tower composed of 18 single-pad boards with a test-beam dedicated interface board. Right: picture of one single-pad used in the FoCal tower prototype [168].

We can focus on a single pad board, that corresponds to one-fifth of the final full-scale 5-pad-layer board to address the calibrations necessary to use the prototype.

The single pad boards were evaluated on a dedicated setup composed of a [FPGA](#) development kit, a test interface board to accommodate the interconnection between the [FPGA](#) Mezzanine Card (FMC) of the kit, an expansion card that attaches to a system directly with pins for other boards, and the single pad board connector and a multichannel charge injector, which mimics a charge deposit up to about 10 pC.

In the following, the calibration procedures for a single board will be presented: the tests have been done using the development kit, which has allowed the implementation of the software for running the calibrations, that are the same as those executed by the prototype.

The results of the calibration procedure applied to a single pad board will be illustrated in the next Section 7.3. Then the results obtained at the test beam campaign at CERN with the prototype will be shown.

7.3 HGCROC-V2 calibration procedure

The calibration procedure is necessary to have a functional sensor: the **ADC** and the **TOT** need to be calibrated, in order to obtain the best accuracy and stability to take data. The assessment used by the **ΩMEGA** group for the **CMS** Collaboration [175] has been followed but with the difference that the **HGCROC** has been characterised in a realistic framework (data taking case) and not only on test-bench. In the following, some parameters used for the calibration are derived from **ΩMEGA** group choice and documentation [175].

The calibration is handled by setting several ReadOut Chip (**ROC**) parameters of the **HGCROC** that are either channel specific, or related to a group of channels or even to a complete half chip. The card is divided into two halves corresponding to the left (L) side, containing channels from 0 to 35, and the right (R) side with channels from 36 to 71. The two sides of the card may indeed have different responses because they come from different Si-PAD glued together. These parameters are programmed in the configuration files of the **HGCROC-V2** card. Part of these parameters are shown in Fig. 7.8.

The calibration procedure has to be done for all cards before the data acquisition either with the internal injection or with the beam. It consists of five steps:

1. pedestals calibration:
 - (a) offset calibration;
 - (b) dynamic range calibration;
2. timing measurement;
3. charge injection response;
4. Time Of Arrival and Time Over Threshold calibrations;

The table shown in Fig. 7.8 refers to the parameters of the shaper and these values are set during the definition of the calibration of the **ADC**.

The offset and the dynamic range calibrations consist of a baseline estimation and therefore they are done without charge injection. This is because if we modify the electronic parameters, we also affect the chip's reaction to an input signal.

7.3. HGCROC-V2 calibration procedure

Name	# bits	I2C Sub-block / sub-address	Description
Probe_noinv	1	Channel-wise	Non inverter shaper output probe ("1" = selected)
Probe_inv	1	Channel-wise	Inverter shaper output probe ("1" = selected)
Ref_dac_inv<4:0>	5	Channel-wise	Local 5b-DAC for ADC pedestal tuning
ON_rtr	1	Global-analog	"1" = enable shaper amplifiers bias
Ibi_sk<1:0>	2	Global-analog	S-K amplifier input stage current
Ibo_sk<5:0>	6	Global-analog	S-K amplifier output stage current
S_sk<2:0>	3	Global-analog	S-K amp Miller cap. $<0> = 50\text{fF}$, $<1> = 100\text{fF}$, $<2> = 200\text{fF}$
Ibi_inv<1:0>	2	Global-analog	Inverter amplifier input stage current
Ibo_inv<5:0>	6	Global-analog	Inverter amplifier output stage current
S_inv<2:0>	3	Global-analog	Inverter amp Miller cap. $<0> = 50\text{fF}$, $<1> = 100\text{fF}$, $<2> = 200\text{fF}$
Ibi_noinv<1:0>	2	Global-analog	Non Inverter amplifier input stage current
Ibo_noinv<5:0>	6	Global-analog	Non Inverter amplifier output stage current
S_noinv<2:0>	3	Global-analog	Non Inverter amp Miller cap. $<0> = 50\text{fF}$, $<1> = 100\text{fF}$, $<2> = 200\text{fF}$
Ibi_inv_buf<1:0>	2	Global-analog	Inverter buffer input stage current
Ibo_inv_buf<5:0>	6	Global-analog	Inverter buffer output stage current
S_inv_buf<2:0>	3	Global-analog	Inverter buffer Miller cap. $<0> = 100\text{fF}$, $<1> = 200\text{fF}$, $<2> = 400\text{fF}$
Ibi_noinv_buf<1:0>	2	Global-analog	Non Inverter buffer input stage current
Ibo_noinv_buf<5:0>	6	Global-analog	Non Inverter buffer output stage current
S_noinv_buf<2:0>	3	Global-analog	Non Inverter buffer Miller cap. $<0> = 100\text{fF}$, $<1> = 200\text{fF}$, $<2> = 400\text{fF}$
Rc<1:0>	2	Global-analog	Shaping time adjustment
Inv_vref<9:0>	10	Voltage references	Inverter shaper global reference
Noinv_vref<9:0>	10	Voltage references	Non Inverter shaper global reference

Figure 7.8: The table contains a part of the ROC parameters of the HGCROC-V2 card.

7.3.1 Pedestals calibration

In an ideal world, if there is no signal or no charge injection, the average values of an **ADC** output should be equal to zero; in reality, there is always a residual noise due to the electronics (e.g. cables, internal or external amplifiers, nonideal power supplies...). This undesired and random signal is called a pedestal and affects all electrical systems, generating a signal baseline.

Figure 7.9–left shows the **ADC** distributions before the pedestal calibration for all channels as a function of the event number, that is the number of taken events.

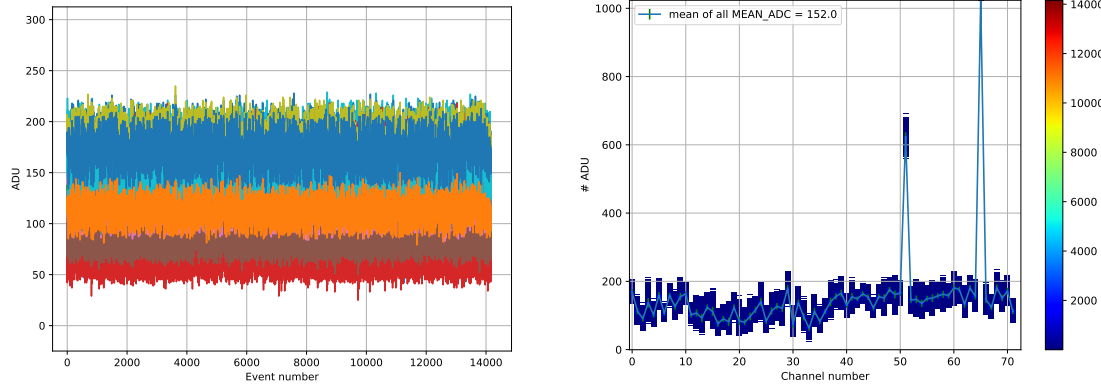


Figure 7.9: ADC distributions before the pedestal calibration. Left: ADC mean distributions for all the channels as a function of the event number. Right: average of the ADC mean distributions as a function of the channel number.

The pedestal value for a given channel is stable with the number of events, thus it is possible to take the average of the **ADC** distributions. This result is reported in Fig 7.9–right. The channels are characterised by different baselines: the means of the **ADC** channels spread from 50 to 220 **ADC** units (ADU).

Channels 51 and 65 are characterised by extremely high **ADC** means, hence they will be discarded in the next discussions.

The aim of the pedestal calibration is to push the baseline close to 0; it involves two steps: the **offset tune**, in which the pedestals of all the channels are equalised, reducing their dispersion; and the **dynamic range tune**, in which the average value of the baseline is reduced as much as possible.

Offset calibration

In order to reduce the spread among the channels, it is possible to play with the HGCROC-V2 parameters, reported in Fig. 7.8 and in particular, with the channel-wise 5b-DAC (**Ref_dac_in** in Fig. 7.8): a 5-bit Digital to Analog Converter which allows to trim the dispersion of every channel. Establishing this trimming for every channel corresponds to defining and applying a compensation current with the 5b-DACs for the leakage currents coming from the analogue part. The effect of this compensation procedure is shown in Fig. 7.10.

The dispersion among the channels is strongly reduced, however, the average **ADC** values are still high: it is necessary to push the baseline close to zero. In order to do that, the dynamic range calibration has to be applied.

7.3. HGCROC-V2 calibration procedure

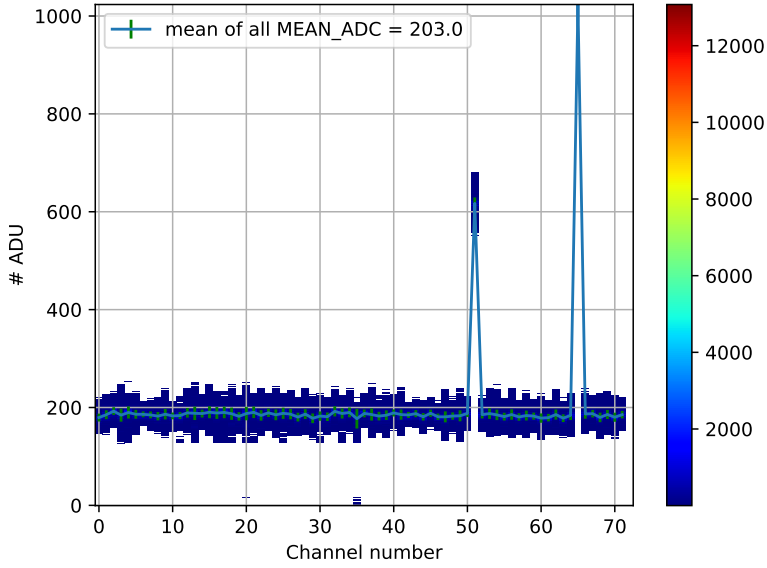


Figure 7.10: Distributions for all the channels, after the pedestal calibration. Average of the ADC distribution as a function of the channel number.

Dynamic range calibration

The shaper, shown in Fig. 7.4, takes care of the frequency response of an input signal, limiting its duration, but it also allows to act on the level of the [ADC](#) output: varying the inverting and the non-inverting reference voltages of the shaper, it is possible to reduce the mean value of the [ADC](#) pedestal.

Therefore, the dynamic range scan consists in estimating the values of the non-inverting reference voltage ([Noinv_vref](#) in Fig. 7.8) and of the inverting one ([Inv_vref](#) in Fig. 7.8) of the shaper to reduce the baseline level. These two voltages are set through two global 10-bit Digital to Analog Converters (10b-DACs) and this permits to test of different inverting and non-inverting reference voltages for each half of channels. Once the [Inv_vref](#) ([Noinv_vref](#)) is set for every channel, the median of the pedestals, that is the median of the means for all channels, related to that inverting reference voltage (non-inverting reference voltage) is evaluated. Figure 7.11 shows the medians as a function of $V_{\text{ref}}^{\text{Inv}}$ ($V_{\text{ref}}^{\text{NoInv}}$).

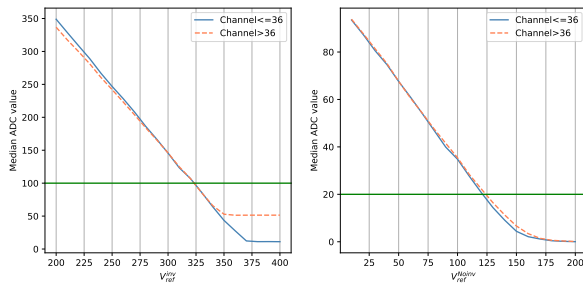


Figure 7.11: Left: median ADC value as a function of inverting voltage. Right: median ADC value as a function of non-inverting one.

The choice of the median instead of the average is because the results obtained with the median are less affected by not working channels. The Ω MEGA group had measured the two median values corresponding to 100 (20) shown in green, used for finding the intersection

between the reference value and the median distribution, determining the best values for the inverting and the non-inverting voltages. Once defined, the inverting and non-inverting reference voltages and modified the corresponding parameters, the effect of the dynamic range scan can be seen in Fig. 7.12.

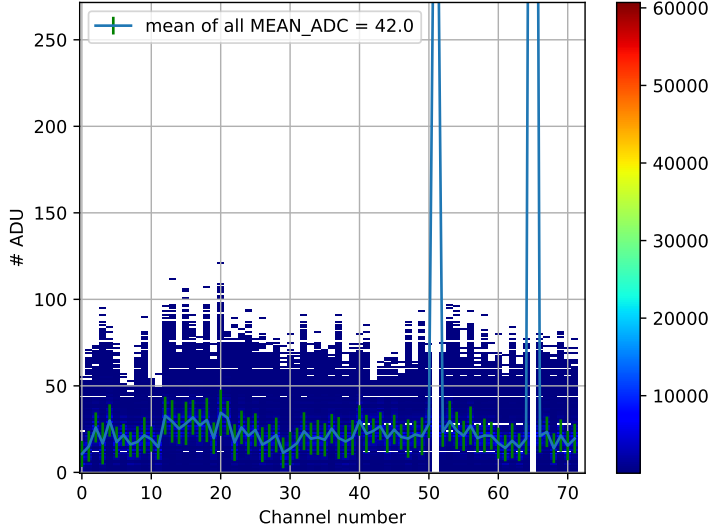


Figure 7.12: Effect of the dynamic range calibration. The mean of the ADC mean distribution for all the channels.

The pedestals are pushed down to zero and the average of the ADC distribution is now around ~ 40 . Since after these two procedures, the baseline of the ADC channels is well defined, it is possible to start to inject charge and evaluate the effect of it.

7.3.2 Timing measurement

Due to all the electronic components and cable lengths and connections, there is an unknown delay between the signal input corresponding to the particle, i.e. the trigger, and the instant given by the clock in which the signal has to be read. The trigger signal is sent to the **HGCROC** and the aggregator, but the propagation time towards them is different and unknown; therefore, it is important to estimate it and understand what receives the signal first. It is known that the propagation time towards the **HGCROC** is shorter than the time towards the aggregator: once the aggregator receives the trigger input, the **ADC** has already encoded and saved the data in the circular buffer. The timing calibration is necessary to evaluate the latency between the trigger and the aggregator request to read the data in the buffer, sort through it and access the correct event of interest. This procedure allows to visualize the arrival and the evolution of the signal.

The entry to be transmitted to the aggregator is extracted from the circular buffer with a programmed offset. This delay or offset, expressed in counts of machine clock cycles (**LHC** clock) is an integer stored in a variable called $L1offset$. The trigger is sampled at the **LHC** clock frequency, that is $40 \text{ MHz} = \frac{1}{\text{BC unit}}$, where the **BC** unit is the period between 2 **BCs** (bunch-crossings): 25 ns. To find in the buffer the event of interest, that corresponds to the maximum of the signal, a window of time in **BC** units is defined to go through the memory.

7.3. HGCROC-V2 calibration procedure

It is possible to measure the delay corresponding to the maximum of the signal. It is expressed by two parameters: the so-called *calib2trig*, expressed in **BC** units and the *adcphase*, expressed in 1/16 **BC** units. The procedure consists of two steps: initially a coarse timing scan is executed to determine the **BC** corresponding to the trigger signal, then a finer delay scan is done to define more precisely the time. The average **ADC** values of every channel and the corresponding timestamps are collected. From them, the **ADC** mean values as a function of the time are produced. The coarse timing scan allows to define the *calib2trig* value and the result of this procedure is shown in Fig. 7.13–left: the maximum of the signal is at 400 ns, e.g 16 **BCs**.

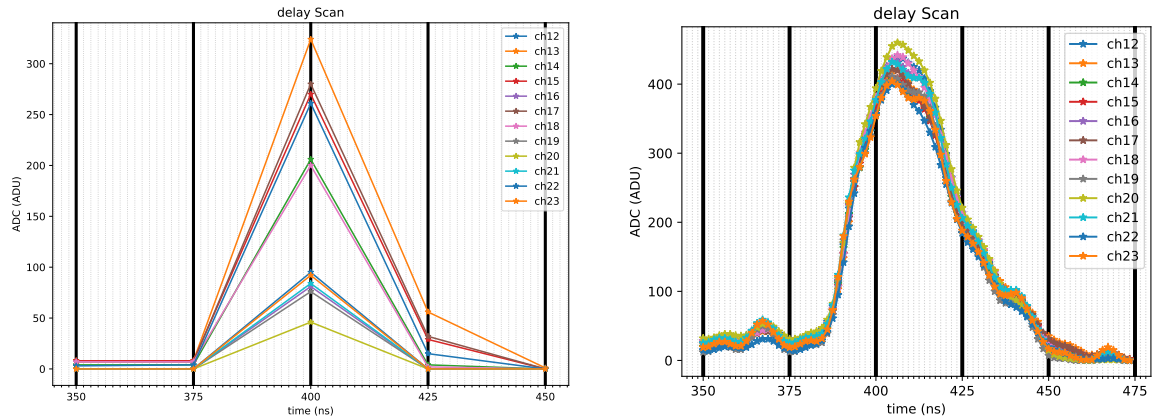


Figure 7.13: ADC mean distribution as a function of the time for channels from 12 to 23. Left: ADC mean distribution for the coarse calibration. Right: ADC mean distribution for the fine calibration.

The coarse delay measurement is improved with the fine one, in which the time axis is segmented in 1/16 **BC**: in fact, the maximum of the trigger signal does not lie to a precise **BC**, but it is usually wider and may drop between 2 **BCs**. Figure 7.13–right shows the fine delay scan procedure in 1/16 **BC** units, from which it is possible to extract the precise values of the *calib2trig* and *adcphase*. After the delay scan calibration, the obtained values are set in the configuration parameter of the **ASIC**.

The results of the delay scan procedure have been obtained using the internal injection of the **HGCROC**, which permits to decide when sending the trigger, setting the initial parameter in the **FPGA** aggregator; this has allowed the implementation of the algorithm to determine the **BC** corresponding to the trigger signal to be saved in the **HGCROC** parameters. In real test beam conditions, the procedure is more complicated because it is not possible to determine the moment of trigger is sent.

7.3.3 Charge injection response

The charge injection is handled by the DAC Calibration injection, shown in Fig. 7.8. It is possible to test different values of charge: the *low range* that corresponds to a charge from 0 to 0.5 pF and the *high range* from 0 to 8 pF.

The calibration consists of executing a charge scan, and evaluating the response of all the channels to different injection values. This procedure permits to verify the correct behaviour of the sensor and check if there are any issues related to the various calibrations.

7.3.4 Calibration of the TOA and of the TOT

The response of a discriminator is dependent on the voltage threshold selected to accept or reject an input signal. Therefore, it is crucial to carefully evaluate and set the threshold value to equalize the responses across different channels. In the case of the HGCROC, the calibration of the **TOA** and **TOT** involves determining the optimal voltage thresholds to ensure that all channels respond similarly to a given input. This calibration is essential for achieving a stable and consistent sensor response across various inputs. In order to determine the voltage thresholds of the Time of Arrival and the Time over Threshold, the charge injector of the HGCROC is used. The **TOA** and the **TOT** have a different response to charge: the **TOT** activates only from 100 fF. The calibration procedure of the two discriminators is the same, and it will be illustrated for the **TOA**; the only difference is the chosen value of the injected charge. For the **TOA** calibration, an injection of 400 DAC units was applied, while for the **TOT** an injection of 600 DAC units was used. This value was selected based on the results obtained by the Ω mega group.

The charge injected cannot be induced in all channels at the same time because of crosstalk effects and noise due to neighbouring cells; hence, the first step of the calibration algorithm is to select the channels to be calibrated at every iteration. The calibration is an iterative procedure, applied in batches of four channels at a time (two for every side of the card, selecting channels that are as far away as possible from each other) until all 72 cells are tested. After injecting the charge into the selected channels, a scan of various voltage thresholds for the **TOA** is conducted, as illustrated in Fig. 7.14–left.

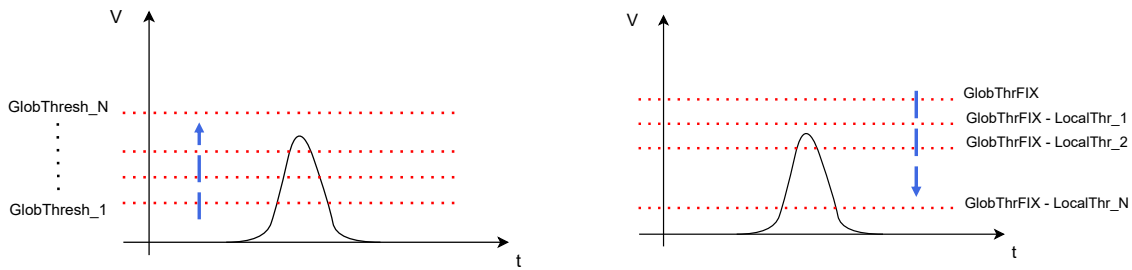


Figure 7.14: Left: Sketch that describes the global thresholds scan. Right: Sketch that describes the local thresholds scan. The blue arrow indicates the direction.

For each channel, an efficiency plot is generated based on its response to the injected charge. This plot indicates the threshold value up to which each channel is able to trigger the input signal. The efficiency plot, also called *s-function*, is reported in Fig. 7.15 as a function of the tested threshold. A global threshold value for each side of the card left and right and common to all channels is extracted in this first phase of the calibration. It corresponds to the threshold of the channel that deactivates as the last one. The no working channels, always or never activated or oscillating, are not included in the evaluation of the global threshold for the two sides. This quantity is encoded over 10-bit DAC and it is a **ROC** parameter (see Sect. 7.3) of the **HGCROC**.

From this scan the global thresholds for the two sides of the card are defined. At this stage, it is necessary to trim each channel relative to the chosen global threshold value using the local thresholds. The **HGCROC-V2** allows for channel-wise parameter adjustments using

7.3. HGCROC-V2 calibration procedure

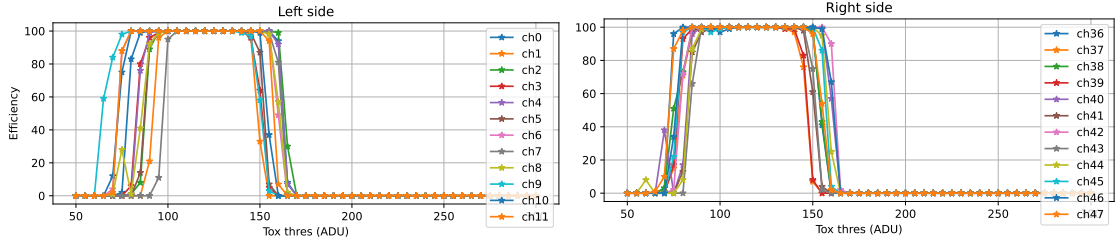


Figure 7.15: Efficiency curves as a function of global thresholds for different channels and for the two sides of the HGCROC, before the calibration procedure.

a 5-bit setting to define the local thresholds. The purpose of these local thresholds is to reduce dispersion among the channels, ensuring that they activate or deactivate at the same threshold value, as can be seen in the right panel of Fig. 7.14. A procedure similar to the one used for evaluating the global threshold is used, in this case, a scan over 32 threshold values is executed. Once all the local thresholds are estimated, the trim value for every channel is saved in the settings of the **ASIC**. At this point it is possible to check the effect of the local thresholds and of calibration. Figure 7.16 shows the efficiency plot for a few channel of the **TOA**, after the calibration procedure.

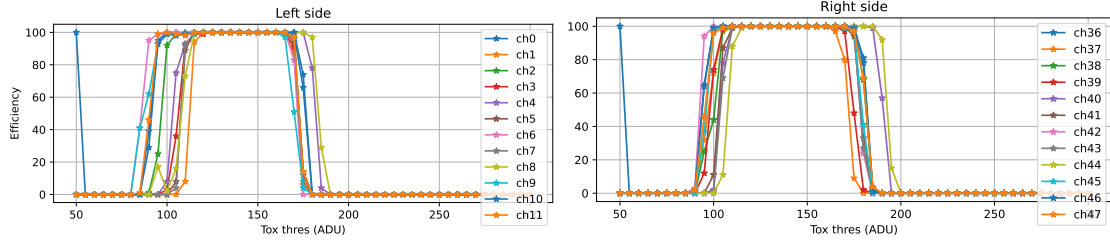


Figure 7.16: Efficiency as a function of global thresholds for different channels and for the two sides of the HGCROC after the calibration.

The response of all the channels are shifted to higher voltage values, as an effect of the local threshold trim. There seems to be a little reduction of the dispersion among the channels: the channel deactivate around the same voltage. The same procedure is repeated for the Time over Threshold, but with an injection value of 600.

7.4 Beam test configuration and calibrations

The FoCal underwent an extensive testing period in 2022. The beam test campaign was conducted at CERN facilities, utilizing particle beams provided by the PS and the SPS. The two facilities allow to testing of different energies, different beam compositions and as a consequence various characteristics of the prototype. The PS can provide electron, positron and hadron beams up to 26 GeV [176] while at the SPS the energies can reach as high as 450 GeV [177]. The first test beam, held at PS, was mainly focused on testing the parameters of the pad sensors and the FoCal-H prototype was included. In the next test beams, held first at the SPS and then at the PS, all the sub-systems utilized the same triggering system which enabled the tests for combined events in FoCal-E and FoCal-H.

The trigger signal was given by the coincidence of four at the PS (three at the SPS) PhotoMultipliers (PMs), located in front of the prototype along the beam axis. The installation of the prototype at CERN PS T9 beamline is shown in Fig. 7.17. The first procedure done

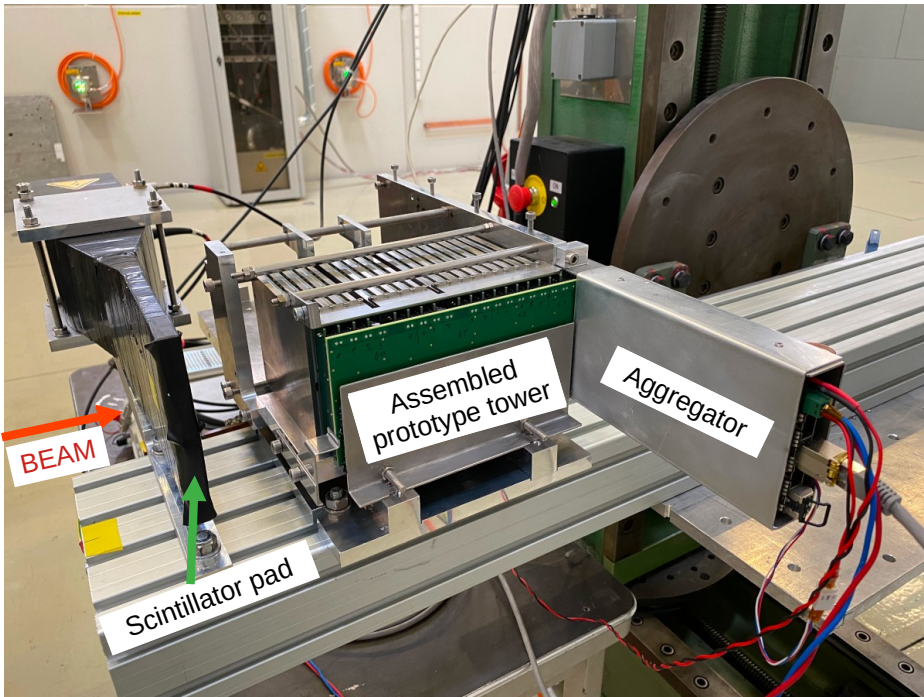


Figure 7.17: Picture of the FoCal tower prototype installed on the T9 beamline at the CERN PS.

was the **timing measurement** (see Sect. 7.3.2) to estimate the delay due to the electronics and determine the time of arrival of the trigger, to extract it from the buffer. In order to determine the window of time in which looking for the trigger it is necessary to evaluate the effects induced by the cables. With respect to the procedure presented in the calibration Sect. 7.3.2, where the internal injection is used as a trigger, now the input signal is the beam, triggered by the coincidence of 4 (3) of PMs, therefore it is essential to take into account the delay due to the electronics chain, shown in Fig. 7.18.

Without beam, it is possible to simulate the coincidence by injecting a pulse in place of the PMs and measuring the delay between the pulse's falling edge and the trigger out's rising edge using an oscilloscope. The determined delay is then used to set the parameters

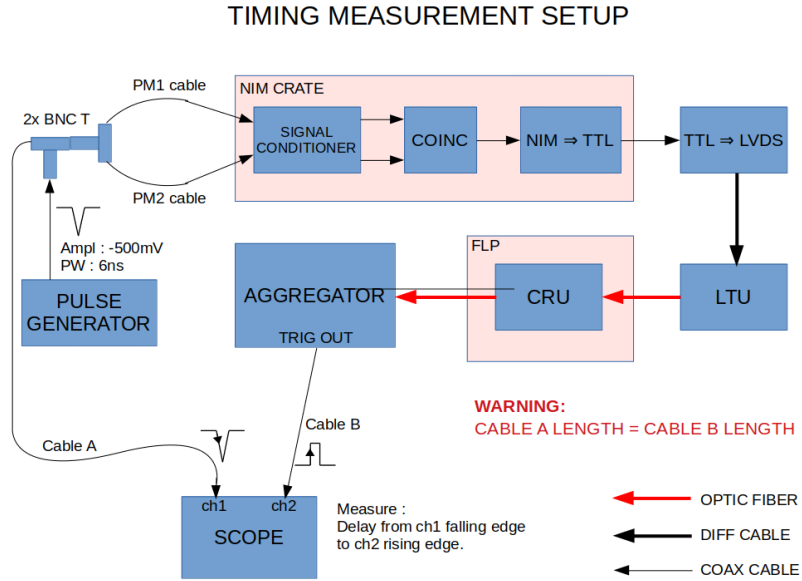


Figure 7.18: Test beam setup used to determine the cables delays to the aggregator. Figure courtesy of D. Tourres.

of the aggregator to account for the external delay, estimate the timing window in which the trigger signal is expected, and run the **timing calibration** (see Sect. 7.3.2).

7.4.1 ADC response

During the test campaign at CERN PS T9 energies, the FoCal-E Pad prototype was irradiated with hadron beams with energies from 5 to 15 GeV, corresponding to MIPs, thus, only the **ADC** of the HGCROC contributed to the energy measurement since the charge generation in the sensor is too low to activate the **TOT** [178].

Standard signal processing techniques were applied to separate the charge deposited by MIPs from contributions of the noise. The two main contributions to the noise were addressed as follows: the pedestal, which results from the combination of the electronics noise in the amplification circuit and the intrinsic fluctuation of the silicon sensor signals, was treated for each channel by fitting the average response in the **ADC** with a Gaussian. A second, smaller contribution to the noise results from phenomena equally affecting all the channels of a layer, namely the Common Mode Noise (CMN). The resulting shape of the distribution can be described with a Landau distribution that models the energy deposition in the detector material convoluted with a Gaussian distribution describing the detector's resolution [179]. Figure 7.19 shows an example of a **MIP** distribution for a specific **ASIC**.

It is possible to distinguish the **MIP** peak from the pedestal, thanks to the subtraction of the per-channel pedestal and of the common noise of all the other channels.

Once the signal due to MIPs was correctly registered, the following characterisation of the **ADC** was done, in order to improve the **PADs** response:

- **voltage scan:** different sensor bias voltages are tested to see if it can affect the **ADC**

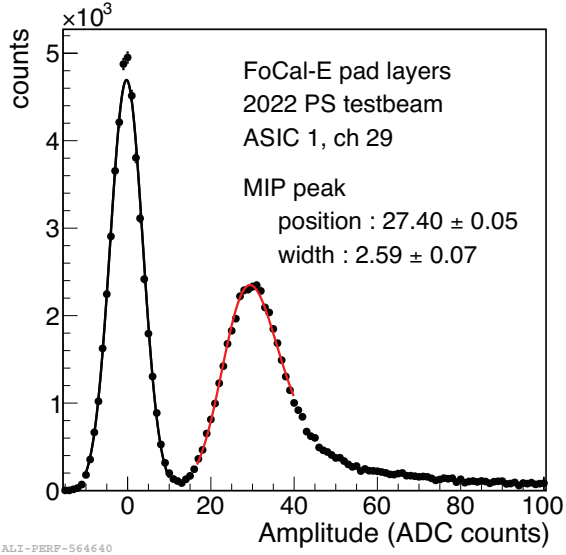


Figure 7.19: MIP peak measured from a single channel of a FoCal-E pad layer in PS 2022 test beam [179].

response;

- **gain scan:** different gains are compared changing the parameters of the preamplifier and of the shaper;
- **position scan:** the answer of all the channels is tested varying the position of the beam and verifying that the **MIP** is visible in all the channels.

Voltage Scan

In order to test the separation between the **MIP** peak and the pedestal, a sensor bias voltage (HV) scan from 0 V to 500 V has been performed. When the sensor is fully depleted, that is when the depletion region thickness equals the sensor thickness, the position and the width of the peak are expected to not change anymore. The results of the voltage scan are shown in Fig. 7.20: the left plot shows the pedestal and the **MIP** distribution obtained for different HV values, while the right figure contains the **MIP** peak position and the peak width in **ADC** unit as function of the voltage (V). Starting from 300 V the peak remains constant as well as the collected energy. The chosen voltage was 500 V.

Gain Scan

As shown in Fig. 7.2, the sensor is characterised by a pre-amplifier and by a Sallen-Key **SH**; varying the gain of the **PA**, that is the feedback resistance and capacitance, and the capacitance of the **SH** allows to see an effect on the **MIP** and to find the best configuration to recognize it. Various settings have been tested, for a total of 24 combinations, and compared with the default one (that is $R_f = 100 \text{ k}\Omega$, $C_f = 300 \text{ fF}$, $C_{f_Sk} = 100 \text{ fF}$). Figure 7.21 shows the **ADC** distributions obtained with different gains. The goal was to choose settings which lead to good separation between the **MIP** signal and noise. As a result of the study, in particular, the setting selected was the one with $R_f = 50 \text{ k}\Omega$, $C_f = 200 \text{ fF}$ and $C_{f_Sk} = 100 \text{ fF}$. This one was selected and used during the **PS** test beam.

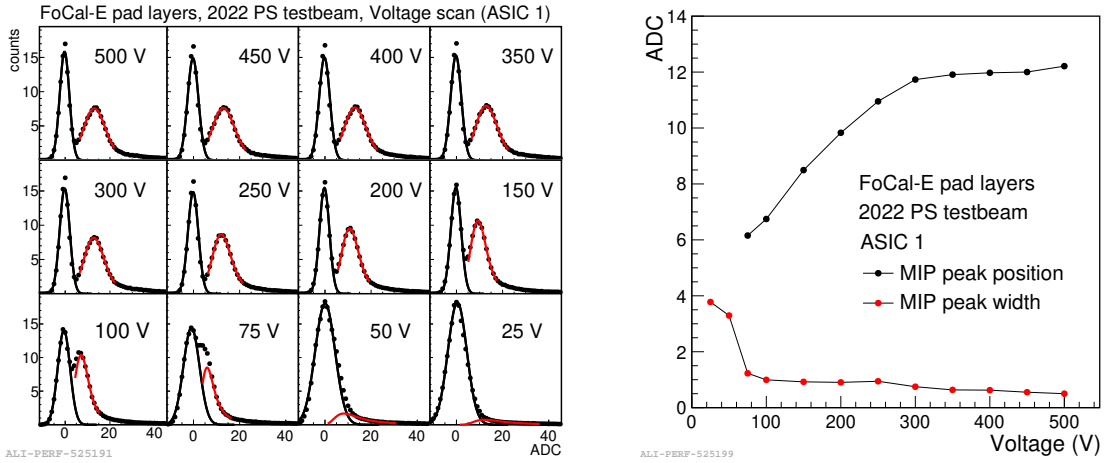


Figure 7.20: Left: ADC distributions as a function of the ADC channel for different voltage values. Right: MIP peak position (full black dot) and MIP peak width (full red dot) as a function of the voltage [179].

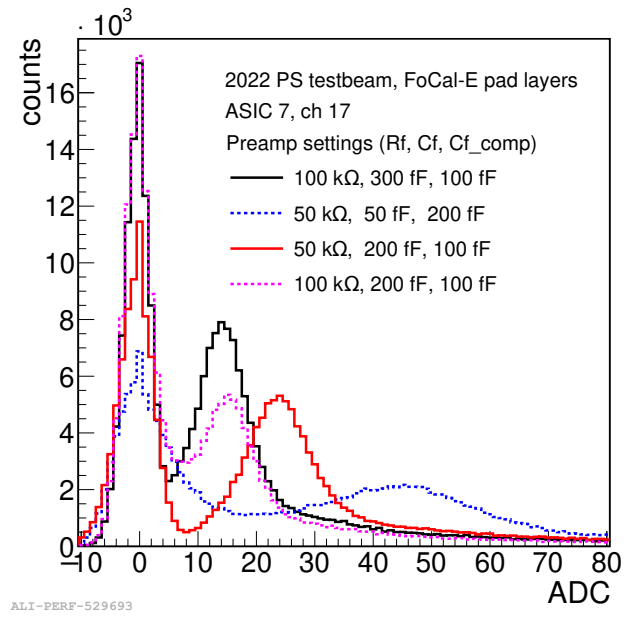


Figure 7.21: ADC response obtained using four different gains for a specific ASIC and channel [179].

Position Scan

Once the best configuration in terms of voltage and gain was defined, the scan of every channel was done. The table under the prototype was moved to “variate” the beam spot and to test the uniformity of the response: ensuring that a **MIP** signal could be seen in every channel. Figure 7.22 shows the **ADC** distribution with the best **MIP** peak of a specific layer (**ASIC**) for every channel.

Position scan, 2022 PS testbeam, FoCal-E pad layers

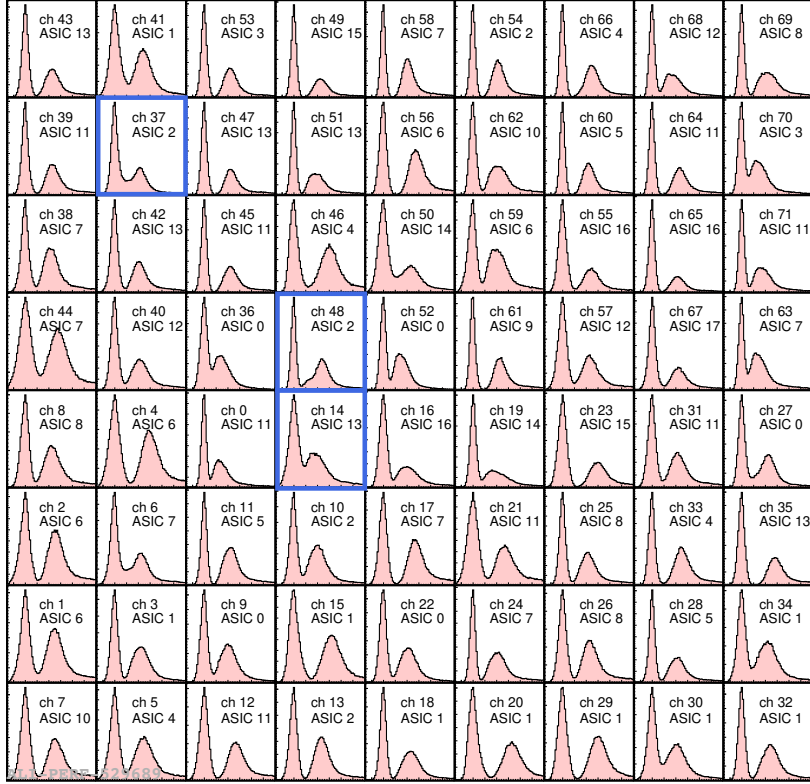


Figure 7.22: Channel scan of MIP’s signal in various ASICs. The squares indicated channels with anomalous MIPs.

It is possible to reconstruct a **MIP** in every channel in different layers of the prototype, although the responses are not the same for every **ASIC**. It is possible to spot differences at a glance for example in channels: 14, 48 and 37. This may be due to malfunctions in the channel or issues with the signal extraction procedure.

7.4.2 TOA and TOT response

MIP measurements were repeated using data collected at the **SPS** beamline to investigate the detector’s behavior at higher energies. When the beam energy becomes too high, the **MIPs** are no longer detected, and the **ADC** response saturates. The **ADC** response for an **ASIC** with the beam spot centred in pad channel 52 is reported in Fig. 7.23. The **ADC** saturation is visible because all its channels are activated and it is not possible to recognise a **MIP** anymore. This confirms the necessity of using the **TOT** for a higher value of charge (hadrons and electrons).

During the **SPS** and **PS** campaigns in September and October, the pixel layers were

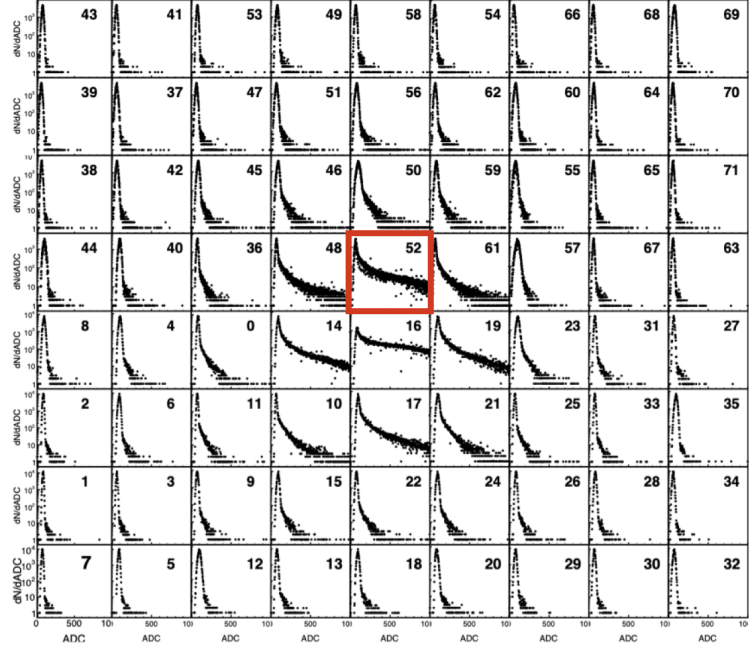


Figure 7.23: ADC response at higher energy. The prototype was irradiated with electrons. The beam spot is in channel 52, indicated by a red square.

included in the measurements and the **FoCal-E DAQ** was based on the ALICE O2 [180] system, providing coherent treatment of the pixel and pad layers. With the occurrence of a coincidence between the two scintillators placed in front of the setup, as shown in Fig. 7.17 the trigger board simultaneously sends out busy signals for the **FoCal-H CAEN** boards and provides an external trigger for the Local Trigger Unit (LTU).

TOA and TOT calibration effects

During the **SPS** campaign the **TOA** and the **TOT** were enabled. The calibration procedures presented in Sect. 7.3.4 have been used. The results related to the **TOA** calibration procedure for one of the layer of the prototype (**ASIC 0**) are illustrated. Figure 7.24 shows the efficiency plots for various channel as a function of the global threshold.

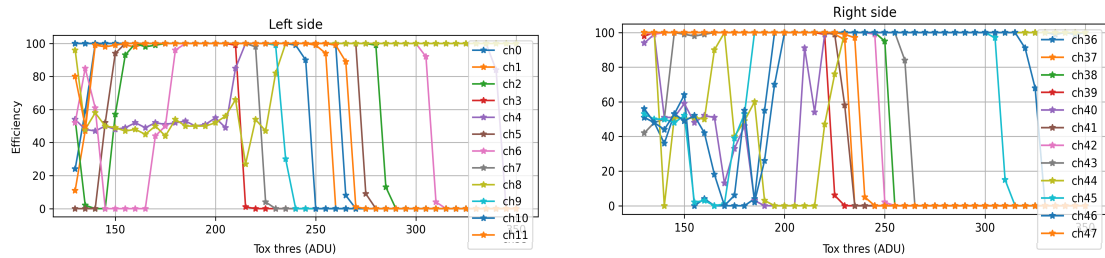


Figure 7.24: Efficiency curves as a function of the global thresholds for different channels and for the two sides of one ASIC of the prototype, before the calibration procedure.

The spread among all the channels is quite large. In addition, there were channels that were always activated or deactivated. This affected the result of the calibration: the trimming with the local thresholds was not enough to reduce the dispersions and to group the channel around a similar global threshold value. The results, obtained after having

applied the global and the local thresholds, are reported in Fig. 7.25. The efficiency plots

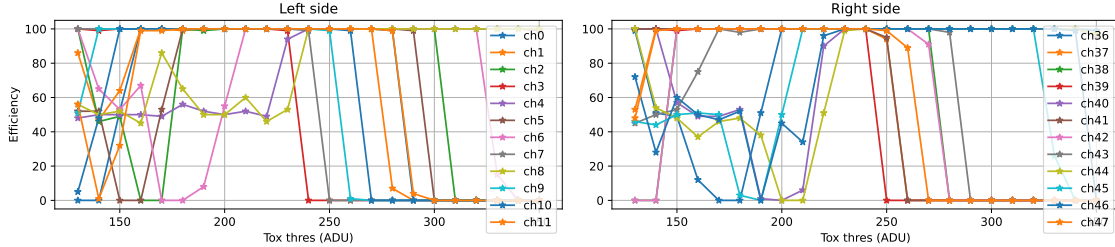


Figure 7.25: Efficiency curves as a function of the global thresholds for different channels and for the two sides of one ASIC of the prototype, after the calibration procedure.

of every channel were pushed towards higher global thresholds, but the dispersion among the channels was not recovered. The same procedure of calibration was done for the **TOT** too.

During the **SPS** data collection, enabling the **TOA** and **TOT** with their settings, as defined by the calibration procedure (see Sect. 7.3.4), led to an unexpected and undesired distortion of the **ADC** distributions. The average baseline of the **ADC** was extremely high, around 100 for all the channels, as shown in Fig. 7.26-right. although the pedestal calibration (see Sect. 7.3.1) has been already executed.

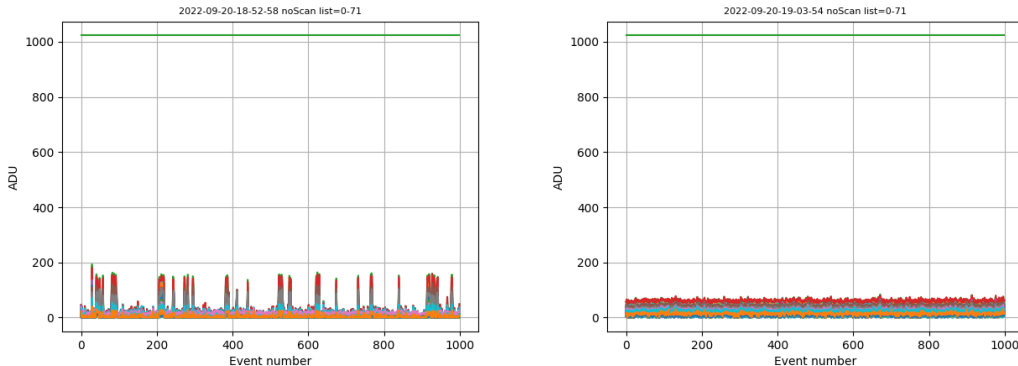


Figure 7.26: Left: ADC pedestals affected by the activation of the **TOA**. Right: ADC pedestals after the variation of **TOA** thresholds.

Figure 7.26-left shows a not uniform **ADC** pedestal distribution of every channel, characterised by random spikes: this was due to a supplementary noise induced by the activation of the **TOA**. This background was not due to particles going through the sensor, but it was a digital noise internal to the **ASIC**.

This problem was impacting the data collection process, so I manually increased the global threshold of the **TOA** to mitigate the amplification of internal noise and restore the pedestals to an acceptable level. The decision to adjust the **TOA** threshold was based on the fact that precise timing measurement from the **TOA** was not expected to be critical for our needs.

This last problem and the difficulties encountered in the **TOA** and **TOT** calibrations are some of the limitations of the **HGCROC-V2**, also highlighted by the **Omega** collaboration. The new **HGCROC-V3** foreseen for the next prototype versions will be characterised by

7.4. Beam test configuration and calibrations

internal noise and will offer a wider range of local thresholds values, which can help to reduce the spread among the channels.

Chapter 8

Conclusions

The γ^{iso} -hadron correlations provide excellent constraints on the kinematics of the scattered parton, and therefore remarkable insight into modifications of the parton in Pb–Pb collisions. However, they remain quite rare in high-energy heavy–ion collisions due to the relatively low cross section of prompt photons compared to decay photons, which made their measurement much more complicated in AA collisions.

We were able to measure the isolated photon-hadron correlations in a p_T^γ range between $18 < p_T^\gamma < 40$ GeV/ c with hadrons with transverse momentum $p_T^{\text{hadr}} > 0.5$ GeV/ c in different centrality bins in Pb–Pb collisions at $\sqrt{s_{\text{NN}}} = 5.02$ TeV. This measurement completes the set of isolated photon-hadron correlation measurements performed by the **ALICE** Collaboration during Run 2. Previous measurements in pp and p–Pb collisions demonstrated the feasibility of such analyses. Our study confirms the viability of the γ^{iso} -hadron correlations in Pb–Pb collisions across three centrality intervals: 0–30%, 30–50%, and 50–90%. The primary observation that we can make is the significant suppression of hadron yield in central events compared to peripheral events and pp NLO simulations. Our findings indicate also a centrality-dependent energy loss, evidenced by the stronger suppression in central collisions relative to peripheral ones. This centrality ordering is also evident when comparing our results to the pp pQCD NLO baseline.

All these observations are well described by theoretical models such as CoLBT and pQCD NLO with quenching, but the current uncertainties prevent a clear distinction between these models.

Our results have been compared with the measurements by the **CMS** Collaboration, by the **PHENIX** experiment and by the **STAR** Collaboration. Although they use different analysis selections, the trends in the same z_T intervals are in agreement and consistent with a larger suppression of high- p_T hadrons at high- z_T .

While this measurement is not intended as a precision study, it serves as an extensive benchmark for Run 3 and upcoming Run 4 (2030–2032) studies. With future data sets offering larger statistics, more accurate correlation measurements will be possible, allowing for more precise investigation of different centrality bins and access to lower p_T^γ values. The increased data will enable differential studies, such as examining correlations in different event plane regions. For instance, in the 30–50% centrality class, where elliptic flow is expected

to be more pronounced, comparisons between in-plane and out-of-plane correlations could be made. Moreover, our results provide a base framework also for photon-tagged jet studies during Run 3 and Run 4, extending our knowledge about jet quenching and obtaining more quantitative results about the amount of jet energy loss induced by the medium.

The [FoCal](#) calorimeter which is a future upgrade for the [ALICE](#) experiment, underwent extensive testing in 2022. The pad sensor performance of the electromagnetic calorimeter is presented here. A comprehensive overview of the pad sensor calibration procedures was presented, alongside selected results from various test beams, providing insights into the overall performance of [FoCal-E](#). This included evaluations of readout parameter selection, bias voltage, and other factors. Clear [MIP](#) signals were successfully measured with the tested sensors. Nevertheless, further investigation is needed to understand the [TOA](#) and [TOT](#) properties and their interactions with the [ADC](#).

While writing this Thesis, additional test beams were conducted, and in May 2024, the FoCal upgrade was officially approved, with the Technical Readiness Document published. This upgrade, scheduled for Run 4, will enable measurements of isolated photon yields and correlations between isolated photons and hadrons at forward rapidity. These observables are directly sensitive to gluon density and saturation effects. Such measurements will allow testing of the x and Q^2 dependence of [QCD](#) evolution in multiple complementary ways. Additionally, jet quenching at forward rapidity in Pb–Pb collisions will be explored, providing a means to map the [QGP](#) density as a function of rapidity.

Appendix A

Data run numbers

This Appendix lists the run numbers and the trigger selection for the different periods of data.

A.1 Data periods

Pb–Pb collisions

- Pb–Pb LHC15o_pass2, trigger: MB (AliVEvent::kINT7), L1- γ (AliVEvent::kEMCEGA) with threshold at 10 GeV.

List of runs:

- 94 runs: 246945, 246928, 246846, 246845, 246844, 246810, 246809, 246808, 246807, 246805, 246804, 246766, 246765, 246760, 246759, 246758, 246757, 246751, 246750, 246434, 246424, 246392, 246391, 246390, 246272, 246271, 246225, 246222, 246217, 246115, 246113, 246089, 246087, 246053, 246052, 246042, 246037, 246003, 246001, 245963, 245954, 245952, 245949, 245705, 245702, 245700, 245554, 245545, 245544, 245543, 245542, 245540, 245535, 245507, 245505, 245504, 245501, 245497, 245496, 245454, 245453, 245446, 245441, 245439, 245411, 245410, 245409, 245407, 245401, 245397, 245396, 245353, 245349, 245347, 245346, 245345, 245343, 245259, 245233, 245232, 245231, 245152, 245151, 245146, 245145, 245068, 245066, 245064, 244983, 244982, 244980, 244975, 244918, 244917.

- Pb–Pb LHC18q(r)_pass3, trigger: MB (AliVEvent::kINT7), AliVEvent::kCentral (0-10%),

AliVEvent::kSemiCentral (30-50%); L1- γ (AliVEvent::kEMCEGA) 2 thresholds: high threshold at 10 GeV (0-50%); low threshold 5 GeV (50-90%).

- LHC18q, 115 runs: 296623, 296622, 296621, 296619, 296618, 296616, 296615, 296594, 296553, 296552, 296551, 296550, 296549, 296548, 296547, 296516, 296512, 296511, 296509, 296472, 296433, 296420, 296419, 296415, 296414, 296383, 296381, 296380, 296379, 296376, 296375, 296312, 296307, 296304, 296303, 296280, 296273, 296270, 296247, 296244, 296243, 296242, 296241, 296240, 296198, 296197, 296196, 296195, 296192, 296143, 296142, 296135, 296134, 296133, 296132, 296123, 296074, 296068, 296066, 296065, 296063, 296062, 296060, 296016, 295942, 295941, 295937, 295936, 295913, 295909, 295908, 295860, 295859, 295856, 295855, 295854, 295853,

A.1. Data periods

- 295831, 295825, 295822, 295819, 295818, 295816, 295791, 295788, 295786, 295763,
295762, 295759, 295758, 295755, 295754, 295725, 295723, 295719, 295718, 295717,
295714, 295712, 295677, 295676, 295673, 295671, 295668, 295667, 295666, 295615,
295612, 295611, 295610, 295589, 295588, 295587, 295586, 295585
- LHC18r, 72 runs: 296690, 296752, 296781, 296784, 296785, 296786, 296790,
296793, 296794, 296799, 296835, 296838, 296839, 296848, 296850, 296851, 296894,
296899, 296903, 296930, 296931, 296932, 296934, 296935, 296941, 296966, 297031,
297117, 297118, 297123, 297132, 297133, 297193, 297195, 297196, 297218, 297221,
297222, 297278, 297310, 297311, 297312, 297315, 297317, 297333, 297335, 297336,
297363, 297366, 297379, 297380, 297405, 297406, 297413, 297414, 297415, 297441,
297442, 297446, 297450, 297451, 297452, 297479, 297512, 297540, 297541, 297542,
297544, 297558, 297588, 297590, 297595

Appendix B

Hit maps

Some cells of the calorimeter may malfunction during data collection, leading to an improper response to energy depositions. This can result in either a noisy signal or no signal at all, causing a discontinuous energy spectrum. These malfunctioning cells are referred to as bad channels and must be masked and excluded from clusterization and subsequent analysis. To identify bad channels, the distribution of hits per cell and the mean energy distribution are analyzed, based on the assumption that these distributions should be similar for all cells within statistical uncertainties.

Once the bad channels are identified, trigger emulation tools are applied to reject in data, these low activity regions or events triggered at lower energy than expected. This permits to define a trigger mask with the spotted dead regions, that can also be applied to MC. The fraction of rejected events is 17% to 19%, similar in all periods, a bit lower limit in peripheral collisions.

The following figures show the selected clusters hit-map in the calorimeter on both data and simulation and their ratio for MB and L1- γ cases when the trigger emulation tools are applied to select the events on data and simulation. Figures show the map of the cells as a function of cell indices in $\eta \times \varphi$ (column \times row) space in Pb–Pb collisions.

One can see the different acceptance maps between the MB and trigger samples due to the trigger-masked regions. The ratio between MC and data hit-maps allow to see how good is the agreement between the active and less active regions in data and simulation. The agreement is rather good although one can see a few small regions not well reproduced.

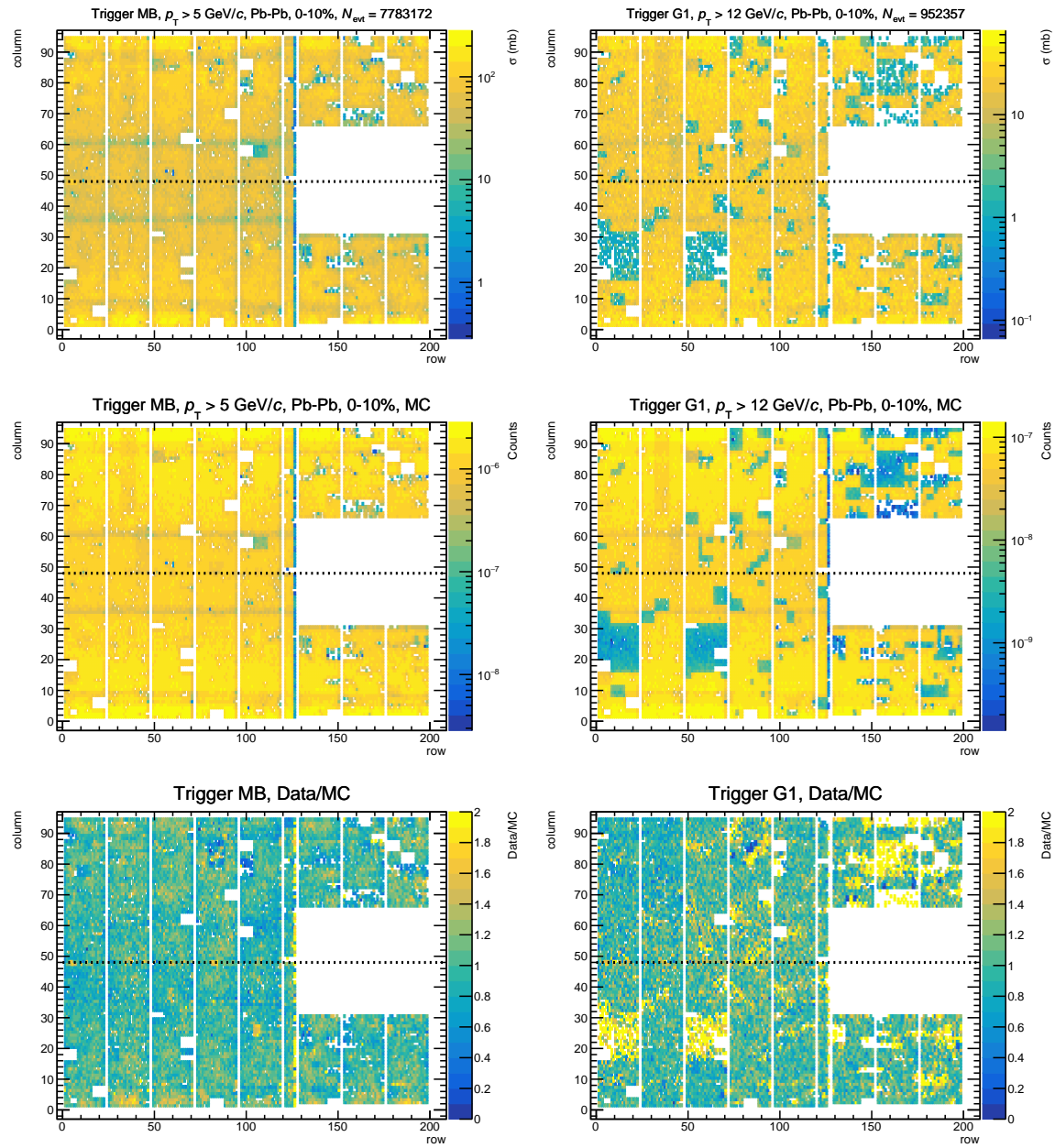


Figure B.1: Calorimeter cell column-row hit map for the period 2015 (LHC15o), Pb-Pb 0-10%, MB (left) and L1- γ (right) triggered data, top row for data, second row for the corresponding embedded MC γ -jet + jet-jet biased events. The last row for the ratio data over simulation, each one normalized by the histogram integral.

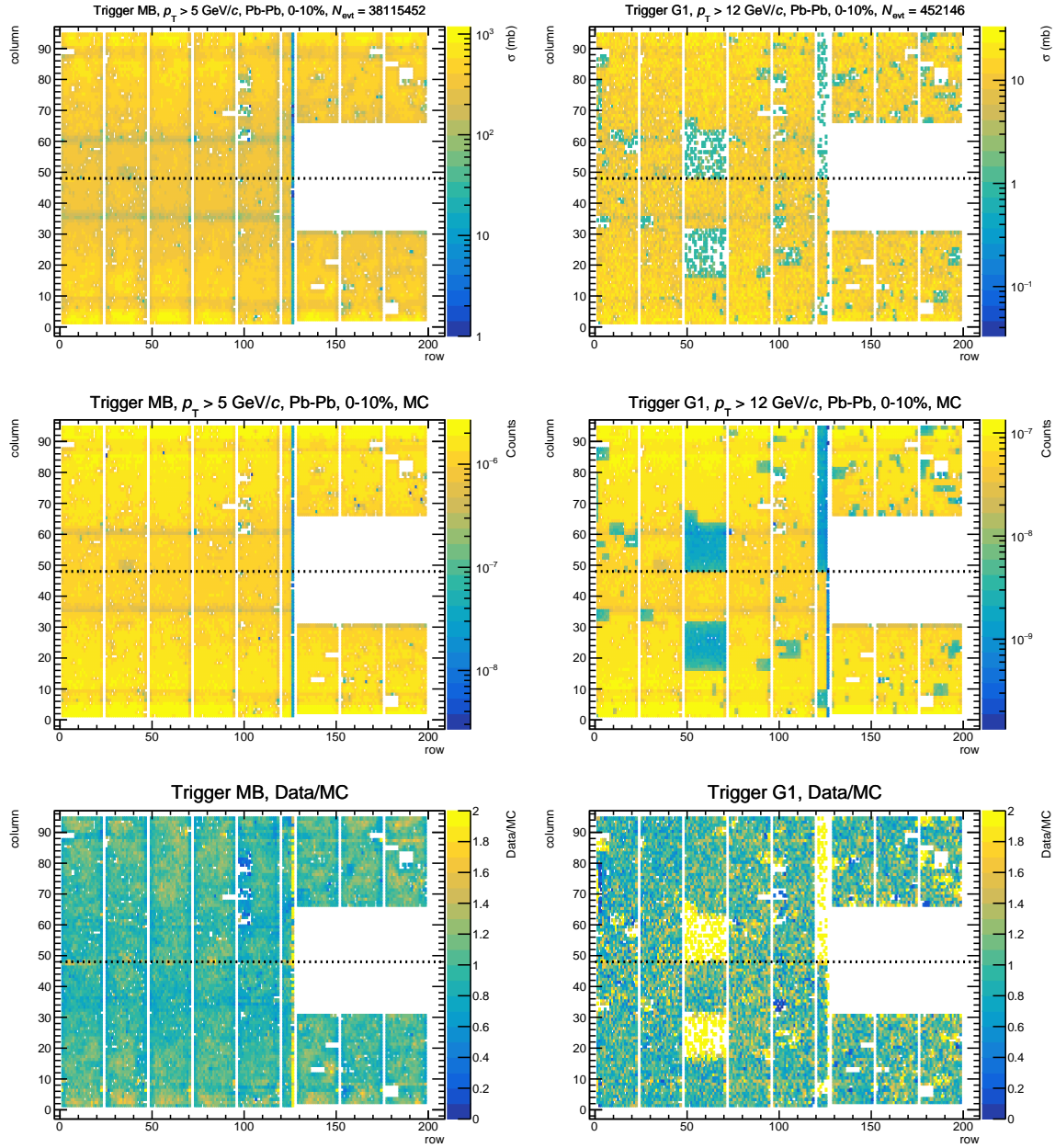


Figure B.2: Calorimeter cell column-row hit map for first period of 2018 (LHC18q), Pb–Pb 0-10%, MB (left) and L1- γ (right) triggered data, top row for data, second row for the corresponding embedded MC γ -jet + jet-jet biased events. The last row for the ratio data over simulation, each one normalized by the histogram integral.

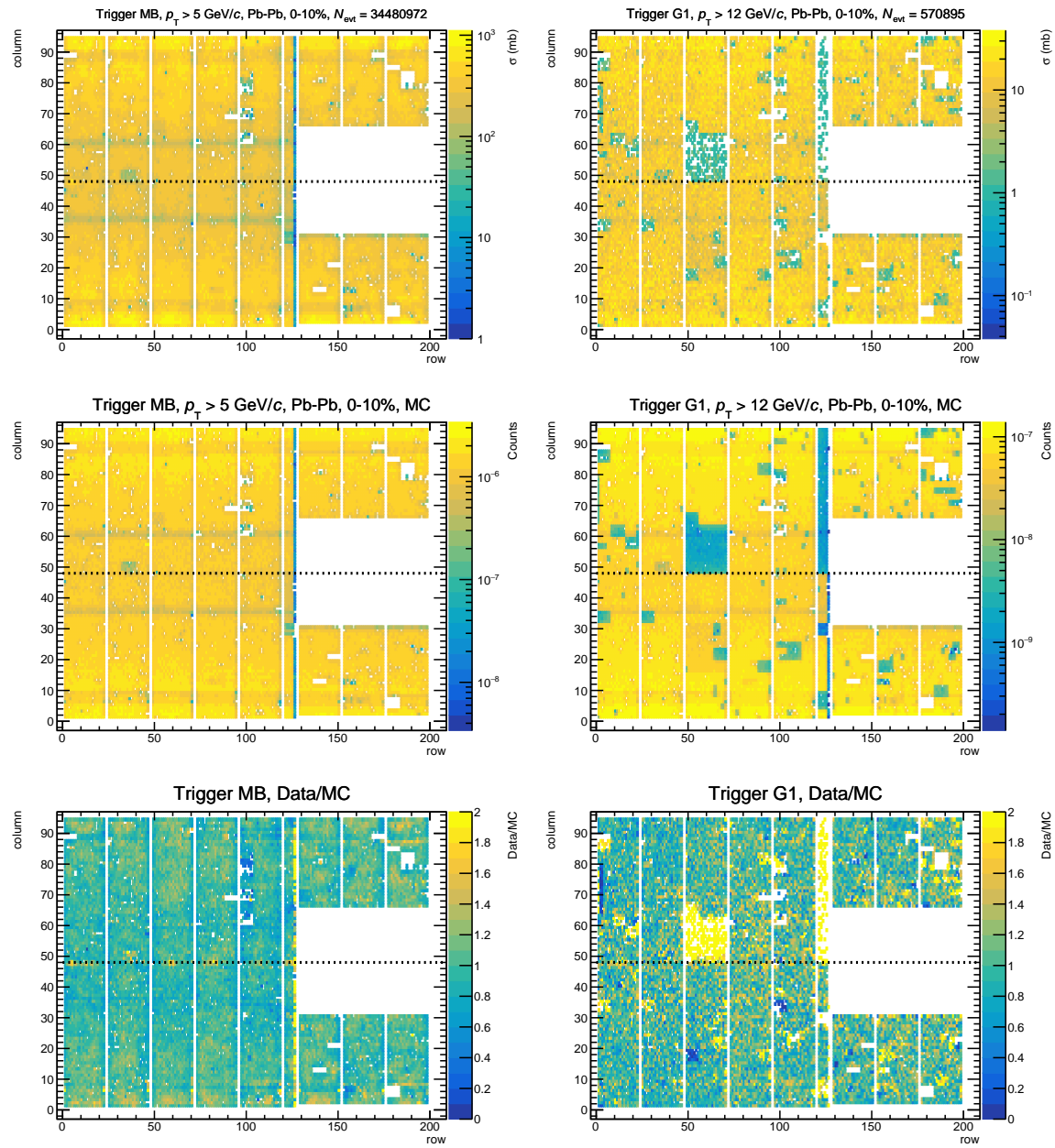


Figure B.3: Calorimeter cell column-row hit map for the second period of 2018 (LHC18r), Pb-Pb 0-10%, MB (left) and L1- γ (right) triggered data, top row for data, second row for the corresponding embedded MC γ -jet + jet-jet biased events. The last row for the ratio data over simulation, each one normalized by the histogram integral.

Appendix C

Azimuthal correlation distributions

This Appendix reports the azimuthal correlations distributions obtained for different p_T^{trig} for isolated narrow and isolated wide clusters in the different centrality classes in Pb–Pb collisions.

C.1 Azimuthal correlation distributions in 0-10% Pb–Pb collisions for isolated cluster narrow

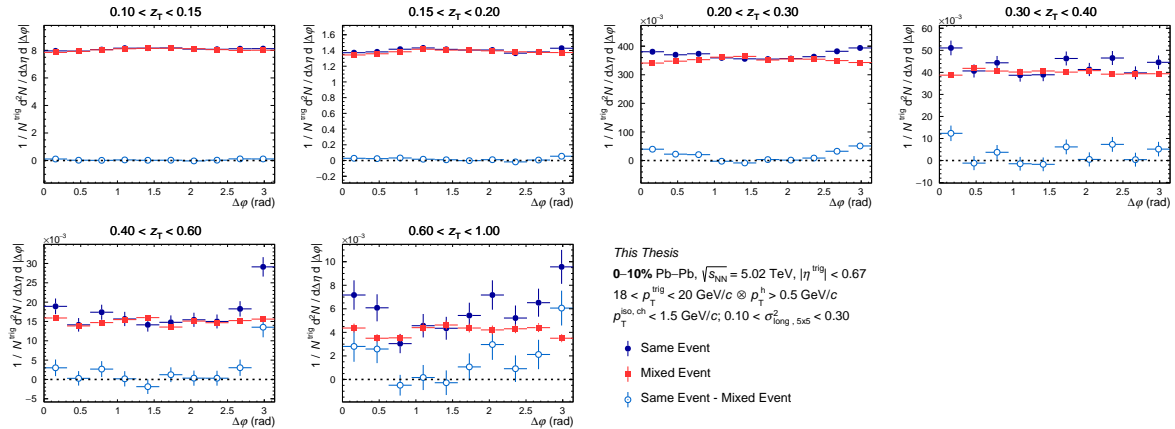


Figure C.1: Azimuthal correlation distribution in **0-10%** for isolated narrow clusters for the same event (full blue circle), for mixed event (full red square) and for the result of the subtraction (empty light blue circle) as a function of $\Delta\varphi$ for different z_T bins with $18 < p_T^{\text{trig}} < 20 \text{ GeV}/c$.

C.1. Azimuthal correlation distributions in 0-10% Pb–Pb collisions for isolated cluster narrow

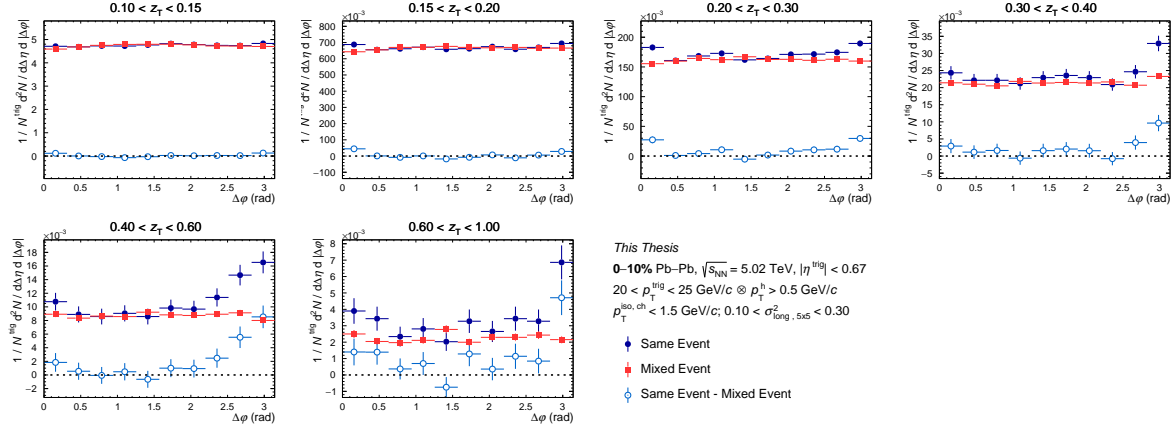


Figure C.2: Azimuthal correlation distribution in **0-10%** for isolated narrow clusters for the same event (full blue circle), for mixed event (full red square) and for result of the subtraction (empty light blue circle) as a function of $\Delta\varphi$ for different z_T bins with $20 < p_T^{\text{trig}} < 25 \text{ GeV}/c$.

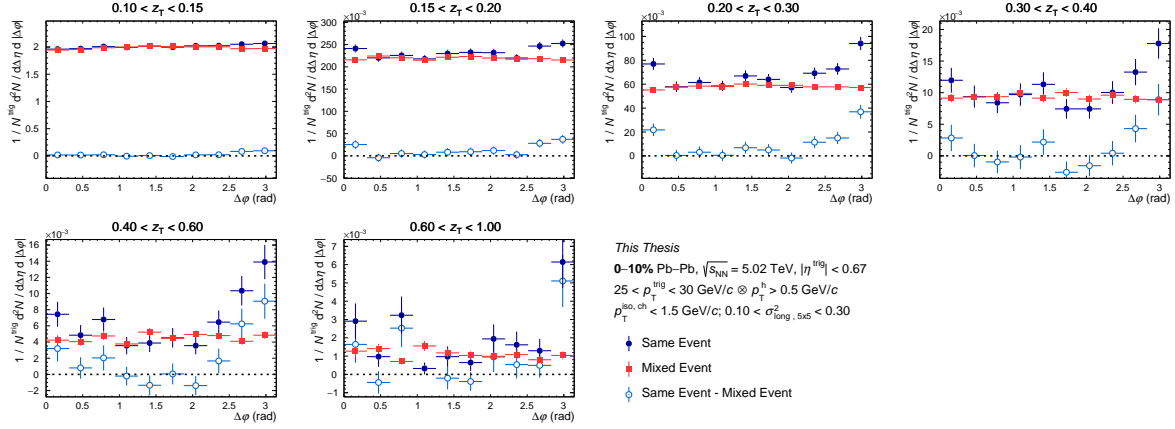


Figure C.3: Azimuthal correlation distribution in **0-10%** for isolated narrow clusters for the same event (full blue circle), for mixed event (full red square) and for result of the subtraction (empty light blue circle) as a function of $\Delta\varphi$ for different z_T bins with $25 < p_T^{\text{trig}} < 30 \text{ GeV}/c$.

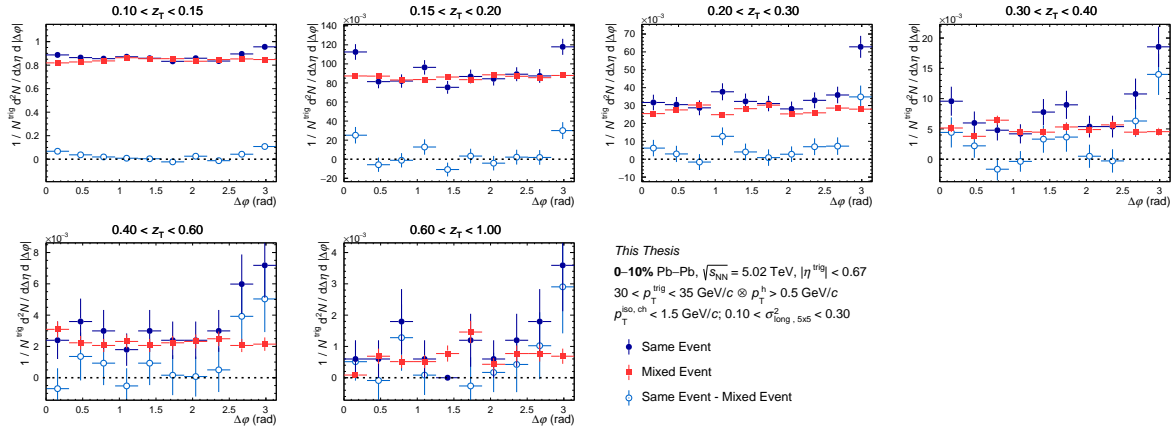


Figure C.4: Azimuthal correlation distribution in **0-10%** for isolated narrow clusters for the same event (full blue circle), for mixed event (full red square) and for result of the subtraction (empty light blue circle) as a function of $\Delta\varphi$ for different z_T bins with $30 < p_T^{\text{trig}} < 35 \text{ GeV}/c$.

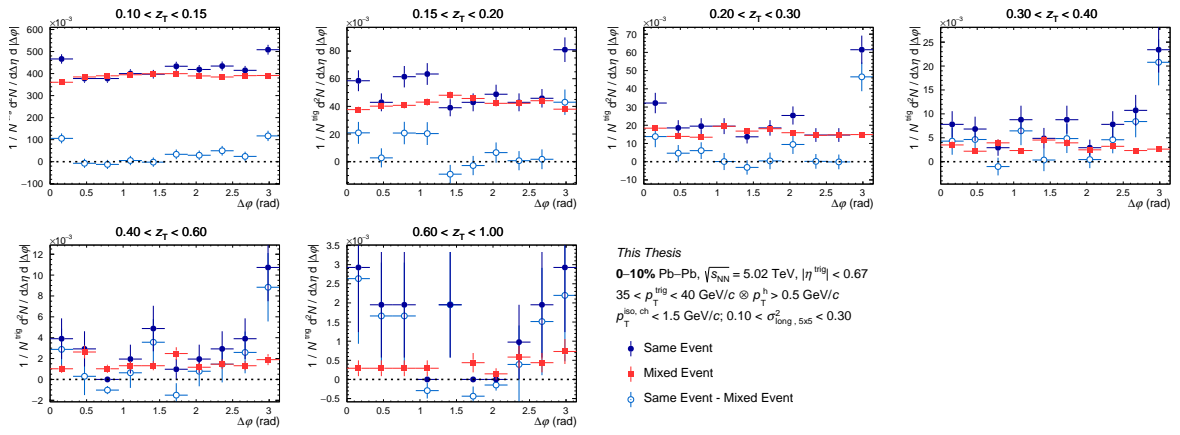


Figure C.5: Azimuthal correlation distribution in **0-10%** for isolated narrow clusters for the same event (full blue circle), for mixed event (full red square) and for the result of the subtraction (empty light blue circle) as a function of $\Delta\varphi$ for different z_T bins with $35 < p_T^{\text{trig}} < 40 \text{ GeV}/c$.

C.2 Azimuthal correlation distributions in 10-30% Pb–Pb collisions for isolated cluster narrow

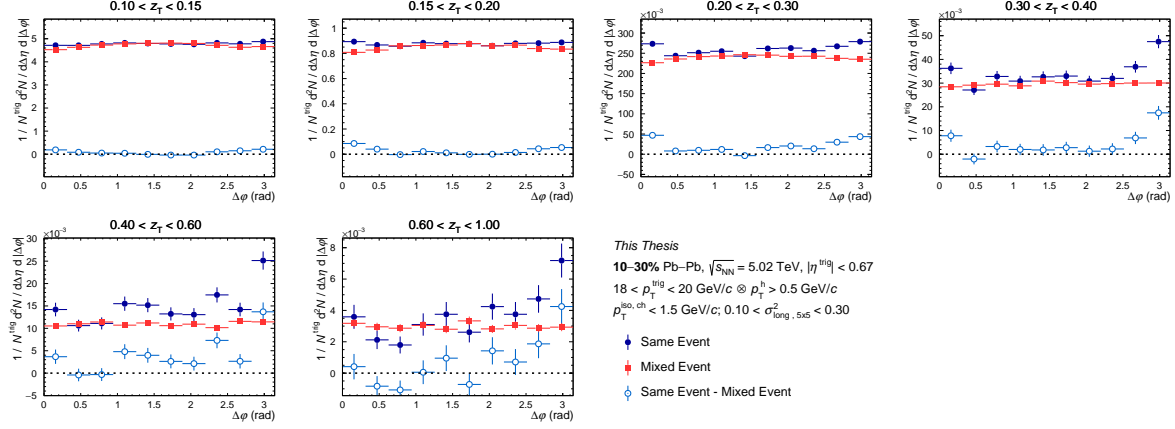


Figure C.6: Azimuthal correlation distribution in **10-30%** for isolated narrow clusters for the same event (full blue circle), for mixed event (full red square) and for the result of the subtraction (empty light blue circle) as a function of $\Delta\varphi$ for different z_T bins with $18 < p_T^{\text{trig}} < 20 \text{ GeV}/c$.

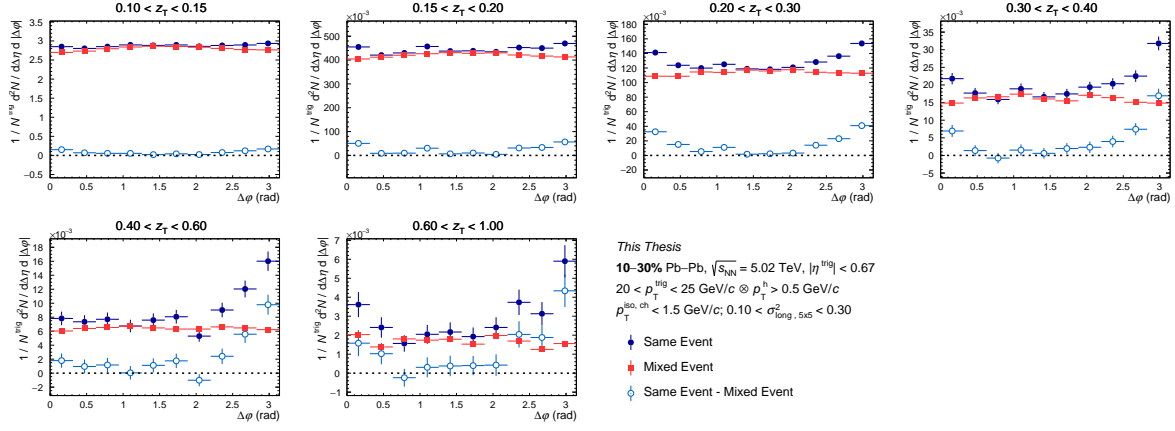


Figure C.7: Azimuthal correlation distribution in **10-30%** for isolated narrow clusters for the same event (full blue circle), for mixed event (full red square) and for the result of the subtraction (empty light blue circle) as a function of $\Delta\varphi$ for different z_T bins with $20 < p_T^{\text{trig}} < 25 \text{ GeV}/c$.

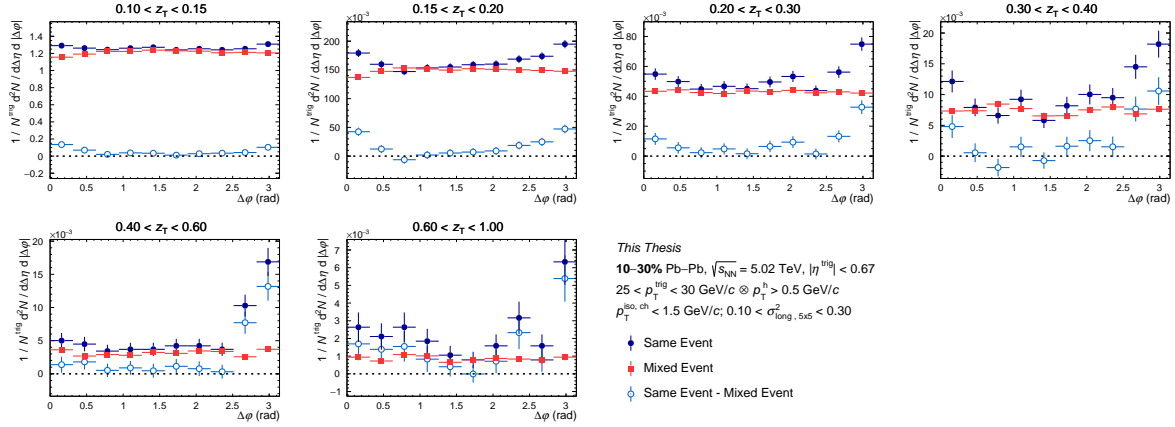


Figure C.8: Azimuthal correlation distribution in **10-30%** for isolated narrow clusters for the same event (full blue circle), for mixed event (full red square) and for the result of the subtraction (empty light blue circle) as a function of $\Delta\varphi$ for different z_T bins with $25 < p_T^{\text{trig}} < 30 \text{ GeV}/c$.

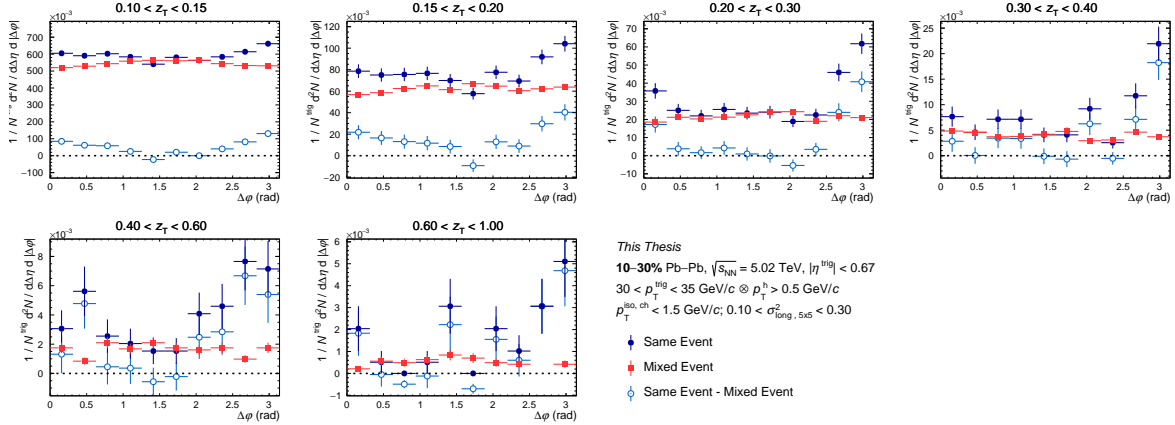


Figure C.9: Azimuthal correlation distribution in **10-30%** for isolated narrow clusters for the same event (full blue circle), for mixed event (full red square) and for the result of the subtraction (empty light blue circle) as a function of $\Delta\varphi$ for different z_T bins with $30 < p_T^{\text{trig}} < 35 \text{ GeV}/c$.

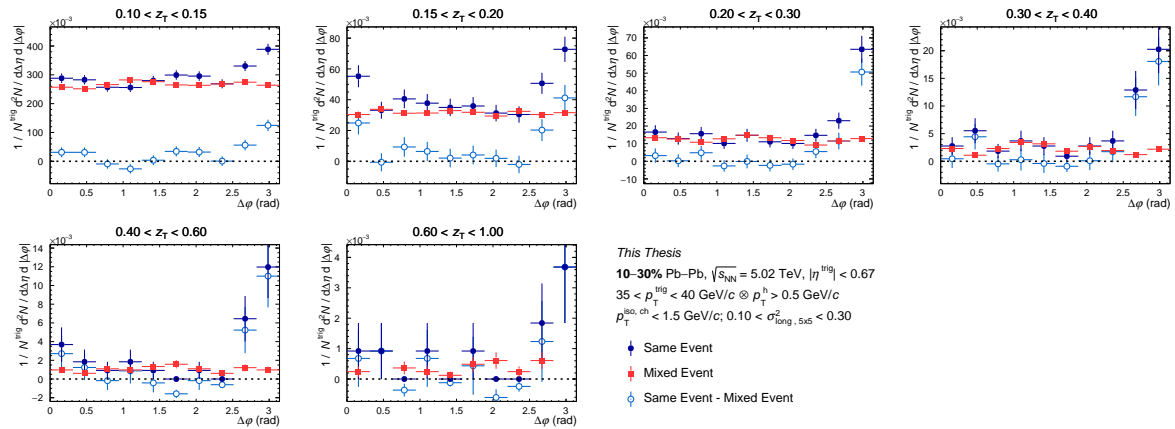


Figure C.10: Azimuthal correlation distribution in **10-30%** for isolated narrow clusters for the same event (full blue circle), for mixed event (full red square) and for the result of the subtraction (empty light blue circle) as a function of $\Delta\varphi$ for different z_T bins with $35 < p_T^{\text{trig}} < 40 \text{ GeV}/c$.

C.3 Azimuthal correlation distributions in 30-50% Pb–Pb collisions for isolated cluster narrow

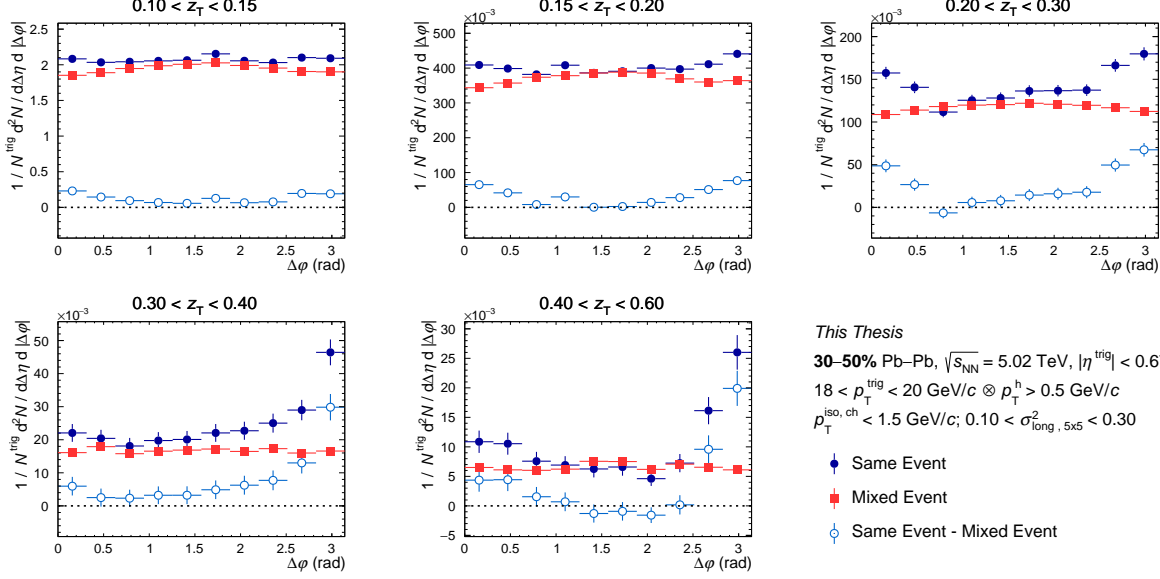


Figure C.11: Azimuthal correlation distribution in **30-50%** for isolated narrow clusters for the same event (full blue circle), for mixed event (full red square) and for result of the subtraction (empty light blue circle) as a function of $\Delta\varphi$ for different z_T bins with $18 < p_T^{\text{trig}} < 20$ GeV/c.

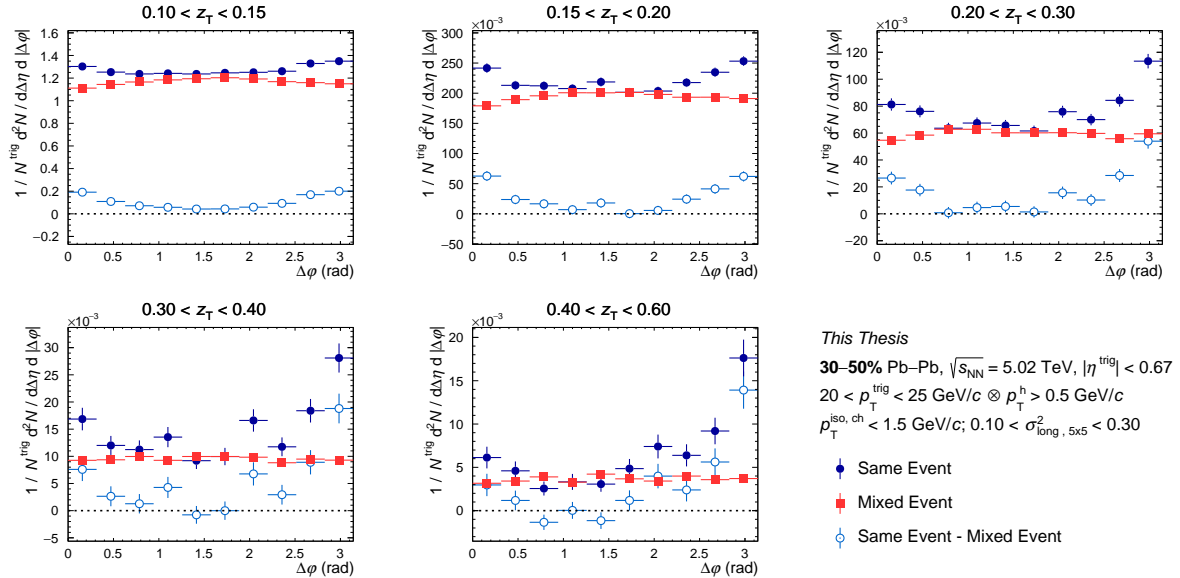


Figure C.12: Azimuthal correlation distribution in **30-50%** for isolated narrow clusters for the same event (full blue circle), for mixed event (full red square) and for result of the subtraction (empty light blue circle) as a function of $\Delta\varphi$ for different z_T bins with $20 < p_T^{\text{trig}} < 25 \text{ GeV}/c$.

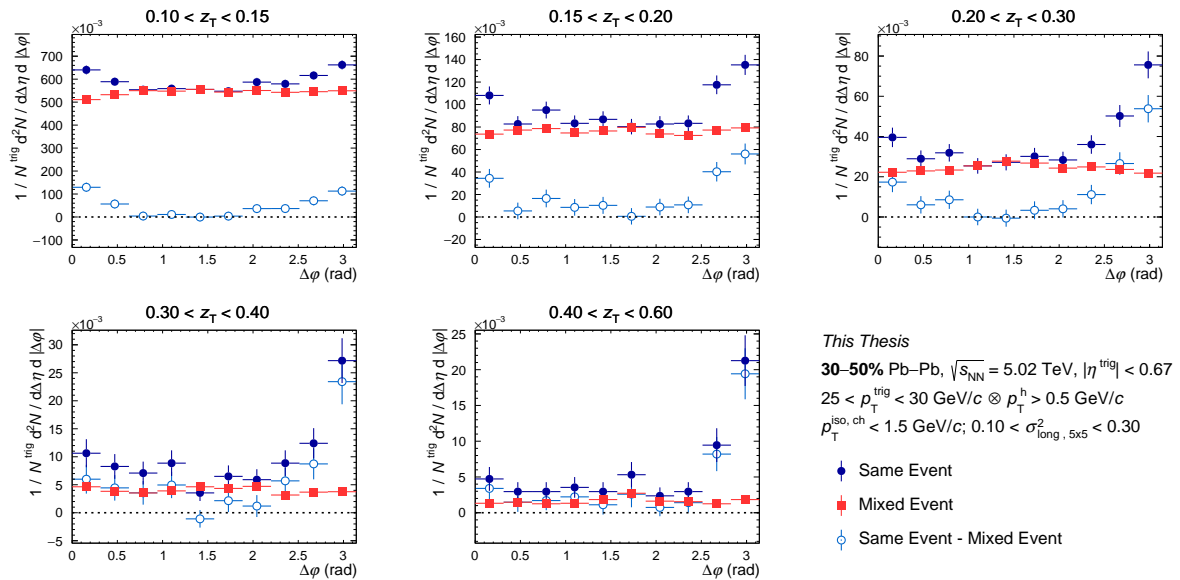


Figure C.13: Azimuthal correlation distribution in **30-50%** for isolated narrow clusters for the same event (full blue circle), for mixed event (full red square) and for result of the subtraction (empty light blue circle) as a function of $\Delta\varphi$ for different z_T bins with $25 < p_T^{\text{trig}} < 30 \text{ GeV}/c$.

C.3. Azimuthal correlation distributions in 30-50% Pb–Pb collisions for isolated cluster narrow

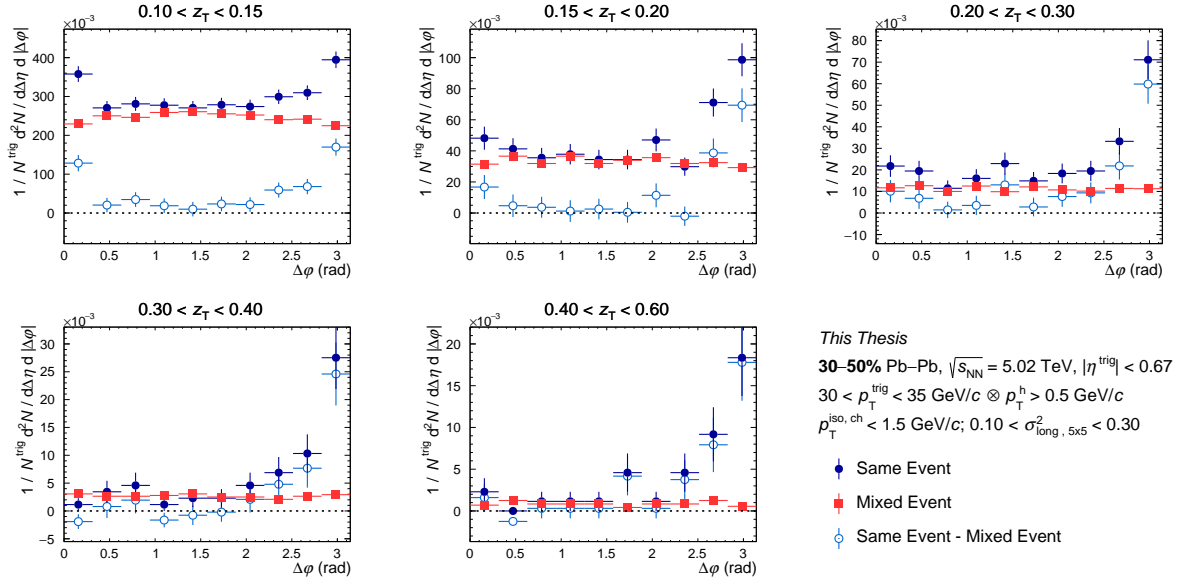


Figure C.14: Azimuthal correlation distribution in **30-50%** for isolated narrow clusters for the same event (full blue circle), for mixed event (full red square) and for result of the subtraction (empty light blue circle) as a function of $\Delta\varphi$ for different z_T bins with $30 < p_T^{\text{trig}} < 35 \text{ GeV}/c$.

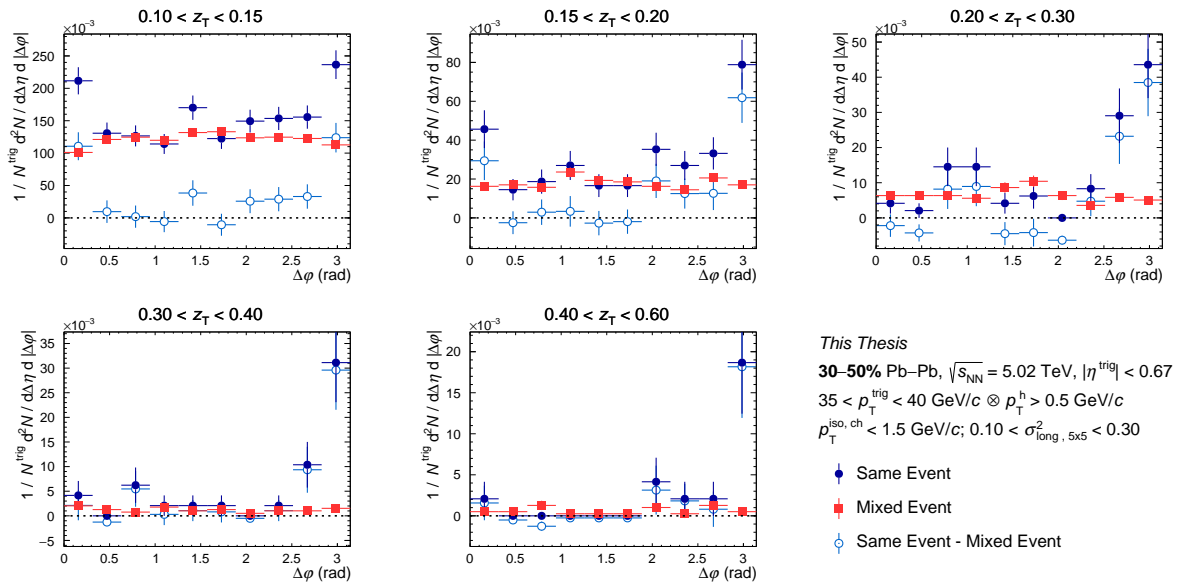


Figure C.15: Azimuthal correlation distribution in **30-50%** for isolated narrow clusters for the same event (full blue circle), for mixed event (full red square) and for result of the subtraction (empty light blue circle) as a function of $\Delta\varphi$ for different z_T bins with $35 < p_T^{\text{trig}} < 40 \text{ GeV}/c$.

C.4 Azimuthal correlation distributions in 50-90% Pb-Pb collisions for isolated cluster narrow

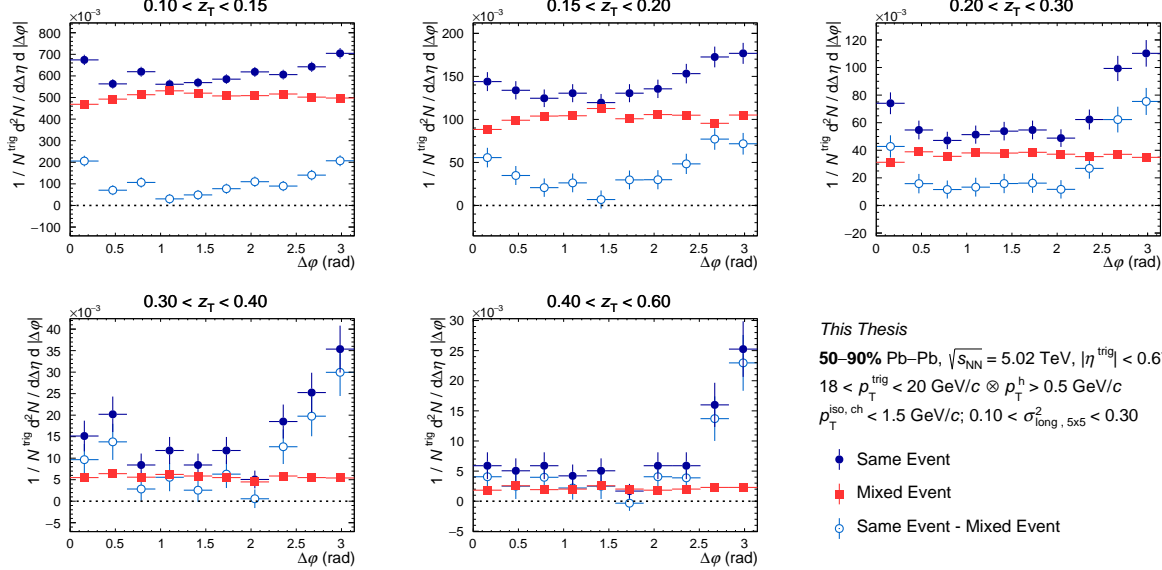


Figure C.16: Azimuthal correlation distribution in **50-90%** for isolated narrow clusters for the same event (full blue circle), for mixed event (full red square) and for result of the subtraction (empty light blue circle) as a function of $\Delta\varphi$ for different z_T bins with $18 < p_T^{\text{trig}} < 20 \text{ GeV}/c$.

This Thesis

**50-90% Pb-Pb, $\sqrt{s_{\text{NN}}} = 5.02 \text{ TeV}, |\eta^{\text{trig}}| < 0.67$
 $18 < p_T^{\text{trig}} < 20 \text{ GeV}/c \otimes p_T^n > 0.5 \text{ GeV}/c$
 $p_T^{\text{iso, ch}} < 1.5 \text{ GeV}/c; 0.10 < \sigma_{\text{long, } 5 \times 5}^2 < 0.30$**

- Same Event
- Mixed Event
- Same Event - Mixed Event

C.4. Azimuthal correlation distributions in 50-90% Pb–Pb collisions for isolated cluster narrow

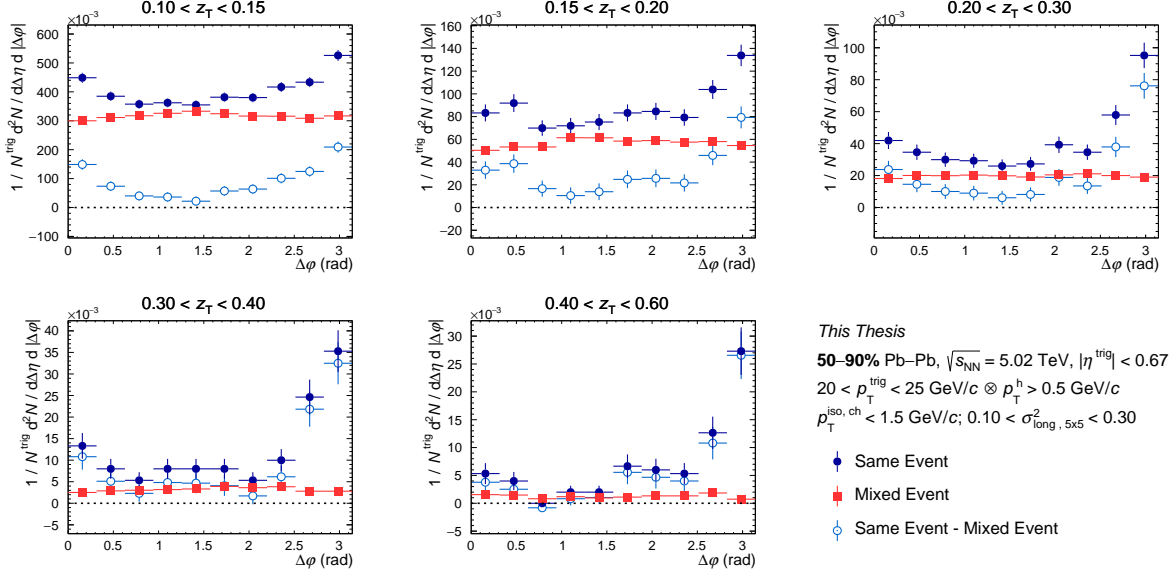


Figure C.17: Azimuthal correlation distribution in 50–90% for isolated narrow clusters for the same event (full blue circle), for mixed event (full red square) and for result of the subtraction (empty light blue circle) as a function of $\Delta\varphi$ for different z_T bins with $20 < p_T^{\text{trig}} < 25 \text{ GeV}/c$.

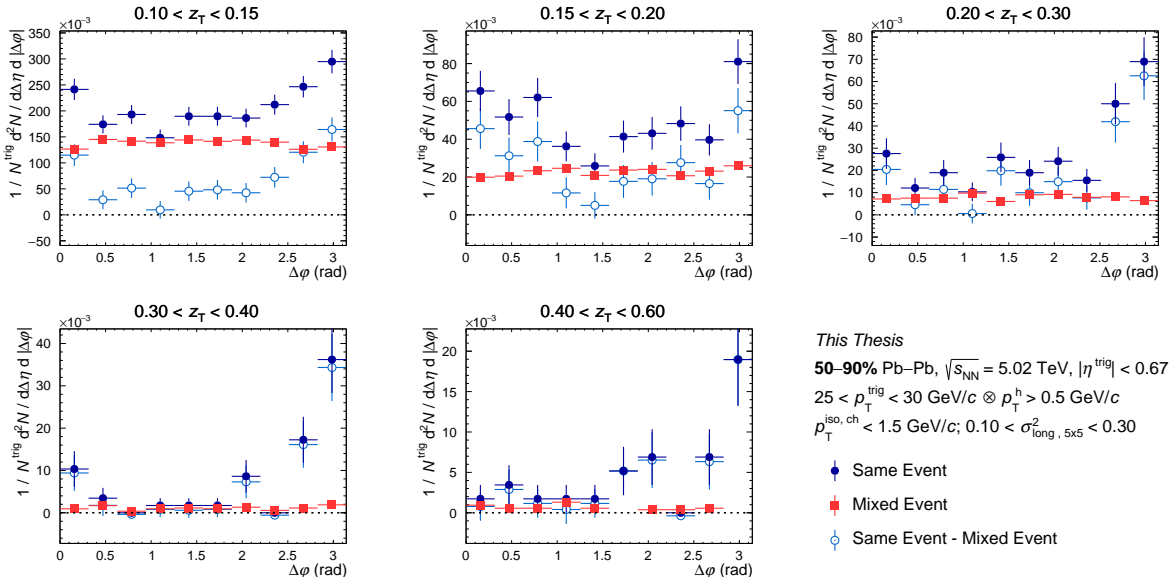


Figure C.18: Azimuthal correlation distribution in 50–90% for isolated narrow clusters for the same event (full blue circle), for mixed event (full red square) and for result of the subtraction (empty light blue circle) as a function of $\Delta\varphi$ for different z_T bins with $25 < p_T^{\text{trig}} < 30 \text{ GeV}/c$.

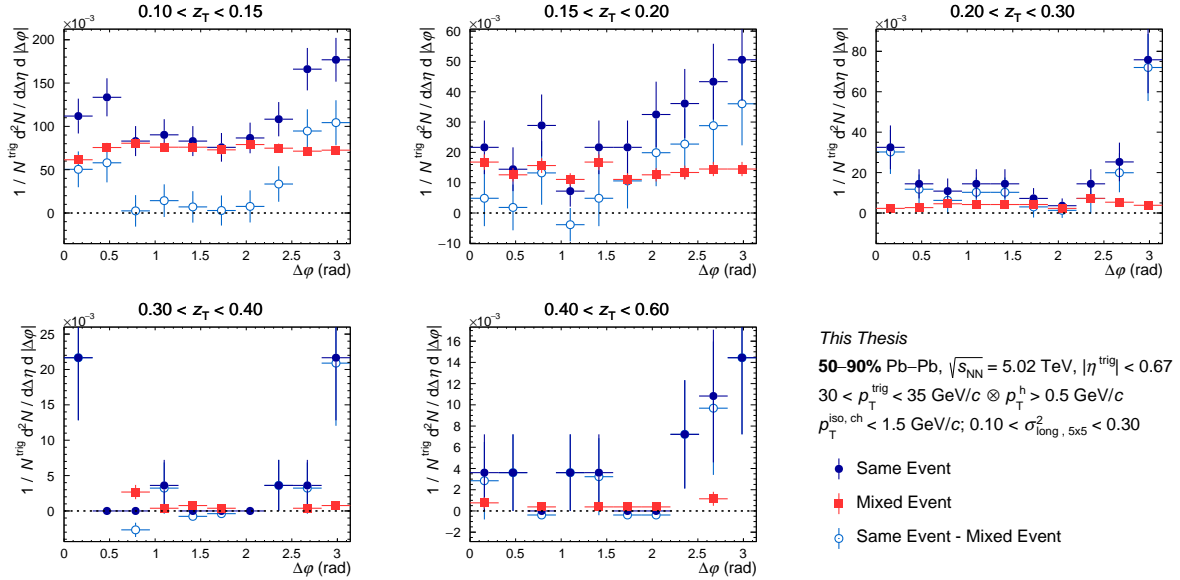


Figure C.19: Azimuthal correlation distribution in **50–90%** for isolated narrow clusters for the same event (full blue circle), for mixed event (full red square) and for result of the subtraction (empty light blue circle) as a function of $\Delta\varphi$ for different z_T bins with $30 < p_T^{\text{trig}} < 35 \text{ GeV}/c$.

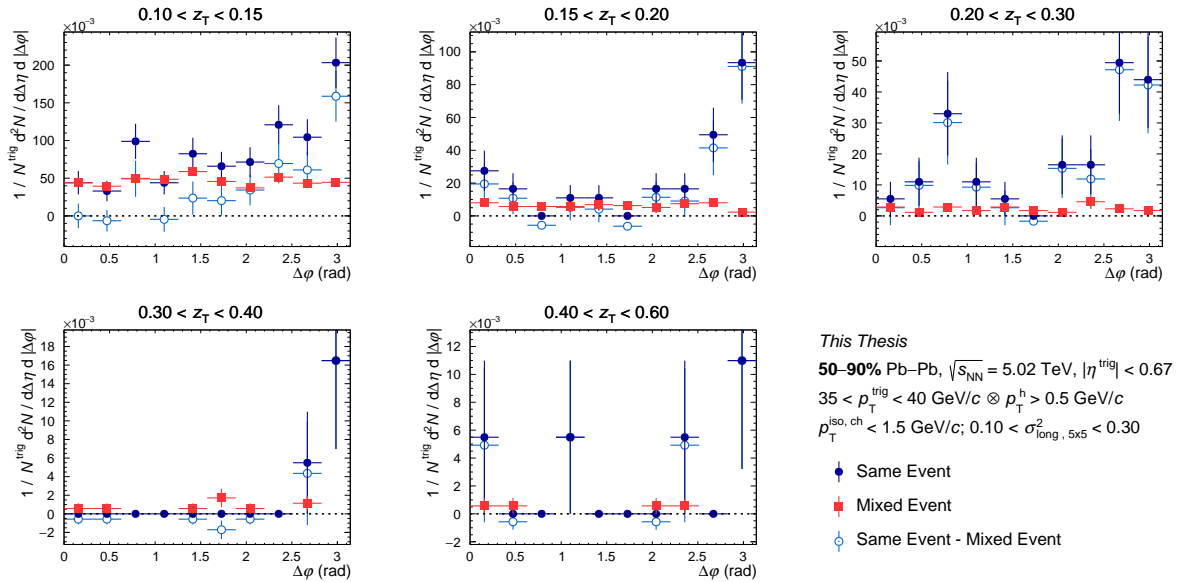


Figure C.20: Azimuthal correlation distribution in **50–90%** for isolated narrow clusters for the same event (full blue circle), for mixed event (full red square) and for result of the subtraction (empty light blue circle) as a function of $\Delta\varphi$ for different z_T bins with $35 < p_T^{\text{trig}} < 40 \text{ GeV}/c$.

C.5 Azimuthal correlation distributions in 0-10% Pb–Pb collisions for isolated cluster wide

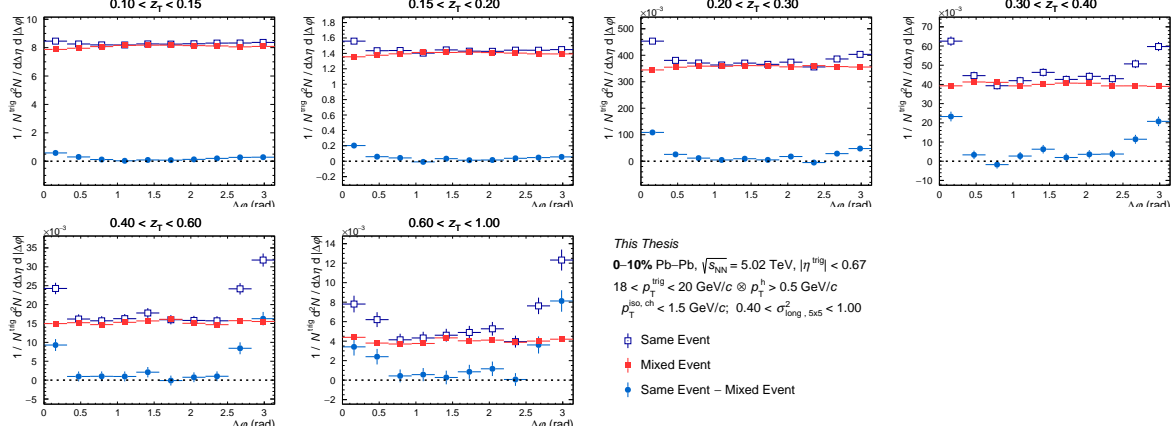


Figure C.21: Azimuthal correlation distribution in 10-30% for isolated wide clusters for the same event (empty blue square), for mixed event (full red square) and for result of the subtraction (full light blue circle) as a function of $\Delta\varphi$ for different z_T bins with $18 < p_T^{\text{trig}} < 20 \text{ GeV}/c$.

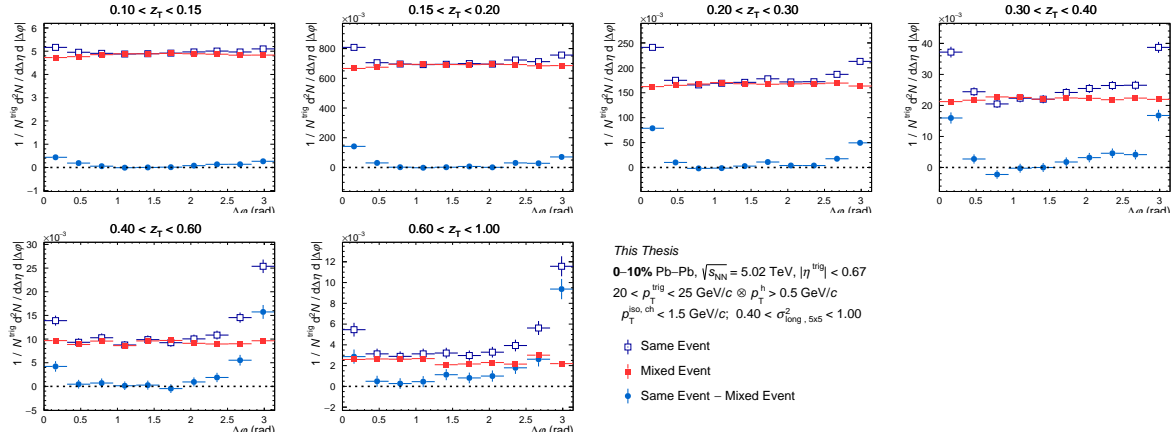


Figure C.22: Azimuthal correlation distribution in 10-30% for isolated wide clusters for the same event (empty blue square), for mixed event (full red square) and for result of the subtraction (full light blue circle) as a function of $\Delta\varphi$ for different z_T bins with $20 < p_T^{\text{trig}} < 25 \text{ GeV}/c$.

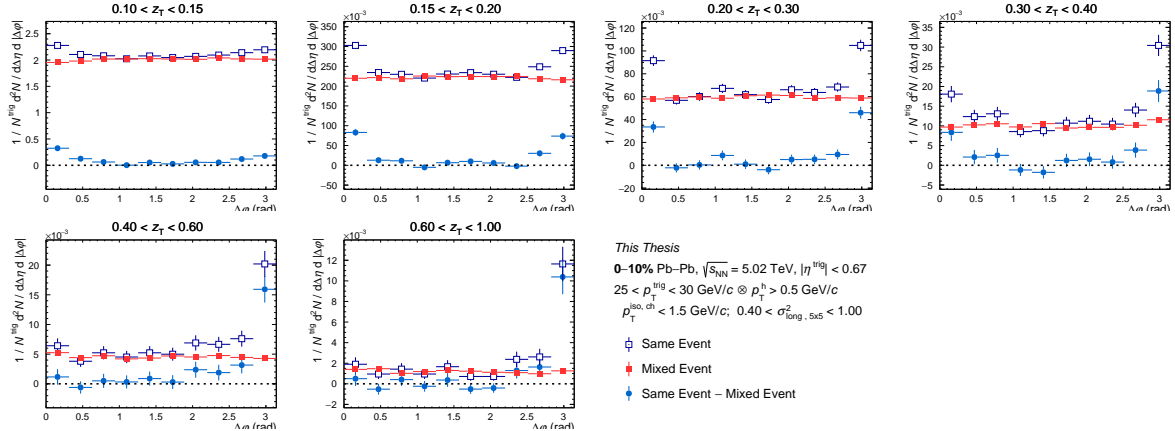


Figure C.23: Azimuthal correlation distribution in 10-30% for isolated wide clusters for the same event (empty blue square), for mixed event (full red square) and for result of the subtraction (full light blue circle) as a function of $\Delta\varphi$ for different z_T bins with $25 < p_T^{\text{trig}} < 30 \text{ GeV}/c$.

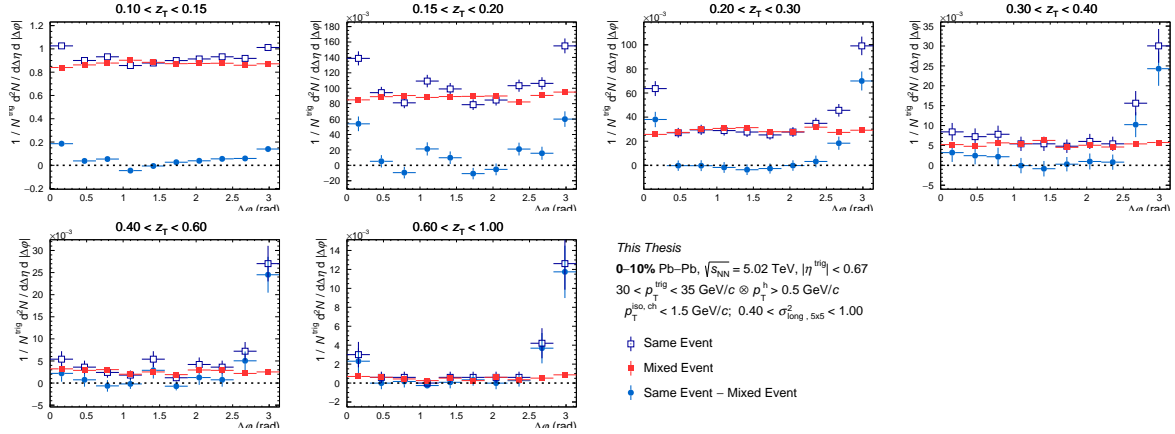


Figure C.24: Azimuthal correlation distribution in 10-30% for isolated wide clusters for the same event (empty blue square), for mixed event (full red square) and for result of the subtraction (full light blue circle) as a function of $\Delta\varphi$ for different z_T bins with $30 < p_T^{\text{trig}} < 35 \text{ GeV}/c$.

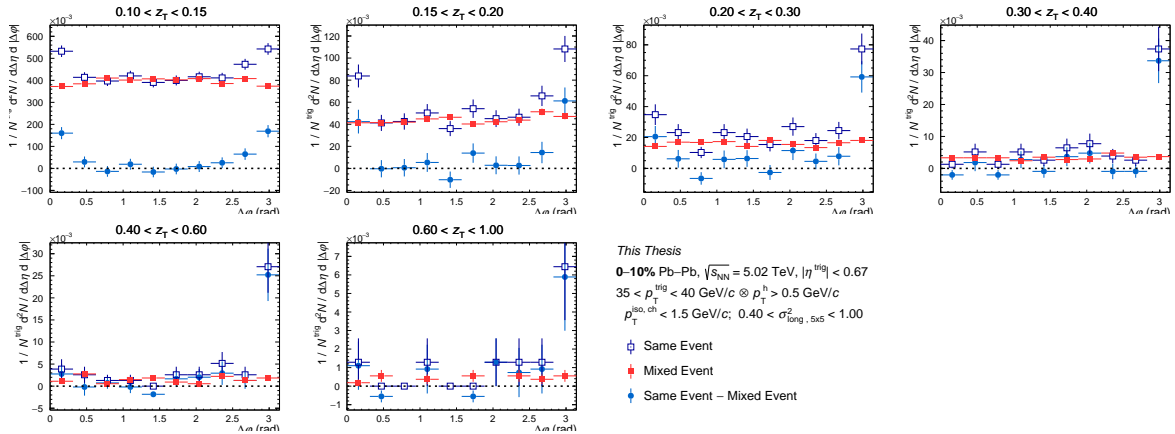


Figure C.25: Azimuthal correlation distribution in 10-30% for isolated wide clusters for the same event (empty blue square), for mixed event (full red square) and for result of the subtraction (full light blue circle) as a function of $\Delta\varphi$ for different z_T bins with $35 < p_T^{\text{trig}} < 40 \text{ GeV}/c$.

C.6 Azimuthal correlation distributions in 10-30% Pb–Pb collisions for isolated cluster wide

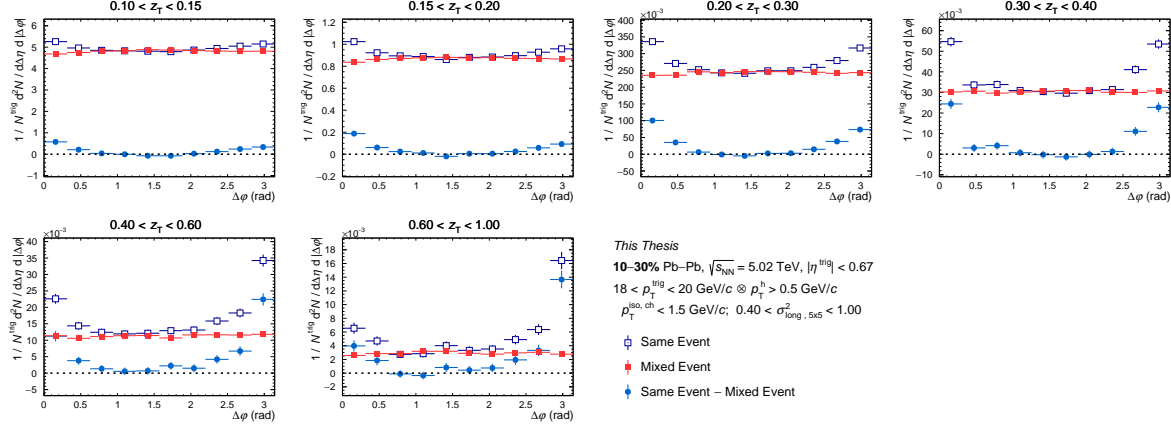


Figure C.26: Azimuthal correlation distribution in 10-30% for isolated wide clusters for the same event (empty blue square), for mixed event (full red square) and for result of the subtraction (full light blue circle) as a function of $\Delta\varphi$ for different z_T bins with $18 < p_T^{\text{trig}} < 20 \text{ GeV}/c$.

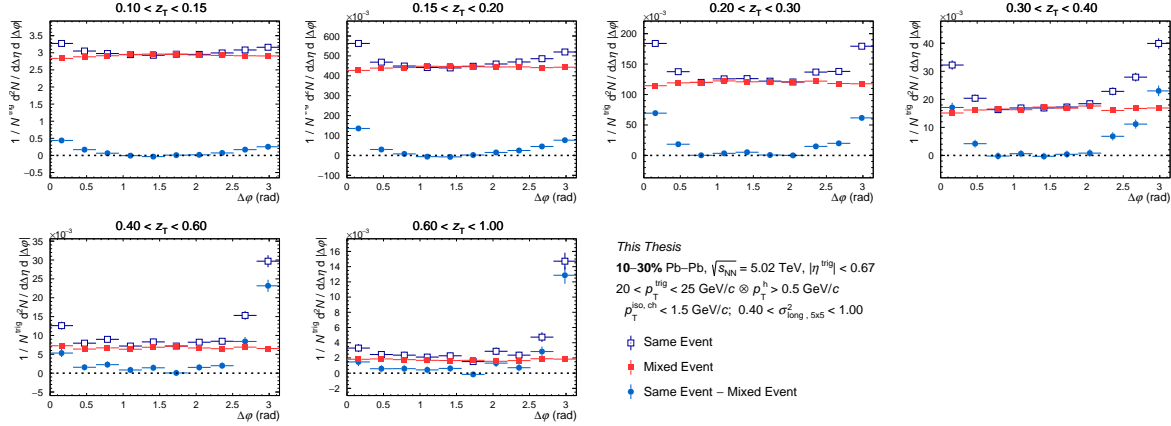


Figure C.27: Azimuthal correlation distribution in 10-30% for isolated wide clusters for the same event (empty blue square), for mixed event (full red square) and for result of the subtraction (full light blue circle) as a function of $\Delta\varphi$ for different z_T bins with $20 < p_T^{\text{trig}} < 25 \text{ GeV}/c$.

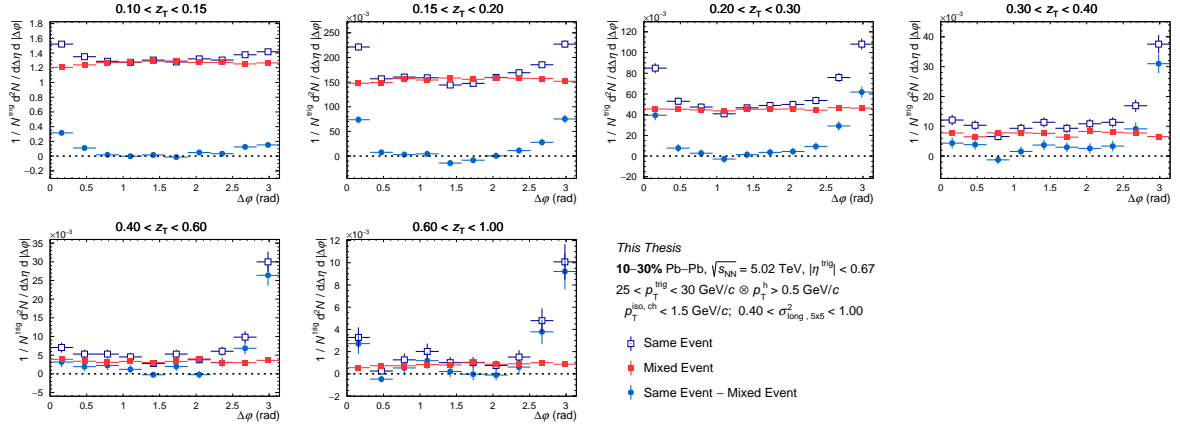


Figure C.28: Azimuthal correlation distribution in 10-30% for isolated wide clusters for the same event (empty blue square), for mixed event (full red square) and for result of the subtraction (full light blue circle) as a function of $\Delta\varphi$ for different z_T bins with $25 < p_T^{\text{trig}} < 30 \text{ GeV}/c$.

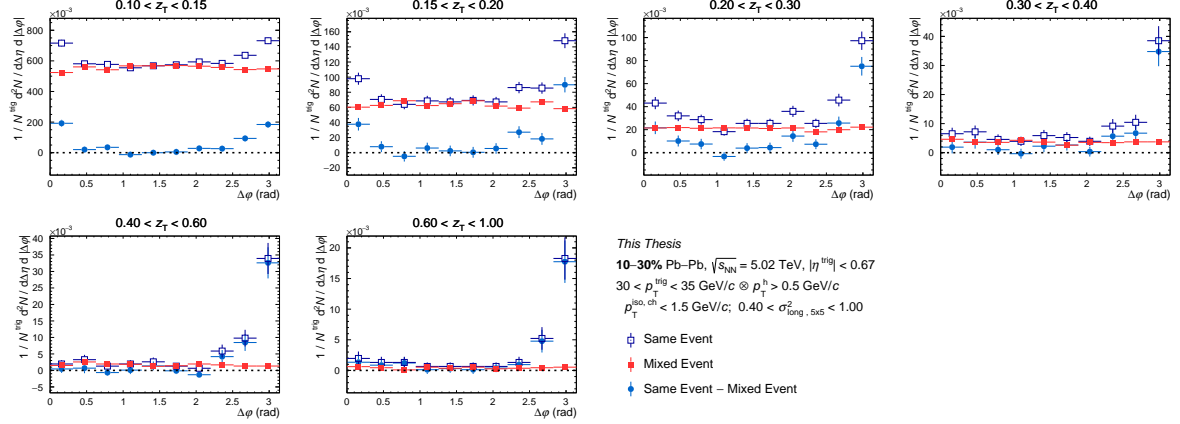


Figure C.29: Azimuthal correlation distribution in 10-30% for isolated wide clusters for the same event (empty blue square), for mixed event (full red square) and for result of the subtraction (full light blue circle) as a function of $\Delta\varphi$ for different z_T bins with $30 < p_T^{\text{trig}} < 35 \text{ GeV}/c$.

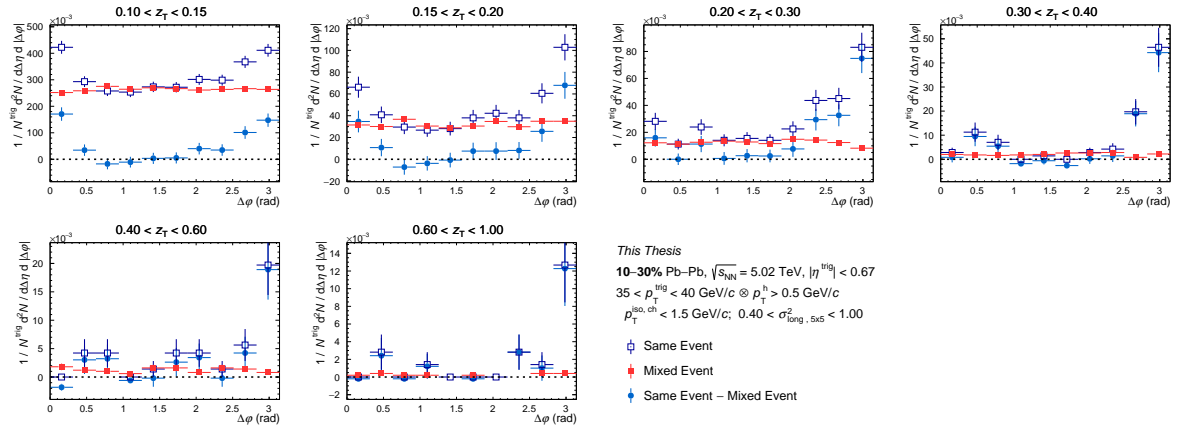


Figure C.30: Azimuthal correlation distribution in 10-30% for isolated wide clusters for the same event (empty blue square), for mixed event (full red square) and for result of the subtraction (full light blue circle) as a function of $\Delta\varphi$ for different z_T bins with $35 < p_T^{\text{trig}} < 40 \text{ GeV}/c$.

C.7 Azimuthal correlation distributions in 30-50% Pb–Pb collisions for isolated cluster wide

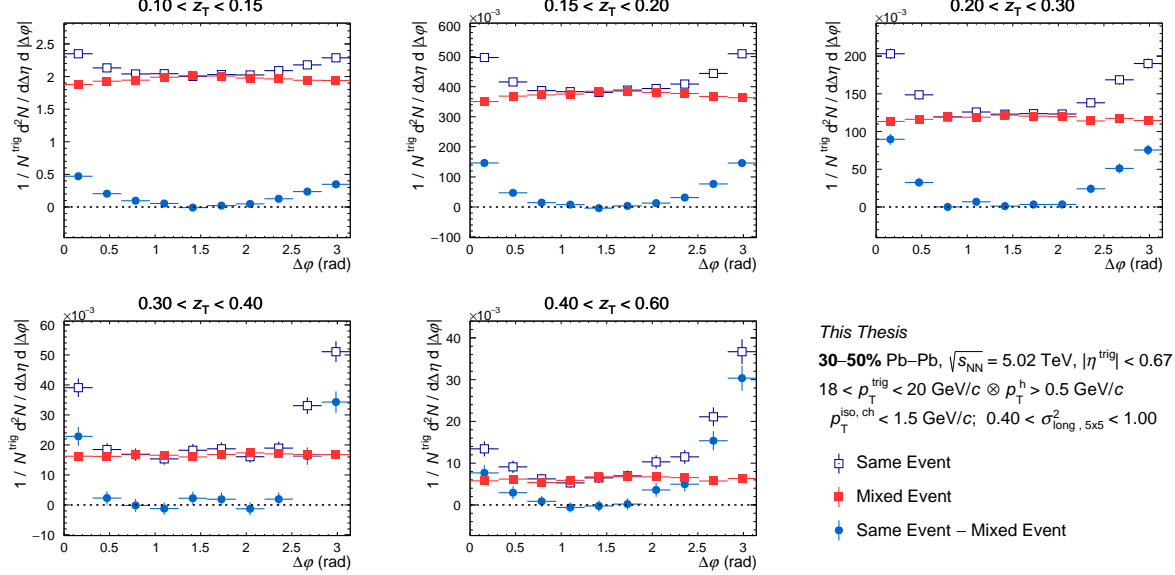


Figure C.31: Azimuthal correlation distribution in **30-50%** for isolated wide clusters for the same event (empty blue square), for mixed event (full red square) and for result of the subtraction (full light blue circle) as a function of $\Delta\varphi$ for different z_T bins with $18 < p_T^{\text{trig}} < 20 \text{ GeV}/c$.

C.8 Azimuthal correlation distributions in 50-90% Pb–Pb collisions for isolated cluster wide

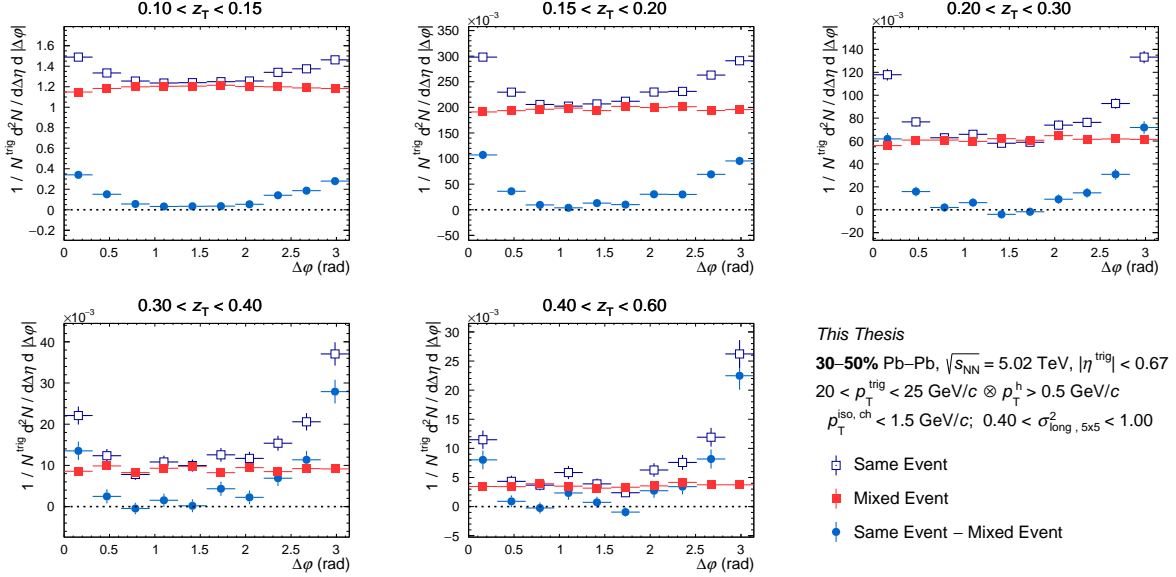


Figure C.32: Azimuthal correlation distribution in **30–50%** for isolated wide clusters for the same event (empty blue square), for mixed event (full red square) and for result of the subtraction (full light blue circle) as a function of $\Delta\varphi$ for different z_T bins with $20 < p_T^{\text{trig}} < 25 \text{ GeV}/c$.

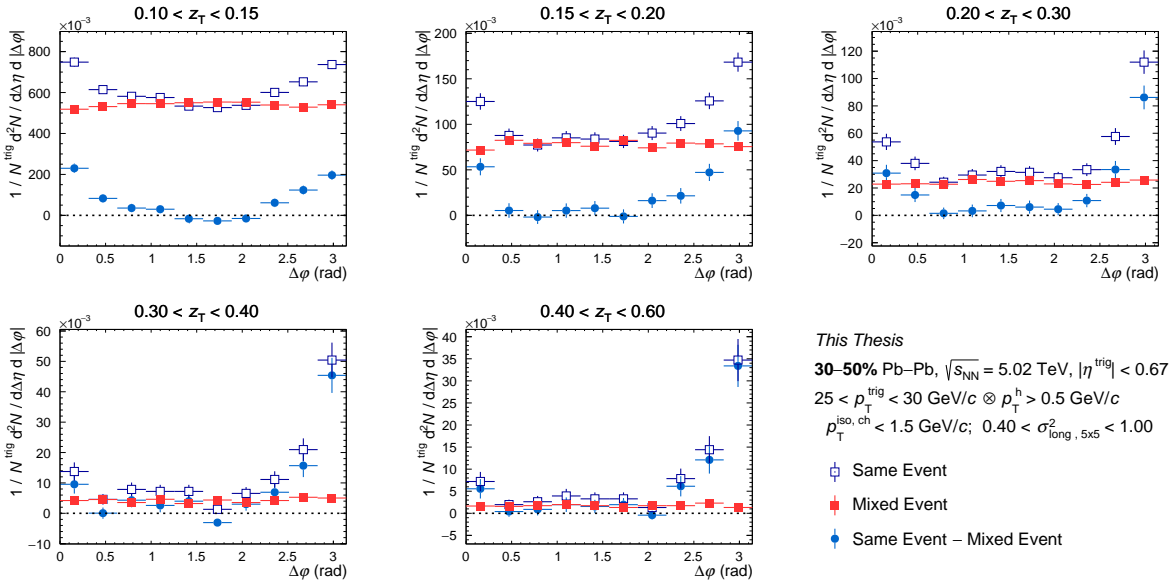


Figure C.33: Azimuthal correlation distribution in **30–50%** for isolated wide clusters for the same event (empty blue square), for mixed event (full red square) and for result of the subtraction (full light blue circle) as a function of $\Delta\varphi$ for different z_T bins with $25 < p_T^{\text{trig}} < 30 \text{ GeV}/c$.

C.8. Azimuthal correlation distributions in 50-90% Pb–Pb collisions for isolated cluster wide

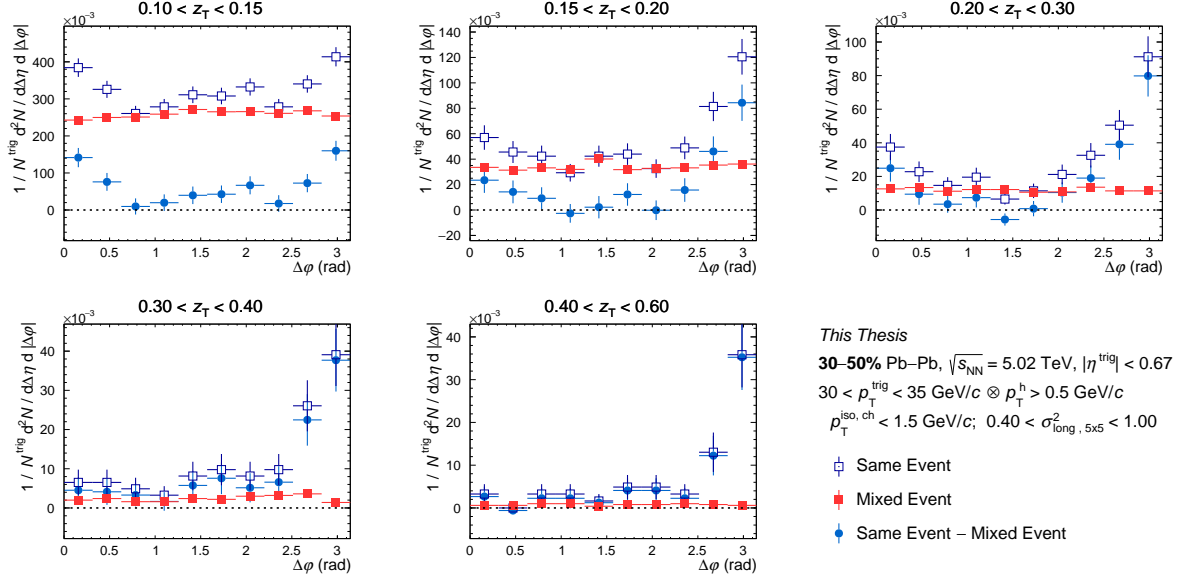


Figure C.34: Azimuthal correlation distribution in **30–50%** for isolated wide clusters for the same event (empty blue square), for mixed event (full red square) and for result of the subtraction (full light blue circle) as a function of $\Delta\varphi$ for different z_T bins with $30 < p_T^{\text{trig}} < 35 \text{ GeV}/c$.

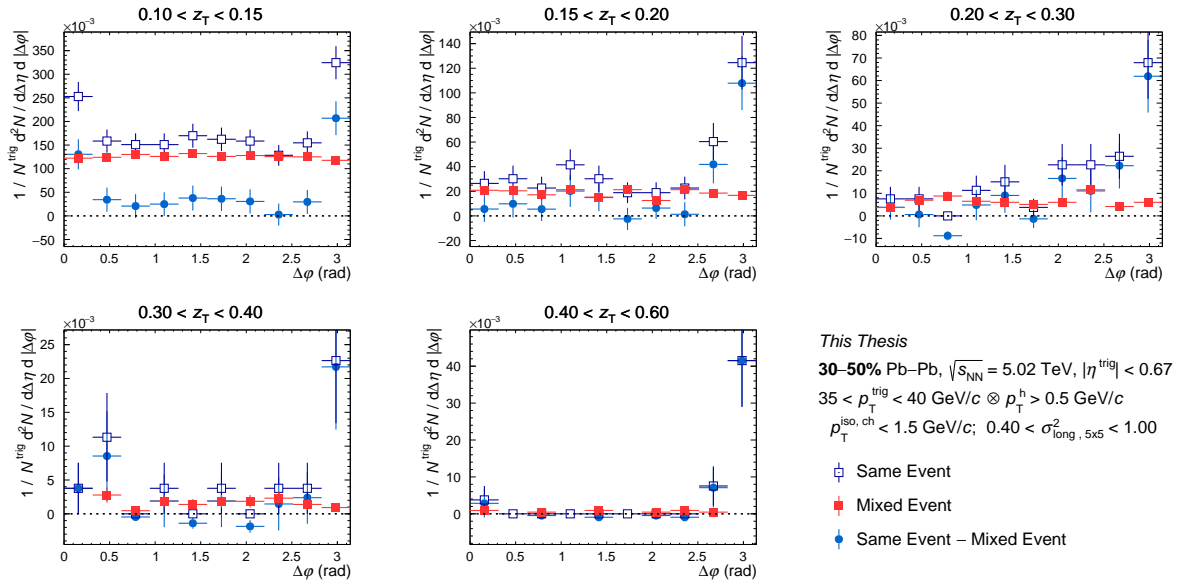


Figure C.35: Azimuthal correlation distribution in **30–50%** for isolated wide clusters for the same event (empty blue square), for mixed event (full red square) and for result of the subtraction (full light blue circle) as a function of $\Delta\varphi$ for different z_T bins with $35 < p_T^{\text{trig}} < 40 \text{ GeV}/c$.

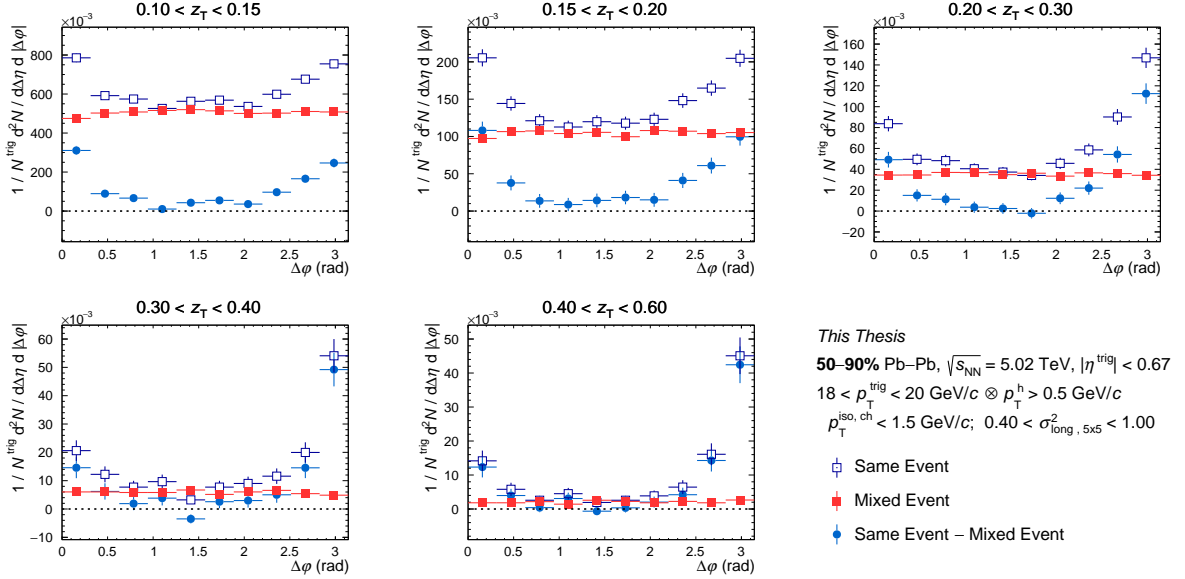


Figure C.36: Azimuthal correlation distribution in 50–90% for isolated wide clusters for the same event (empty blue square), for mixed event (full red square) and for result of the subtraction (full light blue circle) as a function of $\Delta\varphi$ for different z_T bins with $18 < p_T^{\text{trig}} < 20$ GeV/c.

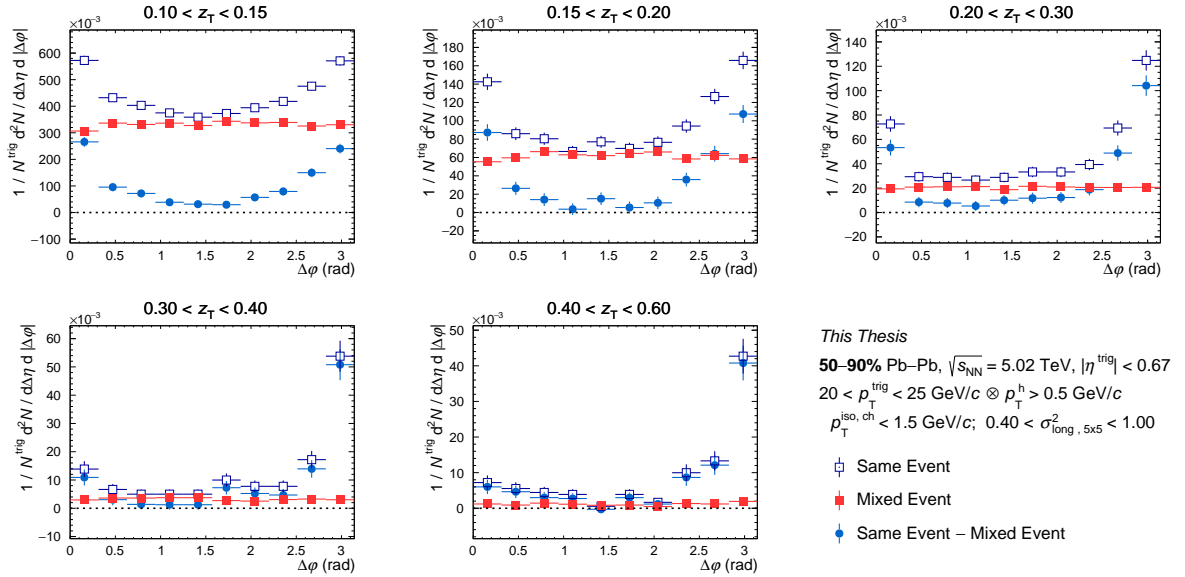


Figure C.37: Azimuthal correlation distribution in 50–90% for isolated wide clusters for the same event (empty blue square), for mixed event (full red square) and for result of the subtraction (full light blue circle) as a function of $\Delta\varphi$ for different z_T bins with $20 < p_T^{\text{trig}} < 25$ GeV/c.

C.8. Azimuthal correlation distributions in 50-90% Pb–Pb collisions for isolated cluster wide

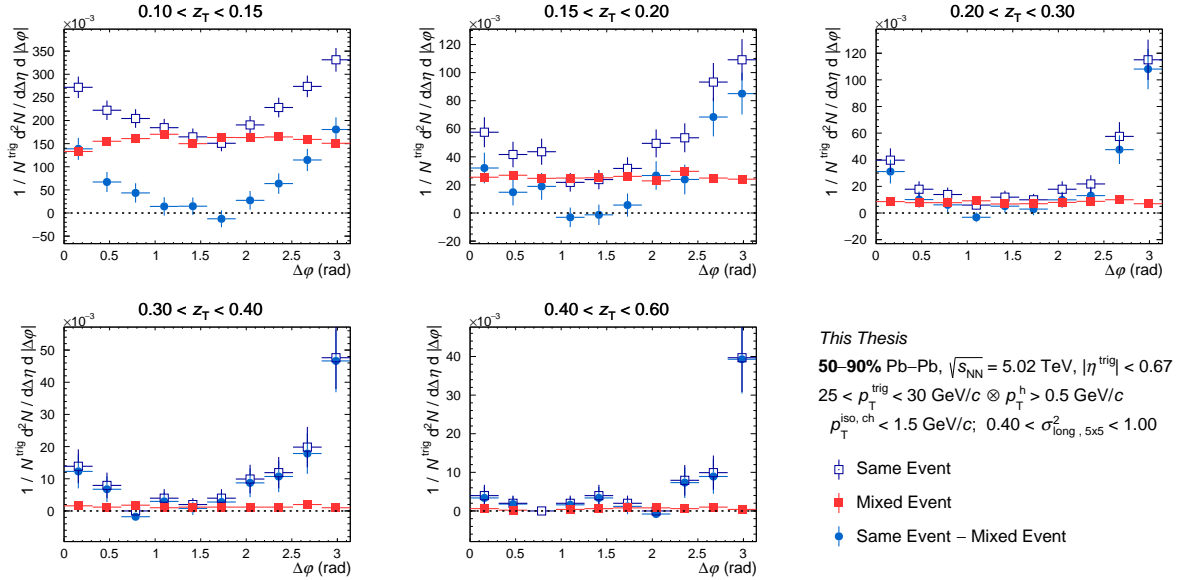


Figure C.38: Azimuthal correlation distribution in **50–90%** for isolated wide clusters for the same event (empty blue square), for mixed event (full red square) and for result of the subtraction (full light blue circle) as a function of $\Delta\varphi$ for different z_T bins with $25 < p_T^{\text{trig}} < 30 \text{ GeV}/c$.

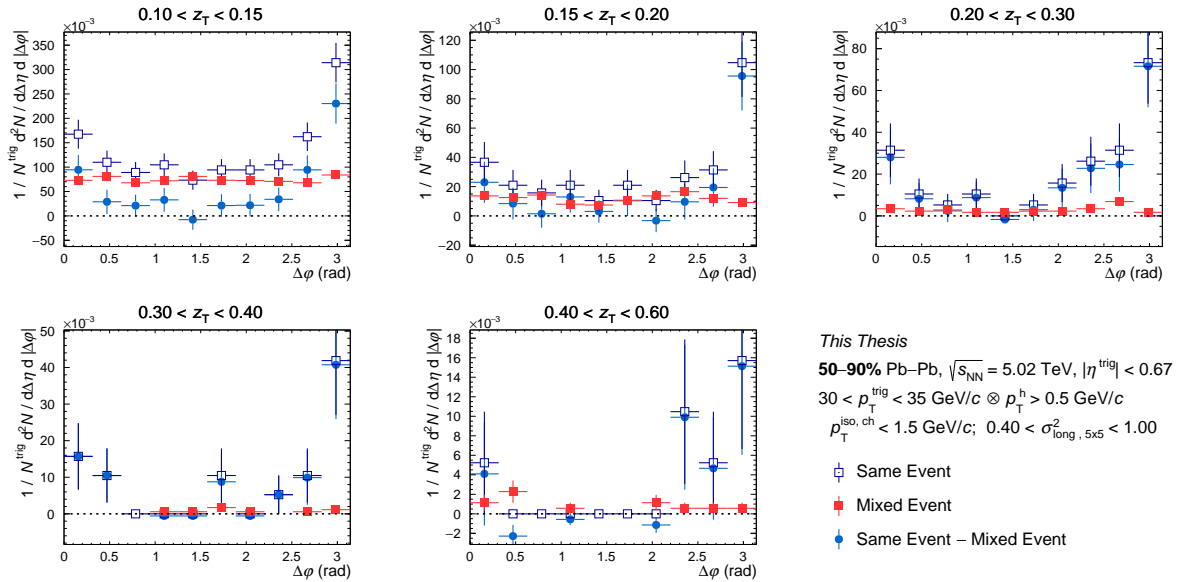


Figure C.39: Azimuthal correlation distribution in **50–90%** for isolated wide clusters for the same event (empty blue square), for mixed event (full red square) and for result of the subtraction (full light blue circle) as a function of $\Delta\varphi$ for different z_T bins with $30 < p_T^{\text{trig}} < 35 \text{ GeV}/c$.

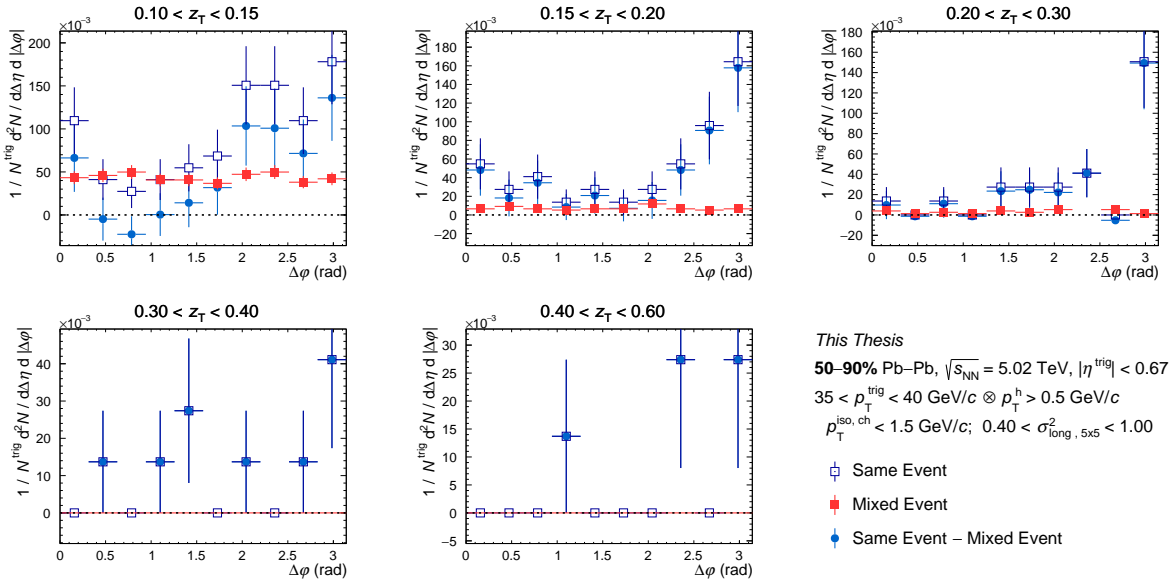


Figure C.40: Azimuthal correlation distribution in **50–90%** for isolated wide clusters for the same event (empty blue square), for mixed event (full red square) and for result of the subtraction (full light blue circle) as a function of $\Delta\varphi$ for different z_T bins with $35 < p_T^{\text{trig}} < 40$ GeV/c.

C.9 Azimuthal correlation distributions: purity correction

Purity correction in 0-10%

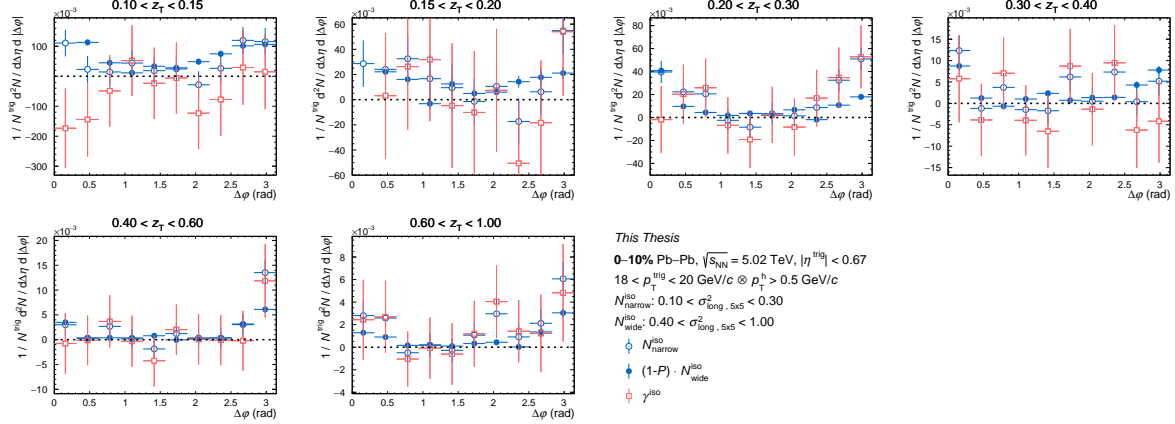


Figure C.41: Azimuthal correlation distributions in **0-10%** for isolated narrow cluster (full light blue circle), for isolated wide cluster (empty light blue circle) and γ^{iso} (empty orange square) as a function of $\Delta\varphi$ for different z_T bins with $18 < p_T^{\text{trig}} < 20 \text{ GeV}/c$.

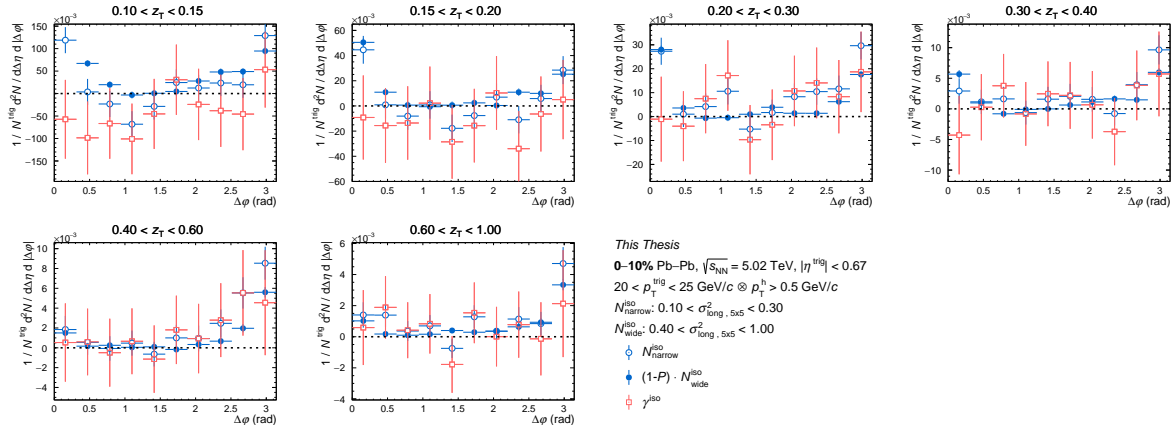


Figure C.42: Azimuthal correlation distributions in **0-10%** for isolated narrow cluster (full light blue circle), for isolated wide cluster (empty light blue circle) and γ^{iso} (empty orange square) as a function of $\Delta\varphi$ for different z_T bins with $20 < p_T^{\text{trig}} < 25 \text{ GeV}/c$.

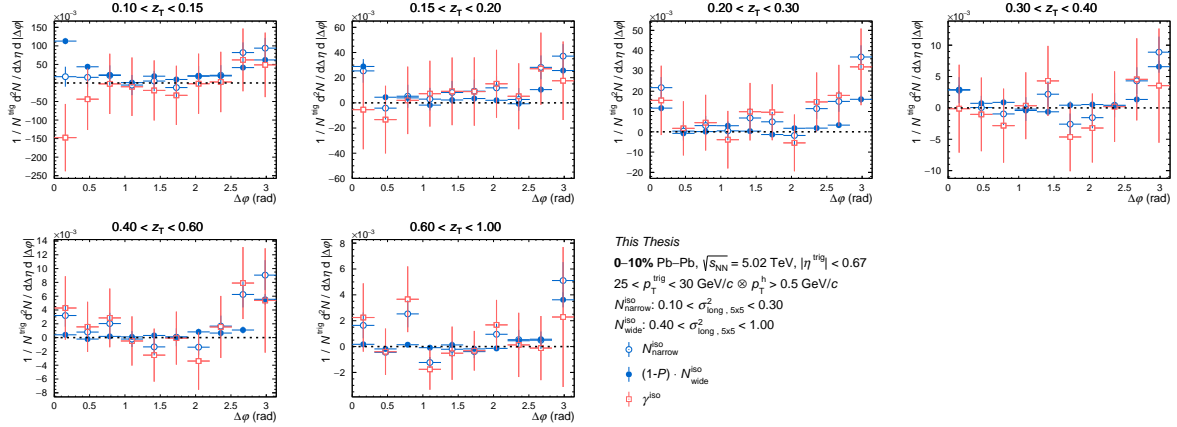


Figure C.43: Azimuthal correlation distributions in **0-10%** for isolated narrow cluster (full light blue circle), for isolated wide cluster (empty light blue circle) and γ^{iso} (empty orange square) as a function of $\Delta\varphi$ for different z_T bins with $25 < p_T^{\text{trig}} < 30 \text{ GeV}/c$.

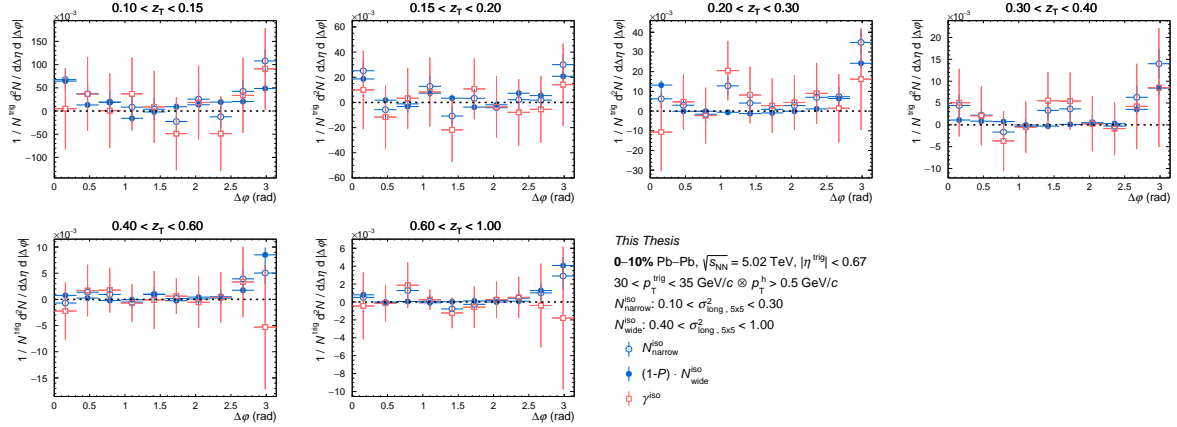


Figure C.44: Azimuthal correlation distributions in **0-10%** for isolated narrow cluster (full light blue circle), for isolated wide cluster (empty light blue circle) and γ^{iso} (empty orange square) as a function of $\Delta\varphi$ for different z_T bins with $30 < p_T^{\text{trig}} < 35 \text{ GeV}/c$.

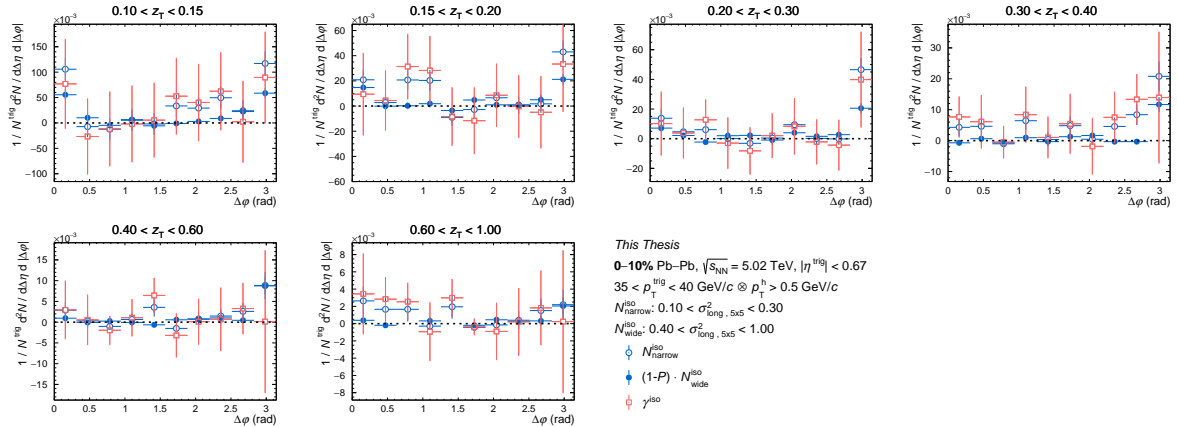


Figure C.45: Azimuthal correlation distributions in **0-10%** for isolated narrow cluster (full light blue circle), for isolated wide cluster (empty light blue circle) and γ^{iso} (empty orange square) as a function of $\Delta\varphi$ for different z_T bins with $35 < p_T^{\text{trig}} < 40 \text{ GeV}/c$.

Purity correction in 10-30%

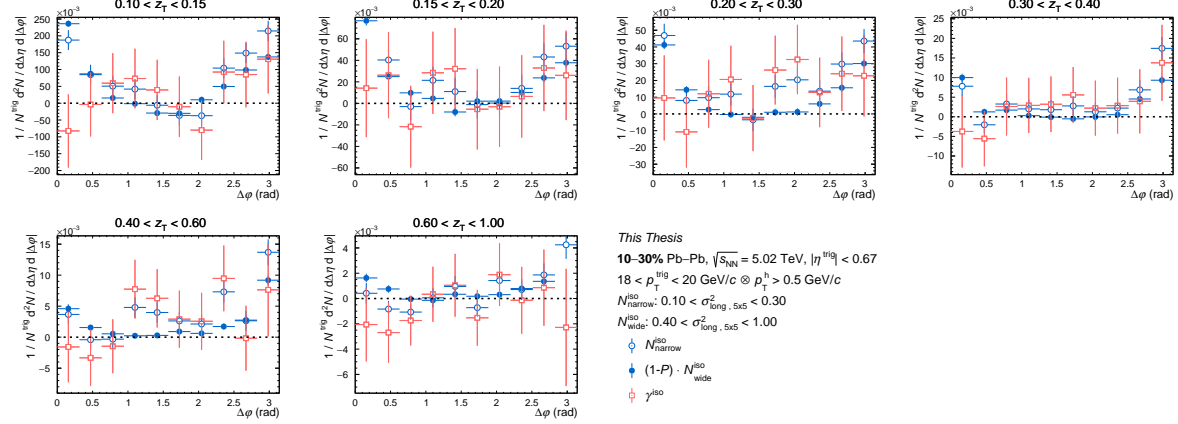


Figure C.46: Azimuthal correlation distributions in **10-30%** for isolated narrow cluster (full light blue circle), for isolated wide cluster (empty light blue circle) and γ^{iso} (empty orange square) as a function of $\Delta\varphi$ for different z_T bins with $18 < p_T^{\text{trig}} < 20 \text{ GeV}/c$.

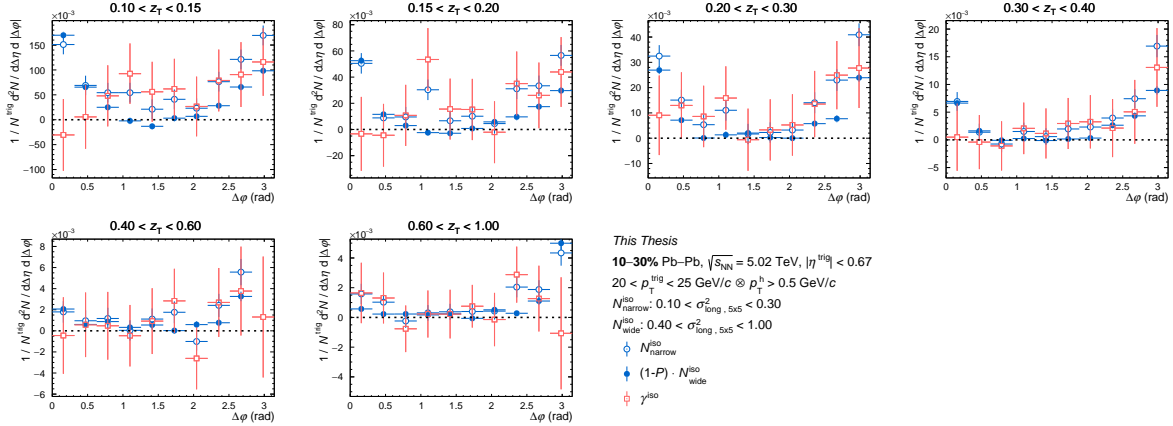


Figure C.47: Azimuthal correlation distributions in **10-30%** for isolated narrow cluster (full light blue circle), for isolated wide cluster (empty light blue circle) and γ^{iso} (empty orange square) as a function of $\Delta\varphi$ for different z_T bins with $20 < p_T^{\text{trig}} < 25 \text{ GeV}/c$.

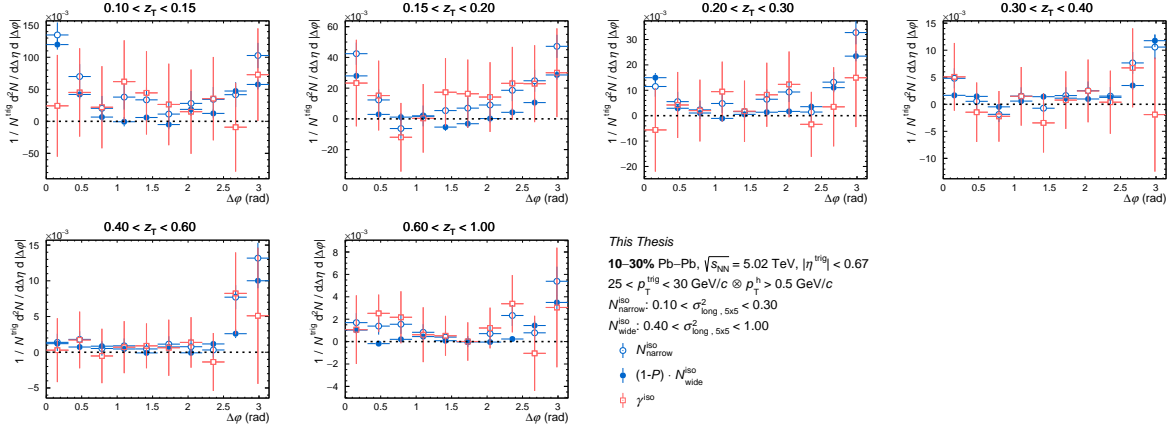


Figure C.48: Azimuthal correlation distributions in 10-30% for isolated narrow cluster (full light blue circle), for isolated wide cluster (empty light blue circle) and γ^{iso} (empty orange square) as a function of $\Delta\varphi$ for different z_T bins with $25 < p_T^{\text{trig}} < 30 \text{ GeV}/c$.

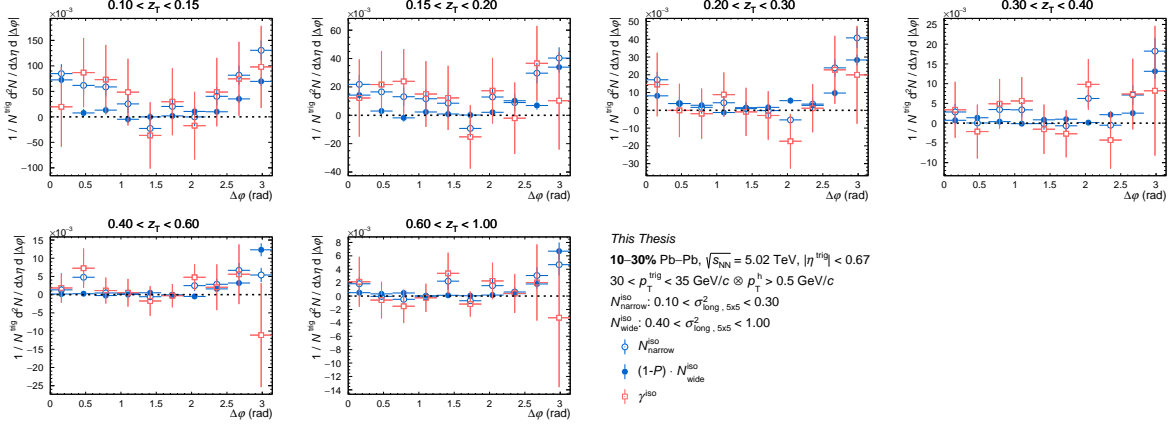


Figure C.49: Azimuthal correlation distributions in 10-30% for isolated narrow cluster (full light blue circle), for isolated wide cluster (empty light blue circle) and γ^{iso} (empty orange square) as a function of $\Delta\varphi$ for different z_T bins with $30 < p_T^{\text{trig}} < 35 \text{ GeV}/c$.

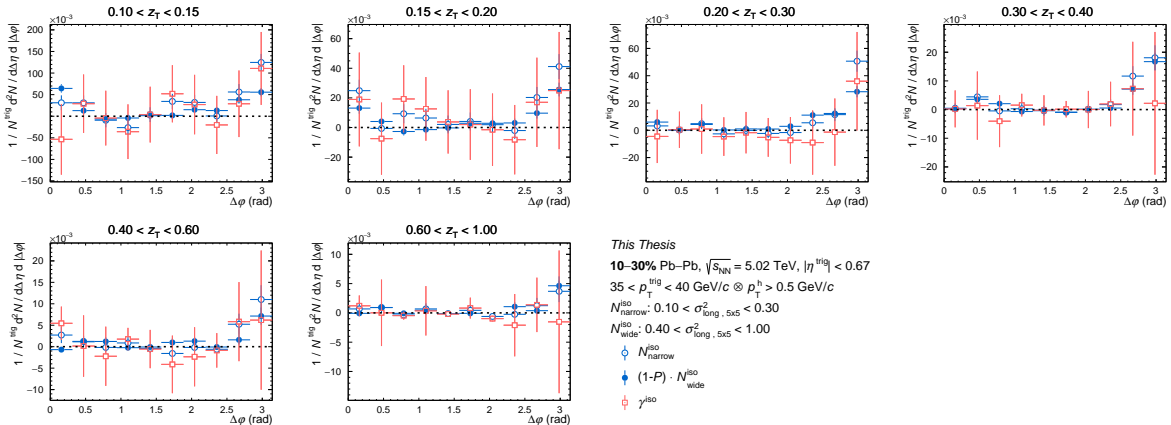


Figure C.50: Azimuthal correlation distributions in 10-30% for isolated narrow cluster (full light blue circle), for isolated wide cluster (empty light blue circle) and γ^{iso} (empty orange square) as a function of $\Delta\varphi$ for different z_T bins with $35 < p_T^{\text{trig}} < 40 \text{ GeV}/c$.

Purity correction in 30-50%

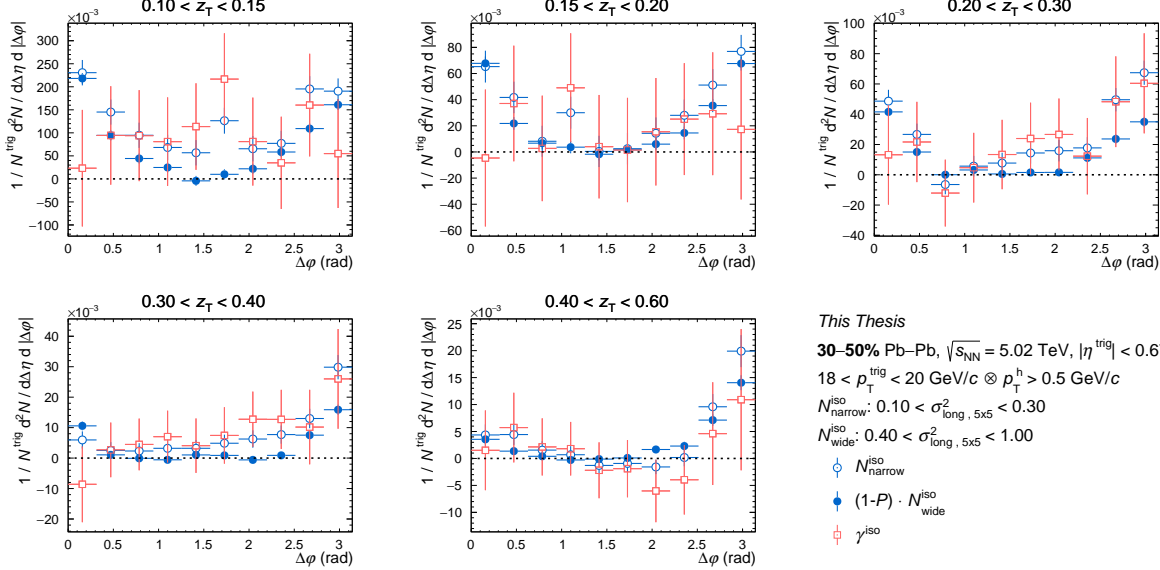


Figure C.51: Azimuthal correlation distributions in **30–50%** for isolated narrow cluster (full light blue circle), for isolated wide cluster (empty light blue circle) and γ^{iso} (empty orange square) as a function of $\Delta\varphi$ for different z_T bins with $18 < p_T^{\text{trig}} < 20 \text{ GeV}/c$.

Purity correction in 50-90%

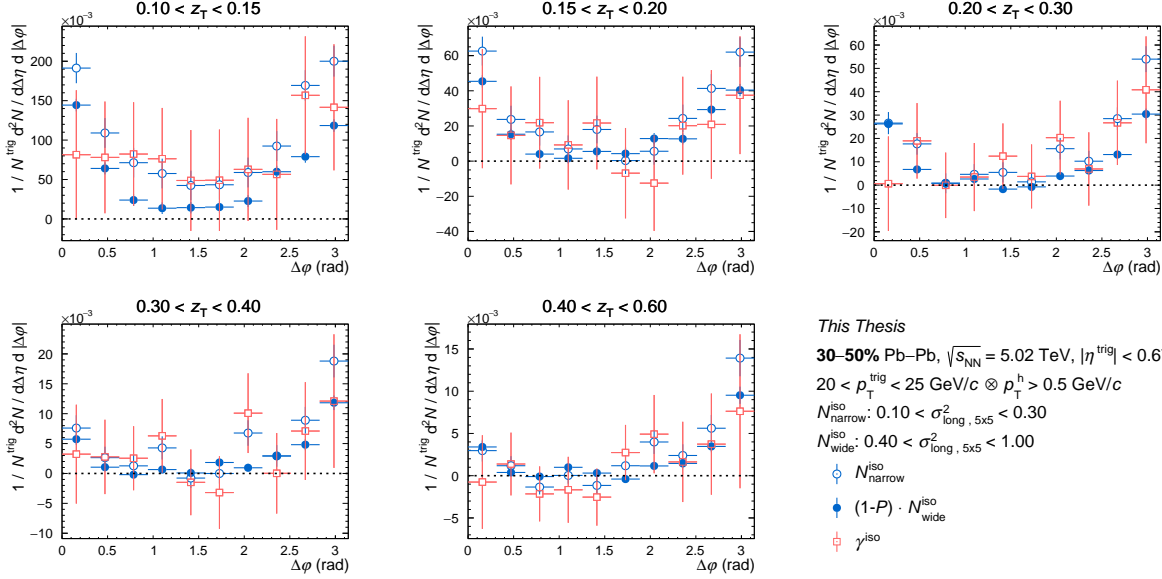


Figure C.52: Azimuthal correlation distributions in **30–50%** for isolated narrow cluster (full light blue circle), for isolated wide cluster (empty light blue circle) and γ^{iso} (empty orange square) as a function of $\Delta\varphi$ for different z_T bins with $20 < p_T^{\text{trig}} < 25 \text{ GeV}/c$.

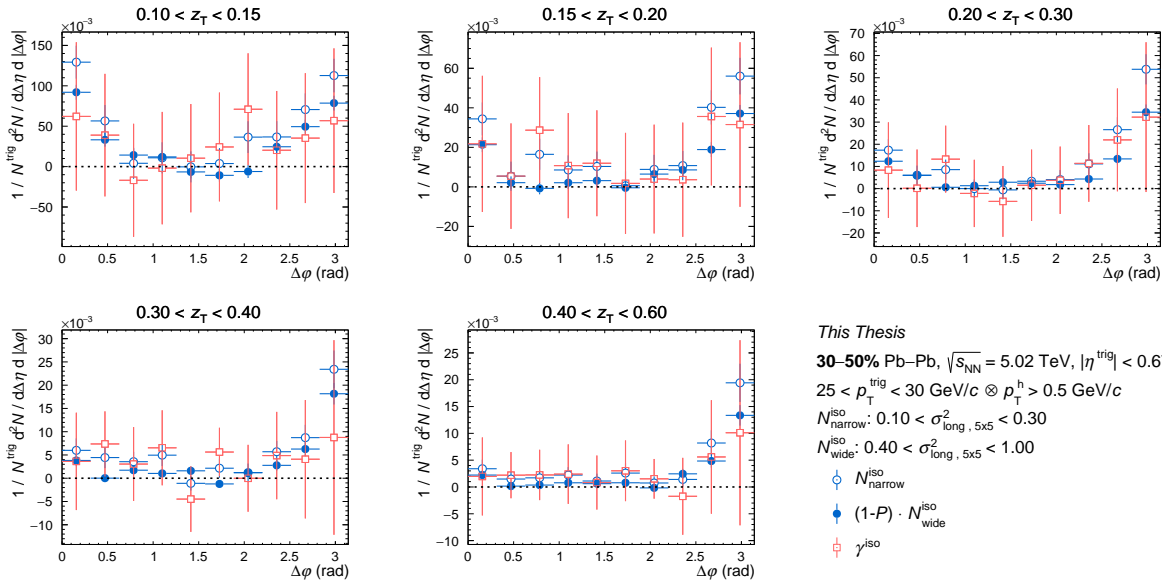


Figure C.53: Azimuthal correlation distributions in **30–50%** for isolated narrow cluster (full light blue circle), for isolated wide cluster (empty light blue circle) and γ^{iso} (empty orange square) as a function of $\Delta\varphi$ for different z_T bins with $25 < p_T^{\text{trig}} < 30 \text{ GeV}/c$.

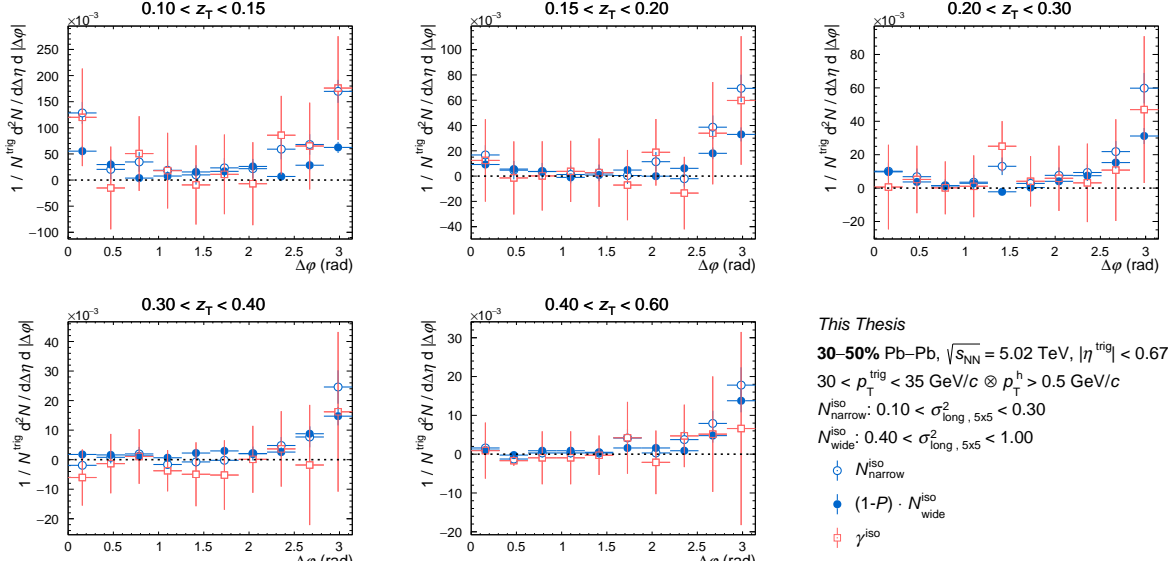


Figure C.54: Azimuthal correlation distributions in **30–50%** for isolated narrow cluster (full light blue circle), for isolated wide cluster (empty light blue circle) and γ^{iso} (empty orange square) as a function of $\Delta\varphi$ for different z_T bins with $30 < p_T^{\text{trig}} < 35$ GeV/c.

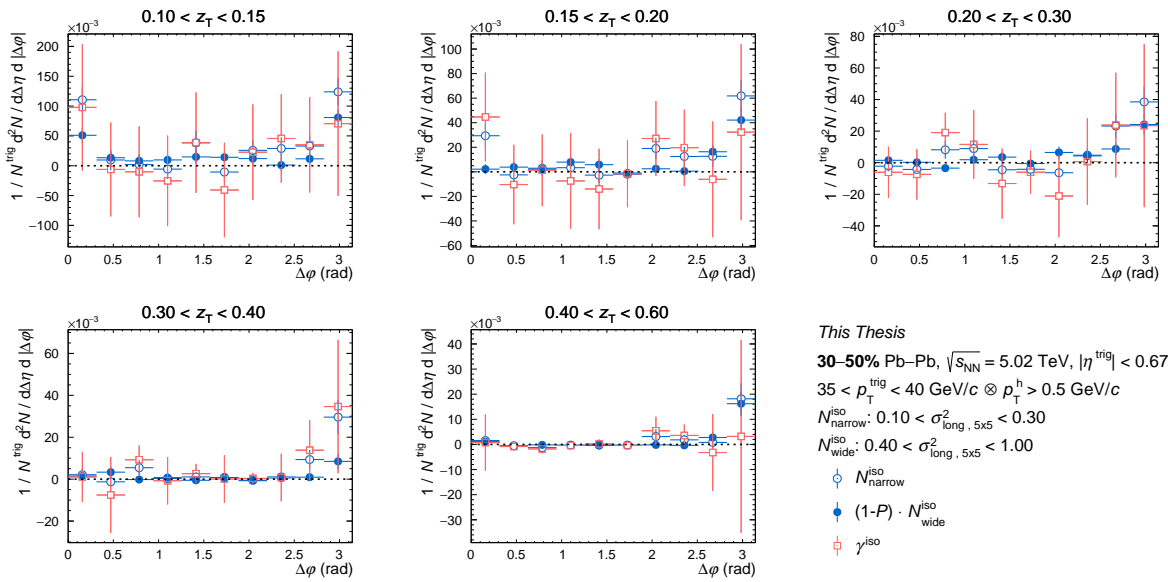


Figure C.55: Azimuthal correlation distributions in **30–50%** for isolated narrow cluster (full light blue circle), for isolated wide cluster (empty light blue circle) and γ^{iso} (empty orange square) as a function of $\Delta\varphi$ for different z_T bins with $35 < p_T^{\text{trig}} < 40$ GeV/c.

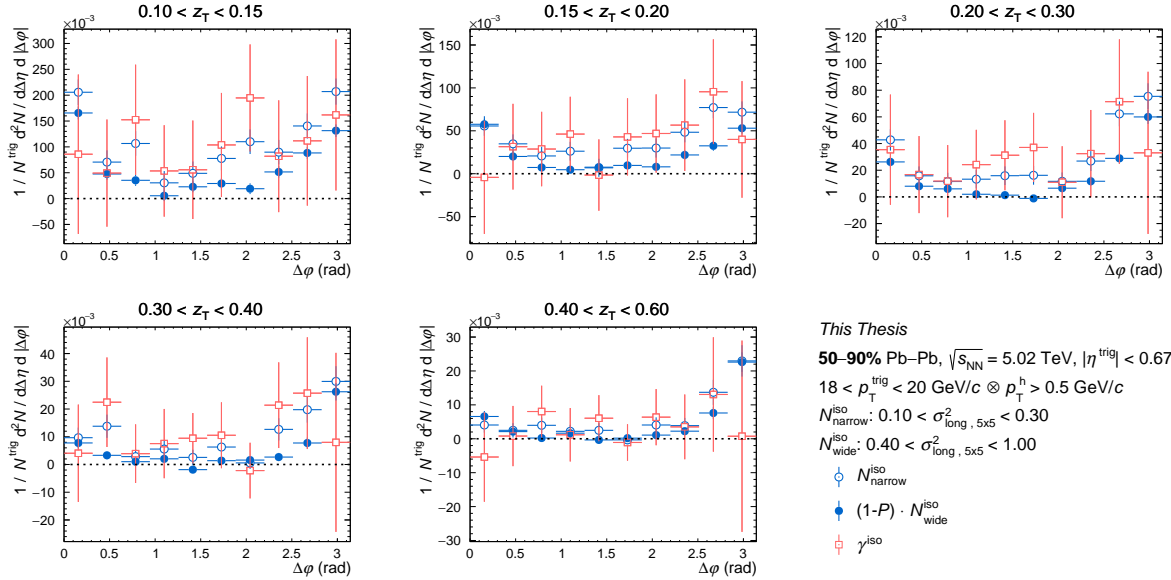


Figure C.56: Azimuthal correlation distributions in 50–90% for isolated narrow cluster (full light blue circle), for isolated wide cluster (empty light blue circle) and γ^{iso} (empty orange square) as a function of $\Delta\varphi$ for different z_T bins with $18 < p_T^{\text{trig}} < 20 \text{ GeV}/c$.

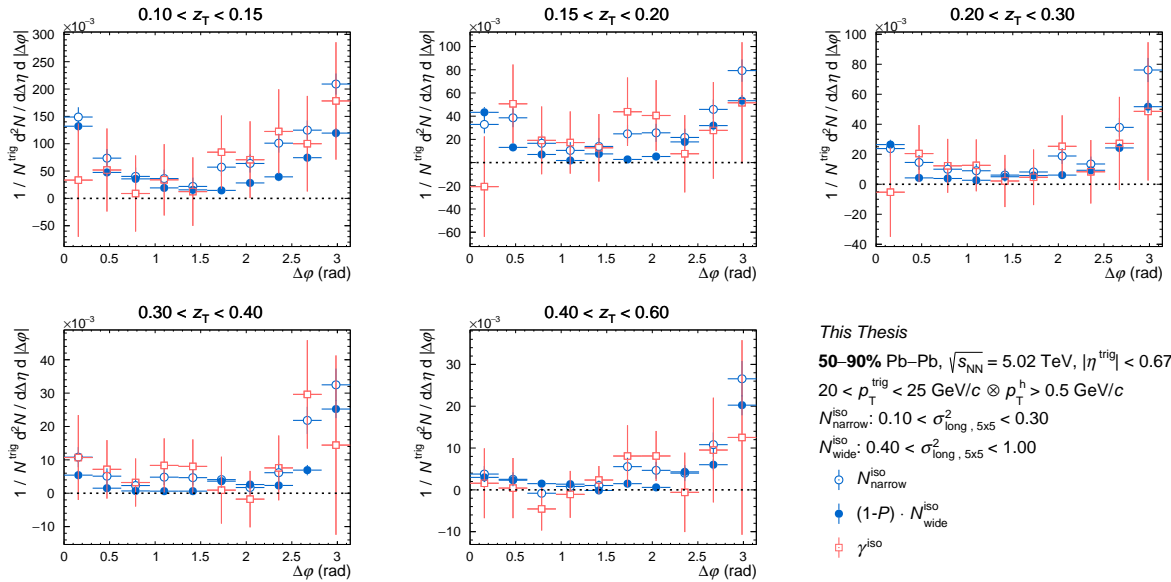


Figure C.57: Azimuthal correlation distributions in 50–90% for isolated narrow cluster (full light blue circle), for isolated wide cluster (empty light blue circle) and γ^{iso} (empty orange square) as a function of $\Delta\varphi$ for different z_T bins with $20 < p_T^{\text{trig}} < 25 \text{ GeV}/c$.

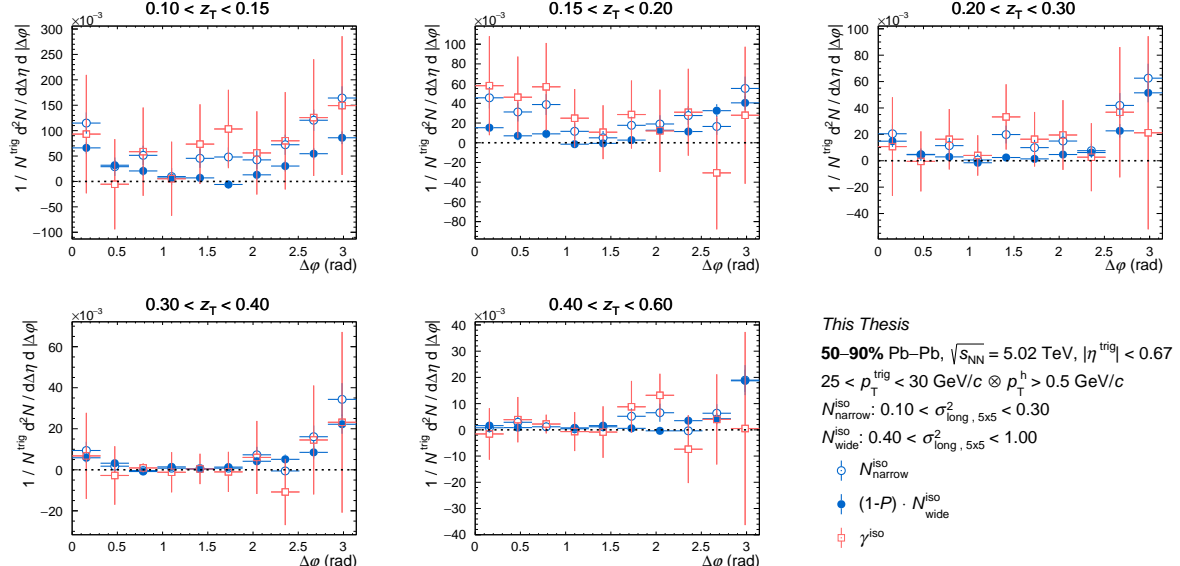


Figure C.58: Azimuthal correlation distributions in **50–90%** for isolated narrow cluster (full light blue circle), for isolated wide cluster (empty light blue circle) and γ^{iso} (empty orange square) as a function of $\Delta\varphi$ for different z_T bins with $25 < p_T^{\text{trig}} < 30$ GeV/c.

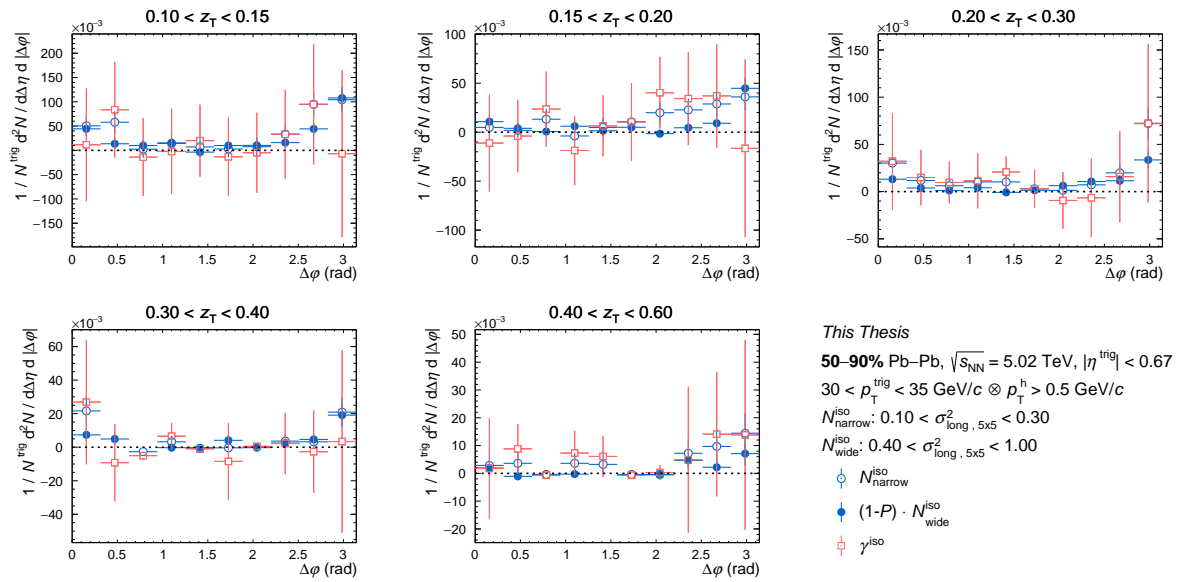


Figure C.59: Azimuthal correlation distributions in **50–90%** for isolated narrow cluster (full light blue circle), for isolated wide cluster (empty light blue circle) and γ^{iso} (empty orange square) as a function of $\Delta\varphi$ for different z_T bins with $30 < p_T^{\text{trig}} < 35$ GeV/c.

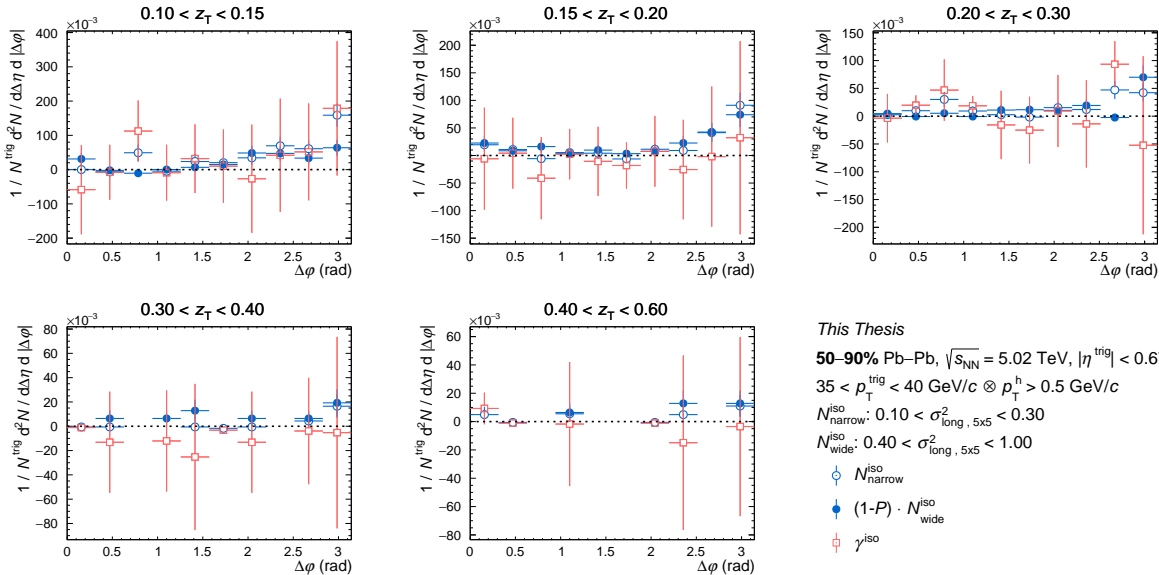


Figure C.60: Azimuthal correlation distributions in **50–90%** for isolated narrow cluster (full light blue circle), for isolated wide cluster (empty light blue circle) and γ^{iso} (empty orange square) as a function of $\Delta\varphi$ for different z_T bins with $35 < p_T^{\text{trig}} < 40 \text{ GeV}/c$.

C.10 $D(z_T)$ distributions for all p_T^γ intervals

Centrality: 0-10%

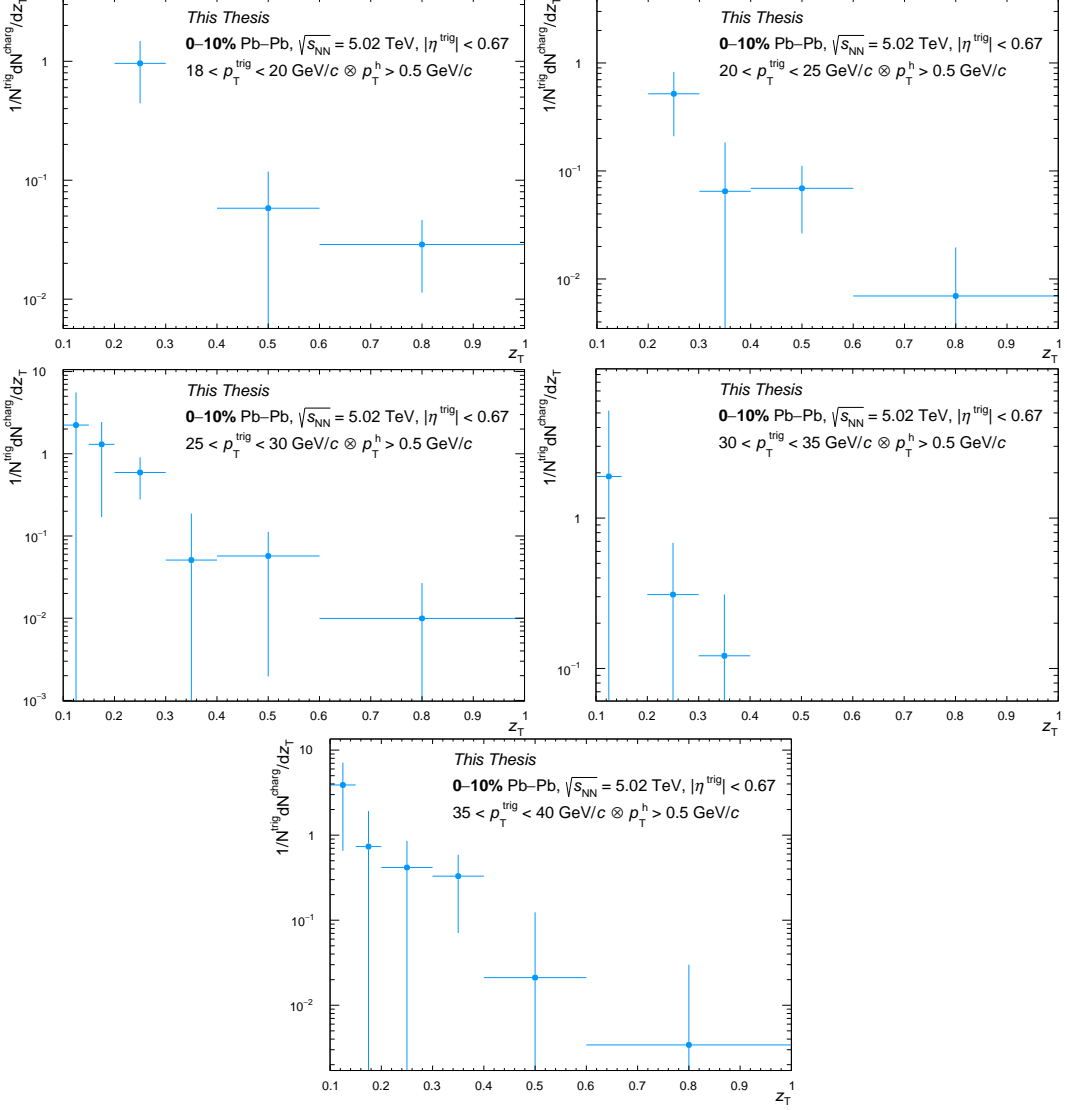


Figure C.61: $D(z_T)$ distribution as a function of z_T in 0-10% Pb-Pb collisions for different p_T^γ intervals. From top to bottom: $18 < p_T^\gamma < 20 \text{ GeV}/c$, $20 < p_T^\gamma < 25 \text{ GeV}/c$, $25 < p_T^\gamma < 30 \text{ GeV}/c$, $30 < p_T^\gamma < 35 \text{ GeV}/c$ and $35 < p_T^\gamma < 40 \text{ GeV}/c$.

Centrality: 10-30%

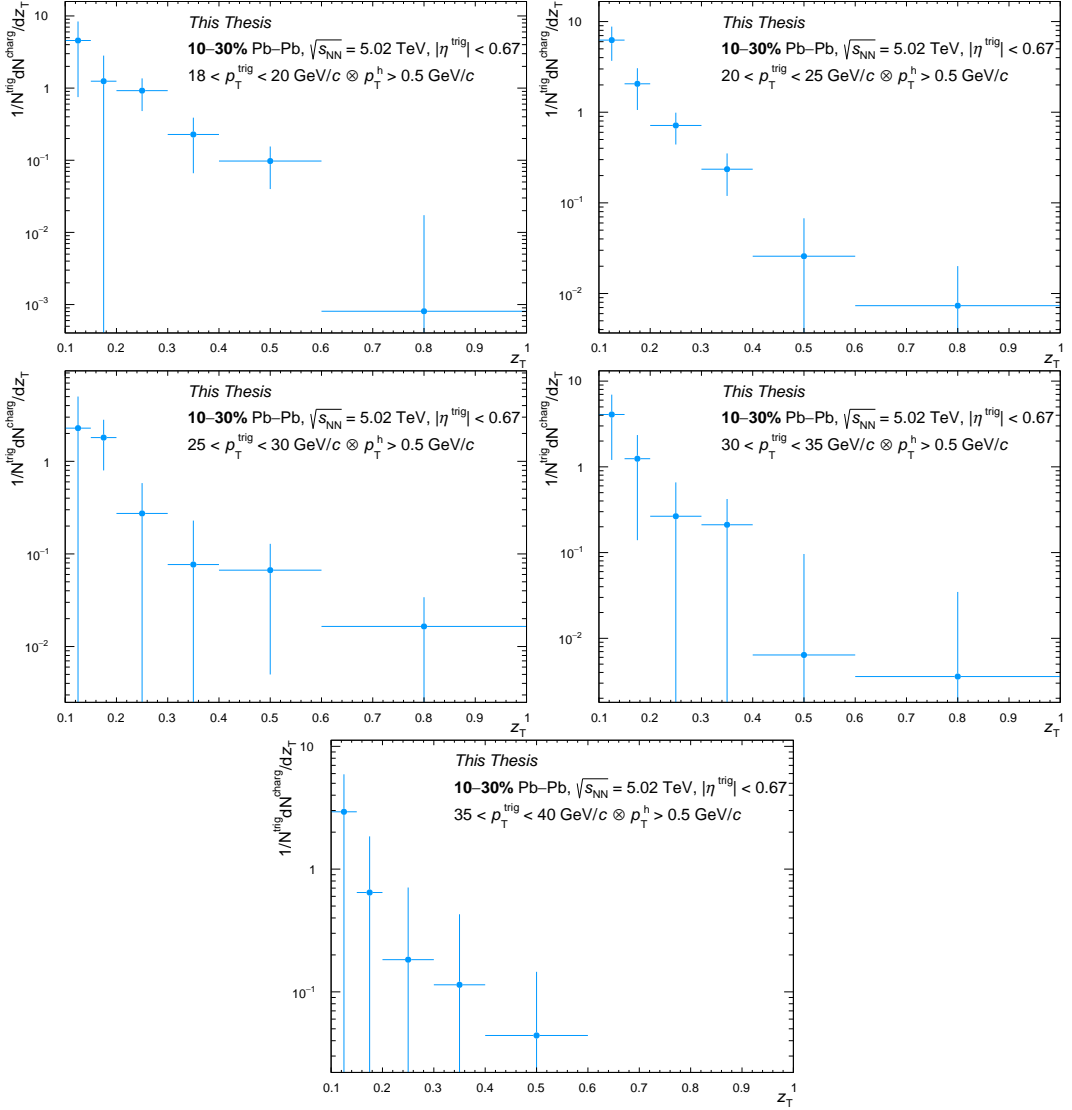


Figure C.62: $D(z_T)$ distribution as a function of z_T in 10-30% Pb-Pb collisions for different p_T^γ intervals. From top to bottom: $18 < p_T^\gamma < 20 \text{ GeV}/c$, $20 < p_T^\gamma < 25 \text{ GeV}/c$, $25 < p_T^\gamma < 30 \text{ GeV}/c$, $30 < p_T^\gamma < 35 \text{ GeV}/c$ and $35 < p_T^\gamma < 40 \text{ GeV}/c$.

Centrality: 30-50%

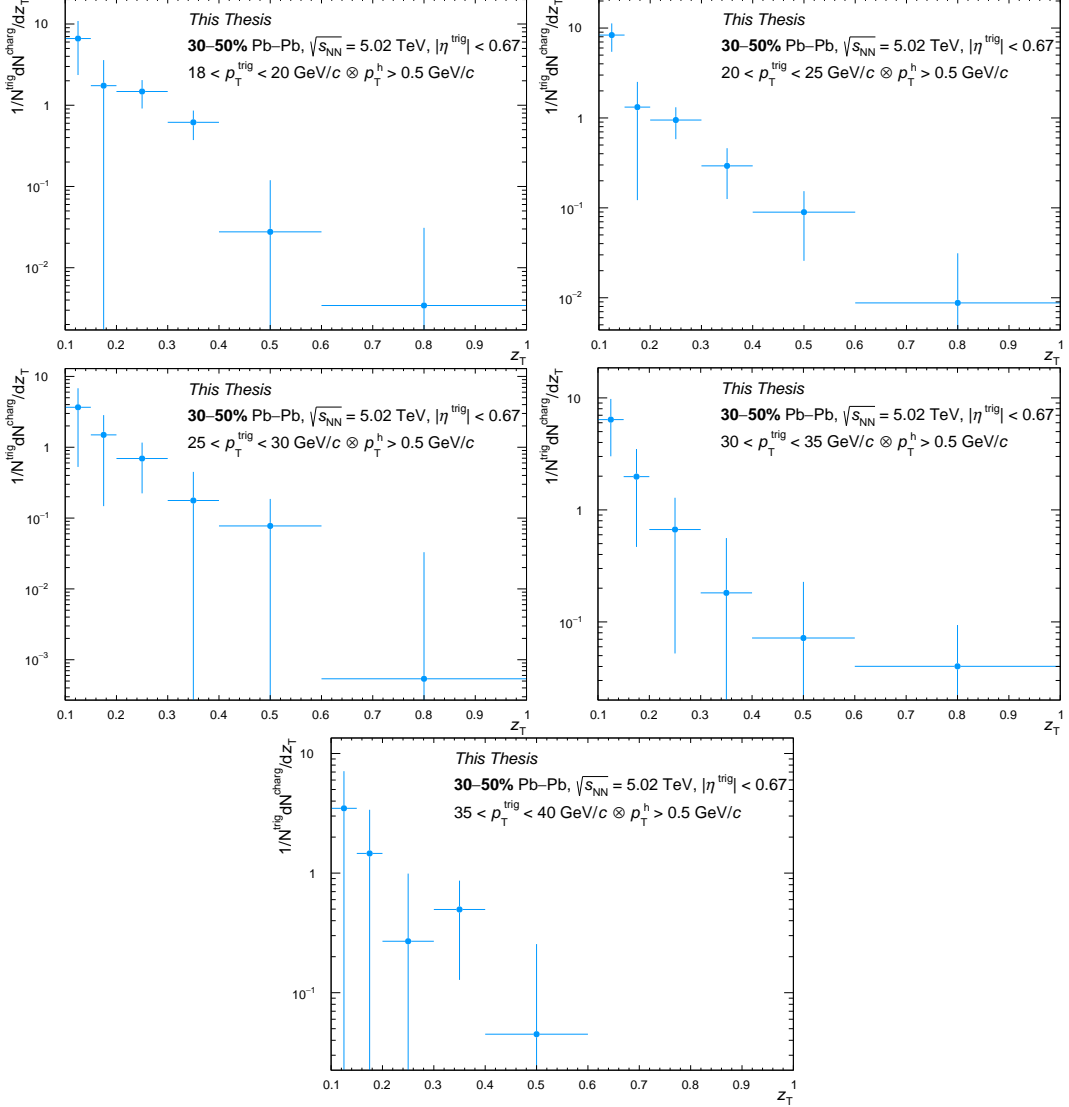


Figure C.63: $D(z_T)$ distribution as a function of z_T in 30-50% Pb-Pb collisions for different p_T^γ intervals. From top to bottom: $18 < p_T^\gamma < 20$ GeV/c, $20 < p_T^\gamma < 25$ GeV/c, $25 < p_T^\gamma < 30$ GeV/c, $30 < p_T^\gamma < 35$ GeV/c and $35 < p_T^\gamma < 40$ GeV/c.

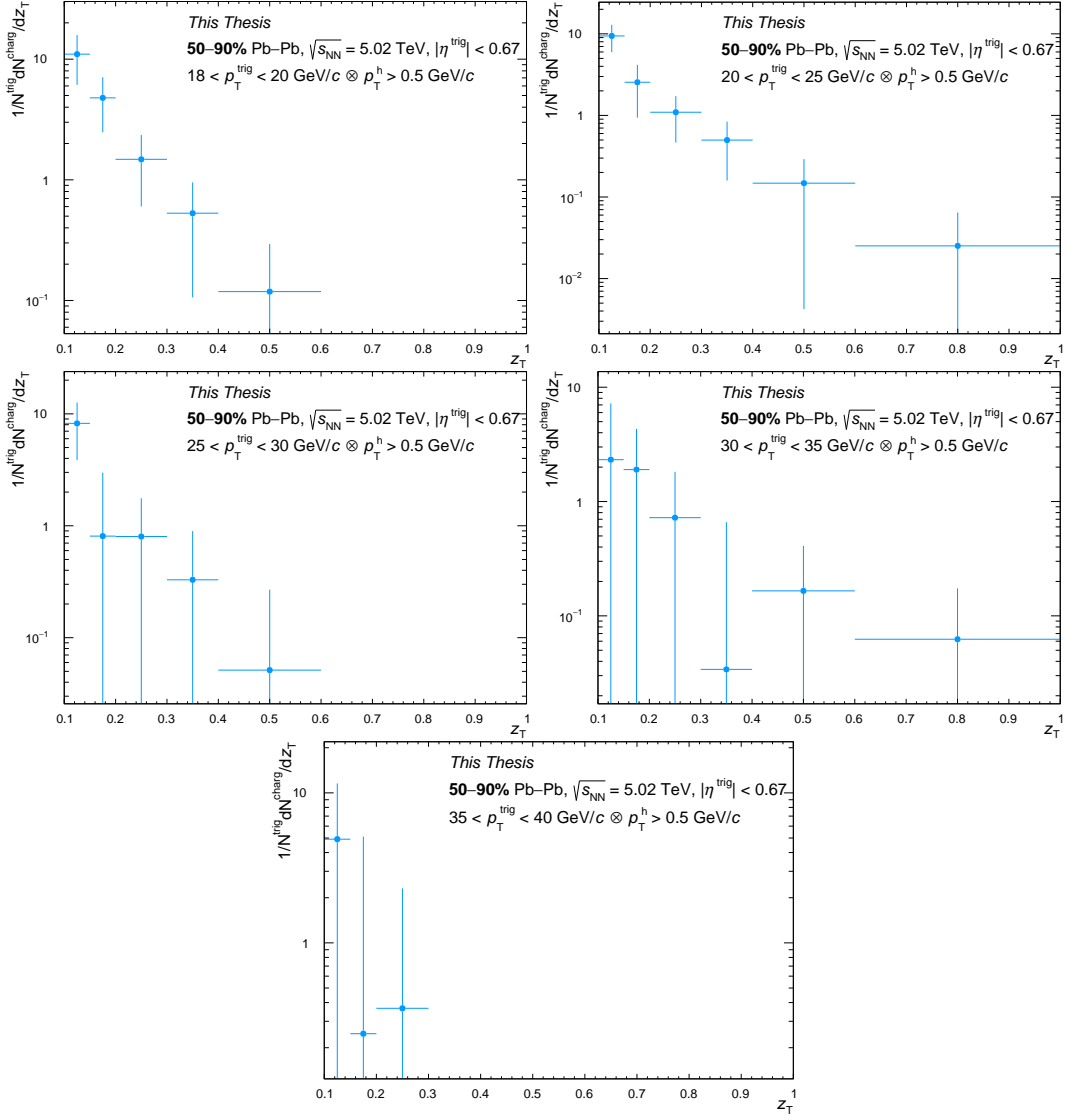
Centrality: 50-90%


Figure C.64: $D(z_T)$ distribution as a function of z_T in 50-90% Pb-Pb collisions for different p_T^γ intervals. From top to bottom: $18 < p_T^\gamma < 20 \text{ GeV}/c$, $20 < p_T^\gamma < 25 \text{ GeV}/c$, $25 < p_T^\gamma < 30 \text{ GeV}/c$, $30 < p_T^\gamma < 35 \text{ GeV}/c$ and $35 < p_T^\gamma < 40 \text{ GeV}/c$.

Appendix D

I_{CP} systematics

As for the fragmentation functions $D(z_T)$, it is necessary to estimate the systematic uncertainties for the I_{CP} . The following variables have been evaluated to see if they introduce any systematic uncertainty:

- the mixed event and its estimation of UE;
- the purity;
- the $\sigma_{\text{long}, 5\times5}$ background range variations;
- the filling of the mixed event pool with the centrality.

Since the I_{CP} is the ratio between the fragmentation functions in central or semi-central collisions relative to peripheral ones, there can be a cancellation of uncertainties. This is the case for the tracking uncertainty, which is not taken into account in this analysis.

The systematics are calculated considering relative variations (in %):

$$\Delta_i^{\text{rel}}(x) = \left| \frac{x_{\text{reference}} - x_i}{x_{\text{reference}}} \right| \times 100 \quad \text{or} \quad \Delta_i^{\text{rel}}(x) = \frac{1}{2} \left| \frac{x_i^{\max} - x_i^{\min}}{x_{\text{reference}}} \right| \times 100 \quad (\text{D.1})$$

D.0.1 Mixed event and UE estimation

The systematic uncertainties due to the UE event estimation on the I_{CP} is obtained by compiling and adding in quadrature the ε_{ME} in central or semicentral collisions and the ε_{ME} in peripheral ones are:

$$\varepsilon_{\text{ME}}^{I_{\text{CP}}} = \sqrt{\varepsilon_{\text{ME}, 0-30\%, 30-50\%}^2 + \varepsilon_{\text{ME}, 50-90\%}^2}. \quad (\text{D.2})$$

The uncertainty $\varepsilon_{\text{ME}, x-x\%}$ is determined in Sect. 6.4.1 for every centrality.

D.0.2 Purity

As already presented in Sect. 6.4.2, the analysis is repeated using the purity values obtained adding or subtracting to it its total uncertainty. The I_{CP} distributions measured with those values are shown in Fig. D.1 as a function of z_T in 0-30% and 30-50% Pb-Pb collisions. The systematic uncertainty is evaluated using the Eq. (D.1)-left and the results are shown in Fig. D.2. At low z_T , the systematic uncertainty is larger in central collisions than in semicentral. At high z_T , the uncertainties are large, because of the fluctuations of the

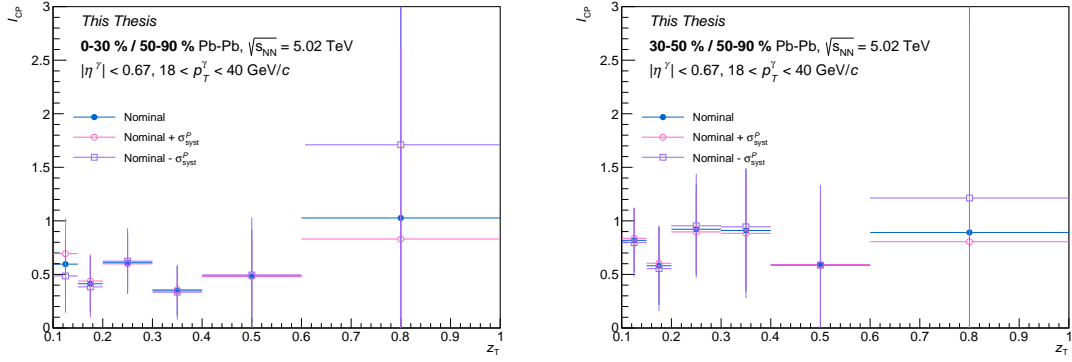


Figure D.1: The I_{CP} ratios for different purity values: nominal (full blue circle), nominal + σ_{syst}^P (empty pink circle) and nominal - σ_{syst}^P (empty violet square) in 0-30% (left panel) and in 30-50% (right panel) Pb-Pb collisions.

peripheral collisions in that bin. The systematic uncertainties due to the purity as a function of z_T are shown in Fig. D.2-left and they have been fitted with an exponential to polish the trend. The result after the fit is reported Fig. D.2-right.

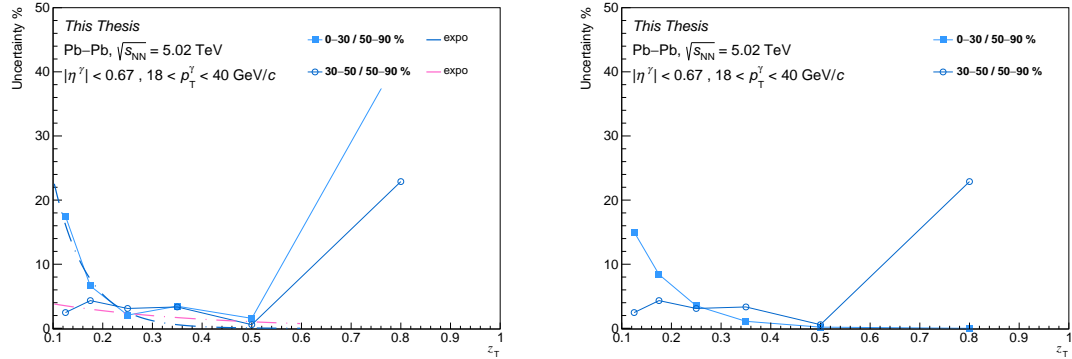


Figure D.2: Left: Systematic uncertainties of the purity on the I_{CP} in 0-30% (full light blue square) and 30-50% (empty blue circle) Pb-Pb collisions. Polishing of the systematic uncertainties using an exponential fit in 0-30% (blue dot-dashed line) and 30-50% (pink dot-dashed line) Pb-Pb collisions. Right: Systematic uncertainties of the purity after the fit.

D.0.3 Variation of the Shower Shape

The $\sigma_{\text{long}, 5 \times 5}^2$ background limits have been varied and the various combinations tested are reported in the following list:

- $0.35 < \sigma_{\text{long}, 5 \times 5}^2 < 1.00$;
- $0.40 < \sigma_{\text{long}, 5 \times 5}^2 < 1.00$ (default);
- $0.40 < \sigma_{\text{long}, 5 \times 5}^2 < 1.50$ [110];
- $0.40 < \sigma_{\text{long}, 5 \times 5}^2 < 2.00$ [149];

The same considerations presented in Sect. 6.4.3, can be repeated here for the selected ranges. Figure D.3 shows the I_{CP} ratios as a function of z_T in 0-30% and 30-50% Pb–Pb collisions. The I_{CP} ratios do not seem to show a clear trend at the varying the $\sigma_{long, 5\times5}^2$. The

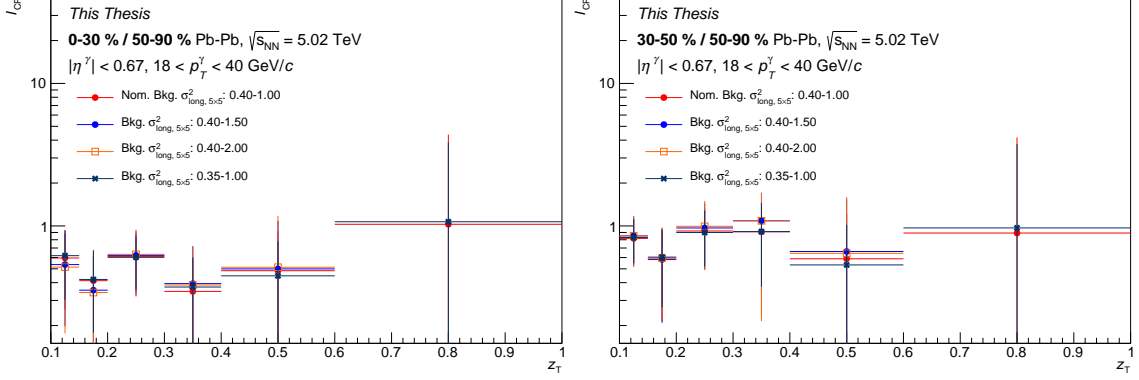


Figure D.3: The I_{CP} distributions obtained using different $\sigma_{long, 5\times5}^2$ background ranges: $0.40 < \sigma_{long, 5\times5}^2 < 1.00$ (full red circle) $0.40 < \sigma_{long, 5\times5}^2 < 1.50$ (full blue circle); $0.40 < \sigma_{long, 5\times5}^2 < 2.00$ (empty orange square) and $0.35 < \sigma_{long, 5\times5}^2 < 1.00$ (full black cross) in 0-30% (top left) and in 30-50% (top right) Pb–Pb collisions.

uncertainties are estimated using the Eq. (D.1)–left and also the average of the uncertainty is calculated. The systematic uncertainties are shown in Fig. D.4 as a function of z_T .

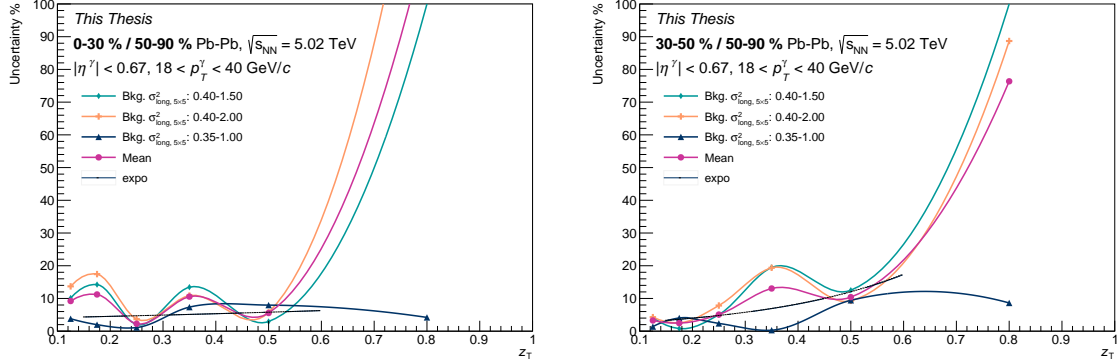


Figure D.4: Systematic uncertainties due to $\sigma_{long, 5\times5}^2$ background ranges: $0.40 < \sigma_{long, 5\times5}^2 < 1.50$ (full green diamond); $0.40 < \sigma_{long, 5\times5}^2 < 2.00$ (full orange cross) and $0.35 < \sigma_{long, 5\times5}^2 < 1.00$ (full black triangle) in 0-30% (top left) and in 30-50% (top right) Pb–Pb collisions. The average of the systematic uncertainties in the three ranges is pink, while the exponential fit is shown with a dashed light blue line.

The uncertainty points fluctuate at high z_T values in central and in particular for semi-central collisions. This is due to the large uncertainty in the last z_T interval between 0.8 and 1.0 in peripheral collisions. To smoothen the trend the last z_T has been excluded and the uncertainty given by the mean of the three systematic uncertainties has been fitted with an exponential in the range $0.15 < z_T < 0.60$. The results are reported in Fig. D.4 and the trend obtained by the fit has been used to describe the systematic uncertainty of the $\sigma_{long, 5\times5}^2$ background range.

D.0.4 Number of centrality bin used for filling the mixed event pool

The I_{CP} ratios obtained using different number of centrality intervals are reported in Fig. D.5. They appear to not be largely affected by the variations. There is only a deviation in the first z_T bin in central collisions. The systematic uncertainty is calculated using Eq. (D.1)–left

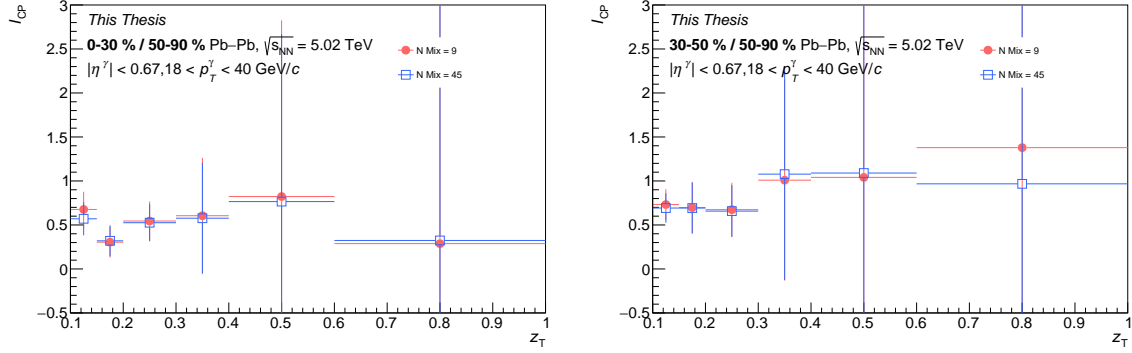


Figure D.5: The I_{CP} distributions obtained using 9 centrality bins (full pink circle) and 45 centrality bins (empty blue square) for filling the mixed event pool in 0-30% (left) and 30-50% (right).

and the results are shown in Fig. D.6. The uncertainty increases for all centralities at high

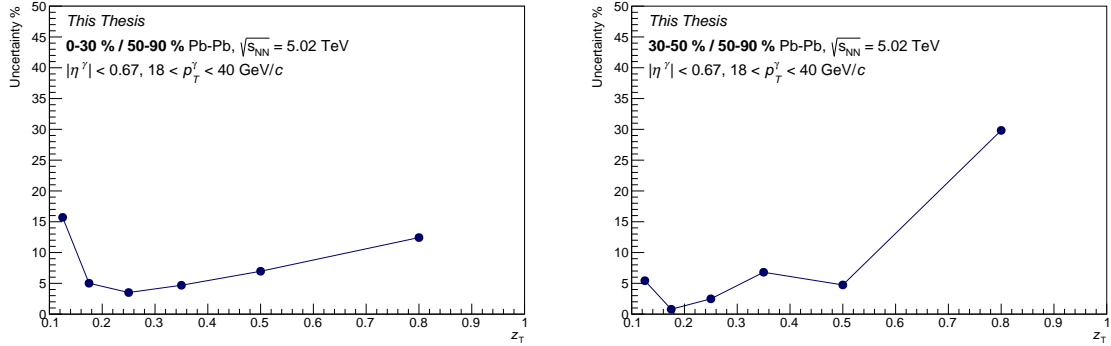


Figure D.6: Systematic uncertainties for different numbers of centrality bins used for filling the mixed event pool in 0-30% (left) and 30-50% (right).

z_T , because of the large statistical fluctuation of the last z_T interval between 0.8 and 1.0 in peripheral collisions. In 0-30%, the deviation of the first z_T bin affects the uncertainty, that is larger than in semi-central collisions. The points have been taken as uncertainties.

D.0.5 Total uncertainties

In this Section, the different systematic uncertainties for the I_{CP} are compiled and added in quadrature.

$$\sigma_{\text{syst}}^{\text{tot}} = \sqrt{\sum_i \sigma_{\text{syst},i}^2}. \quad (\text{D.3})$$

The result of this operation is reported in Fig. D.7. Considered the large statistical uncertainty in the last z_T interval ($0.6 < z_T < 1.00$) in semicentral and in peripheral collisions, that bin has been excluded.

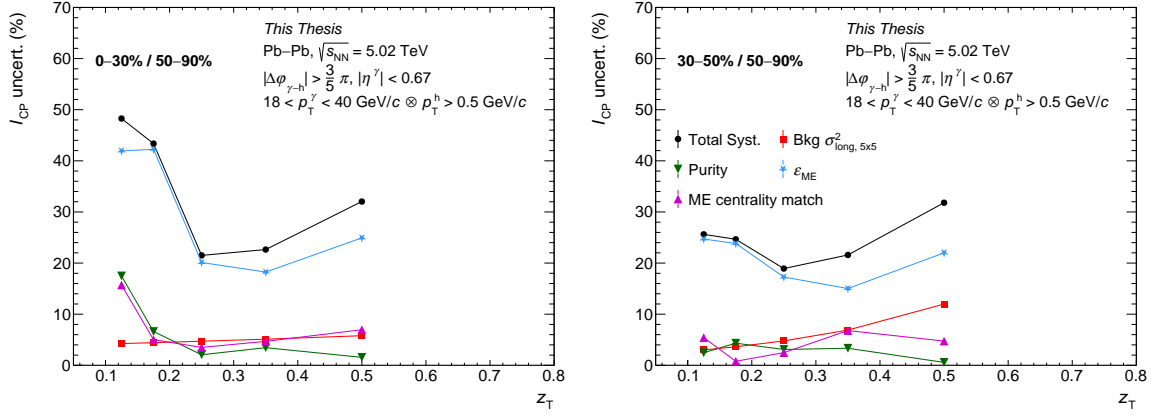


Figure D.7: Various systematic uncertainty sources in 0-30% (left) and 30-50% (right) Pb-Pb collisions.

Appendix E

Synthèse en français

Du Modèle Standard au Plasma de Quarks et de Gluons

La thèse traite des particules fondamentales et des interactions décrites par le Modèle Standard, en se concentrant sur la Chromodynamique Quantique (QCD), la théorie décrivant la force forte entre les quarks et gluons. L'un des objectifs principaux est d'étudier le Plasma de Quarks et de Gluons (QGP), un état particulier de la matière créé dans des conditions de haute énergie et de température extrême, reproduisant celles qui existaient juste après le Big Bang. La recherche de ce plasma est cruciale pour comprendre l'évolution de l'univers primitif.

Le Modèle Standard est une théorie qui explique les interactions fondamentales entre les particules élémentaires telles que les fermions (qui constituent la matière) et les bosons (médialeurs des forces). La QCD, une composante majeure du Modèle Standard, décrit l'interaction forte via un groupe de symétrie appelé SU(3), responsable du confinement des quarks dans des particules comme les protons et neutrons (hadrons). La QCD présente des phénomènes uniques, notamment la liberté asymptotique à haute énergie, où les quarks interagissent plus faiblement, et la confinement de couleur à faible énergie, où ils sont liés à l'intérieur des hadrons.

Les équations de la QCD montrent une dépendance de l'intensité de l'interaction en fonction de l'échelle d'énergie, connue sous le nom de constante de couplage α_s , qui diminue avec l'augmentation du moment transféré (Q^2). Ce phénomène, appelé évolution de α_s , joue un rôle crucial dans la description des interactions à différentes échelles.

Collisions hadroniques et théorie de la factorisation

Les collisions hadroniques, telles que celles réalisées au LHC, permettent de sonder les processus régis par la QCD perturbative, mais aussi des régimes non-perturbatifs liés à la structure complexe des protons et neutrons. Les fonctions de distribution des partons (PDF) décrivent la probabilité de trouver un quark ou un gluon à l'intérieur d'un hadron avec une certaine fraction de sa quantité de mouvement. Les collisions d'ions lourds créent des conditions propices à la formation du QGP, permettant d'étudier ses propriétés sous une forme contrôlée en laboratoire.

Plasma de Quarks et de Gluons (QGP)

La QCD suggère l'existence de différentes phases de la matière nucléaire. À haute température ou densité, les quarks et gluons deviennent déconfinés, formant un état liquide connu sous le nom de Plasma de Quarks et de Gluons. Ce plasma peut être produit dans des expériences de collisions d'ions lourds à haute énergie, telles que celles réalisées au LHC avec l'expérience ALICE. Le QGP est également soupçonné d'exister dans les étoiles à neutrons et pourrait avoir dominé l'univers quelques microsecondes après le Big Bang.

Le diagramme de phase de la QCD montre les transitions entre la matière ordinaire et le QGP en fonction de la température et du potentiel chimique baryonique. À faible potentiel chimique, la transition entre la phase de gaz hadronique et le QGP est un crossover, tandis qu'à haute densité, une transition de phase du premier ordre est attendue.

Collisions d'ions lourds

Les collisions d'ions lourds comme Pb-Pb ou Au-Au sont réalisées pour recréer les conditions extrêmes permettant la formation du QGP. L'évolution de ces collisions passe par plusieurs phases : la collision initiale, suivie d'une phase pré-équilibre, puis la formation du QGP proprement dit. Après cette phase, le plasma se refroidit pour se hadroniser, formant des hadrons qui, après une phase de découplage chimique et de gel thermique, se stabilisent pour être détectés.

Propriétés du QGP

Différentes sondes expérimentales permettent d'étudier les propriétés du QGP. On distingue principalement les probes douces et les probes dures : - Probes douces : telles que la production accrue de particules étranges et le flux collectif. La production de particules étranges, par exemple, est un indicateur important de la formation du QGP, car elle est facilitée par la densité de gluons présente dans ce plasma. - Probes dures : comprennent les particules à haute impulsion transverse (pT) et les particules lourdes comme les charmonia ou bottomonia, dont la suppression ou la régénération dans le plasma peut être observée. Le phénomène de suppression du quarkonium est l'un des signaux importants du QGP, en raison de l'effet de blindage de couleur qui empêche les quarks lourds de se lier dans le plasma.

Modèles théoriques et expérimentations futures

Le modèle théorique de la QGP repose sur des calculs par la QCD sur réseau et des modèles efficaces tels que le modèle MIT Bag, qui permet de modéliser le confinement des quarks. Ces approches sont limitées par les puissances de calcul disponibles et ne peuvent pas explorer toutes les régions du diagramme de phase.

Les futures expérimentations, telles que celles prévues avec l'expérience NA60+, viseront à explorer plus en détail les propriétés du plasma et les effets de saturation des gluons dans les collisions à haute énergie. Ces études permettront de mieux comprendre l'évolution des fonctions de distribution des partons nucléaires (nPDFs) et d'affiner nos connaissances sur le comportement des particules dans des états de matière extrêmes.

Photons, une sonde du plasma de quarks et de gluons

Le plasma de quarks et de gluons (QGP) est un état de la matière produit lors de collisions d'ions lourds à haute énergie, comme celles effectuées dans des expériences telles que l'ALICE au Grand Collisionneur de Hadrons (LHC). Les photons, contrairement aux quarks et gluons, sont insensibles à l'interaction forte, ce qui les rend d'excellentes sondes pour étudier le QGP. Ils sont produits à toutes les étapes de la collision et peuvent être classés en quatre grandes catégories :

- photons directs : créés lors de la diffusion initiale entre partons incidentes via des processus comme Compton ou l'annihilation;
- photons de fragmentation : générés par la fragmentation de partons finaux;
- photons thermiques : émis par le QGP ou le gaz hadronique;
- photons de désintégration : résultant de la désintégration de mésons neutres, principalement du π^0 et de l' η .

Les photons provenant de processus $2 \rightarrow 2$, c'est-à-dire des interactions directes, sont particulièrement intéressants car ils ne sont pas affectés par le QGP, contrairement aux autres types de photons. Ces photons fournissent des informations sur le comportement des particules avant leur passage dans le QGP.

Mesures des photons isolés

Les photons isolés sont ceux qui ne sont pas accompagnés d'activité hadronique significative dans un cône autour d'eux. La technique d'isolation permet de réduire la contribution des photons de fragmentation et de désintégration, ne laissant que les photons directs. Les mesures montrent que pour des impulsions transverses élevées (p_T), les photons directs sont compatibles avec les calculs théoriques basés sur la chromodynamique quantique perturbative (pQCD).

Les résultats de l'expérience ALICE montrent une forte présence de photons thermiques dans la gamme de p_T faible, révélant des températures effectives élevées, suggérant une température initiale du QGP bien au-dessus de la température critique de transition (150 MeV). Cela indique que les conditions créées dans les collisions d'ions lourds au LHC sont extrêmement chaudes, formant l'état le plus chaud jamais observé en laboratoire.

Photons prompts et fragmentation

Les photons prompts résultent principalement des processus de diffusion Compton et d'annihilation parton-antiparton. Ces processus, représentés par des diagrammes de Feynman, sont moins probables que les processus purement QCD, mais ils sont essentiels pour la production de photons de haute énergie. Les mesures expérimentales montrent que les photons fragmentés contribuent surtout à basse énergie, tandis que les photons prompts deviennent dominants à haute énergie.

Application dans les collisions pA et AA

La mesure des photons isolés dans les collisions proton-noyau (pA) permet de tester l'effet des modifications nucléaires des distributions de partons, telles que le shadowing des gluons à faible impulsion transverse. Les expériences menées au LHC montrent que le facteur de modification nucléaire (R_{pA}) pour les photons isolés est compatible avec l'unité à haute énergie, ce qui suggère peu d'effets nucléaires sur la production de photons à ces énergies.

Dans les collisions d'ions lourds (AA), la comparaison des facteurs de modification nucléaire (R_{AA}) des photons avec ceux des hadrons montre un contraste frappant : alors que les hadrons sont fortement supprimés à haute énergie dans les collisions centrales, les photons isolés ne montrent pas cette suppression. Cela confirme que les photons promptes ne sont pas affectés par le QGP, contrairement aux jets de partons qui subissent une perte d'énergie.

Jets associés aux photons

Les jets associés aux photons isolés sont une méthode précieuse pour étudier la perte d'énergie des quarks et gluons dans le QGP, un phénomène connu sous le nom de quenching de jets. Étant donné que les photons ne sont pas affectés par le QGP, ils servent de référence calibrée pour mesurer la perte d'énergie des jets qui leur sont associés. Les études montrent que les jets de gluons subissent une suppression plus importante que les jets de quarks, confirmant ainsi les prédictions théoriques.

Des mesures du déséquilibre en impulsion entre les photons et les jets associés montrent que, dans les collisions les plus centrales, une fraction importante de l'énergie du jet est perdue lorsqu'il traverse le QGP, se manifestant par un excès de particules à faible p_T dans le jet.

Conclusion

Les photons isolés fournissent une fenêtre unique sur les conditions initiales des collisions et permettent de sonder indirectement le comportement des partons dans le plasma de quarks et de gluons. Les études des jets associés aux photons isolés, combinées aux mesures des photons thermiques, permettent de mieux comprendre l'évolution du QGP et la dynamique des partons qui y interagissent.

L'expérience ALICE au Grand collisionneur de hadrons

Le Grand collisionneur de hadrons (LHC) est un accélérateur circulaire de 26,7 km de circonférence situé au CERN, près de Genève, en Suisse. Il accélère des protons et des ions à des vitesses proches de la lumière, les faisant entrer en collision à des niveaux d'énergie sans précédent. Le principal objectif du LHC est d'étudier les forces et les particules fondamentales en observant le comportement de ces collisions à haute énergie, y compris la découverte de particules comme le boson de Higgs et l'étude de phénomènes au-delà du Modèle standard de la physique.

Quatre expériences principales sont hébergées au LHC : ATLAS, CMS, LHCb et ALICE. Alors qu'ATLAS et CMS se concentrent sur la recherche du boson de Higgs et de la nouvelle

physique, et que LHCb étudie la violation de CP dans les systèmes de quarks lourds, ALICE (A Large Ion Collider Experiment) se spécialise dans les collisions d'ions lourds, dans le but d'étudier le plasma quark-gluon , un état de la matière qui aurait existé peu après le Big Bang. ALICE examine les conditions extrêmes dans ces collisions, qui peuvent simuler les conditions de l'univers primitif et fournir des aperçus de la QCD.

Le détecteur ALICE et ses composants

Le détecteur ALICE est un appareil complexe optimisé pour étudier le milieu chaud et dense créé lors des collisions d'ions lourds. Il est conçu pour suivre et identifier les particules sur une large gamme de momenta. Le détecteur comprend plusieurs sous-systèmes :

- système de suivi interne (ITS) : un ensemble de six couches de silicium situées le plus près du point d'interaction, qui reconstruit les trajectoires des particules et localise le vertex de la collision avec une grande précision;
- chambre à projection temporelle (TPC) : un cylindre rempli de gaz qui mesure le moment des particules chargées et fournit une identification des particules à travers la perte d'énergie d'ionisation (dE/dx);
- détecteur V0 : Un ensemble de scintillateurs situés à des angles avant et arrière, utilisés pour mesurer la multiplicité des particules chargées, déclencher des événements et déterminer la centralité des collisions.

Ces sous-systèmes sont divisés en détecteurs en bâillet pour la rapidité centrale et détecteurs avant pour le déclenchement d'événements et le suivi, assurant une collecte complète des données lors des collisions de particules.

Acquisition et analyse des données

ALICE utilise un système avancé d'acquisition de données (DAQ) qui contrôle les détecteurs pendant les collisions et déclenche en fonction de critères d'événements spécifiques. Ce processus comprend un système de déclenchement hiérarchique (L0, L1, L2), qui sélectionne en temps réel les événements intéressants afin de minimiser le stockage des données tout en capturant les informations essentielles. Les données collectées sont distribuées à l'échelle mondiale pour analyse via la Grille de calcul mondiale du LHC, qui traite les vastes ensembles de données produits lors des expériences.

L'analyse des données dans ALICE repose sur le logiciel AliRoot, qui interagit avec des générateurs Monte Carlo comme PYTHIA et des codes de transport détaillés comme GEANT pour simuler les interactions des particules. Le processus d'analyse de données produit des données de résumé d'événements (ESD) et des données d'objet d'analyse (AOD), permettant l'extraction efficace des quantités physiques pertinentes.

Détermination de la centralité et techniques de reconstruction

Dans les collisions d'ions lourds, la détermination de la centralité—une mesure du volume de chevauchement entre les noyaux en collision—est cruciale pour l'étude des propriétés du plasma quark-gluon. La centralité peut être déduite à l'aide du détecteur V0 et du calorimètre de degré zéro (ZDC), qui mesurent la multiplicité des particules chargées et

l'énergie déposée par les nucléons spectateurs. Les classes de centralité sont définies en divisant la subsection efficace en pourcentages, fournissant un moyen de comparer les événements de collision en fonction du paramètre d'impact.

ALICE utilise le filtrage de Kalman pour la reconstruction des trajectoires, garantissant des mesures précises des trajectoires des particules. En combinaison avec des méthodes de reconstruction du vertex, ALICE obtient une grande efficacité de suivi et une bonne résolution du moment.

En plus, le chapitre discute des méthodes pour atténuer les biais dans la sélection de la centralité, en particulier ceux introduits par l'utilisation de la production de particules douces pour la classification, qui peut fausser les résultats liés aux processus durs comme la production de jets. Ces biais doivent être pris en compte lors du calcul des observables telles que le facteur de modification nucléaire (R_{AA}).

Identification et sélection des photons avec l'EMCal d'ALICE

Ce chapitre présente une étude approfondie de l'identification des photons isolés dans les collisions d'ions lourds au LHC à l'aide de l'EMCal (calorimètre électromagnétique) d'ALICE. Elle aborde les méthodes utilisées pour identifier et sélectionner les photons, notamment les techniques de reconstruction des clusters, l'analyse de la forme des clusters et l'isolement des photons, qui permettent de distinguer les photons directs des autres particules produites dans les collisions.

Détection du signal dans les cellules du calorimètre

Lorsqu'une particule interagit avec le calorimètre, elle crée une douche électromagnétique qui répartit son énergie sur plusieurs cellules voisines. Un cluster est défini comme un ensemble de cellules activées par une particule incidente. Différents algorithmes de clusterisation sont utilisés pour regrouper les cellules en clusters, tels que les algorithmes V1 et V2. Le V1 est utilisé dans les collisions pp et p–Pb, tandis que le V2 est préféré pour les collisions Pb–Pb en raison de la plus grande densité de particules.

Méthode d'isolement des photons

Les photons isolés sont produits sans activité hadronique significative dans leur voisinage, contrairement aux photons issus de la fragmentation ou de la désintégration de mésons, souvent accompagnés de jets. Pour les identifier, une méthode d'isolement est utilisée : une zone conique autour du photon est définie, et la somme des impulsions transverses des particules dans cette zone est calculée. Si cette somme (p_T^{iso}) est inférieure à un certain seuil, le photon est considéré comme isolé. Cette méthode permet de filtrer efficacement les photons directs issus de processus comme $2 \rightarrow 2$, qui n'ont pas de fragments associés.

Analyse de la forme des clusters

La forme d'un cluster, représentée par ses axes elliptiques, est un indicateur important pour distinguer les photons directs des photons de désintégration. Les photons directs produisent

des clusters circulaires, tandis que les photons issus de la désintégration de mésons forment des clusters plus elliptiques. L'algorithme V2 permet une meilleure séparation des clusters dans les collisions Pb–Pb où la densité de particules est élevée.

Pureté des photons isolés

Même après la sélection des photons via l'analyse de la forme des clusters et l'isolement, un certain bruit de fond subsiste, principalement dû aux photons de désintégration. La pureté des photons isolés est calculée en utilisant la méthode ABCD-ALICE, qui divise l'espace des variables d'isolation et de forme en quatre régions. Cette méthode permet de quantifier la proportion de vrais photons directs dans l'échantillon mesuré.

Cette chapitre fournit une méthodologie robuste pour identifier les photons directs dans les collisions d'ions lourds au LHC, un aspect essentiel pour l'étude du Plasma de Quarks et de Gluons (QGP). Grâce aux techniques de reconstruction des clusters et à l'analyse de la forme des douches électromagnétiques, l'EMCal d'ALICE permet de sonder les processus fondamentaux dans ces collisions extrêmes.

Correlations des photons isolés et hadrons

Ce chapitre traite de la mesure des corrélations azimutales entre photons isolés et hadrons dans les collisions Pb-Pb, dans le but d'étudier l'effet du plasma de quarks et gluons (QGP) sur la fragmentation des partons. Les expériences sont réalisées à l'aide de l'expérience ALICE au LHC, et les résultats de la thèse visent à mieux comprendre comment les partons interagissent dans le milieu dense créé lors des collisions.

Sélection des données et simulations Monte Carlo

Les données analysées proviennent des collisions d'ions lourds Pb-Pb enregistrées par ALICE en 2015 et 2018 à une énergie de $\sqrt{s_{NN}} = 5,02 \text{ TeV}$. Les événements sont classés en quatre classes de centralité (0-10%, 10-30%, 30-50%, 50-90%) et sont sélectionnés grâce à des déclencheurs spécifiques, tels que EMCal L1- γ , qui permettent de capturer des photons d'intérêt avec des seuils d'énergie définis.

Des simulations Monte Carlo (MC) sont utilisées pour corriger les données expérimentales et estimer la pureté des photons isolés. Les générateurs d'événements tels que PYTHIA 8 simulent les collisions proton-proton en prenant en compte différents processus de diffusion (par exemple, Compton et annihilation), et les événements simulés sont ensuite insérés dans des événements réels pour modéliser les effets du milieu. Les corrections obtenues permettent de tenir compte de l'efficacité du détecteur et des biais introduits par l'arrière-plan.

Définition de la corrélation azimutale

Les corrélations azimutales sont analysées en comparant les angles azimutaux ($\Delta\phi$) entre un photon isolé (particule déclencheuse) et un hadron associé. Le but est de mesurer l'impact du QGP sur la propagation des partons, en se concentrant sur les hadrons produits par la fragmentation des partons. La corrélation est mesurée dans plusieurs intervalles de z_T , qui

représente la fraction de la quantité de mouvement transverse du hadron par rapport à celle du photon.

Les distributions de corrélation sont d'abord corrigées pour soustraire l'arrière-plan dû à l'événement sous-jacent (Underlying Event, UE). Deux méthodes sont utilisées pour estimer l'UE : la méthode Zero Yield At Minimum (ZYAM) et la technique des événements mixtes, cette dernière étant préférée car elle utilise des données réelles et peut mieux reproduire l'état du détecteur.

Après avoir corrigé l'UE, les distributions azimutales montrent un pic sur le côté opposé au photon (côté "away side"), indiquant que les hadrons sont produits principalement dans la direction opposée à celle du photon isolé, comme attendu dans les processus de diffusion de partons.

Correction de la pureté et analyse des résultats

Une correction de la pureté est appliquée pour soustraire la contribution des photons issus de la désintégration de mésons (π^0 et η), qui constituent la principale source de contamination dans les photons isolés. Pour ce faire, la distribution de corrélation des photons contaminés est soustraite de celle des photons isolés. Les distributions corrigées montrent que la corrélation résiduelle sur le côté proche (near side) disparaît, confirmant que les photons isolés sont majoritairement des photons directs.

Les résultats des corrélations azimutales pour différentes classes de centralité (0-10%, 30-50%, 50-90%) montrent des variations importantes en fonction de la centralité. Dans les collisions centrales (0-10%), la suppression des hadrons est plus forte, indiquant une interaction plus intense avec le QGP, tandis que dans les collisions périphériques (50-90%), l'effet du QGP est plus faible, et les pics de corrélation sont plus nets.

Fonctions de fragmentation

Les fonctions de fragmentation ($D(z_T)$) sont extraites des distributions de corrélation pour différents intervalles de (z_T). Ces fonctions décrivent comment l'énergie d'un parton est distribuée parmi les hadrons produits lors de sa fragmentation. Les résultats montrent que les hadrons à faible (p_T) (impulsion transverse) sont plus affectés par la suppression due au QGP que ceux à haute (p_T), ce qui est conforme aux modèles théoriques.

Les résultats obtenus dans cette thèse confirment que les photons isolés sont une sonde efficace pour étudier la fragmentation des partons dans le QGP et fournissent des informations précieuses sur la dynamique des collisions d'ions lourds. Les prochaines étapes consistent à comparer ces résultats avec d'autres expériences et modèles théoriques pour affiner notre compréhension du QGP.

Perspectives futures pour les mesures de photons isolés à grande rapidité avec ALICE

Ce dernier chapitre explore la conception et l'utilisation du FoCal (Forward Calorimeter) dans l'expérience ALICE au LHC, notamment pour mesurer les photons isolés à des pseudorapidités élevées et étudier les densités des partons à faible fraction de moment. Le FoCal

permettra de sonder des aspects fondamentaux de la Chromodynamique Quantique (QCD) en étudiant la saturation des gluons dans les noyaux lourds à faible x , une région jusqu'ici peu explorée.

Le contexte des mesures de photons isolés

Les gluons jouent un rôle central dans la QCD. Ils se distinguent par leur capacité à interagir entre eux en raison de leur charge de couleur, créant ainsi des phénomènes uniques comme la saturation des gluons dans les noyaux à haute énergie. Cette saturation résulte de la croissance rapide de la densité de gluons à de faibles valeurs de x , c'est-à-dire lorsque la fraction du moment des partons devient extrêmement petite.

Les photons isolés, produits principalement par des diffusions Compton entre quarks et gluons, sont un excellent outil pour sonder les fonctions de distribution des partons (PDFs) dans les noyaux à faible x . Ces photons permettent de mieux comprendre la distribution des gluons dans les noyaux lourds, une information cruciale pour étudier le phénomène de shadowing, où la densité de gluons dans les noyaux est plus faible que dans les protons libres.

Le FoCal, qui sera installé après le troisième arrêt long du LHC (LS3) entre 2025 et 2028, couvrira des pseudorapidités allant de 3.4 à 5.8 et mesurera les photons isolés ainsi que les corrélations photon-hadron. Il permettra de sonder des régions de faible x dans les collisions pp, p–Pb, et Pb–Pb, avec une résolution allant jusqu'à $x \sim 10^{-6}$.

Conception du calorimètre FoCal

Le FoCal se compose de deux sous-systèmes principaux : - FoCal-E, un calorimètre électromagnétique compact en tungstène-silicium, et - FoCal-H, un calorimètre hadronique à structure spaghetti pour reconstruire la fraction hadronique des jets.

Le FoCal-E est constitué de 22 modules, chacun composé de 20 couches de capteurs passifs en tungstène alternant avec des couches actives en silicium. Ces capteurs en silicium comprennent 18 couches de détecteurs de type PAD avec une granularité de 1 cm^2 , et 2 couches de capteurs à pixels actifs monolithiques (MAPS) avec une granularité plus fine ($30 \times 30 \mu\text{m}^2$). Ces capteurs à haute granularité permettent de distinguer les photons directs des paires de photons issus de la désintégration des mésons neutres, avec une grande précision.

L'objectif principal du FoCal-E est de mesurer l'énergie et le profil des douches électromagnétiques, en particulier pour les photons isolés. Les couches MAPS permettent également de séparer deux photons proches, essentiels pour discriminer les photons directs des photons de désintégration. Le système de lecture est basé sur le HGCROC (High Granularity Calorimeter Readout Chip), un circuit intégré spécifique qui collecte les signaux analogiques et les convertit en signaux numériques pour l'analyse.

Étalonnage et résultats expérimentaux

Le processus d'étalonnage du FoCal est crucial pour garantir des mesures précises et stables. Il inclut plusieurs étapes : - la calibration des pédestaux (le signal de base sans dépôt d'énergie), - la réponse à l'injection de charge pour évaluer la linéarité de la réponse du capteur, - et la calibration des systèmes de Time of Arrival (TOA) et Time Over Threshold (TOT) pour la mesure du temps de propagation et de l'énergie des signaux.

Les tests en faisceau réalisés en 2022 au PS et au SPS du CERN ont permis de vérifier les performances du FoCal-E. Des faisceaux d'électrons et de hadrons avec des énergies allant de 5 à 15 GeV ont été utilisés pour tester les capteurs PAD, avec des résultats montrant une bonne séparation entre les signaux des particules minimum ionisantes (MIP) et le bruit électronique.

Les résultats montrent que les pics de MIP sont bien visibles dans les canaux de détection, avec une stabilisation de la réponse à partir de 300 V de tension de polarisation. Les différentes configurations de gains ont été testées pour optimiser la réponse des capteurs, avec un choix final de paramètres (par exemple, une résistance de 50 kΩ et une capacité de 200 fF) permettant de maximiser la séparation entre le signal et le bruit.

Perspectives futures

L'ajout du FoCal à l'expérience ALICE permettra d'étendre les études sur les photons isolés et les jets associés à des régions de pseudorapidité élevée, offrant une vue plus complète des processus de quenching de jets à l'avant de la collision. Cela permettra de cartographier la densité du plasma de quarks et gluons (QGP) en fonction de la rapidité et d'examiner les différences de perte d'énergie entre les jets de quarks et de gluons.

L'analyse des jets et des corrélations γ -jet dans des collisions pp, p-Pb, et Pb-Pb fournira des informations uniques pour étudier les fonctions de distribution des partons dans des régions de faible x , contribuant ainsi à notre compréhension de la saturation des gluons et des phénomènes de shadowing dans les noyaux lourds.

En conclusion, l'intégration du FoCal dans ALICE est une avancée majeure qui permettra d'explorer des régimes inédits de la QCD à haute énergie, et d'approfondir notre compréhension des propriétés du QGP et des processus partoniques à faible x .

Conclusions

La thèse explore les corrélations photons isolés-hadrons dans les collisions Pb-Pb à haute énergie au LHC, une méthode cruciale pour étudier les effets du plasma de quarks et de gluons (QGP) sur les partons diffusés. L'analyse des photons isolés permet de mieux comprendre la perte d'énergie des partons dans le QGP, grâce à des mesures de corrélations avec les hadrons associés.

Corrélations photons isolés-hadrons et impact du QGP

Dans les collisions d'ions lourds, les photons isolés sont principalement produits par des processus de diffusion entre quarks et gluons, tels que les processus Compton. Ces photons ne subissent pas d'interaction avec le milieu QGP, contrairement aux jets de partons associés qui traversent ce milieu et perdent de l'énergie. Par conséquent, les corrélations azimutales entre photons isolés et hadrons offrent un aperçu unique des processus de fragmentation des partons, ainsi que des modifications subies par ces partons lors de leur interaction avec le QGP.

L'analyse des corrélations dans différentes classes de centralité (0-30%, 30-50%, 50-90%) a révélé une suppression importante du rendement des hadrons dans les événements centraux par rapport aux événements périphériques et aux simulations pp de QCD perturbative

(NLO). Cette suppression dépendante de la centralité confirme une perte d'énergie plus marquée dans les collisions centrales, où la densité du QGP est plus élevée. Ces résultats sont bien décrits par des modèles théoriques tels que CoLBT et pQCD NLO avec prise en compte du quenching des jets, bien que les incertitudes actuelles empêchent de distinguer clairement entre ces modèles.

Comparaison avec d'autres expériences et implications futures

Les résultats de cette étude ont été comparés avec ceux de collaborations telles que CMS, PHENIX et STAR. Malgré des différences dans les méthodes d'analyse, les tendances observées dans les mêmes intervalles de z_T sont en accord, notamment une plus grande suppression des hadrons à haute impulsion transverse (pT) et à haute z_T dans les collisions d'ions lourds par rapport aux collisions pp.

Bien que cette étude ne soit pas destinée à être une analyse de précision, elle sert de base importante pour les futures études prévues durant le Run 3 et le Run 4 du LHC (2030-2032). Avec des ensembles de données plus importants à venir, des mesures de corrélations plus précises seront possibles, permettant d'examiner des plages d'impulsion transverse (pT) plus basses et de réaliser des études différentielles selon les régions du plan d'événement. Par exemple, dans la classe de centralité 30-50%, où l'on s'attend à ce que le flux elliptique soit plus prononcé, des comparaisons entre les corrélations dans le plan et hors du plan seront réalisables.

Ces futures analyses approfondiront également les études de jets balisés par des photons, offrant un cadre pour étudier plus en détail la perte d'énergie des jets dans le QGP et fourniront une meilleure compréhension des effets de saturation des gluons à faible x .

Perspectives avec le calorimètre FoCal

La thèse discute également de l'importance du FoCal (Forward Calorimeter), une future mise à niveau pour l'expérience ALICE, qui sera installée lors du Run 4. Le FoCal est conçu pour mesurer les photons isolés à des rapidités avant (forward rapidity), ainsi que les corrélations entre photons isolés et hadrons. Ces mesures permettront d'explorer des régions de faible fraction de moment x , où les densités de gluons augmentent rapidement et peuvent mener à un phénomène de saturation. L'étude de la saturation des gluons est essentielle pour comprendre l'évolution de la QCD à faible x et Q^2 .

Le FoCal-E, un calorimètre électromagnétique à base de capteurs en tungstène et silicium, a été testé lors de faisceaux d'essai en 2022. Les résultats montrent que les capteurs PAD du FoCal-E ont réussi à mesurer clairement les signaux des particules minimum ionisantes (MIP), confirmant ainsi la fonctionnalité des capteurs dans des conditions réelles. Cependant, des recherches supplémentaires sont nécessaires pour mieux comprendre les propriétés du Time of Arrival (TOA) et du Time Over Threshold (TOT), ainsi que leurs interactions avec le système ADC.

Le FoCal fournira également des informations précieuses sur le quenching des jets à haute rapidité dans les collisions Pb-Pb, permettant de cartographier la densité du QGP en fonction de la rapidité. Ces nouvelles mesures offriront des contraintes supplémentaires sur la dépendance en x et Q^2 de l'évolution de la QCD, apportant ainsi des réponses aux questions fondamentales sur la structure des noyaux à haute énergie.

Conclusion

Cette thèse apporte une contribution significative à l'étude des corrélations photons isolés-hadrons dans les collisions d'ions lourds, en montrant comment ces corrélations peuvent être utilisées pour sonder les effets du QGP sur la perte d'énergie des partons. Les perspectives futures, notamment avec la mise en place du FoCal, offrent des opportunités uniques pour explorer des phénomènes encore inexplorés dans la QCD à faible x et pour approfondir notre compréhension des propriétés du QGP à différentes échelles d'énergie et de rapidité.

List of Figures

1.1	The elementary particles of the Standard Model [2].	12
1.2	QCD vertices [5].	13
1.3	Left: (a) Illustration of how vacuum polarization in QED shields a bare charge. (b) is the same as (a) but for a QCD charge. (c) shows how in QCD a charge can radiate away its colour via gluon radiation, adapted from [7]. Right: Coupling constants behaviour of the QED and QCD as a function of Q^2 [7].	14
1.4	Summary of measurements of $\alpha_S(Q^2)$ as a function of the respective energy scale Q . The acronyms in the brackets specify the order used in perturbative QCD calculations that went into the extraction of α_s [10].	15
1.5	[11].	16
1.6	NNPDF4.0 NNLO proton PDF as a function of momentum fraction x , evaluated at two different scales $Q = 3.2$ GeV (left) and $Q = 100$ GeV (right). Each colour represents the PDF of a different parton species, as indicated in the legend [15].	17
1.7	Map of QCD as a function of (Q, x)	18
1.8	The QCD phase diagram as a function of the temperature and the baryon-chemical potential [25].	20
1.9	The space-time evolution of heavy-ion collisions at LHC [38].	21
1.10	Measurements of the nuclear modification of the PDFs performed by several experiments in a wide range of Bjorken x	23
1.11	Nuclear modification of nPDFs at $Q^2 = 10$ GeV 2 for different parton species with respect to the free proton baseline. The calculations for nNNPDF30 [43], EPPS16 [44] and nCTEQWZ+SIH [45] are shown, where the bands illustrate the uncertainties at a 68% confidence level [43].	24
1.12	Coordinate system describing a collision between A and B nuclei.	25
1.13	Schematic representation of the Optical Glauber Model geometry, with transverse (a) and longitudinal (b) views [46].	26
1.14	A Glauber Monte Carlo simulation of an Au–Au collision event at $\sqrt{s_{\text{NN}}} = 200$ GeV with impact parameter $b = 6$ fm. (a) shows the transverse plane visualisation, while (b) the visualisation along the beam axis. Darker circles represent participating nucleons [46].	27
1.15	Hyperon enhancements as a function of $\langle N_{\text{wound}} \rangle$ in Pb–Pb p–Pb and p–Be collisions at $\sqrt{s_{\text{NN}}} = 158$ GeV measured by NA57 Collaboration [51].	30

1.16 Ratios of the p_T -integrated yield of hadrons with strange-quark content and charged pions as a function of the charged-particle multiplicity at midrapidity, measured by the ALICE Collaboration in various collision systems and at different center-of-mass energies [53].	30
1.17 Transverse momentum spectra of charged pions, kaons, protons, Λ baryons, and ϕ mesons for central (0–5%) (full marker) and peripheral (80–90%) (empty marker) Pb–Pb collisions at $\sqrt{s_{\text{NN}}} = 2.76$ TeV measured by ALICE [38].	32
1.18 Sketch of a collision to highlight the almond shape.	32
1.19 Elliptic flow coefficient v_2 of charged pions, charged and neutral kaons, protons, ϕ mesons, and hyperons as a function of p_T , measured by the ALICE Collaboration for several centrality classes in Pb–Pb collisions at $\sqrt{s_{\text{NN}}} = 5.02$ TeV [55].	33
1.20 Nuclear modification factors for the $\Upsilon(1S)$, $\Upsilon(2S)$ and $\Upsilon(3S)$ mesons as a function of $\langle N_{\text{part}} \rangle$ measured by CMS [59].	35
1.21 Left: R_{AA} of the J/ψ hadron measured in heavy-ion collisions at different center-of-mass energies as a function of the charged multiplicity by ALICE (red full circle), by NA50 (green full circle) and by STAR (light blue full circle) experiments [38]. Right: v_2 coefficient of charged pions, prompt D mesons, electrons from beauty-hadron decays, J/ψ mesons, and Υ mesons as a function of p_T for Pb–Pb collisions at $\sqrt{s_{\text{NN}}} = 5.02$ TeV in the 30–50% centrality class [38].	35
1.22 Sketch of jet production in pp collisions (left) and in AA collisions (right).	37
1.23 Left: R_{AA} for charged particles in central (0–5%) (full red circle) and peripheral (70–80%) (full blue circle) Pb–Pb collisions and R_{pA} for p–Pb collisions (full green diamond) at $\sqrt{s_{\text{NN}}} = 5.02$ TeV by ALICE [65]. Right: nuclear modification factor for charged particles by ALICE (full violet square) and CMS (empty light blue square) and inclusive jets by ALICE (full green circle) and ATLAS (empty red circle) in central Pb–Pb collisions at $\sqrt{s_{\text{NN}}} = 5.02$ TeV [38].	38
1.24 Left: azimuthal correlation distributions in pp (black line), in central d–Au (full red circle), in minimum bias d–Au (full green triangle) and central Au–Au (full blue star) collisions measured by the STAR Collaboration. The trigger hadron p_T is $4 < p_T < 6$ GeV/ c , while the selected charged particles p_T are between $2 < p_T^{\text{assoc}} < p_T^{\text{trig}}$ GeV/ c [66, 67]. Right: CMS event display at LHC for a single Pb–Pb collision, showing a dijet event [68].	39
1.25 Left: measurement of di-jet yield-normalized x_J distributions measured by the ATLAS Collaboration in 0–10% (full black square) and 40–60% (full blue square) Pb–Pb and in pp (full orange circle) collisions at $\sqrt{s_{\text{NN}}} = 5.02$ TeV [69]. Right: ratio $R_{D(z)}$ between fragmentation functions in central Pb–Pb and pp collisions at $\sqrt{s_{\text{NN}}} = 5.02$ TeV measured by ATLAS. Ratios are shown for three different p_T^{jet} ranges: 126–158 GeV (full black circle), 200–251 GeV (full red diamond) and 316–398 GeV (full blue cross) [70].	40

1.26 Ratio of the jet radial momentum distributions as a function of the angular distance Δr from the jet axis in Pb–Pb for various centrality intervals relative to that measured in pp collisions for leading jets (empty blue circle) with $p_T > 120 \text{ GeV}/c$, $R = 0.4$ and subleading jets (empty red circle) $0.7 < p_T^{\text{track}} < 300 \text{ GeV}/c$ [72].	42
2.1 Sketch of photon production during a heavy-ion collision between nuclei A and B. They include: $\gamma_{2 \rightarrow 2}$, γ_{decay} , γ_{fragm} and γ_{therm}	45
2.2 Left: nuclear modification factor of direct γ (full violet square), inclusive hadrons (full pink star), π^0 mesons (full red circle) and η mesons (empty yellow circle) as a function of p_T for central Au–Au collisions at RHIC [77, 78]. Right: nuclear modification factor for the π^0 (empty red circle), η mesons (full red circle), kaons (full grey circle) and charged pions (empty grey circle) in 0–10% Pb–Pb collisions at $\sqrt{s_{\text{NN}}} = 2.76 \text{ TeV}$ measured by ALICE [79].	46
2.3 Left: R_γ as a function of p_T for 0–10% central (top, red full circle) and 20–40% semi-central (bottom, green full diamond) Pb–Pb collisions at $\sqrt{s_{\text{NN}}} = 2.76 \text{ TeV}$ compared with different model calculations by ALICE. Right: thermal photon spectra as a function of p_T for 0–10% central (red full circle) and 20–40% semi-central (green full diamond) in Pb–Pb collisions at $\sqrt{s_{\text{NN}}} = 2.76 \text{ TeV}$ by the ALICE Collaboration [80]	48
2.4 Feynman diagrams for prompt photon production.	48
2.5 Fraction of different processes, Compton (orange), annihilation (blue) and fragmentation (grey), that contributes to the prompt photon production in pp collisions at $\sqrt{s} = 14 \text{ TeV}$ at LHC from simulation without (left) and with (right) the isolation method [83].	49
2.6 Sketch of a collision in which $\gamma_{2 \rightarrow 2}$, γ_{decay} and γ_{fragm} are produced. The isolation method is applied to select the $\gamma_{2 \rightarrow 2}$	50
2.7 Left: Overview of various isolated-photon spectra in pp and p \bar{p} collisions as a function of $x_T = 2p_T^\gamma/\sqrt{s}$ [85]. Right top: isolated-photon differential cross section (full black square) measured in pp collisions at $\sqrt{s} = 13 \text{ TeV}$. The blue boxes correspond to pQCD calculations with JETPHOX. Right bottom: ratio between JETPHOX calculations and data displayed in the blue boxes, vertical boxes size shows the theory scale and PDF uncertainties. Experimental uncertainties are shown here on the black points centred at unity [85].	51
2.8 Top: R_{pA} of isolated-photon production in p–Pb collisions at $\sqrt{s_{\text{NN}}} = 8.16 \text{ TeV}$ by ALICE (full black circle) and by ATLAS (full pink circle) compared with different JETPHOX calculations using nNNPDF30 (blue line), using CT14 proton PDF + EPPS16 Pb nPDF (red dashed line) and using using CT14 proton PDF + nCTEQ15 Pb nPDF (dotted green line) [91]. Bottom: nuclear modification factor R_{pA} at $\sqrt{s_{\text{NN}}} = 8.16 \text{ TeV}$ in p–Pb collisions measured purely by ATLAS (full black circle) at different rapidities confronted with JETPHOX calculations using CT14 proton PDF (blue dotdashed line) and using CT14 proton PDF + EPPS16 Pb nPDF (red dashed line) [92].	52

2.9 Left: isolated-photon differential cross section measured in pp and Pb–Pb collisions at $\sqrt{s_{\text{NN}}} = 5.02$ TeV for five Pb–Pb centrality classes for $R = 0.2$. Right: ratio of data over JETPHOX NLO pQCD calculations. The bands centred at unity correspond to the JETPHOX pQCD calculations, their width represents the scale (blue) uncertainty and PDF (orange) uncertainty, and blue vertical bars indicate the statistical uncertainty of the calculation [93].	54
2.10 Ratio of isolated-photon spectra measured with $R = 0.4$ over $R = 0.2$, for Pb–Pb and pp collisions at $\sqrt{s_{\text{NN}}} = 5.02$ TeV. Each panel corresponds to a Pb–Pb collisions centrality class or to pp collisions. The pink band corresponds to pQCD calculations with JETPHOX [93].	54
2.11 Nuclear modification factor for isolated photons at $\sqrt{s_{\text{NN}}} = 5.02$ TeV for isolation cone radii $R = 0.2$ (full black circle) and $R = 0.4$ (empty blue circle). Distribution compared to the R_{AA} for charged particles [65] (empty green square) and charged pions [97] (empty orange square) from ALICE, and to the ratio of the Z bosons (full violet square) production in each centrality class to the 0–90% class measured by CMS [98]. The bands correspond to pQCD calculations with JETPHOX for Pb–Pb collisions (nPDF) for 0–100% centrality over pp collisions (PDF). The width of each band corresponds to the scale (orange) and PDF (pink) uncertainties [93].	55
2.12 Left: nuclear modification factor of γ^{iso} -tagged jet as a function of $p_{\text{T}}^{\text{jet}}$ for 0–10% (full pink square), 10–30% (full green diamond) and 30–80% (full blue cross) Pb–Pb collisions at $\sqrt{s_{\text{NN}}} = 5.02$ TeV measured by ATLAS. Right: nuclear modification factor of γ^{iso} -tagged jets (full pink square) and inclusive jets (empty light pink circle) as a function of $p_{\text{T}}^{\text{jet}}$ for 0–10% Pb–Pb collisions at $\sqrt{s_{\text{NN}}} = 5.02$ TeV measured by ATLAS [100].	57
2.13 The p_{T} balance observable as a function of $x_{j\gamma}$ for various centralities in Pb–Pb (full markers) and pp (open markers) collisions. Vertical lines display the statistical uncertainties while the coloured boxes (red for PbPb, green for pp) show the systematic uncertainties [101].	57
2.14 Comparison of photon-tagged fragmentation functions in centrality bins 10–30% (left) and 0–10% (right) as a function of the observables $\xi_{\text{T}}^{\text{jet}}$ (top) and ξ_{T}^{γ} (bottom). The distributions are compared with CoLBT-hydro model (blue line) and HYBRID model with back reaction (yellow line) and without back reaction (pink line) [102, 103].	58
2.15 Top: distributions of $\xi_{\text{T}}^{\text{trk},Z}$ in pp collisions compared to Pb–Pb collisions in various centrality bins. Bottom: ratios of the Pb–Pb to pp distributions. The vertical bars and coloured boxes represent the statistical and systematic uncertainties, respectively. The distributions are compared with CoLBT-hydro model (pink line) and HYBRID model with wake (yellow line) and without wake (brown line) [106].	59
2.16 Top: Differential jet shape, for jets associated with an isolated-photon from peripheral to central Pb–Pb (full circles), and pp (open circles) collisions at $\sqrt{s_{\text{NN}}} = 5.02$ TeV. Bottom: Ratios between the Pb–Pb and pp distributions by CMS [107].	60

2.17 Distributions of jet girth g of γ^{iso} -tagged jets in Pb–Pb (full red square) and pp (empty blue circle) collisions for $x_{j\gamma} = p_T^{\text{jet}}/p_T^\gamma > 0.4$ (left) and for $x_{j\gamma} > 0.8$ (right) measured by CMS [108].	61
2.18 Top: γ^{iso} -hadron azimuthal correlation distributions for pp (full red square), p–Pb (full blue circle) data and PYTHIA 8.2 Monash Tune simulation (dashed green line) at $\sqrt{s} = 5.02$ TeV measured by the ALICE Collaboration. The different panels correspond to different z_T bins [110].	62
2.19 γ^{iso} -hadron fragmentation function for pp (full red square), p–Pb data (full blue circle) and PYTHIA 8.2 simulation (dashed green line). The ratio between p–Pb and pp distributions (black marker) is shown in the bottom panel. The boxes represent the systematic uncertainties while the vertical bars indicate the statistical uncertainties [110].	63
2.20 Left: $D(z_T)$ distributions for γ^{iso} -hadron correlations as a function of z_T for central Au–Au (full red dot) and for pp (empty red dot) collisions measured by the STAR Collaboration. Right: I_{AA} for γ^{iso} -hadron (red squares) and for π^0 -hadron (blue circles) correlations as a function of z_T . The vertical lines represent statistical error and the vertical boxes represent systematic errors. The curves represent theoretical model predictions [111].	63
3.1 Scheme of the CERN accelerator complex. The locations of the four main LHC experiments (ALICE, ATLAS, CMS and LHCb) around the LHC ring are also shown.	67
3.2 The ALICE experimental apparatus with individual sub-detectors labelled during Run 2.	69
3.3 Schema of the Inner Tracking System [122].	70
3.4 Schema of the Time Projection Chamber [122]	71
3.5 Sketches of V0-A and V0-C arrays showing their segmentation. Scintillator thicknesses are 2.5 and 2 cm respectively. The scintillator segments on both sides of the dashed lines are connected to the same PMT [47].	72
3.6 Distribution of the V0 amplitudes measured in Pb–Pb collisions at $\sqrt{s_{\text{NN}}} = 2.76$ TeV. The red line reports the NBD-Glauber fit, while the bands show the different centrality classes [122].	76
3.7 R_{AA} versus centrality for Au–Au and Pb–Pb collisions at $\sqrt{s_{\text{NN}}} = 0.2$ TeV (black markers) and $\sqrt{s_{\text{NN}}} = 5.02$ TeV (red markers), respectively, calculated with HG-PYTHIA model [99].	77
4.1 Photon-matter interaction cross section and its three main contributions as a function of incident photon energy in carbon (left) and lead (right) [136]. Pair production actually has two components, linked to the nuclear (nuc.) and electronic (el.) electric fields of the atom near which the process takes place [137].	79
4.2 Contributions related to the loss of energy per unit radiation length (quantity defined in the text) suffered by an electron or positron in the lead (Pb) as a function of its energy [138].	80

4.3 Sketch of the development of an electromagnetic shower induced by an incident photon. The axes "L" and "l" represent the longitudinal and radial components of this development respectively. Figure taken from [137]	80
4.4 Schematic view of the EMCAL calorimeter illustrating the module position on two approximately opposite locations in azimuth φ . The PHOS calorimeter is inside the DCal and is indicated in brown [135].	82
4.5 Photo and drawing of the EMCAL module components [132].	83
4.6 Illustration of one EMCAL supermodule with the different segmentation levels: tower (green), module (yellow), strip module (pink), T-Card (violet) and FEE-Card (light blue) [132].	84
4.7 Scheme of the EMCAL front end electronics [140].	85
4.8 Digital signal (full black circle) of a tower obtained at the output of a FEE card as a function of time, fitted by the function $\Gamma_n(t)$ (full red line) defined in Eq. (4.3) [132].	86
4.9 Left: L1- γ trigger efficiency for inclusive clusters (see Table 5.1) and isolated narrow clusters (see Sect. 5.3), obtained with PYTHIA simulation combining γ -jet (empty markers) and jet-jet (full markers) processes for pp and embedded in data for Pb–Pb collisions, considering the corresponding trigger thresholds in each system. Right: L1- γ trigger rejection factor calculated by applying the trigger efficiency for each of the pp and Pb–Pb centrality classes considered at $\sqrt{s_{\text{NN}}} = 5.02$ TeV. Solid lines over points result of a constant fit and dashed lines indicate the fit uncertainty [93].	87
4.10 Left: Invariant mass distribution for neutral pion and η meson candidates at intermediate transverse momenta $12 < p_T < 14$ GeV/c reconstructed with both photons in the EMCAL in pp collisions at 13 TeV using the L1- γ trigger sample. Distribution obtained with a fully calibrated EMCAL [135]. Right: Variation of the π^0 energy calibration coefficient in all channels of 2012 data from the last iteration (blue) compared to the first iteration (red), and compared to the last iteration of 2011 data (green).	89
4.11 Left: Energy nonlinearity correction as a function of reconstructed energy for electrons obtained from test beam data (black points), and from MC simulations with GEANT3 (red points) and GEANT4 (cyan points) transport codes. Right: energy resolution of the EMCAL as a function of the incident particle energy [135].	90
5.1 Schematic comparison of different clusterization algorithms: a) V1, b) 3×3 , c) V2. Yellow boxes represent the energy in each cell. E_{agg} is the aggregation energy. Different clusters are indicated by blue and red hatched areas [135].	93
5.2 Distance between a cluster and the closest projected track in $\Delta\eta^{\text{residual}}$ (left) and $\Delta\varphi^{\text{residual}}$ (right) angle versus the track momentum p_T^{track} in pp collisions at $\sqrt{s} = 13$ TeV. The black lines indicate the selection reported in Eq. (5.1) and (5.2) [135].	94

5.3	Positive charge track-cluster matching residuals of $\Delta\eta^{\text{residual}}$ (left) and $\Delta\varphi^{\text{residual}}$ (right) as a function of p_T^{track} for central (0–10%, top rows) and peripheral Pb–Pb collisions (50–90%, bottom rows). The orange dashed lines indicate the limit at high p_T cut given by Eq. (5.1) and (5.2) and the teal dashed line is the loose cut used for systematic studies in the spectrum analysis [93].	95
5.4	The exotoxicity F_+ versus E_{cluster} for 0–10% and 30–50% in minimum bias Pb–Pb collisions at $\sqrt{s_{\text{NN}}} = 5.02$ TeV (top rows) and for 50–90% Pb–Pb collisions at $\sqrt{s_{\text{NN}}} = 5.02$ TeV and pp collisions at $\sqrt{s} = 13$ TeV (bottom rows) with $n_{\text{cells}} > 1$. Lines at $F_+ = 0.97$, 0.95 and 0.93 are added to guide the eye on the exotics upper band limits [93].	96
5.5	Schematic view of cluster energy repartition in cells and the ellipse axes. Darker colours indicate higher energy cells [135].	98
5.6	Schematic view of cluster energy repartition in cells in low particle multiplicity environment, for two decay photons from a neutral meson (π^0 or η for example) at low (left), medium (middle) and high meson energy (right). The opening angle of the decays gets smaller due to the Lorentz boost and thus the two showers tend to merge at high energy. Darker colours indicate higher energy cells [135].	99
5.7	Schematic view of the cell energy repartition of two high-energy decay photons from a neutral meson, each centred in the black-filled cells, on top of a high-multiplicity low-energy particle underlying event environment, the lightest blue cells. The grey lines are the contour of cells selected restricting the growth of the cluster (V2) used to calculate the cluster energy and position. The orange square is the 5×5 region around the highest-energy cell used for the shower shape calculation, excluding cells that only have a common corner, red cross. The red dotted lines are the contour of a cluster without growth restriction (V1), as used in previous pp and p–Pb isolated photon analyses [93].	100
5.8	Inclusive cluster $\sigma_{\text{long}, 5\times 5}^2$ distribution as a function of p_T in data for five different centralities in Pb–Pb collisions and for pp collisions. The dotted line corresponds to the tight value of the upper selection limit ($\sigma_{\text{long}, 5\times 5}^2 = 0.3$) for single photon candidate clusters (narrow clusters), the dashed line corresponds to a looser photon upper selection used in Pb–Pb collisions below 18 GeV/c. The dot-dashed line defines a lower selection limit ($\sigma_{\text{long}, 5\times 5}^2 = 0.1$) used in Pb–Pb and pp collisions.	101
5.9	Inclusive-cluster $\sigma_{\text{long}, 5\times 5}^2$ distribution in data (black bullets) and PYTHIA simulations. The simulation is decomposed in its different particle origins: prompt photons (blue line), not merged decay photons (MC γ_{decay} , blue area), merged decays from π^0 (MC π^0 , red area) or η (brown area). Three different treatments of cross-talk (x-talk) were considered in the simulation: “no x-talk” (open red circles); “x-talk high” (open grey circles), stronger cross talk obtained for the previous isolated-photon measurements [76, 85, 135]; and “x-talk” (open blue circles), obtained for this measurement. The four panels display these distributions for two selected cluster p_T ranges, $12 < p_T < 14$ GeV/c on the left and $40 < p_T < 60$ GeV/c on the right, and two collision systems: pp (top) and Pb–Pb 0–10% central (bottom) at $\sqrt{s_{\text{NN}}} = 5.02$ TeV [93].	102

5.10 Production of different types of photons with the isolation cone sketched. Left: isolated photon produced alone. Middle and right: fragmentation photons and decay photons produced in combination with a jet.	104
5.11 Illustration of the isolation cone and isolation UE estimation regions.	106
5.12 In γ -jet PYTHIA 8 simulation embedded into MB data, $p_T^{\text{iso}, \text{ch}}$ distribution for different UE estimation areas, $p_T > 12 \text{ GeV}/c$ and narrow clusters with $0.1 < \sigma_{\text{long}, 5\times5}^2 < 0.3$ in Pb–Pb central (left), semi-central (middle) and peripheral (right) collisions for $R = 0.2$ (top) and $R = 0.4$ (bottom) [148]. . .	106
5.13 The $\rho_{\text{UE}}^{\text{track}}$ distributions in data calculated in the η -band. Left: for Pb–Pb collisions and the cone radius $R = 0.2$ as a function of centrality. Right: for pp and Pb–Pb collisions for different centrality classes for the cone radius $R = 0.4$ [93].	107
5.14 The $p_T^{\text{iso}, \text{ch}}$ distribution for narrow clusters with $0.1 < \sigma_{\text{long}, 5\times5}^2 < 0.3$ for $p_T > 16 \text{ GeV}/c$, in very central (0–10%) and peripheral (70–90%) Pb–Pb collisions (top left and right, respectively) and in pp ones (lower right frame) with $R = 0.2$ (black bullets) and $R = 0.4$ (blue squares), in data (full markers) and simulation (open markers) PYTHIA 8 γ -jet processes, embedded into data in case of Pb–Pb collisions [93].	108
5.15 $p_T^{\text{iso}, \text{ch}}$ cumulative probability distribution (clusters with $p_T^{\text{iso}, \text{ch}} < p_T^{\text{iso}, \text{ch}}\text{-cut}$ overall) for clusters with $14 < p_T < 16 \text{ GeV}/c$ for signal narrow clusters in a γ -jet simulation (empty blue circle) and background wide clusters in data (full black circle) and background wide clusters in jet-jet simulation (full red circle) with $R = 0.2$. From top to bottom, 0–10% Pb–Pb collisions, 30–50% Pb–Pb collisions, 70–90% Pb–Pb collisions and pp collisions. The η -band is used to subtract the UE from $p_T^{\text{iso}, \text{ch}}$. Dashed line at selected isolation value of $1.5 \text{ GeV}/c$ [148].	109
5.16 Illustration of the parametric-space of the photon p_T^{iso} (or $p_T^{\text{iso}, \text{ch}}$, etc) and σ_{long}^2 ($\sigma_{\text{long}, 5\times5}^2$), used to estimate the background yield in the signal region (A) from the observed yields in the three control regions (B , C , D). The red regions indicate areas dominated by background and the blue regions by the photon signal. The color gradient indicates mixture of signal and background [135].	111
5.17 Illustration of the parametric-space of the photon p_T^{iso} and σ_{long}^2 ($\sigma_{\text{long}, 5\times5}^2$) for and $14 < p_T < 16 \text{ GeV}/c$ in five centrality classes in Pb–Pb collisions and in pp collisions, used to estimate the background yield in the signal region (A) from the observed yields in the three control regions (B, C and D). The dashed boxes indicate the limits of each class [148].	113
5.18 Purity of the isolated-photon sample as a function of p_T^γ in pp and different centrality classes in Pb–Pb collisions at $\sqrt{s_{\text{NN}}} = 5.02 \text{ TeV}$ for $R = 0.2$ (full black circle) and for $R = 0.4$ (empty blue circle). The lines are the result of the two sigmoid functions fit (see Eq. (5.17)) to the points, plain line for low p_T^γ and dashed for high p_T^γ [93].	114
5.19 Purity of the isolated-photon sample as a function of p_T^γ in pp collisions at $\sqrt{s} = 13 \text{ TeV}$. The red and blue lines are the results of a fit to the measured purity using a two-sigmoid-function described by Eq. (5.17) for two different transverse momentum intervals [85].	114

6.1	Centrality distributions for minimum bias events (black marker) or minimum bias plus centrality triggers (blue marker) or EMCAL L1- γ (yellow, orange, pink and red markers). Distributions are shown for events without selection (full markers) and after all the selections (open markers). The L1- γ triggers have an additional offline selection ("accepted" in the legend) based on masked trigger regions offline and energy thresholds.	116
6.2	Left: Not scaled GJ MC distributions as a function of p_T . Right: Scaled GJ MC distributions as a function of p_T . The distributions are presented for various p_T^{hard} intervals.	118
6.3	Left: Not scaled JJ-low (top) and JJ-high (bottom) MC distributions as a function of p_T . Right: Scaled JJ-low (top) and JJ-high (bottom) distributions as a function of p_T . The distributions are presented for various p_T^{hard} intervals.	119
6.4	The R_{AA} distributions for charge hadrons by ALICE (full black circle), by CMS (full black star) and R_{AA} weights (empty pink triangle) as a function of $p_T^{\text{ch, hadron}}$ from central to peripheral Pb–Pb collisions (clock-wise) by ALICE [65] and CMS [152] at $\sqrt{s_{\text{NN}}} = 5.02$ TeV.	120
6.5	Sketch of the three main steps of the analysis.	121
6.6	p_T^{trig} distribution for the same event (blue) and mixed event (red) in 30-50% Pb–Pb collisions. Left: distributions for isolated narrow clusters. Right: distributions for isolated wide clusters. As an example one p_T^{trig} bin has been coloured, corresponding to a certain number of triggers at that transverse momentum.	123
6.7	Azimuthal correlation distributions in 30-50% for isolated narrow clusters for the same event (full blue circle), for the mixed event (full red square) and the result of the subtraction (empty light blue circle) as a function of $\Delta\varphi$ for different z_T bins with $20 < p_T^{\text{trig}} < 25$ GeV/ c	124
6.8	Azimuthal correlation distributions in 30-50% for isolated wide cluster for the same event (empty blue square), for the mixed event (full red square) and the result of the subtraction (full light blue circle) as a function of $\Delta\varphi$ for different z_T bins with $20 < p_T^{\text{trig}} < 25$ GeV/ c	125
6.9	Azimuthal correlation distributions in 0-10% for isolated narrow clusters for the same event (full blue circle), for the mixed event (full red square) and the result of the subtraction (empty light blue circle) as a function of $\Delta\varphi$ for different z_T bins with $20 < p_T^{\text{trig}} < 25$ GeV/ c	125
6.10	Azimuthal correlation distributions in 50-90% for isolated narrow clusters for the same event (full blue circle), for mixed event (full red square) and the result of the subtraction (empty light blue circle) as a function of $\Delta\varphi$ for different z_T bins with $20 < p_T^{\text{trig}} < 25$ GeV/ c	126
6.11	Azimuthal correlation distributions for isolated narrow clusters for the same event (full blue circle), for mixed event (full red square) and the result of the subtraction (empty light blue circle) as a function of $\Delta\varphi$ for two z_T intervals with $20 < p_T^{\text{trig}} < 25$ GeV/ c . Comparing three centralities: 0-10% (left), 30-50% (middle) and 50-90% (right) Pb–Pb collisions.	126

6.12 Azimuthal correlation distributions in 30-50% for isolated narrow clusters (full light blue circle), for isolated wide clusters (empty light blue circle) and γ^{iso} (empty orange square) as a function of $\Delta\varphi$ for different z_T bins with $20 < p_T^{\text{trig}} < 25 \text{ GeV}/c$	127
6.13 Azimuthal correlation distributions in 0-10% for isolated narrow clusters (full light blue circle), for isolated wide clusters (empty light blue circle) and γ^{iso} (empty orange square) as a function of $\Delta\varphi$ for different z_T bins with $20 < p_T^{\text{trig}} < 25 \text{ GeV}/c$	128
6.14 Azimuthal correlation distributions in 50-90% for isolated narrow clusters (full light blue circle), for isolated wide clusters (empty light blue circle) and γ^{iso} (empty orange square) as a function of $\Delta\varphi$ for different z_T bins with $20 < p_T^{\text{trig}} < 25 \text{ GeV}/c$	128
6.15 $D(z_T)$ distributions as a function of z_T for a p_T^{trig} between $20 < p_T^{\text{trig}} < 25 \text{ GeV}/c$. From top to bottom, 0-10% Pb–Pb collisions, 10-30% Pb–Pb collisions, 30-50% Pb–Pb collisions and 50-90% Pb–Pb collisions.	129
6.16 Azimuthal correlation distribution for PYTHIA 8 pp generator level before (empty blue square) and after the subtraction of the UE (full blue square) as a function of $\Delta\varphi$ for different z_T bins with $20 < p_T^{\text{trig}} < 25 \text{ GeV}/c$	130
6.17 Azimuthal correlation distribution 30-50% Pb–Pb collisions for pp PYTHIA 8 γ -jet events embedded into MB data of the Same Event (full pink square), of the Mixed Event (red cross) and of the Same Event without UE (full orange square) as a function of $\Delta\varphi$ for different z_T bins with $20 < p_T^{\text{trig}} < 25 \text{ GeV}/c$	131
6.18 Top panels: the $D(z_T)$ distributions as a function of z_T for GJ MC simulation at generated (full light blue square) and reconstructed (full orange square) levels with $20 < p_T^\gamma < 25 \text{ GeV}/c$. Bottom panels: the α_{corr} factor (full green square) as a function of z_T . From top to bottom, 0-10% Pb–Pb collisions, 10-30% Pb–Pb collisions, 30-50% Pb–Pb collisions and 50-90% Pb–Pb collisions.	132
6.19 The $D(z_T)$ distributions as a function of z_T from γ^{iso} -hadron correlations for a p_T^γ between $20 < p_T^\gamma < 25 \text{ GeV}/c$. From top to bottom, 0-10% Pb–Pb collisions, 10-30% Pb–Pb collisions, 30-50% Pb–Pb collisions and 50-90% Pb–Pb collisions.	133
6.20 The $D(z_T)$ distributions as a function of z_T from γ^{iso} -hadron correlations for a p_T^γ between $18 < p_T^\gamma < 40 \text{ GeV}/c$. From top to bottom, 0-10% Pb–Pb collisions, 10-30% Pb–Pb collisions, 30-50% Pb–Pb collisions and 50-90% Pb–Pb collisions.	134
6.21 z_T distribution in 0-30% for the γ^{iso} -hadron correlation after merging the various $\Delta\varphi$ distributions in 0-10% and 10-30% Pb–Pb collisions for a p_T^γ in $18 < p_T^\gamma < 40 \text{ GeV}/c$	134
6.22 Azimuthal correlation distributions as a function of $\Delta\varphi$ for isolated narrow (full green circle) and for isolated wide (empty green circle) clusters after UE subtraction and corresponding constant fits (narrow: red; wide: blue) for different z_T intervals with $20 < p_T^{\text{trig}} < 25 \text{ GeV}/c$ in 30-50% Pb–Pb collisions.	136
6.23 Systematic uncertainty of the mixed event for isolated narrow (full light blue circle) and wide (empty blue circle) clusters as a function of z_T . From top to bottom, 0-10% Pb–Pb collisions, 10-30% Pb–Pb collisions, 30-50% Pb–Pb collisions and 50-90% Pb–Pb collisions.	137

6.24 Systematic uncertainty of the mixed event for isolated narrow clusters (full light blue circle) as a function of z_T in 0-30% Pb–Pb collisions before smoothing the trend with fits (left) and after (right).	138
6.25 Isolated photon purity uncertainty components for $R = 0.2$ in pp and Pb–Pb collisions. Purity calculated with the ABCD method [93].	139
6.26 The $D(z_T)$ distributions for different purity values: nominal (full blue circle), nominal + σ_{syst}^P (empty pink circle) and nominal – σ_{syst}^P (empty violet square) in 0-30% (top left), in 30-50% (top right) and in 50-90% (bottom) Pb–Pb collisions.	140
6.27 Left: Systematic uncertainties of the purity in 0-30% (full light blue square), 30-50% (empty blue circle) and 50-90% (full blue circle) Pb–Pb collisions. smoothing of the systematic uncertainties using an exponential fit in 0-30% (blue dot-dashed line), 30-50% (pink dot-dashed line) and 50-90% (violet dot-dashed line) Pb–Pb collisions. Right: Systematic uncertainties of the purity obtained from the fit.	140
6.28 The $D(z_T)$ distributions obtained using different $\sigma_{\text{long}, 5\times 5}^2$ background ranges: $0.40 < \sigma_{\text{long}, 5\times 5}^2 < 1.00$ (full red circle) $0.40 < \sigma_{\text{long}, 5\times 5}^2 < 1.50$ (full blue circle); $0.40 < \sigma_{\text{long}, 5\times 5}^2 < 2.00$ (empty orange square) and $0.35 < \sigma_{\text{long}, 5\times 5}^2 < 1.00$ (full black cross) in 0-30% (top left), in 30-50% (top right) and in 50-90% (bottom) Pb–Pb collisions.	142
6.29 Systematic uncertainties due to $\sigma_{\text{long}, 5\times 5}^2$ background ranges: $0.40 < \sigma_{\text{long}, 5\times 5}^2 < 1.50$ (full green diamond); $0.40 < \sigma_{\text{long}, 5\times 5}^2 < 2.00$ (full orange cross) and $0.35 < \sigma_{\text{long}, 5\times 5}^2 < 1.00$ (full black triangle) in 0-30% (top left), in 30-50% (top right) and in 50-90% (bottom) Pb–Pb collisions. The average of the systematic uncertainties in the three ranges is pink, while the exponential fit is shown with a dashed light blue line.	142
6.30 Systematic uncertainty due to the tracking efficiency in 0-30% (top left), 30-50% (top right) and 50-90% (bottom) Pb–Pb collisions.	143
6.31 The differential z_T distributions obtained using 9 centrality bins (full pink circle) and 45 centrality bins (empty blue square) for filling the mixed event pool in 0-30% (left), 30-50% (middle) and 50-90% (right).	144
6.32 Ratio of the z_T distribution obtained with $\text{NcentMix} = 9$ and z_T distribution obtained with $\text{NcentMix} = 45$ in 0-30% (left), 30-50% (middle) and 50-90% (right).	144
6.33 Systematic uncertainty for different numbers of centrality bins used for filling the mixed event pool in 0-30% (left), 30-50% (middle) and 50-90% (right).	145
6.34 Various systematic uncertainty sources for the three centrality classes measured.	145
6.35 Comparison between statistical and systematic uncertainties for the three centrality classes measured.	146
6.36 The $D(z_T)$ distributions as a function of z_T for a p_T^γ between $18 < p_T^\gamma < 40$ GeV/ c in 0-30% (top left), 30-50% (top right) and 50-90% (bottom). The statistical uncertainties are indicated by bar, while the systematics uncertainties are shown with coloured boxed.	147

6.37	Top panels: The $D(z_T)$ distributions as a function of z_T for a p_T^γ between $18 < p_T^\gamma < 40 \text{ GeV}/c$ in 0-30% (full blue square), 30-50% (full orange circle) and 50-90% (empty violet circle). The statistical uncertainties are indicated by bars, while the systematics uncertainties are shown with coloured boxes. Theoretical calculations are included pQCD NLO (pink) and CoLBT-hydro (green) models. Bottom panels: Ratio of $D(z_T)$ in Pb–Pb collisions to pQCD calculations (bottom panels) as a function of z_T	149
6.38	The $I_{\text{pQCD NLO}}$ distributions as a function of z_T in 0-30% (full blue square), 30-50% (full orange circle) and 50-90% (empty violet circle) Pb–Pb collisions.	151
6.39	I_{CP} as a function of z_T for central (full blue square) and for semi-central (full orange circle) Pb–Pb collisions.	151
6.40	Top: The I_{AA} distributions as a function of z_T in central collisions for γ -jet (full blue circle) and Z -hadron (full green cross) correlation from the CMS Collaboration [102, 106] and the $I_{\text{pQCD NLO}}$ from the γ^{iso} -hadron (full red square) correlation by ALICE.	152
6.41	The I_{AA} distributions as a function of z_T in central collisions from γ -hadron correlation from the STAR Collaboration (full light green circle), the PHENIX experiment (full light blue circle) and the $I_{\text{pQCD NLO}}$ by the ALICE experiment (full red square).	153
7.1	ALICE detector configuration for Run 4. FoCal is located in front of the compensator magnet and outside the magnet doors on the A-side, opposite the muon arm. Figure taken from [166].	155
7.2	The longitudinal structure of the FoCal-E has a total of 20 layers: 18 layers of tungsten and silicon pads (blue) interleaved with two layers of tungsten and silicon pixels MAPS (pink) [168]. z is the beam direction.	156
7.3	The pad-layer board is made out of 5 individual pad sensors each with 72 channels of $1 \times 1 \text{ cm}^2$, which will be readout by one HGCROC chip.	156
7.4	Architectural overview of the HGCROC-V2 [172].	157
7.5	Sketch for describing the relationship between the TOA and the TOT. An analogic signal as a function of the time is shown.	158
7.6	Overview of layer stacking in the beam direction. The silicon pad sensor layers and their associated front-end electronics are shown in green, and the MAPS layers (without their readout) are shown in red. The readout partition is shown for a full module: four 5-pad-layer boards per aggregator for the first four groups and two 5-pad-layer boards for the last silicon pad layers. The mechanical adaptation between the 5-pad-layer boards and the aggregator is achieved with a dedicated “final” interface board.	159
7.7	Left: Focal prototype tower composed of 18 single-pad boards with a test-beam dedicated interface board. Right: picture of one single-pad used in the FoCal tower prototype [168].	159
7.8	The table contains a part of the ROC parameters of the HGCROC-V2 card.	161
7.9	ADC distributions before the pedestal calibration. Left: ADC mean distributions for all the channels as a function of the event number. Right: average of the ADC mean distributions as a function of the channel number.	162

7.10	Distributions for all the channels, after the pedestal calibration. Average of the ADC distribution as a function of the channel number.	163
7.11	Left: median ADC value as a function of inverting voltage. Right: median ADC value as a function of non-inverting one.	163
7.12	Effect of the dynamic range calibration. The mean of the ADC mean distribution for all the channels.	164
7.13	ADC mean distribution as a function of the time for channels from 12 to 23. Left: ADC mean distribution for the coarse calibration. Right: ADC mean distribution for the fine calibration.	165
7.14	Left: Sketch that describes the global thresholds scan. Right: Sketch that describes the local thresholds scan. The blue arrow indicates the direction. .	166
7.15	Efficiency curves as a function of global thresholds for different channels and for the two sides of the HGCROC, before the calibration procedure.	167
7.16	Efficiency as a function of global thresholds for different channels and for the two sides of the HGCROC after the calibration.	167
7.17	Picture of the FoCal tower prototype installed on the T9 beamline at the CERN PS.	168
7.18	Test beam setup used to determine the cables delays to the aggregator. Figure courtesy of D. Tourres.	169
7.19	MIP peak measured from a single channel of a FoCal-E pad layer in PS 2022 test beam [179].	170
7.20	Left: ADC distributions as a function of the ADC channel for different voltage values. Right: MIP peak position (full black dot) and MIP peak width (full red dot) as a function of the voltage [179].	171
7.21	ADC response obtained using four different gains for a specific ASIC and channel [179].	171
7.22	Channel scan of MIP's signal in various ASICs. The squares indicated channels with anomalous MIPs.	172
7.23	ADC response at higher energy. The prototype was irradiated with electrons. The beam spot is in channel 52, indicated by a red square.	173
7.24	Efficiency curves as a function of the global thresholds for different channels and for the two sides of one ASIC of the prototype, before the calibration procedure.	173
7.25	Efficiency curves as a function of the global thresholds for different channels and for the two sides of one ASIC of the prototype, after the calibration procedure.	174
7.26	Left: ADC pedestals affected by the activation of the TOA. Right: ADC pedestals after the variation of TOA thresholds.	174
B.1	Calorimeter cell column-row hit map for the period 2015 (LHC15o), Pb–Pb 0–10%, MB (left) and L1- γ (right) triggered data, top row for data, second row for the corresponding embedded MC γ -jet + jet-jet biased events. The last row for the ratio data over simulation, each one normalized by the histogram integral.	181

B.2 Calorimeter cell column-row hit map for first period of 2018 (LHC18q), Pb–Pb 0-10%, MB (left) and L1- γ (right) triggered data, top row for data, second row for the corresponding embedded MC γ -jet + jet-jet biased events. The last row for the ratio data over simulation, each one normalized by the histogram integral.	182
B.3 Calorimeter cell column-row hit map for the second period of 2018 (LHC18r), Pb–Pb 0-10%, MB (left) and L1- γ (right) triggered data, top row for data, second row for the corresponding embedded MC γ -jet + jet-jet biased events. The last row for the ratio data over simulation, each one normalized by the histogram integral.	183
C.1 Azimuthal correlation distribution in 0-10% for isolated narrow clusters for the same event (full blue circle), for mixed event (full red square) and for the result of the subtraction (empty light blue circle) as a function of $\Delta\varphi$ for different z_T bins with $18 < p_T^{\text{trig}} < 20 \text{ GeV}/c$	184
C.2 Azimuthal correlation distribution in 0-10% for isolated narrow clusters for the same event (full blue circle), for mixed event (full red square) and for result of the subtraction (empty light blue circle) as a function of $\Delta\varphi$ for different z_T bins with $20 < p_T^{\text{trig}} < 25 \text{ GeV}/c$	185
C.3 Azimuthal correlation distribution in 0-10% for isolated narrow clusters for the same event (full blue circle), for mixed event (full red square) and for result of the subtraction (empty light blue circle) as a function of $\Delta\varphi$ for different z_T bins with $25 < p_T^{\text{trig}} < 30 \text{ GeV}/c$	185
C.4 Azimuthal correlation distribution in 0-10% for isolated narrow clusters for the same event (full blue circle), for mixed event (full red square) and for result of the subtraction (empty light blue circle) as a function of $\Delta\varphi$ for different z_T bins with $30 < p_T^{\text{trig}} < 35 \text{ GeV}/c$	185
C.5 Azimuthal correlation distribution in 0-10% for isolated narrow clusters for the same event (full blue circle), for mixed event (full red square) and for the result of the subtraction (empty light blue circle) as a function of $\Delta\varphi$ for different z_T bins with $35 < p_T^{\text{trig}} < 40 \text{ GeV}/c$	186
C.6 Azimuthal correlation distribution in 10-30% for isolated narrow clusters for the same event (full blue circle), for mixed event (full red square) and for the result of the subtraction (empty light blue circle) as a function of $\Delta\varphi$ for different z_T bins with $18 < p_T^{\text{trig}} < 20 \text{ GeV}/c$	187
C.7 Azimuthal correlation distribution in 10-30% for isolated narrow clusters for the same event (full blue circle), for mixed event (full red square) and for the result of the subtraction (empty light blue circle) as a function of $\Delta\varphi$ for different z_T bins with $20 < p_T^{\text{trig}} < 25 \text{ GeV}/c$	187
C.8 Azimuthal correlation distribution in 10-30% for isolated narrow clusters for the same event (full blue circle), for mixed event (full red square) and for the result of the subtraction (empty light blue circle) as a function of $\Delta\varphi$ for different z_T bins with $25 < p_T^{\text{trig}} < 30 \text{ GeV}/c$	188

C.9 Azimuthal correlation distribution in 10-30% for isolated narrow clusters for the same event (full blue circle), for mixed event (full red square) and for the result of the subtraction (empty light blue circle) as a function of $\Delta\varphi$ for different z_T bins with $30 < p_T^{\text{trig}} < 35 \text{ GeV}/c$	188
C.10 Azimuthal correlation distribution in 10-30% for isolated narrow clusters for the same event (full blue circle), for mixed event (full red square) and for the result of the subtraction (empty light blue circle) as a function of $\Delta\varphi$ for different z_T bins with $35 < p_T^{\text{trig}} < 40 \text{ GeV}/c$	188
C.11 Azimuthal correlation distribution in 30-50% for isolated narrow clusters for the same event (full blue circle), for mixed event (full red square) and for result of the subtraction (empty light blue circle) as a function of $\Delta\varphi$ for different z_T bins with $18 < p_T^{\text{trig}} < 20 \text{ GeV}/c$	189
C.12 Azimuthal correlation distribution in 30-50% for isolated narrow clusters for the same event (full blue circle), for mixed event (full red square) and for result of the subtraction (empty light blue circle) as a function of $\Delta\varphi$ for different z_T bins with $20 < p_T^{\text{trig}} < 25 \text{ GeV}/c$	190
C.13 Azimuthal correlation distribution in 30-50% for isolated narrow clusters for the same event (full blue circle), for mixed event (full red square) and for result of the subtraction (empty light blue circle) as a function of $\Delta\varphi$ for different z_T bins with $25 < p_T^{\text{trig}} < 30 \text{ GeV}/c$	190
C.14 Azimuthal correlation distribution in 30-50% for isolated narrow clusters for the same event (full blue circle), for mixed event (full red square) and for result of the subtraction (empty light blue circle) as a function of $\Delta\varphi$ for different z_T bins with $30 < p_T^{\text{trig}} < 35 \text{ GeV}/c$	191
C.15 Azimuthal correlation distribution in 30-50% for isolated narrow clusters for the same event (full blue circle), for mixed event (full red square) and for result of the subtraction (empty light blue circle) as a function of $\Delta\varphi$ for different z_T bins with $35 < p_T^{\text{trig}} < 40 \text{ GeV}/c$	191
C.16 Azimuthal correlation distribution in 50-90% for isolated narrow clusters for the same event (full blue circle), for mixed event (full red square) and for result of the subtraction (empty light blue circle) as a function of $\Delta\varphi$ for different z_T bins with $18 < p_T^{\text{trig}} < 20 \text{ GeV}/c$	192
C.17 Azimuthal correlation distribution in 50-90% for isolated narrow clusters for the same event (full blue circle), for mixed event (full red square) and for result of the subtraction (empty light blue circle) as a function of $\Delta\varphi$ for different z_T bins with $20 < p_T^{\text{trig}} < 25 \text{ GeV}/c$	193
C.18 Azimuthal correlation distribution in 50-90% for isolated narrow clusters for the same event (full blue circle), for mixed event (full red square) and for result of the subtraction (empty light blue circle) as a function of $\Delta\varphi$ for different z_T bins with $25 < p_T^{\text{trig}} < 30 \text{ GeV}/c$	193
C.19 Azimuthal correlation distribution in 50-90% for isolated narrow clusters for the same event (full blue circle), for mixed event (full red square) and for result of the subtraction (empty light blue circle) as a function of $\Delta\varphi$ for different z_T bins with $30 < p_T^{\text{trig}} < 35 \text{ GeV}/c$	194

C.20 Azimuthal correlation distribution in 50-90% for isolated narrow clusters for the same event (full blue circle), for mixed event (full red square) and for result of the subtraction (empty light blue circle) as a function of $\Delta\varphi$ for different z_T bins with $35 < p_T^{\text{trig}} < 40 \text{ GeV}/c$	194
C.21 Azimuthal correlation distribution in 10-30% for isolated wide clusters for the same event (empty blue square), for mixed event (full red square) and for result of the subtraction (full light blue circle) as a function of $\Delta\varphi$ for different z_T bins with $18 < p_T^{\text{trig}} < 20 \text{ GeV}/c$	195
C.22 Azimuthal correlation distribution in 10-30% for isolated wide clusters for the same event (empty blue square), for mixed event (full red square) and for result of the subtraction (full light blue circle) as a function of $\Delta\varphi$ for different z_T bins with $20 < p_T^{\text{trig}} < 25 \text{ GeV}/c$	195
C.23 Azimuthal correlation distribution in 10-30% for isolated wide clusters for the same event (empty blue square), for mixed event (full red square) and for result of the subtraction (full light blue circle) as a function of $\Delta\varphi$ for different z_T bins with $25 < p_T^{\text{trig}} < 30 \text{ GeV}/c$	196
C.24 Azimuthal correlation distribution in 10-30% for isolated wide clusters for the same event (empty blue square), for mixed event (full red square) and for result of the subtraction (full light blue circle) as a function of $\Delta\varphi$ for different z_T bins with $30 < p_T^{\text{trig}} < 35 \text{ GeV}/c$	196
C.25 Azimuthal correlation distribution in 10-30% for isolated wide clusters for the same event (empty blue square), for mixed event (full red square) and for result of the subtraction (full light blue circle) as a function of $\Delta\varphi$ for different z_T bins with $35 < p_T^{\text{trig}} < 40 \text{ GeV}/c$	196
C.26 Azimuthal correlation distribution in 10-30% for isolated wide clusters for the same event (empty blue square), for mixed event (full red square) and for result of the subtraction (full light blue circle) as a function of $\Delta\varphi$ for different z_T bins with $18 < p_T^{\text{trig}} < 20 \text{ GeV}/c$	197
C.27 Azimuthal correlation distribution in 10-30% for isolated wide clusters for the same event (empty blue square), for mixed event (full red square) and for result of the subtraction (full light blue circle) as a function of $\Delta\varphi$ for different z_T bins with $20 < p_T^{\text{trig}} < 25 \text{ GeV}/c$	197
C.28 Azimuthal correlation distribution in 10-30% for isolated wide clusters for the same event (empty blue square), for mixed event (full red square) and for result of the subtraction (full light blue circle) as a function of $\Delta\varphi$ for different z_T bins with $25 < p_T^{\text{trig}} < 30 \text{ GeV}/c$	198
C.29 Azimuthal correlation distribution in 10-30% for isolated wide clusters for the same event (empty blue square), for mixed event (full red square) and for result of the subtraction (full light blue circle) as a function of $\Delta\varphi$ for different z_T bins with $30 < p_T^{\text{trig}} < 35 \text{ GeV}/c$	198
C.30 Azimuthal correlation distribution in 10-30% for isolated wide clusters for the same event (empty blue square), for mixed event (full red square) and for result of the subtraction (full light blue circle) as a function of $\Delta\varphi$ for different z_T bins with $35 < p_T^{\text{trig}} < 40 \text{ GeV}/c$	198

C.31 Azimuthal correlation distribution in 30-50% for isolated wide clusters for the same event (empty blue square), for mixed event (full red square) and for result of the subtraction (full light blue circle) as a function of $\Delta\varphi$ for different z_T bins with $18 < p_T^{\text{trig}} < 20 \text{ GeV}/c$	199
C.32 Azimuthal correlation distribution in 30-50% for isolated wide clusters for the same event (empty blue square), for mixed event (full red square) and for result of the subtraction (full light blue circle) as a function of $\Delta\varphi$ for different z_T bins with $20 < p_T^{\text{trig}} < 25 \text{ GeV}/c$	200
C.33 Azimuthal correlation distribution in 30-50% for isolated wide clusters for the same event (empty blue square), for mixed event (full red square) and for result of the subtraction (full light blue circle) as a function of $\Delta\varphi$ for different z_T bins with $25 < p_T^{\text{trig}} < 30 \text{ GeV}/c$	200
C.34 Azimuthal correlation distribution in 30-50% for isolated wide clusters for the same event (empty blue square), for mixed event (full red square) and for result of the subtraction (full light blue circle) as a function of $\Delta\varphi$ for different z_T bins with $30 < p_T^{\text{trig}} < 35 \text{ GeV}/c$	201
C.35 Azimuthal correlation distribution in 30-50% for isolated wide clusters for the same event (empty blue square), for mixed event (full red square) and for result of the subtraction (full light blue circle) as a function of $\Delta\varphi$ for different z_T bins with $35 < p_T^{\text{trig}} < 40 \text{ GeV}/c$	201
C.36 Azimuthal correlation distribution in 50-90% for isolated wide clusters for the same event (empty blue square), for mixed event (full red square) and for result of the subtraction (full light blue circle) as a function of $\Delta\varphi$ for different z_T bins with $18 < p_T^{\text{trig}} < 20 \text{ GeV}/c$	202
C.37 Azimuthal correlation distribution in 50-90% for isolated wide clusters for the same event (empty blue square), for mixed event (full red square) and for result of the subtraction (full light blue circle) as a function of $\Delta\varphi$ for different z_T bins with $20 < p_T^{\text{trig}} < 25 \text{ GeV}/c$	202
C.38 Azimuthal correlation distribution in 50-90% for isolated wide clusters for the same event (empty blue square), for mixed event (full red square) and for result of the subtraction (full light blue circle) as a function of $\Delta\varphi$ for different z_T bins with $25 < p_T^{\text{trig}} < 30 \text{ GeV}/c$	203
C.39 Azimuthal correlation distribution in 50-90% for isolated wide clusters for the same event (empty blue square), for mixed event (full red square) and for result of the subtraction (full light blue circle) as a function of $\Delta\varphi$ for different z_T bins with $30 < p_T^{\text{trig}} < 35 \text{ GeV}/c$	203
C.40 Azimuthal correlation distribution in 50-90% for isolated wide clusters for the same event (empty blue square), for mixed event (full red square) and for result of the subtraction (full light blue circle) as a function of $\Delta\varphi$ for different z_T bins with $35 < p_T^{\text{trig}} < 40 \text{ GeV}/c$	204
C.41 Azimuthal correlation distributions in 0-10% for isolated narrow cluster (full light blue circle), for isolated wide cluster (empty light blue circle) and γ^{iso} (empty orange square) as a function of $\Delta\varphi$ for different z_T bins with $18 < p_T^{\text{trig}} < 20 \text{ GeV}/c$	205

C.42 Azimuthal correlation distributions in 0-10% for isolated narrow cluster (full light blue circle), for isolated wide cluster (empty light blue circle) and γ^{iso} (empty orange square) as a function of $\Delta\varphi$ for different z_T bins with $20 < p_T^{\text{trig}} < 25 \text{ GeV}/c$	205
C.43 Azimuthal correlation distributions in 0-10% for isolated narrow cluster (full light blue circle), for isolated wide cluster (empty light blue circle) and γ^{iso} (empty orange square) as a function of $\Delta\varphi$ for different z_T bins with $25 < p_T^{\text{trig}} < 30 \text{ GeV}/c$	206
C.44 Azimuthal correlation distributions in 0-10% for isolated narrow cluster (full light blue circle), for isolated wide cluster (empty light blue circle) and γ^{iso} (empty orange square) as a function of $\Delta\varphi$ for different z_T bins with $30 < p_T^{\text{trig}} < 35 \text{ GeV}/c$	206
C.45 Azimuthal correlation distributions in 0-10% for isolated narrow cluster (full light blue circle), for isolated wide cluster (empty light blue circle) and γ^{iso} (empty orange square) as a function of $\Delta\varphi$ for different z_T bins with $35 < p_T^{\text{trig}} < 40 \text{ GeV}/c$	206
C.46 Azimuthal correlation distributions in 10-30% for isolated narrow cluster (full light blue circle), for isolated wide cluster (empty light blue circle) and γ^{iso} (empty orange square) as a function of $\Delta\varphi$ for different z_T bins with $18 < p_T^{\text{trig}} < 20 \text{ GeV}/c$	207
C.47 Azimuthal correlation distributions in 10-30% for isolated narrow cluster (full light blue circle), for isolated wide cluster (empty light blue circle) and γ^{iso} (empty orange square) as a function of $\Delta\varphi$ for different z_T bins with $20 < p_T^{\text{trig}} < 25 \text{ GeV}/c$	207
C.48 Azimuthal correlation distributions in 10-30% for isolated narrow cluster (full light blue circle), for isolated wide cluster (empty light blue circle) and γ^{iso} (empty orange square) as a function of $\Delta\varphi$ for different z_T bins with $25 < p_T^{\text{trig}} < 30 \text{ GeV}/c$	208
C.49 Azimuthal correlation distributions in 10-30% for isolated narrow cluster (full light blue circle), for isolated wide cluster (empty light blue circle) and γ^{iso} (empty orange square) as a function of $\Delta\varphi$ for different z_T bins with $30 < p_T^{\text{trig}} < 35 \text{ GeV}/c$	208
C.50 Azimuthal correlation distributions in 10-30% for isolated narrow cluster (full light blue circle), for isolated wide cluster (empty light blue circle) and γ^{iso} (empty orange square) as a function of $\Delta\varphi$ for different z_T bins with $35 < p_T^{\text{trig}} < 40 \text{ GeV}/c$	208
C.51 Azimuthal correlation distributions in 30-50% for isolated narrow cluster (full light blue circle), for isolated wide cluster (empty light blue circle) and γ^{iso} (empty orange square) as a function of $\Delta\varphi$ for different z_T bins with $18 < p_T^{\text{trig}} < 20 \text{ GeV}/c$	209
C.52 Azimuthal correlation distributions in 30-50% for isolated narrow cluster (full light blue circle), for isolated wide cluster (empty light blue circle) and γ^{iso} (empty orange square) as a function of $\Delta\varphi$ for different z_T bins with $20 < p_T^{\text{trig}} < 25 \text{ GeV}/c$	210

C.53 Azimuthal correlation distributions in 30-50% for isolated narrow cluster (full light blue circle), for isolated wide cluster (empty light blue circle) and γ^{iso} (empty orange square) as a function of $\Delta\varphi$ for different z_T bins with $25 < p_T^{\text{trig}} < 30 \text{ GeV}/c$	210
C.54 Azimuthal correlation distributions in 30-50% for isolated narrow cluster (full light blue circle), for isolated wide cluster (empty light blue circle) and γ^{iso} (empty orange square) as a function of $\Delta\varphi$ for different z_T bins with $30 < p_T^{\text{trig}} < 35 \text{ GeV}/c$	211
C.55 Azimuthal correlation distributions in 30-50% for isolated narrow cluster (full light blue circle), for isolated wide cluster (empty light blue circle) and γ^{iso} (empty orange square) as a function of $\Delta\varphi$ for different z_T bins with $35 < p_T^{\text{trig}} < 40 \text{ GeV}/c$	211
C.56 Azimuthal correlation distributions in 50-90% for isolated narrow cluster (full light blue circle), for isolated wide cluster (empty light blue circle) and γ^{iso} (empty orange square) as a function of $\Delta\varphi$ for different z_T bins with $18 < p_T^{\text{trig}} < 20 \text{ GeV}/c$	212
C.57 Azimuthal correlation distributions in 50-90% for isolated narrow cluster (full light blue circle), for isolated wide cluster (empty light blue circle) and γ^{iso} (empty orange square) as a function of $\Delta\varphi$ for different z_T bins with $20 < p_T^{\text{trig}} < 25 \text{ GeV}/c$	212
C.58 Azimuthal correlation distributions in 50-90% for isolated narrow cluster (full light blue circle), for isolated wide cluster (empty light blue circle) and γ^{iso} (empty orange square) as a function of $\Delta\varphi$ for different z_T bins with $25 < p_T^{\text{trig}} < 30 \text{ GeV}/c$	213
C.59 Azimuthal correlation distributions in 50-90% for isolated narrow cluster (full light blue circle), for isolated wide cluster (empty light blue circle) and γ^{iso} (empty orange square) as a function of $\Delta\varphi$ for different z_T bins with $30 < p_T^{\text{trig}} < 35 \text{ GeV}/c$	213
C.60 Azimuthal correlation distributions in 50-90% for isolated narrow cluster (full light blue circle), for isolated wide cluster (empty light blue circle) and γ^{iso} (empty orange square) as a function of $\Delta\varphi$ for different z_T bins with $35 < p_T^{\text{trig}} < 40 \text{ GeV}/c$	214
C.61 $D(z_T)$ distribution as a function of z_T in 0-10% Pb–Pb collisions for different p_T^γ intervals From top to bottom: $18 < p_T^\gamma < 20 \text{ GeV}/c$, $20 < p_T^\gamma < 25 \text{ GeV}/c$, $25 < p_T^\gamma < 30 \text{ GeV}/c$, $30 < p_T^\gamma < 35 \text{ GeV}/c$ and $35 < p_T^\gamma < 40 \text{ GeV}/c$	215
C.62 $D(z_T)$ distribution as a function of z_T in 10-30% Pb–Pb collisions for different p_T^γ intervals From top to bottom: $18 < p_T^\gamma < 20 \text{ GeV}/c$, $20 < p_T^\gamma < 25 \text{ GeV}/c$, $25 < p_T^\gamma < 30 \text{ GeV}/c$, $30 < p_T^\gamma < 35 \text{ GeV}/c$ and $35 < p_T^\gamma < 40 \text{ GeV}/c$	216
C.63 $D(z_T)$ distribution as a function of z_T in 30-50% Pb–Pb collisions for different p_T^γ intervals From top to bottom: $18 < p_T^\gamma < 20 \text{ GeV}/c$, $20 < p_T^\gamma < 25 \text{ GeV}/c$, $25 < p_T^\gamma < 30 \text{ GeV}/c$, $30 < p_T^\gamma < 35 \text{ GeV}/c$ and $35 < p_T^\gamma < 40 \text{ GeV}/c$	217
C.64 $D(z_T)$ distribution as a function of z_T in 50-90% Pb–Pb collisions for different p_T^γ intervals From top to bottom: $18 < p_T^\gamma < 20 \text{ GeV}/c$, $20 < p_T^\gamma < 25 \text{ GeV}/c$, $25 < p_T^\gamma < 30 \text{ GeV}/c$, $30 < p_T^\gamma < 35 \text{ GeV}/c$ and $35 < p_T^\gamma < 40 \text{ GeV}/c$	218

D.1	The I_{CP} ratios for different purity values: nominal (full blue circle), nominal $+\sigma_{\text{syst}}^P$ (empty pink circle) and nominal $-\sigma_{\text{syst}}^P$ (empty violet square) in 0-30% (left panel) and in 30-50% (right panel) Pb–Pb collisions.	220
D.2	Left: Systematic uncertainties of the purity on the I_{CP} in 0-30% (full light blue square) and 30-50% (empty blue circle) Pb–Pb collisions. Polishing of the systematic uncertainties using an exponential fit in 0-30% (blue dot-dashed line) and 30-50% (pink dot-dashed line) Pb–Pb collisions. Right: Systematic uncertainties of the purity after the fit.	220
D.3	The I_{CP} distributions obtained using different $\sigma_{\text{long}, 5\times 5}^2$ background ranges: $0.40 < \sigma_{\text{long}, 5\times 5}^2 < 1.00$ (full red circle) $0.40 < \sigma_{\text{long}, 5\times 5}^2 < 1.50$ (full blue circle); $0.40 < \sigma_{\text{long}, 5\times 5}^2 < 2.00$ (empty orange square) and $0.35 < \sigma_{\text{long}, 5\times 5}^2 < 1.00$ (full black cross) in 0-30% (top left) and in 30-50% (top right) Pb–Pb collisions.	221
D.4	Systematic uncertainties due to $\sigma_{\text{long}, 5\times 5}^2$ background ranges: $0.40 < \sigma_{\text{long}, 5\times 5}^2 < 1.50$ (full green diamond); $0.40 < \sigma_{\text{long}, 5\times 5}^2 < 2.00$ (full orange cross) and $0.35 < \sigma_{\text{long}, 5\times 5}^2 < 1.00$ (full black triangle) in 0-30% (top left) and in 30-50% (top right) Pb–Pb collisions. The average of the systematic uncertainties in the three ranges is pink, while the exponential fit is shown with a dashed light blue line.	221
D.5	The I_{CP} distributions obtained using 9 centrality bins (full pink circle) and 45 centrality bins (empty blue square) for filling the mixed event pool in 0-30% (left) and 30-50% (right).	222
D.6	Systematic uncertainties for different numbers of centrality bins used for filling the mixed event pool in 0-30% (left) and 30-50% (right).	222
D.7	Various systematic uncertainty sources in 0-30% (left) and 30-50% (right) Pb–Pb collisions.	223

List of Tables

3.1	Collision systems and energies at the LHC Run 1 and 2 [117].	66
3.2	Properties of the six layers of the ITS detector [121].	70
3.3	Overview of the track selection criteria.	75
4.1	Summary of the EMCal and DCal properties.	84
5.1	Cluster basic selection cuts for this Thesis.	97
5.2	Parameters used in the cross talk emulation in the simulation, for the different groups of supermodules.	103
6.1	Number of selected events in Pb–Pb collisions, per centrality class.	116
6.2	Configurations for the NLO pQCD calculations.	148

Acronyms

ADC Analog to Digital Converter. 85, 157, 158, 160, 162, 163, 164, 165, 169, 170, 172, 174, 177, 256

ALICE A Large Ion Collider. 28, 30, 31, 33, 35, 38, 46, 48, 52, 53, 55, 56, 62, 64, 65, 66, 67, 68, 69, 71, 72, 73, 74, 75, 78, 79, 81, 86, 87, 88, 105, 111, 113, 116, 117, 120, 141, 143, 150, 152, 153, 154, 156, 176, 177, 238, 240, 256

APD Avalanche PhotoDiode. 83, 85, 96, 256

ASIC Application Specific Integrated Circuit. 156, 165, 167, 169, 172, 173, 174, 256

ATLAS A Toroidal LHC ApparatuS. 40, 41, 52, 53, 55, 56, 59, 64, 66, 256

BC Bunch Crossing. 164, 165, 256

BNL Brookhaven National Laboratory. 20, 256

CERN Conseil Européen pour la Recherche Nucléaire. 20, 65, 73, 160, 168, 256

CGC Colour-Glass Condensate. 18, 256

CMS Compact Muon Solenoid. 35, 39, 42, 52, 55, 57, 58, 59, 60, 61, 62, 64, 66, 96, 120, 152, 156, 160, 176, 256

CNM Cold Nuclear Matter. 21, 256

CoLBT Coupled Linear Boltzmann Transport. 59, 148, 149, 176, 256

CPV Charged Particle Veto. 256

CTP Central Trigger Processor. 72, 87, 256

DAQ Data Acquisition. 72, 73, 86, 87, 173, 256

DCA Distances of Closest Approach. 74, 75, 256

DCal Di-jet Calorimeter. 68, 74, 81, 82, 83, 84, 256

EM ElectroMagnetic. 79, 81, 83, 85, 96, 256

EMCal ElectroMagnetic Calorimeter. 68, 74, 78, 81, 82, 83, 84, 85, 86, 87, 88, 89, 90, 91, 92, 93, 94, 96, 97, 116, 117, 123, 146, 241, 256

- FEE** Front End Electronics. 83, 85, 86, 89, 103, 256
- FF** Fragmentation Function. 16, 57, 148, 256
- FoCal** Forward Calorimeter. 154, 155, 156, 157, 168, 177, 256
- FoCal-H** Forward Calorimeter Hadronic. 155, 168, 173, 256
- FoCal-E** Forward Calorimeter Electromagnetic. 155, 159, 168, 169, 173, 177, 256
- FPGA** Field Programmable Gate Array. 159, 165, 256
- GJ** γ -jet. 117, 118, 130, 131, 143, 256
- HGCROC** High Granularity Calorimeter Readout Chip. 156, 157, 158, 159, 160, 164, 165, 166, 169, 174, 256
- HLT** High-Level software Trigger. 72, 73, 256
- IP** interaction point. 66, 67, 68, 256
- IRC** Infrared and Collinear. 36, 256
- ITS** Inner Tracking System. 68, 69, 74, 93, 143, 256
- JJ** jet-jet. 117, 118, 256
- L0** Level 0 trigger. 72, 86, 256
- L1** Level 1 trigger. 72, 86, 87, 116, 123, 180, 256
- L2** Level 2 trigger. 72, 256
- LEIR** Low-Energy Ion Ring. 66, 256
- LHC** Large Hadron Collider. 11, 15, 16, 20, 21, 22, 28, 29, 30, 35, 46, 47, 48, 49, 51, 56, 65, 66, 67, 72, 73, 79, 82, 89, 96, 97, 152, 153, 154, 158, 164, 256
- LHCb** Large Hadron Collider beauty. 66, 256
- LINAC** Linear Accelerator. 66, 256
- LO** Leading Order. 13, 44, 49, 51, 117, 256
- MB** Minimum Bias. 71, 87, 116, 122, 123, 124, 130, 131, 180, 256
- MC** Monte Carlo. 27, 77, 103, 117, 118, 120, 130, 131, 134, 143, 180, 256
- ME** Mixed event. 122, 256
- MIP** Minimum Ionized Particle. 88, 96, 157, 169, 170, 172, 177, 248, 256
- NBD** negative binomial distribution. 76, 240, 256

NLO Next-to-Leading Order. 44, 51, 52, 53, 55, 56, 148, 149, 150, 176, 256

nPDF nuclear Parton Distribution Function. 23, 51, 53, 256

PA Preamplifier. 157, 170, 256

PAD Silicon Pad. 155, 156, 159, 160, 169, 256

PDF Parton Distribution Function. 16, 17, 18, 22, 23, 49, 51, 52, 53, 56, 148, 154, 256

PHENIX Pioneering High Energy Nuclear Interaction eXperiment. 152, 176, 256

PHOS Photon Spectrometer. 68, 81, 82, 83, 96, 256

PID Particle Identification. 67, 69, 98, 256

PM PhotoMultiplier. 168, 256

pQCD perturbative Quantum Chromodynamics. 15, 16, 37, 47, 51, 52, 53, 55, 148, 149, 150, 176, 256

PS Proton Synchrotron. 66, 168, 169, 170, 172, 256

PSB Proton Synchrotron Booster. 66, 256

QCD Quantum Chromodynamics. 11, 12, 13, 14, 15, 17, 18, 19, 20, 21, 49, 67, 117, 177, 256

QED Quantum Electrodynamics. 11, 13, 14, 78, 256

QFT Quantum Field Theory. 11, 256

QGP Quark-gluon plasma. 19, 20, 21, 22, 28, 29, 30, 31, 34, 36, 37, 40, 41, 43, 44, 45, 46, 47, 48, 51, 55, 56, 58, 60, 64, 65, 148, 150, 155, 177, 256

RHIC Relativistic Heavy-Ion Collider. 20, 28, 34, 39, 46, 47, 51, 61, 62, 64, 152, 153, 256

ROC ReadOut Chip. 160, 166, 256

SDD Silicon Drift Detector. 69, 256

SE Same event. 122, 256

SH Shaper. 157, 170, 256

SM Super Module. 83, 97, 98, 256

SPD Silicon Pixel Detector. 69, 74, 256

SPS Super Proton Synchrotron. 20, 29, 31, 51, 168, 172, 173, 174, 256

SSD Silicon Strip Detector. 69, 74, 256

STAR Solenoidal Tracker at RHIC. 35, 39, 62, 64, 152, 153, 176, 256

T0 TZERO. 68, 256

TOA Time Over Amplitude. 157, 158, 166, 167, 173, 174, 177, 256

TOT Time Over Threshold. 157, 158, 160, 166, 169, 172, 173, 174, 177, 256

TPC Time Projection Chamber. 68, 70, 71, 72, 74, 75, 93, 105, 121, 143, 256

TRU Trigger Readout Unit. 86, 87, 256

UE Underlying event. 99, 100, 101, 104, 105, 107, 120, 121, 122, 123, 124, 127, 128, 130, 135, 136, 150, 219, 256

V0 VZERO. 28, 68, 71, 72, 75, 76, 77, 87, 116, 117, 240, 256

ZDC Zero Degree Calorimeter. 68, 75, 116, 256

ZYAM Zero To Yield At Minimum. 122, 130, 256

Bibliography

- [1] F. Halzen and Alan D. Martin. *QUARKS AND LEPTONS: AN INTRODUCTORY COURSE IN MODERN PARTICLE PHYSICS*. 1984.
- [2] Wikimedia Commons standard model of elementary particles. 2019. https://en.wikipedia.org/wiki/Standard_Model.
- [3] Matthew D. Schwartz. *Quantum Field Theory and the Standard Model*. Cambridge University Press, 3 2014.
- [4] Jeff Greensite. *An introduction to the confinement problem*, volume 821. 2011.
- [5] Michelangelo L Mangano. Introduction to QCD. 2000.
- [6] S. Bethke. Experimental tests of asymptotic freedom. *Progress in Particle and Nuclear Physics*, 58(2):351–386, Apr 2007.
- [7] R. D. Field. *Applications of Perturbative QCD*, volume 77. 1989.
- [8] Mark Thomson. *Modern particle physics*. Cambridge University Press, New York, 2013.
- [9] P. A. Zyla et al. Review of Particle Physics. *PTEP*, 2020(8):083C01, 2020.
- [10] K A Olive. Review of Particle Physics. *Chinese Physics C*, 40(10):100001, 2016.
- [11] Peter Skands. Introduction to QCD. In *Theoretical Advanced Study Institute in Elementary Particle Physics: Searching for New Physics at Small and Large Scales*, pages 341–420, 2013.
- [12] E. Perez and E. Rizvi. The Quark and Gluon Structure of the Proton. *Rept. Prog. Phys.*, 76:046201, 2013.
- [13] V. N. Gribov and L. N. Lipatov. Deep inelastic electron scattering in perturbation theory. *Phys. Lett. B*, 37:78–80, 1971.
- [14] Gavin P. Salam. An Introduction to leading and next-to-leading BFKL. *Acta Phys. Polon. B*, 30:3679–3705, 1999.
- [15] Richard D. Ball et al. The path to proton structure at 1% accuracy. *Eur. Phys. J. C*, 82(5):428, 2022.
- [16] Alfred H. Mueller. A Simple derivation of the JIMWLK equation. *Phys. Lett. B*, 523:243–248, 2001.

- [17] T. Lappi and H. Mäntysaari. Next-to-leading order balitsky-kovchegov equation with resummation. *Phys. Rev. D*, 93:094004, May 2016.
- [18] Javier L. Albacete and Cyrille Marquet. Gluon saturation and initial conditions for relativistic heavy ion collisions. *Prog. Part. Nucl. Phys.*, 76:1–42, 2014.
- [19] Francois Gelis, Edmond Iancu, Jamal Jalilian-Marian, and Raju Venugopalan. The Color Glass Condensate. *Ann. Rev. Nucl. Part. Sci.*, 60:463–489, 2010.
- [20] John C. Collins and M. J. Perry. Superdense Matter: Neutrons Or Asymptotically Free Quarks? *Phys. Rev. Lett.*, 34:1353, 1975.
- [21] F. Karsch and E. Laermann. Thermodynamics and in medium hadron properties from lattice QCD. pages 1–59, 5 2003.
- [22] Gordon Baym, Tetsuo Hatsuda, Toru Kojo, Philip D. Powell, Yifan Song, and Tat-suyuki Takatsuka. From hadrons to quarks in neutron stars: a review. *Rept. Prog. Phys.*, 81(5):056902, 2018.
- [23] Mark G. Alford. Color superconducting quark matter. *Ann. Rev. Nucl. Part. Sci.*, 51:131–160, 2001.
- [24] K. Johnson. The M.I.T. Bag Model. *Acta Phys. Polon. B*, 6:865, 1975.
- [25] Helen Caines. The Search for Critical Behavior and Other Features of the QCD Phase Diagram – Current Status and Future Prospects. *Nucl. Phys. A*, 967:121–128, 2017.
- [26] Y. Aoki, G. Endrodi, Z. Fodor, S. D. Katz, and K. K. Szabo. The Order of the quantum chromodynamics transition predicted by the standard model of particle physics. *Nature*, 443:675–678, 2006.
- [27] C. Spieles, Horst Stoecker, and C. Greiner. Phase transition of a finite quark gluon plasma. *Phys. Rev. C*, 57:908–915, 1998.
- [28] Tanmoy Bhattacharya et al. QCD Phase Transition with Chiral Quarks and Physical Quark Masses. *Phys. Rev. Lett.*, 113(8):082001, 2014.
- [29] Gines Martinez. Advances in Quark Gluon Plasma. 4 2013.
- [30] LHC Machine. *JINST*, 3:S08001, 2008.
- [31] I. B. Issinsky, A. D. Kirillov, A. D. Kovalenko, and P. A. Rukoyatkin. Beams of the Dubna Synchrophasotron and Nuclotron. *Acta Phys. Polon. B*, 25:673–680, 1994.
- [32] A. I. Malakhov. The Main Physical Results at the Dubna Synchrophasotron. In *11th International Workshop on Relativistic Nuclear Physics: from Hundreds of MeV to TeV*, page 6, 2013.
- [33] J. R. Alonso. 30 years at the fore front - a perspective on the Bevatron/Bevalac. In *9th All-union conference on charged particle accelerators*, pages 8–14, 1985.
- [34] Ulrich W. Heinz and Maurice Jacob. Evidence for a new state of matter: An Assessment of the results from the CERN lead beam program. 1 2000.

- [35] C. A. Ogilvie. Review of nuclear reactions at the AGS. *Nucl. Phys. A*, 698:3–12, 2002.
- [36] J. D. Bjorken. Highly Relativistic Nucleus-Nucleus Collisions: The Central Rapidity Region. *Phys. Rev. D*, 27:140–151, 1983.
- [37] Françoise Arleo and Stéphane Peigné. Quenching of light hadron spectra in p - a collisions from fully coherent energy loss. *Phys. Rev. Lett.*, 125:032301, Jul 2020.
- [38] The ALICE experiment – A journey through QCD. 11 2022.
- [39] Charles Gale, Sangyong Jeon, and Bjoern Schenke. Hydrodynamic Modeling of Heavy-Ion Collisions. *Int. J. Mod. Phys. A*, 28:1340011, 2013.
- [40] K. Aamodt et al. Two-pion Bose-Einstein correlations in central Pb-Pb collisions at $\sqrt{s_{NN}} = 2.76$ TeV. *Phys. Lett. B*, 696:328–337, 2011.
- [41] Néstor Armesto. Nuclear shadowing. *Journal of Physics G: Nuclear and Particle Physics*, 32(11):R367–R393, Sep 2006.
- [42] Klaus Rith. Present status of the emc effect, 2014.
- [43] Rabah Abdul Khalek, Rhorry Gauld, Tommaso Giani, Emanuele R. Nocera, Tanguena R. Rabemananjara, and Juan Rojo. nNNPDF3.0: evidence for a modified partonic structure in heavy nuclei. *Eur. Phys. J. C*, 82(6):507, 2022.
- [44] Kari J. Eskola, Petja Paakkinen, Hannu Paukkunen, and Carlos A. Salgado. EPPS16: Nuclear parton distributions with LHC data. *Eur. Phys. J. C*, 77(3):163, 2017.
- [45] P. Duwentäster, L. A. Husová, T. Ježo, M. Klasen, K. Kovařík, A. Kusina, K. F. Muzačka, F. I. Olness, I. Schienbein, and J. Y. Yu. Impact of inclusive hadron production data on nuclear gluon PDFs. *Phys. Rev. D*, 104:094005, 2021.
- [46] Michael L. Miller, Klaus Reygers, Stephen J. Sanders, and Peter Steinberg. Glauber modeling in high energy nuclear collisions. *Ann. Rev. Nucl. Part. Sci.*, 57:205–243, 2007.
- [47] E. Abbas et al. Performance of the ALICE VZERO system. *JINST*, 8:P10016, 2013.
- [48] Anton Andronic, Peter Braun-Munzinger, Krzysztof Redlich, and Johanna Stachel. Decoding the phase structure of QCD via particle production at high energy. *Nature*, 561(7723):321–330, 2018.
- [49] Johann Rafelski and Berndt Müller. Strangeness Production in the Quark - Gluon Plasma. *Phys. Rev. Lett.*, 48:1066, 1982. [Erratum: Phys.Rev.Lett. 56, 2334 (1986)].
- [50] Peter Koch, Berndt Müller, and Johann Rafelski. From Strangeness Enhancement to Quark-Gluon Plasma Discovery. *Int. J. Mod. Phys. A*, 32(31):1730024, 2017.
- [51] F. Antinori et al. Enhancement of hyperon production at central rapidity in 158-A-GeV/c Pb-Pb collisions. *J. Phys. G*, 32:427–442, 2006.
- [52] Betty Bezverkhny Abelev et al. Multi-strange baryon production at mid-rapidity in Pb-Pb collisions at $\sqrt{s_{NN}} = 2.76$ TeV. *Phys. Lett. B*, 728:216–227, 2014. [Erratum: Phys.Lett.B 734, 409–410 (2014)].

- [53] Jaroslav Adam et al. Enhanced production of multi-strange hadrons in high-multiplicity proton-proton collisions. *Nature Phys.*, 13:535–539, 2017.
- [54] C Ahdida et al. Letter of Intent: the NA60+ experiment. Technical report, CERN, Geneva, 2022.
- [55] S. Acharya et al. Anisotropic flow of identified particles in Pb-Pb collisions at $\sqrt{s_{\text{NN}}} = 5.02$ TeV. *JHEP*, 09:006, 2018.
- [56] Denes Molnar and Sergei A. Voloshin. Elliptic flow at large transverse momenta from quark coalescence. *Phys. Rev. Lett.*, 91:092301, 2003.
- [57] Charles Gale, Sangyong Jeon, Björn Schenke, Prithwish Tribedy, and Raju Venugopalan. Event-by-event anisotropic flow in heavy-ion collisions from combined Yang-Mills and viscous fluid dynamics. *Phys. Rev. Lett.*, 110(1):012302, 2013.
- [58] T. Matsui and H. Satz. J/ψ Suppression by Quark-Gluon Plasma Formation. *Phys. Lett. B*, 178:416–422, 1986.
- [59] Albert M Sirunyan et al. Measurement of nuclear modification factors of $\Upsilon(1S)$, $\Upsilon(2S)$, and $\Upsilon(3S)$ mesons in PbPb collisions at $\sqrt{s_{\text{NN}}} = 5.02$ TeV. *Phys. Lett. B*, 790:270–293, 2019.
- [60] Sebastian Sapeta. QCD and Jets at Hadron Colliders. *Prog. Part. Nucl. Phys.*, 89:1–55, 2016. 77 pages, 37 figures; v2: text developments in several places, references added, version published in Prog. Part. Nucl. Phys. 2016.
- [61] Matteo Cacciari, Gavin P. Salam, and Gregory Soyez. FastJet User Manual. *Eur. Phys. J. C*, 72:1896, 2012.
- [62] J. D. Bjorken. Energy Loss of Energetic Partons in Quark - Gluon Plasma: Possible Extinction of High $p(t)$ Jets in Hadron - Hadron Collisions. 8 1982.
- [63] R. Baier, Yuri L. Dokshitzer, Alfred H. Mueller, S. Peigne, and D. Schiff. Radiative energy loss of high-energy quarks and gluons in a finite volume quark - gluon plasma. *Nucl. Phys. B*, 483:291–320, 1997.
- [64] B. G. Zakharov. Radiative energy loss of high-energy quarks in finite size nuclear matter and quark - gluon plasma. *JETP Lett.*, 65:615–620, 1997.
- [65] S. Acharya et al. Transverse momentum spectra and nuclear modification factors of charged particles in pp, p-Pb and Pb-Pb collisions at the LHC. *JHEP*, 11:013, 2018.
- [66] John Adams et al. Experimental and theoretical challenges in the search for the quark gluon plasma: The STAR Collaboration’s critical assessment of the evidence from RHIC collisions. *Nucl. Phys. A*, 757:102–183, 2005.
- [67] J. Adams et al. Evidence from d + Au measurements for final state suppression of high $p(T)$ hadrons in Au+Au collisions at RHIC. *Phys. Rev. Lett.*, 91:072304, 2003.
- [68] Serguei Chatrchyan et al. Observation and studies of jet quenching in PbPb collisions at nucleon-nucleon center-of-mass energy = 2.76 TeV. *Phys. Rev. C*, 84:024906, 2011.

- [69] Georges Aad et al. Measurements of the suppression and correlations of dijets in Pb+Pb collisions at $s_{NN}=5.02$ TeV. *Phys. Rev. C*, 107(5):054908, 2023.
- [70] Morad Aaboud et al. Measurement of jet fragmentation in Pb+Pb and pp collisions at $\sqrt{s_{NN}} = 5.02$ TeV with the ATLAS detector. *Phys. Rev. C*, 98(2):024908, 2018.
- [71] Leticia Cunqueiro and Anne M. Sickles. Studying the QGP with Jets at the LHC and RHIC. *Prog. Part. Nucl. Phys.*, 124:103940, 2022.
- [72] Albert M Sirunyan et al. In-medium modification of dijets in PbPb collisions at $\sqrt{s_{NN}} = 5.02$ TeV. *JHEP*, 05:116, 2021.
- [73] John W. Harris and Berndt Müller. "QGP Signatures" Revisited. 8 2023.
- [74] Gabor David. Direct real photons in relativistic heavy ion collisions. *Rept. Prog. Phys.*, 83(4):046301, 2020.
- [75] Raphaelle Ichou and David d'Enterria. Sensitivity of isolated photon production at TeV hadron colliders to the gluon distribution in the proton. *Phys. Rev. D*, 82:014015, 2010.
- [76] Shreyasi Acharya et al. Measurement of the inclusive isolated photon production cross section in pp collisions at $\sqrt{s} = 7$ TeV. *Eur. Phys. J. C*, 79(11):896, 2019.
- [77] K. Adcox et al. Formation of dense partonic matter in relativistic nucleus-nucleus collisions at RHIC: Experimental evaluation by the PHENIX collaboration. *Nucl. Phys. A*, 757:184–283, 2005.
- [78] Klaus Reygers. High-p(T) direct-photon results from PHENIX. *Acta Phys. Polon. B*, 37:727–732, 2006.
- [79] Shreyasi Acharya et al. Neutral pion and η meson production at mid-rapidity in Pb-Pb collisions at $\sqrt{s_{NN}} = 2.76$ TeV. *Phys. Rev. C*, 98(4):044901, 2018.
- [80] Jaroslav Adam et al. Direct photon production in Pb-Pb collisions at $\sqrt{s_{NN}} = 2.76$ TeV. *Phys. Lett. B*, 754:235–248, 2016.
- [81] Charles Gale. Photon Production in Hot and Dense Strongly Interacting Matter. *Landolt-Bornstein*, 23:445, 2010.
- [82] S. Catani, M. Fontannaz, J. P. Guillet, and E. Pilon. Cross-section of isolated prompt photons in hadron hadron collisions. *JHEP*, 05:028, 2002.
- [83] David d'Enterria and Juan Rojo. Quantitative constraints on the gluon distribution function in the proton from collider isolated-photon data. *Nucl. Phys. B*, 860:311–338, 2012.
- [84] M. McLaughlin, J. Biel, C. Bromberg, B. Brown, C. Chandlee, S. Cihangir, S. R. W. Cooper, T. Ferbel, D. Garelick, G. Glass, M. Glaubman, S. R. Han, K. Heller, S. Hosseini, J. Huston, A. Jonckheere, J. LeBritton, R. A. Lewis, F. Lobkowicz, M. Marshak, C. A. Nelson, E. Peterson, E. Pothier, J. Povlis, K. Ruddick, M. Shupe, P. Slattery, and G. A. Smith. Inclusive production of direct photons in 200-gev/c collisions. *Phys. Rev. Lett.*, 51:971–974, Sep 1983.

- [85] Shreyasi Acharya et al. Measurement of the inclusive isolated-photon production cross section in pp collisions at $\sqrt{s} = 13$ TeV. 7 2024.
- [86] Albert M Sirunyan et al. Measurement of differential cross sections for inclusive isolated-photon and photon+jets production in proton-proton collisions at $\sqrt{s} = 13$ TeV. *Eur. Phys. J. C*, 79(1):20, 2019.
- [87] Morad Aaboud et al. Measurement of the cross section for inclusive isolated-photon production in pp collisions at $\sqrt{s} = 13$ TeV using the ATLAS detector. *Phys. Lett. B*, 770:473–493, 2017.
- [88] Georges Aad et al. Measurement of the inclusive isolated-photon cross section in pp collisions at $\sqrt{s} = 13$ TeV using 36 fb^{-1} of ATLAS data. *JHEP*, 10:203, 2019.
- [89] Francois Arleo, Stanley J. Brodsky, Dae Sung Hwang, and Anne M. Sickles. Higher-Twist Dynamics in Large Transverse Momentum Hadron Production. *Phys. Rev. Lett.*, 105:062002, 2010.
- [90] Georges Aad et al. Inclusive-photon production and its dependence on photon isolation in pp collisions at $\sqrt{s} = 13$ TeV using 139 fb^{-1} of ATLAS data. *JHEP*, 07:086, 2023.
- [91] Florian Jonas. *Probing the initial state of heavy-ion collisions with isolated prompt photons*. PhD thesis, LBL, Berkeley, 5 2023.
- [92] Morad Aaboud et al. Measurement of prompt photon production in $\sqrt{s_{NN}} = 8.16$ TeV $p+\text{Pb}$ collisions with ATLAS. *Phys. Lett. B*, 796:230–252, 2019.
- [93] Shreyasi Acharya et al. Measurement of the inclusive isolated-photon production cross section in pp and pb—pb collisions at $\sqrt{s_{NN}}=5.02$ tev. *xxx*, 2024.
- [94] Patrick Aurenche, Michel Fontannaz, Jean-Philippe Guillet, Eric Pilon, and Monique Werlen. A New critical study of photon production in hadronic collisions. *Phys. Rev. D*, 73:094007, 2006.
- [95] L. Bourhis, M. Fontannaz, and J. P. Guillet. Quarks and gluon fragmentation functions into photons. *Eur. Phys. J. C*, 2:529–537, 1998.
- [96] Xuan Chen, Thomas Gehrmann, Nigel Glover, Marius Höfer, and Alexander Huss. Isolated photon and photon+jet production at NNLO QCD accuracy. *JHEP*, 04:166, 2020.
- [97] Shreyasi Acharya et al. Production of charged pions, kaons, and (anti-)protons in Pb-Pb and inelastic pp collisions at $\sqrt{s_{NN}} = 5.02$ TeV. *Phys. Rev. C*, 101(4):044907, 2020.
- [98] Albert M Sirunyan et al. Constraints on the Initial State of Pb-Pb Collisions via Measurements of Z -Boson Yields and Azimuthal Anisotropy at $\sqrt{s_{NN}}=5.02$ TeV. *Phys. Rev. Lett.*, 127(10):102002, 2021.
- [99] Constantin Loizides and Andreas Morsch. Absence of jet quenching in peripheral nucleus–nucleus collisions. *Phys. Lett. B*, 773:408–411, 2017.

Bibliography

- [100] Georges Aad et al. Comparison of inclusive and photon-tagged jet suppression in 5.02 TeV Pb+Pb collisions with ATLAS. *Phys. Lett. B*, 846:138154, 2023.
- [101] Albert M Sirunyan et al. Study of jet quenching with isolated-photon+jet correlations in PbPb and pp collisions at $\sqrt{s_{NN}} = 5.02$ TeV. *Phys. Lett. B*, 785:14–39, 2018.
- [102] Albert M Sirunyan et al. Observation of Medium-Induced Modifications of Jet Fragmentation in Pb-Pb Collisions at $\sqrt{s_{NN}} = 5.02$ TeV Using Isolated Photon-Tagged Jets. *Phys. Rev. Lett.*, 121(24):242301, 2018.
- [103] Aram Hayrapetyan et al. Overview of high-density QCD studies with the CMS experiment at the LHC. 5 2024.
- [104] Xin-Nian Wang, Zheng Huang, and Ina Sarcevic. Jet quenching in the opposite direction of a tagged photon in high-energy heavy ion collisions. *Phys. Rev. Lett.*, 77:231–234, 1996.
- [105] Jorge Casalderrey-Solana, Doga Can Gulhan, José Guilherme Milhano, Daniel Pablos, and Krishna Rajagopal. Predictions for Boson-Jet Observables and Fragmentation Function Ratios from a Hybrid Strong/Weak Coupling Model for Jet Quenching. *JHEP*, 03:053, 2016.
- [106] Albert M Sirunyan et al. Using Z Boson Events to Study Parton-Medium Interactions in Pb-Pb Collisions. *Phys. Rev. Lett.*, 128(12):122301, 2022.
- [107] Albert M Sirunyan et al. Jet Shapes of Isolated Photon-Tagged Jets in Pb-Pb and pp Collisions at $\sqrt{s_{NN}} = 5.02$ TeV. *Phys. Rev. Lett.*, 122(15):152001, 2019.
- [108] Aram Hayrapetyan et al. Girth and groomed radius of jets recoiling against isolated photons in lead-lead and proton-proton collisions at $\sqrt{s_{NN}} = 5.02$ TeV. 5 2024.
- [109] A. Adare et al. Photon-Hadron Jet Correlations in p+p and Au+Au Collisions at $s^{**}(1/2) = 200$ -GeV. *Phys. Rev. C*, 80:024908, 2009.
- [110] Shreyasi Acharya et al. Measurement of isolated photon-hadron correlations in $\sqrt{s_{NN}} = 5.02$ TeV pp and p-Pb collisions. *Phys. Rev. C*, 102(4):044908, 2020.
- [111] L. Adamczyk et al. Jet-like Correlations with Direct-Photon and Neutral-Pion Triggers at $\sqrt{s_{NN}} = 200$ GeV. *Phys. Lett. B*, 760:689–696, 2016.
- [112] The ALICE experiment at the CERN LHC. *Journal of Instrumentation*, 3(08):S08002–S08002, aug 2008.
- [113] Lyndon Evans and Philip Bryant. LHC machine. *Journal of Instrumentation*, 3(08):S08001–S08001, aug 2008.
- [114] J. Vollaire et al. *Linac4 design report*, volume 6/2020 of *CERN Yellow Reports: Monographs*. CERN, Geneva, 9 2020.
- [115] The Proton Synchrotron Booster. 2012.
- [116] The CERN proton synchrotron. 1 1962.

- [117] Ewa Lopienska. The CERN accelerator complex, layout in 2022. Complex des accélérateurs du CERN en janvier 2022. 2022. General Photo.
- [118] A. Airapetian et al. ATLAS: Detector and physics performance technical design report. Volume 1. 5 1999.
- [119] G. L. Bayatian et al. CMS Physics: Technical Design Report Volume 1: Detector Performance and Software. 2006.
- [120] LHCb technical design report: Reoptimized detector design and performance. 9 2003.
- [121] G. Dellacasa et al. ALICE technical design report of the inner tracking system (ITS). 6 1999.
- [122] K Aamodt et al. Alignment of the ALICE Inner Tracking System with cosmic-ray tracks. *JINST*, 5:P03003, 2010.
- [123] Christian Lippmann. Upgrade of the ALICE Time Projection Chamber. 3 2014.
- [124] K. Bos et al. *LHC computing Grid: Technical Design Report. Version 1.06 (20 Jun 2005)*. Technical design report. LCG. CERN, Geneva, 2005.
- [125] World Wide LHC Computer Grid. url = <https://wlcg-public.web.cern.ch>.
- [126] S. Bagnasco, L. Betev, P. Buncic, F. Carminati, C. Cirstoiu, C. Grigoras, A. Hayrapetyan, A. Harutyunyan, A. J. Peters, and Pablo Saiz. AliEn: ALICE Environment on the GRID. *J. Phys. Conf. Ser.*, 119:062012, 2008.
- [127] ALICE technical design report of the computing. 6 2005.
- [128] R Brun, F Bruyant, M Maire, A C McPherson, and P Zanarini. *GEANT 3: user's guide Geant 3.10, Geant 3.11; rev. version*. CERN, Geneva, 1987.
- [129] S. Agostinelli et al. GEANT4—a simulation toolkit. *Nucl. Instrum. Meth. A*, 506:250–303, 2003.
- [130] Alfredo Ferrari, Paola R. Sala, Alberto Fasso, and Johannes Ranft. FLUKA: A multi-particle transport code (Program version 2005). 10 2005.
- [131] R. Fruhwirth. Application of Kalman filtering to track and vertex fitting. *Nucl. Instrum. Meth. A*, 262:444–450, 1987.
- [132] Betty Bezverkhny Abelev et al. Performance of the ALICE Experiment at the CERN LHC. *Int. J. Mod. Phys. A*, 29:1430044, 2014.
- [133] Centrality determination in heavy ion collisions. 2018.
- [134] Lucio Cerrito. *Electromagnetic and Hadronic Showers: Calorimeters*, pages 171–185. Springer International Publishing, 2017.
- [135] Shreyasi Acharya et al. Performance of the ALICE Electromagnetic Calorimeter. *JINST*, 18(08):P08007, 2023.
- [136] Christian Fabjan and D. Fournier. *Calorimetry*, pages 201–280. 09 2020.

- [137] Erwann Masson. *Mesure de la production de photons isolés dans les collisions proton-proton et proton-plomb au LHC avec l'expérience ALICE*. PhD thesis, SUBATECH, Nantes, 2019.
- [138] M. Tanabashi et al. Review of Particle Physics. *Phys. Rev. D*, 98(3):030001, 2018.
- [139] C. W. Fabjan and F. Gianotti. Calorimetry for particle physics. *Rev. Mod. Phys.*, 75:1243–1286, 2003.
- [140] P. Cortese et al. ALICE electromagnetic calorimeter technical design report. 9 2008.
- [141] O. Bourrion, N. Arbor, G. Conesa-Balbastre, C. Furget, R. Guernane, and G. Marcotte. The ALICE EMCal L1 trigger first year of operation experience. *JINST*, 8:C01013, 2013.
- [142] Gustavo Conesa Balbastre. *Study of the strong interaction with high-energy photons at the LHC: Experience with the ALICE-EMCal detector operation and measurements*. Habilitation à diriger des recherches, UGA (Université Grenoble Alpes), October 2019.
- [143] T. C. Awes, F. E. Obenshain, F. Plasil, S. Saini, S. P. Sorensen, and G. R. Young. A Simple method of shower localization and identification in laterally segmented calorimeters. *Nucl. Instrum. Meth. A*, 311:130–138, 1992.
- [144] W. Bialas and D. A. Petyt. Mitigation of anomalous APD signals in the CMS ECAL. *JINST*, 8:C03020, 2013.
- [145] Measurement of isolated photon cross section and rppb in 5 tev pp and p-pb. <https://alice-notes.web.cern.ch/node/1072>. Accessed: 2024-06-25.
- [146] Measurement of isolated photon production in pp at $\sqrt{s_{\text{NN}}} = 8$ tev with the alice detector at lhc. <https://alice-notes.web.cern.ch/node/1254>. Accessed: 2024-06-25.
- [147] Measurement of isolated photon production in pp and ppb collisions at $\sqrt{s_{\text{NN}}} = 8$ tev and $\sqrt{s_{\text{NN}}} = 8.16$ tev. <https://alice-notes.web.cern.ch/node/1298>. Accessed: 2024-06-25.
- [148] Shreyasi Acharya et al. Public note on: Measurement of the inclusive isolated-photon production cross section in pp and pb—pb collisions at $\sqrt{s_{\text{NN}}}=5.02$ tev. *xxx*, 2024.
- [149] Measurement of isolated photon-jet correlations in 5.02 tev pb-pb collisions. <https://alice-notes.web.cern.ch/node/1281>. Accessed: 2024-06-25.
- [150] Christian Bierlich et al. A comprehensive guide to the physics and usage of PYTHIA 8.3. *SciPost Phys. Codeb.*, 2022:8, 2022.
- [151] Bo Andersson, G. Gustafson, and B. Soderberg. A General Model for Jet Fragmentation. *Z. Phys. C*, 20:317, 1983.
- [152] Albert M Sirunyan et al. The production of isolated photons in PbPb and pp collisions at $\sqrt{s_{\text{NN}}} = 5.02$ TeV. *JHEP*, 07:116, 2020.

- [153] Thomas A. Trainor. Zero yield at minimum (zyam) method and v_2 : Underestimating jet yields from dihadron azimuth correlations. *Phys. Rev. C*, 81:014905, Jan 2010.
- [154] Shreyasi Acharya et al. Measurements of jet quenching using semi-inclusive hadron+jet distributions in pp and central Pb-Pb collisions at $s_{NN}=5.02$ TeV. *Phys. Rev. C*, 110(1):014906, 2024.
- [155] Man Xie, Xin-Nian Wang, and Han-Zhong Zhang. γ -hadron spectra in $p + \text{Pb}$ collisions at $\sqrt{s_{NN}} = 5.02$ tev. *Phys. Rev. C*, 103:034911, Mar 2021.
- [156] Hanzhong Zhang, J. F. Owens, Enke Wang, and Xin-Nian Wang. Tomography of high-energy nuclear collisions with photon-hadron correlations. *Phys. Rev. Lett.*, 103:032302, Jul 2009.
- [157] Wei Chen, Shanshan Cao, Tan Luo, Long-Gang Pang, and Xin-Nian Wang. Effects of jet-induced medium excitation in γ -hadron correlation in A+A collisions. *Phys. Lett. B*, 777:86–90, 2018.
- [158] Tie-Jiun Hou et al. New CTEQ global analysis of quantum chromodynamics with high-precision data from the LHC. *Phys. Rev. D*, 103(1):014013, 2021.
- [159] Bernd A. Kniehl, G. Kramer, and B. Potter. Fragmentation functions for pions, kaons, and protons at next-to-leading order. *Nucl. Phys. B*, 582:514–536, 2000.
- [160] Wei-tian Deng and Xin-Nian Wang. Multiple Parton Scattering in Nuclei: Modified DGLAP Evolution for Fragmentation Functions. *Phys. Rev. C*, 81:024902, 2010.
- [161] Man Xie, Weiyao Ke, Hanzhong Zhang, and Xin-Nian Wang. Global constraint on the jet transport coefficient from single-hadron, dihadron, and γ -hadron spectra in high-energy heavy-ion collisions. *Phys. Rev. C*, 109(6):064917, 2024.
- [162] Xin-Nian Wang. Why the observed jet quenching at RHIC is due to parton energy loss. *Phys. Lett. B*, 579:299–308, 2004.
- [163] A. Adare et al. Medium modification of jet fragmentation in Au + Au collisions at $\sqrt{s_{NN}} = 200$ GeV measured in direct photon-hadron correlations. *Phys. Rev. Lett.*, 111(3):032301, 2013.
- [164] K. J. Eskola, H. Honkanen, V. J. Kolhinen, and C. A. Salgado. Constraints for nuclear gluon shadowing from DIS data. *Phys. Lett. B*, 532:222–230, 2002.
- [165] CERN ALICE Collaboration. Letter of Intent: A Forward Calorimeter (FoCal) in the ALICE experiment. Technical report, CERN, Geneva, 2020.
- [166] Technical Design Report of the ALICE Forward Calorimeter (FoCal). Technical report, CERN, Geneva, 2024.
- [167] M. Mager. Alpide, the monolithic active pixel sensor for the alice its upgrade. *Nuclear Instruments and Methods in Physics Research Section A: Accelerators, Spectrometers, Detectors and Associated Equipment*, 824:434–438, 2016. Frontier Detectors for Frontier Physics: Proceedings of the 13th Pisa Meeting on Advanced Detectors.

- [168] O. Bourrion, D. Tourres, R. Guernane, C. Arata, J. L. Bouly, and N. Ponchant. Prototype electronics for the silicon pad layers of the future Forward Calorimeter (FoCal) of the ALICE experiment at the LHC. 2 2023.
- [169] M. Inaba. FoCal pad prototype and its test results. *JINST*, 15(12):C12003, 2020.
- [170] The Phase-2 Upgrade of the CMS Endcap Calorimeter. Technical report, CERN, Geneva, 2017.
- [171] D. Thienpont and C. de La Taille. Performance study of HGCROC-v2: the front-end electronics for the CMS high granularity calorimeter. *Journal of Instrumentation*, 15(04):C04055–C04055, apr 2020.
- [172] Damien Thienpont and Christophe de La Taille. Performance study of hgcroc-v2: the front-end electronics for the cms high granularity calorimeter. *Journal of Instrumentation*, 15:C04055–C04055, 04 2020.
- [173] M. Barros Marin, S. Baron, S.S. Feger, P. Leitao, E.S. Lupu, C. Soos, P. Vichoudis, and K. Wyllie. The GBT-FPGA core: features and challenges. *Journal of Instrumentation*, 10(03):C03021–C03021, mar 2015.
- [174] O. Bourrion, J. Bouvier, F. Costa, E. Dávid, J. Imrek, T.M. Nguyen, and S. Mukherjee. Versatile firmware for the common readout unit (CRU) of the ALICE experiment at the LHC. *Journal of Instrumentation*, 16(05):P05019, may 2021.
- [175] CMS Omega. "<https://readthedocs.web.cern.ch/display/HGCELE/Characterisation>".
- [176] The proton synchrotron. "<https://home.cern/science/accelerators/proton-synchrotron>". Accessed: 2024-07-03.
- [177] The super proton synchrotron. "<https://home.cern/science/accelerators/super-proton-synchrotron>". Accessed: 2024-07-03.
- [178] Max Philip Rauch. Latest Results from ALICE FoCal Prototypes. *PoS*, ICHEP2022:317, 11 2022.
- [179] M. Aehle et al. Performance of the electromagnetic and hadronic prototype segments of the ALICE Forward Calorimeter. 11 2023.
- [180] P. Buncic, M. Krzewicki, and P. Vande Vyvre. Technical Design Report for the Upgrade of the Online-Offline Computing System. 4 2015.